

Dynamical systems, PDEs and networks for biomedical applications: Mathematical modeling, analysis and simulations

Edited by

André H. Erhardt, Krasimira Tsaneva-Atanasova, Glenn Terje Lines and Erik Andreas Martens

Published in

Frontiers in Physics
Frontiers in Applied Mathematics and Statistics
Frontiers in Physiology



FRONTIERS EBOOK COPYRIGHT STATEMENT

The copyright in the text of individual articles in this ebook is the property of their respective authors or their respective institutions or funders. The copyright in graphics and images within each article may be subject to copyright of other parties. In both cases this is subject to a license granted to Frontiers.

The compilation of articles constituting this ebook is the property of Frontiers.

Each article within this ebook, and the ebook itself, are published under the most recent version of the Creative Commons CC-BY licence. The version current at the date of publication of this ebook is CC-BY 4.0. If the CC-BY licence is updated, the licence granted by Frontiers is automatically updated to the new version.

When exercising any right under the CC-BY licence, Frontiers must be attributed as the original publisher of the article or ebook, as applicable.

Authors have the responsibility of ensuring that any graphics or other materials which are the property of others may be included in the CC-BY licence, but this should be checked before relying on the CC-BY licence to reproduce those materials. Any copyright notices relating to those materials must be complied with.

Copyright and source acknowledgement notices may not be removed and must be displayed in any copy, derivative work or partial copy which includes the elements in question.

All copyright, and all rights therein, are protected by national and international copyright laws. The above represents a summary only. For further information please read Frontiers' Conditions for Website Use and Copyright Statement, and the applicable CC-BY licence.

ISSN 1664-8714
ISBN 978-2-8325-1458-0
DOI 10.3389/978-2-8325-1458-0

About Frontiers

Frontiers is more than just an open access publisher of scholarly articles: it is a pioneering approach to the world of academia, radically improving the way scholarly research is managed. The grand vision of Frontiers is a world where all people have an equal opportunity to seek, share and generate knowledge. Frontiers provides immediate and permanent online open access to all its publications, but this alone is not enough to realize our grand goals.

Frontiers journal series

The Frontiers journal series is a multi-tier and interdisciplinary set of open-access, online journals, promising a paradigm shift from the current review, selection and dissemination processes in academic publishing. All Frontiers journals are driven by researchers for researchers; therefore, they constitute a service to the scholarly community. At the same time, the *Frontiers journal series* operates on a revolutionary invention, the tiered publishing system, initially addressing specific communities of scholars, and gradually climbing up to broader public understanding, thus serving the interests of the lay society, too.

Dedication to quality

Each Frontiers article is a landmark of the highest quality, thanks to genuinely collaborative interactions between authors and review editors, who include some of the world's best academicians. Research must be certified by peers before entering a stream of knowledge that may eventually reach the public - and shape society; therefore, Frontiers only applies the most rigorous and unbiased reviews. Frontiers revolutionizes research publishing by freely delivering the most outstanding research, evaluated with no bias from both the academic and social point of view. By applying the most advanced information technologies, Frontiers is catapulting scholarly publishing into a new generation.

What are Frontiers Research Topics?

Frontiers Research Topics are very popular trademarks of the *Frontiers journals series*: they are collections of at least ten articles, all centered on a particular subject. With their unique mix of varied contributions from Original Research to Review Articles, Frontiers Research Topics unify the most influential researchers, the latest key findings and historical advances in a hot research area.

Find out more on how to host your own Frontiers Research Topic or contribute to one as an author by contacting the Frontiers editorial office: frontiersin.org/about/contact

Dynamical systems, PDEs and networks for biomedical applications: Mathematical modeling, analysis and simulations

Topic editors

André H. Erhardt — Weierstrass Institute for Applied Analysis and Stochastics (LG), Germany

Krasimira Tsaneva-Atanasova — University of Exeter, United Kingdom

Glenn Terje Lines — Simula Research Laboratory, Norway

Erik Andreas Martens — Lund University, Sweden

Citation

Erhardt, A. H., Tsaneva-Atanasova, K., Lines, G. T., Martens, E. A., eds. (2023).

Dynamical systems, PDEs and networks for biomedical applications: Mathematical modeling, analysis and simulations. Lausanne: Frontiers Media SA.

doi: 10.3389/978-2-8325-1458-0

Table of contents

- 05 **Editorial: Dynamical systems, PDEs and networks for biomedical applications: Mathematical modeling, analysis and simulations**
André H. Erhardt, Krasimira Tsaneva-Atanasova, Glenn Terje Lines and Erik Andreas Martens
- 08 **Deriving the Bidomain Model of Cardiac Electrophysiology From a Cell-Based Model; Properties and Comparisons**
Karoline Horgmo Jæger and Aslak Tveito
- 21 **An *In Silico* Study of Electrophysiological Parameters That Affect the Spiral-Wave Frequency in Mathematical Models for Cardiac Tissue**
Mahesh Kumar Mulimani, Soling Zimik and Rahul Pandit
- 32 **Effective Spatio-Temporal Regimes for Wound Treatment by Way of Macrophage Polarization: A Mathematical Model**
Ksenia Zlobina, Jiahao Xue and Marcella Gomez
- 43 **Multiscale and Multiphysics Modeling of Anisotropic Cardiac RFCA: Experimental-Based Model Calibration via Multi-Point Temperature Measurements**
Leonardo Molinari, Martina Zaltieri, Carlo Massaroni, Simonetta Filippi, Alessio Gizzi and Emiliano Schena
- 58 **Geometrically Reduced Modelling of Pulsatile Flow in Perivascular Networks**
Cécile Daversin-Catty, Ingeborg G. Gjerde and Marie E. Rognes
- 73 **Two Domains of Meandering Spiral Waves in a Modified Barkley Model**
Vladimir Zykov and Eberhard Bodenschatz
- 79 **A Scalar Poincaré Map for Anti-phase Bursting in Coupled Inhibitory Neurons With Synaptic Depression**
Mark Olenik and Conor Houghton
- 94 **Corrigendum: A scalar poincaré map for anti-phase bursting in coupled inhibitory neurons with synaptic depression**
Mark Olenik and Conor Houghton
- 97 **Transmissibility in Interactive Nanocomposite Diffusion: The Nonlinear Double-Diffusion Model**
Amit K. Chattopadhyay, Bidisha Kundu, Sujit Kumar Nath and Elias C. Aifantis
- 105 **Resource-Efficient Use of Modern Processor Architectures For Numerically Solving Cardiac Ionic Cell Models**
Kristian Gregorius Hustad and Xing Cai
- 121 **Novel Global Asymptotic Stability and Dissipativity Criteria of BAM Neural Networks With Delays**
Mei Liu, Haijun Jiang, Cheng Hu, Binglong Lu and Zhanfeng Li

- 130 **Optimal Resonances in Multiplex Neural Networks Driven by an STDP Learning Rule**
Marius E. Yamakou, Tat Dat Tran and Jürgen Jost
- 144 **Hydrogen-bond networks for proton couplings in G-Protein coupled receptors**
Ana-Nicoleta Bondar and Mercedes Alfonso-Prieto
- 152 **Computer-assisted modeling of Quorum sensing in bacterial population exposed to antibiotics**
Christina Kuttler and Anna Maslovskaya
- 165 **Fourier filter-based physics- information convolutional recurrent network for 2D incompressible flow**
Chaohao Xiao, Xiaoqian Zhu, Fukang Yin, Xiaoqun Cao, Kecheng Peng and Jun Nie
- 179 **Complex network measures reveal optimal targets for deep brain stimulation and identify clusters of collective brain dynamics**
Konstantinos Spiliotis, Konstantin Butenko, Ursula van Rienen, Jens Starke and Rüdiger Köhling
- 198 **Fluid-structure interaction study of bio-magnetic fluid in a wavy bifurcated channel with elastic walls**
Hasan Shahzad, Xinhua Wang, Zehba Raizah, Arshad Riaz, Afraz Hussain Majeed, Muhammad Adnan Anwar and Sayed M. Eldin



OPEN ACCESS

EDITED BY

Marcel Filoche,
École Supérieure de Physique et de Chimie
Industrielles de la Ville de Paris, France

REVIEWED BY

Alfonso Bueno-Orovio,
University of Oxford, United Kingdom

*CORRESPONDENCE

André H. Erhardt,
✉ andre.erhardt@wias-berlin.de

SPECIALTY SECTION

This article was submitted to Statistical and
Computational Physics,
a section of the journal
Frontiers in Physics

RECEIVED 18 November 2022

ACCEPTED 30 December 2022

PUBLISHED 12 January 2023

CITATION

Erhardt AH, Tsaneva-Atanasova K,
Lines GT and Martens EA (2023), Editorial:
Dynamical systems, PDEs and networks for
biomedical applications: Mathematical
modeling, analysis and simulations.
Front. Phys. 10:1101756.
doi: 10.3389/fphy.2022.1101756

COPYRIGHT

© 2023 Erhardt, Tsaneva-Atanasova, Lines
and Martens. This is an open-access article
distributed under the terms of the [Creative
Commons Attribution License \(CC BY\)](#).
The use, distribution or reproduction in
other forums is permitted, provided the
original author(s) and the copyright
owner(s) are credited and that the original
publication in this journal is cited, in
accordance with accepted academic
practice. No use, distribution or
reproduction is permitted which does not
comply with these terms.

Editorial: Dynamical systems, PDEs and networks for biomedical applications: Mathematical modeling, analysis and simulations

André H. Erhardt^{1*}, Krasimira Tsaneva-Atanasova^{2,3,4,5},
Glenn Terje Lines⁶ and Erik Andreas Martens^{7,8}

¹Weierstrass Institute for Applied Analysis and Stochastics, Berlin, Germany, ²Department of Mathematics and Statistics and Living Systems Institute, University of Exeter, Exeter, United Kingdom, ³EPSRC Hub for Quantitative Modelling in Healthcare, University of Exeter, Exeter, United Kingdom, ⁴The Alan Turing Institute, British Library, London, United Kingdom, ⁵Institute for Advanced Study, Technical University of Munich, Garching, Germany, ⁶Simula Research Laboratory, Department of Computational Physiology, Oslo, Norway, ⁷Centre for Mathematical Sciences, Lund University, Lund, Sweden, ⁸Center for Translational Neurosciences, University of Copenhagen, Copenhagen, Denmark

KEYWORDS

mathematical and computational modeling, biomedical applications, applied analysis, complex dynamic processes, computational medicine, differential equations, network

Editorial on the Research Topic

[Dynamical systems, PDEs and networks for biomedical applications:
Mathematical modeling, analysis and simulations](#)

In recent decades, mathematics for healthcare [1] and quantitative biomedicine have become increasingly important. This research area includes various aspects such as modeling, analysis and simulation of numerous highly relevant processes in clinical practice and combines different scientific disciplines like biology, bioengineering, physics, mathematics and medicine. Important biomedical applications are for instance cellular, biochemical and biomolecular processes, tumour growth, electrophysiology of the heart or the brain, tissue regeneration and biomedical engineering. In this line of research, mathematical and computational modeling, *cf. e.g.* [2–4], have become essential components in interdisciplinary and multidisciplinary research projects and contributes significantly to a better understanding of real-world phenomena. The great importance of this research field also results in the establishment of numerous research centres and research groups in the field of mathematics for healthcare and quantitative biomedicine.

New interdisciplinary research fields like computational cardiology [5], computational neurosciences [6] and computational oncology [7] arise and can be used to develop new therapies and help in improving clinical decision [8–12]. There are plenty of important examples of mathematical and numerical approaches which are applied to drug (safety) testing or drug development, the analysis and simulation of complex dynamics in the heart or the brain such as cardiac arrhythmias [13] or seizures [14], and are becoming more and more relevant these days. Computer modeling of complex dynamic processes like wound and bone healing [15] gives new insights into how such complex biological processes work and helps to make better predictions.

The origins for these developments lie in the great opportunities for developing not only complex (and detailed) models that can be tested against experimental data, which is becoming available in increasing amount and quality, but also computational methods to solve these models. Together, this opens new challenges and prospects for a systematical investigation of both biological and mathematical issues from life science. Thus, this Research Topic is focused on advanced methods

in mathematical and computational modeling of biomedical phenomena using (experimental) data, their analysis and numerical simulations that contribute to a significantly improved comprehension of these phenomena. The main focus of this Research Topic is three-fold: 1) modeling approaches using differential equations or networks describing the behavior of single cells, cell groups, tissue or organs. 2) The analysis of the dynamics and behavior of certain biomedical models improving the state-of-art understanding of certain phenomena like cardiovascular and neurological diseases and disorders. 3) Improved numerical methods to simulate and analyze complex biomedical models.

In computational cardiology, the electrophysiological behavior of cardiac tissue is usually modelled either by the monodomain or bidomain models, which mathematically represent coupled systems of partial and ordinary differential equations, and give insights into the conduction properties of the electrochemical wave traversing the cardiac muscle. The bidomain model is considered to be the gold standard for numerical simulations and the monodomain model is a special case assuming equal anisotropy rates. Jæger et al. studied and compared the bidomain model, which represents the average over a large number of cardiomyocytes, and the EMI model, which is considered to be more accurate since it includes explicitly the extracellular space (E), the cell membrane (M) and the intracellular space (I). The authors showed the limitation of the bidomain model and that it can be derived directly from the cell-based EMI model as well as their similarities. Both models provide remarkably similar results when the parameters of importance for the conduction velocity lie in the normal range. The authors concluded that the bidomain model represents normal cardiac conduction very well if the scale of interest contains many cells, but cannot be used to study conduction in the vicinity of individual cells. Therefore, depending on the biomedical application one has three accurate models of different complexity and different numerical efforts. In this line of research, Mulimani et al. and Zykov et al. studied different types of spiral waves occurring in monodomain models. Monodomain models have been proved to be good approximations of cardiac tissue for wave propagation. Mulimani et al. focused their investigations on the effects of cellular parameters on the properties of the action potential of a myocyte. For instance, this study provides an understanding of how changes in the action potential at single-cell level can be related to changes in spiral-wave frequency at tissue level, which may also result in life-threatening cardiac arrhythmias. Furthermore, Zykov et al. investigated spiral wave instability in a modified Barkley model and showed the existence of two quite different parameter regions of this instability. The first region can be linked to the presence of a Hopf bifurcation and is a well known scenario, while the second region cannot be explained by a Hopf bifurcation and a hysteresis phenomenon was detected on its boundary. Besides the efficient modelling of a certain problem, the development of advanced numerical algorithms are important. Xiao et al. introduced a Fourier filter-based physics-informed convolutional recurrent network that can solve partial differential equations without labeled data. This approach was applied to several problems such as the two-dimensional viscous Burger's equation and FitzHugh–Nagumo reaction-diffusion equations. On single-cell level Hustad et al. pointed out that ODE computations can use a substantial fraction of the total computer time of a heart simulator and they focused on systematically studying how to efficiently use modern multicore CPUs for this costly computational task. Furthermore, they concluded that the largest performance improvement of the ODE solvers arises from using SIMD vectorisation. Molinari et al. established an experimentally calibrated computational model of *ex-vivo* cardiac radiofrequency catheter ablation featuring the inclusion of three-

dimensional myocardial anisotropy, the implementation of a multi-scale time lag thermal ablation model, and the adoption of a model of cell death for the estimation of tissue damage and lesion sizing. The investigation gave new insights into the anisotropic thermal behavior of cardiac tissue and proved that the intrinsic anisotropic microstructure plays a crucial role in the thermo-electrical response of the tissue undergoing hyperthermic treatments.

In the realm of neuroscience, Daversin-Catty et al. introduced a new mathematical and numerical formalism of pulsatile viscous fluid flow in networks based on topological and geometrical model reduction, which is a robust and effective computational approach for large scale *in silico* studies. Moreover, different computational scenarios were studied, e.g. perivascular space flow induced by cardiac pulse wave-induced movement of the inner vascular wall. Furthermore, the framework established a foundation for future computational studies of perivascular flow to improve our understanding of brain transport. Yamakou et al. investigated coherence resonance and self-induced stochastic resonance in multiplex neural networks, which consist of electrically connected FitzHugh–Nagumo model neurons, in the presence of spike-timing-dependent plasticity. Here, several important questions leading to interesting future research directions were addressed, such as: *Which of these noise-induced resonance phenomena is more robust to parametric perturbations?* In order to better understand burst generation in inhibitory half-center central pattern generators, Olenik et al. studied a minimal network of two neurons coupled through depressing synapses. They have shown that synaptic depression of inhibition can enable the two-cell (Morris–Lecar model) network to produce burst solutions of different periods, when the strength of the maximum synaptic conductance is varied. Furthermore, Liu et al. investigated BAM neural networks with delays. By using generalized Halanay inequalities and constructing appropriate Lyapunov functionals, some novelty criteria are obtained for the asymptotic stability of BAM neural systems with time delays. Spiliotis et al. analyzed network dynamics under healthy, Parkinsonian and deep brain stimulation conditions with the aim to improve deep brain stimulation treatment. For this purpose the authors built a large scale computational model that consists of certain elements of the basal ganglia network. This new approach is based on the detection of network communities or modules central to activity distribution. The aim of the paper was two-fold: 1) to identify positions of nodes of high functional impact using network analysis and 2) to explore the relationship between anatomical structure and neural activity using modified Hodgkin–Huxley models. The analysis showed that in all modular areas, Parkinsonian conditions alter power spectrograms.

The last area of this Research Topic concerns modeling and analysis to inform healthcare decision-making in terms of therapy/drug delivery (Zlobina et al.), managing infections (Kuttler et al.), informing new drugs' discovery (Bondar et al.) and managing pandemics (Chattopadhyay et al.). Zlobina et al. proposed that a qualitative model with a proper level of abstraction can be used to predict the response of a wound to dynamic therapy and investigated mathematically the most effective spatio-temporal regimes for drug delivery to accelerate wound closure. This study provides a possible optimal regime of therapy that focuses on macrophage activity and a hypothesis of treatment outcome to be tested in future experiments. Kuttler et al. introduced a mathematical model for bacterial growth and control by antibiotics treatment, including quorum sensing as a special kind of communication. The system is formalized by a system of semi-linear parabolic partial differential equations and can be used for *in silico*

studies of bacterial cooperative behavior in the special case of quorum sensing. The obtained data suggest that even a small bacterial population maintains an essential quorum. Bondar et al. discussed general principles of protonation-coupled protein conformational dynamics and how these apply to G-Protein Coupled Receptors. The authors found that the internal H-bond networks contain sites where structural rearrangements upon protonation change could be transmitted throughout the protein. In Chattopadhyay et al. a novel method of approximating a closed form solution of the ensemble averaged density profiles and correlation statistics of coupled dynamical systems, drawing from a technique used in mathematical biology to calculate a quantity called the basic reproduction number R_0 , was presented. It was shown that the R_0 formulation can be used to calculate the correlation between diffusivity paths, agreeing closely with the exact numerical solution of the double-diffusion model.

The topics covered in this Research Topic are far from exhaustive. Rather, they point to a broader range of problems that can not only be addressed by available mathematical and computational approaches, but also stimulate the development of novel tools and techniques.

Author contributions

AE, KT-A, GL, and EM conceived and wrote the editorial.

References

1. Tsaneva-Atanasova K, Diaz-Zuccarini V. Editorial: Mathematics for healthcare as part of computational medicine. *Front Physiol* (2018) 9:985. doi:10.3389/fphys.2018.00985
2. I. Geris, editor. *Computational modeling in tissue engineering*. Berlin, Germany: Springer (2013). doi:10.1007/978-3-642-32563-2
3. K-A Mardal, ME Rognes, TB Thompson, LM Valnes, editors. *Mathematical modeling of the human brain*. Berlin, Germany: Springer (2022). doi:10.1007/978-3-030-95136-8
4. J Sundnes, G Lines, B Nielsen, KA Mardal, A Tveito, editors. *Computing the electrical activity in the heart*. Berlin, Germany: Springer (2006). doi:10.1007/3-540-33437-8
5. Niederer S, Lumens J, Trayanova N. Computational models in cardiology. *Nat Rev Cardiol* (2019) 16:100–11. doi:10.1038/s41569-018-0104-y
6. Kass RE, Amari SI, Arai K, Brown EN, Diekmann CO, Diesmann M, et al. Computational neuroscience: Mathematical and statistical perspectives. *Annu Rev Stat Its Appl* (2018) 5:183–214. doi:10.1146/annurev-statistics-041715-033733
7. Karolak A, Markov DA, McCawley LJ, Rejniak KA. Towards personalized computational oncology: From spatial models of tumour spheroids, to organoids, to tissues. *J R Soc Interf* (2018) 15:20170703. doi:10.1098/rsif.2017.0703
8. Barbolosi D, Ciccolini J, Lacarelle B, Barlési F, André N. Computational oncology — Mathematical modelling of drug regimens for precision medicine. *Nat Rev Clin Oncol* (2016) 13:242–54. doi:10.1038/nrclinonc.2015.204
9. Kringelbach ML, Deco G. Brain states and transitions: Insights from computational neuroscience. *Cel Rep* (2020) 32:108128. doi:10.1016/j.celrep.2020.108128
10. Owens AP, Allen M, Ondobaka S, Friston KJ. Interoceptive inference: From computational neuroscience to clinic. *Neurosci Biobehavioral Rev* (2018) 90:174–83. doi:10.1016/j.neubiorev.2018.04.017
11. Peirlinck M, Costabal F, Yao J, Guccione JM, Tripathy S, Wang Y, et al. Precision medicine in human heart modeling. *Biomech Model Mechanobiol* (2021) 20:803–31. doi:10.1007/s10237-021-01421-z
12. Trayanova NA, O'Hara T, Bayer JD, Boyle PM, McDowell KS, Constantino J, et al. Computational cardiology: How computer simulations could be used to develop new therapies and advance existing ones. *EP Europace* (2012) 14:v82–9. doi:10.1093/europace/eus277
13. Trayanova NA, Doshi AN, Prakosa A. How personalized heart modeling can help treatment of lethal arrhythmias: A focus on ventricular tachycardia ablation strategies in post-infarction patients. *WIREs Syst Biol Med* (2020) 12:e1477. doi:10.1002/wsbm.1477
14. Depannemaeker D, Destexhe A, Jirsa V, Bernard C. Modeling seizures: From single neurons to networks. *Seizure* (2021) 90:4–8. doi:10.1016/j.seizure.2021.06.015
15. Zhu X, Wang Z, Teng F. A review of regulated self-organizing approaches for tissue regeneration. *Prog Biophys Mol Biol* (2021) 167:63–78. doi:10.1016/j.pbiomolbio.2021.07.006

Acknowledgments

We would like to thank all reviewers for their constructive comments in an attempt to initiate a dialogue between theoreticians and practitioners in the articles of this Research Topic. KT-A gratefully acknowledges the financial support of the EPSRC via grant EP/T017856/1. KT-A also acknowledges the support of the Technical University of Munich—Institute for Advanced Study, funded by the German Excellence Initiative.

Conflict of interest

The authors declare that the research was conducted in the absence of any commercial or financial relationships that could be construed as a potential conflict of interest.

Publisher's note

All claims expressed in this article are solely those of the authors and do not necessarily represent those of their affiliated organizations, or those of the publisher, the editors and the reviewers. Any product that may be evaluated in this article, or claim that may be made by its manufacturer, is not guaranteed or endorsed by the publisher.



Deriving the Bidomain Model of Cardiac Electrophysiology From a Cell-Based Model; Properties and Comparisons

Karoline Horgmo Jæger^{1*} and Aslak Tveito^{1,2}

¹ Simula Research Laboratory, Oslo, Norway, ² Department of Informatics, University of Oslo, Oslo, Norway

OPEN ACCESS

Edited by:

André H. Erhardt,
Weierstrass Institute for Applied
Analysis and Stochastics (LG),
Germany

Reviewed by:

Seth H. Weinberg,
The Ohio State University, United
States
Bradley John Roth,
Oakland University, United States
Nagaiah Chamakuri,
Indian Institute of Science Education
and Research, India

*Correspondence:

Karoline Horgmo Jæger
karolihj@simula.no

Specialty section:

This article was submitted to
Biophysics,
a section of the journal
Frontiers in Physiology

Received: 08 November 2021

Accepted: 13 December 2021

Published: 07 January 2022

Citation:

Jæger KH and Tveito A (2022)
Deriving the Bidomain Model of
Cardiac Electrophysiology From a
Cell-Based Model; Properties and
Comparisons.
Front. Physiol. 12:811029.
doi: 10.3389/fphys.2021.811029

The bidomain model is considered to be the gold standard for numerical simulation of the electrophysiology of cardiac tissue. The model provides important insights into the conduction properties of the electrochemical wave traversing the cardiac muscle in every heartbeat. However, in normal resolution, the model represents the average over a large number of cardiomyocytes, and more accurate models based on representations of all individual cells have therefore been introduced in order to gain insight into the conduction properties close to the myocytes. The more accurate model considered here is referred to as the EMI model since both the extracellular space (E), the cell membrane (M) and the intracellular space (I) are explicitly represented in the model. Here, we show that the bidomain model can be derived from the cell-based EMI model and we thus reveal the close relation between the two models, and obtain an indication of the error introduced in the approximation. Also, we present numerical simulations comparing the results of the two models and thereby highlight both similarities and differences between the models. We observe that the deviations between the solutions of the models become larger for larger cell sizes. Furthermore, we observe that the bidomain model provides solutions that are very similar to the EMI model when conductive properties of the tissue are in the normal range, but large deviations are present when the resistance between cardiomyocytes is increased.

Keywords: bidomain model, EMI model, cell-based model, cardiac electrophysiology, cardiac conduction, cardiac tissue models, numerical simulation

1. INTRODUCTION

Mathematical models are indispensable for understanding the complex processes underlying cardiac electrophysiology. A wide variety of models have been developed for the key processes going on across the membrane of cardiomyocytes (see, e.g., Rudy and Silva, 2006; Rudy, 2012; Qu et al., 2014; Amuzescu et al., 2021), where the latter paper presents a comprehensive overview of the evolution of these models. The models of the membrane dynamics have also been extended to yield descriptions of the electrophysiological properties of cardiac tissue, commonly represented by the bidomain model or the somewhat simpler monodomain model (see Tung, 1978; Neu and Krassowska, 1993; Sundnes et al., 2007; Clayton and Panfilov, 2008; Vigmond et al., 2008; Linge et al., 2009; Niederer et al., 2011a; Franzone et al., 2014). The use of mathematical models for understanding the properties of the cardiac action potential (AP) across the membrane of

cardiomyocytes is very widespread, and so is the use of the bidomain/monodomain models for understanding the properties of the excitation wave traversing cardiac tissue during each heartbeat. However, the spatial bidomain/monodomain models have two inherent limitations. The main limitation is that the extracellular space, the membrane of the myocyte, and the intracellular space are all assumed to be present everywhere. This assumption is indeed courageous but has provided surprisingly accurate results and presently underpins the understanding of cardiac conduction. The second limitation is that convergence is obtained using a relatively coarse mesh ($\Delta x \sim 0.25$ mm, see Xie et al., 2004; Clayton and Panfilov, 2008; Niederer et al., 2011b) and thus a typical mesh block contains several hundred cardiomyocytes (see, e.g., Jæger et al., 2021a,b). Therefore, understanding of the conduction properties (see, e.g., Henriquez, 2014; Veeraraghavan et al., 2014) close to the myocytes cannot be achieved using these models (see, e.g., Jæger et al., 2021a).

These limitations of the homogenized (bidomain/monodomain) models are well known and several authors have developed alternatives where all individual cells are explicitly represented in the models (see, e.g., Spach et al., 2007; Jacquemet and Henriquez, 2009; Hubbard and Henriquez, 2014; Lin and Keener, 2014; Tveito et al., 2017a; Weinberg, 2017; Jæger et al., 2019, 2021a; Domínguez et al., 2021; Jæger and Tveito, 2021). Here, we will apply the EMI model where both the extracellular space (E), the cell membrane (M) and the intracellular space (I) are explicitly represented in the model (see, e.g., Tveito et al., 2017a,b; Jæger and Tveito, 2021), and compare properties with the homogenized bidomain model. First, we will show how the bidomain model can be derived from the more accurate EMI model. Earlier derivations of the bidomain equations (see, e.g., Neu and Krassowska, 1993; Franzone et al., 2014; Henriquez and Ying, 2021) relies on homogenization of cardiac tissue, whereas the derivation given here follows directly from the EMI model. As part of this derivation, we can identify the main sources of deviations between the models.

Next, we will compare the properties of the bidomain model and the EMI model using numerical simulations. We first show that the deviations between the results obtained by the bidomain model and the EMI model become small as the cell size is reduced. This property is consistent with the error introduced in the derivation of the bidomain model. Secondly, we demonstrate that, for conduction properties providing a normal excitation wave with a conduction velocity of about 50 cm/s, the solutions of the EMI model and the bidomain model are very similar. However, as the resistance between the myocytes (through the gap junctions) is increased, the deviation between the solutions increases considerably.

It should be noted that the representation of all individual cardiomyocytes implies a significant increase in the computation load since the mesh resolution needs to be reduced from about $\Delta x \sim 0.25$ mm for a finite difference method (FDM) of the bidomain model to about $\delta x \sim 10$ μ m for a finite element method (FEM) code solving the EMI model (see Jæger et al., 2021a,b). The number of mesh blocks is $\Delta x^3/\delta x^3 = 15,600$ times larger for the EMI model than for the bidomain model, and, therefore, the

computational load increases significantly when every myocyte in the tissue is resolved.

The choice of using either an averaged model like the bidomain model or a cell-based model like the EMI model, depends on the application under consideration. The bidomain model is very useful for simulating large scale problems, whereas EMI is better suited when the dynamics close to individual myocytes, or even inside individual myocytes, are of importance.

2. METHODS

In this section we will derive the bidomain model commonly used to model the electrical activity of the heart from a more detailed model where each cell is represented. This cell-based model is referred to as the EMI model and is derived from Maxwell's equations of electromagnetism in Agudelo-Toro (2012) and Jæger and Tveito (2021). We will start by introducing the equations of the EMI model before we describe the derivation of the bidomain model from these equations. Finally, we discuss how the bidomain model parameters can be defined using the parameter values and tissue geometry of the EMI model.

2.1. The EMI Model

Consider a domain consisting of a single cell, Ω_i , surrounded by an extracellular space, Ω_e , with a cell membrane, Γ , separating the two spaces Ω_i and Ω_e . For such a domain, the electrical activity may be modeled by the EMI model (see, e.g., Roberts et al., 2008; Stinstra et al., 2010; Tveito et al., 2017a; Jæger et al., 2019), given by the equations

$$\nabla \cdot \sigma_i \nabla u_i = 0, \quad \text{in } \Omega_i \quad (1)$$

$$\nabla \cdot \sigma_e \nabla u_e = 0, \quad \text{in } \Omega_e \quad (2)$$

$$\mathbf{n}_e \cdot \sigma_e \nabla u_e = -\mathbf{n}_i \cdot \sigma_i \nabla u_i \equiv I_m, \quad \text{at } \Gamma, \quad (3)$$

$$u_i - u_e = v \quad \text{at } \Gamma, \quad (4)$$

$$I_m = C_m \frac{\partial v}{\partial t} + I_{\text{ion}} \quad \text{at } \Gamma, \quad (5)$$

$$u_e = 0 \quad \text{at } \partial\Omega_e^D, \quad (6)$$

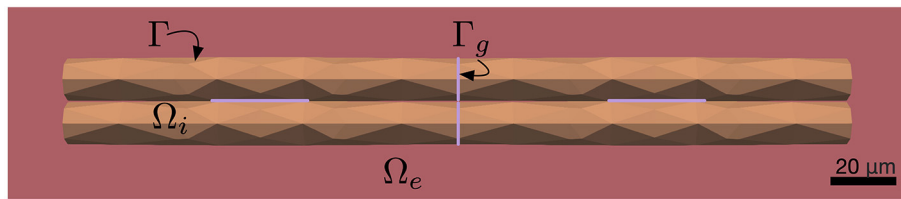
$$\frac{\partial u_e}{\partial \mathbf{n}_e} = 0 \quad \text{at } \partial\Omega_e^N. \quad (7)$$

Here, u_i , u_e , and v are the intracellular, extracellular and membrane potentials (in mV) defined in Ω_i , Ω_e and at Γ , respectively, \mathbf{n}_i and \mathbf{n}_e are the outward pointing normal vectors of the intracellular and extracellular spaces, respectively, C_m is the specific membrane capacitance (in $\mu\text{F}/\text{cm}^2$), I_{ion} is the ionic current density across the membrane (in $\mu\text{A}/\text{cm}^2$), I_m the sum of the capacitive and ionic current densities (in $\mu\text{A}/\text{cm}^2$), and σ_i and σ_e are the intracellular and extracellular conductivities, respectively (in mS/cm). The Equations (6) and (7) are Dirichlet and Neumann boundary conditions, respectively, for the outer boundary of the extracellular space.

2.1.1. Extension to Cells Connected by Gap Junctions

To model collections of connected cardiac cells, e.g., like illustrated in **Figure 1A**, the EMI model for a single cell may be extended to include a model for the currents through the gap

A EMI model domain for four connected cells



B EMI model mesh for a single cell

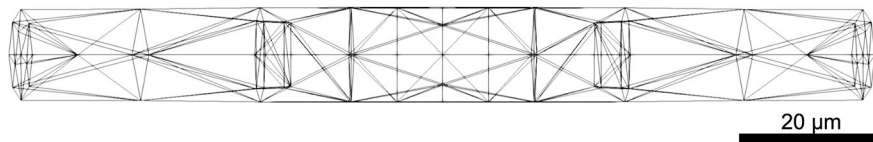


FIGURE 1 | (A) Illustration of an EMI model domain for four connected cells. The intracellular space (orange) is denoted by Ω_i and the extracellular space (red) is denoted by Ω_e . The cell membrane is defined as the interface between the intracellular and extracellular spaces and is denoted by Γ . Similarly, the intercalated discs (purple) are denoted by Γ_g and are defined as the interface between neighboring cells. Each cell is shaped as a cylinder with a diameter increasing slightly toward the center of the cell. **(B)** Illustration of the finite element mesh used to represent a single cell in the EMI model simulations.

junctions connecting neighboring cells (see, e.g., Tveito et al., 2017a; Jæger and Tveito, 2021; Jæger et al., 2021c). For example, for two connected cells 1 and 2, the EMI model can be extended to include equations of the form

$$\mathbf{n}_i^2 \cdot \sigma_i \nabla u_i^2 = -\mathbf{n}_i^1 \cdot \sigma_i \nabla u_i^1 \equiv I_{1,2}, \quad \text{at } \Gamma_g, \quad (8)$$

$$u_i^1 - u_i^2 = w, \quad \text{at } \Gamma_g, \quad (9)$$

$$I_{1,2} = C_g \frac{\partial w}{\partial t} + I_{\text{gap}}, \quad \text{at } \Gamma_g, \quad (10)$$

where Γ_g is the interface between the two cells (i.e., the intercalated disc). Furthermore, u_i^1 and u_i^2 are the intracellular potentials of the two cells, w is the potential difference between the two cells, and \mathbf{n}_i^1 and \mathbf{n}_i^2 are the outward pointing normal vectors of the cells. In addition, C_g is the specific capacitance of the intercalated discs (in $\mu\text{F}/\text{cm}^2$), I_{gap} is the current density through the gap junction proteins located at the intercalated discs (in $\mu\text{A}/\text{cm}^2$), and $I_{1,2}$ is the sum of the capacitive current density over the intercalated discs and the current density through the gap junction proteins connecting the two cells. The current density through the gap junction proteins, I_{gap} , is commonly modeled using the simple passive model

$$I_{\text{gap}} = \frac{1}{R_g} w = G_g w, \quad (11)$$

where R_g is the specific resistance of the gap junctions (in $\text{k}\Omega\text{cm}^2$) and G_g is the corresponding specific conductance (in mS/cm^2). A further explanation of the coupling between two adjacent cells is given in section 1.2.4 of Jæger and Tveito (2021).

2.2. Derivation of the Bidomain Model From the EMI Model

Instead of using the detailed model (Equations 1–11), modeling of the electrical activity of cardiac tissue is usually performed

using the homogenized bidomain and monodomain models. In these models, the detailed geometry of the individual cells and intercalated discs do not have to be represented in the computational mesh because the intracellular space, the extracellular space and the cell membrane are all assumed to exist everywhere in the tissue. We will now describe a possible derivation of the homogenized bidomain model from the EMI model equations described above. Note, however, that more rigorous versions of this derivation, using mathematical two-scale homogenization, have also been presented (see, e.g., Neu and Krassowska, 1993; Franzoni et al., 2014; Henriquez and Ying, 2021).

2.2.1. Starting Point of the Derivation

Assume that we have a relatively large collection of cells, and consider a small volume, Δ , in this cell collection, as illustrated in Figure 2A. We assume that this volume contains a number of cells with an associated surrounding extracellular space, and that the EMI model equations apply in the extracellular domain, in the intracellular domain, at the cell membrane and at the intercalated discs in this small block of tissue.

Step 1: Approximating the Intracellular Conductivity

As a first step in the derivation, we wish to approximate the intracellular conductivity to take both the purely intracellular space and the gap junctions between neighboring cells into account. In other words, we wish to reformulate the full EMI model (Equations 1–11) to a system of the form

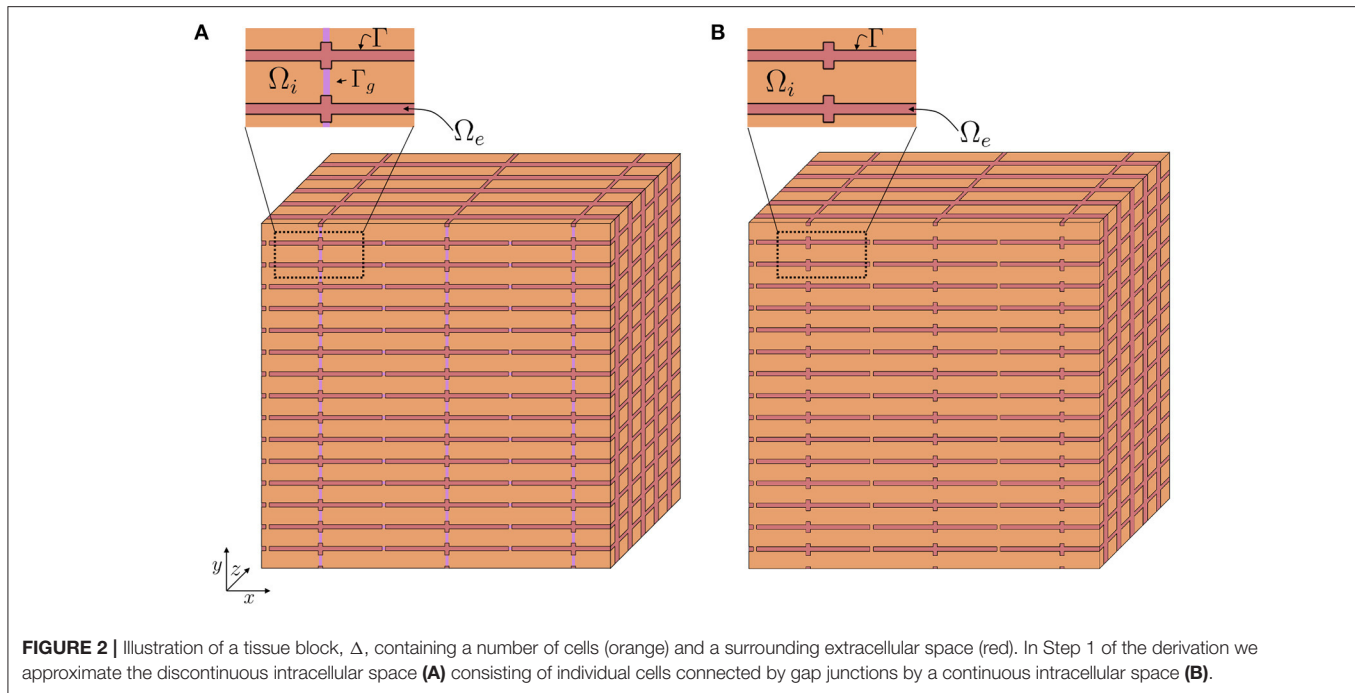
$$\nabla \cdot \bar{\sigma}_i \nabla u_i = 0, \quad \text{in } \Omega_i \quad (12)$$

$$\nabla \cdot \sigma_e \nabla u_e = 0, \quad \text{in } \Omega_e \quad (13)$$

$$\mathbf{n}_e \cdot \sigma_e \nabla u_e = -\mathbf{n}_i \cdot \bar{\sigma}_i \nabla u_i \equiv I_m, \quad \text{at } \Gamma, \quad (14)$$

$$u_i - u_e = v \quad \text{at } \Gamma, \quad (15)$$

$$I_m = C_m \frac{\partial v}{\partial t} + I_{\text{ion}} \quad \text{at } \Gamma, \quad (16)$$



$$u_e = 0 \quad \text{at } \partial\Omega_e^D, \quad (17)$$

$$\frac{\partial u_e}{\partial \mathbf{n}_e} = 0 \quad \text{at } \partial\Omega_e^N, \quad (18)$$

where $\bar{\sigma}_i$ is the average conductivity of the intracellular space including gap junctions. We wish to express $\bar{\sigma}_i$ such that the total intracellular resistance of a tissue block is close to the total intracellular resistance of the tissue block when the full EMI model (Equations 1–11) applies. Such an expression for $\bar{\sigma}_i$ is derived below in section 2.3.3.

In the remaining part of the derivation we will treat the intracellular domain as a continuous domain (see **Figure 2B**), and assume that the simplified EMI system (Equations 12–18) applies.

Step 2: Applying the Divergence Theorem

In the next step of the derivation, we consider the purely intracellular part of the tissue block Δ and apply the divergence theorem for $\bar{\sigma}_i \nabla u_i$ to obtain,

$$\int_{\partial\Omega_i^\Delta} \mathbf{n}_i \cdot \bar{\sigma}_i \nabla u_i dS = \int_{\Omega_i^\Delta} \nabla \cdot \bar{\sigma}_i \nabla u_i dV, \quad (19)$$

where Ω_i^Δ is the intracellular space contained in the tissue block and $\partial\Omega_i^\Delta$ is the boundary of the intracellular space contained in the tissue block. This boundary can be separated into the boundary between the intracellular space and the extracellular space contained in the tissue block, i.e. the cell membrane, and the intracellular part of the outer boundary of the tissue block in each spatial direction. Rewriting the surface integral, we obtain

$$\begin{aligned} & \int_{A_i^{x,+}} \mathbf{n}_i \cdot \bar{\sigma}_i \nabla u_i dS + \int_{A_i^{x,-}} \mathbf{n}_i \cdot \bar{\sigma}_i \nabla u_i dS \\ & + \int_{A_i^{y,+}} \mathbf{n}_i \cdot \bar{\sigma}_i \nabla u_i dS + \int_{A_i^{y,-}} \mathbf{n}_i \cdot \bar{\sigma}_i \nabla u_i dS \\ & + \int_{A_i^{z,+}} \mathbf{n}_i \cdot \bar{\sigma}_i \nabla u_i dS + \int_{A_i^{z,-}} \mathbf{n}_i \cdot \bar{\sigma}_i \nabla u_i dS \\ & + \int_{\Gamma_\Delta} \mathbf{n}_i \cdot \bar{\sigma}_i \nabla u_i dS = \int_{\Omega_i^\Delta} \nabla \cdot \bar{\sigma}_i \nabla u_i dV, \end{aligned} \quad (20)$$

where $A_i^{x,+}$ is the intracellular part of the boundary of the tissue block in the positive x -direction, $A_i^{x,-}$ is the intracellular part of the boundary of the tissue block in the negative x -direction, and the surfaces $A_i^{y,+}$, $A_i^{y,-}$, $A_i^{z,+}$, and $A_i^{z,-}$ are defined similarly for the intracellular part of the boundaries of the tissue block in the y - and z -directions. Furthermore, Γ_Δ is the membrane contained in the tissue block.

By applying the divergence theorem and similar definitions for the extracellular space, we likewise obtain

$$\begin{aligned} & \int_{A_e^{x,+}} \mathbf{n}_e \cdot \sigma_e \nabla u_e dS + \int_{A_e^{x,-}} \mathbf{n}_e \cdot \sigma_e \nabla u_e dS \\ & + \int_{A_e^{y,+}} \mathbf{n}_e \cdot \sigma_e \nabla u_e dS + \int_{A_e^{y,-}} \mathbf{n}_e \cdot \sigma_e \nabla u_e dS \\ & + \int_{A_e^{z,+}} \mathbf{n}_e \cdot \sigma_e \nabla u_e dS + \int_{A_e^{z,-}} \mathbf{n}_e \cdot \sigma_e \nabla u_e dS \\ & + \int_{\Gamma_\Delta} \mathbf{n}_e \cdot \sigma_e \nabla u_e dS = \int_{\Omega_e^\Delta} \nabla \cdot \sigma_e \nabla u_e dV. \end{aligned} \quad (21)$$

Step 3: Applying the EMI Model Equations (12–(14))

By inserting Equations (12) and (13) into Equations (20) and (21), we find that the right hand sides of Equations (20) and (21) are zero. Moreover, by inserting Equation (14), we get

$$\begin{aligned} & \int_{A_i^{x,+}} \mathbf{n}_i \cdot \bar{\sigma}_i \nabla u_i dS + \int_{A_i^{x,-}} \mathbf{n}_i \cdot \bar{\sigma}_i \nabla u_i dS \\ & + \int_{A_i^{y,+}} \mathbf{n}_i \cdot \bar{\sigma}_i \nabla u_i dS + \int_{A_i^{y,-}} \mathbf{n}_i \cdot \bar{\sigma}_i \nabla u_i dS \\ & + \int_{A_i^{z,+}} \mathbf{n}_i \cdot \bar{\sigma}_i \nabla u_i dS + \int_{A_i^{z,-}} \mathbf{n}_i \cdot \bar{\sigma}_i \nabla u_i dS - \int_{\Gamma_\Delta} I_m dS = 0 \end{aligned} \quad (22)$$

for the intracellular part, and

$$\begin{aligned} & \int_{A_e^{x,+}} \mathbf{n}_e \cdot \sigma_e \nabla u_e dS + \int_{A_e^{x,-}} \mathbf{n}_e \cdot \sigma_e \nabla u_e dS \\ & + \int_{A_e^{y,+}} \mathbf{n}_e \cdot \sigma_e \nabla u_e dS + \int_{A_e^{y,-}} \mathbf{n}_e \cdot \sigma_e \nabla u_e dS \\ & + \int_{A_e^{z,+}} \mathbf{n}_e \cdot \sigma_e \nabla u_e dS + \int_{A_e^{z,-}} \mathbf{n}_e \cdot \sigma_e \nabla u_e dS + \int_{\Gamma_\Delta} I_m dS = 0 \end{aligned} \quad (23)$$

for the extracellular part.

Step 4: Extending the Variables and Parameters to Be Defined Everywhere

In order to avoid having to represent the detailed geometry of the cell tissue, we now define some new variables U_i , U_e , and V that each are defined in the entire domain $\Omega = \Omega_i \cup \Omega_e$, and thus also in the entire tissue block, Δ . We want these variables to fulfill the integral conditions specified in Equations (22) and (23). In addition, we assume that the definitions of the membrane potential and I_m specified in Equations (15) and (16) apply in the entire domain. In other words, in an arbitrary tissue block, Δ , of Ω , we seek solutions U_i , U_e , and V such that

$$\begin{aligned} & \int_{A_i^{x,+}} \mathbf{n} \cdot \bar{\sigma}_i \nabla U_i dS + \int_{A_i^{x,-}} \mathbf{n} \cdot \bar{\sigma}_i \nabla U_i dS \\ & + \int_{A_i^{y,+}} \mathbf{n} \cdot \bar{\sigma}_i \nabla U_i dS + \int_{A_i^{y,-}} \mathbf{n} \cdot \bar{\sigma}_i \nabla U_i dS \\ & + \int_{A_i^{z,+}} \mathbf{n} \cdot \bar{\sigma}_i \nabla U_i dS + \int_{A_i^{z,-}} \mathbf{n} \cdot \bar{\sigma}_i \nabla U_i dS - \int_{\Gamma_\Delta} I_m dS = 0, \end{aligned} \quad (24)$$

$$\begin{aligned} & \int_{A_e^{x,+}} \mathbf{n} \cdot \sigma_e \nabla U_e dS + \int_{A_e^{x,-}} \mathbf{n} \cdot \sigma_e \nabla U_e dS \\ & + \int_{A_e^{y,+}} \mathbf{n} \cdot \sigma_e \nabla U_e dS + \int_{A_e^{y,-}} \mathbf{n} \cdot \sigma_e \nabla U_e dS \\ & + \int_{A_e^{z,+}} \mathbf{n} \cdot \sigma_e \nabla U_e dS + \int_{A_e^{z,-}} \mathbf{n} \cdot \sigma_e \nabla U_e dS + \int_{\Gamma_\Delta} I_m dS = 0, \end{aligned} \quad (25)$$

$$V = U_i - U_e, \quad (26)$$

$$I_m = C_m V_t + I_{\text{ion}}. \quad (27)$$

Here, \mathbf{n} is the outward pointing normal vector of the tissue block, and $\bar{\sigma}_i$, σ_e , C_m , I_m and I_{ion} have been extended to be defined in the entire domain.

Step 5: Approximate the Surface Integrals

Since I_m is now defined in the entire tissue block, and not just on the membrane, the surface integral over the membrane can be approximated by

$$\int_{\Gamma_\Delta} I_m dS \approx \int_{\Delta} \chi I_m dV, \quad (28)$$

where Δ is the entire tissue block and χ is the membrane surface to volume ratio, i.e., the surface area of the membrane contained in Δ divided by the volume of Δ .

In addition, the integrals in Equations (24) and (25) over the outer boundary of the tissue block is separated into the intracellular and extracellular parts of the tissue block, and in this step of the derivation, we wish to approximate these integrals to be defined over the entire tissue block boundaries. In order to do this, we apply the approximation

$$\int_{A_i^{x,+}} \mathbf{n} \cdot \bar{\sigma}_i \nabla U_i dS \approx \bar{A}_i^x \int_{A^{x,+}} \mathbf{n} \cdot \bar{\sigma}_i \nabla U_i dS, \quad (29)$$

and similar approximations for the remaining surfaces. Here, \bar{A}_i^x is the average fraction of the cross-sectional area of the tissue block perpendicular to the x -direction that is occupied by the intracellular space and $A^{x,+}$ is the entire boundary of the tissue block in the positive x -direction. Inserting this type of approximation in all the integrals over the outer boundaries of the tissue block, Equations (24) and (25) can be approximated as

$$\begin{aligned} & \int_{A^{x,+}} \mathbf{n} \cdot \bar{A}_i^x \bar{\sigma}_i \nabla U_i dS + \int_{A^{x,-}} \mathbf{n} \cdot \bar{A}_i^x \bar{\sigma}_i \nabla U_i dS \\ & + \int_{A^{y,+}} \mathbf{n} \cdot \bar{A}_i^y \bar{\sigma}_i \nabla U_i dS + \int_{A^{y,-}} \mathbf{n} \cdot \bar{A}_i^y \bar{\sigma}_i \nabla U_i dS \\ & + \int_{A^{z,+}} \mathbf{n} \cdot \bar{A}_i^z \bar{\sigma}_i \nabla U_i dS + \int_{A^{z,-}} \mathbf{n} \cdot \bar{A}_i^z \bar{\sigma}_i \nabla U_i dS - \int_{\Delta} \chi I_m dV = 0, \end{aligned} \quad (30)$$

$$\begin{aligned} & \int_{A^{x,+}} \mathbf{n} \cdot \bar{A}_e^x \sigma_e \nabla U_e dS + \int_{A^{x,-}} \mathbf{n} \cdot \bar{A}_e^x \sigma_e \nabla U_e dS \\ & + \int_{A^{y,+}} \mathbf{n} \cdot \bar{A}_e^y \sigma_e \nabla U_e dS + \int_{A^{y,-}} \mathbf{n} \cdot \bar{A}_e^y \sigma_e \nabla U_e dS \\ & + \int_{A^{z,+}} \mathbf{n} \cdot \bar{A}_e^z \sigma_e \nabla U_e dS + \int_{A^{z,-}} \mathbf{n} \cdot \bar{A}_e^z \sigma_e \nabla U_e dS + \int_{\Delta} \chi I_m dV = 0. \end{aligned} \quad (31)$$

Furthermore, we may define a set of scaled bidomain conductivities,

$$\bar{\sigma}_i^x = \bar{A}_i^x \bar{\sigma}_i^x, \quad \bar{\sigma}_i^y = \bar{A}_i^y \bar{\sigma}_i^y, \quad \bar{\sigma}_i^z = \bar{A}_i^z \bar{\sigma}_i^z, \quad (32)$$

$$\bar{\sigma}_e^x = \bar{A}_e^x \sigma_e^x, \quad \bar{\sigma}_e^y = \bar{A}_e^y \sigma_e^y, \quad \bar{\sigma}_e^z = \bar{A}_e^z \sigma_e^z, \quad (33)$$

where $\tilde{\sigma}_i^x$, $\tilde{\sigma}_i^y$ and $\tilde{\sigma}_i^z$ and σ_e^x , σ_e^y and σ_e^z refer to the possible directional dependence of $\tilde{\sigma}_i$ and σ_e . We also define the associated bidomain conductivity tensors,

$$M_i = \begin{pmatrix} \tilde{\sigma}_i^x & 0 & 0 \\ 0 & \tilde{\sigma}_i^y & 0 \\ 0 & 0 & \tilde{\sigma}_i^z \end{pmatrix}, \quad M_e = \begin{pmatrix} \sigma_e^x & 0 & 0 \\ 0 & \sigma_e^y & 0 \\ 0 & 0 & \sigma_e^z \end{pmatrix}. \quad (34)$$

By introducing these tensors, Equations (30) and (31) can be rewritten as

$$\int_{\partial\Delta} \mathbf{n} \cdot (M_i \nabla U_i) dS - \int_{\Delta} \chi I_m dV = 0, \quad (35)$$

$$\int_{\partial\Delta} \mathbf{n} \cdot (M_e \nabla U_e) dS + \int_{\Delta} \chi I_m dV = 0, \quad (36)$$

where $\partial\Delta$ represents the entire outer surface of the tissue block.

Step 6: Reapply the Divergence Theorem for the New Variables

We may now reapply the divergence theorem for the newly defined variables U_i and U_e defined in the entire tissue block. This yields

$$\int_{\Delta} \nabla \cdot (M_i \nabla U_i) dV - \int_{\Delta} \chi I_m dV = 0, \quad (37)$$

$$\int_{\Delta} \nabla \cdot (M_e \nabla U_e) dV + \int_{\Delta} \chi I_m dV = 0. \quad (38)$$

We also note that the volume Δ was chosen arbitrarily. Therefore, the more general relation

$$\nabla \cdot (M_i \nabla U_i) - \chi I_m = 0, \quad (39)$$

$$\nabla \cdot (M_e \nabla U_e) + \chi I_m = 0, \quad (40)$$

holds.

Step 7: Rearranging the Terms and Inserting Equations (26) and (27)

By rearranging Equation (39) and adding Equations (39) and (40), these equations may be rewritten as

$$\nabla \cdot (M_i \nabla U_i) = \chi I_m, \quad (41)$$

$$\nabla \cdot (M_i \nabla U_i) + \nabla \cdot (M_e \nabla U_e) = 0. \quad (42)$$

Finally, by inserting Equations (26) and (27), we obtain the bidomain model equations

$$\nabla \cdot (M_i \nabla V) + \nabla \cdot (M_e \nabla U_e) = \chi \left(C_m \frac{\partial V}{\partial t} + I_{\text{ion}} \right), \quad (43)$$

$$\nabla \cdot (M_i \nabla V) + \nabla \cdot ((M_i + M_e) \nabla U_e) = 0, \quad (44)$$

where we recall that M_i and M_e are intracellular and extracellular conductivity tensors (in mS/cm) defined in Equations (32)–(34), χ is the membrane surface to volume ratio (in cm^{-1}), C_m is the specific membrane capacitance (in $\mu\text{F}/\text{cm}^2$), I_{ion} is the

current density through ion channels, pumps and exchangers on the cell membrane (in $\mu\text{A}/\text{cm}^2$) and V and U_e (in mV) are the bidomain model membrane and extracellular potentials, respectively, defined in the entire domain. Furthermore, the intracellular potential (in mV) may be computed by

$$U_i = V + U_e. \quad (45)$$

In addition, the boundary conditions

$$U_e = 0 \quad \text{at } \partial\Omega^D, \quad (46)$$

$$\frac{\partial U_e}{\partial \mathbf{n}} = 0 \quad \text{at } \partial\Omega^N, \quad (47)$$

are assumed to hold at the boundary of the domain where Ω^D coincides with the EMI model boundary Ω_e^D , and Ω^N coincides with the EMI model boundary Ω_e^N .

2.3. Expressions for the Bidomain Model Parameters

The bidomain model as derived above introduces a set of new parameters, namely the conductivity tensors, M_i and M_e , and the surface to volume ratio, χ . Considering their definitions, values for these parameters may be derived from the geometry and parameters of the EMI model. In this subsection, we suggest an approach for making these definitions by considering an EMI model mesh of a volume Ω , containing an intracellular volume, Ω_i , and extracellular volume, Ω_e , a surface for the cell membranes, Γ , and a collection of surfaces for the intercalated discs, Γ_g . For simplicity, we assume that the value of all the EMI model parameters and the tissue geometry do not vary in different parts of the domain, so that the bidomain model parameters can be treated as constants throughout the domain. In addition, we assume that the total domain $\Omega = \Omega_i \cup \Omega_e$ is shaped as a rectangular cuboid with lengths L_x , L_y and L_z in the x -, y - and z -directions, respectively. An alternative approach for setting up the bidomain model conductivities from the EMI model parameters and a simplified tissue geometry is presented in Henriquez and Ying (2021).

2.3.1. Surface to Volume Ratio, χ

In order to compute the surface to volume ratio from an EMI model mesh, we may simply compute

$$A_{\Gamma,\Omega} = \int_{\Gamma} 1 dS, \quad (48)$$

$$V_{\Omega} = \int_{\Omega} 1 dS, \quad (49)$$

where $A_{\Gamma,\Omega}$ represents the total membrane area in the domain and V_{Ω} represents the volume of the domain. Assuming an even distribution of cells throughout the domain, the surface to volume ratio can then be defined as

$$\chi = \frac{A_{\Gamma,\Omega}}{V_{\Omega}}. \quad (50)$$

2.3.2. Average Cross-Sectional Area Fractions

We first consider the average intracellular fraction of the cross-sectional area perpendicular to the x -axis, \bar{A}_i^x . Let $A^x(x)$ be the cross-sectional area of Ω perpendicular to the x -axis, and let $A_i^x(x)$ be the fraction belonging to Ω_i . Then

$$V_{\Omega_i} = \int_0^{L_x} A_i^x(x) A^x(x) dx = \bar{A}_i^x \int_0^{L_x} A^x(x) dx = \bar{A}_i^x V_{\Omega}. \quad (51)$$

Hence,

$$\bar{A}_i^x = \frac{V_{\Omega_i}}{V_{\Omega}}. \quad (52)$$

Similar arguments yield

$$\bar{A}_i^x = \bar{A}_i^y = \bar{A}_i^z = \frac{V_{\Omega_i}}{V_{\Omega}}, \quad (53)$$

$$\bar{A}_e^x = \bar{A}_e^y = \bar{A}_e^z = \frac{V_{\Omega_e}}{V_{\Omega}} = \left(1 - \frac{V_{\Omega_i}}{V_{\Omega}}\right). \quad (54)$$

Here, V_{Ω_i} can be computed from the EMI model mesh as

$$V_{\Omega_i} = \int_{\Gamma_{\Omega_i}^x} 1 dS. \quad (55)$$

2.3.3. Average Intracellular Conductivity

As described above, we wish to define an average conductivity $\bar{\sigma}_i$ such that the simplified EMI model (Equations 12–18) is a good approximation of the full EMI model (Equations 1–11). In particular, we wish to find a $\bar{\sigma}_i$ such that the total intracellular resistance of the simplified model is close to the total intracellular resistance of the full model. To simplify this argument, we assume that there is no capacitive current across the intercalated discs, i.e. that the current between two cells is given by I_{gap} (see Equation 11).

We start by considering the total resistance in the x -direction of the domain. In the full EMI model (Equations 1–11) with the capacitive current set to zero, this is given by the sum of the resistance over the purely intracellular space (R_c^x) and the resistance over the gap junctions (R_j^x) (Shaw and Rudy, 1997):

$$R_i^x = R_c^x + R_j^x. \quad (56)$$

The total resistance in the purely intracellular space is given by (Plonsey and Barr, 2007)

$$R_c^x = \frac{L_x}{\sigma_i \bar{A}_i^x L_y L_z}, \quad (57)$$

where $\bar{A}_i^x L_y L_z$ is the average intracellular cross-sectional area of the domain perpendicular to the x -direction. Assuming that the cells are organized as a regular grid in the x -, y - and z -directions, the total resistance through gap junctions in the x -direction is given by

$$R_j^x = \frac{(N_x - 1)R_g}{N_y N_z A_j^x}, \quad (58)$$

where R_g is the specific gap junction resistance (in $\text{k}\Omega\text{cm}^2$), as it appears in the full EMI model, A_j^x is the area of a single intercalated disc perpendicular to the x -direction and N_x , N_y , and N_z are the number of cells in the x -, y -, and z -directions, respectively. Thus, $N_x - 1$ is the number of intercalated disc collections along the length of the domain in the x -direction, $N_y N_z$ is the number of intercalated disc for each such collection, and $N_y N_z A_j^x$ is the total cross-sectional area of each of the intercalated disc collections.

In the simplified model (Equations 12–18), the total resistance is given by (Plonsey and Barr, 2007)

$$R_i^x = \frac{L_x}{\bar{\sigma}_i^x \bar{A}_i^x L_y L_z}. \quad (59)$$

Therefore, in order for the total resistance to be the same in the two formulations, we wish $\bar{\sigma}_i^x$ to satisfy

$$\frac{L_x}{\bar{\sigma}_i^x \bar{A}_i^x L_y L_z} = \frac{L_x}{\sigma_i \bar{A}_i^x L_y L_z} + \frac{(N_x - 1)R_g}{N_y N_z A_j^x}, \quad (60)$$

which yields

$$\bar{\sigma}_i^x = \frac{\sigma_i}{1 + \frac{\sigma_i R_g (N_x - 1) \bar{A}_i^x L_y L_z}{L_x N_y N_z A_j^x}}. \quad (61)$$

From the EMI model mesh, we may compute

$$A_{j,\Omega}^x = \int_{\Gamma_{\Omega}^x} 1 dS, \quad (62)$$

as the total area of all intercalated discs perpendicular to the x -direction, Γ_{Ω}^x . Since A_j^x is defined as the area of a single intercalated disc perpendicular to the x -direction, we note that

$$A_j^x = \frac{A_{j,\Omega}^x}{(N_x - 1)N_y N_z}, \quad (63)$$

where $(N_x - 1)N_y N_z$ is the total number of intercalated discs in the x -direction. Inserting Equations (63) into Equation (61) yields

$$\bar{\sigma}_i^x = \frac{\sigma_i}{1 + \frac{(N_x - 1)^2 \bar{A}_i^x L_y L_z \sigma_i R_g}{L_x A_{j,\Omega}^x}}. \quad (64)$$

We also note that from Equation (52), we have that

$$\bar{A}_i^x = \frac{V_{\Omega_i}}{V_{\Omega}} = \frac{V_{\Omega_i}}{L_x L_y L_z} \Rightarrow \bar{A}_i^x L_y L_z = \frac{V_{\Omega_i}}{L_x}, \quad (65)$$

and inserting this into Equation (64), we obtain

$$\bar{\sigma}_i^x = \frac{\sigma_i}{1 + \frac{\sigma_i R_g V_{\Omega_i}}{\delta_x^2 A_{j,\Omega}^x}}. \quad (66)$$

where $\delta_x = L_x/(N_x - 1)$. Similar arguments for the y - and z -directions result in

$$\bar{\sigma}_i^y = \frac{\sigma_i}{1 + \frac{\sigma_i R_g V_{\Omega_i}}{\delta_y^2 A_{j,\Omega}^y}}, \quad (67)$$

$$\bar{\sigma}_i^z = \frac{\sigma_i}{1 + \frac{\sigma_i R_g V_{\Omega_i}}{\delta_z^2 A_{j,\Omega}^z}}. \quad (68)$$

Since

$$\frac{\bar{\sigma}_i^x}{\bar{\sigma}_i^y} = \frac{1 + \frac{\sigma_i R_g V_{\Omega_i}}{\delta_y^2 A_{j,\Omega}^y}}{1 + \frac{\sigma_i R_g V_{\Omega_i}}{\delta_x^2 A_{j,\Omega}^x}}, \quad (69)$$

the anisotropy is governed by the difference between $\delta_x^2 A_{j,\Omega}^x$ and $\delta_y^2 A_{j,\Omega}^y$, and similar for the other combination of axes.

2.3.4. Intracellular Conductivity Tensor

Inserting Equations (52) and (66)–(68) into Equation (32), we get

$$\tilde{\sigma}_i^x = \bar{A}_i^x \bar{\sigma}_i^x = \frac{V_{\Omega_i}}{V_{\Omega}} \frac{\sigma_i}{1 + \frac{\sigma_i (N_x - 1)^2 R_g V_{\Omega_i}}{L_x^2 A_{j,\Omega}^x}}, \quad (70)$$

$$\tilde{\sigma}_i^y = \bar{A}_i^y \bar{\sigma}_i^y = \frac{V_{\Omega_i}}{V_{\Omega}} \frac{\sigma_i}{1 + \frac{\sigma_i (N_y - 1)^2 R_g V_{\Omega_i}}{L_y^2 A_{j,\Omega}^y}}, \quad (71)$$

$$\tilde{\sigma}_i^z = \bar{A}_i^z \bar{\sigma}_i^z = \frac{V_{\Omega_i}}{V_{\Omega}} \frac{\sigma_i}{1 + \frac{\sigma_i (N_z - 1)^2 R_g V_{\Omega_i}}{L_z^2 A_{j,\Omega}^z}}. \quad (72)$$

2.3.5. Extracellular Conductivity Tensor

The extracellular conductivity tensor can be found directly from the cross-sectional area fractions and we get

$$\tilde{\sigma}_e^x = \tilde{\sigma}_e^y = \tilde{\sigma}_e^z = \frac{V_{\Omega_e}}{V_{\Omega}} \sigma_e = \left(1 - \frac{V_{\Omega_i}}{V_{\Omega}}\right) \sigma_e. \quad (73)$$

3. RESULTS

In order to compare the EMI model with the homogenized bidomain model, we set up a few example applications and perform numerical simulations of the two models. Note here that all EMI model simulations are performed in three dimensions (3D), whereas the bidomain model simulations are performed in two dimensions (2D) or one dimension (1D).

3.1. Simulation Set-Up

In our numerical simulations of the EMI model, we consider collections of cells shaped as cylinders with a slightly varying diameter. In all simulations, except for the ones where the cell length is varied and is explicitly specified, each cell is 120 μm long (in the x -direction) and has a radius varying from 6 μm at the cell ends to 7 μm at the center of the cell (see **Figure 1**). We let the distance from the boundary of the extracellular space to the cell collection be 2 μm in all spatial directions. The parameter values used in the simulations are specified in **Table 1**. The parameters

TABLE 1 | Default parameter values used in the simulations.

Parameter	Value	Parameter	Value
σ_i	4 mS/cm	σ_e	20 mS/cm
C_m	1 $\mu\text{F}/\text{cm}^2$	C_g	0.5 $\mu\text{F}/\text{cm}^2$
R_g	0.0015 $\text{k}\Omega\text{cm}^2$		

The bidomain model parameters M_i , M_e and χ are computed from the EMI model parameters and mesh as described in section 2.3.

used in the bidomain model are computed from the EMI model parameters and mesh as described in section 2.3.

All EMI model simulations are performed in 3D. However, for our example test cases with a 1D strand of cells and a 2D grid of cells, we use 1D and 2D versions, respectively, of the bidomain model. In the simulations of a 1D strand of cells, we apply homogenous Neumann boundary conditions on the outer boundary of the extracellular domain in the y - and z -directions and homogenous Dirichlet boundary conditions in the x -direction. In the simulations of a 2D grid of cells, we apply homogenous Neumann boundary conditions on the outer boundary of the extracellular domain in the z -direction and homogenous Dirichlet boundary conditions in the x - and y -directions.

3.2. Numerical Methods

The EMI model simulations are performed using the operator splitting procedure described in Jæger et al. (2021c,d), the numerical methods applied to (Jæger et al., 2021d) and the MFEM C++ finite element method library (Anderson et al., 2020; MFEM, 2021). For details on the numerical methods applied to solve the EMI model, we refer to Jæger et al. (2021a,c,d). The bidomain model simulations are performed in Matlab using a first-order temporal operator splitting procedure as described in Sundnes et al. (2006), where the ordinary differential part of the equations is solved using forward Euler and the partial differential part of the equations is solved using an implicit finite difference scheme. Unless otherwise specified, we use a time step of $\Delta t = 0.001$ ms in the simulations of both models. In the bidomain model simulations, we use a spatial discretization of $\Delta x = \Delta y = 10$ μm , roughly matching the typical edge length in the applied EMI model finite element mesh.

3.3. 1D Strand of Cells With a Passive Membrane Model

We first consider an example with a 1D strand of cells connected in the longitudinal direction (x -direction). The total length of the cell strand is 2 mm and we consider a number of different choices for the length of a single cell (and the associated total number of cells). In addition, we vary the value of the specific gap junction resistance, R_g . The membrane dynamics, I_{ion} , is modeled by a simple passive membrane model

$$I_{\text{ion}} = \frac{1}{R_m} (v - v_0), \quad (74)$$

where $R_m = 5$ $\text{k}\Omega\text{cm}^2$ is the specific membrane resistance and $v_0 = -80$ mV is the resting membrane potential. We stimulate

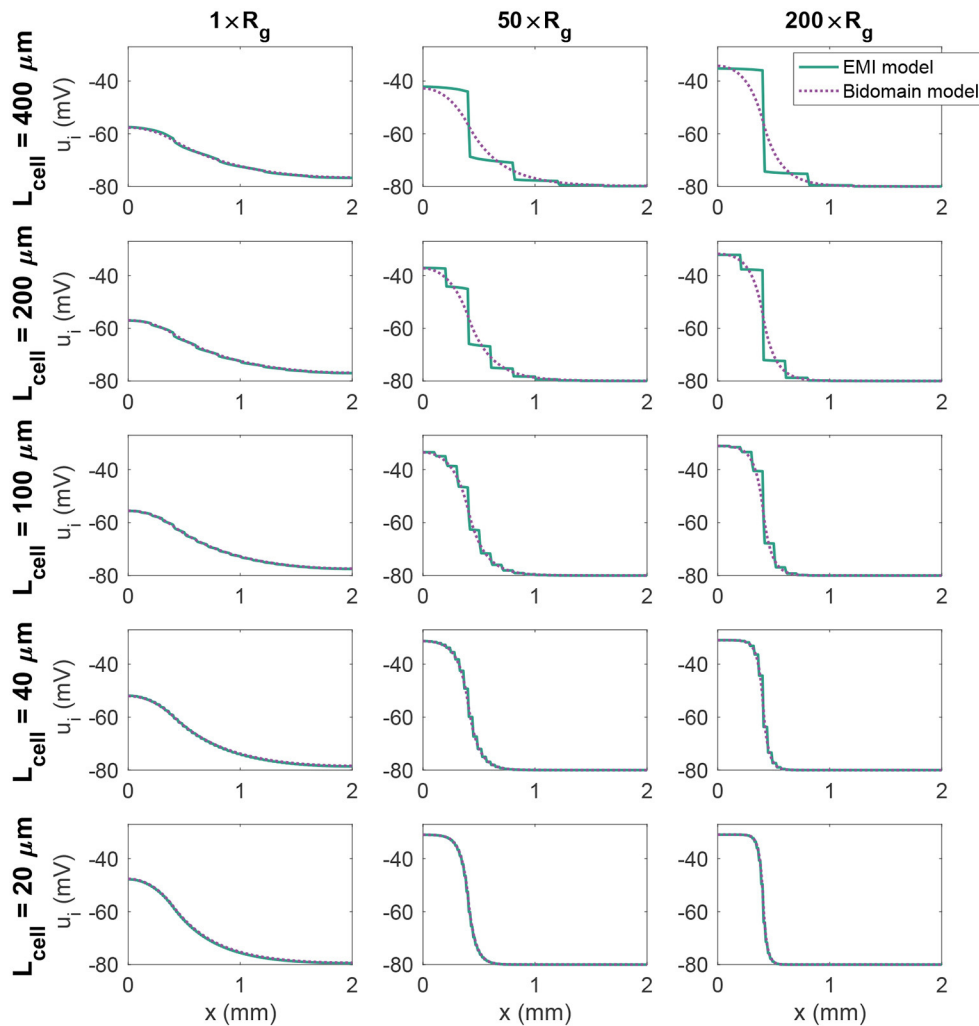


FIGURE 3 | Intracellular potential, u_i , at time $t = 20$ ms in EMI model and bidomain model simulations using a passive membrane model (Equation 74) and the default parameter values specified in **Table 1**, except that the value of R_g is increased by the factor indicated by the column titles. In addition, the cell length (L_{cell}) is varied as described for each row of plots.

the first (leftmost) $400 \mu\text{m}$ of membrane in the x -direction by a constant stimulus current of size $-10 \mu\text{A}/\text{cm}^2$. **Figure 3** shows the intracellular potential at time $t = 20$ ms along a line in the x -direction in the center of the domain for the EMI model and the associated solution of the bidomain model for a few combinations of cell length and R_g values. We observe that for small cells (lower panels), the solution of the bidomain model is in very good agreement with the results of the EMI model. However, if the cell size is increased, and the gap junction resistance is increased, there is a significant difference between the results of the EMI model and the bidomain model.

3.4. 1D Strand of Cells With an Active Membrane Model

Next, we consider an example with a 1D strand of 20 cells of length $120 \mu\text{m}$ with an active membrane model, modeled by the human left atrial base model from Jæger et al. (2021b). We initiate

a traveling wave by stimulating the first $360 \mu\text{m}$ of cell membrane in the x -direction (corresponding to three cardiomyocytes) by a 1 ms long constant stimulus current of size $-40 \mu\text{A}/\text{cm}^2$. We measure the conduction velocity as the distance between a point a in the center of the domain in the x -direction and a point b located at $4/5$ of the total domain length, divided by the difference in time between when the membrane potential in these two points reach a value above -20 mV. Using the default parameter values specified in **Table 1**, we get a conduction velocity of 50.8 cm/s in the bidomain model simulation. This is close to the value found in the EMI model simulation, which is 53.3 cm/s .

In **Figure 4**, we further investigate the relationship between the conduction velocity found in the bidomain and EMI model simulations when R_g is increased, representing reduced cell coupling. We consider two different discretization resolutions, the default resolution of $\Delta t = 0.001 \text{ ms}$ and $\Delta x \sim 10 \mu\text{m}$

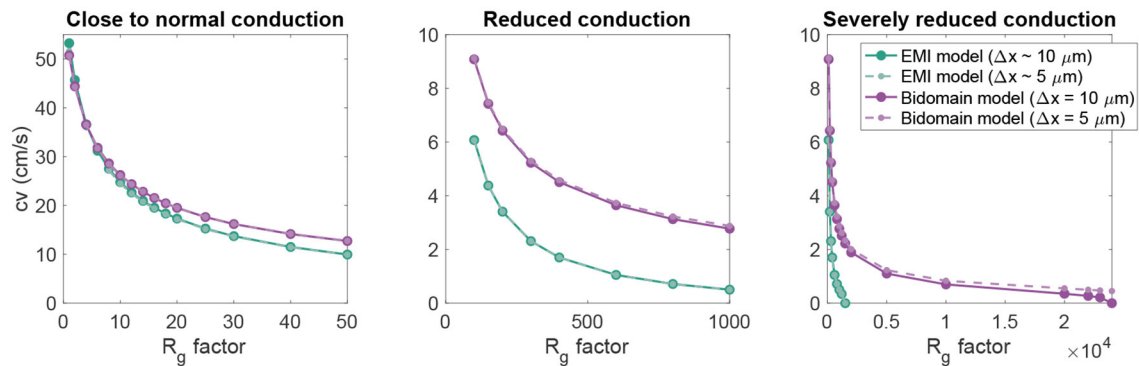


FIGURE 4 | Conduction velocity as R_g is increased in EMI model and bidomain model simulations of a strand of 20 connected cells with an active membrane model (Jæger et al., 2021b). The values on the x-axis represent the factor with which the default R_g value in **Table 1** is multiplied. The remaining parameter values are as specified in **Table 1**. Note that the plot is separated into three panels in order to improve the visibility of the data. Note also that we consider two different discretization resolutions in the simulations of each model. In the default case, $\Delta t = 0.001$ ms and Δx in the bidomain model and the typical edge length in the EMI model is $10 \mu\text{m}$, whereas in the refined case (dashed lines), both the spatial and temporal discretization steps are reduced to half of the default values.

and a refined resolution of $\Delta t = 0.0005$ ms and $\Delta x \sim 5 \mu\text{m}$. We observe that for values of R_g relatively close to the default value, the conduction velocities found in simulations of the bidomain and EMI models are very similar. However, when R_g is considerably increased, the difference between the two model formulations appears to be more significant and the conduction velocity is considerably higher in the bidomain model simulations than in the corresponding EMI model simulations. Furthermore, we observe that for the EMI model, conduction is blocked when R_g is increased by a factor larger than about 2,000, whereas for the bidomain model, R_g can be increased by a factor of about 20,000 before conduction is blocked for the default resolution and conduction is not blocked for the considered values of R_g for the refined resolution. In addition, we note that the simulations of refined resolution appears to give very similar conduction velocities as for the default resolution in the EMI model simulations. For the bidomain model simulations, the two resolutions give very similar results for the first range of R_g values, but as the R_g value is severely increased, we can observe a difference between the two resolutions.

3.5. 2D Grid of Cells With an Active Membrane Model

Next, we consider a case of a grid of 25×25 connected cells with the same active membrane model as for the 1D strand simulations. We stimulate the membrane of an area corresponding to the 5×5 cells in the lower left corner by the same stimulation current as in the 1D case. **Figure 5** shows the membrane potential, v , and the extracellular potential, u_e , from the EMI model and bidomain model simulations using the default parameter values specified in **Table 1** at time $t = 5$ ms. The solution of the two models appears to be very similar. However, in **Figure 6**, we have performed a similar simulation where R_g is increased by a factor of 200. We consider the solution at $t = 20$ ms and observe that the traveling excitation wave has clearly traveled faster and reached further in the bidomain model

simulation than in the EMI model simulation, consistent with the results of **Figure 4**.

4. DISCUSSION

The bidomain model continues to provide essential insights into cardiac conduction and how the electrochemical dynamics of the heart is affected by blocking ion channels (see, e.g., Zemzemi et al., 2013; Sharifi, 2017), increasing gap junction resistance (see, e.g., Roth, 1988; Bruce et al., 2014), introducing ischemia (see, e.g., Stinstra et al., 2004, 2005; Heidenreich et al., 2012) or performing defibrillation (see, e.g., Skouibine et al., 2000; Trayanova et al., 2006, 2011; Quarteroni et al., 2017). However, as almost any model, its utility is limited by the inherent resolution of the model. It is useful for understanding cardiac conduction at the tissue level, but it cannot be applied for analyses of conduction close to individual cardiomyocytes. Therefore, detailed models representing individual myocytes have been developed.

Here, we show that the bidomain model can be derived directly from the cell-based EMI model. Classically, the bidomain model is derived using elegant homogenization techniques (see Neu and Krassowska, 1993; Henriquez and Ying, 2021). In the derivation presented here, the deviation between the properties of the bidomain model and the EMI model is seen directly as part of the derivation. In short, the advantage of the present derivation is that it is more straightforward to follow and that it gives indications of where the deviations in the results between the two models stem from.

4.1. Source of Difference Between EMI and Bidomain Solutions

There are essentially three steps in the derivation of the bidomain model where approximations are introduced and thus, most likely, are responsible for the difference in the solutions of the two models. First; the resistance of the intracellular

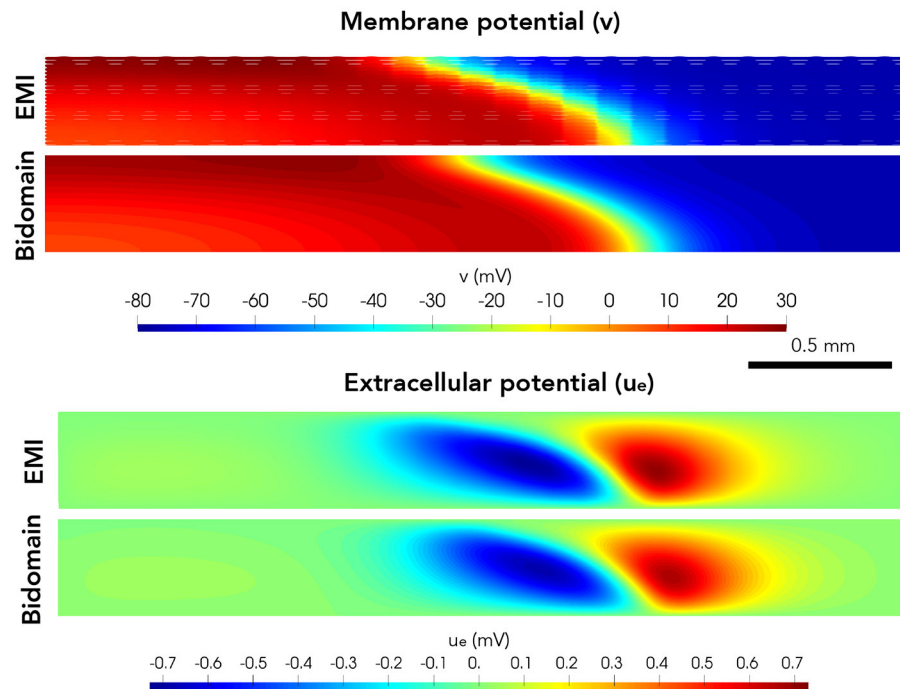


FIGURE 5 | Membrane potential, v , and extracellular potential, u_e , at time $t = 5$ ms in EMI model and bidomain model simulations using the default parameter values specified in **Table 1** and an active membrane model (Jæger et al., 2021b). This simulation required a CPU time of 132 min for the EMI model and 2 min for the bidomain model.

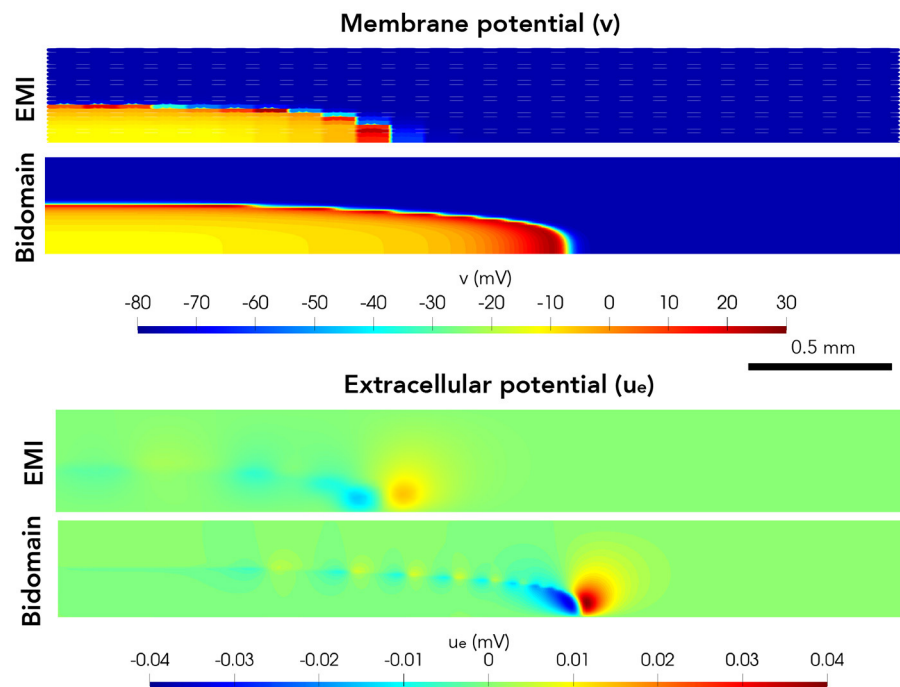


FIGURE 6 | Membrane potential, v , and extracellular potential, u_e , at time $t = 20$ ms in EMI model and bidomain model simulations using and active membrane model (Jæger et al., 2021b) and the default parameter values specified in **Table 1**, except that the value of R_g is increased by a factor of 200.

space and the gap junctions are combined into one common and averaged resistance. Second, the average of a function over a volume is approximated by the average of the same function over the surface of the volume. Third, the average of a function on a surface is approximated by the average of the same function on an extended surface. It is beyond the scope of this paper to perform a detailed analysis of these deviations, but based on these observations, it comes as no surprise that the error becomes smaller when the cell size is reduced.

4.2. Differences and Similarities

The EMI model and the bidomain model provide remarkably similar results when the parameters of importance for the conduction velocity are in the normal range. It is safe to claim that the bidomain model represents normal cardiac conduction very well if the scale of interest contains many cells. Certainly, the bidomain model cannot be used to study conduction in the vicinity of individual cells, and it also runs into difficulties for large cells combined with high values of resistance across the gap junctions. It is observed that the bidomain model consistently overestimates the conduction velocity. For normal parameters,

the difference is small, but for strongly increased resistance across the gap junctions, the bidomain model significantly overestimates the conduction velocity.

DATA AVAILABILITY STATEMENT

The original contributions presented in the study are included in the article/supplementary material, further inquiries can be directed to the corresponding author.

AUTHOR CONTRIBUTIONS

KH and AT: concept and writing. KH: derivation of models and simulations. AT: definition of test problems. Both authors contributed to the article and approved the submitted version.

FUNDING

This project was supported by the Norwegian Research Council through the EMIX project; 324239.

REFERENCES

- Agudelo-Toro, A. (2012). *Numerical simulations on the biophysical foundations of the neuronal extracellular space* (Ph.D. thesis). Niedersächsische Staats- und Universitätsbibliothek Göttingen.
- Amuzescu, B., Airini, R., Epureanu, F. B., Mann, S. A., Knott, T., and Radu, B. M. (2021). Evolution of mathematical models of cardiomyocyte electrophysiology. *Math. Biosci.* 334:108567. doi: 10.1016/j.mbs.2021.108567
- Anderson, R., Andrej, J., Barker, A., Bramwell, J., Camier, J.-S., Dobrev, J. C. V., et al. (2020). MFEM: a modular finite element library. *Comput. Math. Appl.* 81, 42–74. doi: 10.1016/j.camwa.2020.06.009
- Bruce, D., Pathmanathan, P., and Whiteley, J. P. (2014). Modelling the effect of gap junctions on tissue-level cardiac electrophysiology. *Bull. Math. Biol.* 76, 431–454. doi: 10.1007/s11538-013-9927-1
- Clayton, R., and Panfilov, A. (2008). A guide to modelling cardiac electrical activity in anatomically detailed ventricles. *Prog. Biophys. Mol. Biol.* 96, 19–43. doi: 10.1016/j.pbiomolbio.2007.07.004
- Domínguez, S., Reimer, J., Green, K. R., Zolfaghari, R., and Spiteri, R. J. (2021). “A simulation-based method to study the LQT1 syndrome remotely using the EMI model,” in *Emerging Technologies in Biomedical Engineering and Sustainable TeleMedicine* (Cham: Springer), 179–189.
- Franzone, P. C., Pavarino, L. F., and Scacchi, S. (2014). *Mathematical Cardiac Electrophysiology, Vol. 13*. Cham: Springer.
- Heidenreich, E., Ferrero, J., and Rodríguez, J. (2012). “Modeling the human heart under acute ischemia,” in *Patient-Specific Computational Modeling. Lecture Notes in Computational Vision and Biomechanics, Vol. 5* (Dordrecht: Springer), 81–103.
- Henriquez, C. S. (2014). A brief history of tissue models for cardiac electrophysiology. *IEEE Trans. Biomed. Eng.* 61, 1457–1465. doi: 10.1109/TBME.2014.2310515
- Henriquez, C. S., and Ying, W. (2021). “The bidomain model of cardiac tissue: from microscale to macroscale,” in *Cardiac Bioelectric Therapy* (Boston, MA: Springer), 211–223.
- Hubbard, M. L., and Henriquez, C. S. (2014). A microstructural model of reentry arising from focal breakthrough at sites of source-load mismatch in a central region of slow conduction. *Am. J. Physiol. Heart Circ. Physiol.* 306, H1341–H1352. doi: 10.1152/ajpheart.00385.2013
- Jæger, K. H., Edwards, A. G., Giles, W. R., and Tveito, A. (2021a). From millimeters to micrometers; re-introducing myocytes in models of cardiac electrophysiology. *Front. Physiol.* 12:763584. doi: 10.3389/fphys.2021.763584
- Jæger, K. H., Edwards, A. G., Giles, W. R., and Tveito, A. (2021b). Mutations change excitability and the probability of re-entry in a computational model of cardiac myocytes in the sleeve of the pulmonary vein. *bioRxiv*. doi: 10.1101/2021.09.24.461636
- Jæger, K. H., Edwards, A. G., McCulloch, A., and Tveito, A. (2019). Properties of cardiac conduction in a cell-based computational model. *PLoS Comput. Biol.* 15:e1007042. doi: 10.1371/journal.pcbi.1007042
- Jæger, K. H., Hustad, K. G., Cai, X., and Tveito, A. (2021c). Efficient numerical solution of the EMI model representing the extracellular space (E), cell membrane (M) and intracellular space (I) of a collection of cardiac cells. *Front. Phys.* 8:579461. doi: 10.3389/fphys.2020.579461
- Jæger, K. H., Hustad, K. G., Cai, X., and Tveito, A. (2021d). “Operator splitting and finite difference schemes for solving the EMI model,” in *Modeling Excitable Tissue* (Cham: Springer), 44–55.
- Jæger, K. H., and Tveito, A. (2021). “Derivation of a cell-based mathematical model of excitable cells,” in *Modeling Excitable Tissue* (Cham: Springer), 1–13.
- Jacquemet, V., and Henriquez, C. S. (2009). Genesis of complex fractionated atrial electrograms in zones of slow conduction: a computer model of microfibrosis. *Heart Rhythm* 6, 803–810. doi: 10.1016/j.hrthm.2009.02.026
- Lin, J., and Keener, J. P. (2014). Microdomain effects on transverse cardiac propagation. *Biophys. J.* 106, 925–931. doi: 10.1016/j.bpj.2013.11.1117
- Linge, S., Sundnes, J., Hanslien, M., Lines, G. T., and Tveito, A. (2009). Numerical solution of the bidomain equations. *Philos. Trans. R. Soc. Lond. A* 367, 1931–1950. doi: 10.1098/rsta.2008.0306
- MFEM (2021). *MFEM: Modular Finite Element Methods [Software]*. Available online at: www.mfem.org.
- Neu, J., and Krassowska, W. (1993). Homogenization of syncytial tissues. *Crit. Rev. Biomed. Eng.* 21, 137–199.
- Niederer, S., Mitchell, L., Smith, N., and Plank, G. (2011a). Simulating human cardiac electrophysiology on clinical time-scales. *Front. Physiol.* 2:14. doi: 10.3389/fphys.2011.00014
- Niederer, S. A., Kerfoot, E., Benson, A. P., Bernabeu, M. O., Bernus, O., Bradley, C., et al. (2011b). Verification of cardiac tissue electrophysiology simulators

- using an n-version benchmark. *Philos. Trans. R. Soc. A* 369, 4331–4351. doi: 10.1098/rsta.2011.0139
- Plonsey, R., and Barr, R. C. (2007). *Bioelectricity: A Quantitative Approach*. Boston, MA: Springer Science & Business Media.
- Qu, Z., Hu, G., Garfinkel, A., and Weiss, J. N. (2014). Nonlinear and stochastic dynamics in the heart. *Phys. Rep.* 543, 61–162. doi: 10.1016/j.physrep.2014.05.002
- Quarteroni, A., Manzoni, A., and Vergara, C. (2017). The cardiovascular system: mathematical modelling, numerical algorithms and clinical applications. *Acta Numerica* 26, 365–590. doi: 10.1017/S0962492917000046
- Roberts, S. F., Stinstra, J. G., and Henriquez, C. S. (2008). Effect of nonuniform interstitial space properties on impulse propagation: a discrete multidomain model. *Biophys. J.* 95, 3724–3737. doi: 10.1529/biophysj.108.137349
- Roth, B. J. (1988). The electrical potential produced by a strand of cardiac muscle: a bidomain analysis. *Ann. Biomed. Eng.* 16, 609–637. doi: 10.1007/BF02368018
- Rudy, Y. (2012). From genes and molecules to organs and organisms: heart. *Comprehensive Biophys.* 268–327. doi: 10.1016/B978-0-12-374920-8.00924-3
- Rudy, Y., and Silva, J. R. (2006). Computational biology in the study of cardiac ion channels and cell electrophysiology. *Q. Rev. Biophys.* 39, 57–116. doi: 10.1017/S0033583506004227
- Sharifi, M. (2017). Computational approaches to understand the adverse drug effect on potassium, sodium and calcium channels for predicting tdp cardiac arrhythmias. *J. Mol. Graphics Modell.* 76, 152–160. doi: 10.1016/j.jmgm.2017.06.012
- Shaw, R. M., and Rudy, Y. (1997). Ionic mechanisms of propagation in cardiac tissue: roles of the sodium and L-type calcium currents during reduced excitability and decreased gap junction coupling. *Circ. Res.* 81, 727–741. doi: 10.1161/01.RES.81.5.727
- Skouibine, K., Trayanova, N., and Moore, P. (2000). A numerically efficient model for simulation of defibrillation in an active bidomain sheet of myocardium. *Math. Biosci.* 166, 85–100. doi: 10.1016/S0025-5564(00)00019-5
- Spach, M. S., Heidlage, J. F., Dolber, P. C., and Barr, R. C. (2007). Mechanism of origin of conduction disturbances in aging human atrial bundles: experimental and model study. *Heart Rhythm* 4, 175–185. doi: 10.1016/j.hrthm.2006.10.023
- Stinstra, J., MacLeod, R., and Henriquez, C. (2010). Incorporating histology into a 3D microscopic computer model of myocardium to study propagation at a cellular level. *Ann. Biomed. Eng.* 38, 1399–1414. doi: 10.1007/s10439-009-9883-y
- Stinstra, J. G., Hopenfeld, B., and Macleod, R. S. (2004). Using models of the passive cardiac conductivity and full heart anisotropic bidomain to study the epicardial potentials in ischemia. *Conf. Proc. IEEE Eng. Med. Biol. Soc.* 2, 3555–3558. doi: 10.1109/IEMBS.2004.1403999
- Stinstra, J. G., Shome, S., Hopenfeld, B., and MacLeod, R. S. (2005). Modelling passive cardiac conductivity during ischaemia. *Med. Biol. Eng. Comput.* 43, 776–782. doi: 10.1007/BF02430957
- Sundnes, J., Lines, G. T., Cai, X., Nielsen, B. F., Mardal, K.-A., and Tveito, A. (2007). *Computing the Electrical Activity in the Heart, Vol. 1*. Berlin: Springer Science & Business Media.
- Sundnes, J., Nielsen, B. F., Mardal, K. A., Cai, X., Lines, G. T., and Tveito, A. (2006). On the computational complexity of the bidomain and the monodomain models of electrophysiology. *Ann. Biomed. Eng.* 34, 1088–1097. doi: 10.1007/s10439-006-9082-z
- Trayanova, N., Constantino, J., Ashihara, T., and Plank, G. (2011). Modeling defibrillation of the heart: approaches and insights. *IEEE Rev. Biomed. Eng.* 4, 89–102. doi: 10.1109/RBME.2011.2173761
- Trayanova, N., Plank, G., and Rodríguez, B. (2006). What have we learned from mathematical models of defibrillation and postshock arrhythmogenesis? application of bidomain simulations. *Heart Rhythm* 3, 1232–1235. doi: 10.1016/j.hrthm.2006.04.015
- Tung, L. (1978). *A bi-domain model for describing ischemic myocardial dc potentials* (Ph.D. thesis). Massachusetts Institute of Technology.
- Tveito, A., Jæger, K. H., Kuchta, M., Mardal, K.-A., and Rognes, M. E. (2017a). A cell-based framework for numerical modeling of electrical conduction in cardiac tissue. *Front. Phys.* 5:48. doi: 10.3389/fphy.2017.00048
- Tveito, A., Jæger, K. H., Lines, G. T., Paszkowski, L., Sundnes, J., Edwards, A. G., et al. (2017b). An evaluation of the accuracy of classical models for computing the membrane potential and extracellular potential for neurons. *Front. Comput. Neurosci.* 11:27. doi: 10.3389/fncom.2017.00027
- Veeraraghavan, R., Gourdie, R. G., and Poelzing, S. (2014). Mechanisms of cardiac conduction: a history of revisions. *Am. J. Physiol. Heart Circ. Physiol.* 306, H619–H627. doi: 10.1152/ajpheart.00760.2013
- Vigmond, E., Dos Santos, R. W., Prassl, A., Deo, M., and Plank, G. (2008). Solvers for the cardiac bidomain equations. *Prog. Biophys. Mol. Biol.* 96, 3–18. doi: 10.1016/j.pbimolbio.2007.07.012
- Weinberg, S. (2017). Ephaptic coupling rescues conduction failure in weakly coupled cardiac tissue with voltage-gated gap junctions. *Chaos* 27, 093908. doi: 10.1063/1.4999602
- Xie, F., Qu, Z., Yang, J., Baher, A., Weiss, J. N., Garfinkel, A., et al. (2004). A simulation study of the effects of cardiac anatomy in ventricular fibrillation. *J. Clin. Invest.* 113, 686–693. doi: 10.1172/JCI17341
- Zemzemi, N., Bernabeu, M. O., Saiz, J., Cooper, J., Pathmanathan, P., Mirams, G. R., et al. (2013). Computational assessment of drug-induced effects on the electrocardiogram: from ion channel to body surface potentials. *Br. J. Pharmacol.* 168, 718–733. doi: 10.1111/j.1476-5381.2012.02200.x

Conflict of Interest: The authors declare that the research was conducted in the absence of any commercial or financial relationships that could be construed as a potential conflict of interest.

Publisher's Note: All claims expressed in this article are solely those of the authors and do not necessarily represent those of their affiliated organizations, or those of the publisher, the editors and the reviewers. Any product that may be evaluated in this article, or claim that may be made by its manufacturer, is not guaranteed or endorsed by the publisher.

Copyright © 2022 Jæger and Tveito. This is an open-access article distributed under the terms of the Creative Commons Attribution License (CC BY). The use, distribution or reproduction in other forums is permitted, provided the original author(s) and the copyright owner(s) are credited and that the original publication in this journal is cited, in accordance with accepted academic practice. No use, distribution or reproduction is permitted which does not comply with these terms.



An *In Silico* Study of Electrophysiological Parameters That Affect the Spiral-Wave Frequency in Mathematical Models for Cardiac Tissue

Mahesh Kumar Mulimani¹, Soling Zimik² and Rahul Pandit^{1*}

¹Centre for Condensed Matter Theory, Department of Physics, Indian Institute of Science, Bangalore, India, ²Computational Biology Group, Institute of Mathematical Sciences, Chennai, India

OPEN ACCESS

Edited by:

André H. Erhardt,
Weierstrass Institute for Applied
Analysis and Stochastics (LG),
Germany

Reviewed by:

Kunichika Tsumoto,
Kanazawa Medical University, Japan
Nele Vandersickel,
Ghent University, Belgium

*Correspondence:

Rahul Pandit
rahul@iisc.ac.in

[†]Present address:

Rahul Pandit,
Department of Physics, Indian Institute
of Science, Bangalore, India

Specialty section:

This article was submitted to
Biophysics,
a section of the journal
Frontiers in Physics

Received: 22 November 2021

Accepted: 23 December 2021

Published: 03 February 2022

Citation:

Mulimani MK, Zimik S and Pandit R
(2022) An *In Silico* Study of
Electrophysiological Parameters That
Affect the Spiral-Wave Frequency in
Mathematical Models for
Cardiac Tissue.
Front. Phys. 9:819873.
doi: 10.3389/fphy.2021.819873

Spiral waves of excitation in cardiac tissue are associated with life-threatening cardiac arrhythmias. It is, therefore, important to study the electrophysiological factors that affect the dynamics of these spiral waves. By using an electrophysiologically detailed mathematical model of a myocyte (cardiac cell), we study the effects of cellular parameters, such as membrane-ion-channel conductances, on the properties of the action-potential (AP) of a myocyte. We then investigate how changes in these properties, specifically the upstroke velocity and the AP duration (APD), affect the frequency ω of a spiral wave in the mathematical model that we use for human-ventricular tissue. We find that an increase (decrease) in this upstroke-velocity or a decrease (increase) in the AP duration increases (decreases) ω . We also study how other intercellular factors, such as the fibroblast-myocyte coupling, diffusive coupling strength, and the effective number of neighboring myocytes and fibroblasts, modulate ω . Finally, we demonstrate how a spiral wave can drift to a region with a high density of fibroblasts. Our results provide a natural explanation for the anchoring of spiral waves in highly fibrotic regions in fibrotic hearts.

Keywords: mathematical models of cardiac tissue, action-potential (AP), cardiac fibrosis, spiral waves, drift of spiral waves

1 INTRODUCTION

Nonlinear waves in the form of rotating spirals are ubiquitous spatiotemporal patterns that occur in a variety of biological or physical systems; these include chemical-reaction waves in the Belousov-Zhabotinsky system [1–5], oxidation waves of carbon monoxide on the surface of platinum [6–8], calcium-signalling waves in *Xenopus* oocytes [9], cyclic-AMP signalling waves in the aggregation process of *Dictyostelium discoideum* [10, 11], and, notably, action-potential (AP) waves that mediate muscle contraction in cardiac tissue. The organization of these AP waves in the form of spirals or scrolls in cardiac tissue is associated with abnormal and life-threatening heart rhythms known as arrhythmias. In particular, ventricular arrhythmias can lead to sudden cardiac death; therefore, it is important to understand the dynamics of such waves.

The rhythm of a normal heart is maintained by the trains of waves that are generated by its pacemaker, the sino-atrial node (SAN). This normal rhythm in a heart can be disturbed by the

formation of a spiral wave, which can override the function of the SAN as the primary source of waves and entrain the heart to follow the spiral-rotation frequency. There are multiple mechanisms through which spiral waves can occur in cardiac tissue [12–18].

Ex vivo and *in vitro* studies [19–27] show that VT is associated with functional reentry that leads to the formation of a spiral wave. A multiple-spiral state is linked to ventricular fibrillation (VF) that results in a chaotic heart rate [13–15, 23, 28–30], and a quivering of the left ventricle, which renders it incapable of pumping oxygenated blood to the body; and, in the absence of medical intervention, this leads to death in a few minutes. It is crucial, therefore, to develop a detailed understanding of how spiral waves in cardiac tissue can get destabilized and form multiple spiral waves. Some studies have shown that heterogeneity-induced spatial gradients in the frequency ω of a spiral wave can lead to such an instability [31, 32] or to the drifting of this spiral wave [28, 33–35]. We build on the results of these studies to investigate which physiological factors affect ω and how they modulate it. In mammalian hearts, cardiac tissue is heterogeneous: there can be cellular heterogeneity, e.g., cardiac fibroblasts in addition to myocytes, or a spatial variation of electrophysiological properties, e.g., along the apico-basal direction in a heart, or between intermural layers [36] of the heart, or because of conduction inhomogeneities [37].

We investigate the effects of various intracellular (ion-channel conductances) and intercellular (gap-junctional factors) parameters on the spiral-wave frequency. At the single-cell level, we show how changes in ion-channel conductances modulate action-potential (AP) properties, such as its upstroke velocity $\frac{dV}{dt}_{max}$ and duration (APD). We then examine how these changes in AP properties affect the spiral-wave frequency ω at the tissue level. We find that an increase (decrease) in $\frac{dV}{dt}_{max}$ (APD) increases (decreases) ω . We then investigate the effects of intercellular coupling strength on ω by changing the coupling strength in the following two ways: a) by modifying the diffusion constant D of the medium; b) by interspersing inexcitable point obstacles in the medium, thereby reducing the effective number of neighboring myocytes. We find that ω is unaffected by a change in D , but, with point obstacles, ω decreases with an increase in the density of these obstacles. We examine two models for fibrosis, which occurs in diseased hearts and is usually accompanied by a proliferation of fibroblasts [38–42]. These models allow us to study how various fibroblast parameters, e.g., the fibroblast-myocyte coupling and the AP of the coupled myocyte, affect ω and spiral-wave dynamics; the fibroblast parameters include its resting potential and the number of fibroblasts coupled to a myocyte. Moreover, we show that a spiral in a medium with a heterogeneous distribution of fibroblasts, drifts towards the region with a high density of fibroblasts.

The paper is organized as follows. The Materials and Methods **Section 2** contains (a) the details of the myocyte and tissue models that we use in our simulations and (b) the numerical techniques we use to solve the governing equations.

TABLE 1 | The various ionic currents in the TP06 model [43]. The details of the ion-channel and ion-pump equations for the currents and the parameter values that we use for the TP06 model are given in the **Supplementary Material**.

Symbol	Ion-channel or ion pump current
I_{Na}	fast inward Na^+ current
I_{CaL}	L-type inward Ca^{2+} current
I_{to}	Transient outward current
I_{Ks}	Slow delayed rectifier outward K^+ current
I_{Kr}	Rapid delayed rectifier outward K^+ current
I_{K1}	Inward rectifier outward K^+ current
I_{NaCa}	Na^+/Ca^{++} exchanger current
I_{NaK}	Na^+/K^+ pump current
I_{pCa}	plateau Ca^{++} current
I_{pK}	plateau K^+ current
I_{bNa}	background inward Na^+ current
I_{bCa}	background inward Ca^{++} current

We then provide the findings of our study in **Section 3** on Results. Finally, in the Discussion, **Section 4**, we discuss our results in the light of other past studies and mention some of the limitations in our study.

2 MATERIALS AND METHODS

2.1 Model

For myocytes we use the TP06 human-ventricular-cell model [43], in which the transmembrane potential V_m of an isolated myocyte is governed by the following ordinary differential equation (ODE):

$$\frac{dV_m}{dt} = -\frac{I_{ion}}{C_m}; \quad I_{ion} = \sum_i I_i; \quad (1)$$

I_{ion} is the sum of all the ion-channel currents with I_i the i th ion-channel current, and C_m the normalized transmembrane capacitance. In **Table 1** we list the currents in the TP06 model; their dependence on V_m is given, e.g., in Ref. 43.

The spatiotemporal evolution of V_m in mathematical models for cardiac tissue is governed by the following reaction-diffusion partial differential equation (PDE):

$$\frac{\partial V_m}{\partial t} = D \nabla^2 V - \frac{I_{ion}}{C_m}; \quad (2)$$

D is the diffusion coefficient; we restrict ourselves to a scalar D for simplicity; the TP06 case is described in detail in Ref. 43. It is convenient to use the following non-dimensionalised ion-channel conductances and diffusion coefficients:

$$S_G = \frac{G}{G_c}; \quad S_D = \frac{D}{D_0}; \quad (3)$$

where G stands for a typical conductance, G_c is the control value of the conductance, and the control diffusion constant $D_0 = 0.001$ $54 \text{ cm}^2/\text{ms}$; for the conductances we consider, $G_c = 14.838, 0.000$ 039 $8, 0.153$ nS/pF for G_{Na}, G_{CaL} , and G_{Kr} , respectively.

We use the following two models for the fibroblast cells:

- **Model-I:** We model the fibroblast cells as inexcitable obstacles and we replace the myocytes at random with these inexcitable obstacles throughout our simulation domain such that the percentage of sites with obstacles is p_o . The gap-junctional current between the myocyte and inexcitable obstacles in this model is zero (see Refs. 37, 44).
- **Model-II:** We model the fibroblasts in our study as an electrically passive cells, as in Ref. 45. Each myocyte is coupled to N_f fibroblasts; and the myocyte and fibroblast transmembrane potentials V_m and V_f , respectively, obey the following coupled ODEs:

$$\begin{aligned}\frac{dV_m}{dt} &= -\left(\frac{I_{ion}}{C_m} + N_f \times \frac{I_{gap}}{C_m}\right); \\ \frac{dV_f}{dt} &= \frac{(I_{gap} - I_f)}{C_f}; \\ I_f &= G_f (V_f - E_f); \\ I_{gap} &= G_{gap} (V_m - V_f).\end{aligned}\quad (4)$$

C_f , E_f and G_{gap} are the membrane capacitance of a fibroblast, the fibroblast resting potential, and the fibroblast-myocyte gap-junctional coupling, respectively. We use a *bilayer model* for fibroblast-myocyte couplings: fibroblasts, in the top layer, are coupled to myocytes in the bottom layer, as in Ref. 16, which contains a schematic diagram of this bilayer and the PDEs that describe the spatiotemporal evolution of waves of activation in this model; we do not include fibroblast-fibroblast couplings. Moreover, when we consider a heterogeneous distribution of fibroblasts in **Section 3.4**, we first consider a homogeneous region in which each myocyte is coupled to N_f fibroblasts, which are in a layer above the myocyte cell layer as described in detail in Ref. 16. Now we introduce heterogeneity, which results in a gradient in the density of fibroblasts, we removing all the N_f fibroblasts that are coupled to a myocyte at a site, so that the percentage of myocyte cells, at which we retain the myocyte-fibroblast coupling, is p_f . To study gradients in the density of fibroblasts, we use a space-dependent density that varies linearly as we move away from chosen central site:

$$p_f(r_i) = p_f(r_0) - \frac{[p_f(r_0) - p_f(r_{max})]}{[r_{max} - r_0]} \times r_i, \quad (5)$$

where r_i is the distance from the centre, r_0 is the position of the centre, and r_{max} is maximum radial distance from the centre.

2.2 Numerical Methods

We update the ODEs via the forward-Euler method for **Eqs 1, 4**. For our two-dimensional (2D) tissue simulations as in **Eq. 2** we use a square domain with $N \times N$ grid points with $N = 512$, the forward-Euler scheme for time marching, and a central-difference scheme with a five-point stencil for the Laplacian, with the time and space steps $\Delta t = 0.02$ ms and $\Delta x = 0.025$ cm, respectively. The control value of the diffusion coefficient $D = D_0$, with $D_0 = 0.001$ 54 cm²/ms, which gives us a conduction velocity

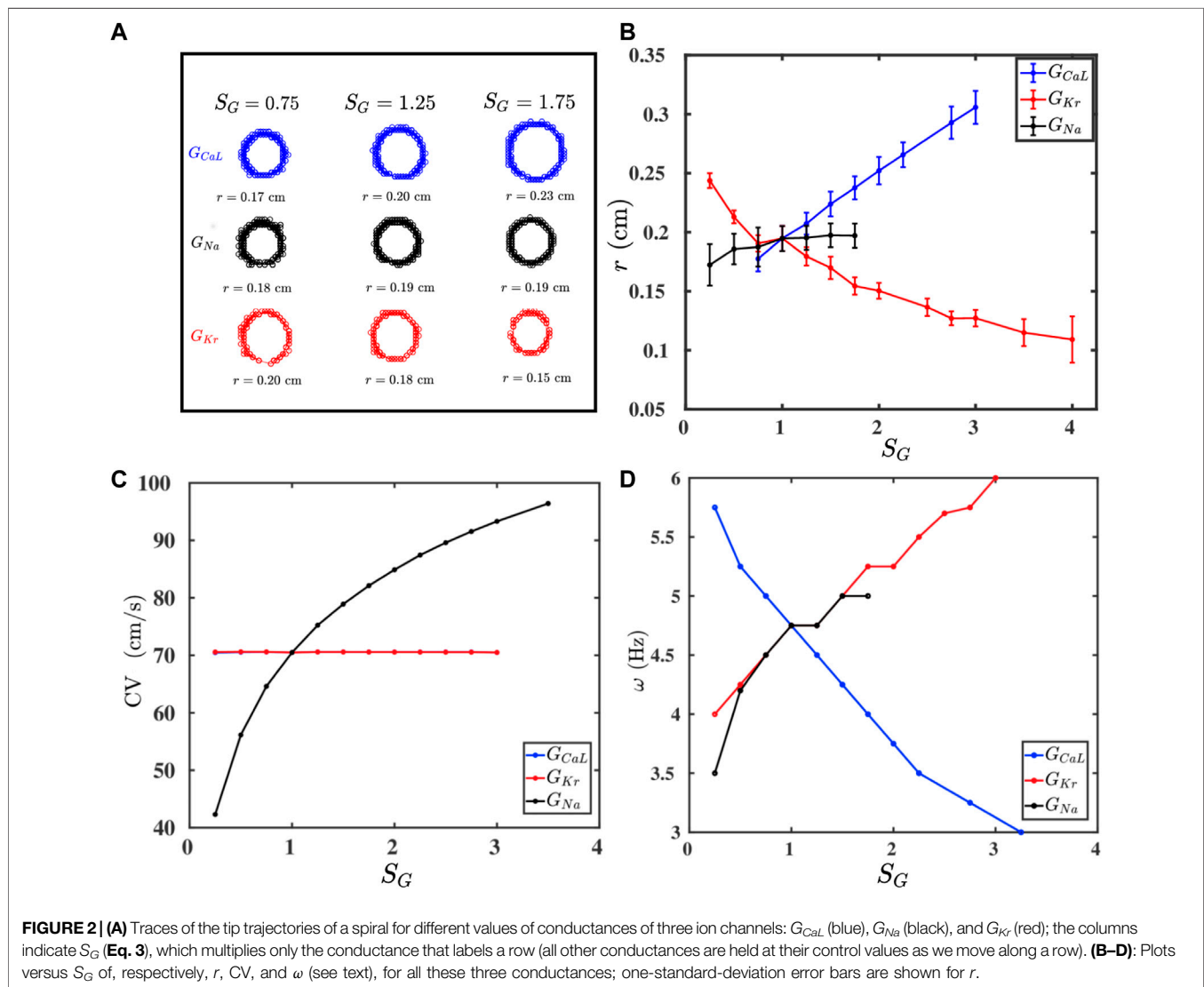
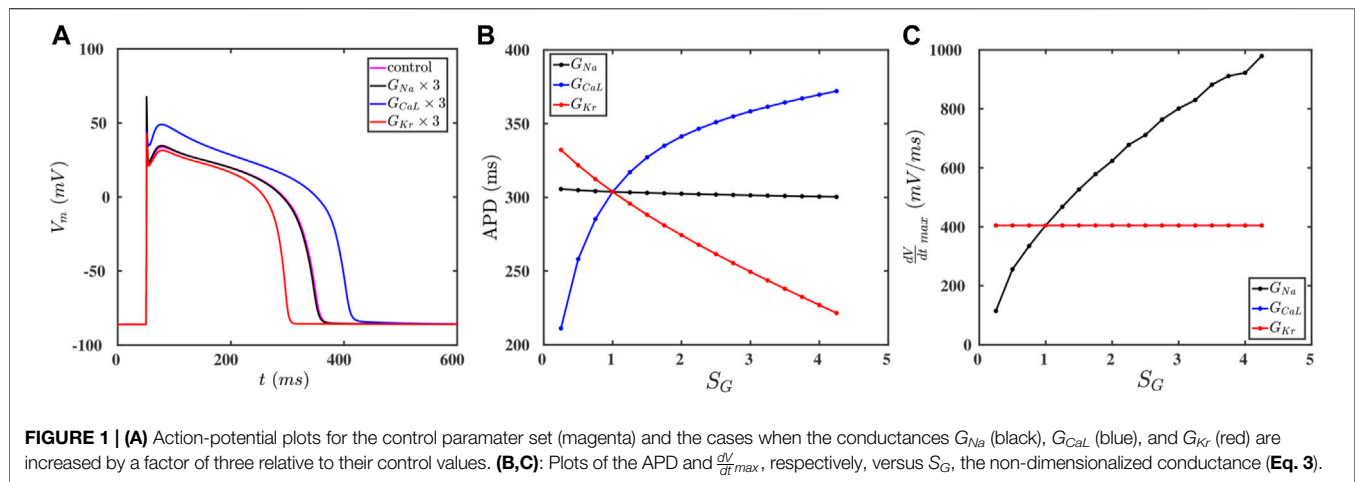
$CV \approx 70$ cm/s, as has been reported for human-ventricular-tissue models [43, 46].

2.3 Data Acquisition

- We generate a spiral wave by the cross-field protocol; we pass a traveling plane wave (S1) from one end of the domain; and when the wave back of S1 reaches the middle of the domain, we pass another plane wave (S2) perpendicular to S1; when the wavefront of S2 meets the wave back of S1, a phase singularity is created at the junction; this creates a spiral wave [see **Supplementary Figure S1**].
- We calculate the frequency ω by recording the time-series of the transmembrane potential V_m at four representative positions in the simulation domain. From the principal peak in the Fourier transforms of these time series, we obtain ω (we take the average of the values at the four representative positions). [We show in **Supplementary Table S1**] that this frequency is within error bars of the frequency ω_{tip} of rotation of the tip of the spiral wave.]
- For the radius of the tip trajectory of rigidly rotating spiral waves, which is, on average, circular, we fit the average trajectory to a circle with radius r and center (x_c, y_c) , by using a nonlinear regression model, to obtain the mean radius and the mean values of the coordinates of the center of the circle; we also calculate the standard deviation of the fluctuations in r by using the mean position of the center (x_c, y_c) and the coordinates (x, y) of the points that lie on the unaveraged tip trajectory that we compute.
- We calculate CV by pacing the simulation domain at one end with a pacing cycle length of 1 Hz; we use 20 pulses. We record the time series of V_m at two designated grid points A and B , which are separated by a distance l_{AB} . These grid points are chosen such that the line between the two grid points is normal to the wavefront. We obtain the times t_A and t_B at which the wavefront hits the grid points A and B , respectively; the difference $t_B - t_A$ gives the time taken by the wavefront to propagate A to B ; therefore, $CV = \frac{l_{AB}}{(t_B - t_A)}$. In the disordered case, with inexcitable obstacles distributed at random in the simulation domain, we record the time series of V_m at multiple points and repeat the above procedure; we then take the mean of the CVs obtained from these points; we also compute the standard deviation of the CVs (see **Supplementary Table S2**).

3 RESULTS

We present the results of our *in-silico* studies as follows: In **Section 3.1** we examine the dependence of the AP and of ω on various ion-channel conductances. **Section 3.2** is devoted to the effects of the gap-junctional coupling on ω . In **Section 3.3** we investigate the effects of the fibroblast-myocyte coupling on the myocyte AP and ω . We elucidate the drift of spiral waves in domains with an inhomogeneous distribution of fibroblasts in **Section 3.4**.



3.1 Effects of Conductances on the AP and the Spiral-Wave Frequency ω

The cell membrane of a myocyte is embedded with various ion channels, which we list in **Table 1**; V_m depends on the currents through these ion channels (**Eq. 1**), so, if we vary the conductances of these channels, we can modulate the AP of the myocyte. To study the effects of these ion channels on the AP, we choose three representative major ionic currents for our study: I_{Na} , I_{CaL} , and I_{Kr} . **Figure 1A** shows the APs of a myocyte for control values (magenta) and for the cases where the conductances G_{Na} (black), G_{CaL} (blue), and G_{Kr} (red) are increased three-fold. We find that increasing G_{CaL} (G_{Kr}) increases (decreases) the APD, whereas G_{Na} has no significant effect on the APD (**Figure 1B**). This is because the inward current I_{CaL} augments depolarization, and I_{Kr} , being an outward current, enhances repolarization; although I_{Na} is an inward current, it is active only during the early upstroke phase of the AP, therefore, it cannot affect the APD significantly. Furthermore, we find that increasing G_{Na} increases the upstroke velocity $\frac{dV}{dt}_{max}$, but G_{CaL} and G_{Kr} do not affect on $\frac{dV}{dt}_{max}$ (**Figure 1**). We have also checked the effects of other ion-channel conductances and ion-pump parameters on the AP. The results are consistent with our findings above, namely, increasing (decreasing) the conductances of inward (outward) currents increases (decreases) the APD of the myocyte; and I_{Na} is the only current that can change the value of $\frac{dV}{dt}_{max}$. We give details in **Supplementary Figure S1**.

We now study how these changes in $\frac{dV}{dt}_{max}$ and the APD affect the dynamics of a spiral wave. In **Figure 2A** we show spiral-tip trajectories and how the radius r , of the averaged circular trajectory, varies with the three conductances G_{CaL} (blue), G_{Na} (black), and G_{Kr} (red); the columns are labelled by the values of S_G (**Eq. 3**), which multiply only the conductance that labels a row (all other conductances are held at their control values as we move along a row in **Figure 2A**). In **Figures 2B–D** we give plots versus S_G of, respectively, r , CV, and ω , for all these three conductances. In particular, we find that ω increases if we increase the values of G_{Na} and G_{Kr} ; by contrast, ω decreases as we increase G_{CaL} . This is consistent with the variation of r and of CV with S_G (**Figures 2B,C**), for ω is related to r and CV as in **Eq. 6**.

$$\omega \propto \frac{CV}{2\pi r} \quad (6)$$

If we raise the values of G_{CaL} and G_{Kr} , then we find an increase and decrease the spiral core radius r , respectively, whereas G_{Na} has no significant effect on the value of r (**Figure 2B**). Furthermore, **Figure 2C** shows that CV increases with G_{Na} , whereas G_{CaL} and G_{Kr} do not affect CV; this is because only G_{Na} affects the value of $\frac{dV}{dt}_{max}$ (**Figure 1C**), which determines how fast a myocyte is excited and, therefore, how rapidly a wave of excitation propagates through our cardiac-tissue model. This result, along with **Figure 1B**, implies that the change in the APD is associated with the change in the value of r ; a large (small) value of the APD is associated with a large (small) value of r ; and conductances such as G_{Na} have no significant effect on the APD because they do not affect r substantially. We have also checked

this correlation between the APD and r for other conductances (see **Supplementary Figure S2**) and have found similar results. In summary, the rise of ω with the increase of G_{Na} is primarily because of the increase in CV, and the decline (rise) of ω , with the increase of G_{CaL} (G_{Kr}), can be attributed principally because to the increase (decrease) in r .

3.2 Effect of the Gap-Junctional Coupling on ω

The strength of the gap-junctional coupling between the cells in cardiac tissue can change in diseased conditions, e.g., in the wake of a myocardial infarction [47–49]. It is, therefore, instructive to investigate the role of the diffusive coupling between the cells on spiral-wave dynamics. To study the effect of D on ω , we first plot, in **Figure 3A**, r (blue curve) and CV (red curve) versus S_D , the non-dimensionalised diffusion constant in **Eq. 3**; this shows that both r and CV increase with S_D , because a high diffusive coupling enhances the propagation of waves. The increase in CV is offset by the increase in r , so ω (see **Eq. 6**) does not depend on S_D significantly, as we show in **Figure 3B**.

We can also reduce the effective coupling strength between the cells in the medium by interspersing the medium with inexcitable point obstacles. These obstacles mimic collagen deposits in fibrotic tissue [38, 50]. The random distribution of these obstacles disrupts the propagation of a wave, as we show by the pseudocolor plots of V_m in **Figure 4A**; and it reduces the velocity of the wave [37, 44, 47]. In **Figure 4B** we plot CV versus p_o ; clearly, CV decreases as the obstacle density p_o increases; and beyond $p_o \approx 38\%$, we observe conduction block with CV = 0. This result is consistent with the earlier study in Ref. 51. This reduction in CV, with the increase of p_o , contributes to the decline of ω with increasing p_o , which we depict by the plot in **Figure 4C**. Furthermore, because of the disorder-induced corrugated wavefront (**Figure 4A**), it becomes difficult to track the spiral-tip trajectory for $p_o > 10\%$; for $p_o < 10\%$, the value of r remains unaltered (see **Supplementary Figure S3**). Nonetheless, the simultaneous decrease of ω and CV, as we increase p_o , tells us that the change in CV is responsible principally for the variation of ω .

3.3 Effect of the Fibroblast-Myocyte Coupling on AP Properties and ω

Fibroblast cells, which maintain the structural integrity of a heart, are known to (a) proliferate in diseased conditions [38, 39] and (b) form gap-junctional couplings with myocytes. Such couplings can modulate the electrophysiological properties, e.g., of the AP, of the myocytes [45, 52, 53]. We show in **Figures 5A,B**, how the fibroblast-myocyte coupling affects the AP morphology, APD, and $\frac{dV}{dt}_{max}$ for different values of fibroblast resting potential E_f and the number N_f of fibroblasts coupled to a myocyte in **Model-II**. We see that the APD and $\frac{dV}{dt}_{max}$ increase and decrease, respectively, as we increase E_f . For a fixed value of E_f , increasing N_f decreases both APD and $\frac{dV}{dt}_{max}$. This is because fibroblasts act as current sinks when coupled to myocytes. These changes in the properties of the AP, because of the fibroblast-myocyte coupling, affect the dynamics of wave at the tissue level. We show in **Figure 5C** that the rise in the APD and the decline in

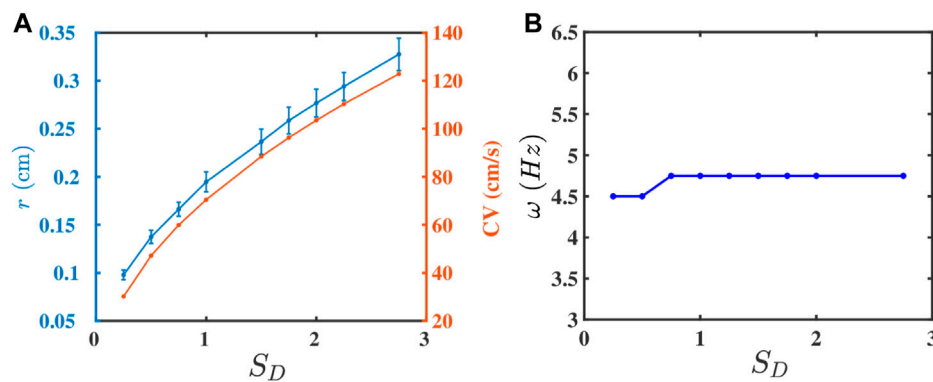


FIGURE 3 | Plots versus S_D (Eq. 3) of (A) r (blue curve) and CV (red curve) and (B) ω .

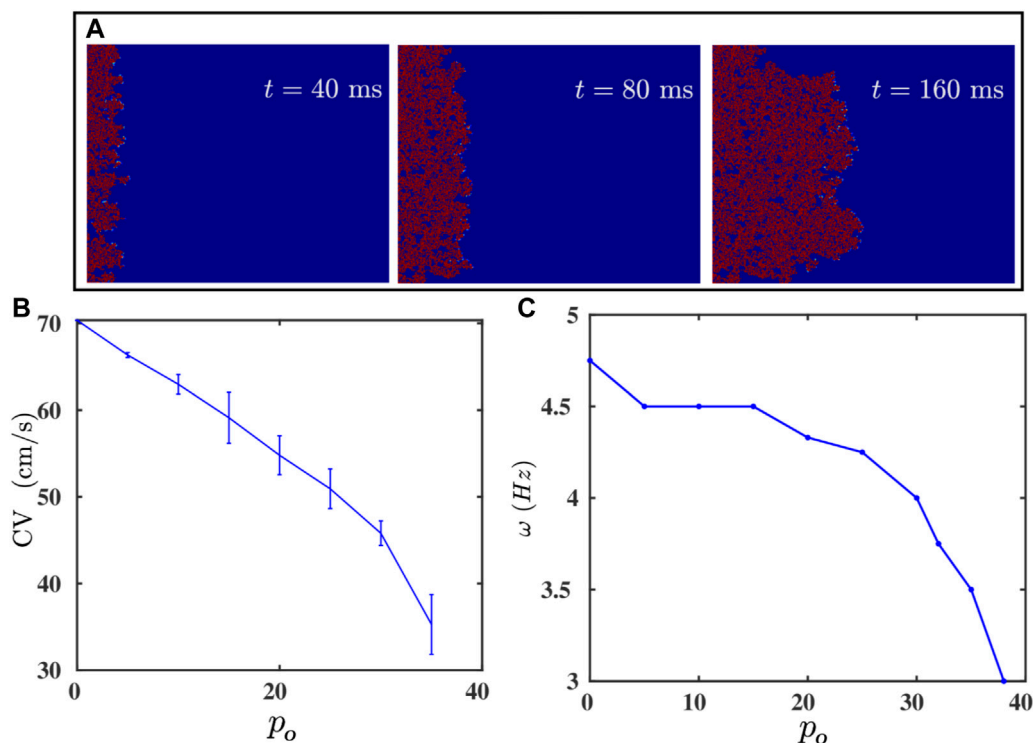


FIGURE 4 | (A) Pseudocolor plots of V_m illustrating the propagation of a plane wave through the simulation domain with randomly distributed inexcitable obstacles (Model-I); the obstacle density $p_o = 35\%$. (B,C): Plots versus p_o of the plane-wave conduction velocity CV and the spiral-wave frequency ω . CV vanishes after $p_o \geq 38\%$; i.e., there is conduction block.

$\frac{dV}{dt}_{max}$ (Figure 5B) increases and decreases the values of r and CV, respectively, as we increase E_f . In Figure 5D we show how the combination of these effects on CV and r affect the variation of ω with E_f and N_f .

3.4 Drift of Spiral Waves in Domains With an Inhomogeneous Distribution of Fibroblasts

Fibrosis is a natural wound-healing process that occurs in the heart after a patient suffers from a condition such as infarction

or heart attack [40–42], and such fibrotic tissue can affect the propagation of excitation waves [14, 37, 47, 48, 54, 55], which can promote arrhythmias. We now show how a heterogeneous density of fibroblasts in the medium (Model-II) can affect the dynamics of a spiral wave. Figure 6A shows the heterogeneous distribution of fibroblasts in the medium; here, yellow indicates fibroblast-myocyte composites and blue indicates myocytes. The density of fibroblasts decreases radially outwards from the centre that is marked by a red octagram in Figure 6A (Section 2; Eq. 5). Figure 6B shows the spatial variation of the

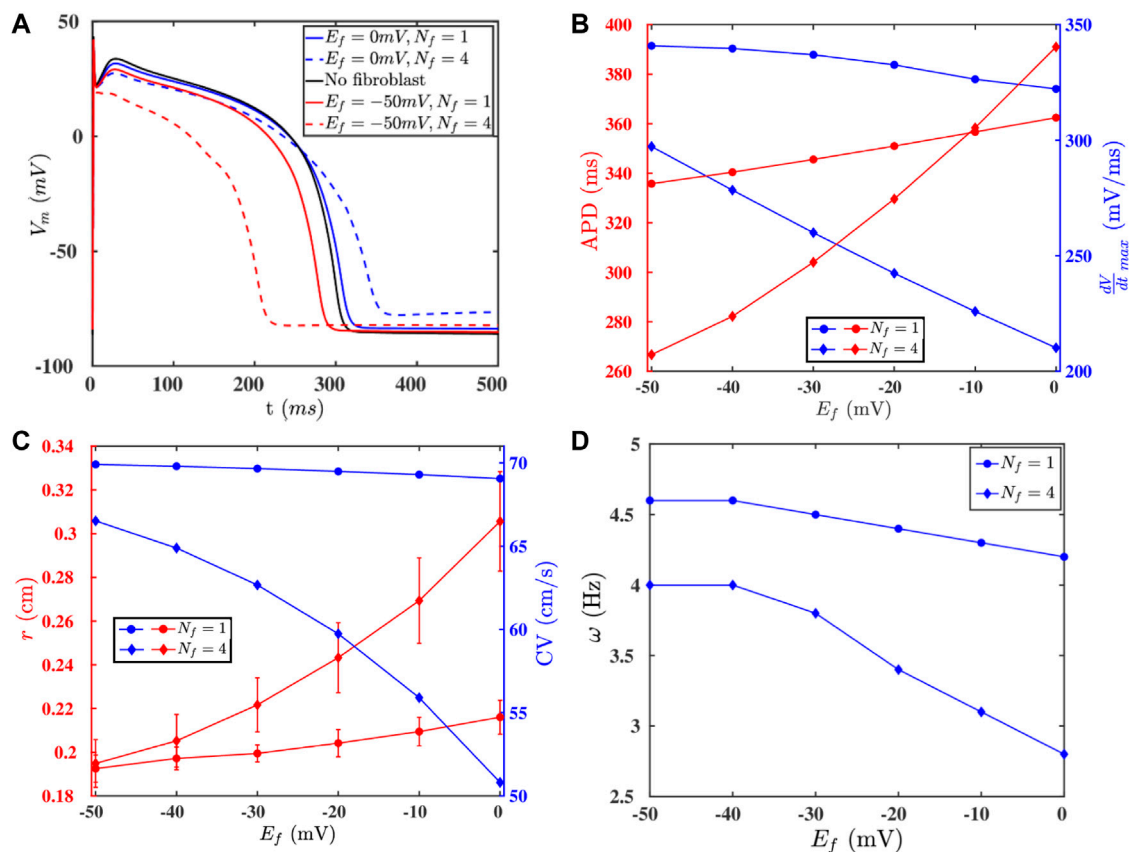


FIGURE 5 | (A) APs of an isolated myocyte (black -) and a myocyte coupled to fibroblasts with various parameters: $E_f = 0$ mV, $N_f = 1$ (blue -); $E_f = 0$ mV, $N_f = 4$ (blue - -); $E_f = -50$ mV, $N_f = 1$ (red -); $E_f = -50$ mV, $N_f = 4$ (red - -). **(B)** The values of the APD and $\frac{dV}{dt}_{max}$ for different values of E_f and two different values of N_f . **(C)** The values of r and CV for different values of E_f and two different values of N_f . **(D)** The variation of ω with changes in E_f for two different values of N_f .

APD in the medium because of the heterogeneous fibroblast density. **Figures 6C,D** show the spatiotemporal evolution of a spiral in this case. It shows that a spiral, initiated at the left side of the domain in the region with a low density of fibroblasts, drifts towards the region with a high density of fibroblasts; and the spiral remains anchored to the central region, where the fibroblast density is maximum. The trajectory of the spiral tip is shown in white in **Figure 6D** (see also the **Supplementary Movie M1**). In **Figure 6D**, we have shown the drift data up until a simulation duration of $t = 60$ s. The spiral indeed goes near to the red star (highest fibrotic density region shown in **Figure 6A**), anchors to it, and becomes stable (at $t = 114$ s); and the spiral does not meander after anchoring. This can be observed in the **Supplementary Movie M1** provided in the **Supplementary Material**. This drifting of a spiral towards the region with a high density of fibroblasts is associated with the tendency of the spiral wave to drift towards the region with the highest value of the APD [33, 34, 56–58]. Such anchoring of a spiral wave to a region with a high density of fibrosis has been seen in experiments on real hearts [23, 28, 59–61]. Our study illustrates how a region with a high density of fibroblasts can behave like an attractor and an anchoring point for spiral waves in fibrotic tissue. Such drifting of a spiral wave, in a medium

with heterogeneity, has also been reported in other studies in contexts other than fibrosis [33, 34, 56–58].

4 DISCUSSION

We have used *in silico* simulations of detailed mathematical models for cardiac tissue to examine the effects of various electrophysiological parameters of a cardiac cell and cardiac tissue on the AP properties and on electrical-wave dynamics. Our work is of relevance when spiral waves are formed in real hearts where there are gradients in electrophysiological parameters along the transmural [36, 62, 63] and the apico-basal [64, 65] directions. Moreover, heterogeneities can also be induced in the heart because of diseases [64, 66–68]. In this context, we have shown how changes in various ion-channel conductances of a myocyte or the fibroblast-myocyte coupling can modulate the AP of a myocyte. We have then checked how these changes affect the spiral-wave frequency ω . We find that an increase (decrease) in $\frac{dV}{dt}_{max}$ or decrease (increase) in the APD increases (decreases) ω : large values of $\frac{dV}{dt}_{max}$ increase CV; and a low APD is associated with low values of the mean spiral-tip-trajectory radius r ; these are related to ω through **Eq. 6**. Our study

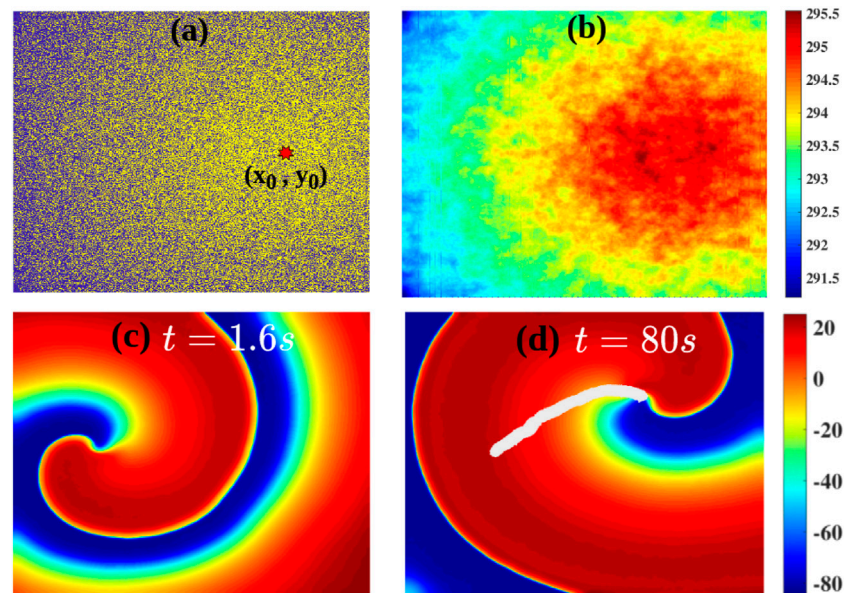


FIGURE 6 | (A) The radially decreasing distribution of the fibroblast density (**Model-II Eq. 5**) away from a center, marked by a red octagram; yellow indicates fibroblast-myocyte composites and blue denoted myocytes. **(B)** The distribution of the APD because of the gradient in fibroblast density. **(C,D)**: Pseudocolor plots of V_m showing a spiral wave in the simulation domain: a spiral initiated in the small-APD region, proximal to the left boundary, drifts towards the large-APD (low- ω) region. The tip trajectory of the spiral is marked by the white line.

has provided a natural understanding of how changes in the AP, at the single-myocyte level, can be related to changes in ω at the cardiac-tissue level. Moreover, we have investigated how changes in the gap-junctional coupling between the cells and S_D affect ω . We have also reduced the effective coupling between the cells by interspersing the medium with inexcitable obstacles; ω changes with the density of the obstacles. It is of interest to investigate such effects on ω , because they provide insights into spiral-wave dynamics in excitable media with heterogeneities [68]. We illustrate this in detail in **Figure 6** for a simulation domain with a heterogeneous distribution of fibroblast; here, we demonstrate the drift of a spiral wave towards the region with a high density of fibroblasts; such a drift has been seen in real hearts [23, 59–61].

We have explored the validity of the frequency relation **Eq. 6** (Ref. 15) for a wide range of electrophysiological parameters in the models that we use. We show in **Supplementary Figure S1** that our measurements of ω and $\frac{CV}{r}$ are consistent with a linear relation (see the fit that is indicated by a black line); at very low values of CV, e.g., near conduction block in **Model-I** which accounts for fibrosis-induced disorder, this linear relation breaks down. The randomness in these models introduces errors in the determination of r of the spiral wave, especially for large randomness; e.g., as we increase p_f , we observe, in **Supplementary Figure S6** that the tip trajectory of the spiral wave becomes very noisy. Note also that the CV of a plane wave is distinct from CV_{tip} the velocity of the tip of the spiral wave as it goes around its trajectory (on average a circle with radius r); clearly, $\omega_{tip} = CV_{tip}/(2\pi r)$ (see **Supplementary Table S1**).

Some earlier studies have investigated the properties of spiral waves in two-variable mathematical models for cardiac [69–75].

However, such studies have been conducted in the weak- or strong-excitability limits; real cardiac tissue exhibits various degrees of excitability depending on different electrophysiological parameters. Our study, which employs electrophysiologically detailed mathematical models for cardiac tissue, has allowed us to study spiral-wave dynamics with greater realism than is possible with two-variable models for cardiac tissue. The drifting of a spiral wave towards regions with a large APD has been reported in contexts other than fibrosis [33, 34, 56–58]. Moreover, anomalous drift of a spiral towards a region with a small APD, which has been observed in generic models [34], is not seen in our study; and it is yet to be reported in any of the electrophysiologically-detailed mathematical models for the cardiac tissue. It is also observed in the two-variable models that the radius of the spiral tip trajectory is very large, in the weakly excitable limit, compared to what is observed in the strongly excitable limit [72, 76].

In our realistic models, if we consider two parameters that control excitability, e.g., G_{Na} and D , then we observe that r does not increase with a decrease in the value of G_{Na} (**Figure 2**); but we observe an increase in r , as we increase the value of D (see **Supplementary Figure S5**). Hence, our systematic study, which uses a detailed human-ventricular-tissue mathematical model, provides an important point of reference for future *in silico* and experimental studies of such spiral waves in cardiac tissue.

For the study of spiral-wave dynamics in the fibrosis, we have considered two types of models for fibrosis: (a) **Model-I** and (b) **Model-II** (**Section 2**). With these models we have investigated the following: The change of ω in (i) **Model-I** and (ii) **Model-II** as we change fibrosis parameters such as p_o (in **Model-I**) and N_f and E_f (in **Model-II**). (iii) In **Model-II** we show that ω decreases with an

increase in N_f in homogeneous fibrotic tissue. Furthermore, we consider a heterogeneous model, based on **Model-II**, in which the fibroblast density P_f (number density of myocyte cells coupled to N_f fibroblast cells at a site) is highest at a central site and decreases outwards from this center. We find that a spiral wave, initiated far away from the center where P_f is low, drifts towards the region with the highest fibroblast density, i.e., the center, which has the lowest ω . There are earlier studies in this direction such as in Refs. 77, 78 that uses **Model-I** type fibrosis. The study of Ref. 77, induces spiral waves by a bursting or pacing mechanism and investigates the dependence of ω on the fibrosis density (Model of type I). This study shows that ω is dependent on the maximal local fibrosis density. The study in Ref. 78, considers a local fibrotic region (**Model-I** type) and studies the anchoring of a spiral wave initiated far from this region. The mechanism of anchoring here involves the breaking up of the spiral waves around the fibrotic tissue and a consequent alteration of the initial spiral wave; this is eventually driven near to the fibrotic tissue and is then anchored around it. However, our study investigates the drift of the spiral wave in **Model-II** and shows the experimentally observed drift of spiral waves towards the region of highest fibroblast density. Also, our gradient in the fibroblast density based on **Model-II**, in contrast to that of Refs. 77, 78, uses a continuous gradient in the fibroblast density and, in addition, with fibroblasts that are treated as passive, but electrically active, cells. We note that, multiple studies have shown that fibroblast cells are electrically active, especially in the context of infarction (see, e.g., Refs. 14, 49, 53, 79, 80). Such fibroblasts are used in our **Model-II** but not in the studies mentioned in Refs. 77, 78. Thus, our work extends considerably these earlier studies.

4.1 Limitations of Our Study

We end our discussion with some limitations in our study. We have used a monodomain model for cardiac tissue. Bidomain models of cardiac tissue account for the extracellular matrix. However, monodomain models have been proved to be good approximations of cardiac tissue for wave propagation [81] for the types of excitations we consider. Furthermore, our tissue model does not incorporate the effects of mechanical deformations, stretch-activated channels, and stress-dependent diffusion tensors [82–84]. Such deformations

can affect the dynamics of spiral waves [85] and the drift of spirals in a heterogeneous medium; we defer an investigation of the interplay between deformation and drift for future work.

DATA AVAILABILITY STATEMENT

The equations of the ionic currents, ion-dynamics and the parameter values used in the TP06 model required to reproduce our simulations are been provided in the data sheet 2 file.

AUTHOR CONTRIBUTIONS

MKM and SZ designed the problem; MKM performed the numerical simulations; MKM together with SZ and RP, did the analysis; MKM, SZ and RP wrote the manuscript.

FUNDING

We thank SERB (India) JC Bose fellowship grant no: SR/S2/JCB-17/2007 and the National Supercomputing Mission (NSM-India) grant no: DST/NSM/HPC_Applications/2021-1500, and CSIR (India) for the financial support and the Supercomputer Education and Research Centre (SERC, IISc) for computational resources.

SUPPLEMENTARY MATERIAL

The Supplementary Material for this article can be found online at: <https://www.frontiersin.org/articles/10.3389/fphy.2021.819873/full#supplementary-material>

Data Sheet 1 | We provide the additional details of our simulations in this file.

Data Sheet 2 | The normal parameter values and the equations for the 12 currents and ion-dynamics of the TP06 model is provided in this file.

Movie-M1 | This movie shows the drift of the spiral waves in the gradient of the fibroblast density.

REFERENCES

1. Zaikin AN, Zhabotinsky AM. Concentration Wave Propagation in Two-Dimensional Liquid-phase Self-Oscillating System. *Nature* (1970) 225(5232):535–7. doi:10.1038/225535b0
2. Winfree AT. Spiral Waves of Chemical Activity. *Science* (1972) 175(4022):634–6. doi:10.1126/science.175.4022.634
3. Field RJ. *Chaos in Chemistry and Biochemistry*. Singapore: World Scientific (1993).
4. Ott E. *Chaos in Dynamical Systems*. Cambridge, United Kingdom: Cambridge University Press (2002).
5. Strogatz SH. *Nonlinear Dynamics and Chaos with Student Solutions Manual: With Applications to Physics, Biology, Chemistry, and Engineering*. Boca Raton, FL: CRC Press (2018).
6. Falcke M, Bär M, Engel H, Eiswirth M. Traveling Waves in the CO Oxidation on Pt(110): Theory. *J Chem Phys* (1992) 97(6):4555–63. doi:10.1063/1.463900
7. Imbihl R, Ertl G. Oscillatory Kinetics in Heterogeneous Catalysis. *Chem Rev* (1995) 95(3):697–733. doi:10.1021/cr00035a012
8. Pande A, Pandit R. Spatiotemporal Chaos in a Model for Co Oxidation on Pt (110). In: 4th Meeting of the Royal-Society-Unilever-Indo-UK Forum in Materials Science and Engineering (1999).
9. Lechleiter J, Girard S, Peralta E, Clapham D. Spiral Calcium Wave Propagation and Annihilation in xenopus Laevis Oocytes. *Science* (1991) 252(5002):123–6. doi:10.1126/science.2011747
10. Tyson JJ, Murray JD. Cyclic Amp Waves During Aggregation of Dictyostelium Amoebae. *Development* (1989) 106(3):421–6. doi:10.1242/dev.106.3.421
11. Rietdorf J, Siegert F, Weijer CJ. Analysis of Optical Density Wave Propagation and Cell Movement During Mound Formation in *Dictyostelium discoideum*. *Developmental Biol* (1996) 177(2):427–38. doi:10.1006/dbio.1996.0175

12. Panfilov AV, Vasiev BN. Vortex Initiation in a Heterogeneous Excitable Medium. *Physica D: Nonlinear Phenomena* (1991) 49(1-2):107. doi:10.1016/0167-2789(91)90200-s
13. Lim ZY, Maskara B, Aguel F, Emokpae R, Tung L. Spiral Wave Attachment to Millimeter-Sized Obstacles. *Circulation* (2006) 114(20):2113–21. doi:10.1161/circulationaha.105.598631
14. Xie Y, Garfinkel A, Camelliti P, Kohl P, Weiss JN, Qu Z. Effects of Fibroblast-Myocyte Coupling on Cardiac Conduction and Vulnerability to Reentry: a Computational Study. *Heart Rhythm* (2009) 6(11):1641–9. doi:10.1016/j.hrthm.2009.08.003
15. Qu Z, Hu G, Garfinkel A, Weiss JN. Nonlinear and Stochastic Dynamics in the Heart. *Phys Rep* (2014) 543(2):61–162. doi:10.1016/j.physrep.2014.05.002
16. Nayak AR, Shajahan TK, Panfilov AV, Pandit R. Spiral-wave Dynamics in a Mathematical Model of Human Ventricular Tissue with Myocytes and Fibroblasts. *PLoS one* (2013) 8(9):e72950. doi:10.1371/journal.pone.0072950
17. Nayak AR, Pandit R. Turbulent States and Their Transitions in Mathematical Models for Ventricular Tissue: The Effects of Random Interstitial Fibroblasts. *Phys Rev E Stat Nonlin Soft Matter Phys* (2015) 92(3):032720. doi:10.1103/PhysRevE.92.032720
18. Zimik S, Pandit R. Reentry via High-Frequency Pacing in a Mathematical Model for Human-Ventricular Cardiac Tissue With a Localized Fibrotic Region. *Sci Rep* (2017) 7(1):15350. doi:10.1038/s41598-017-15735-5
19. Allesie MA, Bonke FI, Schopman FJ. Circus Movement in Rabbit Atrial Muscle as a Mechanism of Tachycardia. III. The "Leading Circle" Concept: a New Model of circus Movement in Cardiac Tissue Without the Involvement of an Anatomical Obstacle. *Circ Res* (1977) 41(1):9–18. doi:10.1161/01.res.41.1.9
20. Gray RA, Pertsov AM, Salomonsz R, Jafar J. Spatial and Temporal Organization During Cardiac Fibrillation. *Nature* (1998) 392(6671):75–8. doi:10.1038/32164
21. Pertsov AM, Davidenko JM, Salomonsz R, Baxter WT, Jafar J. Spiral Waves of Excitation Underlie Reentrant Activity in Isolated Cardiac Muscle. *Circ Res* (1993) 72(3):631–50. doi:10.1161/01.res.72.3.631
22. Davidenko JM, Kent PF, Chialvo DR, Michaels DC, Jafar J. Sustained Vortex-Like Waves in Normal Isolated Ventricular Muscle. *Proc Natl Acad Sci* (1990) 87(22):8785–9. doi:10.1073/pnas.87.22.8785
23. Davidenko JM, Pertsov AM, Salomonsz R, Baxter W, Jafar J. Stationary and Drifting Spiral Waves of Excitation in Isolated Cardiac Muscle. *Nature* (1992) 355(6358):349–51. doi:10.1038/355349a0
24. Gray RA, Jafar J, Panfilov A, Baxter WT, Cabo C, Davidenko JM, et al. Nonstationary Vortexlike Reentrant Activity as a Mechanism of Polymorphic Ventricular Tachycardia in the Isolated Rabbit Heart. *Circulation* (1995) 91(9):2454–69. doi:10.1161/01.cir.91.9.2454
25. Bray M-A, Lin S-F, Wikswo J. Three-Dimensional Visualization of Phase Singularities on the Isolated Rabbit Heart. *J Cardiovasc Electrophysiol* (2002) 13(12):1311. doi:10.1046/j.1540-8167.2002.01311.x
26. Valderrábano M, Chen PS, Lin SF. Spatial Distribution of Phase Singularities in Ventricular Fibrillation. *Circulation* (2003) 108(3):354–9. doi:10.1161/01.CIR.0000080322.67408.B4
27. Pandit SV, Jafar J. Rotors and the Dynamics of Cardiac Fibrillation. *Circ Res* (2013) 112(5):849–62. doi:10.1161/CIRCRESAHA.111.300158
28. ten Tusscher KH, Panfilov AV. Reentry in Heterogeneous Cardiac Tissue Described by the Luo-Rudy Ventricular Action Potential Model. *Am J Physiol Heart Circ Physiol* (2003) 284(2):H542–8. doi:10.1152/ajpheart.00608.2002
29. Clayton RH, Bernus O, Cherry EM, Dierckx H, Fenton FH, Mirabella L, et al. Models of Cardiac Tissue Electrophysiology: Progress, Challenges and Open Questions. *Prog Biophys Mol Biol* (2011) 104(1):22–48. doi:10.1016/j.pbiomolbio.2010.05.008
30. Alonso S, dos Santos RW, Bär M. Reentry and Ectopic Pacemakers Emerge in a Three-Dimensional Model for a Slab of Cardiac Tissue With Diffuse Microfibrosis Near the Percolation Threshold. *PLoS one* (2016) 11(11):e0166972. doi:10.1371/journal.pone.0166972
31. Zimik S, Pandit R. Instability of Spiral and Scroll Waves in the Presence of a Gradient in the Fibroblast Density: the Effects of Fibroblast-Myocyte Coupling. *New J Phys* (2016) 18(12):123014. doi:10.1088/1367-2630/18/12/123014
32. Zimik S, Pandit R, Majumder R. Anisotropic Shortening in the Wavelength of Electrical Waves Promotes Onset of Electrical Turbulence in Cardiac Tissue: An In Silico Study. *Plos one* (2020) 15(3):e0230214. doi:10.1371/journal.pone.0230214
33. Krinsky V, Hamm E, Voignier V. Dense and Sparse Vortices in Excitable media Drift in Opposite Directions in Electric Field. *Phys Rev Lett* (1996) 76(20):3854–7. doi:10.1103/physrevlett.76.3854
34. Sridhar S, Sinha S, Panfilov AV. Anomalous Drift of Spiral Waves in Heterogeneous Excitable media. *Phys Rev E Stat Nonlin Soft Matter Phys* (2010) 82(5):051908. doi:10.1103/PhysRevE.82.051908
35. Biktashev VN, Biktasheva IV, Sarvazyan NA. Evolution of Spiral and Scroll Waves of Excitation in a Mathematical Model of Ischaemic Border Zone. *PLoS One* (2011) 6(9):e24388. doi:10.1371/journal.pone.0024388
36. Wolk R, Cobbe SM, Hicks MN, Kane KA. Functional, Structural, and Dynamic Basis of Electrical Heterogeneity in Healthy and Diseased Cardiac Muscle Implications for Arrhythmogenesis and Anti-arrhythmic Drug Therapy. *Pharmacol Ther* (1999) 84(2):207–31. doi:10.1016/s0163-7258(99)00033-9
37. ten Tusscher KH, Alexander V. Wave Propagation in Excitable media with Randomly Distributed Obstacles. *Multiscale Model Simulation* (2005) 3(2):265–82. doi:10.1137/030602654
38. Weber KT, Sun Y, Tyagi SC, Cleutjens JPM. Collagen Network of the Myocardium: Function, Structural Remodeling and Regulatory Mechanisms. *J Mol Cell Cardiol* (1994) 26(3):279–92. doi:10.1006/jmcc.1994.1036
39. Manabe I, Shindo T, Nagai R. Gene Expression in Fibroblasts and Fibrosis. *Circ Res* (2002) 91(12):1103–13. doi:10.1161/01.res.0000046452.67724.b8
40. Gurtner GC, Werner S, Barrandon Y, Longaker MT. Wound Repair and Regeneration. *Nature* (2008) 453:314–21. doi:10.1038/nature07039
41. Biernacka A, Frangogiannis NG. Aging and Cardiac Fibrosis. *Aging Dis* (2011) 2(2):158–73.
42. Hinderer S, Schenke-Layland K. Cardiac Fibrosis - A Short Review of Causes and Therapeutic Strategies. *Adv Drug Deliv Rev* (2019) 146:77–82. doi:10.1016/j.addr.2019.05.011
43. ten Tusscher KH, Panfilov AV. Alternans and Spiral Breakup in a Human Ventricular Tissue Model. *Am J Physiol Heart Circ Physiol* (2006) 291(3):H1088–100. doi:10.1152/ajpheart.00109.2006
44. Majumder R, Nayak AR, Pandit R. Nonequilibrium Arrhythmic States and Transitions in a Mathematical Model for Diffuse Fibrosis in Human Cardiac Tissue. *PLoS one* (2012) 7(10):e45040. doi:10.1371/journal.pone.0045040
45. Andrew MacCannell K, Bazzazi H, Chilton L, Shibukawa Y, Clark RB, Giles WR. A Mathematical Model of Electrotone Interactions between Ventricular Myocytes and Fibroblasts. *Biophysical J* (2007) 92(11):4121–32. doi:10.1529/biophysj.106.101410
46. ten Tusscher KH, Noble D, Noble PJ, Panfilov AV. A Model for Human Ventricular Tissue. *Am J Physiol Heart Circ Physiol* (2004) 286(4):H1573–89. doi:10.1152/ajpheart.00794.2003
47. de Bakker JM, van Capelle FJ, Janse MJ, Tasseron-Vermeulen S, Vermeulen JT, de Jonge-Lahpor N, et al. Slow Conduction in the Infarcted Human Heart. "Zigzag" Course of Activation. *Circulation* (1993) 88(3):915–26. doi:10.1161/01.cir.88.3.915
48. King JH, Huang CL, Fraser JA. Determinants of Myocardial Conduction Velocity: Implications for Arrhythmogenesis. *Front Physiol* (2013) 4:154. doi:10.3389/fphys.2013.00154
49. McDowell KS, Arevalo HJ, Maleckar MM, Trayanova NA. Susceptibility to Arrhythmia in the Infarcted Heart Depends on Myofibroblast Density. *Biophysical J* (2011) 101(6):1307–15. doi:10.1016/j.bpj.2011.08.009
50. Spach MS, Boineau JP. Microfibrosis Produces Electrical Load Variations Due to Loss of Side-To-Side Cell Connections; a Major Mechanism of Structural Heart Disease Arrhythmias. *Pacing Clin Electro* (1997) 20(2):397–413. doi:10.1111/j.1540-8159.1997.tb06199.x
51. Vigmond E, Pashaei A, Amraoui S, Cochet H, Hassaguerre M. Percolation as a Mechanism to Explain Atrial Fractionated Electrograms and Reentry in a Fibrosis Model Based on Imaging Data. *Heart rhythm* (2016) 13(7):1536–43. doi:10.1016/j.hrthm.2016.03.019
52. Jacquemet V, Henriquez CS. Modelling Cardiac Fibroblasts: Interactions with Myocytes and Their Impact on Impulse Propagation. *Europace* (2007) 9 Suppl 6(Suppl. 1):vi29–37. doi:10.1093/europace/eum207
53. Zlochiver S, Muñoz V, Vikstrom KL, Taffet SM, Berenfeld O, Jafar J. Electrotone Myofibroblast-To-Myocyte Coupling Increases Propensity to Reentrant Arrhythmias in Two-Dimensional Cardiac Monolayers. *Biophysical J* (2008) 95(9):4469–80. doi:10.1529/biophysj.108.136473

54. Kawara T, Derksen R, de Groot JR, Coronel R, Tasseron S, Linnenbank AC, et al. Activation Delay after Premature Stimulation in Chronically Diseased Human Myocardium Relates to the Architecture of Interstitial Fibrosis. *Circulation* (2001) 104(25):3069–75. doi:10.1161/hc5001.100833
55. Morgan R, Colman MA, Chubb H, Seemann G, Aslanidi OV. Slow Conduction in the Border Zones of Patchy Fibrosis Stabilizes the Drivers for Atrial Fibrillation: Insights From Multi-Scale Human Atrial Modeling. *Front Physiol* (2016) 7:474. doi:10.3389/fphys.2016.00474
56. An R, Alexander P. Drift and Interaction of Vortices in Two-Dimensional Heterogeneous Active Medium. *Studia Biophys* (1983) 98(3):183–8.
57. Qu Z, Weiss JN. Effects of Na⁺ and K⁺ Channel Blockade on Vulnerability to and Termination of Fibrillation in Simulated Normal Cardiac Tissue. *Am J Physiology-Heart Circulatory Physiol* (2005) 289(4):H1692–H1701. doi:10.1152/ajpheart.00241.2005
58. Berenfeld O. The Major Role of Ik1 in Mechanisms of Rotor Drift in the Atria: A Computational Study. *Clin Med Insights Cardiol* (2016) 10:71–9. doi:10.4137/CMC.S39773
59. Fast VG, Pertsov AM. Drift of Vortex in the Myocardium. *Biofizika* (1990) 35(3):478–82.
60. Jalife J, Gray R. Drifting Vortices of Electrical Waves Underlie Ventricular Fibrillation in the Rabbit Heart. *Acta Physiol Scand* (1996) 157(2):123–32. doi:10.1046/j.1365-201x.1996.505249000.x
61. Roney CH, Bayer JD, Zahid S, Meo M, Boyle PMJ, Trayanova NA, et al. Modelling Methodology of Atrial Fibrosis Affects Rotor Dynamics and Electrograms. *EP Europace* (2016) 18(Suppl. 1_4):iv146–iv155. doi:10.1093/europace/euw365
62. Antzelevitch C, Fish J. Electrical Heterogeneity Within the Ventricular wall. *Basic Res Cardiol* (2001) 96(6):517–27. doi:10.1007/s003950170002
63. McCrossan ZA, Illeter R, White E. Transmural Changes in Size, Contractile and Electrical Properties of Shr Left Ventricular Myocytes During Compensated Hypertrophy. *Cardiovasc Res* (2004) 63(2):283–92. doi:10.1016/j.cardiores.2004.04.013
64. Burton F, Cobbe SM. Dispersion of Ventricular Repolarization and Refractory Period. *Cardiovasc Res* (2001) 50(1):10–23. doi:10.1016/s0008-6363(01)00197-3
65. Szentadassy N, Banyasz T, Biro T, Szabo G, Toth B, Magyar J, et al. Apico? basal Inhomogeneity in Distribution of Ion Channels in Canine and Human Ventricular Myocardium. *Cardiovasc Res* (2005) 65(4):851–60. doi:10.1016/j.cardiores.2004.11.022
66. Viswanathan PC, Rudy Y. Cellular Arrhythmogenic Effects of Congenital and Acquired Long-Qt Syndrome in the Heterogeneous Myocardium. *Circulation* (2000) 101(10):1192–8. doi:10.1161/01.cir.101.10.1192
67. Schmidt A, Azevedo CF, Cheng A, Gupta SN, Bluemke DA, Foo TK, et al. Infarct Tissue Heterogeneity by Magnetic Resonance Imaging Identifies Enhanced Cardiac Arrhythmia Susceptibility in Patients with Left Ventricular Dysfunction. *Circulation* (2006) 115(15):2006–14. doi:10.1161/CIRCULATIONAHA.106.653568
68. Antzelevitch C. Heterogeneity and Cardiac Arrhythmias: an Overview. *Heart Rhythm* (2007) 4:964. doi:10.1016/j.hrthm.2007.03.036
69. Mikhailov AS, Krinsky VI. Rotating Spiral Waves in Excitable media: the Analytical Results. *Physica D: Nonlinear Phenomena* (1983) 9(3):346–71. doi:10.1016/0167-2789(83)90277-4
70. Winfree AT. Varieties of Spiral Wave Behavior: An Experimentalist's Approach to the Theory of Excitable media. *Chaos* (1991) 1(3):303–34. doi:10.1063/1.165844
71. Mikhailov AS, Davydov VA, Zykov VS. Complex Dynamics of Spiral Waves and Motion of Curves. *Physica D: Nonlinear Phenomena* (1994) 70(1-2):1–39. doi:10.1016/0167-2789(94)90054-x
72. Hakim V, Karma A. Theory of Spiral Wave Dynamics in Weakly Excitable media: Asymptotic Reduction to a Kinematic Model and Applications. *Phys Rev E* (1999) 60(5):5073–105. doi:10.1103/physreve.60.5073
73. Margerit D, Barkley D. Cookbook Asymptotics for Spiral and Scroll Waves in Excitable media. *Chaos* (2002) 12(3):636–49. doi:10.1063/1.1494875
74. Zykov VS. Kinematics of Rigidly Rotating Spiral Waves. *Physica D: Nonlinear Phenomena* (2009) 238(11-12):931–40. doi:10.1016/j.physd.2008.06.009
75. Löber J, Engel H. Analytical Approximations for Spiral Waves. *Chaos* (2013) 23(4):043135. doi:10.1063/1.4848576
76. Barkley D. Euclidean Symmetry and the Dynamics of Rotating Spiral Waves. *Phys Rev Lett* (1994) 72(1):164–7. doi:10.1103/physrevlett.72.164
77. Kazbanov IV, ten Tusscher KH, Panfilov AV. Effects of Heterogeneous Diffuse Fibrosis on Arrhythmia Dynamics and Mechanism. *Sci Rep* (2016) 6:20835. doi:10.1038/srep20835
78. Vandersickel N, Watanabe M, Tao Q, Fostier J, Zeppenfeld K, Panfilov AV. Dynamical Anchoring of Distant Arrhythmia Sources by Fibrotic Regions via Restructuring of the Activation Pattern. *Plos Comput Biol* (2018) 14(12):e1006637. doi:10.1371/journal.pcbi.1006637
79. Camelliti P, Green CR, Kohl P. Structural and Functional Coupling of Cardiac Myocytes and Fibroblasts. *Cardiovasc Gap Junctions* (2006) 42:132–49. doi:10.1159/000092566
80. Gaudesius G, Miragoli M, Thomas SP, Rohr S. Coupling of Cardiac Electrical Activity over Extended Distances by Fibroblasts of Cardiac Origin. *Circ Res* (2003) 93(5):421–8. doi:10.1161/01.res.0000089258.40661.0c
81. Potse M, Dube B, Richer J, Vinet A, Gulrajani RM. A Comparison of Monodomain and Bidomain Reaction-Diffusion Models for Action Potential Propagation in the Human Heart. *IEEE Trans Biomed Eng* (2006) 53(12):2425–35. doi:10.1109/tbme.2006.880875
82. Zeng T, Bett GCL, Sachs F. Stretch-Activated Whole Cell Currents in Adult Rat Cardiac Myocytes. *Am J Physiology-Heart Circulatory Physiol* (2000) 278(2):H548–H557. doi:10.1152/ajpheart.2000.278.2.h548
83. Kamkin A, Kiseleva I, Isenberg G. Stretch-activated Currents in Ventricular Myocytes: Amplitude and Arrhythmogenic Effects Increase with Hypertrophy. *Cardiovasc Res* (2000) 48(3):409–20. doi:10.1016/s0008-6363(00)00208-x
84. Thompson SA, Copeland CR, Reich DH, Tung L. Mechanical Coupling between Myofibroblasts and Cardiomyocytes Slows Electric Conduction in Fibrotic Cell Monolayers. *Circulation* (2011) 123(19):2083–93. doi:10.1161/circulationaha.110.015057
85. Panfilov AV, Keldermann RH, Nash MP. Drift and Breakup of Spiral Waves in Reaction Diffusion Mechanics Systems. *Proc Natl Acad Sci* (2007) 104(19):7922–6. doi:10.1073/pnas.0701895104

Conflict of Interest: The authors declare that the research was conducted in the absence of any commercial or financial relationships that could be construed as a potential conflict of interest.

Publisher's Note: All claims expressed in this article are solely those of the authors and do not necessarily represent those of their affiliated organizations, or those of the publisher, the editors and the reviewers. Any product that may be evaluated in this article, or claim that may be made by its manufacturer, is not guaranteed or endorsed by the publisher.

Copyright © 2022 Mulimani, Zimik and Pandit. This is an open-access article distributed under the terms of the Creative Commons Attribution License (CC BY). The use, distribution or reproduction in other forums is permitted, provided the original author(s) and the copyright owner(s) are credited and that the original publication in this journal is cited, in accordance with accepted academic practice. No use, distribution or reproduction is permitted which does not comply with these terms.



Effective Spatio-Temporal Regimes for Wound Treatment by Way of Macrophage Polarization: A Mathematical Model

Ksenia Zlobina^{1*}, Jiahao Xue² and Marcella Gomez¹

¹ Department of Applied Mathematics, University of California, Santa Cruz, Santa Cruz, CA, United States, ² Department of Electrical and Computer Engineering, University of California, Santa Cruz, Santa Cruz, CA, United States

OPEN ACCESS

Edited by:

Krasimira Tsaneva-Atanasova,
University of Exeter, United Kingdom

Reviewed by:

Giri Gopalan,
California Polytechnic State University,
United States
Arran Hodgkinson,
University of Exeter, United Kingdom

*Correspondence:

Ksenia Zlobina
kzlobina@ucsc.edu

Specialty section:

This article was submitted to
Mathematical Biology,
a section of the journal
Frontiers in Applied Mathematics and
Statistics

Received: 07 October 2021

Accepted: 27 January 2022

Published: 22 February 2022

Citation:

Zlobina K, Xue J and Gomez M (2022)
Effective Spatio-Temporal Regimes for
Wound Treatment by Way of
Macrophage Polarization: A
Mathematical Model.
Front. Appl. Math. Stat. 8:791064.
doi: 10.3389/fams.2022.791064

Wound healing consists of a sequence of biological processes often grouped into different stages. Interventions applied to accelerate normal wound healing must take into consideration timing with respect to wound healing stages in order to maximize treatment effectiveness. Macrophage polarization from M1 to M2 represents a transition from the inflammatory to the proliferative stage of wound healing. Accelerating this transition may be an effective way to accelerate wound healing; however, it must be induced at the appropriate time. We search for an optimal spatio-temporal regime to apply wound healing treatment in a mathematical model of wound healing. In this work we show that to maximize effectiveness, treatment must not be applied too early or too late with respect to peak inflammation. We also show that the effective spatial distribution of treatment depends on the heterogeneity of the wound surface. In conclusion, this research provides a possible optimal regime of therapy that focuses on macrophage activity and a hypothesis of treatment outcome to be tested in future experiments. Finding optimal regimes for treatment application is a first step toward the development of intelligent algorithms for wound treatment that minimize healing time.

Keywords: wound healing, mathematical model, macrophage polarization, optimal treatment regime, partial differential equations (PDE)

1. INTRODUCTION

Delayed wound healing presents an important health-care problem. There is no decisive finding regarding the best therapy for delayed wound healing due to the variety of complications that can ensue [1]. In the case of acute wounds, a growing research area in wound healing has focused on methods to accelerate wound healing such as application of an electric field, application of stem cells, and the passive release of therapeutic molecules in so-called smart bandages [2]. Less attention has been given to the timing of any given therapy. A treatment may exert no effect or even a negative effect on healing tissues if not applied appropriately [3]. For example, certain treatments can accelerate specific stages of inflammation but have little effect on others [4, 5]. In other cases, treatment can induce toxic side-effects [6]. For this reason each treatment should be applied only at the appropriate stages of wound healing. The emergence of bioelectronic devices provides the opportunity to achieve drug delivery in a continuous and controlled fashion [7, 8].

Wound healing consists of several stages: hemostasis, inflammation, proliferation, and remodeling [9–11]. During hemostasis, a blood clot is formed to stop bleeding [12]. Inflammation begins immediately after a blood clot formation. At this time, chemokines are released to attract immune cells - neutrophils and macrophages. During the proliferative stage, angiogenesis, collagen deposition, and the formation of granulation tissue occur. The main participants in this stage are fibroblasts and anti-inflammatory macrophages. During remodeling, unnecessary blood vessels are removed, the extracellular matrix is remodeled, and tissue architecture is restored.

Wound acceleration can be achieved by shortening the duration of one or more of the wound healing stages. Determining the optimal timing for a therapy requires one to map the direct effect of the therapy on the targeted biological processes to the overall wound closure time.

Mathematical modeling in this field may help to predict optimal treatment regimes and to plan future experiments. Existing mathematical models have served to investigate different aspects/stages of wound healing [13–15]. Models of inflammation have suggested strategies to avoid chronic inflammation by control of neutrophil apoptosis and macrophage phagocytosis [16]. The model presented in Xue et al. [17] suggests a mechanism by which a deficiency in oxygen supply can limit macrophage recruitment and slow healing. The models describing production of the extracellular matrix by fibroblasts allowed researchers to investigate scar formation [18]. The role of cell migration and proliferation on wound closure was investigated in Javierre et al. [19]. Thus, we propose that a qualitative model with a proper level of abstraction can be used to predict the response of a wound to dynamic therapy.

In this study, we investigate mathematically the most effective spatio-temporal regimes for drug delivery to accelerate wound closure. In particular, we identify the effects of delivering substances that can accelerate macrophage polarization on wound closure times. Macrophage polarization modeling, to our knowledge, has been applied to several biological situations but not to wound healing [20, 21].

Macrophages play important roles at all stages of wound healing [9–11, 22]—from clearing the wound of debris by phagocytosis to maintaining cell proliferation of the tissue being repaired. Macrophages can perform various tasks due to their ability to transform into several phenotypes depending on external stimuli [23]. The most famous phenotypes are M1 (pro-inflammatory) and M2 (anti-inflammatory), identified *in vitro* [24]. In a wound, the set of stimuli received by macrophages is constantly changing and their phenotype undergoes a dynamic transition. The ability to regulate the macrophage phenotype and achieve a controlled time-dependent transition from the M1 phenotype to the M2 phenotype is a promising approach to accelerate wound healing [25–27]. There are several substances that can induce macrophage polarization from the pro-inflammatory to the anti-inflammatory subtype [28–30]. This type of treatment can have adverse effects if applied improperly [31, 32]. For example, a fast transition from the inflammatory to the proliferative stage may slow down the

cleaning of the wound of debris (e.g., removal of harmful bacteria and damaged cells).

We focus our attention on accelerating wound closure of acute wounds. For simplicity, and to this end, we consider a simple model with only one stable state – the healthy one. That is, our model does not capture switching between chronic and normal wound healing regimes. However, in order to appropriately capture trade-offs of early treatment, we model wound debris over time, which is actively degraded by M1 macrophages. Tracking this state, we quantify wound cleaning time with the understanding that any remaining wound debris can be an indicator of prolonged inflammation and potential infection preventing wound closure. That is, wound debris should decay in a timely manner for the treatment to be realizable.

In summary, we examine wound healing time and wound debris cleaning time in response to different spatio-temporal signals inducing macrophage polarization. Overall, decoupling the different modalities of wound healing trajectories reduces complexity of the model and allows us to gain intuition for optimal treatment strategies. We find that actuation of M1–M2 polarization must be applied with care and optimal timing can depend on the duration of the treatment, time of initiation, placement of the actuator, and initial distribution of wound debris.

2. MATHEMATICAL MODEL

2.1. Background

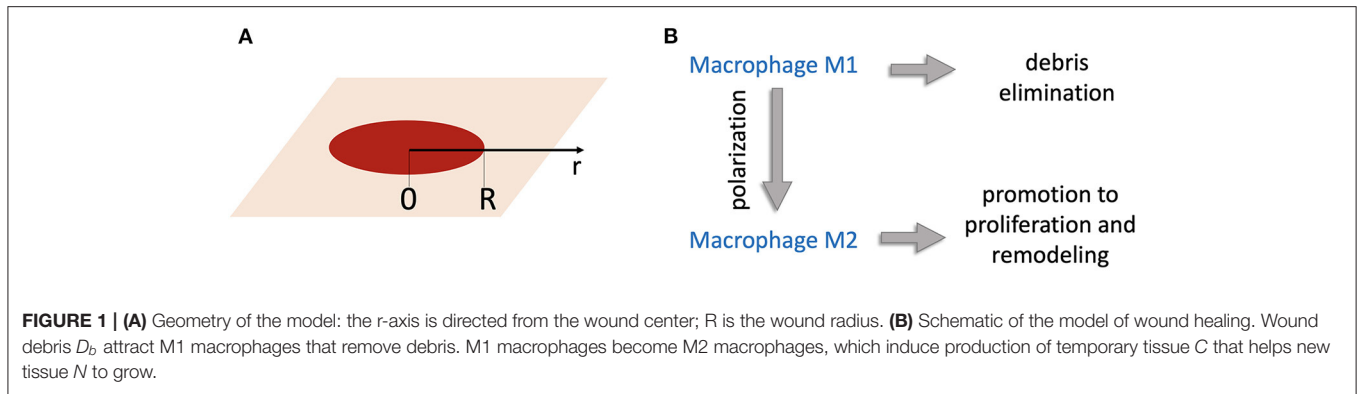
The timing and coordination of biological processes involved in wound healing are complex, however, many of them can be lumped into a single state [33]. A good model should contain the minimal number of variables needed to describe the process [14].

We consider a five state system, which provides an appropriate level of abstraction for our study. In order to study the effects of macrophage polarization we must make them explicit states. M1 macrophages are associated with the early stages of inflammation [11, 34] and the upregulation of M2 signals corresponds to initiation of the proliferation stage [9, 10]. The remaining states defined as wound debris, temporary tissue, and new tissue represent primary activity in early and later stages of wound healing.

Debris of both internal and external origin appear in the wound at the moment of injury, when healthy tissue is damaged. The debris activate M1 macrophages and are then removed by them.

M1 macrophages clean up debris mainly by phagocytosis [35]. Soon after that, M1 macrophages become anti-inflammatory M2 macrophages in a process called efferocytosis (M1 macrophages phagocytose apoptotic neutrophils, transforming into M2 macrophages) [36, 37]. The upregulation of M2 macrophages is associated with the end of inflammation [38] and the onset of proliferation during wound healing [10, 11].

The proliferative stage is characterized by the production of an extracellular matrix facilitated by fibroblasts and the growth of new blood vessels [39, 40]. These processes are regulated by M2 macrophages [10] and are needed to help new tissue form



correctly, thus, we consider these agents as “temporary tissue” in our model.

During the remodeling stage, the extracellular matrix is remodeled and extra blood vessels are removed [39]; new healthy tissue replaces temporary tissue indicating wound closure. Here, we consider a wound where only the top epithelial layer is damaged and new tissue grows from the edge of the wound as epithelial cells proliferate and migrate inward. Thus, new tissue in our model is growing as a sheet from the wound edge [41].

These five states capture the well characterized wound healing stages and changing wound conditions inducing a biological response.

2.2. Equations

Consider a wound of radius R . Let the axis r to be directed from the wound center to the edge (**Figure 1A**). Concentrations of substances and populations of cells are functions of r . A schematic of the interaction between the modeled biological processes including macrophage participation in wound healing is shown in **Figure 1B**.

D_b is wound debris consisting of damaged cells and bacterial cells promoting infection. We assume the wound debris to be non-active and only eliminated by M1 macrophages:

$$\dot{D}_b = -k_1 D_b M_1, \quad (1)$$

where M_1 is the population of M1 macrophages, which are attracted by debris ($k_2 D_b$) and removed in the reactions corresponding to debris elimination ($k_1 D_b M_1$), macrophage polarization ($k_4 \frac{M_1^q}{K^q + M_1^q}$), and natural death ($k_{d1} M_1$). Spatial migration of macrophages is described by a classical diffusion term [42]. Thus, the dynamics of M1 macrophages are described by the following equation:

$$\begin{aligned} \dot{M}_1 = & k_2 D_b - k_1 D_b M_1 - k_4 \frac{M_1^q}{K^q + M_1^q} \\ & - k_{d1} M_1 + D \left(\frac{1}{r} \frac{\partial M_1}{\partial r} + \frac{\partial^2 M_1}{\partial r^2} \right), \end{aligned} \quad (2)$$

where the diffusion is written in a cylindrical coordinate system. M_2 is the population of M2 macrophages whose dynamics are

driven by M1 polarization ($k_4 \frac{M_1^q}{K^q + M_1^q}$), their death rate ($-k_{d2} M_2$), and migration as follows:

$$\dot{M}_2 = k_4 \frac{M_1^q}{K^q + M_1^q} - k_{d2} M_2 + D \left(\frac{1}{r} \frac{\partial M_2}{\partial r} + \frac{\partial^2 M_2}{\partial r^2} \right). \quad (3)$$

Proliferation is a complex process involving fibroblasts. The extracellular matrix (ECM) formation and its partial destruction is controlled by a complex coordination of enzymes [39, 40]. This finely tuned system supporting new tissue growth has been modeled in several works [18, 43, 44]. Here, we use a simplified model of proliferation. The temporary tissue variable C represents the temporarily formed ECM and active enzymes. Temporary tissue production is induced by M2 macrophages ($k_5 M_2$) and is destroyed thereafter ($-k_r C$). The dynamics are described by the following equation:

$$\dot{C} = k_5 M_2 - k_r C. \quad (4)$$

The state C is an intermediate state leading to the growth of new healthy tissue, N . To model growth of new healthy tissue, we assume that the top layer of the skin, the epithelium, grows as a sheet from the edge of the wound [41]. Epithelial cells divide, but this process slows down if there are too many cells. Thus, the epithelial growth velocity is described as $N(1 - N)$. If the amount of new tissue reaches $N = 1$ it does not grow any more. New tissue cells can migrate to adjacent areas with a migration rate D_n that is much slower than that of macrophages. The equation $\dot{N} = \alpha N(1 - N) + \frac{\partial^2 N}{\partial x^2}$ is known in the theory of nonlinear dynamical systems as the Fisher-Kolmogorov equation [45], and its solution can be represented as a running wave [42]. However, this is possible only in the presence of temporary tissue, so the rate of new tissue growth is proportional to C . The dynamics of new tissue are described by the following equation:

$$\dot{N} = C \left[\alpha N(1 - N) + D_n \left(\frac{1}{r} \frac{\partial N}{\partial r} + \frac{\partial^2 N}{\partial r^2} \right) \right]. \quad (5)$$

TABLE 1 | The values of parameters used in numerical simulations.

Parameter	Value	Reference
R	3 mm	
L	0.03 mm	
T	1/3 day	
δ	1/3 day	
β	1	[46, 47]
ρ	0.1	[48]
k	0.05	[48]
q	5	[48]
γ_1	0.1	[34, 49]
γ_2	0.1	[34, 49]
μ	0.2	[39]
\tilde{D}	0.32	[50, 51]
\tilde{D}_n	0.0003	[52]
$\tilde{\alpha}$	1.8	[52]

In order to reduce the number of parameters, we reparameterize the model by introducing new variables:

$$\begin{aligned} a &= D_b k_1 T & m_1 &= M_1 k_1 T & m_2 &= M_2 k_1 T \\ c &= C \frac{k_1}{k_5} & n &= N & \tau &= \frac{t}{T} \\ \tilde{r} &= \frac{r}{L} \end{aligned}$$

where T and L are characteristic time and length scales. The system of equations in the reparameterized form is:

$$\dot{a} = -am_1, \quad (6)$$

$$\dot{m}_1 = \beta a - am_1 - \rho \frac{m_1^q}{k^q + m_1^q} - \gamma_1 m_1 + \tilde{D} \left(\frac{1}{\tilde{r}} \frac{\partial m_1}{\partial \tilde{r}} + \frac{\partial^2 m_1}{\partial \tilde{r}^2} \right), \quad (7)$$

$$\dot{m}_2 = \rho \frac{m_1^q}{k^q + m_1^q} - \gamma_2 m_2 + \tilde{D} \left(\frac{1}{\tilde{r}} \frac{\partial m_2}{\partial \tilde{r}} + \frac{\partial^2 m_2}{\partial \tilde{r}^2} \right), \quad (8)$$

$$\dot{c} = m_2 - \mu c, \quad (9)$$

$$\dot{n} = c[\tilde{\alpha}n(1-n) + \tilde{D}_n \left(\frac{1}{\tilde{r}} \frac{\partial n}{\partial \tilde{r}} + \frac{\partial^2 n}{\partial \tilde{r}^2} \right)], \quad (10)$$

where $\beta = k_2 T$, $\rho = k_1 k_4 T^2$, $\gamma_1 = k_{d1} T$, $\gamma_2 = k_{d2} T$, $\mu = k_r T$, $\tilde{D} = \frac{DT}{L^2}$, $\tilde{D}_n = \frac{D_n T k_5}{L^2 k_1}$, $\tilde{\alpha} = \alpha T \frac{k_5}{k_1}$, $k = K k_1 T$. The parameter values used in numerical simulations are listed in **Table 1**.

We assume a time scale of 8 h and a spatial scale of 0.03 mm. For β the rate of attraction of macrophages by debris/pathogen was reported in Hau et al. [46] as 1/day and in Andersson

et al. [47] as 0.5/day. We set $\beta = 1$. The degradation rate of macrophages varies in literature from 0.014/h [34] to 0.12/h [49]. We accept the values $\gamma_1 = \gamma_2 = 0.1$. We select parameters k , q and ρ such that $M1$ and $M2$ dynamics agree with those found in Du et al. [48]. The value of μ was set such that temporary tissue is removed 3 weeks after injury [39]. The coefficient of diffusion for macrophages can be deduced from cell migration experiments. In Wheeler et al. [51], the mean displacement of cells on plastic was 20–30 μm in 6.5 h, giving the estimate for the diffusion coefficient [50] $\tilde{D} = 0.27 - 0.61$. We assume $\tilde{D} = 0.32$.

Finally, the parameters $\tilde{D}_n = 0.0003$ and $\tilde{\alpha} = 1.8$ were selected in such a way that complete wound closure was observed by day 14, while no changes in wound closure were observed in the first 2 days as is consistent with some experiments [52]. The sensitivity analysis of the model to variations in parameters is shown in **Supplementary Figures S5, S6**.

The initial conditions are:

$$a|_{t=0} = 1, \quad m_1|_{t=0} = m_2|_{t=0} = c|_{t=0} = n|_{t=0} = 0. \quad (11)$$

We assume zero-flux boundary conditions for macrophages on the right and left boundaries of the considered region:

$$\frac{\partial m_1}{\partial \tilde{r}}|_{\tilde{r}=0} = \frac{\partial m_2}{\partial \tilde{r}}|_{\tilde{r}=0} = \frac{\partial m_1}{\partial \tilde{r}}|_{\tilde{r}=R/L} = \frac{\partial m_2}{\partial \tilde{r}}|_{\tilde{r}=R/L} = 0. \quad (12)$$

New tissue is assumed to be constant at the edge of the wound and non-moving through the center of the wound:

$$\frac{\partial n}{\partial \tilde{r}}|_{\tilde{r}=0} = 0, \quad n|_{\tilde{r}=R/L} = 1. \quad (13)$$

The system of Equations (6)–(10) was solved numerically on a uniform mesh consisting of 100 spatial cells. Five equations were written in each cell, with the diffusion term approximated using a central difference scheme. The resulting system of 500 ordinary differential equations was solved in Matlab R2020a by the ode15s solver. The results of wound healing model simulations are shown in **Figure 2**. The wound radius is measured as the distance from wound center to the location r , where $n(r) > 0.95$.

2.3. Model of Wound With Actuator

In order to investigate regimes of wound healing treatment we include actuator induced macrophage polarization into the model. This actuator is applied at a radius $r = r_p$. We assume that the actuator delivers a biochemical at the point of application and its concentration θ is described by the following function in time and space (see **Figure 3A**):

$$\begin{aligned} \theta(r, t) &= \theta_0(t) \cdot \begin{cases} 0 & r \in (-\infty, r_p - \sigma_1] \cup [r_p + \sigma_1, \infty) \\ 1 & r \in [r_p - \sigma_2, r_p + \sigma_2] \\ \frac{r - (r_p - \sigma_1)}{(\sigma_1 - \sigma_2)} & r \in (r_p - \sigma_1, r_p - \sigma_2) \\ -\frac{r - (r_p + \sigma_1)}{(\sigma_1 - \sigma_2)} & r \in (r_p + \sigma_2, r_p + \sigma_1) \end{cases} \quad (14) \end{aligned}$$

where θ_0 is the amplitude of the treatment controlled by the actuator. One can see that $\theta = \theta_0$ at the location of the actuator,

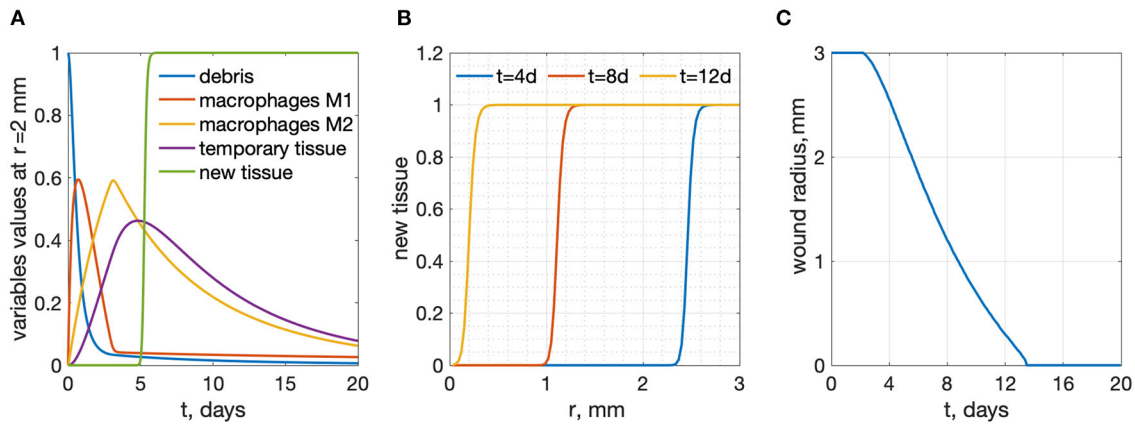


FIGURE 2 | Results of wound healing model simulations, $R = 3$ mm. **(A)** time-dependence of all variables at a radius $r = 2$ mm from the wound center **(B)** new tissue profiles as functions of r for several time points. **(C)** wound radius vs. time: wound healing time is 13.47 days.

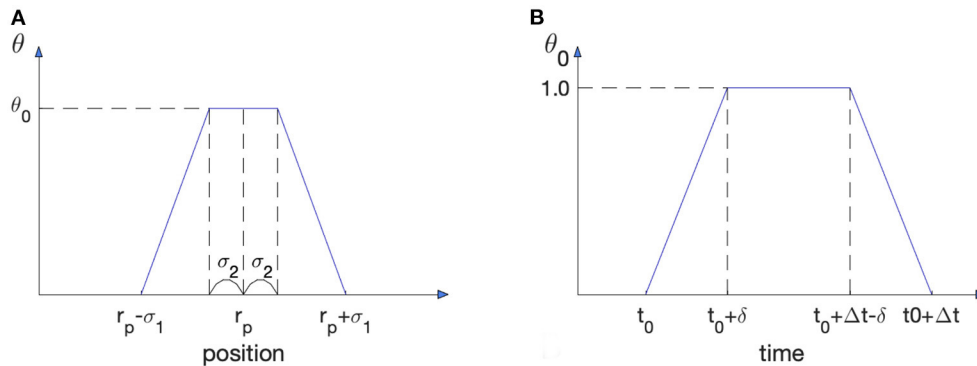


FIGURE 3 | Spatio-temporal characteristics of treatment induced by actuation. **(A)** Treatment substance distribution in space. The actuator is located at $r = r_p$. **(B)** Time dependence of the actuator amplitude.

$r = r_p$. In this work we assumed $\sigma_1 = 0.3$ mm and $\sigma_2 = 0.09$ mm. The treatment substance delivered affects macrophage polarization, so equations for m_1 and m_2 with actuators may be rewritten as follows:

$$\dot{m}_1 = \beta a - a m_1 - \rho \frac{m_1^q}{k^q + m_1^q} - \gamma_1 m_1 + \tilde{D} \left(\frac{1}{\tilde{r}} \frac{\partial m_1}{\partial \tilde{r}} + \frac{\partial^2 m_1}{\partial \tilde{r}^2} \right) - \theta m_1, \quad (15)$$

$$\dot{m}_2 = \rho \frac{m_1^q}{k^q + m_1^q} - \gamma_2 m_2 + \tilde{D} \left(\frac{1}{\tilde{r}} \frac{\partial m_2}{\partial \tilde{r}} + \frac{\partial^2 m_2}{\partial \tilde{r}^2} \right) + \theta m_1, \quad (16)$$

In order to find the optimal regime, we test the model with impulses of actuator treatment of duration Δt beginning at time t_0 (see Figure 3B):

$$\theta_0 = \begin{cases} \frac{t-t_0}{\delta} & t_0 \leq t < t_0 + \delta \\ 1 & t_0 + \delta \leq t < t_0 + \Delta t - \delta \\ \frac{t_0 + \Delta t - t}{\delta} & t_0 + \Delta t - \delta \leq t < t_0 + \Delta t \end{cases}, \quad (17)$$

We present a piece-wise linear function for simplicity. We assume linear growth and a decrease at the beginning and end of the signal. We tested other impulse-like shapes for actuation and found that the general behavior of the system response remained unchanged.

3. RESULTS

We define wound healing time as the time from injury ($t=0$) to the moment when the wound radius reaches zero. Application of an actuator that accelerates macrophage polarization in the model decreases the time of wound healing. The results are shown in Figures 4–6.

The beginning time of actuation plays an important role in wound healing (see Figure 4). Large values of t_0 make the treatment less effective: wound healing time increases as t_0 increases. In our simulations for $t_0 > 3d$ the treatment does not have any effect: the value of healing time tends to the value of healing without treatment (13.47 days for the given set of parameters).

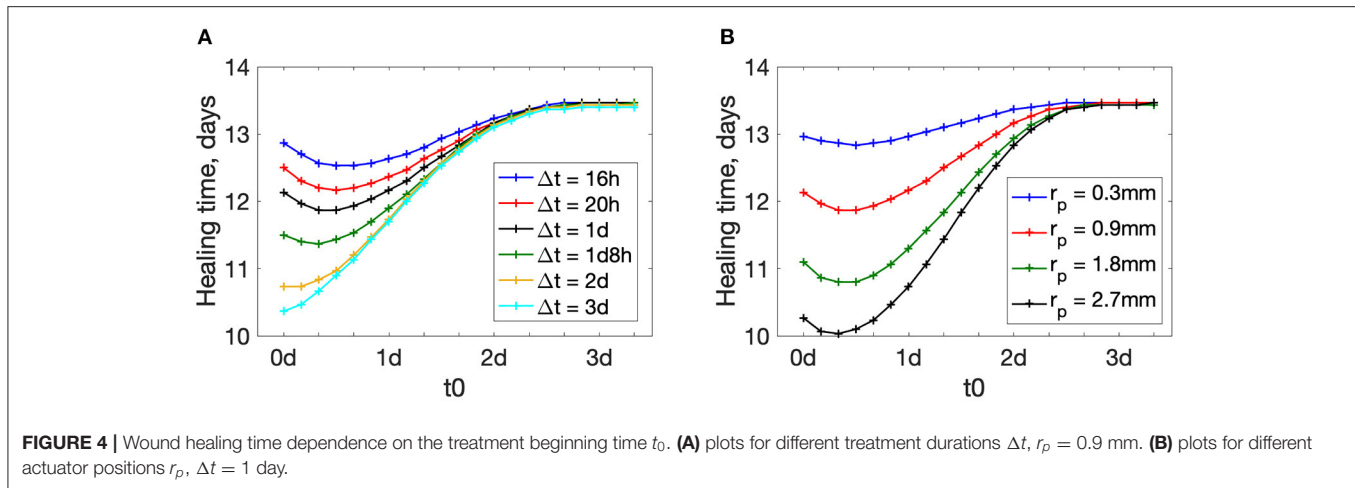


FIGURE 4 | Wound healing time dependence on the treatment beginning time t_0 . (A) plots for different treatment durations Δt , $r_p = 0.9$ mm. (B) plots for different actuator positions r_p , $\Delta t = 1$ day.

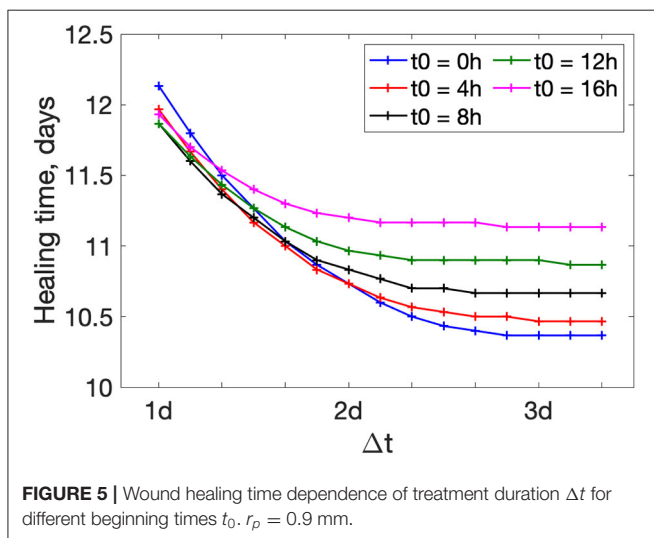


FIGURE 5 | Wound healing time dependence of treatment duration Δt for different beginning times t_0 , $r_p = 0.9$ mm.

Interestingly, for shorter treatment durations Δt , healing time plots have a minimum away from the extremes (see plots for $\Delta t < 2d$ in **Figure 4A**). There exists a time-window in the wound healing process when treatment is most effective. This time-window is likely characterized by some underlying biological process. If the treatment duration is short and applied early, the treatment ends before the most effective time-window is reached. This is not observed for longer treatments ($\Delta t = 2 - 3$ days) because even with early application at $t_0 = 0$, the treatment duration overlaps with the most effective time-window for treatment.

This means that there is a non-trivial optimal treatment beginning time t_0 . In other words, there is a short window of time during wound healing when artificial acceleration of macrophage polarization is most effective. The plots for other actuator positions r_p are shown in the **Supplementary Figure S1**. Similar trends are observed for different placement of the actuators.

Figure 5 shows how wound healing time depends on the duration of treatment. The longer the treatment time Δt is, the more effective it is at accelerating wound healing. However, for Δt larger than 2–3 days, wound healing time approaches a lower bound. This means that further prolongation of the treatment has minor effects. The plots for other values of r_p are shown in **Supplementary Figure S2**. Again, we find a similar trend regardless of actuator placement.

Figure 6A shows the dependence of wound healing time on the actuator position r_p . The treatment substance in this model is approximated by a piece-wise function (14) on a bounded domain. To ensure the bounded domain stays within the region of interest we constrain the actuator placement: $0.3 \text{ mm} \leq r \leq 2.7 \text{ mm}$. The plots are decreasing from the wound center to the edge. This implies that an actuator located close to the wound edge is beneficial. The plots for other Δt and t_0 are shown in **Supplementary Figures S3, S4**.

The results above might be the consequence of the initial uniform distribution of the debris in the wound (see initial conditions). We provide additional simulations with debris accumulation in the center and at the edge of the wound. Alternative initial conditions for the debris variable take the following form:

$$a(r)|_{t=0} = 2(1 - r/R) \quad (18)$$

and

$$a(r)|_{t=0} = 2r/R. \quad (19)$$

Wound healing time dependence on r_p for the three different types of initial conditions on debris distribution is shown in **Figure 6B**. One can see that debris distribution in the wound bed affects the dependence of healing time on actuator placement.

For the case $a(r) = 2r/R$, there is more debris on the edge. If the actuator is placed near the edge, we can get much shorter healing times. For the case $2(1 - r/R)$ (more debris in the wound center), there exists an optimal position of the actuator away from the edge ($r_p \approx 1.8$ mm). One can see that the optimal actuator

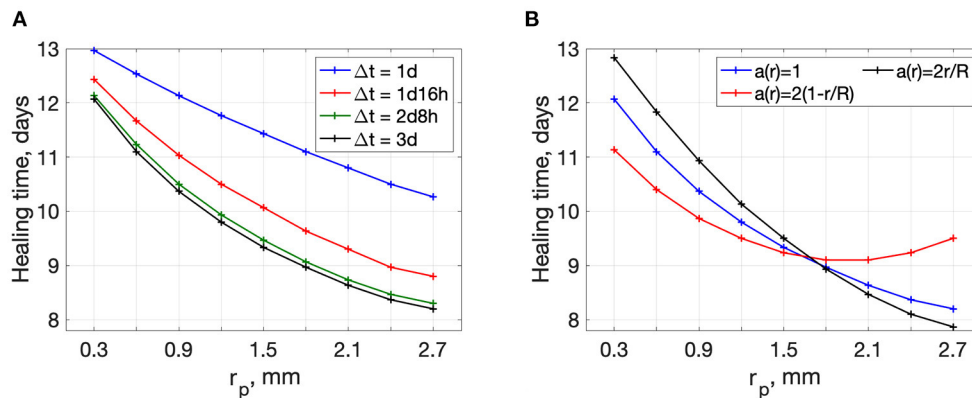


FIGURE 6 | Wound healing time dependence on the actuator position r_p . **(A)** plots for different treatment durations Δt , $t_0 = 0h$ **(B)** plots for different initial distributions of debris in the wound, $t_0 = 0h$ $\Delta t = 3days$.

position is sensitive to the distribution of the debris in the wound. Debris distribution cannot be estimated in the framework of this rough modeling and must be investigated experimentally.

Figure 7 demonstrates the limitations of treatment regimes. In addition to wound healing time, we define the wound cleaning time for debris removal. Because debris is a diminishing variable in our model, it tends to zero as time goes to infinity. We define wound cleaning time as the time when the maximal value of debris across the wound bed falls below a small threshold 0.025:

$$\max_r a < 0.025. \quad (20)$$

Because the treatment applied in this model accelerates M1 to M2 transition, it not only accelerates the proliferation-remodeling stages but removes M1 cells performing debris removal. Too large application of this treatment can make debris removal too slow—this is the cost of accelerating the proliferative and remodeling stages. **Figure 7A** shows that a shorter wound healing time corresponds to a longer time required for wound cleaning or debris removal. For some scenarios, wound cleaning may take even longer than wound closure, which is physically unrealizable and indicative of complications in wound healing.

We can see two main limitations of the treatment regimes, divided by vertical dotted lines in **Figure 7A**. The regimes with small t_0 (left of the first dotted line) lead to too slow wound cleaning. Regimes with very large t_0 (to the right of the second dotted line) result in insufficient improvement in wound healing. We define “insufficient” by a less than 10% reduction in wound healing time when treatment is applied. This threshold is of course arbitrary and can be chosen by the user. For reference, in Liang et al. [53], the authors demonstrated accelerated wound closure on a pig wound by applying a continuous external electric field and reduced the time for wound closure by ~ 12 –18%. Thus, we opine that below a 10% threshold, the cost and potential side effects of applying the treatment outweigh the benefit.

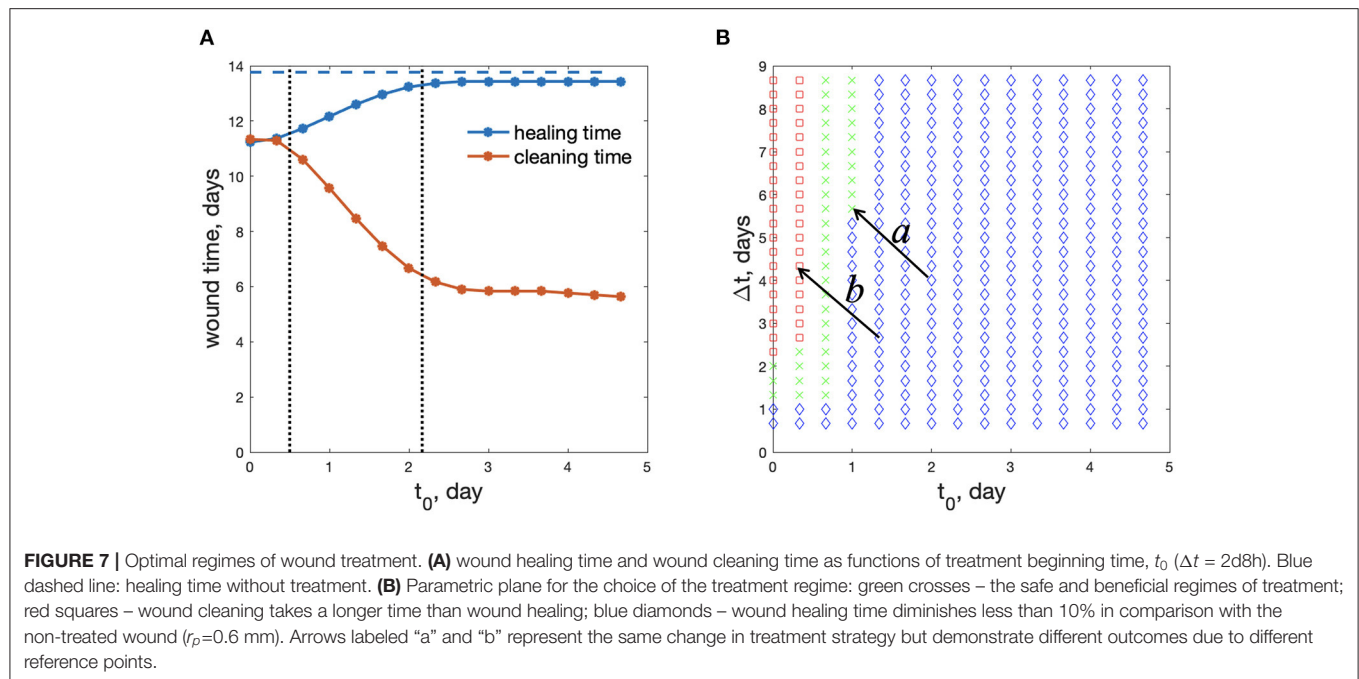
Only the regimes with middle values of t_0 , between the vertical dotted lines in **Figure 7A**, shorten wound healing time sufficiently, while keeping a reasonable wound cleaning time.

Figure 7B shows these 3 types of regimes in the $(t_0, \Delta t)$ parametric plane. The regimes marked as red squares correspond to regimes when wound cleaning takes a longer time than wound healing, whereas blue diamonds correspond to regimes when wound healing time diminishes less than 10% in comparison with a non-treated wound. Green crosses represent the effective regimes of wound treatment. We find that the treatment should be applied between 0 and 1 days. Applying treatment past 1 day in all scenarios does not significantly reduce the wound healing time, hence, the treatment is ineffective. We note that in our simulations, M1 macrophage activity, which is associated with inflammation, peaks at around 24 h. Thus, we may hypothesize that treatment is best applied shortly after or just shy of peak inflammation, thereby, accelerating the transition from the inflammatory state to the proliferative state. Applying treatment too early can result in chronic wounds given a less than reasonable time is provided for inflammation, a stage in wound healing critical for preventing infections.

Of course, one can choose more stringent conditions for optimal regimes (maybe 10% healing time improvement is not enough, or the threshold in the condition (20) should be smaller. Some variants of other threshold selections are shown in **Supplementary Figure S7**). Among all the regimes presented in **Figure 7B** the smallest healing time (11.37 days) is observed for the treatment regime $t_0 = 8h$ and $\Delta t = 2days\ 8h$. This reduces wound healing time by approximately 2 days. In practical situations there might be additional constraints on the duration of treatment, or maximum concentration that is not considered here. However, our model demonstrates the principles of wound treatment regime optimization.

4. DISCUSSION

To our knowledge, the mathematical model presented here is the first one that considers the role of macrophage polarization explicitly in wound healing. The model takes into account the presence of two types of macrophages in the wound—M1 and M2. It is believed that in addition to these primary



subtypes, there are several other subtypes of macrophages. All subtypes of macrophages were found *in vitro* as a result of identifying corresponding activating stimuli. The exact subtypes of macrophages in wounds have not been established and are considered to be roughly similar to those found *in vitro*. It is most likely that macrophages of different types can be present in the wound simultaneously. However, the functions that these macrophages perform are more important for the healing process than the markers found *in vitro*. Therefore, in this model, we clearly divide the functions of the macrophages into inflammatory and reparative, keeping in mind that such pure cell lines may not exist in reality. This separation of functions of macrophages gave us the opportunity to draw up a rather simple naive model and identify general patterns for the effect of varying treatment regimens on wound healing time.

Admittedly, this model has its limitations. The model constructed in this work does not take into account the details of macrophages polarization due to the poor knowledge of this mechanism *in vivo* [34]. It is known that M2 macrophages can appear in response to stimulation by certain cytokines, for example, IL4, produced by basophils and mast cells [11]. There are indications that M1 macrophages are converted to M2 subtypes after they phagocyte apoptotic neutrophils [38]. We made a model in which the M1 population is replaced by M2 although the mechanisms of this transition *in vivo* are not well understood. Thus the mechanisms of polarization and their effects on timing cannot be included. Still we derive biologically meaningful results.

Our results imply that a treatment targeting macrophage polarization should not take place too early. Otherwise, M1 macrophages do not have enough time to eliminate wound debris and wound healing can be delayed. Details of this scenario is out

of scope of our model. The onset of this scenario is especially important for infected wounds when the debris consists not only of damaged cells but of bacterial pathogen [54]. In the case of bacterial pathogen, the first equation in the model should include pathogen reproduction and regimes where pathogen persistence may occur. This may lead to continuation of M1 recruitment, inflammation persistence, and prevent full wound closure. On the other hand, treatment targeting macrophage polarization should not begin too late, because it becomes ineffective and toxic side effects are unknown.

The model can still be used to guide experiments. The parametric plane of treatment regimes in the $(t_0, \Delta t)$ coordinate plane (**Figure 7B**) may serve as a first approximation for planning wound treatment strategies. Although the boundaries separating the three regimes in **Figure 7B** may shift across experiments, we might expect the general pattern to hold. For example, if an experimentally tested treatment regimen is found to not shorten healing time to a desirable extent, then the implication is that the domain of actuation is in the blue region of **Figure 7B**. A reasonable choice for the next strategy is to decrease t_0 and increase Δt with the goal of shifting the system from the blue to green region (arrow *a* in **Figure 7B**). However, if the new regimen leads to complications in the inflammatory stage, this implies the shift pushed the actuation domain into the red region, as shown by arrow *b* in **Figure 7B**. Having this mathematically derived parametric plane may help experimenters orient in an unknown field of regimes. The specific values of the thresholds and the corresponding shapes of the boundaries can be clarified experimentally.

We note that the geometry of the domain of actuation corresponds to a ring of a given width at a given radius. Recent

advances in the design of bioelectronic devices provide the ability to deliver biochemicals with spatio-temporal precision [7]. Thus, we would like to take full advantage of these capabilities to understand the dependence of treatment effectiveness on proximity to the wound center compared to the wound edge. The lack of knowledge about debris distribution in the wound makes it difficult to predict the optimal actuator position. However, we demonstrate several possible solutions for different debris distributions in the wound. Experiments on wound treatment should be done to clarify the optimal spatial distribution of treatment actuators.

Nonetheless, the general trends for changes in wound healing times with respect to changes in actuation timing are similar for various fixed spatial profiles. The importance of considering spatial context in wound treatment remains an open question. If considering spatial information can significantly improve treatment strategies, then such numerical studies can inform future actuator design.

5. CONCLUSION

Wound healing consists of a sequence of stages with different cells performing different functions. Therefore, it is reasonable to assume that at each stage, different medications should be applied to improve healing. However, to our knowledge, there are not many studies of dynamic wound treatment regimens. In this work, we attempted to find the optimal wound treatment regimen by affecting macrophage polarization.

Actuating macrophage polarization for acceleration of wound healing must be done in a narrow time interval, beginning from the peak time of M1. Too early and too strong treatment of this type may slow down wound cleaning and lead to chronic inflammation. Delayed treatment may have too small of an effect. For the particular parameter values chosen here, the optimal actuating time is between 0.7 and 3.1 days. The shortest observed wound healing time was 11.37 days for a $\sim 15.5\%$ reduction in wound healing time. This is comparable to the results in Liang et al. [53], where time for wound closure was reduced by $\sim 12\text{--}18\%$.

REFERENCES

- Schreml S, Szeimies RM, Prantl L, Landthaler M, Babilas P. Wound healing in the 21st century. *Am Acad Dermatol.* (2010) 63:866–81. doi: 10.1016/j.jaad.2009.10.048
- Kasuya A, Tokura Y. Attempts to accelerate wound healing. *J Dermatol Sci.* (2014) 76:169–72. doi: 10.1016/j.jdermsci.2014.11.001
- Dreifke MB, Jayasuriya AA, Jayasuriya AC. Current wound healing procedures and potential care. *Mater Sci Eng C Mater Biol Appl.* (2015) 48:651–62. doi: 10.1016/j.msec.2014.12.068
- Baron JM, Glatz M, Proksch E. Optimal support of wound healing: new insights. *Dermatology.* (2020) 236:593–600. doi: 10.1159/000505291
- Ubbink DT, Brolmann FE, Go PM, Vermeulen H. Evidence-Based care of acute wounds: a perspective. *Adv Wound Care (New Rochelle).* (2015) 4:286–94. doi: 10.1089/wound.2014.0592
- Murphy PS, Evans GR. Advances in wound healing: a review of current wound healing products. *Plast Surg Int.* (2012) 2012:190436. doi: 10.1155/2012/190436
- Selberg J, Jafari M, Mathews J, Jia M, Pansodtee P, Dechiraju H, et al. Machine learning-driven bioelectronics for closed-loop control of cells. *Adv Intell Syst.* (2020) 2:2000140. doi: 10.1002/aisy.202000140
- Mostafalu P, Tamayol A, Rahimi R, Ochoa M, Khalilpour A, Kiaee G, et al. Smart bandage for monitoring and treatment of chronic wounds. *Small.* (2018) 14:e1703509. doi: 10.1002/sml.201703509
- Hesketh M, Sahin KB, West ZE, Murray RZ. Macrophage phenotypes regulate scar formation and chronic wound healing. *Int J Mol Sci.* (2017) 18:1545. doi: 10.3390/ijms18071545
- Roszer T. Understanding the mysterious M2 macrophage through activation markers and effector mechanisms. *Mediators Inflamm.* (2015) 2015:816460. doi: 10.1155/2015/816460
- Mosser DM, Edwards JP. Exploring the full spectrum of macrophage activation. *Nat Rev Immunol.* (2008) 8:958–69. doi: 10.1038/nri2448

To our knowledge, this is the first work in search of an optimal spatio-temporal regime of wound treatment, which can be tested experimentally. We also note that we are only presenting one method of intervention. In the future, this study can be expanded to include additional intervention strategies targeting other biological processes. Thus, this naive modeling approach may help to predict optimal regimes for various treatments with known distinct actions. Combining approaches could potentially lead to unprecedented reductions in wound healing times. We believe this is the first step toward designing smart treatment and development of algorithms for smart wound healing devices.

DATA AVAILABILITY STATEMENT

The raw data supporting the conclusions of this article will be made available by the authors, without undue reservation.

AUTHOR CONTRIBUTIONS

KZ provided context and background, significantly contributed to the model, performed numerical analysis, prepared images, and wrote parts of the original draft. JX performed numerical analysis, prepared images, and parts of the original draft. MG contributed to conceptualization, supervised the work, reviewed, and edited the article. All authors contributed to the article and approved the submitted version.

FUNDING

Research was sponsored by the Office of Naval Research and the DARPA Biotechnologies Office (DARPA/BTO) and was accomplished under Cooperative Agreement Number DC20AC00003.

SUPPLEMENTARY MATERIAL

The Supplementary Material for this article can be found online at: <https://www.frontiersin.org/articles/10.3389/fams.2022.791064/full#supplementary-material>

12. Hoehn K, Marieb EN. *Human Anatomy & Physiology*. San Francisco, CA: Benjamin Cummings (2010).
13. Sherratt JA, Murray JD. Mathematical analysis of a basic model for epidermal wound healing. *J Math Biol.* (1991) 29:389–404. doi: 10.1007/BF00160468
14. Flegg JA, Menon SN, Maini PK, McElwain DL. On the mathematical modeling of wound healing angiogenesis in skin as a reaction-transport process. *Front Physiol.* (2015) 6:262. doi: 10.3389/fphys.2015.00262
15. Jorgensen SN, Sanders JR. Mathematical models of wound healing and closure: a comprehensive review. *Med Biol Eng Comput.* (2016) 54:1297–316. doi: 10.1007/s11517-015-1435-z
16. Dunster JL, Byrne HM, King JR. The resolution of inflammation: a mathematical model of neutrophil and macrophage interactions. *Bull Math Biol.* (2014) 76:1953–80. doi: 10.1007/s11538-014-9987-x
17. Xue C, Friedman A, Sen CK. A mathematical model of ischemic cutaneous wounds. *Proc Natl Acad Sci USA.* (2009) 106:16782–7. doi: 10.1073/pnas.0909115106
18. Cumming BD, McElwain DL, Upton Z. A mathematical model of wound healing and subsequent scarring. *J R Soc Interface.* (2010) 7:19–34. doi: 10.1098/rsif.2008.0536
19. Javierre E, Vermolen FJ, Vuik C, van der Zwaag S. A mathematical analysis of physiological and morphological aspects of wound closure. *J Math Biol.* (2009) 59:605–30. doi: 10.1007/s00285-008-0242-7
20. den Breems NY, Eftimie R. The re-polarisation of M2 and M1 macrophages and its role on cancer outcomes. *J Theor Biol.* (2016) 390:23–39. doi: 10.1016/j.jtbi.2015.10.034
21. Torres M, Wang J, Yannie PJ, Ghosh S, Segal RA, Reynolds A. Identifying important parameters in the inflammatory process with a mathematical model of immune cell influx and macrophage polarization. *PLoS Comput Biol.* (2019) 15:e1007172. doi: 10.1371/journal.pcbi.1007172
22. Delavary BM, van der Veer WM, van Egmond M, Niessen FB, Beelen RH. Macrophages in skin injury and repair. *Immunobiology.* (2011) 216:753–62. doi: 10.1016/j.imbio.2011.01.001
23. Mantovani A, Sica A, Sozzani S, Allavena P, Vecchi A, Locati M. The chemokine system in diverse forms of macrophage activation and polarization. *Trends Immunol.* (2004) 25:677–86. doi: 10.1016/j.it.2004.09.015
24. Mills CD, Kincaid K, Alt JM, Heilman MJ, Hill AM. M-1/M-2 macrophages and the Th1/Th2 paradigm. *J Immunol.* (2000) 164:6166–73. doi: 10.4049/jimmunol.164.12.6166
25. Sindrilaru A, Peters T, Wieschalka S, Baican C, Baican A, Peter H, et al. An unrestrained proinflammatory M1 macrophage population induced by iron impairs wound healing in humans and mice. *J Clin Invest.* (2011) 121:985–97. doi: 10.1172/JCI44490
26. Mirza RE, Fang MM, Ennis WJ, Koh TJ. Blocking interleukin-1 β induces a healing-associated wound macrophage phenotype and improves healing in type 2 diabetes. *Diabetes.* (2013) 62:2579–87. doi: 10.2337/db12-1450
27. Alvarez MM, Liu JC, de Santiago GT, Cha BH, Vishwakarma A, Ghaemmaghami AM, et al. Delivery strategies to control inflammatory response: modulating M1-M2 polarization in tissue engineering applications. *J Control Release.* (2016) 240:349–63. doi: 10.1016/j.jconrel.2016.01.026
28. Qing L, Fu J, Wu P, Zhou Z, Yu F, Tang J. Metformin induces the M2 macrophage polarization to accelerate the wound healing via regulating AMPK/mTOR/NLRP3 inflammasome signaling pathway. *Am J Transl Res.* (2019) 11:655–68.
29. Kotwal GJ, Chien S. Macrophage differentiation in normal and accelerated wound healing. *Results Probl Cell Differ.* (2017) 62:353–364. doi: 10.1007/978-3-319-54090-0_14
30. Kim H, Wang SY, Kwak G, Yang Y, Kwon IC, Kim SH. Exosome-Guided phenotypic switch of M1 to M2 macrophages for cutaneous wound healing. *Adv Sci (Weinh).* (2019) 6:1900513. doi: 10.1002/adv.201900513
31. Goren I, Muller E, Schiefelbein D, Christen U, Pfeilschifter J, Muhl H, et al. Systemic anti-TNF α treatment restores diabetes-impaired skin repair in ob/ob mice by inactivation of macrophages. *J Invest Dermatol.* (2007) 127:2259–67. doi: 10.1038/sj.jid.5700842
32. Weagel E, Smith C, Liu PG, Robison R, O'Neill K. Macrophage polarization and its role in cancer. *J Clin Cell Immunol.* (2015) 6:4. doi: 10.4172/2155-9899.1000338
33. Ziraldo C, Soloviyev A, Allegritti A, Krishnan S, Henzel MK, Sowa GA, et al. A computational, tissue-realistic model of pressure ulcer formation in individuals with spinal cord injury. *PLoS Comput Biol.* (2015) 11:e1004309. doi: 10.1371/journal.pcbi.1004309
34. Krzyszczyk P, Schloss R, Palmer A, Berthiaume F. the role of macrophages in acute and chronic wound healing and interventions to promote pro-wound healing phenotypes. *Front Physiol.* (2018) 9:419. doi: 10.3389/fphys.2018.00419
35. Frykberg RG, Banks J. Challenges in the treatment of chronic wounds. *Adv Wound Care (New Rochelle).* (2015) 4:560–82. doi: 10.1089/wound.2015.0635
36. Doran AC, A JY, Tabas I. Efferocytosis in health and disease. *Nat Rev Immunol.* (2020) 20:254–67. doi: 10.1038/s41577-019-0240-6
37. Landen NX, Li D, Stahle M. Transition from inflammation to proliferation: a critical step during wound healing. *Cell Mol Life Sci.* (2016) 73:3861–85. doi: 10.1007/s00018-016-2268-0
38. Fadok VA, Bratton DL, Konowal A, Freed PW, Westcott JY, Henson PM. Macrophages that have ingested apoptotic cells *in vitro* inhibit proinflammatory cytokine production through autocrine/paracrine mechanisms involving TGF- β , PGE $_2$, and PAF. *J Clin Invest.* (1998) 101:890–8. doi: 10.1172/JCI1112
39. Tracy LE, Minasian RA, Catterson EJ. Extracellular matrix and dermal fibroblast function in the healing wound. *Adv Wound Care (New Rochelle).* (2016) 5:119–36. doi: 10.1089/wound.2014.0561
40. Li B, Wang JH. Fibroblasts and myofibroblasts in wound healing: force generation and measurement. *J Tissue Viability.* (2011) 20:108–20. doi: 10.1016/j.jtv.2009.11.004
41. Zhao M, Song B, Pu J, Forrester JV, McCaig CD. Direct visualization of a stratified epithelium reveals that wounds heal by unified sliding of cell sheets. *FASEB J.* (2003) 17:397–406. doi: 10.1096/fj.02-0610com
42. Murray JD. *Mathematical Biology, 3rd Edn.* New York, NY: Springer (2002).
43. Olsen L, Sherratt JA, Maini PK. A mathematical model for fibro-proliferative wound healing disorders. *Bull Math Biol.* (1996) 58:787–808. doi: 10.1007/BF02459482
44. Painter KJ. Modelling cell migration strategies in the extracellular matrix. *J Math Biol.* (2009) 58:511–43. doi: 10.1007/s00285-008-0217-8
45. Kolmogorov A, Petrovskii I, Piskunov N. A study of the diffusion equation with increase in the amount of substance, and its application to a biological problem. *Bull Moscow Univ Math Mech.* (1937) 1:1–26.
46. Hau T, Hoffman R, Simmons RL. Mechanisms of the adjuvant effect of hemoglobin in experimental peritonitis. I. In vivo inhibition of peritoneal leukocytosis. *Surgery.* (1978) 83:223–9.
47. Andersson U, Wang H, Palmblad K, Aveberger AC, Bloom O, Erlandsson-Harris H, et al. High mobility group 1 protein (HMG-1) stimulates proinflammatory cytokine synthesis in human monocytes. *J Exp Med.* (2000) 192:565–70. doi: 10.1084/jem.192.4.565
48. Du Y, Ren P, Wang Q, Jiang SK, Zhang M, Li JY, et al. Cannabinoid 2 receptor attenuates inflammation during skin wound healing by inhibiting M1 macrophages rather than activating M2 macrophages. *J Inflamm (Lond).* (2018) 15:25. doi: 10.1186/s12950-018-0201-z
49. Coxon A, Tang T, Mayadas TN. Cytokine-activated endothelial cells delay neutrophil apoptosis *in vitro* and *in vivo*. A role for granulocyte/macrophage colony-stimulating factor. *J Exp Med.* (1999) 190:923–34. doi: 10.1084/jem.190.7.923
50. Berg HC. *Random Walks in Biology*. Princeton, NJ: Princeton University Press (1993).
51. Wheeler AP, Wells CM, Smith SD, Vega FM, Henderson RB, Tybulewicz VL, et al. Rac1 and Rac2 regulate macrophage morphology but are not essential for migration. *J Cell Sci.* (2006) 119(Pt 13):2749–57. doi: 10.1242/jcs.03024
52. Godwin A, Sharma A, Yang WL, Wang Z, Nicastro J, Coppa GF, et al. Receptor-Interacting protein kinase 3 deficiency delays cutaneous wound healing. *PLoS ONE.* (2015) 10:e0140514. doi: 10.1371/journal.pone.0140514

53. Liang Y, Tian H, Liu J, Lv Y, Wang Y, Zhang J, et al. Application of stable continuous external electric field promotes wound healing in pig wound model. *Bioelectrochemistry*. (2020) 135:107578. doi: 10.1016/j.bioelechem.2020.107578
54. Yoon DJ, Fregoso DR, Nguyen D, Chen V, Strbo N, Fuentes JJ, et al. A tractable, simplified ex vivo human skin model of wound infection. *Wound Repair Regen*. (2019) 27:421–5. doi: 10.1111/wrr.12712

Author Disclaimer: The views and conclusions contained in this document are those of the authors and should not be interpreted as representing the official policies, either expressed or implied, of the Office of Naval Research and the DARPA Biotechnologies Office (DARPA/BTO) or the U.S. Government. The U.S. Government is authorized to reproduce and distribute reprints for Government purposes notwithstanding any copyright notation herein.

Conflict of Interest: The authors declare that the research was conducted in the absence of any commercial or financial relationships that could be construed as a potential conflict of interest.

Publisher's Note: All claims expressed in this article are solely those of the authors and do not necessarily represent those of their affiliated organizations, or those of the publisher, the editors and the reviewers. Any product that may be evaluated in this article, or claim that may be made by its manufacturer, is not guaranteed or endorsed by the publisher.

Copyright © 2022 Zlobina, Xue and Gomez. This is an open-access article distributed under the terms of the Creative Commons Attribution License (CC BY). The use, distribution or reproduction in other forums is permitted, provided the original author(s) and the copyright owner(s) are credited and that the original publication in this journal is cited, in accordance with accepted academic practice. No use, distribution or reproduction is permitted which does not comply with these terms.



Multiscale and Multiphysics Modeling of Anisotropic Cardiac RFCA: Experimental-Based Model Calibration *via* Multi-Point Temperature Measurements

Leonardo Molinari¹, Martina Zaltieri², Carlo Massaroni², Simonetta Filippi³, Alessio Gizzi^{3*} and Emiliano Schena²

OPEN ACCESS

Edited by:

André H. Erhardt,
Weierstrass Institute for Applied
Analysis and Stochastics (LG),
Germany

Reviewed by:

Bradley John Roth,
Oakland University, United States
Olivier Bernus,
Université de Bordeaux, France

*Correspondence:

Alessio Gizzi
a.gizzi@unicampus.it

Specialty section:

This article was submitted to
Computational Physiology and
Medicine,
a section of the journal
Frontiers in Physiology

Received: 30 December 2021

Accepted: 22 March 2022

Published: 19 April 2022

Citation:

Molinari L, Zaltieri M, Massaroni C,
Filippi S, Gizzi A and Schena E (2022)
Multiscale and Multiphysics Modeling
of Anisotropic Cardiac RFCA:
Experimental-Based Model Calibration
via Multi-Point
Temperature Measurements.
Front. Physiol. 13:845896.
doi: 10.3389/fphys.2022.845896

¹Department of Mathematics and Computer Science, Emory University, Atlanta, GA, United States, ²Laboratory of Measurement and Biomedical Instrumentation, Department of Engineering, University of Rome Campus Bio-Medico, Rome, Italy, ³Nonlinear Physics and Mathematical Modeling Lab, Department of Engineering, University of Rome Campus Bio-Medico, Rome, Italy

Radiofrequency catheter ablation (RFCA) is the mainstream treatment for drug-refractory cardiac fibrillation. Multiple studies demonstrated that incorrect dosage of radiofrequency energy to the myocardium could lead to uncontrolled tissue damage or treatment failure, with the consequent need for unplanned reoperations. Monitoring tissue temperature during thermal therapy and predicting the extent of lesions may improve treatment efficacy. Cardiac computational modeling represents a viable tool for identifying optimal RFCA settings, though predictability issues still limit a widespread usage of such a technology in clinical scenarios. We aim to fill this gap by assessing the influence of the intrinsic myocardial microstructure on the thermo-electric behavior at the tissue level. By performing multi-point temperature measurements on *ex-vivo* swine cardiac tissue samples, the experimental characterization of myocardial thermal anisotropy allowed us to assemble a fine-tuned thermo-electric material model of the cardiac tissue. We implemented a multiphysics and multiscale computational framework, encompassing thermo-electric anisotropic conduction, phase-lagging for heat transfer, and a three-state dynamical system for cellular death and lesion estimation. Our analysis resulted in a remarkable agreement between *ex-vivo* measurements and numerical results. Accordingly, we identified myocardium anisotropy as the driving effect on the outcomes of hyperthermic treatments. Furthermore, we characterized the complex nonlinear couplings regulating tissue behavior during RFCA, discussing model calibration, limitations, and perspectives.

Keywords: radiofrequency ablation, myocardial anisotropy, hyperthermal tissue damage, fiber Bragg grating sensors, finite element analysis

1 INTRODUCTION

Cardiac arrhythmias are the most common and disabling pathologies worldwide (Pires et al., 1995; Kornej et al., 2020; Siontis et al., 2021) with increasing incidence—it is estimated that about 16 million people in the United States will suffer from this condition by 2050 (Patel et al., 2014). In the context of minimally invasive procedures, cardiac radiofrequency catheter ablation (RFCA) emerged as the leading clinical routine for treating cardiac arrhythmias (Nath et al., 1994). RFCA causes hyperthermic lesions destroying myocardial regions responsible for arrhythmias foci. Radiofrequency (RF) energy is carried out through a delivery antenna to target areas where the temperature is raised to at least 50°C (Wood et al., 2011). Cellular excitability is eliminated in correspondence with the ablation sites, and thermal damage is produced (Morady, 1999).

Despite the extensive clinical achievements which result in a high success rate and low mortality, RFCA is still subject to several drawbacks. An excessive thermal increase can produce steam pops and unwanted tissue lesions (Zaltieri et al., 2021). On the contrary, failure to achieve target temperatures can lead to incomplete tissue ablations, which may provoke recurrent arrhythmias that often require repeated clinical interventions. Since the temperature profoundly affects the outcome of this procedure, considerable interest has matured in predicting macroscopic thermal patterns and, in turn, estimating the expected lesion size to make RFCA risk-free and prevent failures.

Computational modeling has emerged as a feasible way to predict the outcome of cardiac RFCA procedures and to tackle specific unanswered questions. Numerical techniques, including the Finite Element Method (FEM), have been extensively used in numerous studies on cardiac RFCA (Dillon-Murphy et al., 2018; Roney et al., 2020) and, more generally, RFCA of biological tissues. Within the spectrum of RFCA, the electromagnetic source is approximated by a quasi-static form of Maxwell's equations, often disregarding the effects of external factors. Heat transfer is usually modeled *via* the classical Pennes' bio-heat equation due to its relative ease of implementation (Trujillo and Berjano, 2013; González-Suárez and Berjano, 2015; Park et al., 2016; Qadri et al., 2017; Petras et al., 2019). Only a few more complex models incorporating non-Fourier effects have been proposed in the literature (Tzou, 1995; Sahoo et al., 2014; Singh and Melnik, 2019). Besides, the vast majority of computational studies include simplified two-dimensional geometries (Schutt et al., 2009; Joseph and Rajappan, 2012; Hamaya et al., 2018; Singh and Melnik, 2019). The 2D nature of the current models dramatically reduces their reliability and predictability—planar domains cannot investigate cardiac microstructural features, i.e., rotational anisotropic conduction.

The role of the myocardial fibers on thermal conductive properties remains unexamined mainly, both from the experimental and computational points of view. Previous works claimed the anisotropic thermal and electrically conductive nature of the myocardium as a possible explanation for the discrepancies found between elliptical

experimental/clinical lesions and the computed spherical ones (Petras et al., 2019, 2018). Only one study hitherto was found, which integrates anisotropic conductive properties in the analysis of cardiac ablation (Xie and Zemlin, 2016). Nevertheless, the work focused on pulsed-field ablation with penetrating needles and neglected tissue heat transfer. In a recent contribution (Molinari et al., 2022), we derived a novel thermo-mechanical framework for cardiac RFCA based on energetic reasoning and variational procedures also accounting for tissue microstructure. We showed that complex patterns of tissue damage and residual strains appear depending on the applied contact force and local material properties. Here, we aim at generalizing the classical thermo-electric model from the literature, considering, for the first time, a three-dimensional model of RFCA including anisotropic thermo-electrical conduction, a three-state cellular death model, and a higher-order formulation for heat transfer. In addition, we work out an experimental-based model tuning considering an innovative high-resolution measure of the thermal profile during the RFCA procedure employing Fiber Bragg Grating (FBG) sensors.

The final aim of the work is to assess the influence of the underlying myocardial microstructure on the thermal behavior at the tissue level. Accordingly, we present a multiphysics material model, implemented in a multiscale computational framework fine-tuned via multi-point temperature measurements on *ex-vivo* swine cardiac tissue undergoing RFCA. We exploited FBG sensors due to their excellent metrological and physical characteristics (i.e., small size, high thermal sensitivity, good accuracy and spatial resolution, short response time, immune to electromagnetic fields (Schena et al., 2016)), obtaining high spatio-temporal resolution of temperature maps in tissue depth. Ultimately, we integrated the space and time evolution of thermal ablation into a simplified three-dimensional finite element model of the cardiac tissue. We further considered multiscale boundary conditions, incorporating the effect of blood flow, electrical impedance, and power dissipation circuit, thus addressing and discussing several open questions of clinical relevance.

The manuscript is organized as follows. In **Section 2** we provide the experimental setup developed and the RFCA protocol adopted. Besides, a description of FBGs for temperature measurements is described in terms of working principle, sensors positioning, and tissue damage estimation. In **Section 3** we detail the computational model developed in terms of geometry, microstructured, and boundary conditions. We work out our generalized theory of heat transfer, further introducing an additional coupled model of thermal damage by means of cellular death and thermal dependency of material properties. **Section 4** presents experimental and modeling results based on numerical convergence, sensitivity analysis, and fine-tuning of the anisotropic constitutive parameters. In particular, we discuss model accuracy and predictability quantifying the relative error between simulations and experiments. **Section 5** closes the manuscript with a critical discussion of the results, highlighting limitations and perspectives.

TABLE 1 | Impedance values at the starting (li) and ending (lf) instants of each of the six experimental RF delivery process.

Trial	li [Ω]	lf [Ω]
1	58	56
2	59	57
3	54.5	52
4	57	55
5	61	58
6	51	50

2 RFCA ON EX-VIVO SWINE MYOCARDIUM

This section describes the experimental setup and the RFCA protocol used to investigate the temperature variation (ΔT) in the porcine myocardium. A focus on the FBG sensors' working principle is provided.

2.1 Experimental Setup and RFCA Protocol

Two freshly excised swine hearts were collected from the local slaughterhouse. Three myocardial specimens with a thickness of at least 30 mm were extracted from the left ventricular area (such

a thickness ensures that the RFCA treatment is confined within the ventricular wall) and put into a water bath at $\approx 37^\circ\text{C}$ to achieve body temperature. Each specimen was then positioned in a container filled with saline solution, placed upon a precision digital scale (EU C7500, Gibertini Elettronica, Novate Milanese, MI). An RF antenna (FlexAbility™ Ablation Catheter Sensor Enabled™, Abbott Medical, MN, United States) with 2.5 mm of tip diameter and connected to a cooling system (Cool Point™, Abbott Medical, MN, United States) delivering 17 [mL/min] of saline solution was positioned on the surface of the tissue. A slight pressure was exerted on the antenna until the value of about 12 gf (i.e., about 0.118 N) was displayed by the scale, to simulate clinical pressure conditions. A perforated plexiglass positioner was exploited to hold the RF antenna in place. Four optical FBG arrays were inserted into the specimen with the help of four steel needles 20 Gauge calipered. RF impulses were produced by a RF generator (Generatore Ampere, Abbott Medical, MN, United States). A spectrum analyzer (si255 based on Hyperion Platform, Micron Optics, Atlanta, GA, United States) connected to a personal computer was employed during all the RFCAs to collect the fibers' outputs at 1 kHz of sampling frequency. Impedance measurement was performed during the ablation

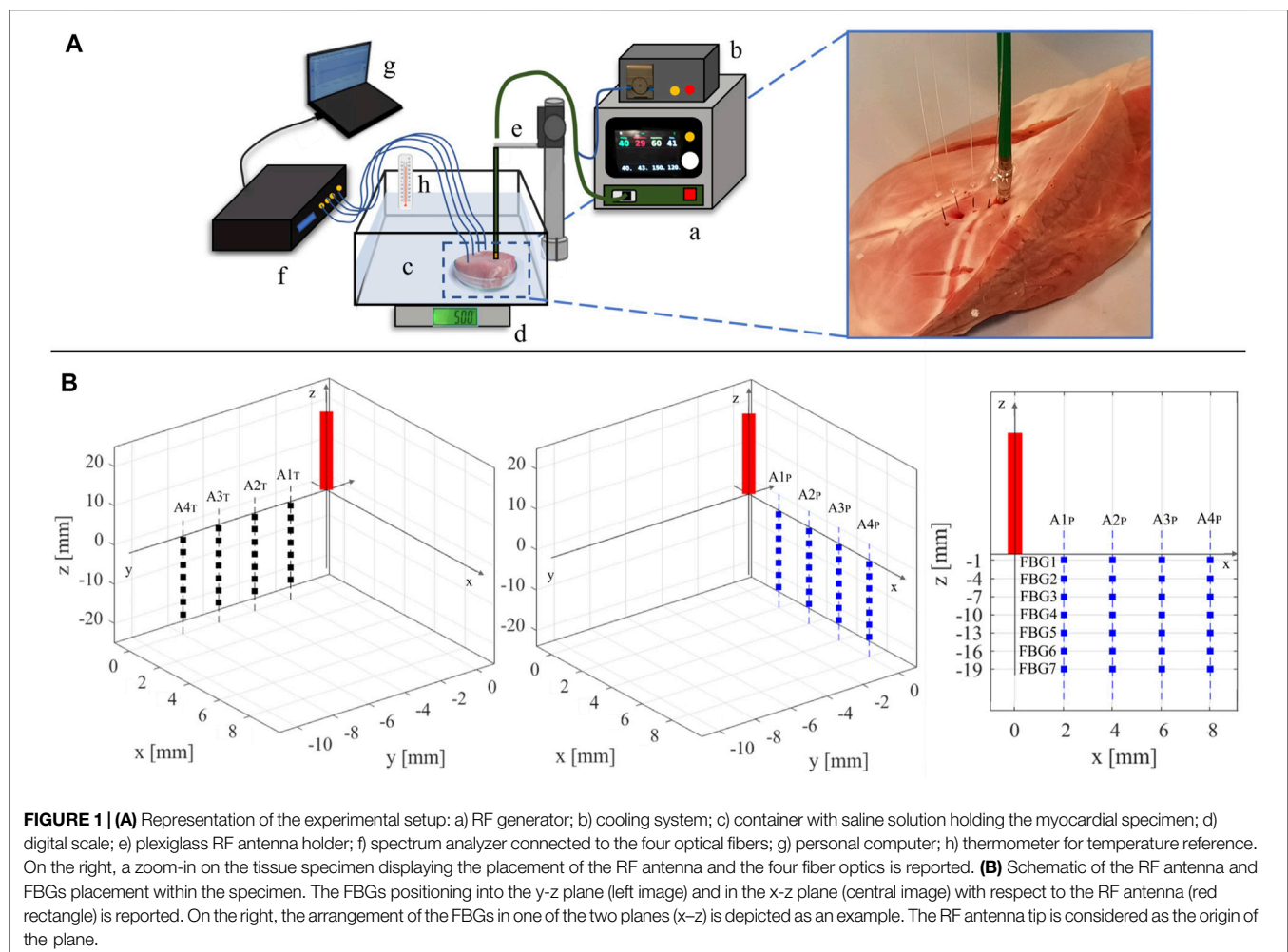


FIGURE 1 | (A) Representation of the experimental setup: a) RF generator; b) cooling system; c) container with saline solution holding the myocardial specimen; d) digital scale; e) plexiglass RF antenna holder; f) spectrum analyzer connected to the four optical fibers; g) personal computer; h) thermometer for temperature reference. On the right, a zoom-in on the tissue specimen displaying the placement of the RF antenna and the four fiber optics is reported. (B) Schematic of the RF antenna and FBGs placement within the specimen. The FBGs positioning into the y-z plane (left image) and in the x-z plane (central image) with respect to the RF antenna (red rectangle) is reported. On the right, the arrangement of the FBGs in one of the two planes (x-z) is depicted as an example. The RF antenna tip is considered as the origin of the plane.

procedure. The values at the starting and ending instants of each RF delivery process of the protocol described below are provided in **Table 1**. In **Figure 1A**, the experimental setup is shown.

Two RFCAs were performed for 60 s of treatment time at 30 W of power delivery in two different points of each specimen. On every tissue sample, fibers placement and RF deliveries were executed according to the experimental protocol detailed as follows: 1) the RF antenna was set in a specific point of the tissue surface; 2) the four optical fibers were placed in a x-z plane parallel to the longitudinal axis of the antenna; 3) a first RF delivery was performed; 4) the optical fibers were removed, and the antenna was moved about 4 cm below the previous application site; 5) the four optical fibers were inserted in a y-z plane parallel to the longitudinal axis of the antenna and mutually orthogonal to the previous x-z plane; 6) a second RFCA was performed. For the sake of clarity, an example of fiber positioning is shown in **Figure 1B**.

2.2 FBGs for Temperature Measurements

Multi-point ΔT measurements were performed into swine myocardial specimens (starting from the initial tissue temperature $T_0 \approx 37^\circ\text{C}$) during RFCA by means of four nominally identical FBG arrays (FiSens GmbH, Braunschweig, Germany). Each array enclosed 7 FBGs (acrylate coating, reflectivity value $>20\%$, FWHM value $<2\text{ nm}$, and declared thermal sensitivity $S_T = 0.01\text{ nm}^\circ\text{C}$) of 1 mm in length and 2 mm of edge-to-edge distance (total sensing length of 19 mm), each of whose set at a specific wavelength (i.e., Bragg wavelength, $\lambda_B\text{ nm}$) ranging from 1,500 to 1,600 nm.

2.2.1 Working Principle

Once illuminated by a broadband source, an FBG operates as a notch filter which reflects a narrow spectrum of light centered around its λ_B . As shown in (1), λ_B is function of the core effective refractive index ($\eta_{\text{eff}} [\cdot]$) and the grating period ($\Lambda [\text{nm}]$) (Erdogan, 1997):

$$\lambda_B = 2\eta_{\text{eff}}\Lambda \quad (1)$$

Both η_{eff} and Λ depend on ΔT and strain (ϵ). These two parameters cause a shift in the reflected spectrum, thus of λ_B ($\Delta\lambda_B$). As the experiments were performed in a strain-free configuration, the $\Delta\lambda_B$ was attributable to the ΔT contribute only, as also proven in a previous work (Zaltieri et al., 2020). The relationship between $\Delta\lambda_B$ and ΔT reads:

$$\frac{\Delta\lambda_B}{\lambda_B} = S_T\Delta T \quad (1a)$$

2.2.2 Sensors Positioning Within Tissue

Before each RFCA, the optical fibers were inserted into the myocardial tissue and placed into the specimen (according to anatomical landmarks), parallel to the longitudinal axis of the RF antenna and spaced 2 mm, 4 mm, 6 mm, and 8 mm apart from it. The fiber insertion was adjusted to have all the FBGs as reported in **Figure 1B**. For ease of reference, the optical FBG arrays are denoted with “A” associated to a number from 1 to 4, starting

from the closest to the RF antenna to the farthest one. Also, the fibers belonging to the x-z plane (which is parallel to the RF antenna) are denoted by the subscript “P” (i.e., $A1_P, A2_P, A3_P$, and $A4_P$), while the ones lying in the y-z plane (which is transversal to the x-z plane) are denoted by the subscript “T” (i.e., $A1_T, A2_T, A3_T$, and $A4_T$).

The 7 FBGs embedded in each array are labelled with a progressive number from 1 to 7 (i.e., FBG1, FBG2, FBG3, FBG4, FBG5, FBG6 and FBG7), starting from the outermost to the innermost. In each plane, a total amount of 28 sensing points distributed in a tissue area of $6\text{ mm} \times 19\text{ mm}$ are positioned.

2.2.3 Hyperthermal Tissue Damage Estimation

At the end of the experimental session, the hyperthermal damage caused to the myocardial tissue by RFCA was evaluated. For each specimen, in correspondence with every ablation site, tissue was sectioned along the insertion plane of the arrays. The dimensions of each lesion (intended as the area that visually showed a lighter coloring, as common in the literature (Calzolari et al., 2017)) were manually estimated in terms of length and depth by means of a digital caliper.

3 COMPUTATIONAL MODEL

3.1 Computational Domain and Myocardial Fiber Modeling

The computational model developed in the present work replicates the experimental setup described before by means of a simplified geometry model. We included a tissue sample of $8\text{ cm} \times 8\text{ cm} \times 3\text{ cm}$ and the surrounding domain of saline solution $13\text{ cm} \times 13\text{ cm} \times 9\text{ cm}$ (see **Figure 2A**). The chosen dimensions, with constant thickness, are in line with the physical dimensions of a porcine ventricular wall and do not affect the overall numerical results as discussed in the following. The catheter and electrode geometries have been omitted to reduce the overall computational burden and have been considered by appropriate thermal and electrical boundary conditions detailed in the next sections. The geometry is encapsulated in a larger box to which a coordinate scaling was applied. Therefore, these regions are treated as having an infinite extent compared to the scale length of the model, thereby minimizing boundary effects. According to well-established evidence, ventricular myocardial rotational anisotropy was implemented assuming a 120° counterclockwise rotation of the fibers, from epicardium to endocardium (Lombaert et al., 2012). To set a direct comparison with experimental data, fibers were assumed parallel to the tissue surface and aligned to the x-axis of the epicardial layer (see **Figure 2B**). We remark that myocardial fibers rotate continuously throughout the ventricular wall building up a sheet-like transverse isotropic material changing the conductivity properties along the depth. In other words, the material is both anisotropic and heterogeneous. The fiber rotational anisotropy is thus described by the law:

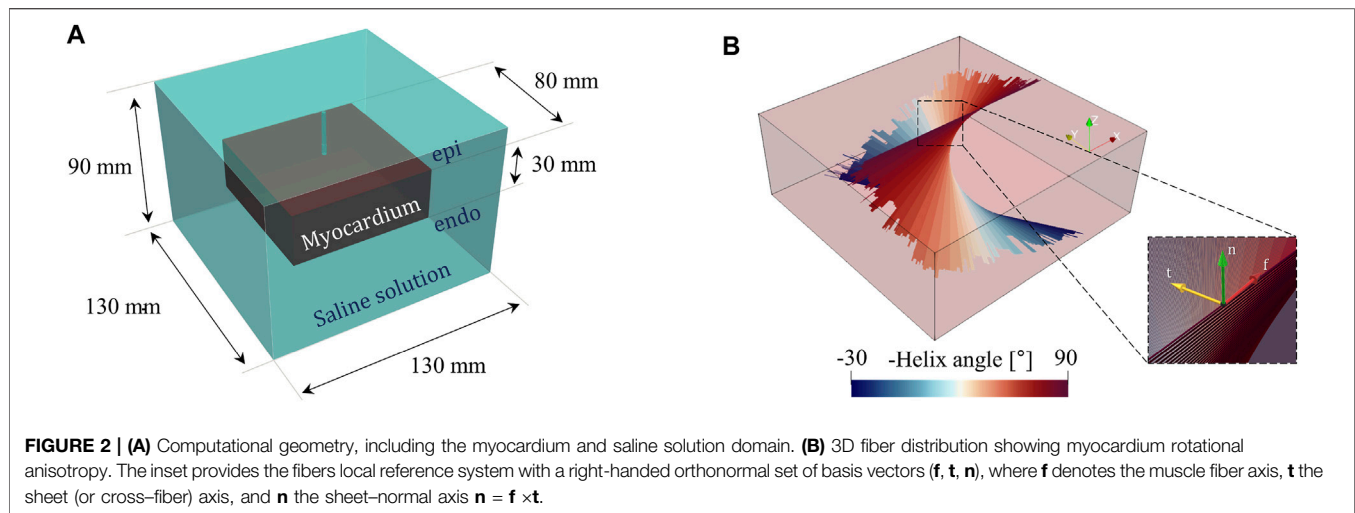


FIGURE 2 | (A) Computational geometry, including the myocardium and saline solution domain. **(B)** 3D fiber distribution showing myocardium rotational anisotropy. The inset provides the fibers local reference system with a right-handed orthonormal set of basis vectors (\mathbf{f} , \mathbf{t} , \mathbf{n}), where \mathbf{f} denotes the muscle fiber axis, \mathbf{t} the sheet (or cross-fiber) axis, and \mathbf{n} the sheet-normal axis $\mathbf{n} = \mathbf{f} \times \mathbf{t}$.

$$\theta(z) = \theta_{\text{epi}} + \frac{z - z_{\text{epi}}}{z_{\text{endo}} - z_{\text{epi}}} (\theta_{\text{endo}} - \theta_{\text{epi}}) \quad (2)$$

being z the thickness direction with versor \mathbf{n} .

3.2 Multiscale Electrical Model

The electric potential due to the ablative procedure was determined by solving the time-harmonic Maxwell's equations (quasi-static regime), complemented by the constitutive relations:

$$\nabla \cdot \mathbf{J} = 0, \quad \mathbf{J} = \sigma \mathbf{E} + j\omega \mathbf{D}, \quad \mathbf{E} = -\nabla V, \quad \mathbf{D} = \epsilon \mathbf{E} \quad (2a - d)$$

where V is the electric potential, \mathbf{E} the electric field vector, \mathbf{J} the current density vector, \mathbf{D} the electric displacement vector, ϵ the electrical permittivity constant, and ω the angular frequency. Considering the frequency spectrum of RFCA, the wavelength of the electromagnetic field is $\sim 600 \text{ m}$, several orders of magnitude larger than the spatial scale of the system, i.e., $\sim 10 \text{ cm}$. Accordingly, we can assume the biological medium as resistive and solve the quasi-static form of the electrical problem.

The second-order conductivity tensor σ is introduced to model the anisotropic electrical conduction in the ventricular wall as:

$$\sigma = \mathbf{R} \begin{bmatrix} \sigma_f & 0 & 0 \\ 0 & \sigma_t & 0 \\ 0 & 0 & \sigma_n \end{bmatrix} \mathbf{R}^T \quad (3)$$

where σ_f , σ_t , σ_n [S/m] are the conductivities in the fiber and transverse directions, respectively, and $\mathbf{R} = [\mathbf{f} \ \mathbf{t} \ \mathbf{n}]$ is the rotation matrix tensor, based on the local fiber reference system see **Figure 2B**):

$$\mathbf{R} = \begin{bmatrix} \cos(\theta) & -\sin(\theta) & 0 \\ \sin(\theta) & \cos(\theta) & 0 \\ 0 & 0 & 1 \end{bmatrix} \quad (4)$$

The saline solution was modelled as an isotropic medium with constant conductivity σ_{sol} .

We further adopted a multiscale modeling approach, coupling the 3D computational domain with an external 0D electrical

circuit composed of an AC voltage generator, an input, and output resistance. The latter is fine-tuned in a pre-processing step to match the experimentally measured impedance and the applied power source, according to the RFCA protocol (see **Figure 3**). The electric potential from the AC voltage generator follows a sigmoidal increase from 0 to $V_0 = \sqrt{2PR_{\text{ref}}}$ in a time window of 1s, with $p = 30 \text{ W}$ being the applied power; Dirichlet boundary conditions were applied to the electrode tip ($V = V_{R_{\text{in}}}$) and the outer surface of the saline solution ($V = V_{R_{\text{out}}}$) to simulate the connection with the external circuit; a homogeneous Neuman boundary condition ($-\sigma \nabla V \cdot \mathbf{n} = 0$) was applied at the catheter surface to simulate electrical insulation.

3.3 Heat Transfer Model

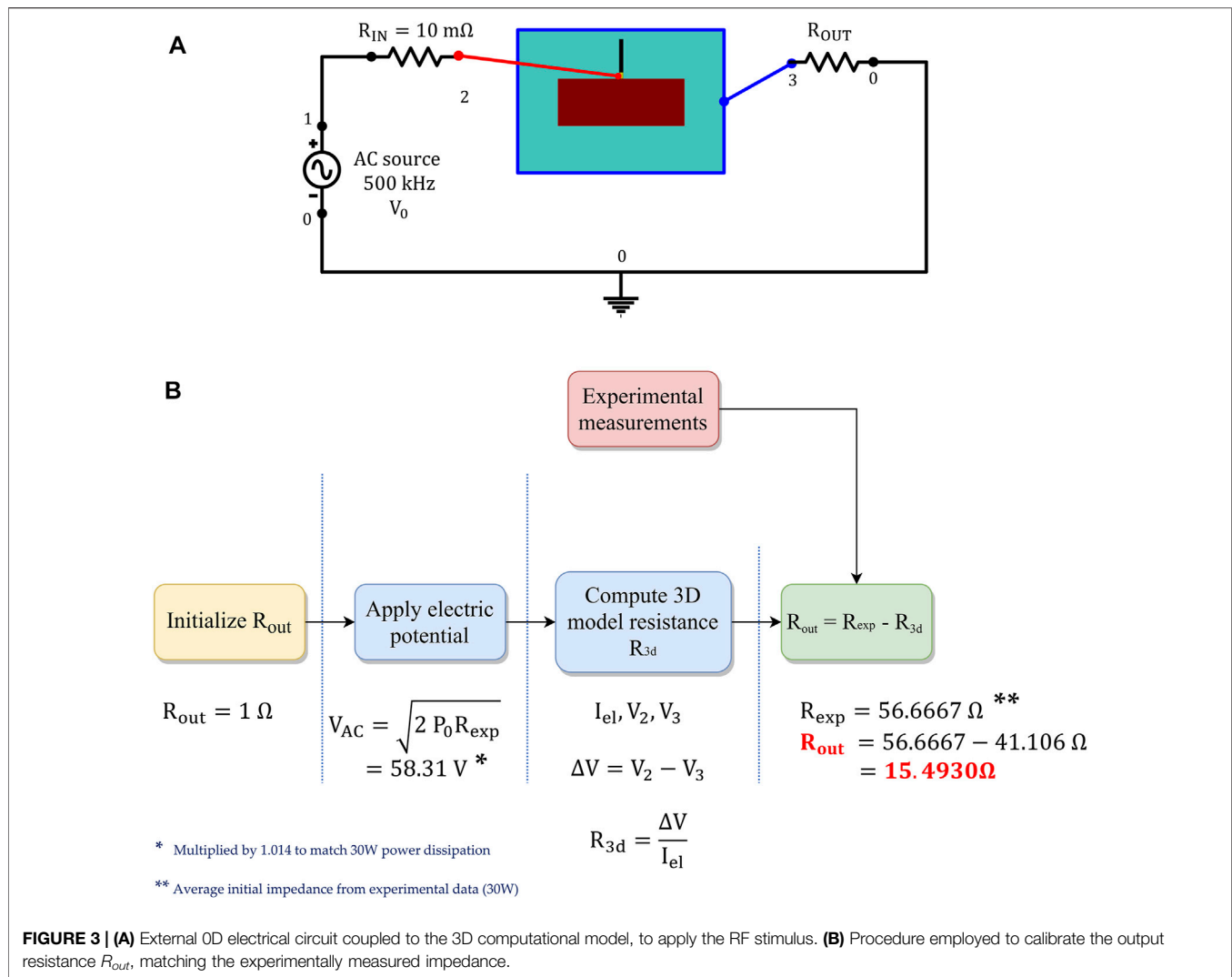
Heat transfer was described using two alternative formulations:

$$\rho c \frac{\partial T}{\partial t} = k \nabla^2 T \quad (5a)$$

$$\tau_q \rho c \frac{\partial^2 T}{\partial t^2} + \rho c \frac{\partial T}{\partial t} = \nabla \cdot (\mathbf{k} \nabla T) + \tau_t \nabla \cdot \left(\mathbf{k} \frac{\partial \nabla T}{\partial t} \right) + Q_s \quad (5b)$$

where **Eq. 5a** refers to the parabolic heat equation based on the classical Fourier's theory (Pennes, 1998) employed for the saline solution domain, and **Eq. 5b** denotes the so called dual-phase-lag (DPL) equation (Tzou, 1995), which is solved for the myocardium. Here, T [K] is the temperature, ρ [kg/m³] the density, c the heat capacity [J/kg · K], \mathbf{k} [W/m · K] the thermal conductivity tensor, $Q_s = \mathbf{J} \cdot \mathbf{E}$ [W/m³] the external electromagnetic heating source, and τ_q , τ_t [s] the phase-lag time constants.

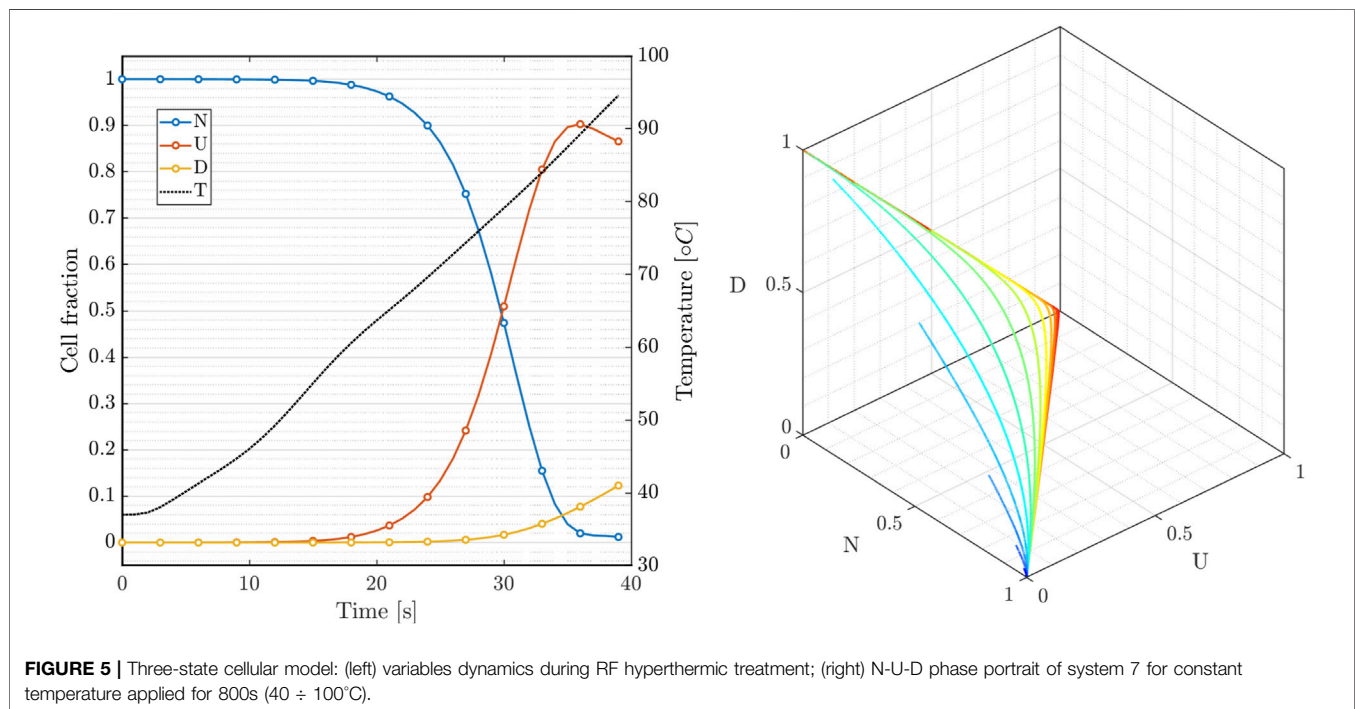
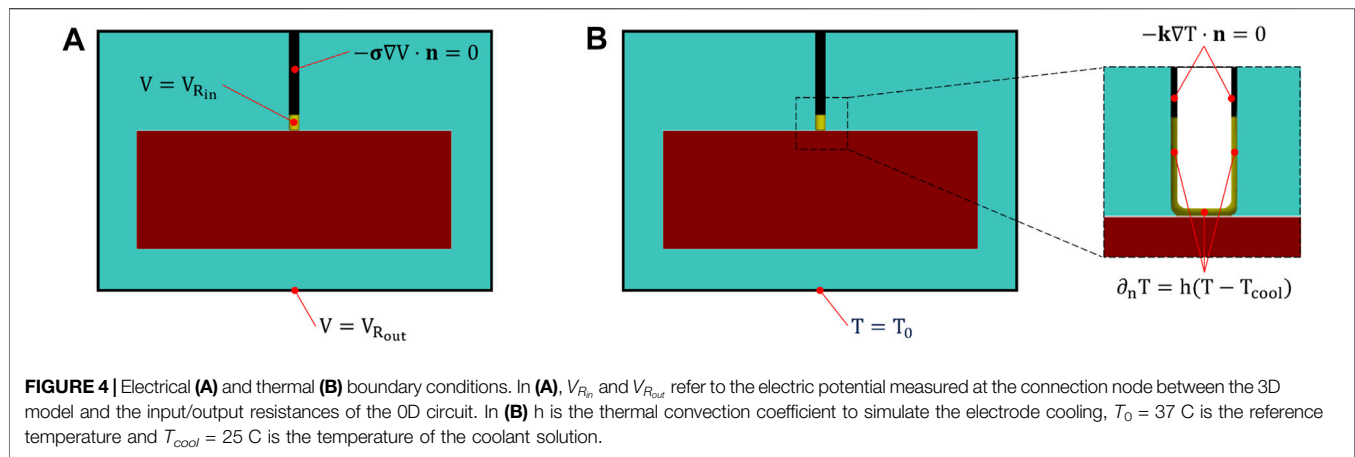
Classical Fourier-based models fail to capture the finite thermal propagation speed due to the inherently heterogeneous microstructure of the biological medium and fast transient temperature increase occurring in hyperthermal treatments due to the small time scales and high-temperature gradients involved. Different theories have been proposed to account for non-Fourier behavior (e.g., hyperbolic heat



equations and relativistic heat transfer). Among them, the so-called dual-phase-lag proposed by (Tzou, 1995) characterizes this phenomenon by means of a hyperbolic heat equation including two thermal relaxation time constants τ_q and τ_t , to control the delayed response between the heat flux and temperature gradient induced in the medium. In such a framework, τ_q defines the time lag between the heat flux and temperature gradient, while τ_t governs the phase lag in establishing the temperature gradient in the conductive medium, accounting for microstructural inhomogeneities of the biological tissue. Notably, the constraint $\tau_q < \tau_t$ (i.e., heat flux precedes the temperature gradient established in the tissue) must be satisfied not to violate the causality principle (Singh and Melnik, 2019). As shown in (López Molina et al., 2014), parabolic heat equation (Fourier's theory) and hyperbolic heat conduction (DPL) converge for infinite time or infinite distance from the electrode. Our findings confirm the assumption that both heat conduction models recover the steady-state solution. In contrast, the DPL model is required to catch the initial transient

temperature increase, which has a critical impact on the evolution of the damage pattern in the tissue.

Consistently with the electrical problem, Eq. 3, we introduce tissue thermal anisotropy by means of the conductivity tensor \mathbf{k} , with k_f , k_t , k_n , the fiber and transverse thermal conductivities, respectively; the saline solution was modeled as an isotropic medium, with a constant thermal conductivity k_{sol} . According to the experimental setup, we did not consider blood perfusion in the ventricle and applied the following boundary conditions for the heat transfer model (see Figure 4): a constant temperature $T_0 = 37^\circ\text{C}$ was imposed to the outer boundaries of the saline solution domain; thermal insulation ($-\mathbf{k}\nabla T \cdot \mathbf{n} = 0$) was assumed at the catheter surface; a Robin convective boundary condition ($-\mathbf{k}\nabla T \cdot \mathbf{n} = h(T - T_c)$) was applied at the electrode-solution and electrode-tissue interface to simulate the effect of saline cooling, assuming a coolant temperature $T_c = 25^\circ\text{C}$, and a heat transfer coefficient $h = 5,927 \text{ [W/m}^2 \cdot \text{K]}$ calculated as in (González-Suárez and Berjano, 2015) by assuming an irrigation rate of 17 [mL/min].



3.4 Thermal Damage Modeling

Thermal damage in ventricular tissue was assessed by using the three-state variable model of hyperthermic cell death proposed by (O'Neill et al., 2011). Such a compartment model assumes the occurrence of three cell states, i.e., alive or native (N), vulnerable or unfolded (U), and dead or denatured (D). The system allows for cell reversibility to the native state N if the thermal history is short enough (reverse transition between N and U states) and preceding irreversible damage in state D. Accordingly, the kinetic equations read:



resulting in a system of 3 coupled ODEs controlling the dynamics of each state, readily:

$$\frac{dN}{dt} = -\alpha_1 N + \alpha_2 U, \quad \frac{dU}{dt} = \alpha_1 N - (\alpha_2 + \alpha_3) U, \quad \frac{dD}{dt} = \alpha_3 U. \quad (7)$$

The model must satisfy the global volumetric constraint $N + U + D = 1$ (conserved cell population). The reaction rates $\alpha_i = A_i e^{-\Delta E_i / (RT)}$ are temperature dependent and determined by the Arrhenius law, where ΔE_i [J/mol] is the activation energy, A_i [1/s] the frequency factor, T [K] the absolute temperature and R [J/mol · K] the universal gas constant. Consistently with previous works (Qadri et al., 2017; Singh and Melnik, 2019), such a dynamic model allows us to predict and quantify several key features of the RFCA procedure. In particular, the tissue is considered to be completely damaged if $N < N_{thr}$, with N_{thr} a tissue-dependent threshold.

TABLE 2 | Material properties for the 3D model including the myocardium and saline solution domains.

Parameter		Value	Ref
Electrical model			
Myocardium fiber electrical conductivity [S/m]	σ_f^0	0.3367	Wang et al. (2001)
Myocardium transverse electrical conductivity [S/m]	σ_t^0, σ_n^0	0.1683	Wang et al. (2001)
Saline solution electrical conductivity [S/m]	σ_{sal}	1.4	Sauerheber and Heinz, (2015)
Myocardium electrical permittivity [F/m]	ϵ_{myo}	3,260	(Gabriel, 1996; Raghavan et al., 2009)
Saline solution electrical permittivity [F/m]	ϵ_{sal}	80	Raghavan et al. (2009) Maribo-Mogensen et al. (2013) Nörtemann et al. (1997)
Thermal model			
Myocardium fiber thermal conductivity [W/m · K]	k_f^0	0.6 ^a	Končan et al. (2000)
Saline solution thermal conductivity [W/m · K]	k_{sal}	0.6	Ozbek and Phillips, (1979)
Myocardium heat capacity [J/kg · K]	c_{myo}^0	3,017	Petrás et al. (2019)
Saline solution heat capacity [J/kg · K]	c_{sal}	4,178	Kho et al. (2021)
Myocardium density [kg/m ³]	ρ_{myo}	1,076	Petrás et al. (2019)
Saline solution density [kg/m ³]	ρ_{sal}	997	Kho et al. (2021)
Relaxation time heat flux [s]	τ_q	8 ^a	Sahoo et al. (2014)
Relaxation time temperature gradient [s]	τ_t	0.045 ^a	Sahoo et al. (2014)
Cell-death model			
Frequency factor $N \rightarrow U$ [1/s]	A_1	3.68×10^{30}	Park et al. (2016)
Frequency factor $U \rightarrow D$ [1/s]	A_2	5.68×10^3	Park et al. (2016)
Frequency factor $U \rightarrow N$ [1/s]	A_3	2.58×10^5	Park et al. (2016)
Activation energy $N \rightarrow U$ [J/mol]	ΔE_1	210, ×, 10^3	Park et al. (2016)
Activation energy $U \rightarrow D$ [J/mol]	ΔE_2	38.6×10^3	Park et al. (2016)
Activation energy $U \rightarrow N$ [J/mol]	ΔE_3	47.2×10^3	Park et al. (2016)

^aParameter included in the parametric analysis.

In **Figure 5**(left), we show the time course of the three state variables applying the RFCA heating curve compared with the temperature rise (black). The model replicates the nonlinear features observed experimentally and characterizes the latency of the cell death rate. Interestingly, the intermediate state balances the transition towards the irreversible dead state. **Figure 5**(right) also provides the phase portrait parametrized by the temperature value in the range $40 \div 100^\circ\text{C}$ for 800 s. The dynamical system is characterized by the fixed point $[N, U, D] = [0, 0, D]$ that changes to $[0, 0, 1]$ once the cell population constraint is included. It is worth mentioning that the fast temperature increase due to RFCA critically modifies the reaction rates α_i driving the system towards the vulnerable state. Such dynamics is much faster than the system's natural evolution towards the global fix point (dead state), enriching the nonlinear evolution of the lesion.

3.5 Thermal Dependency of Material Properties

Predictive simulations of RFCA have been shown to critically depend on the biophysical modeling of tissue parameters (Trujillo and Berjano, 2013). All parameters included in the simulations were gathered from literature and reported in **Table 2**. Consistently with the phenomenological approach adopted, we assumed temperature dependency for the following myocardial constitutive parameters (c , k , σ). In particular σ increases with

temperature while k and c decrease. As a part of the model calibration, different mathematical functions were tested to describe such a temperature dependency (Petrás et al., 2019):

$$c(T) = c_0 [1 - 0.0041 (T - T_0)] \quad (8a)$$

$$k_i^{\text{lin}}(T) = k_i^0 [1 - \lambda_k (T - T_0)], \quad i = f, n, t \quad (8b)$$

$$k_i^{\text{step}}(T) = k_i^0 f(T - T_m, \Delta T_m, \lambda_k), \quad i = f, n, t \quad (8c)$$

$$\sigma_i^{\text{lin}}(T) = \sigma_i^0 [1 - \lambda_\sigma (T - T_0)], \quad i = f, n, t \quad (8d)$$

$$\sigma_i^{\text{step}}(T) = \sigma_i^0 f(T_m - T, \Delta T_m, \lambda_\sigma), \quad i = f, n, t \quad (8e)$$

where $(\cdot)_0$ refers to the baseline value of the parameter at body core temperature $T_0 = 37^\circ\text{C}$, λ_i are rates of increase/decrease, $f(\cdot, \cdot, \cdot)$ is a smoothed Heaviside function with a continuous second derivative, implemented via piecewise 5th-degree polynomials; the parameters $T_m = 68.5^\circ\text{C}$ and ΔT_m in (**Eqs 8c–8e**) control the step reference temperature and the transition zone, respectively. Possible generalizations of the chosen formulation are discussed in the conclusions.

4 RESULTS AND DISCUSSION

4.1 Experimental Results

FBGs data were exported and processed in MATLAB® (Mathworks, Natick, MA, United States) environment. For each experiment, the ΔT trends estimated by the 28 FBGs embedded in the four arrays are analyzed with respect to T_0

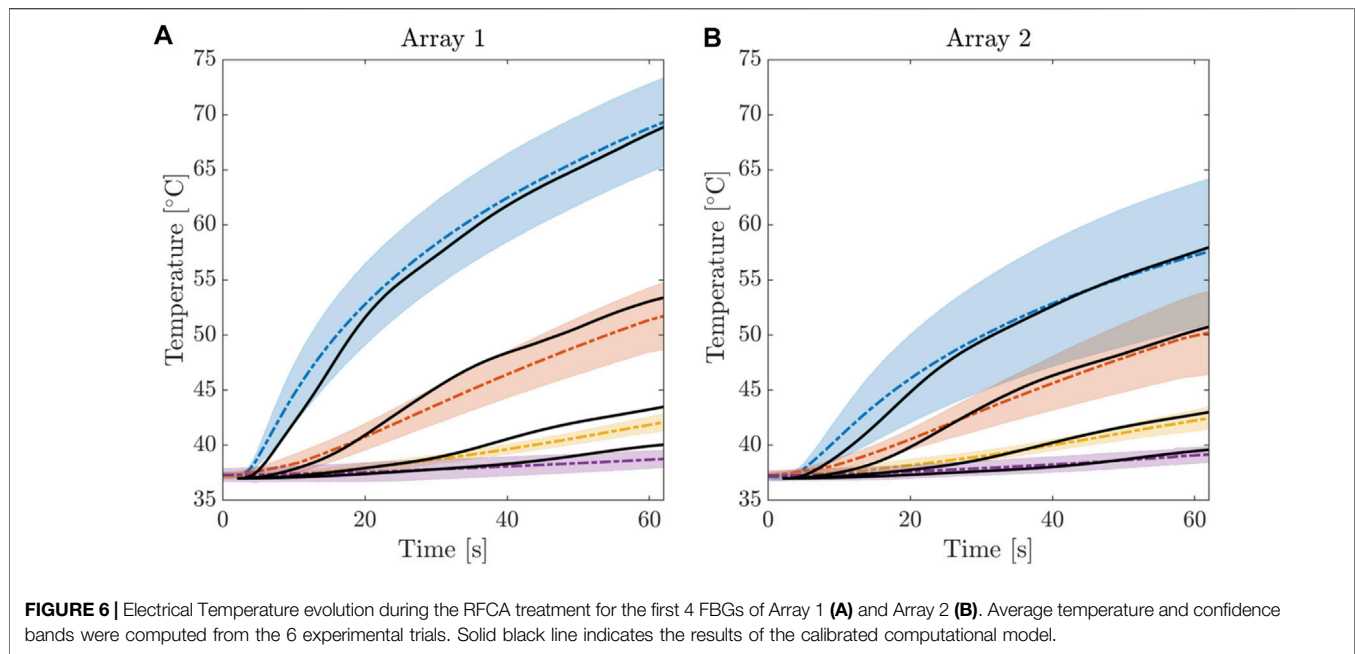


FIGURE 6 | Electrical Temperature evolution during the RFCA treatment for the first 4 FBGs of Array 1 (A) and Array 2 (B). Average temperature and confidence bands were computed from the 6 experimental trials. Solid black line indicates the results of the calibrated computational model.

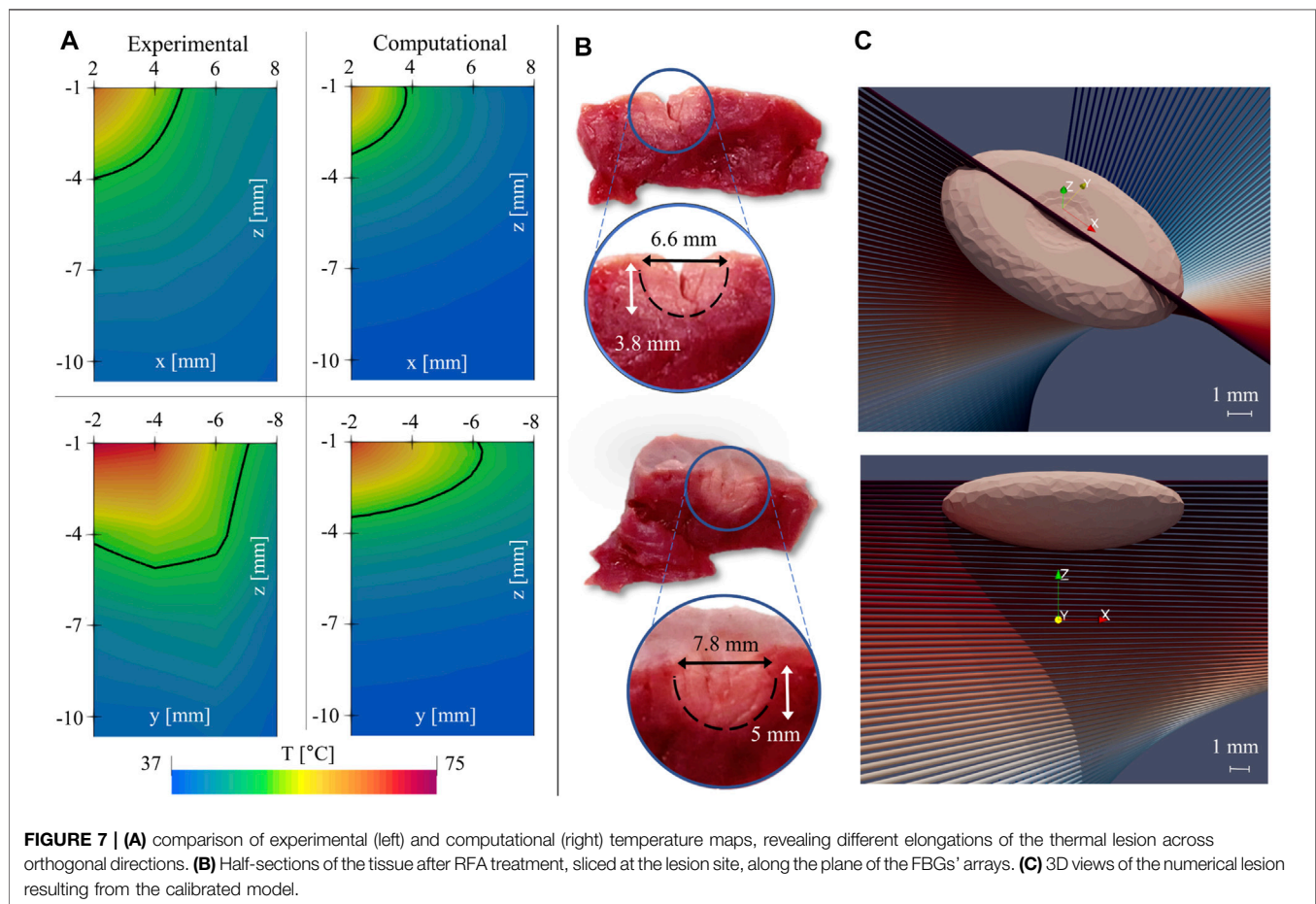


FIGURE 7 | (A) comparison of experimental (left) and computational (right) temperature maps, revealing different elongations of the thermal lesion across orthogonal directions. (B) Half-sections of the tissue after RFCA treatment, sliced at the lesion site, along the plane of the FBGs' arrays. (C) 3D views of the numerical lesion resulting from the calibrated model.

during the 60 s of RFCA. In the **Supplementary Material (SM)**, the plots showing the temperature increase caused by the RF heating effect are reported for all the six experiments. The ΔT measured by each FBG strictly depends on its placement with respect to the RF antenna tip. In fact, FBGs positioned closer to the antenna (see **Figure 1B**, right image), measured higher ΔT than the distant ones, also exhibiting faster temperature rises. For example, among the sensors belonging to the same array (e.g., from FBG1 to FBG7 of A1_T), FBG1 always measures the maximal ΔT values. Also, proceeding deeper into the tissue from FBG1 to FBG7, the obtained ΔT trends decrease. Furthermore, referring to FBGs placed into the tissue at the same depth but belonging to different arrays (e.g., all the FBGs of A1_T, A2_T, A3_T, and A4_T), the ΔT trends are progressively lower starting from A1_T to A4_T. For the sake of completeness, for each FBG the average temperature was computed across the six experiments, together with the standard deviation. **Figure 6** shows the average temperature trends relative to FBG1, FBG2, FBG3 and FBG4 of the arrays A1 and A2, respectively. Such multi-point measurement enabled the identification and quantification of two-dimensional temperature maps to depict the temperature spatial distribution into the treated tissues at the end of each RFCA. More precisely, FBGs data were collected from the start of treatment to the moment of RF discharge. A total amount of 28 experimental values related to the 28 measurement sites as previously depicted were obtained. A linear interpolation was implemented along such temperature values and 2D experimental temperature maps were produced for all the performed RFCAs, both along x-z and y-z planes.

We remark that statistical averages were derived from the whole data set to represent a robust information bandwidth to fit the computational model. As described in the following, the tuning procedure was developed such to identify the optimal anisotropy ratio matching average and variance in tissue depth at different locations.

In **Figure 7A**, two representative experimental temperature maps showing the temperature distributions at the final instant of the treatment (i.e., 60th s) are provided.

The temperature maps evaluated on the x-z plane (top) and on the y-z plane (bottom), and the isothermal level at $T = 50^\circ\text{C}$ (solid black curve) are reported. Temperatures greater than 50°C are considered responsible of myocardial tissue permanent injury. As consequence, it is supposed that the area included into the curve may be representative of the damaged tissue (Zhang et al., 2016). However, the two temperature maps differ in terms of dimension and size of the tissue area surrounded by the 50°C isotherm (which is larger in the y-z plane with respect to the x-z plane). These results confirm the occurrence of a preferential direction along which the heat diffuses. In this specific case, heat transport is higher along the y-axis (**Figure 7A**, bottom) than the x-axis (**Figure 7A**, top). Moreover, heat spreads mostly in the y-z plane than in the x-z plane. We remark that the observed anisotropic evolutions critically depend on FGB location with respect to ventricular microstructure. However, though following anatomical landmarks, FGB positioning does not get information on the underlying fiber structure. Moreover, the in-depth measure along the seven sensors gathers thermal information from twisted myocardial fibers (see **Figure 1**). The definition of the appropriate

myocardial anisotropy requires then an accurate parametric tuning as described in the following section.

Such findings are supported by comparing the hyperthermal damages' dimensions obtained manually by means of the digital caliper. In **Figure 7B**, the two images of the produced lesions sectioned along the x-z plane (upper image) and y-z plane (down image) are shown. As expected, both length and depth of the damage evaluated in the y-z plane are greater than the ones evaluated in the x-z plane (i.e., 7.8 mm vs. 6.6 mm in length, 5 vs. 3.8 mm in depth). In both cases, the lesions which were manually assessed result in larger dimensions than the ones obtained from the 2D temperature maps by using the thermal isocontour method: for instance, widths were 6.6 and 7.8 mm (**Figure 7B**) vs. almost 10 and 18 mm (**Figure 7A**), respectively. Two main motivations can justify such a discrepancy: 1) the occurrence of measurement errors caused by possible inaccuracies in the visual evaluation of the damaged area as there is no unequivocal method for visually assessing the extent of the lesions (no evidence is given that the damaged area uniquely consists of the zone with lighter color), and 2) the adoption of the isothermal curve at 50°C as the sole criterion for the lesion evaluation. Significantly, using this approach, the lesion is determined only based on the local temperature and does not account for the effects of the thermal treatment duration. In addition, there have been concerns about the actual value of the temperature threshold, and various alternatives have been proposed in the literature, e.g., 55 and 59°C (Zhang et al., 2016). To cope with such a non-unique definition, in the following, we provide a rationale based on the three-state dynamics cell model.

4.2 Model Setup and Convergence Analysis

Numerical simulations were performed with the finite element software COMSOL Multiphysics® (Comsol 5.6, COMSOL, Stockholm, Sweden). We discretized the computational domain with mixed linear tetrahedral and hexahedral elements. In particular, hexahedral elements were used to discretize the additional domain for the coordinate scaling (see **Section 2.1**), with a significantly reduced number of elements in the mesh. From a relatively coarse discretization, the mesh was gradually refined near the electrode area, which is strongly affected by hyperthermic treatment. To solve the problem in the time domain, an implicit BDF scheme with adaptive time stepping was adopted. A preliminary convergence analysis ensured that the results were independent of the numerical approximation. Specifically, five different meshes were tested, and the optimal discretization (71,501 degrees of freedom) was chosen to achieve an error below 1% for the maximum temperature of each FBG, compared to the reference solution, i.e., the one with the finest mesh (see Molinari et al. (2021)).

4.3 Sensitivity Analysis and Model Calibration

In the following, we present the extensive sensitivity analysis performed to fine-tune the computational model and match experimental data. Virtual probes were positioned in the computational model following FBG positions in the experimental setup to obtain consistency for quantitative comparison. Initially, a preliminary model tuning was conducted using the parabolic Fourier model **Eq. 5a** getting a

basal thermo-electric profile in the myocardium. Then, the DPL model **Eq. 5b** was introduced to better replicate the transient temperature rise during RFCA treatment. Finally, the parameters for anisotropic thermal conductivity were adjusted to match the spatial temperature distribution obtained from the multi-point measurements. For the sake of conciseness, the complete set of numerical analyses are available at (Molinari et al., 2021). In the following, we will rather present how the calibration process was carried out and discuss the main findings of the study.

4.3.1 Electrical Model Tuning

Different functional forms for the electrical conductivity were tested, as described in **Section 3.5**, with the linear function resulting in better compatibility with reference data. The linear increase rate λ_σ was calibrated to achieve an impedance drop at the end of ablation in the range of experimental measurements ($2 \pm 0.63 \Omega$). A value of $\lambda_\sigma = 0.1$ was selected and included in the upcoming analyses.

4.3.2 Fourier Thermal Model Tuning

A preliminary numerical examination confirmed that the baseline value of thermal conductivity $k_0 = 0.6$ [W/m · K], gathered from literature, provided optimal results in terms of temperature distribution within the tissue. Afterwards, we calibrated the two proposed functions for thermal conductivity, i.e., smoothed step ($\Delta T_m = 55^\circ\text{C}$, $\lambda_k = -0.006$) and linear ($\lambda_k = -0.001$). Results comparison shows that both strategies furnish similar values, albeit with significantly reduced computational time in the case of the linear decrease of k . Accordingly, we assumed a linear temperature dependence for the thermal conductivity.

4.3.3 DPL Model Time Constant Tuning

After calibrating the myocardium's thermal and electrical constitutive properties using the parabolic heat conduction, we investigated the effect of phase lag on the model outcome. To handle separately the two phase-lagging phenomena reproduced in the model (i.e., heat flux and temperature gradient delays), we performed two different tests by modifying the value of one of the time constants while keeping the other fixed. Our investigations determined that the values reported in (Sahoo et al., 2014) ($\tau_q = 8$ s, $\tau_t = 0.045$ s) best fit our experimental data.

4.3.4 Thermal Anisotropy Tuning

Experimental results outlined in **Section 4.1** showed a higher temperature increase in the longitudinal direction than in the tissue depth due to myocardial fiber architecture. To achieve optimal agreement with the time course of temperature curves, we performed multiple numerical tests by varying the coefficients k_f and k_n introduced in **Section 3.3**, i.e., the heat conduction values in the fiber and sheet-normal directions, respectively. Starting from an isotropic conductive medium (i.e., $k_f = k_t = k_n = k$), multiple combinations were tested, with increased conductivity along the fibers ($k_f = 2k, 3k, 5k, 6k$) and decreased conductivity in the sheet-normal direction ($k_n = 0.8k, 0.7k, 0.6k, 0.5k$), holding $\mathbf{k} = \mathbf{k}(T)$ the thermal dependent conductivity tensor as in **Eq. 8b**. Our parametric analysis revealed negligible sensitivity to the cross-fiber conductivity k_r , and we identified $[k_f, k_r, k_n] = [6k, k, 0.5k]$ as the optimal values that

provide the best fit for the experimental temperature curves. We note that, during the optimization process, thermal anisotropy mainly influences the initial temperature increase. In contrast, both contributions, electrical and thermal anisotropies, are required to reproduce experimental transient temperature increases and steady-state values. As a representative example, **Figure 8** compares thermal and electrical anisotropy fitting for different ratios versus the corresponding isotropic case.

A conclusive study was conducted to test the sensitivity of the computational model to the alignment of the FBG arrays and myocardial fibers. We tested five different fiber distributions by gradually rotating the fibers at epicardial level by 10° . As expected, due to the higher conductivity in the fiber direction, we noticed a decrease in temperature as the level of misalignment increases. However, this effect was negligible, particularly for FBGs that are distant from the RF antenna. We remark that FBG arrays have been placed according to anatomical landmarks on the surface of the ventricular surface and the adopted fitting procedure considered the statistical average-variance over the total experiments. Accordingly, the conducted parametric analysis was able to identify the rotational anisotropy ratio recovering the temperature rise with negligible error (see next Section).

4.4 Model Accuracy and Damage Prediction

We present the results obtained from the calibrated model, which are thoroughly compared with the experimental counterpart. In **Figure 6**, we provide the time evolution of the simulated temperature profiles (solid black) over imposed to the average value and confidence bands of the experimental recordings (dashed color) for each FBG. Though clear accordance among calibrated model and *ex-vivo* measurements is obtained, we quantified the goodness of fit using two different strategies. First, we computed the relative error (ΔFBG_i) between the numerical and the average experimental temperature at each instant of the RFCA (**Figures 9A, B**). Additionally, we analyzed the relationship between experimental and simulated temperatures using the Pearson correlation coefficient ρ (**Figure 9C, D**). The plots display the statistical analysis results for the first FBGs of A1 and A2. The error settles below 5% for each FBG of the two arrays, with a slightly higher value (6%) for FBG1/A1 in the initial phase of the RFCA treatment. However, given the non-critical temperature (below 43°C) experienced by the tissue, we reasonably considered this result of minor importance.

As confirmed in **Table 3**, we found an excellent correlation between the predicted and experimental data. More significant relative errors, still below 10%, were found for FBG1 and FBG2 of the remaining arrays, while the correlation remained positive ($\hat{\rho} > 0.98$). Nevertheless, given the distance of the FBGs from the ablation site, the absolute temperature increase was limited (below 43°C). Therefore the marginal discrepancies between the model and the measurements were not considered meaningful. The complete results, including the 28 FBGs traces, are provided in (Molinari et al., 2021).

Finally, we provide a quantitative analysis of damage assessment and lesion prediction criterium. The lesion was first computed with the 50°C thermal isocontour method (consistently with the visual post-processing of experimental data). The computed damage

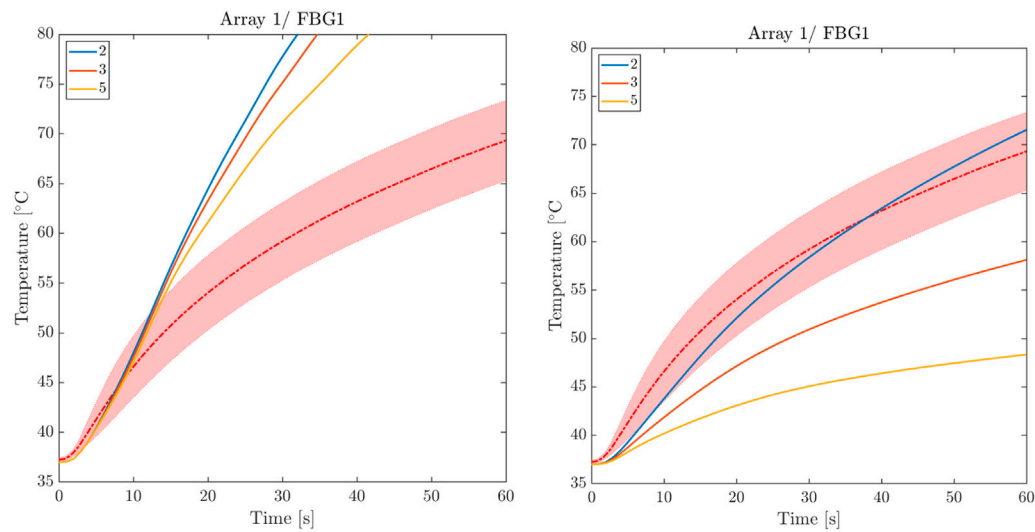


FIGURE 8 | Comparison between thermal and electrical anisotropy fitting. Left: thermal isotropy for three levels of electrical anisotropy. Right: electrical isotropy for three levels of thermal anisotropy.

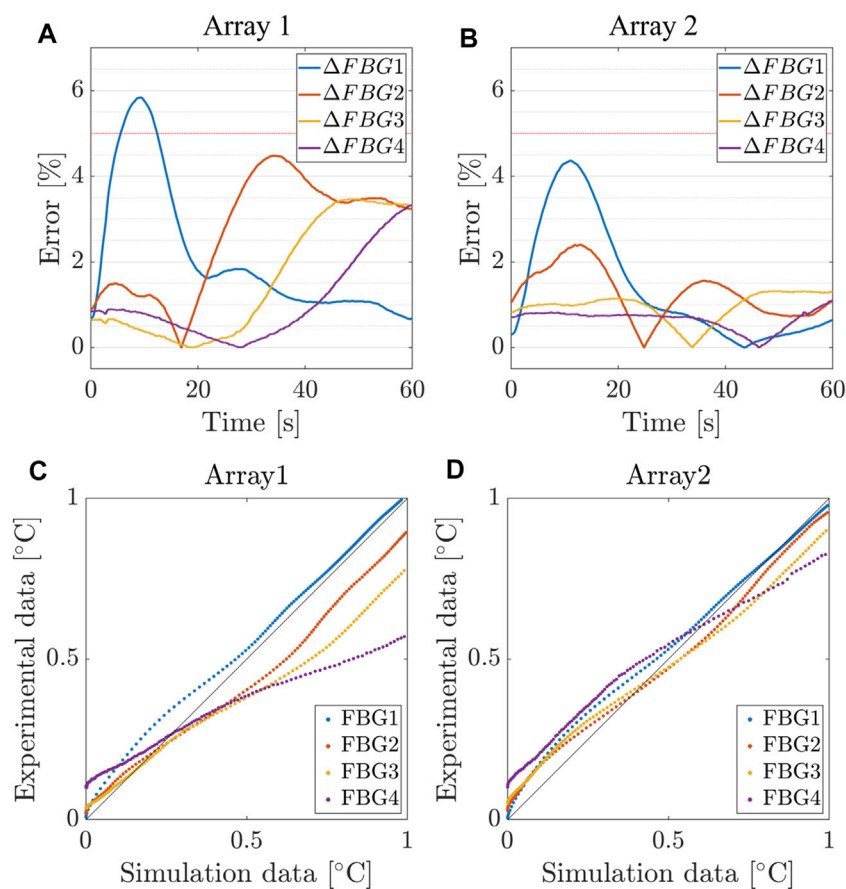


FIGURE 9 | Relative error between simulated and measured temperatures for the first 4 FBGs of Array 1, 2. (A,B) Relative error and (C,D) Pearson correlation coefficient between the numerical and the average experimental temperature at each instant of the RFCA.

TABLE 3 | Maximum absolute error and correlation coefficients for the simulated and measured temperatures for the first 4 FBGs of Array 1 and 2.

FBG	Max $ \Delta\text{FBG} $ [%]	$\hat{\rho}$
Array 1		
FBG1	5.84	0.9987
FBG2	4.48	0.9972
FBG3	3.47	0.9963
FBG4	3.32	0.9934
Array 2		
FBG1	4.36	0.9979
FBG2	2.40	0.9976
FBG3	1.32	0.9978
FBG4	1.10	0.9915

volume, shown in **Figure 7**, is 12.6 mm in width and 3.6 mm in depth. Both experimental and computational lesions exhibit an ellipsoidal shape, with the major axis oriented towards the muscular fibers. Then, a numerical sensitivity analysis was performed by using the cell-death model varying the threshold value $N_{thr} \in [0.8 \div 0.99]$. **Figure 10** shows how the cell-based computed damage volume grows as the threshold increases also depending on the ablation time. We identify $N_{thr} \approx 0.95 \div 0.98$ as the optimal value for the present model vs. experimental lesions. We further note that the computational lesion follows the fiber rotation across the tissue and that the irreversible damage volume concentrates below the tissue surface according to the expected RF concentration in the presence of blood flow and saline boundary conditions. This result broadly supports the work of (Xie and Zemlin, 2016) though an extended validation in this direction is required.

5 DISCUSSION

In the present study, we developed an experimentally calibrated finite element computational model of *ex-vivo* cardiac RFCA. The key innovative features of the proposed methodology are the inclusion of three-dimensional myocardial anisotropy, the implementation of a multi-scale time lag thermal ablation model, and the adoption of a dynamical model of cell death for the estimation of tissue damage and lesion sizing.

Remarkably, model calibration relies on accurate multi-point temperature measurements obtained via FBG sensors. The study

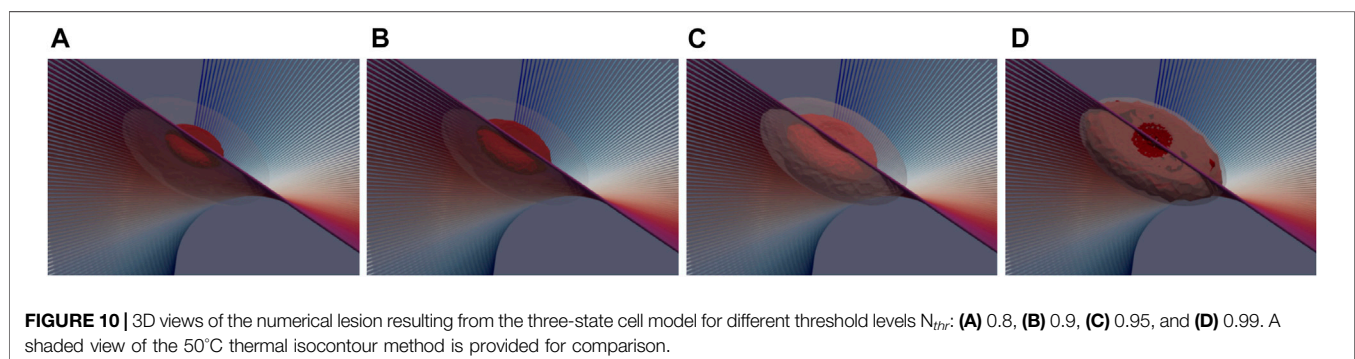
offered novel insights into the anisotropic thermal behavior of cardiac tissue, which was poorly addressed in the literature. In a combined experimental-computational modeling framework, we proved that the intrinsic anisotropic microstructure of the myocardium plays a pivotal role in the thermo-electrical response of the tissue undergoing hyperthermic treatments. Furthermore, we showed that a comprehensive sensitivity analysis must comply with complex nonlinear couplings and heterogeneous materials properties.

5.1 Limitations

Limitations to this study need to be acknowledged. First, the computational domain was idealized. Experimental thickness variation, and associated microstructure, may represent a possible source of error in model tuning. However, a priori sensitivity analysis of varying tissue thickness indicated that overall results do not change since temperature decreases rapidly with tissue depth and significant heating only occurs in the vicinity of the electrode. Because of clinical applications, however, a patient-specific image-based realistic geometry will be mandatory for maximizing model reliability and further improving its predictability (Sung et al., 2021).

Second, material modeling lacks of cardiac electro-mechanical couplings (Singh and Melnik, 2019; Pandolfi et al., 2016, 2017; Gizzi et al., 2015; Ruiz-Baier et al., 2020), as well as tissue-electrode contact mechanics (Petras et al., 2018). Besides, three-dimensional blood hemodynamics and saline irrigation (accounted in the present study by means of multiscale boundary conditions) shall be considered in line with recent computational studies (Petras et al., 2019). We remark that our experimental calibration is performed on *ex-vivo* samples, with no external perfusion. Accordingly, we did not include the perfusion term in the heat equation to be consistent with our experimental dataset. However, additional volumetric sources (accounting for blood perfusion, metabolism, to name a few) and multi-field coupling phenomena should be included when modeling *in-vivo* cardiac ablation. In addition state-of-the-art machine learning algorithms and data assimilation procedures (Barone et al., 2020a,b; Zaman et al., 2021) are also foreseen in view of a patient-specific optimization applications (Lopez-Perez et al., 2019; Aronis et al., 2021).

From the experimental point of view, it was not possible to ensure an identical placement of the sensors within the tissues for all the experiments and no measurements were performed contemporary in the x-y plane due to difficulties in sensors positioning. We opted for a solution minimizing the positioning error of the FBGs caused



by the manual insertion of the optical fibers. A dedicated 3D-printed holding setup for FBG insertion is a route we are exploring for further improving the current measurement technique.

Finally, more objective criteria for the estimation of tissue damage taking advantage of histological techniques are expected. We investigated a smooth transition of the damage criterium through a parametric analysis of the threshold value. In view of generalized robust and reliable multiscale modeling approaches, an extended validation of the damage criterium is foreseen to cope with a broad spectrum of clinical applications.

5.2 CONCLUSION

The present work has the ultimate purpose of improving the predictive capabilities of RFCA computational models in view of personalized therapy planning, design, and development of new RFCA systems and protocols and ultimately paving the way to a dramatic improvement in the safety of clinical procedures.

DATA AVAILABILITY STATEMENT

The original contributions presented in the study are included in the article/**Supplementary Material**, further inquiries can be directed to the corresponding author.

REFERENCES

- Aronis, K. N., Prakosa, A., Bergamaschi, T., Berger, R. D., Boyle, P. M., Chrispin, J., et al. (2021). Characterization of the Electrophysiologic Remodeling of Patients with Ischemic Cardiomyopathy by Clinical Measurements and Computer Simulations Coupled with Machine Learning. *Front. Physiol.* 12, 1079. doi:10.3389/fphys.2021.684149
- Barone, A., Carlino, M. G., Gizzi, A., Perotto, S., and Veneziani, A. (2020a). Efficient Estimation of Cardiac Conductivities: A Proper Generalized Decomposition Approach. *J. Comput. Phys.* 423, 109810. doi:10.1016/j.jcp.2020.109810
- Barone, A., Gizzi, A., Fenton, F., Filippi, S., and Veneziani, A. (2020b). Experimental Validation of a Variational Data Assimilation Procedure for Estimating Space-dependent Cardiac Conductivities. *Comput. Methods Appl. Mech. Eng.* 358, 112615. doi:10.1016/j.cma.2019.112615
- Calzolari, V., De Mattia, L., Indiani, S., Crosato, M., Furlanetto, A., Licciardello, C., et al. (2017). *In Vitro* validation of the Lesion Size index to Predict Lesion Width and Depth after Irrigated Radiofrequency Ablation in a Porcine Model. *JACC: Clin. Electrophysiol.* 3, 1126–1135. doi:10.1016/j.jacep.2017.08.016
- Dillon-Murphy, D., Marlevi, D., Ruijsink, B., Qureshi, A., Chubb, H., Kerfoot, E., et al. (2018). Modeling Left Atrial Flow, Energy, Blood Heating Distribution in Response to Catheter Ablation Therapy. *Front. Physiol.* 9, 1757. doi:10.3389/fphys.2018.01757
- Erdogan, T. (1997). Fiber Grating Spectra. *J. Lightwave Technol.* 15, 1277–1294. doi:10.1109/50.618322
- Gabriel, C. (1996). Compilation of the Dielectric Properties of Body Tissues at RF and Microwave Frequencies. *Tech. rep., King's Coll. Lond. (United Kingdom) Dept Phys.* doi:10.21236/ada303903
- Gizzi, A., Cherubini, C., Filippi, S., and Pandolfi, A. (2015). Theoretical and Numerical Modeling of Nonlinear Electromechanics with Applications to Biological Active media. *Commun. Comput. Phys.* 17, 93–126. doi:10.4208/cicp.091213.260614a
- González-Suárez, A., and Berjano, E. (2015). Comparative Analysis of Different Methods of Modeling the thermal Effect of Circulating Blood Flow during Rf Cardiac Ablation. *IEEE Trans. Biomed. Eng.* 63, 250–259.

ETHICS STATEMENT

The animal study was reviewed and approved by University of Rome Campus Bio-Medico.

AUTHOR CONTRIBUTIONS

LM, MZ, AG and ES conceived the study, LM, MZ and CM conducted the experiments, LM and AG conceived and conducted the numerical study, LM and MZ analyzed the results. LM, and MZ drafted the original manuscript. All authors reviewed the manuscript.

FUNDING

The authors acknowledge the support of the Italian National Group for Mathematical Physics (GNFM-INDAM).

SUPPLEMENTARY MATERIAL

The Supplementary Material for this article can be found online at: <https://www.frontiersin.org/articles/10.3389/fphys.2022.845896/full#supplementary-material>

- Hamaya, R., Miyazaki, S., Kajiyama, T., Watanabe, T., Kusa, S., Nakamura, H., et al. (2018). Efficacy and Safety Comparison between Different Types of Novel Design Enhanced Open-Irrigated Ablation Catheters in Creating Cavo-Tricuspid Isthmus Block. *J. Cardiol.* 71, 513–516. doi:10.1016/j.jjcc.2017.10.015
- Joseph, J. P., and Rajappan, K. (2012). Radiofrequency Ablation of Cardiac Arrhythmias: Past, Present and Future. *Qjm* 105, 303–314. doi:10.1093/qjmed/hcr189
- Kho, A. S., Ooi, E. H., Foo, J. J., and Ooi, E. T. (2021). Role of saline Concentration during saline-infused Radiofrequency Ablation: Observation of Secondary Joule Heating along the saline-tissue Interface. *Comput. Biol. Med.* 128, 104112. doi:10.1016/j.compbiomed.2020.104112
- Končan, D., Rifel, J., Drevenšek, G., Kocijančič, S., Ogorelec, S., and Budihna, M. V. (2000). Thermal Conductivity of the Porcine Heart Tissue. *Pflügers Archiv-European J. Physiol.* 440, R143
- Kornej, J., Börschel, C. S., Benjamin, E. J., and Schnabel, R. B. (2020). Epidemiology of Atrial Fibrillation in the 21st Century. *Circ. Res.* 127, 4–20. doi:10.1161/circresaha.120.316340
- Lombaert, H., Peyrat, J., Croisille, P., Rapacchi, S., Fanton, L., Cheriet, F., et al. (2012). Human Atlas of the Cardiac Fiber Architecture: Study on a Healthy Population. *IEEE Trans. Med. Imaging* 31, 1436–1447. doi:10.1109/tmi.2012.2192743
- López Molina, J. A., Rivera, M. J., and Berjano, E. (2014). Fourier, Hyperbolic and Relativistic Heat Transfer Equations: a Comparative Analytical Study. *Proc. R. Soc. A.* 470, 20140547. doi:10.1098/rspa.2014.0547
- Lopez-Perez, A., Sebastian, R., Izquierdo, M., Ruiz, R., Bishop, M., and Ferrero, J. M. (2019). Personalized Cardiac Computational Models: From Clinical Data to Simulation of Infarct-Related Ventricular Tachycardia. *Front. Physiol.* 10, 580. doi:10.3389/fphys.2019.00580
- Maribo-Mogensen, B., Kontogeorgis, G. M., and Thomsen, K. (2013). Modeling of Dielectric Properties of Aqueous Salt Solutions with an Equation of State. *J. Phys. Chem. B* 117, 10523–10533. doi:10.1021/jp403375t
- Molinari, L., Gerardo-Giorda, L., and Gizzi, A. (2022). A Transversely Isotropic Thermo-Hyperelastic Constitutive Model of Myocardial Tissue with a Three-State Cell Death Dynamics for Cardiac Radiofrequency Ablation. *J. Mech. Phys. Sol.* 161, 104810. doi:10.1016/j.jmps.2022.104810

- Molinari, L. (2021). Results of Rfca Computational Model Calibration via Fbgs Multi-point Temperature Measurements. doi:10.6084/m9.figshare.15077952
- Morady, F. (1999). Radio-frequency Ablation as Treatment for Cardiac Arrhythmias. *N. Engl. J. Med.* 340, 534–544. doi:10.1056/nejm199902183400707
- Nath, S., DiMARCO, J. P., and Haines, D. E. (1994). Basic Aspects of Radiofrequency Catheter Ablation. *J. Cardiovasc. Electrophysiol.* 5, 863–876. doi:10.1111/j.1540-8167.1994.tb01125.x
- Nörtemann, K., Hilland, J., and Kaatz, U. (1997). Dielectric Properties of Aqueous NaCl Solutions at Microwave Frequencies. *The J. Phys. Chem. A* 101, 6864–6869.
- O'Neill, D. P., Peng, T., Stiegler, P., Mayrhauser, U., Koestenbauer, S., Tscheliessnigg, K., et al. (2011). A Three-State Mathematical Model of Hyperthermic Cell Death. *Ann. Biomed. Eng.* 39, 570–579. doi:10.1007/s10439-010-0177-1
- Ozbek, H., and Phillips, S. L. (1979). *Thermal Conductivity of Aqueous NaCl Solution from 20 °C to 330 °C*. Berkeley, CA: Technical Report
- Pandolfi, A., Gizzi, A., and Vasta, M. (2016). Coupled Electro-Mechanical Models of Fiber-Distributed Active Tissues. *J. Biomech.* 49, 2436–2444. doi:10.1016/j.jbiomech.2016.01.038
- Pandolfi, A., Gizzi, A., and Vasta, M. (2017). Visco-electro-elastic Models of Fiber-Distributed Active Tissues. *Meccanica* 52, 3399–3415. doi:10.1007/s11012-017-0622-4
- Park, C. S., Hall, S. K., Liu, C., and Payne, S. J. (2016). A Model of Tissue Contraction during thermal Ablation. *Physiol. Meas.* 37, 1474–1484. doi:10.1088/0967-3334/37/9/1474
- Patel, N. J., Deshmukh, A., Pant, S., Singh, V., Patel, N., Arora, S., et al. (2014). Contemporary Trends of Hospitalization for Atrial Fibrillation in the United States, 2000 through 2010. *Circulation* 129, 2371–2379. doi:10.1161/circulationaha.114.008201
- Pennes, H. H. (1998). Analysis of Tissue and Arterial Blood Temperatures in the Resting Human Forearm. *J. Appl. Physiol.* 85, 5–34. doi:10.1152/jappl.1998.85.1.5
- Petrás, A., Leoni, M., Guerra, J. M., Jansson, J., and Gerardo-Giorda, L. (2019). A Computational Model of Open-Irrigated Radiofrequency Catheter Ablation Accounting for Mechanical Properties of the Cardiac Tissue. *Int. J. Numer. Method Biomed. Eng.* 35, e3232. doi:10.1002/cnm.3232
- Petrás, A., Leoni, M., Guerra, J. M., Jansson, J., and Gerardo-Giorda, L. (2018). Effect of Tissue Elasticity in Cardiac Radiofrequency Catheter Ablation Models. *Comput. Cardiol. Conference(CinC) (Ieee)* 45, 1–4. doi:10.22489/cinc.2018.035
- Pires, L. A., Wagshal, A. B., Lancey, R., and Huang, S. K. S. (1995). Arrhythmias and Conduction Disturbances after Coronary Artery Bypass Graft Surgery: Epidemiology, Management, and Prognosis. *Am. Heart J.* 129, 799–808. doi:10.1016/0002-8703(95)90332-1
- Qadri, A. M., Chia, N. J. Y., and Ooi, E. H. (2017). Effects of saline Volume on Lesion Formation during saline-infused Radiofrequency Ablation. *Appl. Math. Model.* 43, 360–371. doi:10.1016/j.apm.2016.11.032
- Raghavan, K., Porterfield, J. E., Kottam, A. T. G., Feldman, M. D., Escobedo, D., Valvano, J. W., et al. (2009). Electrical Conductivity and Permittivity of Murine Myocardium. *IEEE Trans. Biomed. Eng.* 56, 2044–2053. doi:10.1109/tbme.2009.2012401
- Roney, C. H., Beach, M. L., Mehta, A. M., Sim, I., Corrado, C., Bendikas, R., et al. (2020). In Silico comparison of Left Atrial Ablation Techniques that Target the Anatomical, Structural, and Electrical Substrates of Atrial Fibrillation. *Front. Physiol.* 11, 572874. doi:10.3389/fphys.2020.572874
- Ruiz-Baier, R., Gizzi, A., Loppini, A., Cherubini, C., and Filippi, S. (2020). Modelling Thermo-Electro-Mechanical Effects in Orthotropic Cardiac Tissue. *CiCP* 27, 87–115. doi:10.4208/cicp.oa-2018-0253
- Sahoo, N., Ghosh, S., Narasimhan, A., and Das, S. K. (2014). Investigation of Non-fourier Effects in Bio-Tissues during Laser Assisted Photothermal Therapy. *Int. J. Therm. Sci.* 76, 208–220. doi:10.1016/j.ijthermalsci.2013.08.014
- Sauerheber, R., and Heinz, B. (2015). Temperature Effects on Conductivity of Seawater and Physiologic saline, Mechanism and Significance. *Chem. Sci. J.* 6, 109. doi:10.4172/2150-3494.1000109
- Schena, E., Tosi, D., Saccomandi, P., Lewis, E., and Kim, T. (2016). Fiber Optic Sensors for Temperature Monitoring during thermal Treatments: an Overview. *Sensors* 16, 1144. doi:10.3390/s16071144
- Schutt, D., Berjano, E. J., and Haemmerich, D. (2009). Effect of Electrode thermal Conductivity in Cardiac Radiofrequency Catheter Ablation: a Computational Modeling Study. *Int. J. hyperthermia* 25, 99–107. doi:10.1080/02656730802563051
- Singh, S., and Melnik, R. (2019). Coupled Thermo-Electro-Mechanical Models for thermal Ablation of Biological Tissues and Heat Relaxation Time Effects. *Phys. Med. Biol.* 64, 245008. doi:10.1088/1361-6560/ab4cc5
- Siontis, K. C., Noseworthy, P. A., and Ruddy, K. J. (2021). Atrial Fibrillation and Cancer. *JACC: CardioOncology* 3, 233–235. doi:10.1016/j.jacc.2021.04.003
- Sung, E., Etoz, S., Zhang, Y., and Trayanova, N. A. (2021). Whole-heart Ventricular Arrhythmia Modeling Moving Forward: Mechanistic Insights and Translational Applications. *Biophys. Rev.* 2, 031304. doi:10.1063/5.0058050
- Trujillo, M., and Berjano, E. (2013). Review of the Mathematical Functions Used to Model the Temperature Dependence of Electrical and thermal Conductivities of Biological Tissue in Radiofrequency Ablation. *Int. J. Hyperthermia* 29, 590–597. doi:10.3109/02656736.2013.807438
- Tzou, D. Y. (1995). The Generalized Lagging Response in Small-Scale and High-Rate Heating. *Int. J. Heat Mass Transfer* 38, 3231–3240. doi:10.1016/0017-9310(95)00052-b
- Wang, Y., Haynor, D. R., and Kim, Y. (2001). An Investigation of the Importance of Myocardial Anisotropy in Finite-Element Modeling of the Heart: Methodology and Application to the Estimation of Defibrillation Efficacy. *IEEE Trans. Biomed. Eng.* 48, 1377–1389. doi:10.1109/10.966597
- Wood, M., Goldberg, S., Lau, M., Goel, A., Alexander, D., Han, F., et al. (2011). Direct Measurement of the Lethal Isotherm for Radiofrequency Ablation of Myocardial Tissue. *Circ. Arrhythmia Electrophysiol.* 4, 373–378. doi:10.1161/circ.110.961169
- Xie, F., and Zemlin, C. W. (2016). Effect of Twisted Fiber Anisotropy in Cardiac Tissue on Ablation with Pulsed Electric fields. *PLoS one* 11, e0152262. doi:10.1371/journal.pone.0152262
- Zaltieri, M., Allegretti, G., Massaroni, C., Schena, E., and Cauti, F. M. (2020). Fiber Bragg Grating Sensors for Millimetric-Scale Temperature Monitoring of Cardiac Tissue Undergoing Radiofrequency Ablation: A Feasibility Assessment. *Sensors* 20, 6490. doi:10.3390/s20226490
- Zaltieri, M., Massaroni, C., Cauti, F. M., and Schena, E. (2021). Techniques for Temperature Monitoring of Myocardial Tissue Undergoing Radiofrequency Ablation Treatments: An Overview. *Sensors* 21, 1453. doi:10.3390/s21041453
- Zaman, M. S., Dhamala, J., Bajracharya, P., Sapp, J. L., Horáček, B. M., Wu, K. C., et al. (2021). Fast Posterior Estimation of Cardiac Electrophysiological Model Parameters via Bayesian Active Learning. *Front. Physiol.* 12, 740306. doi:10.3389/fphys.2021.740306
- Zhang, B., Moser, M. A. J., Zhang, E. M., Luo, Y., Liu, C., and Zhang, W. (2016). A Review of Radiofrequency Ablation: Large Target Tissue Necrosis and Mathematical Modelling. *Physica Med.* 32, 961–971. doi:10.1016/j.ejmp.2016.07.092

Conflict of Interest: The authors declare that the research was conducted in the absence of any commercial or financial relationships that could be construed as a potential conflict of interest.

Publisher's Note: All claims expressed in this article are solely those of the authors and do not necessarily represent those of their affiliated organizations, or those of the publisher, the editors and the reviewers. Any product that may be evaluated in this article, or claim that may be made by its manufacturer, is not guaranteed or endorsed by the publisher.

Copyright © 2022 Molinari, Zaltieri, Massaroni, Filippi, Gizzi and Schena. This is an open-access article distributed under the terms of the Creative Commons Attribution License (CC BY). The use, distribution or reproduction in other forums is permitted, provided the original author(s) and the copyright owner(s) are credited and that the original publication in this journal is cited, in accordance with accepted academic practice. No use, distribution or reproduction is permitted which does not comply with these terms.



Geometrically Reduced Modelling of Pulsatile Flow in Perivascular Networks

Cécile Daversin-Catty ^{1*}, Ingeborg G. Gjerde ² and Marie E. Rognes ^{1,2}

¹Simula Research Laboratory, Oslo, Norway, ²Department of Mathematics, University of Bergen, Bergen, Norway

OPEN ACCESS

Edited by:

André H. Erhardt,
Weierstrass Institute for Applied
Analysis and Stochastics (LG),
Germany

Reviewed by:

Kartik Jain,
University of Twente, Netherlands
Jeff Heys,
Montana State University,
United States

*Correspondence:

Cécile Daversin-Catty
cecile@simula.no

Specialty section:

This article was submitted to
Statistical and Computational Physics,
a section of the journal
Frontiers in Physics

Received: 23 February 2022

Accepted: 06 April 2022

Published: 11 May 2022

Citation:

Daversin-Catty C, Gjerde IG and
Rognes ME (2022) Geometrically
Reduced Modelling of Pulsatile Flow in
Perivascular Networks.
Front. Phys. 10:882260.
doi: 10.3389/fphy.2022.882260

Flow of cerebrospinal fluid in perivascular spaces is a key mechanism underlying brain transport and clearance. In this paper, we present a mathematical and numerical formalism for reduced models of pulsatile viscous fluid flow in networks of generalized annular cylinders. We apply this framework to study cerebrospinal fluid flow in perivascular spaces induced by pressure differences, cardiac pulse wave-induced vascular wall motion and vasomotion. The reduced models provide approximations of the cross-section average pressure and cross-section flux, both defined over the topologically one-dimensional centerlines of the network geometry. Comparing the full and reduced model predictions, we find that the reduced models capture pulsatile flow characteristics and provide accurate pressure and flux predictions across the range of idealized and image-based scenarios investigated—at a fraction of the computational cost of the corresponding full models. The framework presented thus provides a robust and effective computational approach for large scale in-silico studies of pulsatile perivascular fluid flow and transport.

Keywords: biomedical flows, low-dimensional models, bifurcation, variational methods, computational methods

1 INTRODUCTION

Flow of cerebrospinal fluid (CSF) in perivascular spaces (PVSs) is a key transport mechanism in and around the brain [1–3]. A PVS is a space or potential space along or around a blood vessel through which fluid and particles can pass [4]. Such spaces appear along blood vessels on the brain surface (surface or pial PVSs) or along blood vessels within the brain parenchyma (parenchymal PVSs). While their shape and structure, and to some extent existence, remain disputed [4–8], PVSs are typically represented as (elliptic) annular structures surrounding the blood vessels. As such, surface and parenchymal PVSs form structural networks, dual to and in close interaction with the vascular network, and the surrounding brain tissue and/or subarachnoid space.

Mathematical and computational models are playing an increasingly important role in understanding and predicting PVS flow characteristics [9]. Theoretical models have quantified the resistance in PVS networks [10], while detailed numerical simulations can predict perivascular fluid velocities and pressures in idealized [11–17] and image-based geometries [18]. However, computational fluid dynamics simulations rapidly become prohibitively expensive for large, three-dimensional PVS networks. A natural question is therefore whether reduced models can accurately capture PVS flow and transport characteristics and magnitudes. Of particular interest and relevance are geometrically-reduced models for which the computational domain is reduced from an initial three-dimensional representation to a network of topologically one-dimensional branches. Such models have been subject to active research over the last decades in the context of the vasculature, arterial blood flow, and tissue perfusion [19–29]. For the one-dimensional arterial blood flow models,

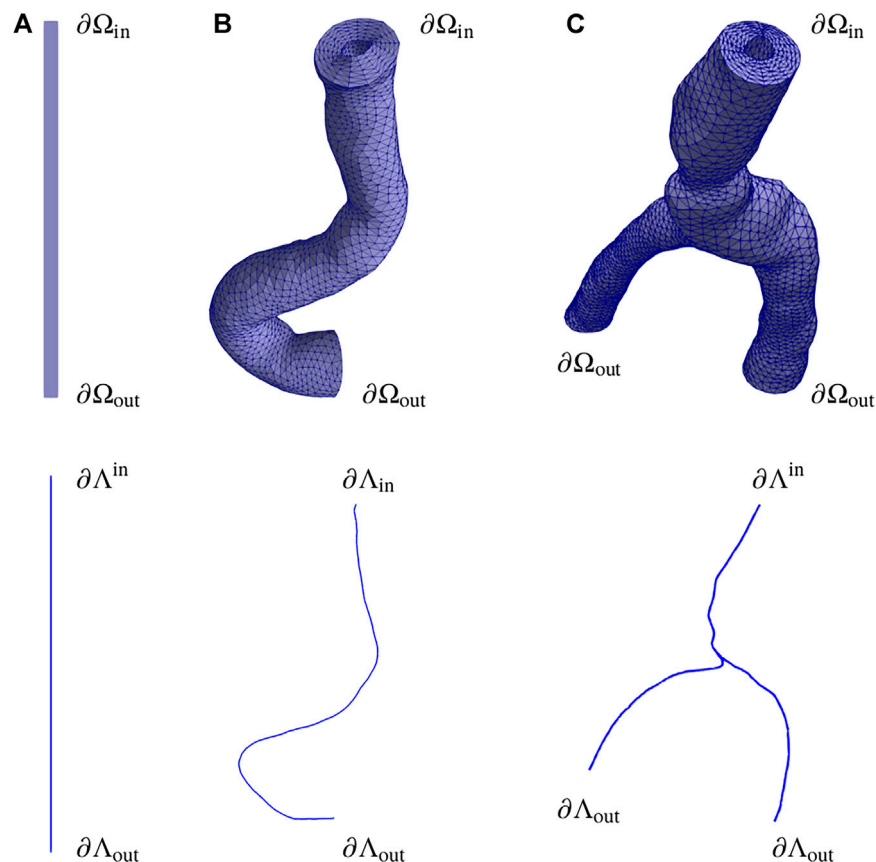


FIGURE 1 | Overview of the full three-dimensional and topologically one-dimensional reduced model domains. The idealized geometry **(A)** (the *axisymmetric PVS*) is a single 1 mm long axisymmetric annular cylinder represented by its two-dimensional angular cross-section. Geometry **(B)** (the *image-based PVS*) is generated from a cerebral artery segment (Aneurisk dataset repository, case id C0092) and represents an image-based perivascular space without bifurcation. Geometry **(C)** (the *bifurcating image-based PVS*) is generated from a middle cerebral artery (MCA M1–M2) segment (Aneurisk dataset repository, case id C0075) and represents an image-based perivascular space including a bifurcation.

see e.g., the seminal work of Olufsen [19], the vasculature is typically represented by a branching network of centerlines, and the model variables are the time-varying cross-section flux and vascular area. The corresponding PVS flow setting has received less attention from the mathematical and numerical community on the other hand.

In this work, we introduce a geometrically-reduced mathematical model and numerical solution techniques for the time-dependent flow of an incompressible viscous fluid such as CSF in surface PVS networks. The cross-section flux and average pressure are the primary model variables. We consider different computational scenarios including PVS flow induced by a systemic pressure gradient, by cardiac pulse wave-induced movement of the inner vascular wall and by vasomotion in idealized or image-based model geometries. We evaluate the accuracy and efficiency of the reduced models by qualitative and quantitative comparison with the full three-dimensional model analogues.

The reduced models provide accurate approximations of the cross-section average pressure, cross-section flux and net flow in all geometries considered with relative model discrepancies in the

peak flux between 0 and 35% and in the peak pressure between 0 and 52%. For realistic three-dimensional geometries, the reduced model reduces the computational costs (memory and runtime) by factors of 50–200× with higher factors expected for larger scale networks.

2 MATERIALS AND METHODS

2.1 PVS Geometries (3D and 1D)

In general, we consider a perivascular tree-like domain Ω consisting of a network of branching generalized annular cylinders Ω^i , with $\Omega \subseteq \cup_{i \in I} \Omega^i$, spatial coordinates $x \in \Omega$ and time $t \geq 0$. The boundary is denoted $\partial\Omega$, with boundary normal n . We assume that each generalized annular cylinder Ω^i has a well-defined and oriented, topologically one-dimensional centerline Λ^i with coordinate s . We set $\Lambda = \cup_{i \in I} \Lambda^i$. Along s , we define the cross-sections $C^i = C^i(s, t)$ of Λ^i with area $A^i = A^i(s, t)$. We denote the inner radius of Ω^i by R_1^i and the outer radius of Ω^i by R_2^i ; these radii will in practice vary with s , t and the angular coordinate θ . We denote the set

TABLE 1 | Geometrical or numerical PVS domain characteristics for domains A, B, C.

Domain	L (mm)	D_a (mm)	D_{pvs} (mm)	Mesh (full)			Mesh (reduced)	
				cells	vertices	hmin (mm)	vertices	hmin (mm)
A	1	0.04	0.06	1920	1053	1.3×10^{-2}	65	1.6×10^{-2}
B	≈ 1	0.036–0.047	0.035–0.044	63144	12404	9.4×10^{-3}	356	2.8×10^{-4}
C	≈ 1	0.024–0.046	0.023–0.044	88074	17318	6.4×10^{-3}	249	9.9×10^{-5}

L denotes an approximate domain length, $D_a = 2R_1$ is the range of the arterial diameters, D_{pvs} indicates the range of widths of the perivascular space ($D_{pvs} = R_2 - R_1$, so that $R_2 = 2.95R_1$) cells and vertices indicate the number of mesh cells and mesh vertices respectively for the full (2D or 3D) model and reduced models, and h_{max} denotes the maximal mesh cell size for each mesh. The vertices for the one-dimensional geometries are uniformly spaced in the interior of the domain

of bifurcation points i.e. the points at which the centerlines of branches meet by \mathcal{B} .

We introduce three specific geometries of increasing complexity: from an axisymmetric cylinder (A) to an image-based perivascular geometry without any bifurcations (B) and one with a bifurcation (C) (**Figure 1** and **Table 1**). The image-based geometries (B) and (C) are constructed from non-pathological artery segments from the Aneurisk dataset repository [30], and thus define high-fidelity 3D representations of human brain surface arteries. In each of these geometries, the PVS domain is defined by creating a generalized annular cylinder surrounding the vascular segment with the vascular wall as the inner surface of the PVS. The width of the PVS is set proportional to the blood vessel diameter (by factor of 0.95) and scaled (to a mouse scale) [18, 31]. Three-dimensional PVS flow in geometries A and C have been studied previously [18] and will be used for comparison. We define as PVS inlets and outlets ($\partial\Omega_{in}$ and $\partial\Omega_{out}$) the PVS ends surrounding the vascular inlets and outlets, respectively, noting however that fluid may flow both in and out of both the inlet and outlets. We denote the inner PVS wall (boundary) by $\partial\Omega_{inner}$ and outer wall by $\partial\Omega_{outer}$.

The 3D PVS construction and the 1D centerline extraction are performed using *PVS-meshing-tools* [32], largely based on VMTK [33]. The extracted centerline comes with underlying data including the branch lengths and vessel radii. The centerline radius refers to the radius of the maximal inscribed circle of the vessel cross-sections. The meshing of both 3D and 1D PVS domains is performed within *PVS-meshing-tools* [32] using meshio [34] and GMSH [35]. The centerline meshes consist of topologically one-dimensional intervals embedded in three dimensions. The bifurcation points $b \in \mathcal{B} \subset \Omega$ are explicitly labeled within each centerline mesh. Each branch is also separately tagged and given a consistent orientation. This procedure allows for the identification of bifurcation points as the outlet of one (parent) centerline and the inlet of other (daughter) centerlines, and a split of the full perivascular network into oriented mesh branches.

2.2 Stokes Flow in a Deforming Perivascular Domain

Flow of CSF in surface PVSs is reported to be laminar, with low Reynolds numbers (10^{-4} – 10^{-2}) and moderate Péclet numbers (10^2 – 10^4) for $1\mu\text{m}$ spherical particles transported at low Reynolds number [31], a mean flow speed of up to $60\mu\text{m/s}$,

and parabolic flow profiles [31]. We therefore model the flow of an incompressible, viscous fluid flowing at low Reynolds and Womersley numbers via the time-dependent Stokes equations over a time-dependent domain $\Omega = \Omega(t)$ representing the PVS. The fluid velocity $v = v(x, t)$ for $x \in \Omega(t)$ at time t and the CSF pressure $p = p(x, t)$ then solve the following system of time-dependent partial differential equations (PDEs) [18, 36]:

$$\rho \partial_t v - \mu \nabla^2 v + \nabla p = 0 \quad \text{in } \Omega(t), \quad (1a)$$

$$\nabla \cdot v = 0 \quad \text{in } \Omega(t), \quad (1b)$$

where ρ is the fluid density and μ is the dynamic fluid viscosity. To model CSF at body temperature, we set the fluid density to $\rho = 10^3 \text{ kg/m}^3$ and the dynamic viscosity to $\mu = 0.697 \times 10^{-3} \text{ Pa s}$. As in our previous full models of perivascular flow [18], the initial PVS mesh defines the reference domain $\Omega(0)$, and we assume that $\Omega(t)$ at time $t > 0$ is given by a deformation d of the reference domain: $\Omega(0) \mapsto \Omega(t)$ with $x = d(X, t)$, $X \in \Omega(0)$, $x \in \Omega(t)$. We denote the domain velocity associated with d by w (thus $\dot{d} = w$).

2.3 Boundary Conditions, Initial Conditions and Periodicity

At the PVS ends, we prescribe a traction condition corresponding to a known, applied pressure $\tilde{p} = \tilde{p}(x, t)$:

$$\sigma_n \equiv (\mu \nabla u - pI) \cdot n = -\tilde{p}n \quad \text{on } \partial\Omega_{in} \text{ and } \partial\Omega_{out}. \quad (2)$$

We either prescribe (i) zero pressure at both ends $\tilde{p} = 0$, or (ii) a constant-in-time pressure gradient $\Delta \tilde{p} > 0$ by setting $\tilde{p}_{in} = L_{out} \Delta \tilde{p}$ at the inlet, letting $\tilde{p}_{out} = 0$ at the outlet furthest from the inlet with distance L_{out} , and setting \tilde{p}_{out} at any other outlets such that the average pressure gradient over each branch path $(\tilde{p}_i - \tilde{p}_{out})/L_{out}$ is constant and equal to the prescribed pressure gradient $\Delta \tilde{p}$ mmHg/m. This static pressure difference can represent e.g., a hydrostatic pressure difference, a venous pressure differential, or some other systemic pressure difference. Other types of boundary conditions could also be considered, see e.g., a discussion of compliance conditions in [18], or [37].

On the inner and outer PVS walls (along the length of the PVS), we set the fluid velocity v to match a known, prescribed domain velocity $w = w(x, t)$. For the inner PVS wall, we either (i) consider a rigid wall and set $v = w = 0$, or (ii) impose a pulsating wall displacement:

$$d|_{\partial\Omega_{\text{inner}}}(X, t) = A(X, t)n, \quad (3)$$

with reference to the initial (fixed) mesh with coordinates X and prescribe $v = w = \dot{d}$. To represent wall motion induced by the cardiac pulse wave, we let the amplitude A be defined by the juxtaposition of an experimentally-observed wall motion time series [31] either applied uniformly along the length of the PVS or as a travelling wave along the PVS length with wave speed $c = 1$ m/s and frequency 10 Hz. We refer to [18] for the detailed description. To represent wall motion due to vasomotion, we consider a similar set-up but with a travelling sinusoidal wave in time with a frequency of 0.1 Hz and wave length $\lambda = 8$ mm [38], and an amplitude A of 7.5% of the initial inner radius R_1 . We note that for all models, the wall moves in the normal (radial) direction only. For the outer PVS wall $\partial\Omega_{\text{outer}}$, we set $v = w = 0$.

The system starts at rest with $v = w = 0$ at $t = 0$. The system reaches the periodic steady state nearly immediately, and we report results starting from the first cycle.

2.4 Model Reduction Assumptions

We define a reduced, topologically one-dimensional, model approximation of the full PVS flow model [(1) with the given boundary and initial conditions] under the following stipulations. For each branch $\Omega^i(t)$ with centerline Λ^i and local coordinate system (s, r, θ) , where s represents the path length (or axial coordinate), r is the radial coordinate and θ is the angular coordinate, we suppose that:

- (I) Axial symmetry. Fields and input parameters are independent of the angular coordinate θ ;
- (II) Radial displacements. Boundaries displace in the radial direction only;
- (III) Fixed centerline. The centerline Λ is fixed in time and defines the axial direction;
- (IV) Constant cross-section pressure. The pressure field is independent of the angular and radial coordinates i.e., $p = p(s, t)$;
- (V) Axial velocity profile. The axial velocity v_s , i.e., the velocity component in the axial direction can be decomposed in the form

$$v \cdot s = v_s = v_s(s, r, t) = \hat{v}(s, t)v_{\text{vp}}(r), \quad (4)$$

where v_{vp} is a given velocity profile varying radially only, \hat{v} is to be determined.

For the velocity profile v_{vp} , we here choose a normalized annular Poiseuille flow:

$$v_{\text{vp}}(r) = \frac{v_{\text{poise}}(r)}{v_{\text{poise}}\left(\frac{R_1+R_2}{2}\right)}, \quad v_{\text{poise}}(r) = \left(1 - \frac{r^2}{R_1^2} + \frac{R_2^2 - R_1^2}{R_1^2 \ln(R_2/R_1)} \ln(r/R_1)\right). \quad (5)$$

This velocity profile is parabolic in r (as for Poiseuille flow in a cylinder) with a logarithmic correction that accounts for the annulus.

In particular, the domain velocity w is assumed independent of the angular coordinate θ . Note that we do not assume other

velocity components (than the axial) to necessarily be zero. We emphasize that these assumptions will in general not be satisfied by realistic geometries and flows. Thus, the reduced model defines a model approximation associated with a certain modelling error.

2.5 Reduced Model Equations

Under the assumptions (I–V), the full PVS flow model can be reduced to the following system of time-dependent differential equations: find the cross-section flux $\hat{q} = \hat{q}(s, t)$ and the cross-section average pressure $\hat{p} = \hat{p}(s, t)$ such that for each centerline Λ^i (denoting $\hat{q}|_{\Lambda^i} = \hat{q}^i$ and $\hat{p}|_{\Lambda^i} = \hat{p}^i$):

$$\frac{\rho}{A^i} \partial_t \hat{q}^i - \frac{\mu}{A^i} \partial_{ss} \hat{q}^i + \mu \frac{\alpha^i}{A^i} \hat{q}^i + \partial_s \hat{p}^i = 0 \text{ on } \Lambda^i, \quad (6a)$$

$$\partial_s \hat{q}^i = \hat{f}^i \text{ on } \Lambda^i, \quad (6b)$$

hold.

$$\begin{aligned} \hat{f}^i(s) \equiv & 2\pi R_1^i(s, t) w(R_1, s, t) \cdot n|_{\partial\Omega_{\text{inner}}} \\ & + 2\pi R_2^i(s, t) w(R_2, s, t) \cdot n|_{\partial\Omega_{\text{outer}}}. \end{aligned} \quad (7)$$

Moreover, $A^i = A^i(s, t)$ denotes the cross-section area, while $\alpha^i = \alpha^i(s, t)$ is a lumped flow parameter that depends on the domain geometry and the choice of velocity profile v_{vp} :

$$\begin{aligned} \alpha^i(s, t) \equiv & \frac{1}{A \bar{v}_{\text{vp}}(s)} (2\pi R_1^i(s, t) \partial_r v_{\text{vp}}(R_1^i(s, t)) \\ & - 2\pi R_2^i(s, t) \partial_r v_{\text{vp}}(R_2^i(s, t))), \end{aligned} \quad (8)$$

and where \bar{v}_{vp} is the velocity profile integrated over each cross-section:

$$\bar{v}_{\text{vp}} \equiv \int_{C(s)} v_{\text{vp}} r dr d\theta. \quad (9)$$

We also define the (one-dimensional) normal stress induced by \hat{q} and \hat{p} :

$$\hat{\sigma} \equiv \frac{\mu}{A} \partial_s \hat{q} - \hat{p}, \quad (10)$$

which corresponds to an average of the axial (s -)component of the normal stress in (2) over each cross-section

At the bifurcation points $b \in \mathcal{B} \subset \Omega$, we impose the following two conditions representing conservation of flux and continuity of normal stress, respectively:

$$\hat{q}^p(s^p) = \hat{q}^{d_1}(s^{d_1}) + \hat{q}^{d_2}(s^{d_2}), \quad (11)$$

$$\hat{\sigma}^p(s^p) = \hat{\sigma}^{d_1}(s^{d_1}) = \hat{\sigma}^{d_2}(s^{d_2}), \quad (12)$$

where Λ^p and $\Lambda^{d_1}, \Lambda^{d_2}$ represent the centerlines of the parent and two daughter branches, respectively, associated with the bifurcation point b and $s' = \iota(b)$ where ι denotes the map from three-dimensional bifurcation point to the one-dimensional centerline coordinate for each branch Ω^i .

System (6) defines a set of equations for each branch centerline Λ_i and is closed by the bifurcation conditions (11, 12), together with boundary conditions at the PVS inlet and outlets, as well as initial conditions for the cross-section flux. Specifically, in place of

the traction condition (2), we prescribe the corresponding pressure difference for the (average) normal stress $\hat{\sigma}$ cf. (10). In this manner, the (one-dimensional) solutions \hat{q}^i and \hat{p}^i of the reduced model (6) define approximations of the (three-dimensional) axial flux and pressure solving (1) integrated or averaged over each cross-section:

$$\begin{aligned}\hat{q}^i(s) &\approx \int_{C^i(s)} v_s(s, r, t) r \, dr \, d\theta \equiv A^i(s) \bar{q}^i(s), \\ \hat{p}^i(s) &\approx \frac{1}{A^i(s)} \int_{C^i(s)} p(s, r, t) r \, dr \, d\theta.\end{aligned}$$

The factor r originates from integrating in cylindrical coordinates. We note that the wall velocity w , which defines a boundary condition for the full PVS model (1), enters as a body force in the reduced model (6).

2.6 Numerical Solution and Software

We solve the full PVS (1) *via* a previously developed and verified arbitrary Lagrangian-Eulerian (ALE) formulation and finite element discretization [18]. This solver builds on the standard FEniCS finite element software suite [39], and is openly available [40].

To compute numerical solutions to the reduced model (6), we consider a first-order implicit Euler scheme in time and a higher-order finite element method in space. The finite element mesh \mathcal{T} of the centerline Λ is composed of mesh segments \mathcal{T}^i , one for each centerline branch Λ^i . Each mesh segment is a mesh consisting of intervals embedded in \mathbb{R}^3 . We label the set of bifurcation points \mathcal{B} , inlet points \mathcal{I} and outlet points \mathcal{O} , and define the following finite element spaces:

- The flux space V_h is the space of continuous piecewise quadratics over \mathcal{T}^i for each i .
- The (average) pressure space Q_h is the space of continuous piecewise linears on \mathcal{T} .
- The Lagrange multiplier space $R_h = \mathbb{R}^B$ where B is the number of bifurcation points.

The flux is thus solved on each mesh segment representing the PVS network branches and may be discontinuous across bifurcations. We impose the flux conservation condition (11) weakly using a Lagrange multiplier formulation. The pressure is solved on the whole mesh and is continuous at bifurcations by construction.

For each discrete time t^k , given \hat{q}_h^{k-1} at the previous time t^{k-1} and time step $\Delta t = t^k - t^{k-1}$, we solve for the approximate cross-section flux $\hat{q}_h^k \in V_h$, average pressure $\hat{p}_h^k \in Q_h$ and a Lagrange multiplier [corresponding to the normal stress (10) at the bifurcation points] $\lambda_h^k \in R_h$ solving

$$a((\hat{q}_h^k, \hat{p}_h^k, \lambda_h^k), (\psi, \phi, \xi)) = L^k((\psi, \phi, \xi)), \quad (13)$$

for all finite element test functions $\psi \in V_h$, $\phi \in Q_h$, and $\xi \in R_h$. The left-hand side bilinear form a is defined by:

$$\begin{aligned}a((q, p, \lambda), (\psi, \phi, \xi)) = & \sum_{i \in \mathcal{I}} \int_{\Lambda^i} \frac{1}{A^i} (\rho + \Delta t \mu \alpha^i) q^i \psi^i + \frac{\Delta t \mu}{A^i} \partial_s q^i \partial_s \psi^i + \partial_s q^i \phi^i - \Delta t \partial_s \psi^i p^i \, ds \\ & + \sum_{b \in \mathcal{B}} \lambda^b [\psi]^b + \xi^b [q]^b,\end{aligned} \quad (14)$$

where λ^b (or ξ^b) is simply the entry of the vector λ (or ξ) corresponding to bifurcation point b , and we define the natural jump:

$$[\psi]^b = \psi^p(b) - \psi^{d_1}(b) - \psi^{d_2}(b). \quad (15)$$

The right-hand side linear form L is:

$$\begin{aligned}L^k(\psi, \phi, \xi) = & \sum_{i \in \mathcal{I}} \int_{\Lambda^i} \frac{\rho}{A^i} \hat{q}_h^{k-1,i} \psi^i + f^i \phi^i \, ds - \sum_{x \in \mathcal{I}} \Delta t \tilde{p}_{\text{in}}(x) \psi^{i_I}(x) \\ & + \sum_{x \in \mathcal{O}} \Delta t \tilde{p}_{\text{out}}(x) \psi^{i_O}(x),\end{aligned} \quad (16)$$

where the superscript i_I (i_O) in the inlet (outlet) terms above refers to the unique centerline branch associated with the inlet (outlet) points.

The numerical solver for the reduced model was implemented in the well-established FEniCS Project finite element software [39]. The solver, and in particular the definition of the partially continuous flux space, builds on mixed-domain features [41] and relies on the latest development version of FEniCS. All data and source code are available via Zenodo [42].

2.7 Overview of Computational Models, Output Functionals and Model Error Measures

An overview of the six computational models considered is given in Table 2. Each model is labeled with reference to its domain (A, B, or C) followed by a number indicating the driving forces included: (1) a given pressure drop, (2) wall movement due to cardiac pulsations and (3) wall movement due to vasomotion. For each model, we consider the full three-dimensional version as well as the reduced model.

To compare the solutions from the full and reduced models, we consider the following quantities of interest. For each domain, we define a set of cross-sections as follows. For domain A, we define the left-most end as the inlet ($s = 0$) and define an upper cross-section. For domain B, we consider the inlet and outlet ends of the PVS, as well as upper and lower cross-sections. For domain C, we consider the inlet at $s = 0$, and the two outlets, as well as three additional cross sections near the inlet, on the largest daughter branch relatively close to the bifurcation, and near the outlet of the other daughter branch.

We then compute for each cross section $C(s)$ the averaged pressure $\bar{p}_h(s, t)$ and the cross-section flux $\bar{q}_h(s, t)$:

TABLE 2 | Overview of computational models parameterized by domain, prescribed pressure gradient $\Delta\bar{p}$ and wall motion pattern (see Methods).

	Domain	Pressure Gradient $\Delta\bar{p}$ [Pa/mm]	Wall motion pattern	Model assumptions				
				(I)	(II)	(III)	(IV)	(V)
Model A1	A	0.1995	None	✓	✓	✓	✓	✓
Model A2	A	0.0	Cardiac pulsations (uniform)	✓	✓	✓	✗	✗
Model B1	B	0.1995	None	✗	✓	✓	✗	✗
Model B2	B	0.0	Cardiac pulsations (travelling)	✗	✓	✓	✗	✗
Model B3	B	0.0	Vasomotion (travelling)	✗	✓	✓	✗	✗
Model C12	C	0.1995	Cardiac pulsations (travelling)	✗	✓	✓	✗	✗

Wall pulsations are applied uniformly in space (uniform) or as a travelling wave in space (travelling). Each of the models satisfy some of the reduced model assumptions (I–V), but only Model A1 satisfies all

$$\begin{aligned}\bar{p}_h(s, t) &= \frac{1}{|C|} \sum_k w_k p_h(x_k, t), \\ \bar{q}_h(s, t) &= \sum_k w_k v_h(x_k, t) \cdot n_C(x_k)\end{aligned}\quad (17)$$

for a quadrature scheme with points x_k and weights w_k defined over C and an approximation $|C|$ of the cross-section area. Here n_C is the normal vector of the cross-section. The averaging is implemented by using the Frenet frame associated with Λ to map from an annular cylinder in a reference domain onto the cross-section, similar to the implementation of the averaging operator in `fenics_ii` [43].

With this in hand we define the percentagewise relative model discrepancy $E_q(t)$ in the flux by

$$E_q(t) = \frac{\|\bar{q}_h(t) - \hat{q}_h(t)\|_{L^2(\Lambda)}}{\|\bar{q}_h(t)\|_{L^2(\Lambda)}} \cdot 100\% \quad (18)$$

and similarly for the pressure E_p . We typically compute this quantity if the flow is driven by a constant pressure gradient. In this case the fluid starts at rests and then quickly develops to stationary, annular Poiseuille flow. We then compute $E_q(T)$ and $E_p(T)$, where T denotes the final time.

For pulsatile flow, we typically compare the percentagewise relative error in peak pressure $e_p^{\text{peak}}(s')$ and peak cross-section flow $e_q^{\text{peak}}(s')$ at some cross section $C(s', t)$, where

$$e_q^{\text{peak}}(s') = \frac{|\max_{t \in (0, T)} \hat{q}_h(s', t) - \max_{t \in (0, T)} \bar{q}_h(s', t)|}{|\max_{t \in (0, T)} \bar{q}_h(s', t)|} \cdot 100\% \quad (19)$$

and $e_p^{\text{peak}}(s')$ is similarly defined. Finally, we compare the net fluxes Q of the full and reduced model, where Q associated with the velocity $v = v(x, t)$ can be computed as:

$$Q = \int_0^T \int_{\partial\Omega_{\text{in}}} v \cdot n \, dx \, dt, \quad (20)$$

and the corresponding quantity associated with the flux $\hat{q} = \hat{q}(s)$ by:

$$Q = \int_0^T \sum_{x \in \mathcal{I}} \hat{q}(x) \, dt \quad (21)$$

where the integration in time is over one period $[0, T]$.

3 RESULTS

The prescribed pressure gradient and the pulsating PVS walls each induce pressure gradients and fluid flow in the different PVS geometries. For each of the models (Table 2), we compare the simulation results from the full PVS (1) defined over the three-dimensional model domains and the reduced system (6) defined over the topologically one-dimensional domains, quantify the discrepancies between the models and the computational costs.

3.1 Reduced Model Exactly Predicts Pressure-Driven Axisymmetric Flow Characteristics

Flow in an axisymmetric annular cylinder of length ℓ driven by a constant pressure difference Δp (Model A1) is described by the analytic expression:

$$\begin{aligned}\hat{q}(s, t) &= A \frac{\Delta p}{\mu \alpha \ell} \left(1 - \exp\left(-\frac{\mu \alpha t}{\rho}\right) \right), \\ \hat{p}(s, t) &= \frac{\Delta p}{\ell} s + \hat{p}(0),\end{aligned}\quad (22)$$

where α is the lumped flow parameter given by (8) and which is constant in time and space in this case. For the velocity profile (5) defined over geometry A (cf. Table 1), $\alpha = 7325.3/\text{m}^2$, and $\mu\alpha/\rho = 5105.7/\text{s}$. Thus, the time-dependency is negligible after only a few milliseconds, and the flow develops near-instantaneously to steady-state Poiseuille flow.

Both the full and reduced models reproduce the exact annular Poiseuille flow characteristics of this case (Figure 2A). The numerical difference between the analytic and computed reduced solutions for the cross-section flux \hat{q} and average pressure \hat{p} is at machine precision ($\|\hat{q}(T) - \hat{q}_h(T)\| = 1.7 \times 10^{-14}$ and $\|\hat{p}(T) - \hat{p}_h(T)\| = 2.6 \times 10^{-17}$) ($T = 1$ s). In general, the total error is the sum of the model error and the numerical error associated with the space-time discrete approximation (13). For Model A1, the model error is zero as the model reduction assumptions (I–V) are exactly fulfilled by the geometry and flow pattern. As the total error also vanishes, we note that the numerical error is also negligible for this case.

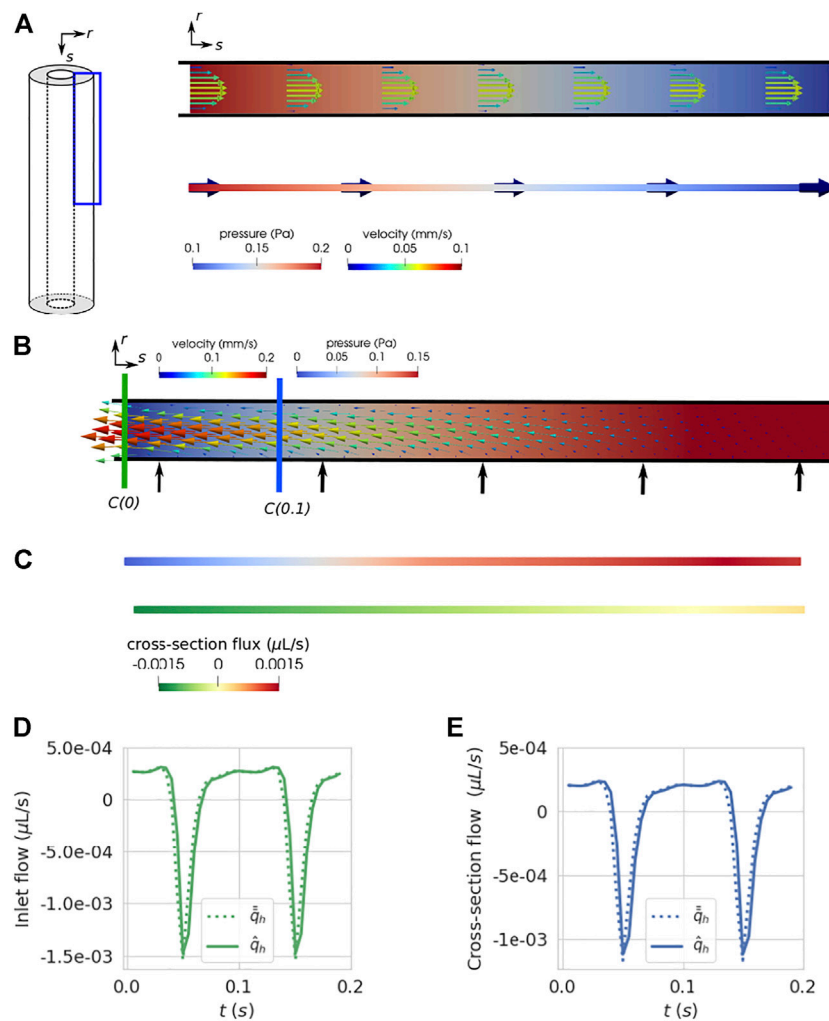


FIGURE 2 | PVS flux and pressure in an axisymmetric annular cylinder induced by a constant pressure difference or cardiac wall motion (Models A1, A2). **(A)** Model A1: A constant pressure gradient induces annular Poiseuille flow in both the full axisymmetric model (upper panel) and the reduced model (lower panel); snapshot of steady solution at $T = 0.1$. **(B–E)** Model A2: Inner wall pulsations induce bidirectional and oscillatory flow. **(B)** Snapshot of the full model solutions at peak outflux ($t = 0.05$). Different cross-sections are marked in green (at the inlet) and blue (in the interior). **(C)** Pressure (upper panel) and cross-section flux \bar{q}_h (lower panel). **(D)** Cross-section flux predicted by the full model (dotted line) and the reduced model (solid line) at inlet versus time. **(E)** As for **(C)** but at the interior cross-section marked in **(B)**.

3.2 Reduced Model Accurately Captures Axisymmetric PVS Wall Pulsations

Next, we examine the PVS flow and pressure generated by uniform axisymmetric pulsations of the inner PVS wall (Model A2, **Figures 2B–E**). The inner wall movement changes the inner domain radius R_1 in time. The fluid is pushed out at the both ends as the PVS width decreases, and flows back in at both ends as the PVS width returns to baseline. This behaviour is reproduced by both the full (**Figure 2B** [18]) and reduced models (**Figure 2C**). We note that the reduced model assumptions (IV, V) do not hold in this scenario as the PVS axial velocity profile is no longer identical to the Poiseuille velocity profile, and the pressure is not perfectly constant on each cross-section. Comparing the full and reduced cross-section fluxes \bar{q}_h and \hat{q}_h , we observe however that the two

models still agree closely (**Figures 2D,E**), both at the inlet and at an interior cross-section. Moreover, the time-profile of the reduced and full cross-section flux approximations are very similar (both at the inlet and at the interior cross-section, Table), though with small (Δt s) shifts in time. The peak outfluxes occur at the inlet and outlet; the peak outflux for the full model is $1.53 \times 10^{-3} \mu\text{m}^3/\text{s}$, and $1.47 \times 10^{-3} \mu\text{m}^3/\text{s}$ for the reduced model (**Figure 2D**). The peak pressure occurs in the middle of the domain; the peak pressure for the full model is 0.194 and 0.193 Pa for the reduced model. Using (19) the relative error in the peak cross-section flux at the inlet is $e_q^{\text{peak}}(0) = 4.0\%$ and in the peak cross-section (average) pressure $e_p^{\text{peak}}(0) = 0.8\%$. There is thus a small discrepancy between the two models, as expected by the violation of the reduced model assumptions.

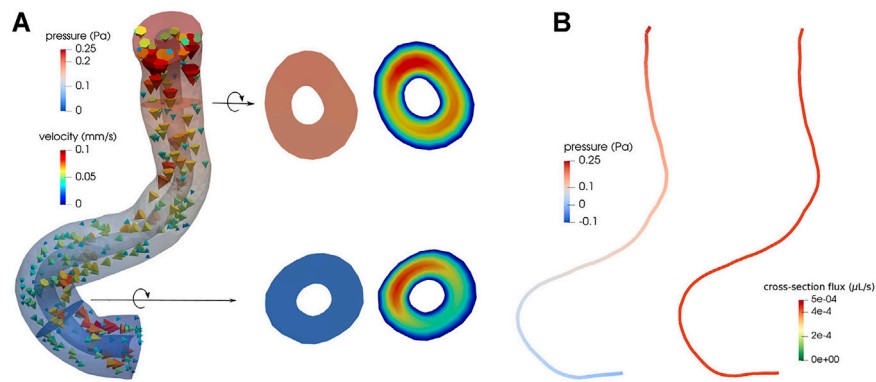


FIGURE 3 | In an image-based perivascular segment with varying radii, a pressure difference between inlet and outlet induces a pressure field that is nearly constant on each cross-section, but a velocity field that varies with the radial, angular and axial coordinates. **(A)** Full pressure and velocity approximations in the domain (left) along with close-up views of the pressure (middle) and velocity magnitude (right) at two cross-sections; **(B)** Reduced average cross-section pressure (left) and cross-section flux approximations (right).

3.3 Radial Geometry Variations Induce Small Model Errors

In contrast to the axisymmetric geometry A, the image-based geometries B and C express angular and axial variations in radius. The inner and outer radii of these geometries vary along the length of the domain (with s) and depend on the angular coordinate θ , with the latter violating model assumption I. To study the resulting model error in isolation, we again examine the pressure-driven flow predicted in full and reduced models but now of geometry B (Model B1, **Figure 3**). The full numerical approximation of the pressure is nearly constant over each cross-section. On the other hand, the velocity profile varies between cross-sections and with the angular coordinate within each cross-section (**Figure 3A**). Therefore, we expect a larger model error in the reduced model compared to the previous case(s). At steady state ($t = 0.5$), the reduced pressure approximation \hat{p} varies nearly linearly along the length of the domain as expected, and the reduced flux approximation \hat{q} is essentially constant along the centerline with value $\hat{q} = 4.28 \times 10^{-4} \mu\text{L/s}$. Computing the corresponding cross-section flux from the full model, we find values ranging from 3.5×10^{-4} to $5.31 \times 10^{-4} \mu\text{L/s}$. The relative model discrepancy (18) in the pressure is $E_p = 2.6\%$ and for the flux $E_q = 12.6\%$.

3.4 Reduced Model is Robust with Respect to Wall Motion Amplitude and Frequency

Cardiac wall motion and vasomotion may drive pulsatile perivascular flow with different flow characteristics. To evaluate the model discrepancy induced by different physiological drivers, we compare the full and reduced models over an image-based PVS segment driven by wall motion induced by the cardiac pulse wave (Model B2) and by vasomotion (Model B3). The cardiac pulse wave induces wall motion at a higher frequency (10 Hz) travelling at a higher wave speed (1000 mm/s), while vasomotion creates pulsations at lower frequencies (0.1 Hz) and at a lower wave speed (0.8 mm/s). Both models include

angularly, axially and temporally varying radii, and we expect model assumptions I, IV-V to not hold.

Both pairs of models induce pulsatile bidirectional flow in and out of the PVS segment in synchrony with the pulsating wall (**Figure 4**, **Supplementary Video S1**) with peak pressure magnitude in the middle of the segment, and conversely, low velocities in the middle of the domain and higher velocities near the PVS ends. Both model scenarios lead to pressure fields that are nearly constant on each cross-section (**Figures 4C, 5**), but with angularly varying velocity profiles (**Figures 4B, 5**).

For the cardiac wall motion, the overall cross-section average of the full pressure \bar{p}_h ranges from -0.05 to 0.26 Pa, while the full cross-section flux \bar{v}_h ranges from -1.54×10^{-3} to $1.95 \times 10^{-3} \mu\text{L/s}$. The reduced model accurately captures the temporal and spatial characteristics of the full model (**Figures 4D–G**). For the reduced model, the overall cross-section pressure \hat{p}_h ranges from -0.06 to 0.29 Pa, while the cross-section flux \hat{q}_h is between -1.61×10^{-3} and $2.23 \times 10^{-3} \mu\text{L/s}$. Comparing the full and reduced pressure and flux over time at an interior, lower cross-section with axial coordinate s' (**Figures 4B,C**), we observe that the reduced model slightly overestimates the peak pressure and flux when compared to the full model (**Figures 4F,G**). Using (19) at this cross-section we find that the relative error of the peak pressure is $e_p^{\text{peak}}(s') = 19.0\%$ and the relative error of the peak flux is $e_q^{\text{peak}}(s') = 1.2\%$. One shall note that the space discretization of the initial 3D model has a non negligible impact on these relative errors. Indeed, using a finer 3D mesh composed of 333000 tetrahedrons instead of the initial 63000 lowers the relative error of the peak pressure $e_p^{\text{peak}}(s')$ to 12.1%. The relative error on peak flux is not significantly impacted but $e_q^{\text{peak}}(s')$ was already very small.

For the vasomotion scenario, the domain movement is larger compared to the cardiac wall motion, but the wall velocity is lower (peak wall speed of 0.001 vs. 0.005 mm/s). The resulting peak (in terms of magnitude) cross-section pressure is -0.012 Pa and peak cross-section flux is $9.14 \times 10^{-5} \mu\text{L/s}$ (**Figure 5**, **Supplementary Video S2**). These are one-to-two orders of magnitude lower than for the cardiac wall motion scenario. Comparing the full and reduced models in two interior (upper and lower) cross-sections,

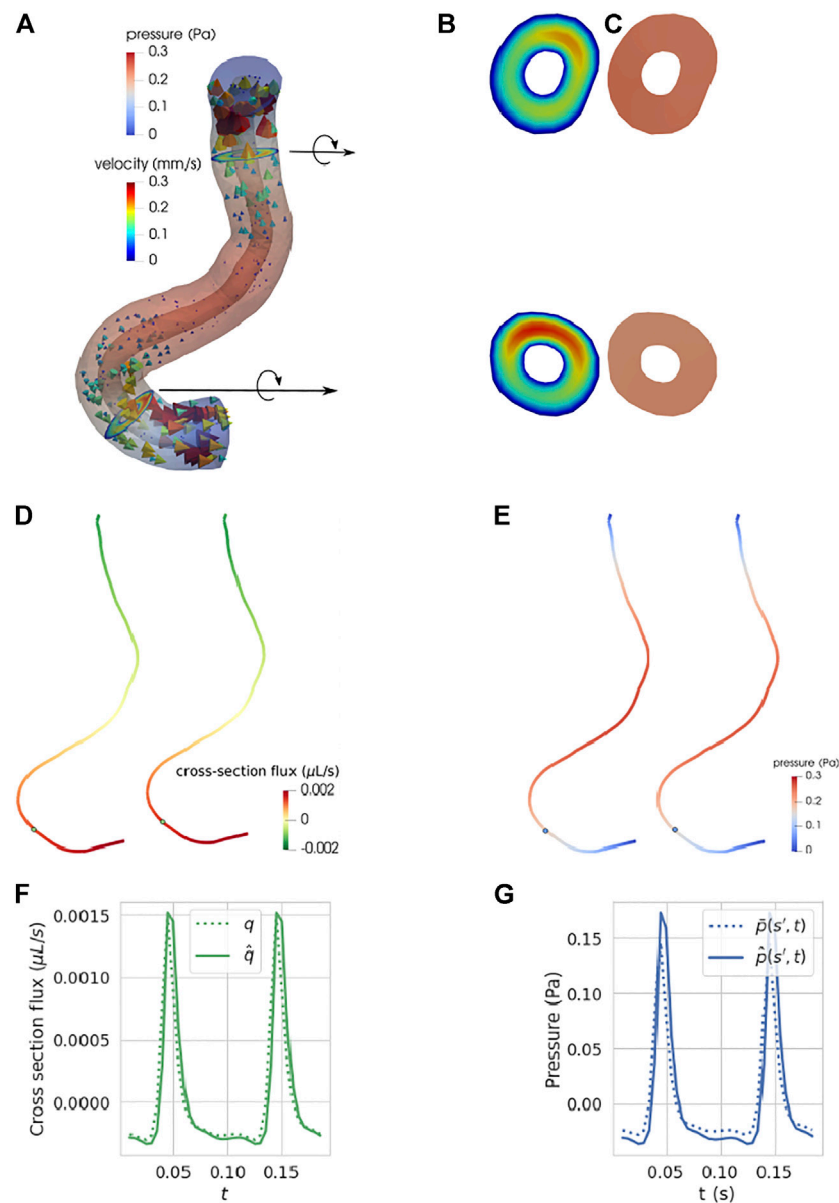


FIGURE 4 | Cardiac wall motion induces substantial pulsatile pressures and velocities in an image-based perivascular space segment, with the reduced model accurately capturing flow, pressure and transport characteristics. **(A)** Snapshot of the pressure and velocity at time of peak pressure ($t = 0.05$ s); **(B)** Velocity at upper and lower cross-section [zoom of **(A)**]; **(C)** Pressure at upper and lower cross-sections [zoom of **(A)**]; **(D)** Cross-section flux from reduced model (left) and full model (right); **(E)** cross-section average pressure from reduced model (left) and full model (right); **(F)** full and reduced model cross-section fluxes at the lower cross-section over time; **(G)** full and reduced model pressures at the lower cross-section over time.

we observe that the cross-section pressure \hat{q}_h matches pulsatile behaviour of the average cross-section pressure in the full model \bar{q}_h (**Figure 5B**) but that the peak amplitude is higher. The largest model differences in pressure at the lower cross-section is at the peak pressure; there the relative difference in peak pressure is $e_p^{\text{peak}}(s') = 52.7\%$. The similar observations hold for the flux, but the model discrepancies are lower: the relative difference in peak flux is $e_q^{\text{peak}}(s') = 15.6\%$. Moreover, the full and reduced models agree on a pressure phase shift of 0.5s. In agreement with our previous findings, the reduced pressure approximation displays a

greater model discrepancy with higher predicted pressure variations in the reduced model (**Figure 5B**).

3.5 Reduced Model Captures Flow and Transport Characteristics Through Bifurcations

Now, we turn to compare the full and reduced model predictions of physiologically realistic perivascular flow in an image-based PVS surrounding a vascular bifurcation

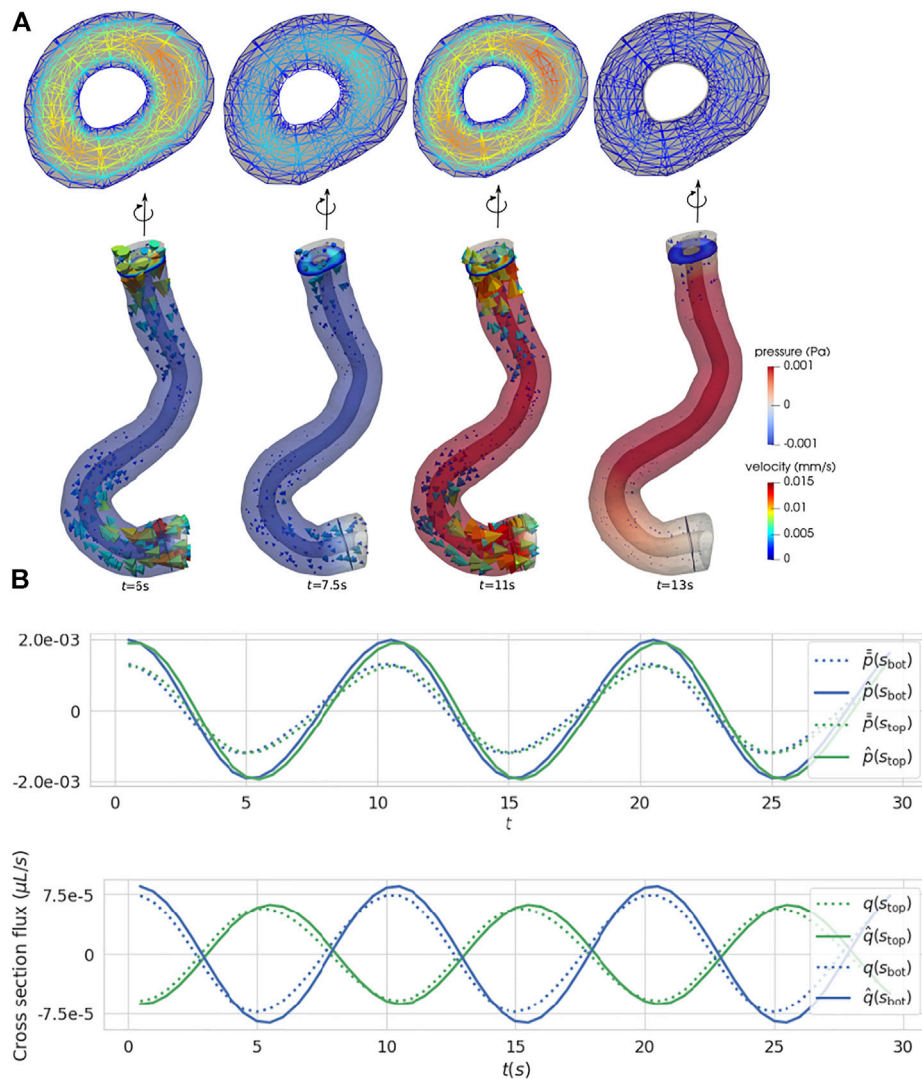


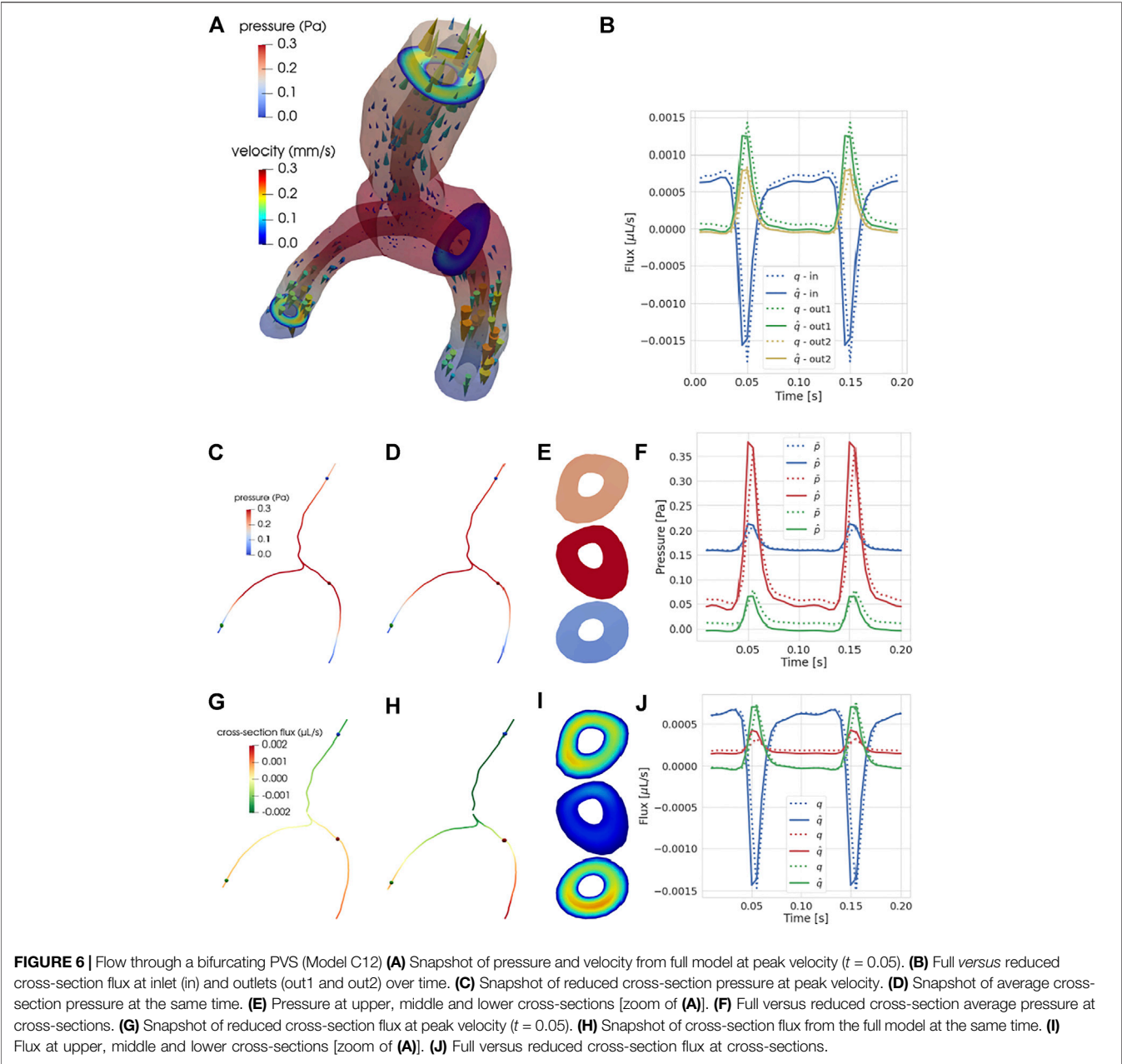
FIGURE 5 | Vasomotion induces higher domain deformations but lower wall velocities, pressure differences and cross-section fluxes. **(A)** Snapshots of the full model pressure and velocity at different time points with cross-section velocities (top). **(B)** Average pressure (upper panel) and flux (lower panel) for the full and reduced models at upper and lower cross-sections over time. The values at the different cross-sections are slightly shifted in time due to the travelling vasomotion. The pressure model discrepancy dominates the flux differences.

(Model C12). The prescribed pressure difference between inlet and outlets as well as the cardiac wall motion induces pulsatile flow with a net flow component [18] (Figure 6A, Supplementary Video S3). We note that the domain radii vary both angularly and axially, also for the initial domain, and also that the presence of a bifurcation region induces non-Poiseuille/non-Womersley-type velocity profiles. Comparing the full and reduced average pressure and flux at the time of peak velocity (Figures 6F,J), we note that the reduced model captures the qualitative and quantitative flow and pressure characteristics. The bifurcation conditions are satisfied at the bifurcation point b (Figures 6C,G) with a parent branch flux $\hat{q}(b)|_{\Lambda^P} = -5.52 \times 10^{-4} \mu L/s$ and daughter branch fluxes $\hat{q}(b)|_{\Lambda^{d_1}} = -7.8 \times 10^{-5} \mu L/s$ and $\hat{q}(b)|_{\Lambda^{d_2}} = -4.74 \times 10^{-4} \mu L/s$. The uneven flux distribution is induced by the smaller

average width of one of the daughter vessels. The predicted stress $\hat{\sigma}$ is continuous (data not shown).

The reduced peak cross-section flux (over time) at the inlet is $-1.5 \times 10^{-3} \mu L/s$, and $1.2 \times 10^{-3} \mu L/s$ and $7.9 \times 10^{-4} \mu L/s$ at the outlets (Figure 6B).

Comparing the relative difference in peak flux at the inlet and outlets, we note that the discrepancy is largest at larger daughter outlet (s_{out}) with a relative difference $e_p^{peak}(s_{out}) = 12.7\%$. Comparing the full and reduced peak pressures at the upper (s_u), middle (s_m) and lower (s_l) cross-sections, we find relative differences $e_p^{peak}(s_u) = 1.1\%$, $e_p^{peak}(s_m) = 4.1\%$, and $e_p^{peak}(s_l) = 16.4\%$. The analogous numbers for the fluxes are $e_q^{peak}(s_u) = 1.0\%$, $e_q^{peak}(s_m) = 33.5\%$, and $e_q^{peak}(s_l) = 5.1\%$. Thus, the relative differences in peak flux are larger near the bifurcation region (Figures 6F,J).



The net flow is a key quantity of interest for the physiological relevance of perivascular flow and transport. The net flow per cycle in the full model is 3.5×10^{-5} , and $2.9 \times 10^{-5} \mu\text{L}$ for the reduced model, corresponding to a relative difference of 17%.

3.6 Reduced Models Offer Orders of Magnitude Saving in Computational Resources

Accurate direct three-dimensional simulations of pulsatile perivascular fluid flow in large, deforming vascular networks

TABLE 3 | The geometrically-reduced models reduce computational cost by orders of magnitude.

Model	d.o.fs		Time (s)		Memory (MB)	
	Full	Reduced	Full	Reduced	Full	Reduced
A2	9, 103	194	0.16	0.35	180	146
B2	287, 432	1067	42.33	0.83	6261	133
C12	401, 156	749	130.57	0.76	8874	176

Number of degrees of freedom d.o.f.s, computational tim (average time for a single time step) and memory usage (peak memory usage throughout the simulation) for the full models (2D/3D) and reduced models (1D).

involve a significant computational cost. The expense is dominated by solving large linear systems of equations at each time step. For instance, even the moderate-resolution single-bifurcation model considered here (model C12) includes more than 17 000 vertices, 88 000 mesh cells and 400,000 degrees of freedom. For a small-scale idealized model such as axisymmetric Model A2, the reduced model uses 2.1% of the number of degrees of freedom but approximately the same amount of memory and longer runtime (0.16 vs. 0.35 s per time step, **Table 3**). However, the one-dimensional models reduce computational cost substantially for the image-based geometries (**Table 3**). For the image-based perivascular segment (Model B2), the reduced model uses 0.4% of the number of degrees of freedom, 2.0% of the runtime, and 2.1% of the memory of the full model. For the image-based bifurcating PVS (Model C12), the reduced model uses 0.18% of the number of degrees of freedom, 0.6% of the runtime and 2.0% of the memory of the full model. Overall, the reduced model reduces the computational expense, both in terms of computational time and memory, by several orders of magnitude for image-based PVS segments.

DISCUSSION

We have proposed a new mathematical and numerical framework based on topological and geometrical model reduction for computational modelling and simulation of steady and pulsatile fluid flow in deformable perivascular space networks. The reduced model is defined over a perivascular centerline network and predicts the fluid flux and average pressure in each cross-section of each network branch. By numerically comparing direct three-dimensional simulations of the fluid flow with the reduced model results for a range of physiological scenarios, we find that the reduced model accurately captures the important flow characteristics with cross-section peak pressure discrepancies ranging from 0% to 52% and peak flux discrepancies ranging from 0% to 35%. Our findings indicate that reduced model is robust with respect to physiologically relevant spatial and temporal variations in the vascular radius. Moreover and importantly, the computational cost of the reduced model is several orders of magnitude lower than that of the corresponding full model.

While geometrically-reduced network models of pulsatile blood flow have become a standard computational tool [19, 23, 44], network models of perivascular fluid flow have mainly focused either on quantifying flow resistance [7, 10] or predicting steady flow [45]. In the latter, Tithof et al present the results of a network model of glymphatic flow under different parameters, using resistance models to compute flow in idealized domains. For the open channel flow, they compute the flow therein via Darcy's law $v = -(\kappa A/\nu)\nabla p$ with permeability

$$\kappa = \frac{1}{8} \left(R_2^2 + R_1^2 - \frac{R_2^2 - R_1^2}{\ln(R_2/R_1)} \right). \quad (23)$$

This relationship holds under the assumption of Poiseuille flow in the open, annular channel (for which there is an analytic

solution) and corresponds to the permeability required for this solution to satisfy Darcy's law. For steady-state flow ($\partial_t v = \partial_{ss} v = 0$) driven by a constant pressure difference, the reduced model (6) simplify to the Darcy flow equation with permeability

$$\kappa = \frac{1}{\alpha}. \quad (24)$$

In the idealized Model A1 scenario, the two definitions of κ (23, 24) agree, with $\kappa = 1.36 \times 10^{-4} \text{ mm}^2$, and thus the models coincide within this regime.

Rey and Sarntinoranont [13] also introduced two hydraulic models to predict fluid flow induced by blood pressure wave pulsations, and in particular net flow and transport. Their models also capture the pulsatile flow generated by the volume changes induced by a pulsating inner boundary, but under other modelling assumptions and without considering bifurcations, and thus differ from the one considered here. However, their peak fluid velocities of the order tens of $\mu\text{m/s}$ is of the same order as the fluid velocities predicted in single branches here (Models A2, B2, B3), as are the pressures on the order of up to 0.3 Pa.

Several different bifurcation conditions have been proposed in the literature. In one-dimensional blood flow models, the most common conditions are conservation of flux combined with continuity of pressure [44, 46]. These conditions may be imposed directly on the pressure and flux solution variables [44], or weakly in the variational formulation [46]. Here, we also enforce conservation of flux, but in place of the strong pressure continuity condition, we weakly impose the continuity of the normal stress. This approach gives a natural setting for Stokes flow and allows for a compatible variational formulation using a Lagrange multiplier space.

In terms of limitations, we here focus on models of perivascular flow and the effect of vascular pulsations on perivascular flow, and not on the full interplay between vascular, perivascular and interstitial flow and deformation, nor on the transfer across the blood-brain barrier or the glial limitans. For healthy arterial and venous regions, in which the blood flow dynamics dominate the perivascular flow and pressure, we expect this one-way (vascular-to-perivascular) coupling to capture the leading order dynamics. Moreover, in light of the expected high resistance of the interstitial space [13, 45, 47, 48], we expect the perivascular-interstitial transfer and interstitial flow to be relatively small under physiological conditions. However, in light of the importance of quantifying and characterizing the different potential pathways, coupled fluid dynamics in vascular, perivascular and interstitial spaces will be considered in subsequent work.

We here consider open (in contrast to porous) domains. This is an appropriate modelling choice for surface perivascular spaces surrounding arteries or veins [6, 8]. For parenchymal perivascular spaces, within the pial-glial interface or within the smooth muscle cell basement membranes [49], however, a porous media representation may be more appropriate. In such a case, the Stokes flow (1) are naturally replaced by a Darcy or Brinkman flow model with an additional permeability κ [50]. The analogous reduced model [corresponding to (6)] would include an

additional lower order term for the flux \hat{q} weighted by this permeability. For parenchymal and capillary perivascular spaces, we would also expect the coupled interplay between vascular, perivascular and interstitial spaces to be non-negligible.

Surface PVSs may be of different shapes ranging from annular cylinders with no or some ellipticity to fully separated segments [7], or be defined as more irregular expansions of the subarachnoid space [6, 51]. The image-based vascular geometries used here define high-fidelity representations of inner boundaries of human surface PVSs. However, the representation of surrounding PVSs as annular structures is clearly an approximation, and a response to the lack of appropriate three-dimensional data of human surface PVSs. An interesting point in this regard, and an opportunity for further study, is the quantification of the model error introduced by approximating these non-regular structures by elliptic annular cylinders with a fixed centerline. We would expect more irregular geometries to induce larger differences between the full and reduced models, but the relative importance and role of ellipticity and other geometrical irregularities remain undetermined.

Our simulations rely on a high-order discretization in space to ensure stability of the model, combined with a first-order discretization in time. A temporal sensitivity analysis on key output quantities i.e. pressure and cross-section flux showed expected convergence as the time resolution is reduced, and was used to determine the employed time step. The use of a higher-order discretization in time could also be considered. We also note that we have considered simplified (prescribed traction) boundary conditions at the PVS inlet and outlets. Compliance or resistance-based boundary conditions could of course also be considered, e.g., as in previous work [18], or [37]. We have focused on cardiac pulse wave-induced wall motion and vasomotion, two physiological factors that generate changes in vascular radius of up to 15% [31, 38] and only moderate wall velocities. However, the vascular and perivascular diameters may change more dramatically. For instance, Enger et al [52] report of a nearly 40% increase and 50% decrease in arteriole diameter during cortical spreading depression, and intriguingly the vascular and perivascular wall motions may differ between e.g., sleep states [53]. If these changes lead to significantly higher wall velocities than those considered here, we would expect a further breakdown of the reduced model assumptions, specifically assumption V, which in turn would be expected to impact the accuracy of the reduced models.

While many aspects of brain influx and clearance remain enigmatic, perivascular fluid flow along the cerebral vasculature is widely recognized as a key transport mechanism. The

computationally inexpensive yet accurate reduced models presented here give an efficient and flexible framework for computational modelling and simulation of pulsatile flow in idealized or realistic networks including complete representations of e.g., the cerebral arteries or veins and many generations of arterioles/capillaries. This framework thus establishes a foundation for future computational studies of perivascular flow to improve our understanding of brain transport.

DATA AVAILABILITY STATEMENT

The datasets presented in this study can be found in online repositories. The names of the repository/repositories and accession number(s) can be found below: <https://doi.org/10.5281/zenodo.5729484>.

AUTHOR CONTRIBUTIONS

CD-C, IG, and MR conceived the experiments. CD-C created the PVS geometries. CD-C, IG, and MR developed the simulation code. CD-C and IG conducted the experiments and analyzed the results. CD-C, IG, and MR created figures. CD-C, IG, and MR wrote the paper. All authors reviewed and approved the final manuscript.

FUNDING

This study has received funding from the European Research Council (ERC) under the European Union's Horizon 2020 research and innovation programme under grant agreement 714892.

ACKNOWLEDGMENTS

We thank Miroslav Kuchta (Simula Research Laboratory) for constructive discussion on topics related to the manuscript.

SUPPLEMENTARY MATERIAL

The Supplementary Material for this article can be found online at: <https://www.frontiersin.org/articles/10.3389/fphy.2022.882260/full#supplementary-material>

REFERENCES

1. Rennels ML, Gregory TF, Blaumanis OR, Fujimoto K, Grady PA. Evidence for a 'Paravascular' Fluid Circulation in the Mammalian central Nervous System, provided by the Rapid Distribution of Tracer Protein throughout the Brain from the Subarachnoid Space. *Brain Res* (1985) 326:47–63. doi:10.1016/0006-8993(85)91383-6
2. Carare RO, Bernardes-Silva M, Newman TA, Page AM, Nicoll JAR, Perry VH, et al. Solutes, but Not Cells, drain from the Brain Parenchyma along Basement Membranes of Capillaries and Arteries: Significance for Cerebral Amyloid Angiopathy and Neuroimmunology. *Neuropathol Appl Neurobiol* (2008) 34:131–44. doi:10.1111/j.1365-2990.2007.00926.x
3. Iliff JJ, Wang M, Liao Y, Plogg BA, Peng W, Gundersen GA, et al. A Paravascular Pathway Facilitates CSF Flow through the Brain Parenchyma

- and the Clearance of Interstitial Solutes, Including Amyloid β . *Sci Transl Med* (2012) 4:147ra111. doi:10.1126/scitranslmed.3003748
4. Wardlaw JM, Benveniste H, Nedergaard M, Zlokovic BV, Mestre H, Lee H, et al. Perivascular Spaces in the Brain: Anatomy, Physiology and Pathology. *Nat Rev Neurol* (2020) 16:137–53. doi:10.1038/s41582-020-0312-z
 5. Zhang ET, Inman CB, Weller RO. Interrelationships of the Pia Mater and the Perivascular (Virchow-Robin) Spaces in the Human Cerebrum. *J Anat* (1990) 170:111–23.
 6. Bedussi B, Almasian M, de Vos J, VanBavel E, Bakker EN. Paravascular Spaces at the Brain Surface: Low Resistance Pathways for Cerebrospinal Fluid Flow. *J Cereb Blood Flow Metab* (2018) 38:719–26. doi:10.1177/0271678x17737984
 7. Thifof J, Kelley DH, Mestre H, Nedergaard M, Thomas JH. Hydraulic Resistance of Periarterial Spaces in the Brain. *Fluids Barriers CNS* (2019) 16:19–3. doi:10.1186/s12987-019-0140-y
 8. Min Rivas F, Liu J, Martell BC, Du T, Mestre H, Nedergaard M, et al. Surface Periarterial Spaces of the Mouse Brain Are Open, Not Porous. *J R Soc Interf* (2020) 17:20200593. doi:10.1098/rsif.2020.0593
 9. Martinac AD, Bilston LE. Computational Modelling of Fluid and Solute Transport in the Brain. *Biomech Model Mechanobiol* (2019) 19:1–20. doi:10.1007/s10237-019-01253-y
 10. Faghhi MM, Sharp MK. Is Bulk Flow Plausible in Perivascular, Paravascular and Paravenous Channels? *Fluids Barriers CNS* (2018) 15:17. doi:10.1186/s12987-018-0103-8
 11. Asgari M, de Zélicourt D, Kurtcuoglu V. Glymphatic Solute Transport Does Not Require Bulk Flow. *Sci Rep* (2016) 6:38635–11. doi:10.1038/srep38635
 12. Diem AK, MacGregor Sharp M, Gatherer M, Bressloff NW, Carare RO, Richardson G. Arterial Pulsations Cannot Drive Intramural Periarterial Drainage: Significance for A β Drainage. *Front Neurosci* (2017) 11:475. doi:10.3389/fnins.2017.00475
 13. Rey J, Sarntinoranont M. Pulsatile Flow Drivers in Brain Parenchyma and Perivascular Spaces: a Resistance Network Model Study. *Fluids Barriers CNS* (2018) 15:20. doi:10.1186/s12987-018-0105-6
 14. Keith Sharp M, Carare RO, Martin BA. Dispersion in Porous media in Oscillatory Flow between Flat Plates: Applications to Intrathecal, Periarterial and Paraarterial Solute Transport in the central Nervous System. *Fluids Barriers CNS* (2019) 16:13. doi:10.1186/s12987-019-0132-y
 15. Lloyd RA, Stoodley MA, Fletcher DF, Bilston LE. The Effects of Variation in the Arterial Pulse Waveform on Perivascular Flow. *J Biomech* (2019) 90:65–70. doi:10.1016/j.jbiomech.2019.04.030
 16. Kedarasetti RT, Drew PJ, Costanzo F. Arterial Pulsations Drive Oscillatory Flow of CSF but Not Directional Pumping. *Sci Rep* (2020) 10:10102–12. doi:10.1038/s41598-020-66887-w
 17. Kedarasetti RT, Turner KL, Echagarruga C, Gluckman BJ, Drew PJ, Costanzo F. Functional Hyperemia Drives Fluid Exchange in the Paravascular Space. *Fluids Barriers CNS* (2020) 17:52–25. doi:10.1186/s12987-020-00214-3
 18. Daversin-Catty C, Vinje V, Mardal K-A, Rognes ME. The Mechanisms behind Perivascular Fluid Flow. *PLOS ONE* (2020) 15:e0244442. doi:10.1371/journal.pone.0244442
 19. Olufsen MS. Structured Tree Outflow Condition for Blood Flow in Larger Systemic Arteries. *Am J Physiol Heart Circulatory Physiol* (1999) 276: H257–H268. doi:10.1152/ajpheart.1999.276.1.h257
 20. Sherwin SJ, Franke V, Peiró J, Parker K. One-dimensional Modelling of a Vascular Network in Space-Time Variables. *J Eng Math* (2003) 47:217–50. doi:10.1023/b:engi.0000007979.32871.e2
 21. D'Angelo C, Quarteroni A. On the Coupling of 1d and 3d Diffusion-Reaction Equations: Application to Tissue Perfusion Problems. *Math Models Methods Appl Sci* (2008) 18:1481–504. doi:10.1142/S0218202508003108
 22. Lesinigo M, D'Angelo C, Quarteroni A. A Multiscale Darcy-Brinkman Model for Fluid Flow in Fractured Porous media. *Numer Math* (2011) 117:717–52. doi:10.1007/s00211-010-0343-2
 23. Coccarelli A, Carson JM, Aggarwal A, Pant S. A Framework for Incorporating 3d Hyperelastic Vascular wall Models in 1d Blood Flow Simulations. *Biomech Model Mechanobiol* (2021) 20:1231. doi:10.1007/s10237-021-01437-5
 24. Köppl T, Vidotto E, Wohlmuth B. A 3D-1D Coupled Blood Flow and Oxygen Transport Model to Generate Microvascular Networks. *Int J Numer Meth Biomed Engng* (2020) 36:e3386. doi:10.1002/cnm.3386
 25. Koch T, Schneider M, Helmig R, Jenny P. Modeling Tissue Perfusion in Terms of 1d-3d Embedded Mixed-Dimension Coupled Problems with Distributed Sources. *J Comput Phys* (2020) 410:109370. doi:10.1016/j.jcp.2020.109370
 26. Vidotto E, Koch T, Köppl T, Helmig R, Wohlmuth B. Hybrid Models for Simulating Blood Flow in Microvascular Networks. *Multiscale Model Simul* (2019) 17:1076–102. doi:10.1137/18m1228712
 27. Cattaneo L, Zunino P. A Computational Model of Drug Delivery through Microcirculation to Compare Different Tumor Treatments. *Int J Numer Meth Biomed Engng* (2014) 30:1347–71. doi:10.1002/cnm.2661
 28. Possenti L, di Gregorio S, Gerosa FM, Raimondi G, Casagrande G, Costantino ML, et al. A Computational Model for Microcirculation Including Fahraeus-Lindqvist Effect, Plasma Skimming and Fluid Exchange with the Tissue Interstitium. *Int J Numer Meth Biomed Engng* (2018) 35:e3165. doi:10.1002/cnm.3165
 29. Possenti L, Cicchetti A, Rosati R, Cerroni D, Costantino ML, Rancati T, et al. A Mesoscale Computational Model for Microvascular Oxygen Transfer. *Ann Biomed Eng* (2021) 49:3356. doi:10.1007/s10439-021-02807-x
 30. Aneurisk-Team. *AneuriskWeb Project Website*. [Dataset] (2012). Available at: <http://ecm2.mathcs.emory.edu/aneuriskweb> Accessed April 19, 2021.
 31. Mestre H, Thifof J, Du T, Song W, Peng W, Sweeney AM, et al. Flow of Cerebrospinal Fluid Is Driven by Arterial Pulsations and Is Reduced in Hypertension. *Nat Commun* (2018) 9:4878. doi:10.1038/s41467-018-07318-3
 32. Daversin-Catty C. *PVS Meshing Tools*. [Dataset]. Github (2020). Available at: <https://github.com/cdaversin/PVS-meshing-tools>
 33. Antiga L, Piccinelli M, Botti L, Ene-Iordache B, Remuzzi A, Steinman DA. An Image-Based Modeling Framework for Patient-specific Computational Hemodynamics. *Med Biol Eng Comput* (2008) 46:1097–112. doi:10.1007/s11517-008-0420-1
 34. Schlömer N. *Meshio v4.3.10*. [Dataset]. Zenodo (2020). doi:10.5281/zenodo.4555995
 35. Geuzaine C, Remacle J-F. Gmsh: A 3-d Finite Element Mesh Generator with Built-In Pre- and post-processing Facilities. *Int J Numer Meth Engng* (2009) 79: 1309–31. doi:10.1002/nme.2579
 36. San Martín J, Smaranda L, Takahashi T. Convergence of a Finite element/ALE Method for the Stokes Equations in a Domain Depending on Time. *J Comput Appl Math* (2009) 230:521–45. doi:10.1016/j.cam.2008.12.021
 37. Ladrón-de-Guevara A, Shang JK, Nedergaard M, Kelley DH. Perivascular Pumping in the Mouse Brain: Improved Boundary Conditions Reconcile Theory, Simulation, and experiment. *J Theor Biol* (2022) 542:111103. doi:10.1016/j.jtbi.2022.111103
 38. Aldea R, Weller RO, Wilcock DM, Carare RO, Richardson G. Cerebrovascular Smooth Muscle Cells as the Drivers of Intramural Periarterial Drainage of the Brain. *Front Aging Neurosci* (2019) 11:1. doi:10.3389/fnagi.2019.00001
 39. Alnæs MS, Blechta J, Hake J, Johansson A, Kehlet B, Logg A, et al. The FEniCS Project Version 1.5. *Archive Numer Softw* (2015) 3:9–23. doi:10.11588/ans.2015.100.20553
 40. Daversin-Catty C, Vinje V, Mardal K-A, Rognes ME. Mechanisms-behind-pvs-flow-v1.0. [Dataset] (2020). doi:10.5281/zenodo.3890133
 41. Daversin-Catty C, Richardson CN, Ellingsrud AJ, Rognes ME. Abstractions and Automated Algorithms for Mixed-Dimensional Finite Element Methods. *ACM Trans Math Softw* (2021) 47:1–36. doi:10.1145/3471138
 42. Daversin-Catty C, Gjerde IG, Rognes ME. Geometrically-reduced-pvs-flow-v1.0. [Dataset] (2021). doi:10.5281/zenodo.5729484
 43. Kuchta M. Assembly of Multiscale Linear PDE Operators. In: *Lecture Notes in Computational Science and Engineering*. Cham: Springer International Publishing (2020). p. 641–50. doi:10.1007/978-3-030-55874-1_63
 44. Olufsen M, Nadim A. On Deriving Lumped Models for Blood Flow and Pressure in the Systemic Arteries. *Mbe* (2004) 1:61–80. doi:10.3934/mbe.2004.1.61
 45. Thifof J, Boster KAS, Bork PAR, Nedergaard M, Thomas JH, Kelley DH. A Network Model of Glymphatic Flow under Different Experimentally-Motivated Parametric Scenarios. *bioRxiv*:104258 (2021). doi:10.1101/2021.09.23.461519
 46. Notaro D, Cattaneo L, Formaggia L, Scotti A, Zunino P. A Mixed Finite Element Method for Modeling the Fluid Exchange between Microcirculation and Tissue Interstitium. In: G Ventura E Benvenuti, editors. *Advances in Discretization Methods: Discontinuities, Virtual Elements, Fictitious Domain*

- Methods*. Cham: Springer International Publishing (2016). p. 3–25. doi:10.1007/978-3-319-41246-7_1
47. Holter KE, Kuchta M, Mardal K-A. Sub-voxel Perfusion Modeling in Terms of Coupled 3d-1d Problem. In: FA Radu, K Kumar, I Berre, JM Nordbotten, IS Pop, editors. *Numerical Mathematics and Advanced Applications ENUMATH 2017*. Cham: Springer International Publishing (2019). p. 35–47. doi:10.1007/978-3-319-96415-7_2
 48. Vinje V, Eklund A, Mardal KA, Rognes ME, Støverud KH. Intracranial Pressure Elevation Alters CSF Clearance Pathways. *Fluids Barriers CNS* (2020) 17:29–19. doi:10.1186/s12987-020-00189-1
 49. Albargothy NJ, Johnston DA, MacGregor-Sharp M, Weller RO, Verma A, Hawkes CA, et al. Convective Influx/glymphatic System: Tracers Injected into the CSF Enter and Leave the Brain along Separate Periarterial Basement Membrane Pathways. *Acta Neuropathol* (2018) 136:139–52. doi:10.1007/s00401-018-1862-7
 50. Brinkman HC. A Calculation of the Viscous Force Exerted by a Flowing Fluid on a Dense Swarm of Particles. *Appl Sci Res* (1949) 1:27–34. doi:10.1007/bf02120313
 51. Vinje V, Bakker ENTP, Rognes ME. Brain Solute Transport Is More Rapid in Periarterial Than Perivenous Spaces. *Scientific Rep* (2021) 11:16085. doi:10.1038/s41598-021-95306-x
 52. Enger R, Tang W, Vindedal GF, Jensen V, Johannes Helm P, Sprengel R, et al. Dynamics of Ionic Shifts in Cortical Spreading Depression. *Cereb Cortex* (2015) 25:4469–76. doi:10.1093/cercor/bhv054
 53. Bojarskaite L, Bjørnstad DM, Pettersen KH, Cunen C, Hermansen GH, Åbjørsbråten KS, et al. Astrocytic Ca²⁺ Signaling Is Reduced during Sleep and Is Involved in the Regulation of Slow Wave Sleep. *Nat Commun* (2020) 11:3240–16. doi:10.1038/s41467-020-17062-2
- Conflict of Interest:** The authors declare that the research was conducted in the absence of any commercial or financial relationships that could be construed as a potential conflict of interest.
- Publisher's Note:** All claims expressed in this article are solely those of the authors and do not necessarily represent those of their affiliated organizations, or those of the publisher, the editors and the reviewers. Any product that may be evaluated in this article, or claim that may be made by its manufacturer, is not guaranteed or endorsed by the publisher.
- Copyright © 2022 Daversin-Catty, Gjerde and Rognes. This is an open-access article distributed under the terms of the Creative Commons Attribution License (CC BY). The use, distribution or reproduction in other forums is permitted, provided the original author(s) and the copyright owner(s) are credited and that the original publication in this journal is cited, in accordance with accepted academic practice. No use, distribution or reproduction is permitted which does not comply with these terms.



Two Domains of Meandering Spiral Waves in a Modified Barkley Model

Vladimir Zykov^{1*} and Eberhard Bodenschatz^{1,2,3,4}

¹ Max-Planck-Institute for Dynamics and Self-Organization, Göttingen, Germany, ² German Center for Cardiovascular Research, Partner Site Göttingen, Göttingen, Germany, ³ Institute for the Dynamics of Complex Systems, Georg-August-University Göttingen, Göttingen, Germany, ⁴ Laboratory of Atomic and Solid-State Physics and Sibley School of Mechanical and Aerospace Engineering, Cornell University, Ithaca, NY, United States

The stability of rigidly rotating spiral waves is a very important topic in the study of nonlinear reaction-diffusion media. Computer experiments carried out with a slightly modified Barkley model showed that, in addition to one region of instability observed earlier in the original Barkley model, there is another one exhibiting completely different properties. The wave instability in the second region is not related to the Hopf bifurcation. Moreover, hysteresis effects are observed at the boundary of the region. This means that in the vicinity of this region of instability, direct integration of the model equations leads either to a rigidly rotating or meandering spiral, depending on the initial conditions.

Keywords: excitable media, spiral wave, instability, hysteresis, modified Barkley model

OPEN ACCESS

Edited by:

Erik Andreas Martens,
Lund University, Sweden

Reviewed by:

Vadim N. Biktashev,
University of Exeter, United Kingdom
Zhouchao Wei,
China University of Geosciences
Wuhan, China

*Correspondence:

Vladimir Zykov
vladimir.zykov@ds.mpg.de

Specialty section:

This article was submitted to
Dynamical Systems,
a section of the journal
Frontiers in Applied Mathematics and
Statistics

Received: 24 March 2022

Accepted: 25 April 2022

Published: 13 May 2022

Citation:

Zykov V and Bodenschatz E (2022)
Two Domains of Meandering Spiral
Waves in a Modified Barkley Model.
Front. Appl. Math. Stat. 8:903563.
doi: 10.3389/fams.2022.903563

1. INTRODUCTION

Excitable media represent a broad class of non-equilibrium reaction-diffusion systems that play an important role in physical, chemical, and biological applications [1–4]. For example, wave processes in excitable media are intensively studied in various distributed systems, including the colonies of *Dictyostelium discoideum* [5], the Belousov-Zhabotinsky chemical reaction [6], the heart muscle [7], the eye retina [8], the neocortex [9], CO oxidation on the platinum single crystal surface [10], and many others.

An excitable medium can be viewed as an ensemble of active elements coupled locally by diffusion-like transport processes. Each individual active element has a resting state, resistant to small external perturbations. However, it can be excited by the application of a suprathreshold stimulus or by interacting with their neighbors. Therefore, locally induced excitation can propagate through the medium as a self-sustaining wave. Such a wave represents a rapid transition from a stable resting state to an excited one followed by a slow recovery transition (refractory) back to the resting state. Under normal conditions, the wave back follows the wavefront, and they never touch each other.

However, under some special conditions, the propagating wavefront can be broken [1, 11]. Then the front and the back of the wave propagating in a two-dimensional medium coincide at one point called a phase change point [2]. Near this point, the front and the back are moving in opposite directions and the boundary of the excited region curls around this singularity point. As a result, the broken wave is winding up into a spiral permanently rotating within the medium.

Such self-sustained activity unexpectedly appearing in cardiac or neuronal tissues strongly destroys their dynamics that results in life-threatening diseases. In this context, an understanding of possible scenarios of spiral wave dynamics is of great theoretical importance and has many practical applications.

One important aspect of this study is investigation of spiral wave stability. In a homogeneous low excitable two-dimensional medium spiral wave rigidly rotates around a round core. However,

under a variation of the medium's parameters this well-ordered dynamics can be destroyed that leads to a transformation of a circular trajectory of the spiral wave tip into the so-called meandering one, e.g., hypotrochoid or epitrochoid [12, 13].

Spiral wave meander has been observed in experiments with chemical solutions [14] and in computations performed with different reaction-diffusion models [15–17]. The investigation of spiral wave instability attracts a great attention from a theoretical point of view [18–21].

In this study we would like to find out domains of the spiral wave meandering within the parameter space of a slightly modified Barkley model of an excitable medium.

2. MODEL

In many studies it was demonstrated that the basic features of the wave dynamics can be reproduced by the two-component reaction-diffusion system

$$\frac{\partial u}{\partial t} = D\nabla^2 u + F(u, v), \quad \frac{\partial v}{\partial t} = \epsilon G(u, v), \quad (1)$$

where the variables u and v represent the activator and inhibitor species, respectively. Typically the nullcline $F(u, v) = 0$ is a non-monotonic function creating possibility for undamped wave propagation. The second nullcline $G(u, v) = 0$ is monotone and intersects the first one at only one point (u_0, v_0) . Below the functions $F(u, v)$ and $G(u, v)$ are taken in the form proposed by Barkley [22]:

$$F(u, v) = u(1 - u)[u - (v + b)/a], \quad (2)$$

$$G(u, v) = \begin{cases} u - v, & u \geq v, \\ k_\epsilon(u - v), & u < v. \end{cases} \quad (3)$$

Note, that in the original Barkley model the value of the parameter k_ϵ is fixed as $k_\epsilon = 1$. Three other constants a , b , and ϵ have been used as important control parameters. A variation of each of these three parameters results in a simultaneous influence on such important medium's characteristics as the propagation velocity, pulse duration and refractoriness. In the modified model under consideration the constant k_ϵ is introduced, which has no influence on the duration of a single pulse and its propagation velocity. However, this parameter allow us to control the recovery process because its characteristic time is determined as the product $k_\epsilon \epsilon$. Thus the activation and the recovery processes have different time constants, if $k_\epsilon \neq 1$. Such a jump in the characteristic time constant is a fairly common and useful tool in simulations of excitable media [12, 23, 24].

In all computations below the parameter D is fixed as $D = 1$. The Laplacian in Equation (1) was approximated using the five-point finite-difference method on the rectangular 500×500 grid with spatial step $\Delta x = \Delta y = 0.3$. After this spatial discretization the model equations are integrated in time with the explicit forward Euler method with time step $\Delta t = 0.01$ and no-flux boundary conditions. The spiral wave tip is determined as a point where $u = 0.5$ and $du/dt = 0$. A part of an isoconcentration line $u(x, y, t) = 0.5$ corresponds to the wave front where $du/dt > 0$, and another part, where $du/dt < 0$, represents the wave back.

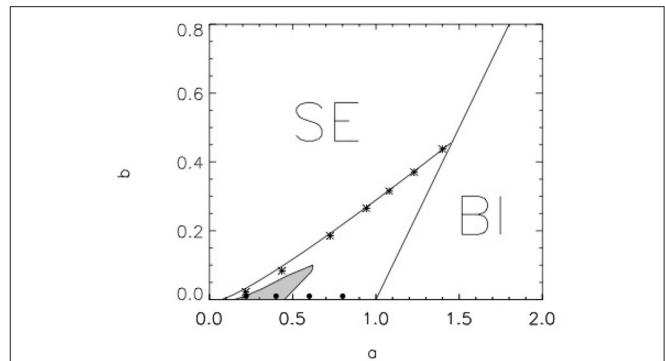


FIGURE 1 | Parameter space of the modified Barkley model with $\epsilon = 0.01$ and $k_\epsilon = 2$. Within the SE region wave segments created in two dimensional medium are shrinking. Within the BI region the system (1)–(3) exhibits the bistability. Rotating spiral waves are analyzed between these two regions. Within the white domain spiral waves rotates around a circular core, while they are meandering within the light gray domain. Black spots correspond to parameter values used in **Figure 2**.

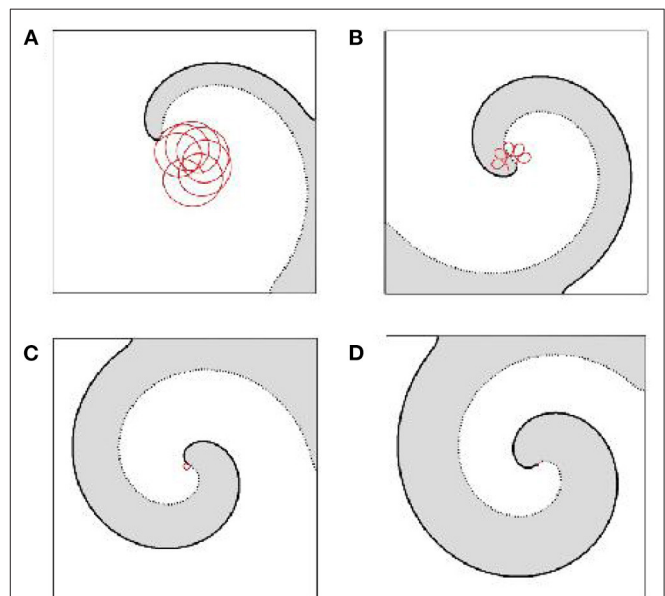


FIGURE 2 | Spiral waves dynamics obtained for the system (1)–(3) with $\epsilon = 0.01$, $k_\epsilon = 2$ and $b = 0.01$ for different values of the parameter a . In **(A)** $a = 0.22$, in **(B)** $a = 0.4$, in **(C)** $a = 0.6$, and in **(D)** $a = 0.8$. Thick and dotted solids represent the wave front and back, correspondingly. The trajectory of the spiral wave tip is shown in red.

3. RESULTS

3.1. Single Domain of Meandering Spiral Waves

As the first step of our study the parameters are fixed as $\epsilon = 0.01$ and $k_\epsilon = 2$, while the constants a and b are used as important control parameters. The obtained computational results are illustrated in **Figures 1, 2**.

Within the parameter space shown in **Figure 1** there is a line

$$b = a - 1, \quad (4)$$

which determines the boundary of the bistability (BI) domain, where $b < a - 1$. Here the nullclines of the system (1)–(3) have two intersections points.

We analyse another part of the parameter space, where $b > a - 1$ and the system has only one rest point. Here the existence of spiral waves is limited by another line, where the radius of the core of the spiral wave becomes infinitely large. In the subexcitable (SE) region above this line, the wave segments formed after a wave break are not able to curl around the created singularity point, but simply shrink and disappear. An analytical expression for this line was obtained earlier [25] and has the form

$$b = [a - (\frac{4\epsilon a^2}{B_c})^{1/3}]/2, \quad (5)$$

where $B_c = 0.535$ is a critical value of the parameter $B = \frac{2D}{d_u c_p^2}$, as it was shown in [26]. Here d_u and c_p are the duration and the propagation velocity of a single pulse through a one dimensional medium, correspondingly. It can be seen, that the analytical approximation expressed by Equation (4) is in good agreement with the direct reaction-diffusion calculations illustrated by asterisk in **Figure 1**.

In order to analyse the dynamics of the spiral wave, numerous calculations were performed at various points in the parameter space. A broken plane excitation wave [2] was used as initial conditions. Initially, we fixed a relatively small value of the parameter b . A rigidly rotating spiral wave with a large core was generated near the boundary of the SE region. Then the parameter a increases step by step from one calculation to the next. The size of the core decreases as a increases, and the rotation period decreases. At some computational step, rigid rotation becomes impossible, and a meandering trajectory of the spiral wave tip is observed. This occurs on the left boundary of the light gray region in the **Figure 1**.

Meandering spirals were observed in the entire light gray region. It is found that in this meandering region the trajectory of the spiral wave tip may look like an epitrochoid (**Figure 2A**) or a hypotrochoid (**Figure 2B**). In the white region, to the right of the light gray region and until the BI domain, the tip of the spiral wave moves along a circular trajectory. The radius of this trajectory strongly decreases as a increases.

The computational data shown in **Figures 1, 2** look qualitatively similar to ones obtained earlier for the original Barkley model with $k_\epsilon = 1$ and $\epsilon = 0.02$ [22, 27]. However, the size of the instability domain is considerably smaller in the case under consideration. Note, that while the used value of the parameter ϵ is smaller, the characteristic recovery time determined by the product $k_\epsilon \epsilon$ remains the same.

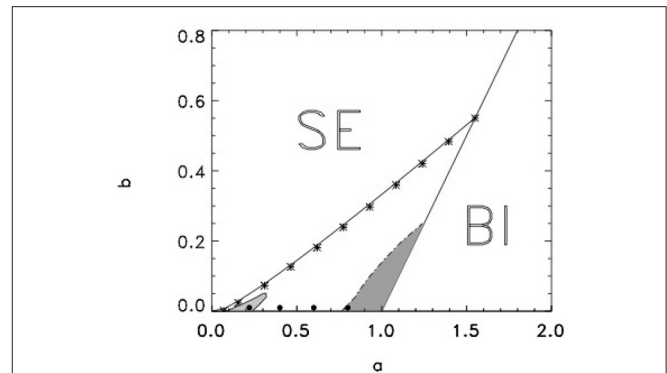


FIGURE 3 | Parameter space of the modified Barkley model with $k_\epsilon = 4$ and $\epsilon = 0.005$. Within the light gray domain tip trajectories look like epi- or hypo-trochoids, like in **Figure 1**. Within the dark gray domain the tip trajectories are more complicated and disordered. Within the white domain spiral waves rotates around a circular core. Black spots correspond to parameter values used in **Figure 4**.

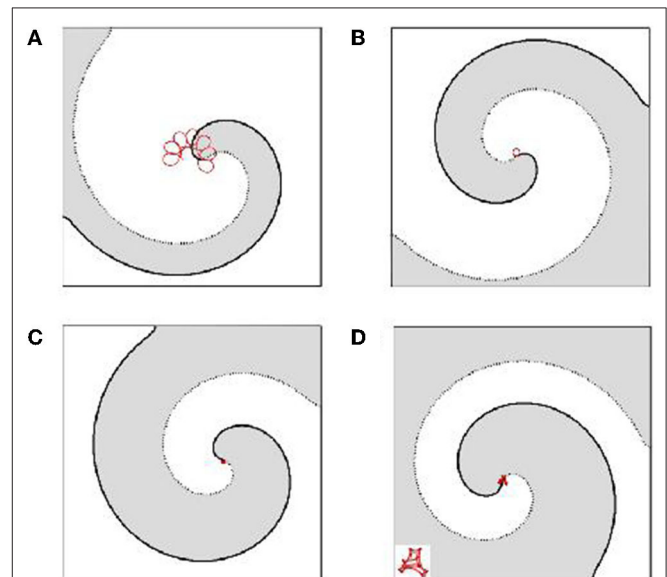
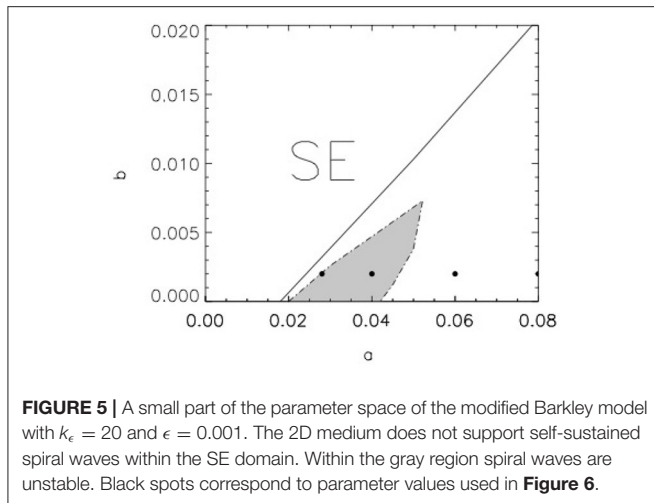


FIGURE 4 | Spiral waves dynamics obtained for the system (1)–(3) with $\epsilon = 0.005$, $k_\epsilon = 4$, and $b = 0.01$ for different values of the parameter a . In **(A)** $a = 0.22$, in **(B)** $a = 0.4$, in **(C)** $a = 0.6$, and in **(D)** $a = 0.8$. Thick and dotted solids represent the wave front and back, correspondingly. The trajectory of the spiral wave tip is shown in red. In the left lower corner of **(D)** the trajectory is magnified.

4. SECOND DOMAIN OF MEANDERING SPIRAL WAVES

In the second part of our study the value of the parameter ϵ is further decreased to $\epsilon = 0.005$ and k_ϵ is increased to $k_\epsilon = 4$ in order to conserve the characteristic recovery time. The data obtained in the corresponding computations are shown in **Figures 3, 4**.



As well as in the previous case, the existence of spiral waves here is limited by the lines defined by Equations (4) and (5). Note that the accuracy of the analytical estimate represented by Equation (5) becomes better as ϵ decreases.

Figure 3 clearly shows that there are two regions of instability in the parameter space. The spiral waves in the light gray region show dynamics very similar to those observed in the light gray region in **Figure 1**. Here, the trajectories of the spiral wave tips resemble epitrochoids or hypotrochoids, for example (see **Figure 4A**).

In the dark gray region, the tip trajectories become much more complex and are not as well ordered as shown in **Figure 4D**. In the parameter region surrounding these two regions, the trajectory of the spiral tip is circular.

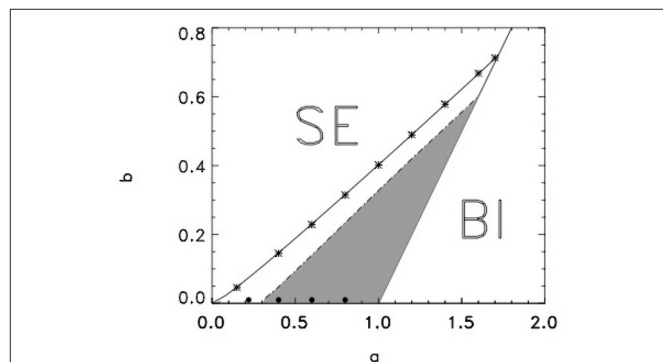
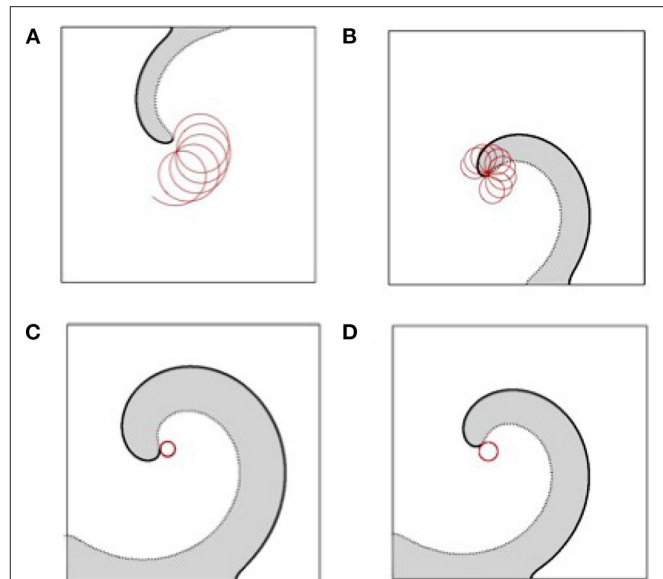
Note that the light gray domain in **Figure 3** is much smaller than in **Figure 1**. You can also see that the radius of the circular trajectory of the spiral tip is much smaller for these ϵ and k_ϵ values, while the values of a and b are the same. This follows from a comparison of **Figures 1B,C** with **Figures 3B,C**.

5. HYSTERESIS PHENOMENON

As the next step of our study the value of the parameter ϵ is considerably decreased to $\epsilon = 0.001$ in the numerical computations. Simultaneously the parameter k_ϵ is increased to $k_\epsilon = 20$ in order to conserve the characteristic recovery time.

Under these modified values a part of the parameter space shown in **Figure 5** looks qualitatively similar to the picture obtained for the original Barkley model as well as for one shown in **Figure 1**. Within the subexcitable region SE there are no self-sustained spiral waves. Wave segments initiated in this parameter region are shrinking and disappear. Within the rest of the parameter space presented in **Figure 5** self-sustained spiral waves have been observed. They are rotating rigidly within the white region, while inside the light gray region they are meandering. Some examples of spiral wave dynamics are shown in **Figure 6**.

However, this is only a very small part of the entire parameter space investigated at these parameter values. The results obtained



in a wider parameter space are shown in **Figure 7**. The regions of subexcitability (SE) and bistability (BI) are indicated here. Self-sustaining spiral waves are observed between these two regions. Within the narrow white region, the rigid rotation of spiral waves is stable. The transition to meandering spiral motion occurs in a very small light gray region with $a \ll 1$ and $b \ll 1$, which is almost invisible in **Figure 7** but is shown in **Figure 5**.

In the dark gray region, the trajectories of the spiral tips are very different from those of the hypotrochoids and epitrochoids shown in **Figure 6**. A step by step increase of the parameter a within the dark gray domain results in a strong transformation of the spiral tip trajectory. Indeed, rigidly rotating spiral describing

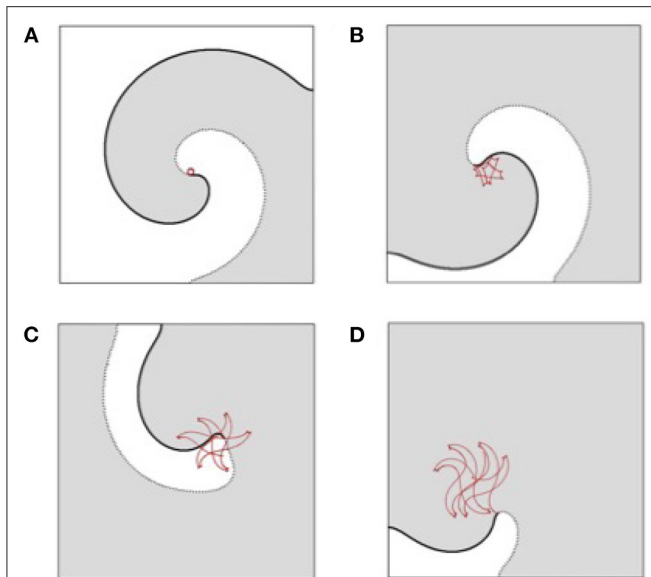


FIGURE 8 | Four examples of the trajectories of the spiral wave tip observed within the gray parameter region shown in **Figure 5** with $b = 0.01$ and (A) $a = 0.22$, (B) $a = 0.4$, (C) $a = 0.6$, (D) $a = 0.8$.

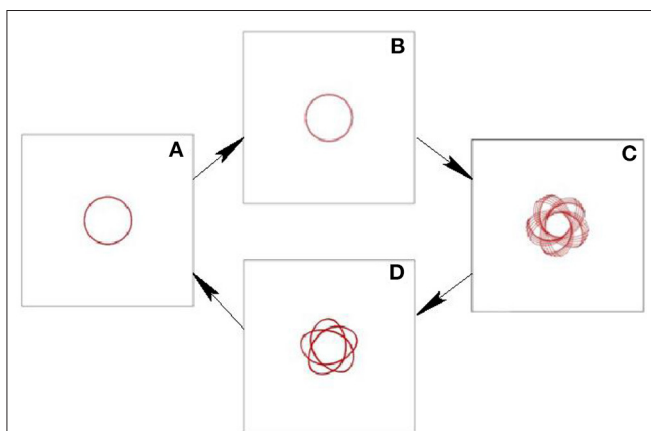


FIGURE 9 | The trajectories of the spiral wave tips obtained numerically for the modified Barkley model with the parameter b fixed as $b = 0.015$ and varied parameter a . (A) $a = 0.31$, (B) $a = 0.32$, (C) $a = 0.325$, (D) $a = 0.32$.

a perfect circular shown in **Figure 8A** transforms into a jagged trajectory in **Figure 8B**. Further increase of a results in increasing of angular loops of the trajectory in **Figure 8C** and their dynamics becomes more irregular in **Figure 8D**.

Moreover, at the boundary of this region a hysteresis effect in the spiral wave dynamics has been observed. This phenomenon is illustrated in **Figure 9**. Here the trajectories of the spiral wave tip are shown obtained for different values of the parameter a and $b = 0.015$. The computations have been started at $a = 0.31$ and result in rigidly rotating spiral shown in **Figure 9A**. This stationary rotating wave is used as the initial conditions

for the next computations performed with $a = 0.32$ and illustrated in **Figure 9B**. After a short transient process the spiral wave trajectory approaches the circular shape. However, a jump to $a = 0.325$ leads to a destabilization of the rigid rotation and appearance of a rather complicated trajectory, shown in **Figure 9C**. This wave pattern has been used as the initial conditions for the computations in which the parameter a has been returned back to $a = 0.32$. However, the spiral tip trajectory does not return back to a circular one, as can be seen in **Figure 9D**. A rigid rotation restores only for $a = 0.31$. The further decrease of a also results in a circular trajectory. Thus, it is demonstrated that for $a = 0.32$ the shape of the spiral tip trajectory depends on the initial conditions.

The observed hysteresis effect exists not only for $b = 0.015$, but for all other values of b corresponding to the boundary of the instability domain represented by a dashed-dotted line in **Figure 9**. In particular for $a = 1.0$ and $b = 0.328$, as well as for $a = 1.4$ and $b = 0.51$. It has been observed not only by a variation of the parameter a and fixed parameter b , but also by a variation of the parameter b and fixed a .

6. SUMMARY

Thus, the numerical computations performed with a slightly modified Barkley model demonstrate the existence of two quite different parameter regions of spiral wave instability. Within a region located near the SE domain a transition from rigid rotation to spiral meandering follows a well known scenario. Here the instability is induced by the Hopf bifurcation that results in a hypotrichoidal or epitrichoidal trajectory of the spiral wave tip.

The spiral tip trajectories look more complex in the new found region (see **Figure 4**). The smooth circular trajectory transforms here into a jagged one and even becomes randomized (see **Figure 8**). This resembles a transition to hypermeandering spiral dynamics reported for the FitzHugh-Nagumo model [13], but is very unusual for the well studied Barkley model. The observed instability cannot be explained by the Hopf bifurcation as was done for the original Barkley model.

At the boundary of this new found instability region the hysteresis phenomenon was detected (see **Figure 9**). Note, that the similar hysteresis phenomenon was recently observed in the context of the Barkley model within the bistability region [25]. Moreover, a hysteresis phenomenon has been described in context of the FitzHugh-Nagumo model [28, 29].

Thus, the results obtained are quite general and applicable to quite different reaction-diffusion models, which should stimulate further research in this area.

DATA AVAILABILITY STATEMENT

The original contributions presented in the study are included in the article/supplementary material, further inquiries can be directed to the corresponding author.

AUTHOR CONTRIBUTIONS

VZ performed the computations. Both authors conceived of the presented idea, discussed the results, and contributed to the final manuscript.

FUNDING

This work was supported by the Max Planck Society and the German Center for Cardiovascular Research (DZHK).

REFERENCES

1. Winfree AT. *When Time Breaks Down*. Princeton, NJ: Princeton University Press (1987).
2. Zykov VS. *Simulation of Wave Processes in Excitable Media*. New York, NY: Manchester University Press (1987).
3. Mikhailov AS. *Foundations of Synergetics*. Berlin; Heidelberg: Springer (1990). doi: 10.1007/978-3-642-97269-0
4. Kaplan D, Glass L. *Understanding Nonlinear Dynamics*. New York, NY: Springer; (1995).
5. Gerisch G. Periodische Signale steuern die Musterbildung in Zellverbänden. *Naturwissenschaften* (1971) 58:430–8. doi: 10.1007/BF00624616
6. Zaikin AN, Zhabotinsky AM. Concentration wave propagation in two-dimensional liquid-phase self-oscillating systems. *Nature*. (1970) 225:535–7. doi: 10.1038/225535b0
7. Allesie MA, Bonke FIM, Schopman FJG. Circus movement in rabbit atrial muscle as a mechanism of tachycardia. *Circ Res*. (1973) 41:9–18. doi: 10.1161/01.RES.41.1.9
8. Gorelova NA, Bures J. Spiral waves of spreading depression in the isolated chicken retina. *J Neurobiol*. (1983) 14:353–63. doi: 10.1002/neu.480140503
9. Huang X, Xu W, Liang J, Takagaki K, Gao X, Wu J-Y. Spiral wave dynamics in neocortex. *J Neurobiol*. (2010) 68:978–90. doi: 10.1016/j.neuron.2010.11.007
10. Jakubith S, Rotermund HH, Engel W, von Oertzen A, Ertl G. Spatiotemporal concentration patterns in a surface-reaction - propagating and standing waves, rotating spirals, and turbulence. *Phys Rev Lett*. (1990) 65:3013–6. doi: 10.1103/PhysRevLett.65.3013
11. Zykov VS. Spiral wave initiation in excitable media. *Philos Trans R Soc A*. (2018) 376:2017. doi: 10.1098/rsta.2017.0379
12. Zykov VS. Cycloidal circulation of spiral waves in excitable media. *Biofizika*. (1986) 31:862–5.
13. Winfree AT. Varieties of spiral wave behavior: an experimentalists approach to the theory of excitable media. *Chaos*. (1971) 1:303–34. doi: 10.1063/1.165844
14. Winfree AT. Spatial and temporal organization in the zhabotinsky reaction. *Adv Biol Med Phys*. (1977) 16:115–36. doi: 10.1016/B978-0-12-005216-5.50011-6
15. Rössler OE, Kahlert C. Winfree meandering in a 2-dimensional 2-variable excitable medium. *Z Naturforsch*. (1979) 34:565–70. doi: 10.1515/zna-1979-0507
16. van Capelle FJ, Durrer D. Computer simulation of arrhythmias in a network of coupled excitable elements. *Circ Res*. (1979) 47:454–66. doi: 10.1161/01.RES.47.3.454
17. Pertsov AM, Panfilov A, Medvedeva FU. Instabilities of autowaves in excitable media associated with critical curvature phenomenon. *Biofizika*. (1983) 28:100–2.
18. Lugi E. Analysis of meandering in Zykov kinetics. *Phys D*. (1989) 40:331–7. doi: 10.1016/0167-2789(89)90047-X
19. Barkley D. Linear stability analysis of rotating spiral waves in excitable media. *Phys Rev Lett*. (1992) 68:2090–3. doi: 10.1103/PhysRevLett.68.2090
20. Ouyang Q, Swinney HL, Li G. Transition from spirals to defect-mediated turbulence driven by a Doppler instability. *Phys Rev Lett*. (2000) 84:1047–50. doi: 10.1103/PhysRevLett.84.1047
21. Qu Z, Xie F, Garfinkel A, Weiss JN. Origins of spiral wave meander and breakup in a two-dimensional cardiac tissue model. *Ann Biomed Eng*. (2000) 40:755–71. doi: 10.1114/1.1289474
22. Barkley D. A model for fast computer-simulation of waves in excitable media. *Phys D*. (1991) 49:61–70. doi: 10.1016/0167-2789(91)90194-E
23. Fenton F, Karma A. Vortex dynamics in three-dimensional continuous myocardium with fiber rotation: filament instability and fibrillation. *Chaos*. (1998) 8:20–47. doi: 10.1063/1.166311
24. Zykov VS, Bodenschatz E. Periodic sequence of stabilized wave segments in an excitable medium. *Phys Rev E*. (2018) 97:030201. doi: 10.1103/physreve.97.03.030201
25. Zykov VS, Bodenschatz E. Spiral waves within a bistability parameter region of an excitable medium. *New J Phys*. (2022) 24: 3036. doi: 10.1088/1367-2630/ac47ca
26. Karma A. Universal limit of spiral wave propagation in excitable media. *Phys Rev Lett*. (1991) 66:2274–7. doi: 10.1103/PhysRevLett.66.2274
27. Alonso, S., Sagues, F. and Mikhailov, A S, *Taming Winfree turbulence of scroll waves in 223 excitable media*, *Science*. (2003) 299:1722. doi: 10.1126/science.1080207
28. Winfree AT. Alternative stable rotors in an excitable medium. *Phys D*. (1991) 102:125–40. doi: 10.1016/0167-2789(91)90202-K
29. Sehgal S, Foulkes AJ. Numerical analysis of subcritical Hopf bifurcations in the two-dimensional FitzHugh-Nagumo model. *Phys Rev E*. (2020) 49:2212. doi: 10.1103/PhysRevE.102.02212

Conflict of Interest: The authors declare that the research was conducted in the absence of any commercial or financial relationships that could be construed as a potential conflict of interest.

Publisher's Note: All claims expressed in this article are solely those of the authors and do not necessarily represent those of their affiliated organizations, or those of the publisher, the editors and the reviewers. Any product that may be evaluated in this article, or claim that may be made by its manufacturer, is not guaranteed or endorsed by the publisher.

Copyright © 2022 Zykov and Bodenschatz. This is an open-access article distributed under the terms of the Creative Commons Attribution License (CC BY). The use, distribution or reproduction in other forums is permitted, provided the original author(s) and the copyright owner(s) are credited and that the original publication in this journal is cited, in accordance with accepted academic practice. No use, distribution or reproduction is permitted which does not comply with these terms.



A Scalar Poincaré Map for Anti-phase Bursting in Coupled Inhibitory Neurons With Synaptic Depression

Mark Olenik^{1*} and Conor Houghton²

¹ School of Biological Sciences, Faculty of Life Sciences, University of Bristol, Bristol, United Kingdom, ² School of Computer Science, Electrical and Electronic Engineering, and Engineering Mathematics, Faculty of Engineering, University of Bristol, Bristol, United Kingdom

OPEN ACCESS

Edited by:

Erik Andreas Martens,
Lund University, Sweden

Reviewed by:

Jonathan E. Rubin,
University of Pittsburgh, United States
Anastasiia Panchuk,
Institute of Mathematics (NAN
Ukraine), Ukraine

*Correspondence:

Mark Olenik
m.olenik@bristol.ac.uk

Specialty section:

This article was submitted to
Dynamical Systems,
a section of the journal
Frontiers in Applied Mathematics and
Statistics

Received: 26 November 2021

Accepted: 26 April 2022

Published: 02 June 2022

Citation:

Olenik M and Houghton C (2022) A
Scalar Poincaré Map for Anti-phase
Bursting in Coupled Inhibitory
Neurons With Synaptic Depression.
Front. Appl. Math. Stat. 8:822782.
doi: 10.3389/fams.2022.822782

Short-term synaptic plasticity is found in many areas of the central nervous system. In the inhibitory half-center central pattern generators involved in locomotion, synaptic depression is believed to act as a burst termination mechanism, allowing networks to generate anti-phase bursting patterns of varying periods. To better understand burst generation in these central pattern generators, we study a minimal network of two neurons coupled through depressing synapses. Depending on the strength of the synaptic conductance between the two neurons, this network can produce symmetric $n:n$ anti-phase bursts, where neurons fire n spikes in alternation, with the period of such solutions increasing with the strength of the synaptic conductance. Relying on the timescale disparity in the model, we reduce the eight-dimensional network equations to a fully-explicit scalar Poincaré burst map. This map tracks the state of synaptic depression from one burst to the next and captures the complex bursting dynamics of the network. Fixed points of this map are associated with stable burst solutions of the full network model, and are created through fold bifurcations of maps. We derive conditions that predict the bifurcations between $n:n$ and $(n+1):(n+1)$ solutions, producing a full bifurcation diagram of the burst cycle period. Predictions of the Poincaré map fit excellently with numerical simulations of the full network model and allow the study of parameter sensitivity for rhythm generation.

Keywords: Poincaré map, neuronal bursting, dynamical system (DS), synaptic depression, central pattern generator

1. INTRODUCTION

Short-term synaptic plasticity may have a role in burst activity in central pattern generators (CPGs). Short-term synaptic depression is commonly found in neuronal networks involved in the generation of rhythmic movements, such as in the pyloric CPG of the spiny lobster [1, 2], or in the lumbosacral cord of the chick embryo [3]. Synaptic depression modulates the strength of synapses in response to changes to the presynaptic firing frequency. At a high neuronal firing frequency, depression weakens the strength of synapses and therefore reduces the magnitude of the postsynaptic response. At low firing frequency, it allows sufficient time for the synapse to recover from depression between spikes, leading to a stronger postsynaptic response. In reciprocal networks, synaptic depression has been shown to act as a “switch,” giving rise to a wide range of network dynamics such as synchronous and multi-stable rhythms, as well as fine tuning the frequency of network oscillations [4–6].

Brown [7] pioneered the idea that synaptic depression acts as a burst termination mechanism in CPGs composed of reciprocally inhibitory neurons and involved in rhythm generation of locomotion. When one side is firing during a burst the other, antagonistic side, is prevented from firing by synaptic inhibition. However, the weakening of inhibition as a result of synaptic depression eventually releases the antagonistic side so that it starts firing, terminating the burst on the side that had originally been firing. This rhythmogenesis hypothesis has been considered one of a handful of standard mechanisms for generating locomotion rhythms in vertebrates [8–10]. It has been proposed as an explanation of the antiphase burst rhythm in struggling in *Xenopus* tadpoles [11].

Bose and Booth [6] investigated burst generation in a generic half-center CPG that consists of two identical, tonically active Morris-Lecar [12] neurons coupled through inhibitory depressing synapses. Numerical simulations showed that when the reciprocal synaptic conductance between the two neurons is varied, the network produces symmetric $n:n$ anti-phase bursts, with stronger synaptic coupling leading to longer bursts. They used methods from geometric singular perturbation theory to separate the timescales of the fast membrane, and the slow synaptic dynamics of the network to derive one-dimensional conditions necessary for the existence of stable $n:n$ solutions (for $n \leq 2$). According to these conditions the type of firing pattern largely depends on the slow depression dynamics of the synapses between the two neurons, and can therefore be predicted by knowing the strengths of the synaptic conductances of the two synapses. Thus, the scalar conditions derived in Bose and Booth [6] provide a method to numerically identify the type of stable $n:n$ pattern for any given value of the coupling strength and $n \leq 2$. However, they do not predict the exact period of such solutions. Furthermore, while they provide good arguments for the validity of their reduction assumptions and the resulting scalar conditions, they do not verify them numerically.

Here we extend the previous analysis by providing a Poincaré map of the slow depression dynamics. This allows us not only to predict the types of stable $n:n$ solutions the full network can produce, (for any n), but also to study how varying the coupling strength affects the period of such solutions. To do this, we build on, and numerically test, the assumptions on the fast-slow timescale disparity made in Bose and Booth [6]. We reduce the two-cell model to a scalar Poincaré map that tracks the evolution of the depression from the beginning of one burst to the beginning of the next burst. Stable fixed points of our map are associated with stable $n:n$ burst solutions. Our map construction is motivated by the burst length map of a T-type calcium current, utilized by Matveev et al. [13], which approximates the anti-phase bursting dynamics of a network of two coupled Morris-Lecar neurons. In contrast to our model, the network described in the Matveev et al. [13] paper does not contain short-term synaptic depression, and burst termination is instead accomplished through the dynamics of a slow T-type calcium current.

The Poincaré map derived here replicates the results from numerical simulations of the full two-cell ODE system: Given the strength of maximum conductance between the two neurons,

fixed points of our map predict the type and period of $n:n$ patterns, the switch between burst solutions of different periods, as well as the occurrence of co-existent solutions. In addition to proving the existence and stability of fixed points, our map shows that fixed points are created via a fold bifurcation of maps. Finally, we use our map to derive algebraic conditions that allow us to predict parameter values of the maximum conductance at which $n:n$ solutions bifurcate to $(n+1):(n+1)$ solutions, and vice versa. Because our map is fully explicit, it lays the framework for studying the effects of other model parameters on network dynamics without the need to run expensive numerical integrations of the ODEs.

This paper is organized as follows. First, we introduce the network of two neurons, and describe the properties of single cell and synapse dynamics. We use numerical simulations of the network to provide an intuition for the range of possible burst dynamics the system can produce. Next, we state and justify the simplifying assumptions that are necessary for the map construction. Finally, we analytically derive the first return map of the depression variable as well as the conditions that are required for stable $n:n$ solutions. We end this work with a discussion.

2. MATERIALS AND METHODS

We consider a pair of identical Morris-Lecar neurons [12], with parameters from Bose and Booth [6]. The Morris-Lecar model is a set of two first-order differential equations that describe the membrane dynamics of a spiking neuron. The depolarisation is modeled by an instantaneous calcium current, and the hyperpolarisation by a slow potassium current and a leak current. The membrane potential v_i and potassium activation w_i of neuron i ($i, j = 1, 2$) is described by:

$$\dot{v}_i = f(v_i, w_i) - \bar{g}s_j(v_i - v_s), \quad (1)$$

$$\dot{w}_i = h(v_i, w_i). \quad (2)$$

Here v_s is the inhibitory reversal potential, and \bar{g} and s_j are the maximal synaptic conductance and the synaptic gating, respectively, constituting the total inhibitory conductance $\bar{g}s_j$ from neuron j to neuron i . Function $f(v_i, w_i)$ describes the membrane currents of a single cell:

$$f(v_i, w_i) = -g_{Ca}m_\infty(v_i)(v_i - v_{Ca}) - g_Kw_i(v_i - v_K) - g_L(v_i - v_L) + I. \quad (3)$$

The currents include a constant current I , and three ionic currents: an instantaneous calcium current, a potassium current, and a leak current, with respective reversal potentials v_{Ca} , v_K , and v_L , as well as maximum conductances g_{Ca} , g_K , and g_L . The function $h(v_i, w_i)$ models the kinetics of the potassium gating variable w_i , and is given by

$$h(v_i, w_i) = \frac{w_\infty(v_i) - w_i}{\tau_w}. \quad (4)$$

The steady-state activation functions m_∞ and w_∞ as well as the default model parameters are described in the **Supplementary Material 1**.

The dynamics of the synaptic interactions between the neurons are governed by a synaptic gating variable s_i and a depression variable d_i :

$$\dot{d}_i = \begin{cases} (1 - d_i)/\tau_a & \text{if } v_i < v_\theta, \\ -d_i/\tau_b & \text{if } v_i > v_\theta, \end{cases} \quad (5)$$

$$\dot{s}_i = \begin{cases} -s_i/\tau_\kappa & \text{if } v_i < v_\theta, \\ 0 & \text{if } v_i > v_\theta. \end{cases} \quad (6)$$

Variable d_i describes a firing rate dependent depletion mechanism that governs the amount of depression acting on the synapse. The model is agnostic with respect to the exact mechanism of this depletion, be it pre- or post-synaptic. When the voltage of cell i is above firing threshold ($v_i > v_\theta$), variable d_i decays with time constant τ_b , and recovers with time constant τ_a when voltage is below firing threshold ($v_i < v_\theta$). Since the synaptic inhibition occurs on a much faster timescale than synaptic depression, we assume that s_i is instantaneously reset to d_i whenever v_i increases above v_θ , where it remains throughout $v_i > v_\theta$. Whenever $v_i < v_\theta$, the synaptic variable decays exponentially with time constant τ_κ . The equations for the depression model are identical to the Bose and Booth [14] model. These equations are a mathematically tractable simplification of the established phenomenological depression model previously described by Tsodyks and Markram [15].

When the total inhibitory conductance $\bar{g}s_j$ is constant, the membrane dynamics are determined by the cubic v -nullcline $v_\infty(v_i)$ and the sigmoid w -nullcline $w_\infty(v_i)$, satisfying $\dot{v}_i = 0$ and $\dot{w}_i = 0$, respectively. In case of no inhibition ($\bar{g} = 0$), the two curves intersect near the local minimum of v_∞ to the left of v_θ (commonly referred to as “left knee” of v_∞), creating an unstable fixed point p_f with a surrounding stable limit cycle of period $T = T_a + T_s$ (**Figure 1A**). Here T_a is the amount of time the membrane potential spends above firing threshold ($v_i > v_\theta$), while T_s is the time it spends below firing threshold ($v_i < v_\theta$). Trajectories along that limit cycle have the familiar shape of the action potential (**Figure 1B**). Applying a constant nonzero inhibition, e.g., by letting $s_j = 1$ and $\bar{g} > 0$, moves the cubic v_∞ with the ensuing unstable fixed point down w_∞ in the (v_i, w_i) -plane. When \bar{g} is large enough, the fixed point moves past the left knee and becomes stable via a subcritical Andronov-Hopf bifurcation, attracting all previously periodic trajectories. In the following section we will refer to the value of the total conductance $\bar{g}s_j$ at the bifurcation point as g_{bif} .

The two-cell network model is numerically integrated using an adaptive step-size integrator for stiff differential equations implemented with XPPAUT [16] and controlled through the Python packages SciPy [17] and PyXPP [18]. The following mathematical analysis is performed on the equations of a single cell. Unless required for clarity, we will therefore omit the subscripts i, j from here on.

3. RESULTS

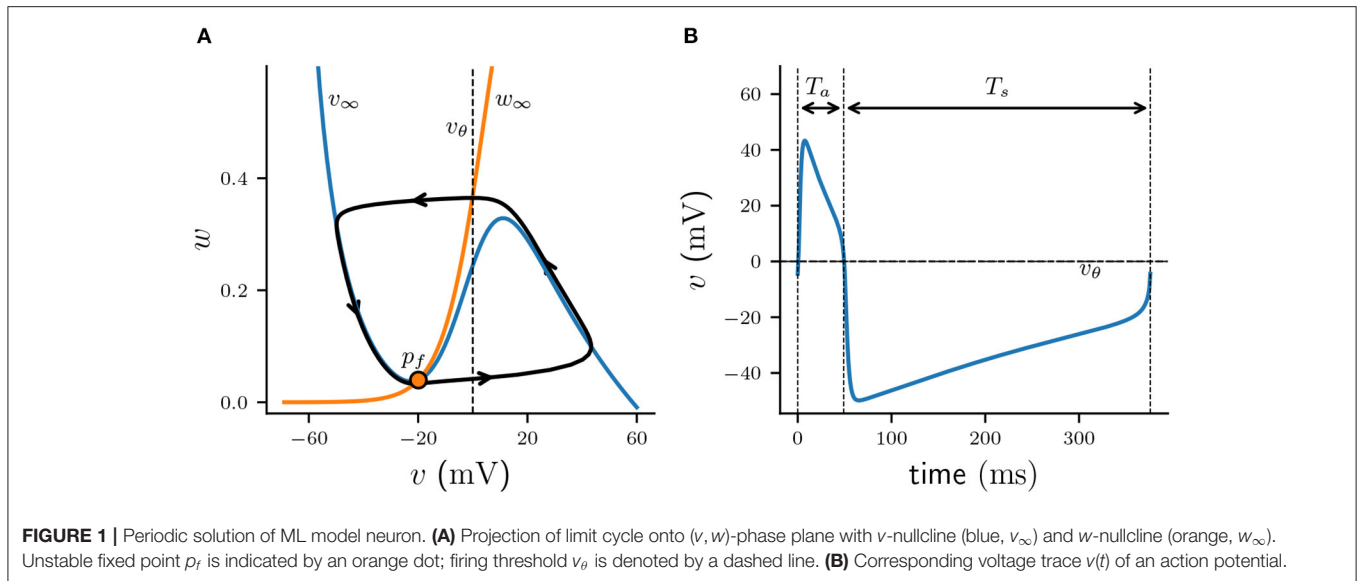
3.1. Anti-phase Burst Solutions

Short-term synaptic depression of inhibition in a half-center oscillator acts as a *burst termination* mechanism [7] and is known to produce $n:n$ anti-phase burst solutions of varying period. Such $n:n$ solutions consist of cells firing bursts of n spikes in alternation. **Figure 2D** shows the timecourse of a typical 4:4 burst. While one cell is firing a burst it provides an inhibitory conductance to the other cell, preventing it from firing.

Therefore, at any given moment one cell is spiking while the other is suppressed and does not spike. We will refer to the currently firing cell as “active” and we will call the suppressed cell “silent.” Additionally, we will distinguish between two phases of a $n:n$ solution: We will refer to the time interval when a cell is firing as the “active phase,” and we will call the remaining duration of a cycle, when a cell is not firing, the “silent phase.”

With each action potential of the active cell, short-term depression leads to a decrease of d , and consequently of s . If d depresses faster at spike time than it can recover in the inter-spike-intervals (ISIs), the total synaptic conductance $\bar{g}s$ will eventually become sufficiently small to allow for the silent cell to be released [19, 20] and start firing, thus inhibiting the previously active cell. While a cell is silent its depression variable can recover. Once the silent cell becomes active again its synaptic inhibition will be sufficient to terminate the burst of the previously active cell and commence a new cycle. As previously demonstrated by Bose and Booth [6], in a two-cell reciprocally inhibitory network with synaptic depression the coupling strength \bar{g} determines the type of $n:n$ solution. Increasing \bar{g} produces higher $n:n$ burst solutions with more spikes per burst and a longer cycle period. **Figure 2** shows numerically stable $n:n$ solutions for varying values of \bar{g} . For small values of \bar{g} the network produces anti-phase spiking 1:1 solutions (**Figure 2A**). As \bar{g} is increased the network generates solutions of increasing n , that is 2:2 (**Figure 2B**), 3:3 (**Figure 2C**), and 4:4 (**Figure 2D**). When \bar{g} is sufficiently large (**Figure 2E**), one of the cells continuously spikes at its uncoupled period T while the other cell remains fully suppressed. Depending on the initial conditions either of the two cells can become the suppressed cell, which is why the suppressed solution is numerically bistable.

Branches of numerically stable $n:n$ solutions and their associated limit cycle period for varying values of \bar{g} are depicted in **Figure 3** (see **Supplementary Material 2** for algorithm description). Not only do higher $n:n$ solutions branches require stronger coupling \bar{g} , but also within $n:n$ branches the period increases with \bar{g} . In line with Bose and Booth [6] we find small overlaps between solution branches indicating numerical bistability, for example such as between the 2:2 and 3:3 solution branches. Branches of higher $n:n$ burst solutions occur on increasingly smaller intervals of \bar{g} , for instance is the \bar{g} interval of the 5:5 branch shorter than that of the 4:4 branch and so on. The interval between the 5:5 branch and the suppressed solution (region between dotted lines in **Figure 3**) not only contains even higher numerically stable $n:n$ solutions, such as 11:11 bursts, but also other non-symmetric $n:m$ solutions as well as irregular, non-periodic solutions. However, the analysis in the following



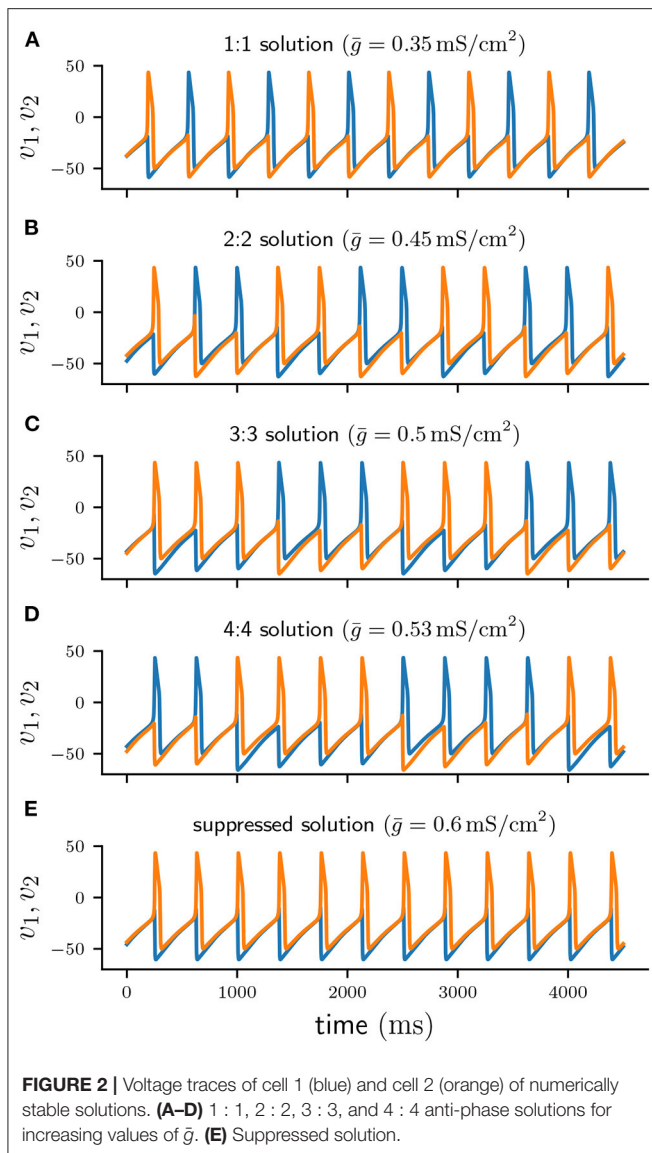
sections will only be concerned with the numerically stable and symmetric $n:n$ solutions.

3.2. Mathematical Analysis of Two-Cell Network

The goal of the following mathematical analysis is to reduce the complexity of the eight-dimensional system to a more tractable problem. As we will explain, we do this by approximating the full dynamics by a reduced system that describes the evolution of the depression variable d of either of the two cells. We will construct the solution of d in a piecewise manner from one spike to the next, first during the active phase, and then during the silent phase. This construction will require two assumptions about the membrane and synaptic dynamics. The first assumption states that during a burst the active cell fires at its uncoupled period T , which simplifies the construction of the solution of d . The second assumption states that once the inhibitory conductance acting on the silent cell drops below a critical threshold, the cell is immediately released and fires. The second assumption is necessary to predict the release time of the silent cell, which allows us to model the recovery of d during the silent phase. In other words, the second assumption requires that the release of the silent cell from inhibition depends only on the timecourse of the inhibition, and not on the membrane dynamics of the silent cell. The approximate validity of both assumptions can be observed in coupled relaxation-oscillator types of neurons such as the Morris-Lecar model we use, and will be numerically verified below. Both assumptions were first used in Bose and Booth [6] to derive algebraic conditions that guarantee the periodicity of the depression variable for different $n:n$ solutions. However, here we will use these assumptions to construct a Poincaré map of d , which will provide a geometric intuition for the dynamics of the full two-cell network and its dependence on model parameters.

Our first assumption about the model states that the active cell fires at its uncoupled period T , that is, during the active phase of a burst we have $ISI = T$. Solution profiles in **Figure 2** suggest that the $ISIs$ are indeed approximately constant. Numerically computing $ISIs$ for all stable $n:n$ solutions in **Figure 3** reveals that $ISIs$ differ by at most 1 ms from the intrinsic firing period $T \approx 376$ ms. Assuming $ISI = T$ seems reasonable given that inhibition acting on the silent cell decays exponentially on a much shorter timescale τ_κ than the duration of the ISI . Therefore, once the silent cell is released its trajectory quickly approaches the spiking limit cycle. Naturally the above assumption requires a sufficiently small τ_κ , and fails when τ_κ is large. In the **Supplementary Material 3** we numerically explore how different values of τ_κ affect the $ISIs$ of the active cell. Finally, assuming $ISI = T$ allows us to ignore the non-linear membrane dynamics during the active phase, and to construct the evolution of the synaptic variables iteratively from spike to spike.

Our second assumption states that the silent cell is released and spikes as soon as the total inhibitory conductance $\bar{g}s$ acting on it drops below some threshold value. We call this critical threshold value the “release conductance,” and define it as the value of $\bar{g}s$ at the time when the voltage of the silent cell first crosses the firing threshold v_θ , that is when that cell is released and fires its first spike. Recall that when a cell is silent its v - and w -nullclines intersect at a stable fixed point and $\bar{g}s > g_{bif}$. A sufficient condition for the silent cell to be released is therefore $\bar{g}s < g_{bif}$. However, depending on the topology of the stable manifold, the (v, w) -trajectory of the silent cell can escape the stable fixed point and allow the cell to produce a spike for $\bar{g}s > g_{bif}$. In this case the value of the release conductance depends on the type of $n:n$ solution and the coupling strength \bar{g} . For any stable $n:n$ solution in **Figure 3** we can compute an associated release conductance numerically by recording the value of $\bar{g}s$ at the time of the first spike of the silent cell. Such values of the release conductance are shown in **Figure 4A**, and the graph suggests that as n increases, the value of the release



conductance converges to some constant conductance value $g^* \approx 0.0068 \text{ mS/cm}^2$. Here g^* is the value of $\bar{g}s$ at the end of a cycle of a suppressed solution, just before the active cell spikes. Using g^* as a constant approximation for the release conductance will allow us to formulate a scalar condition that predicts the release time of the silent cell. Moreover, using g^* is convenient because its exact value can be derived explicitly, as will be shown in the following section.

Assuming a constant release conductance for all $n : n$ solutions will naturally introduce some error in the prediction of the release time of the silent cell. We can compute that error for any associated solution in **Figure 4A** by calculating the time interval between the first spike of the silent cell and the time when $\bar{g}s$ first crosses g^* . We will call this time interval the “release delay.” **Figure 4B** shows the numerically computed graph of such release delays. For $n > 1$ the absolute delays are smaller than 2 ms. Therefore, using

$$\bar{g}s = g^* \quad (7)$$

as a constant release condition for all $n : n$ solutions allows us to accurately predict the timing of the release of the silent cell. And to simplify the terminology, from now on we will refer to Equation (7) simply as the “release condition.”

In summary: We assume that the release condition is sufficient to predict when the silent cell is released. Due to the symmetry of $n : n$ solutions the release occurs at exactly half the period of the full cycle. The release time therefore uniquely determines the type of $n : n$ solution. Furthermore, computation of the release time does not depend on the membrane nor the synaptic dynamics of the silent cell. Instead, the solution of the synaptic variable s of the active cell is sufficient to predict when $\bar{g}s = g^*$ is satisfied. Finally, the value of s at each spike time is determined by the evolution of the depression variable d of the active cell. Constructing a solution of d during the active phase of either cell will therefore uniquely determine the solution of the full eight-dimensional network. However, finding the solution d requires us to know the initial value $d(0)$ at the start of a cycle at $t = 0$. In the next section we will construct a scalar return map that tracks these initial values $d(0)$ from cycle to cycle of stable $n : n$ solutions.

3.3. Construction of the Scalar Poincaré Map

In this section we construct the scalar Poincaré map $\Pi_n : d^* \mapsto d^*$. Here the discrete variable d^* tracks the values of the continuous depression variable d at the beginning of each $n : n$ burst. The map Π_n therefore describes the evolution of d , of either of the two cells, from the beginning of one cycle to the beginning of the next cycle. To simplify the map construction we will assume that an active cell fires exactly n times before it becomes silent. We will construct Π_n by evolving d first during the active phase and then during the silent phase of the $n : n$ limit cycle. The terms “active” and “silent” phases will be defined in terms of the state of the depression variable. During the active phase the depression variable of the active cell both decays and recovers, while during the silent phase it only recovers. First, let us give explicit definitions of the active and silent phases of a burst. A schematic illustration of both phases is given in **Figure 5**.

Suppose that at $t = 0$ cell 1 becomes active with some initial $d(0)$. Cell 1 then fires n spikes at the uncoupled period $T = T_a + T_s$. Let $s(t)$ and $d(t)$ be the corresponding solutions of the synaptic and depression variables of cell 1. After n spikes the total conductance $\bar{g}s(t)$ acting on the silent cell 2 has decayed sufficiently to satisfy the release condition (Equation 7). That is at some time $t = (n - 1)T + T_a + \Delta t$, where $\Delta t < T_s$ will be determined below, we have $\bar{g}s(t) = g^*$ [6]. Cell 2 is then released and prevents cell 1 from further spiking. Once released, cell 2 also fires n spikes until cell 1 becomes active once again. Let P_n denote the full cycle period of a $n : n$ solution:

$$P_n = 2[(n - 1)T + T_a + \Delta t]. \quad (8)$$

We can now define the active and silent phases of cell 1 explicitly. The active phase of a burst is the interval that lasts from the first

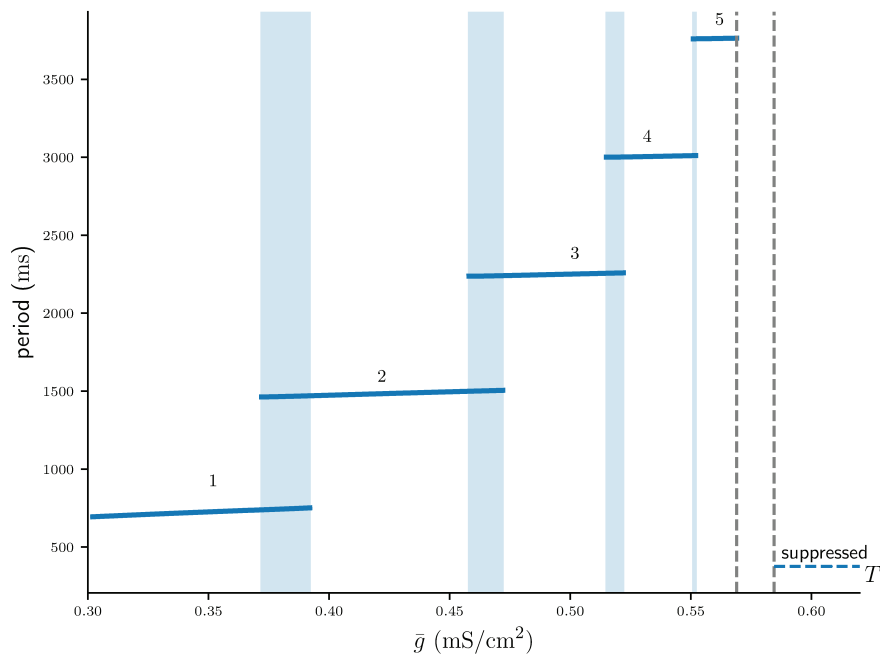


FIGURE 3 | Numerically computed bifurcation diagram of the cycle period of stable $n:n$ solutions for increasing coupling strength \bar{g} . Regions of bistability are indicated by light blue vertical stripes. Dashed lines show the interval between the 5:5 and the suppressed solution, where higher period $n:n$ solutions occur on increasingly smaller intervals of \bar{g} .

spike time up until the beginning of the silent phase of the last spike, that is for time $0 < t < (n-1)T + T_a$. During the active phase of cell 1, the silent cell 2 is inhibited sufficiently strong to prevent it from firing, hence $\bar{g}s > g^*$. The silent phase of cell 1 is the remaining duration of the cycle when the cell is not firing, that is for $(n-1)T + T_a < t < P_n$. The silent phase lasts for $(n-1)T + T_a + 2\Delta t$.

Note that only the silent phase depends on Δt , which will play a central role in the construction of Π_n . From Equation (8) Δt can be computed as

$$\Delta t = \frac{1}{2}P_n - (n-1)T - T_a. \quad (9)$$

We can use Equation (9) and the numerically computed bifurcation diagram of the period for stable $n:n$ solutions in **Figure 3** to obtain the graph of Δt as a function of \bar{g} (**Figure 6**). Each continuous branch of Δt is monotonically increasing and corresponds to a $n:n$ burst: Stronger coupling \bar{g} increases the total synaptic conductance $\bar{g}s$ that acts on the silent cell, thus delaying its release. It is easy to see that for any n -branch we have $\Delta t < T_s$: Once Δt crosses T_s , the active cell can “squeeze in” an additional spike and the solutions bifurcate into a $(n+1):(n+1)$ burst.

Distinguishing between the active and silent phases of a $n:n$ cycle allows us to describe the dynamics of the depression variable d explicitly for each phase. As can be seen from **Figure 5C**, during the active phase d depresses when $v > v_\theta$ and recovers when $v < v_\theta$. In contrast, during the silent phase d only recovers and does not depress. Given the initial $d^* = d(0)$ at

the beginning of the cycle and the number of spikes in the active phase n , we can now construct the burst map Π_n . The map

$$\Pi_n(d^*) = Q_n[F_n(d^*)] \quad (10)$$

is a composition of two maps. Map

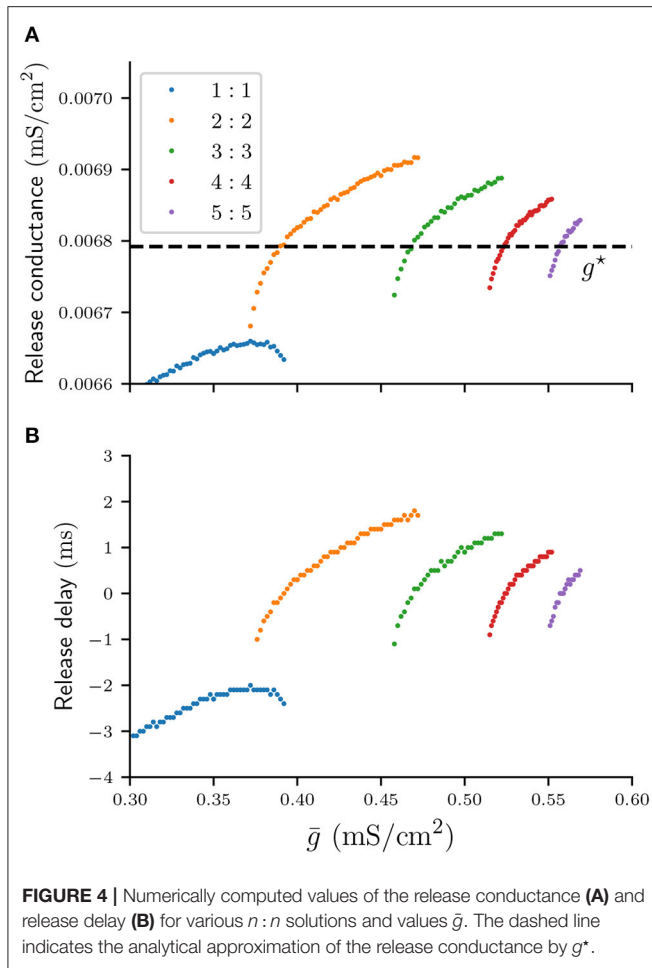
$$F_n: d^* \mapsto \Delta t \quad (11)$$

models the evolution of d in the active phase. F_n takes an initial value d^* and calculates Δt . Map

$$Q_n: \Delta t \mapsto d^* \quad (12)$$

models the recovery of d in the silent phase. Given some Δt map Q_n computes d^* at the start of the next cycle.

Our aim in the following analysis is to elucidate the properties of Π_n and to understand the structure of its parameter space by exploring how the stable and unstable fixed points of Π_n are created. To that effect it will be useful to include not only positive, but also negative values of d^* to the domain of Π_n . But it is important to add that values $d^* < 0$ are biologically impossible as the depression variable models a finite pool of neurotransmitters, and therefore must be positive. Because Π_n maps first from d^* to Δt , and then back to d^* , we will also consider negative values of Δt , interpreting them as $n:n$ solutions with partially overlapping bursts. As will become evident, $\Delta t < 0$ is only a formal violation of the biological realism of the map Π_n , as numerically stable $n:n$ solutions of the full system of ODEs only exist for $\Delta t > 0$.



We start the construction of Π_n by first considering the active phase and building the map F_n . At each spike time t_k where $d(t_k) = d_k$, variable d decays first for the duration of T_a , as described by the solution to Equation (5). At $t = t_k + T_a$ we have

$$d(t_k + T_a) = d_k e^{-T_a/\tau_b}. \quad (13)$$

The depression variable then recovers for T_s until t_{k+1} , where for $0 < t < T_s$:

$$d(t_{k+1}) = 1 - (1 - d_k e^{-T_a/\tau_b}) e^{-t/\tau_a}. \quad (14)$$

By substituting $t = T_s$ we can build a linear map that models the depression of d from spike time t_k to the subsequent spike time t_{k+1} during the active phase:

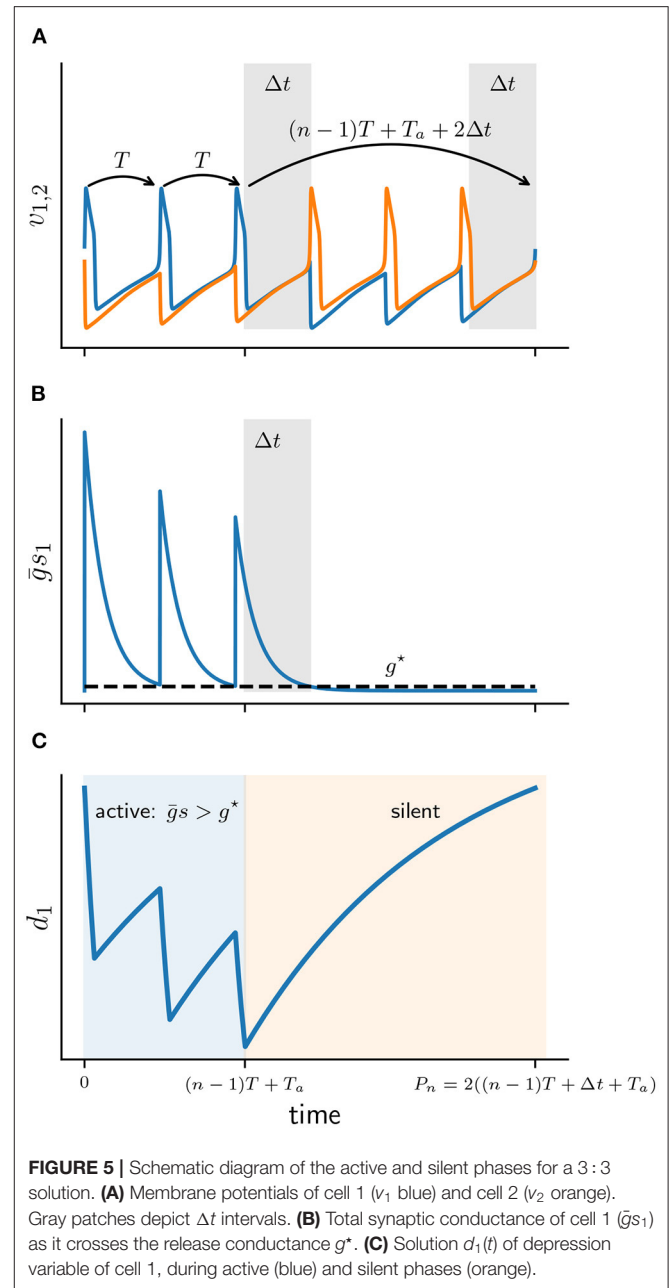
$$d_{k+1} = \lambda \rho d_k + (1 - \rho), \quad (15)$$

where to keep the notation simple we let

$$\lambda := \exp(-T_a/\tau_b), \quad (16)$$

$$\rho := \exp(-T_s/\tau_a). \quad (17)$$

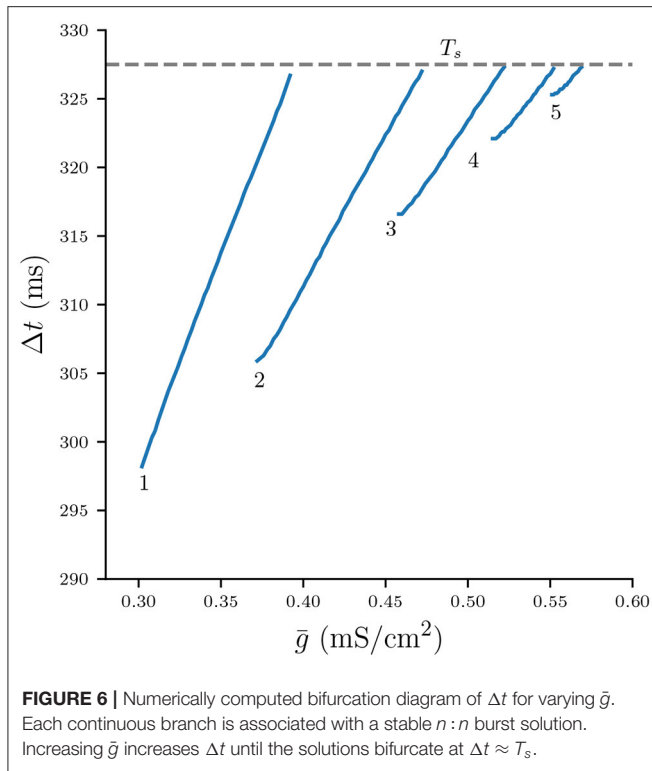
Given constant T_a and T_s , the derived parameter λ determines how much the synapses depresses when $v > v_\theta$, while ρ



determines how much it recovers when $v < v_\theta$. Since $0 < \lambda, \rho < 1$, the map in Equation (15) is increasing and contracting, with a fixed point at

$$d_s = \frac{1 - \rho}{1 - \lambda \rho}, \quad (18)$$

where $0 < d_s < 1$. The value d_s is the maximum depression value that can be observed in the suppressed solution where the active cell fires at its uncoupled period T (see **Figure 2E**). Using the release condition in Equation (7) allows us to derive the value of the minimum coupling strength that will produce the full suppressed solution, denoted as \bar{g}_s . Solving Equation (7) for $s(t)$



with $t = T_s$ and setting the initial value $s(0) = d_s \lambda$ then gives us the aforementioned approximation of the release conductance g^* :

$$\bar{g}_s d_s \lambda e^{-T_s/\tau_\kappa} = g^* \approx 0.0068 \text{ mS/cm}^2. \quad (19)$$

By substituting the definition of d_s in Equation (18) and rearranging, we can also write \bar{g}_s as a function of λ and ρ :

$$\bar{g}_s(\lambda, \rho) = \frac{1/\lambda - \rho}{1 - \rho} e^{T_s/\tau_\kappa} g^*. \quad (20)$$

Note that the above dependence of \bar{g}_s on λ is linear and monotonically decreasing. Increasing λ reduces the strength of the depression of the active cell. This in turn allows the active cell to fully suppress the silent cell at smaller values of \bar{g} .

Solving Equation (15) gives us the linear map δ_n , that for some initial d^* computes the depression at the n th spike time, that is $d(t_n)$:

$$\delta_n(d^*) = (\lambda \rho)^{n-1} d^* + (1 - \rho) \sum_{i=0}^{n-2} (\lambda \rho)^i. \quad (21)$$

Since $\lambda < 1$, function δ_n is a linearly increasing function of d^* with a fixed point at d_s for all n . Having identified d after n spikes, we can now use the release condition $\bar{g}_s = g^*$ (Equation 7) to find Δt . At the last (n th) spike of the active phase at time $t_n = (n-1)T$ the synapse variable s is set to the respective value of $d(t_n) = \delta_n(d^*)$, and mirrors the value of d for the duration of

T_a . At the end of the active phase at time $t_n + T_a$ variable d has decayed to $\delta_n(d^*)\lambda$, therefore

$$s(t_n + T_a) = \delta_n(d^*)\lambda. \quad (22)$$

Finally s decays exponentially for $\Delta t < T_s$. Solving (Equation 6) with initial condition $s(0) = \delta_n(d^*)\lambda$ yields:

$$s(\Delta t) = \delta_n(d^*)\lambda e^{-\Delta t/\tau_\kappa}. \quad (23)$$

Substituting $s(\Delta t)$ into s of the release condition (Equation 7) gives then

$$\bar{g} \delta_n(d^*)\lambda e^{-\Delta t/\tau_\kappa} = g^*. \quad (24)$$

Our assumption of the release condition guarantees that the silent cell 2 spikes and becomes active when $\bar{g}s - g^*$ crosses zero. Solving (Equation 24) for Δt allows us to compute Δt as a function of d^* , which defines the map F_n :

$$F_n(d^*) := \tau_\kappa \ln \left(\frac{\bar{g}}{g^*} \lambda \delta_n(d^*) \right) = \Delta t. \quad (25)$$

Figure 7A shows F_n for various n , which is a strict monotonically increasing function of d^* as well as \bar{g} . Larger values of d^* and \bar{g} , respectively, cause stronger inhibition of the silent cell, and therefore prolong its release time and the associated Δt . Map F_n is defined on $d^* > d_a$, where d_a is a vertical asymptote found by solving $\delta_n(d^*) = 0$ in Equation (21) for d^* , which yields

$$d_a(n) = -\frac{(1 - \rho) \sum_{i=0}^{n-2} (\lambda \rho)^i}{(\lambda \rho)^{n-1}} \leq 0. \quad (26)$$

We now turn to the construction of map Q_n , which describes the recovery of the depression variable during the silent phase. As we have identified earlier, the recovery of d in the silent phase of a $n:n$ solution starts at time $t_n + T_a$ and lasts for the duration of $(n-1)T + T_a + 2\Delta t$. Substituting that duration into the solution of d (Equation 5) with the initial condition $d(0) = \delta_n(d^*)\lambda$ yields the map Q_n :

$$Q_n(\Delta t) := 1 - [1 - \delta_n(d^*)\lambda] e^{-[(n-1)T + T_a + 2\Delta t]/\tau_a}. \quad (27)$$

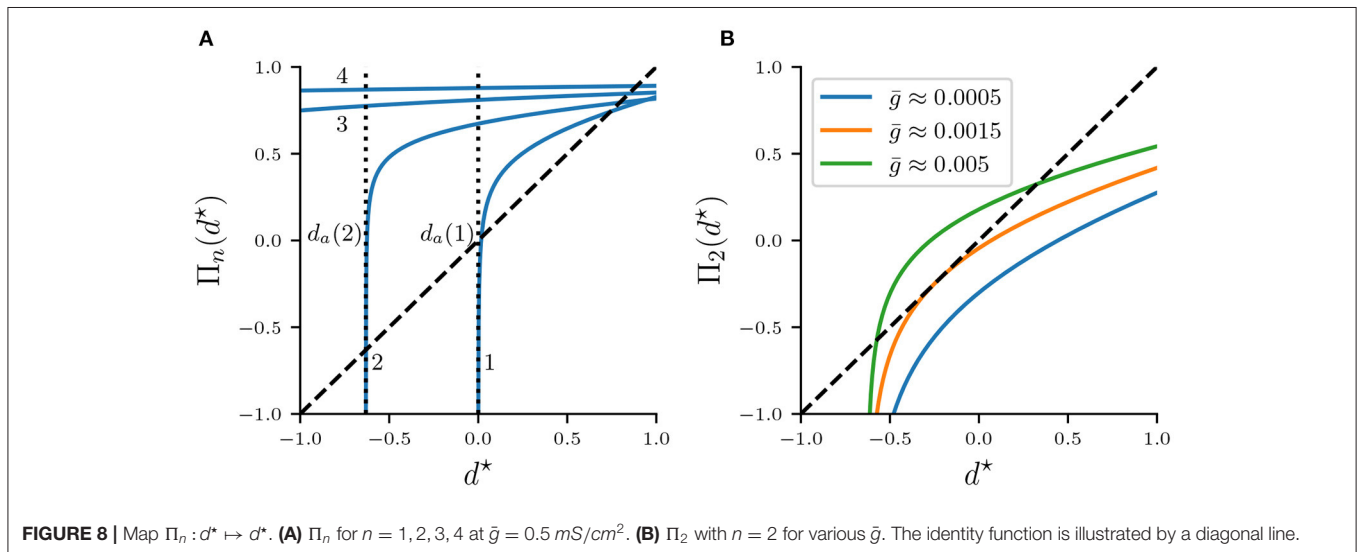
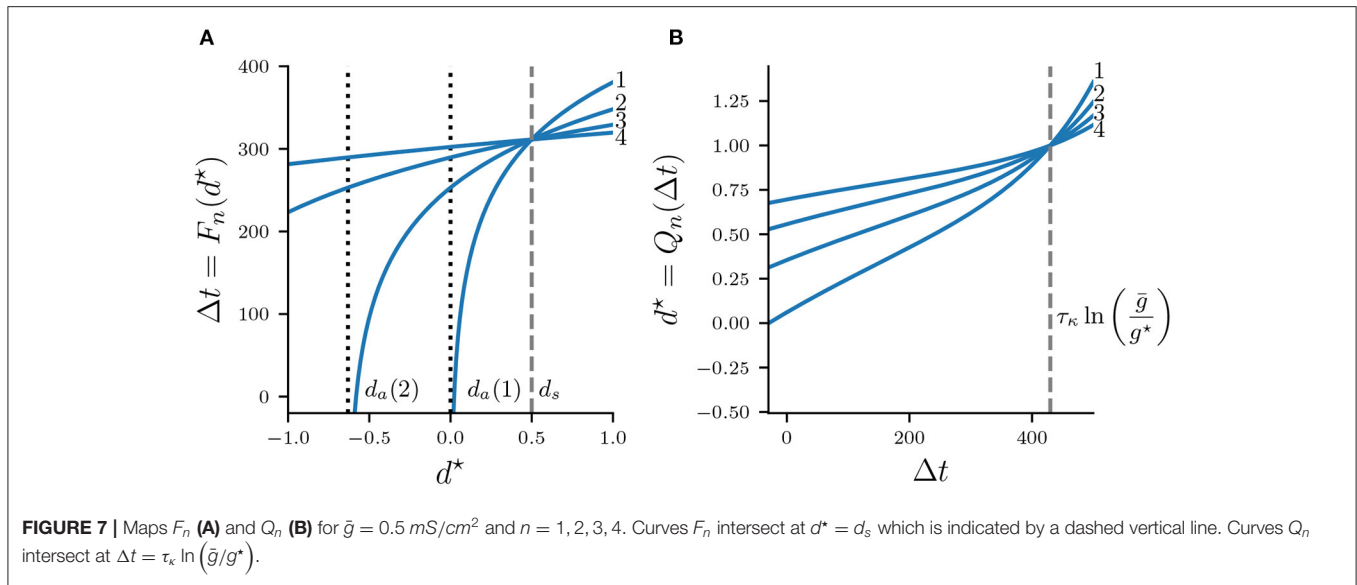
We can find $\delta_n(d^*)$, i.e., the value of d at the n th spike time, by rearranging the release condition in Equation (24):

$$\delta_n(d^*) = \frac{1}{\bar{g}\lambda} g^* e^{\Delta t/\tau_\kappa}. \quad (28)$$

Map Q_n is shown in Figure 7B for various values n . Note that Q_n is monotonically increasing as larger values Δt imply a longer recovery time, and hence Q_n grows without bound. All curves Q_n intersect at some $\Delta t = \tau_\kappa \ln [\bar{g}/g^*]$ where

$$Q_n \left[\tau_\kappa \ln \left(\frac{\bar{g}}{g^*} \right) \right] = 1. \quad (29)$$

As we will show in the next section, all fixed points of the full map Π_n occur for $d^* < 1$. We will therefore restrict the domain



of Q_n to $(-\infty, \tau_\kappa \ln[\bar{g}/(g^*)])$ and the codomain to $(-\infty, 1)$. Additionally, while values $\Delta t > T$ will be helpful in exploring the geometry of Π_n , recall from **Figure 6** that in the flow system $n:n$ solutions bifurcate into $(n+1):(n+1)$ solutions exactly when $\Delta t = T_s$, and we will address this concern in the last part of our map analysis.

Having found F_n and Q_n , we can now construct the full map $\Pi_n(d^*) = Q_n[F_n(d^*)]$:

$$\Pi_n(d^*) = 1 - \left[1 - \delta_n(d^*)\lambda \right] \left[\frac{\bar{g}}{g^*} \delta_n(d^*)\lambda \right]^{-\tau} e^{-[(n-1)T+T_a]/\tau_a}, \quad (30)$$

where we substituted $\tau = 2\tau_k/\tau_a$. Recall that $\delta_n(d^*)$ and g^* are obtained from Equations (21) and (19), respectively. Since d is the slowest variable of the system and $\tau_a \gg \tau_k$, we will also assume $\tau < 1$. **Figure 8A** depicts Π_n for various n . Intersections

of Π_n with the diagonal are fixed points of the map. **Figure 8B** shows Π_2 with $n = 2$. Varying the synaptic strength \bar{g} moves the curves Π_n up and down the (d^*, Π_n) -plane. For $\bar{g} < 0.0015 \text{ mS/cm}^2$ map Π_2 has no fixed points. As \bar{g} is increased to $\bar{g} \approx 0.0015 \text{ mS/cm}^2$, curve Π_2 coalesces with the diagonal tangentially. When $\bar{g} > 0.0015 \text{ mS/cm}^2$, a pair of fixed points emerge, one stable and one unstable fixed point, indicating the occurrence of a fold bifurcation of maps.

Π_n is monotonically increasing with respect to \bar{g} and also d^* :

$$\frac{d\Pi_n}{d\bar{g}} > 0, \quad (31)$$

$$\frac{d\Pi_n}{dd^*} > 0, \quad (32)$$

The monotonicity of Π_n w.r.t. \bar{g} is evident from Equation (30), while the monotonicity w.r.t. d^* follows from the monotonicity

of both Q_n and F_n . In the following sections we will heavily rely on this monotonicity property of Π_n . Just as F_n , curves Π_n spawn at the asymptote d_a (Equation 26), and because

$$\lim_{\bar{g} \rightarrow \infty} \Pi_n = 1 \text{ for all } n, \quad (33)$$

fixed points of Π_n lie in $(d_a, 1)$.

3.4. Existence and Stability of Fixed Points

We introduce the fixed point notation d_f^* with $\Pi_n(d_f^*) = d_f^*$. The existence of fixed points d_f^* for \bar{g} sufficiently large can be shown from the strict monotonicity of Π_n with respect to \bar{g} and d^* (Equations 32, 31), as well as the fact that the slope of Π_n is monotonically decreasing,

$$\left(\frac{d}{dd^*}\right)^2 \Pi_n < 0. \quad (34)$$

In the limit $d^* \rightarrow d_a$ the value of Π_n decreases without bound for any $\bar{g} > 0$. In the limit $\bar{g} \rightarrow 0$, Π_n also decreases without bound, but as $\bar{g} \rightarrow \infty$ values of Π_n approach 1. It follows from Equation (31) and the intermediate value theorem that for some \bar{g} large enough Π_n intersects the diagonal. Moreover, because Π_n and its slope are monotonic with respect to d^* , there exists some critical fixed point (d_b^*, \bar{g}_b) where Π_n aligns with the diagonal tangentially with

$$\Pi_n(d_b^*, \bar{g}_b) = d_b^*, \quad (35)$$

$$\frac{d}{dd^*} \Pi_n(d_b^*, \bar{g}_b) = 1. \quad (36)$$

3.5. Fold Bifurcations of Maps

Fixed points of Π_n satisfy the fixed point equation

$$\Phi_n(d^*, \bar{g}) := \Pi_n(d^*, \bar{g}) - d^* = 0. \quad (37)$$

As we have already shown, for $\bar{g} > \bar{g}_b(n)$ solutions to Equation (37) exist in pairs of stable and unstable fixed points. Solving (Equation 37) explicitly for d^* is not trivial, but solving for \bar{g} is straightforward and given by $\bar{g} = G_n(d^*)$, where

$$G_n(d^*) := \frac{g^*}{\delta_n(d^*)\lambda} \left(\frac{[1 - \lambda\delta_n(d^*)]}{1 - d^*} e^{-[(n-1)T + T_a]/\tau_a} \right)^{1/\tau} \quad (38)$$

is defined for $d^* < 1$ and $\delta_n(d^*) > 0$. Plotting d^* against \bar{g} gives the fixed point curves, which are shown in **Figure 9A**. Note the typical quadratic shape of a fold bifurcation of maps. It is also evident that the fold bifurcations occur for increasingly smaller \bar{g} as n is increased. Moreover, the graph suggests that for $n > 1$ unstable fixed points have negative values of d^* .

Equation (38) also allows us to find the critical fixed point connected with the fold bifurcation, namely $[d_b^*(n), \bar{g}_b(n)]$, which is the global minimum of $G_n(d_f^*)$:

$$d_b^*(n) = \operatorname{argmin} G_n(d_f^*), \quad (39)$$

$$\bar{g}_b(n) = \min G_n(d_f^*). \quad (40)$$

Function G_n is strictly monotonic on the respective intervals of d_f^* that correspond to the stable and unstable fixed points, that is

$$\frac{dG_n}{dd_f^*} > 0, \quad \text{for } d_f^* > d_b^*(n) \text{ stable}, \quad (41)$$

$$\frac{dG_n}{dd_f^*} < 0, \quad \text{for } d_f^* < d_b^*(n) \text{ unstable}, \quad (42)$$

which allows us to express the stable and unstable fixed points as the inverse of G_n on their respective intervals of d_f^* . Because we are primarily interested in the stable fixed points $d_f^* > d_b^*(n)$, we define the stable fixed point function $d_f^* = \phi_n(\bar{g})$ as

$$\phi_n(\bar{g}) := G_n^{-1}(\bar{g}). \quad (43)$$

Function $\phi_n(\bar{g})$ is also monotonic, and is therefore straightforward to compute numerically. We use the Python package Pynverse [21] for that purpose.

Having found the stable fixed points d_f^* as a function of \bar{g} , we can now compute the associated cycle period. Recall that the period is given by Equation (8), which can be written as a function of \bar{g} :

$$P_n(\bar{g}) = 2 \left((n-1)T + T_a + F_n \left[\underbrace{\phi_n(\bar{g}), \bar{g}}_{d_f^*} \right] \right), \quad (44)$$

where map F_n (Equation 25) calculates Δt given a stable fixed point $d_f^* = \phi_n(\bar{g})$. **Figure 9B** shows the period $P_n(\bar{g})$ computed from Equation (44) versus the cycle period of stable $n:n$ solutions, computed from numerically integrating the full system of ODEs. The overlap between blue and orange curves suggests that stable fixed points of Π_n accurately predict the cycle period of stable solutions of the flow system.

It is evident from **Figure 9A** that ϕ_n is strictly increasing with \bar{g} . This property follows directly from the quadratic normal form of the fold bifurcation, but can also be shown using implicit differentiation and the fixed point equation $\Phi_n[\phi_n(\bar{g}), \bar{g}] = 0$ in Equation (37). For $d_f^* = \phi_n(\bar{g}) > d_b(n)$ we get:

$$\frac{d\phi_n}{d\bar{g}} = - \frac{\partial \Phi_n / \partial \bar{g}}{\partial \Phi_n / \partial d^*} = \frac{\partial \Pi_n / \partial \bar{g}}{1 - \partial \Pi_n / \partial d^*} > 0. \quad (45)$$

The inequality follows from $\partial \Pi_n / \partial \bar{g} > 0$ and the fact that $\partial \Pi_n / \partial d^* < 1$ for $d^* > d_b(n)$. Equation (45) allows us to explain why the period P_n increases with \bar{g} , as seen in **Figure 9B**. Differentiating P_n gives:

$$\frac{dP_n}{d\bar{g}} = 2 \nabla F_n(d_f^*, \bar{g}) \cdot \begin{bmatrix} \partial \phi_n / \partial \bar{g} \\ 1 \end{bmatrix} > 0, \quad (46)$$

where the partial derivatives of $F_n(d_f^*, \bar{g})$ are:

$$\frac{\partial F_n}{\partial d_f^*} = \tau_\kappa \frac{(\lambda\rho)^{n-1}}{\delta_n(d_f^*)} > 0. \quad (47)$$

$$\frac{\partial F_n}{\partial \bar{g}} = \frac{\tau_\kappa}{\bar{g}} > 0. \quad (48)$$

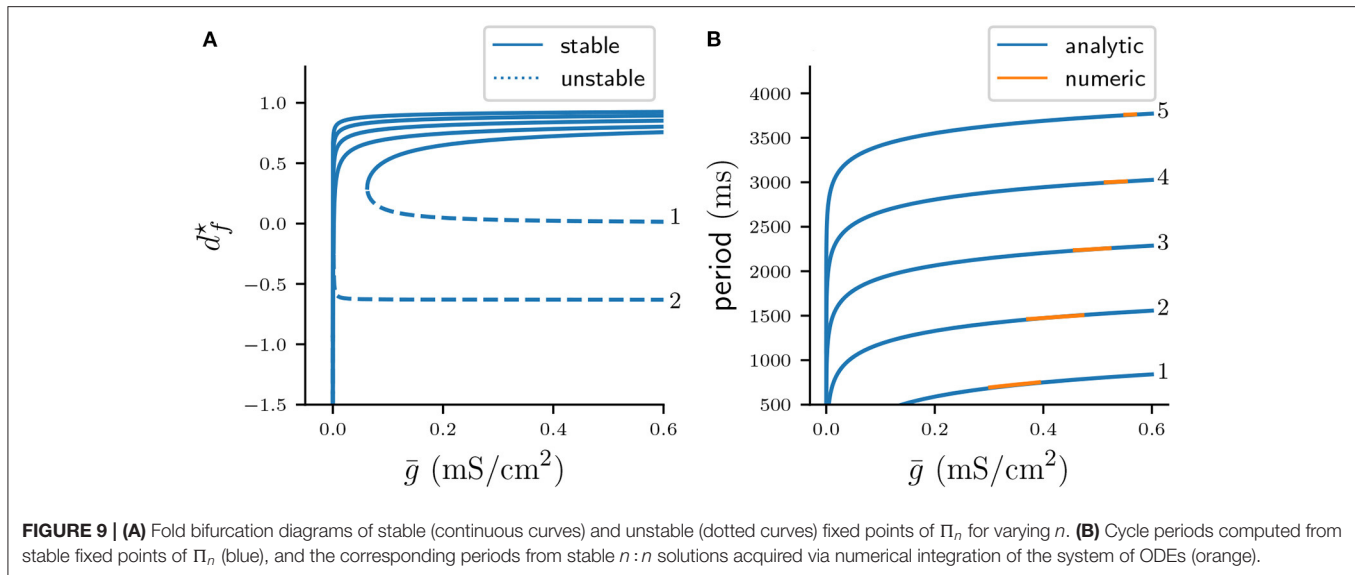


FIGURE 9 | (A) Fold bifurcation diagrams of stable (continuous curves) and unstable (dotted curves) fixed points of Π_n for varying n . **(B)** Cycle periods computed from stable fixed points of Π_n (blue), and the corresponding periods from stable $n:n$ solutions acquired via numerical integration of the system of ODEs (orange).

Equation (46) and (47) have an intuitive biological interpretation: Increasing the coupling strength between the neurons leads to overall stronger inhibition of the silent cell, which delays its release and leads to a longer cycle period. The latter allows more time for the synapse to depress in the active phase and recover in the silent phase, resulting in overall larger values of d_f^* , that is weaker depression at the burst onset.

While fixed points of our Poincaré map predict the cycle period of the flow system excellently, its construction relies on the strong assumption that the active phase contains exactly n spikes. As is evident from **Figure 9B** this assumption is clearly violated in the flow system, as stable $n:n$ bursts exists only on certain parameter intervals of \bar{g} . The multi-stability of fixed points of maps Π_n in **Figure 9B** does therefore not imply a similar multi-stability of the flow system. In the last sub-section we will analyze the mechanisms that guide how the stable $n:n$ are created and destroyed, and use our previous analysis to derive the corresponding parameter intervals of \bar{g} where such solutions exist.

3.6. Stable Solution Branch Borders

Let $\bar{g}_L(n)$ and $\bar{g}_R(n)$ denote the left and right parameter borders on \bar{g} where stable $n:n$ solutions exist. That is, as \bar{g} is increased stable $n:n$ solutions are created at $\bar{g}_L(n)$ and destroyed at $\bar{g}_R(n)$. When \bar{g} is reduced beyond $\bar{g}_L(n)$, $n:n$ solutions bifurcate into $(n-1):(n-1)$ solutions, while when \bar{g} is increased beyond $\bar{g}_R(n)$, $n:n$ solutions bifurcate into $(n+1):(n+1)$ solutions. Let us briefly recap our observations regarding $\bar{g}_L(n)$ and $\bar{g}_R(n)$ from the numerical bifurcation diagram in **Figure 9B**. For $n > 1$ there are the following relations:

$$\bar{g}_L(n) < \bar{g}_R(n), \quad (49)$$

$$\bar{g}_L(n) < \bar{g}_R(n+1) \text{ and } \bar{g}_R(n) < \bar{g}_L(n+1), \quad (50)$$

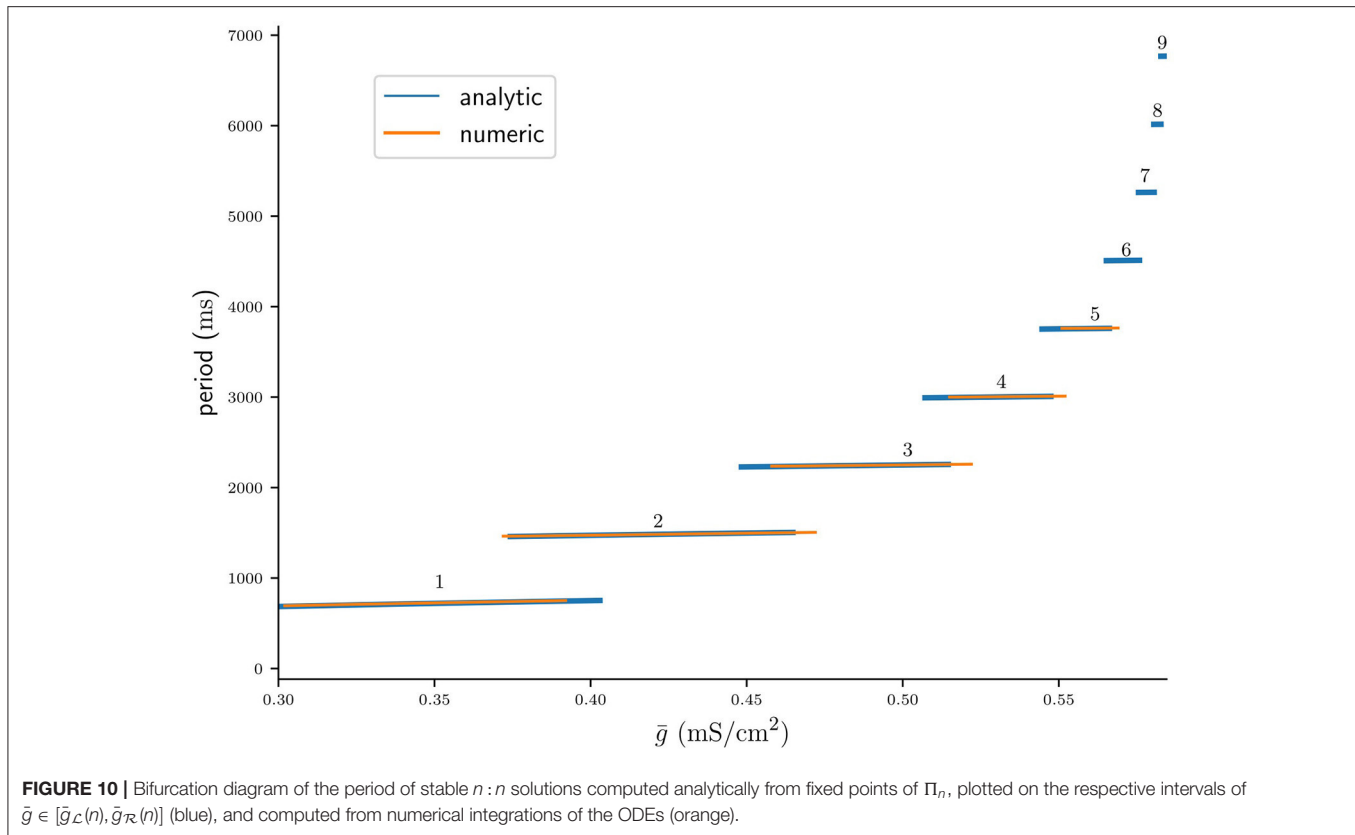
$$\bar{g}_L(n) < \bar{g}_R(n) \quad (51)$$

$$\bar{g}_L(n) < \bar{g}_L(n+1) \text{ and } \bar{g}_R(n) < \bar{g}_R(n+1) \quad (52)$$

Equations (49, 50) are self-explanatory. Equation (51) formally describes occurrence of co-existence between stable $n:n$ and $(n+1):(n+1)$ solutions. Equation (52) implies that the parameter interval on \bar{g} of $n:n$ solutions decreases with n , in other words, bursts with more spikes occur on increasingly smaller intervals of the coupling strength. All of the above relations are reminiscent of the bifurcation scenario of type period increment with co-existent attractors, first described for piecewise-linear scalar maps with a single discontinuity by Avrutin and colleagues [e.g., see 22–24]. While our maps Π_n are fully continuous, the above observation suggests that a different piecewise-linear scalar map that captures such period increment dynamics of the full system might exist. We will explore what such a map might look like in the discussion.

Let us now find algebraic equations that will allow us to calculate the critical parameters $\bar{g}_L(n)$ and $\bar{g}_R(n)$ associated with the left and right $n:n$ branch borders. Recall that the period P_n derived from the fixed points of Π_n is an increasing function of \bar{g} (Equation 46). That is, as the coupling strength increases, it takes longer for the total synaptic conductance to fall below the value of the release conductance, which delays the release of the silent cell, and Δt becomes larger. When $\Delta t > T_s$, the active cell can produce another spike and the solution bifurcates into a $(n+1):(n+1)$ solution. Note, however, that at $\bar{g}_L(n)$ the bifurcation into a $(n-1):(n-1)$ does not occur at $\Delta t = 0$. Here the mechanism is different: A sufficient reduction of \bar{g} causes the total synaptic conductance to drop below the release conductance in the *previous* ISI, which allows the silent cell to be released one spike earlier.

Using the above reasoning we can now formulate the conditions for both bifurcations at $\bar{g}_L(n)$ and $\bar{g}_R(n)$. As in the previous sections, we will only restrict ourselves to the analysis of



the stable fixed points given implicitly by $d_f^* = \phi_n(\bar{g})$ (Equation 43). At the right bifurcation border $\bar{g}_{\mathcal{R}}(n)$ we have $\Delta t = T_s$, and after substituting our F_n map (Equation 25) this translates into

$$\bar{g}_{\mathcal{L}}(n+1) < \bar{g}_{\mathcal{R}}(n) \quad (53)$$

which lets us define a function

$$\bar{g}_{\mathcal{R}}(n+1) - \bar{g}_{\mathcal{L}}(n+1) < \bar{g}_{\mathcal{R}}(n) - \bar{g}_{\mathcal{L}}(n) \quad (54)$$

whose root is the desired right bifurcation border $\bar{g}_{\mathcal{R}}(n)$. In case of the left bifurcation border at $\bar{g}_{\mathcal{L}}(n)$, the release condition is satisfied just before the active cell has produced its n th spike, where total synaptic conductance is given by

$$\bar{g}_{\delta_{n-1}}[\phi_n(\bar{g})]\lambda e^{-T_s/\tau_k} = g^*, \quad (55)$$

which can be rewritten as a function

$$\mathcal{L}_n(\bar{g}) := \bar{g}_{\delta_{n-1}}[\phi_n(\bar{g})]\lambda e^{-T_s/\tau_k} - g^*, \quad (56)$$

whose root is $\bar{g}_{\mathcal{L}}(n)$. Both \mathcal{R}_n and \mathcal{L}_n are increasing with respect to \bar{g} , which makes finding their roots numerically straightforward.

Figure 10 shows the period $P_n(\bar{g})$ as predicted by the fixed points of Π_n (Equation 44) plotted on their respective intervals $\bar{g} \in [\bar{g}_{\mathcal{L}}(n), \bar{g}_{\mathcal{R}}(n)]$ (blue), as well as the cycle period acquired from numerical integration of the full system of ODEs (orange).

Here $g_{\mathcal{L}}(n)$ and $\bar{g}_{\mathcal{R}}(n)$ were computed from Equations (56) and (54), respectively. Note that the width of $n:n$ branches decreases with n , which confirms the inequality in Equation (52). That is, bursts with more spikes occur on increasingly smaller intervals of \bar{g} , which can be interpreted as a loss of robustness with respect to the coupling strength of long-cyclic solutions. We also note the occurrence of bistability between pairs of $n:n$ and $(n+1):(n+1)$ branches, which also confirms our initial observation in Equation (51). As previously observed in **Figure 9B** our maps prediction of the cycle period is accurate. However, the mismatch in the left and right branch borders is significant. This mismatch might be due to the millisecond release delay error (**Figure 4B**) induced by our assumption of a constant release conductance for all $n:n$ solutions (see Equation 7). Another explanation for the border mismatch could be that our assumptions on the time scales of (v, w) vs s - and d -dynamics do not hold near the stability borders, and that they can only be captured by more complex approximations. Nevertheless, our map allows approximate extrapolation of the cycle period and the respective bifurcation borders where numerical integration of the ODEs would require a very small time step.

4. DISCUSSION

Synaptic depression of inhibition is believed to play an important role in the generation of rhythmic activity involved in many motor rhythms such as in leech swimming [25] and leech

heart beat [26], and in the lobster pyloric system [1, 2]. In inhibitory half-center CPGs, such as believed to be found in the struggling network of *Xenopus* tadpoles, synaptic depression can act as a burst termination mechanism, enabling the alternation of bursting between the two sides of the CPG [11]. Modeling can shed light on the underlying mathematical principles that enable the generation of such anti-phase bursts, and help identify the components that control this rhythm allowing it to switch between different patterns.

To study the mechanisms of burst generation in half-center CPGs we have analyzed a neuronal model network that consists of a pair of inhibitory neurons that undergo a frequency dependent synaptic depression. When the strength of synaptic inhibition between the neurons is varied, such a simple network can display a range of different $n:n$ burst patterns. Using the timescale disparity between neuronal and synaptic dynamics, we have reduced the network model of eight ODEs to a scalar first return map Π_n of the slow depression variable d . This map Π_n is a composition of two maps, F_n and Q_n , that model the evolution of the depression during the active and silent phases of $n:n$ solutions respectively. Both F_n and Q_n maps are constructed by using the dynamics of a single uncoupled neuron. Fixed points of Π_n are created in pairs through a fold bifurcation of maps, where the stable fixed point correspond to stable $n:n$ burst solutions of the full two-cell system of ODEs. The results from our one-dimensional map match excellently with numerical simulation of the full network. Our results are also in line with Brown's [7] rhythmogenesis hypothesis, namely that synaptic depression of inhibition is a mechanism by which anti-phase bursting may arise.

We have studied $n:n$ solutions assuming that the synaptic coupling \bar{g} between the two cells is symmetrical. However, Bose and Booth [6] have shown that asymmetrical coupling (\bar{g}_1, \bar{g}_2) can result in network solutions of type $m:n$, where one cell fires m spikes, while the other n spikes. It is conceivable that our map construction can be extended to also capture such $m:n$ solutions. Remember, in the case of symmetrical coupling with $n:n$ solutions, the timecourse of the depression variables d_1 and d_2 were in anti-phase, and it was therefore sufficient to track only one of the two variables. To capture the full network dynamics in case of asymmetrical coupling one would also have to account for burst patterns of type $m:n$, where the solutions of the depression variables d_1 and d_2 are not simply time-shifted versions of each other. To do that, one could track the state of both variables by constructing a two-dimensional Poincaré map $\Pi(d_1, d_2)$. While geometrical interpretation of two-dimensional maps remains challenging, there exist a number of recent studies which have employed novel geometrical analysis methods to understand the dynamics of two-dimensional maps of small neuronal networks [27–29]. Generally speaking, our map construction approach is applicable to any small network, even with more than two neurons. As long as the network dynamics occur on separable timescales the main challenges to the map construction lie in identifying the slowest variables, and finding an appropriate, simplified description of their respective

timecourses. In theory, the reduction approach can be also applied to neuronal systems with more than two timescales [e.g., see 30].

In tadpoles, struggling is believed to be initiated by an increase in the firing frequency of reciprocally inhibitory commissural interneurons, which has been hypothesized to lead to stronger synaptic depression of inhibition and result in the iconic anti-phase bursting [11]. It would therefore be interesting to study how varying the cell intrinsic firing period T could affect the network rhythm. While we have laid out the framework to perform such an investigation, due to the choice of neural model we have avoided varying T . Recall that T is a derived parameter in the Morris and Lecar [12] model, and can therefore not be varied in isolation of other model parameters. This makes verifying any analytical results from our map analysis via numerical integration of the ODEs difficult. A more abstract model such as the quadratic integrate-and-fire model [31] allows varying T independently of other model parameters, and could be more fitting for such an investigation.

Our simulations of the network showed that $n:n$ solutions lose robustness as their period is increased. That is, solutions with a larger cycle period occur on increasingly smaller intervals of the coupling strength. We were able to replicate this finding by numerically finding the respective left and right borders of stable $n:n$ branches of fixed points of Π_n , and showing that the distance between these borders shrinks with n . We have also noted the resemblance of our bifurcation diagram to one where such $n:n$ branches are created via the bifurcation scenario of type period-increment with co-existent attractors, first described for scalar linear maps with a discontinuity [24, 32]. It is worthwhile noting that the bifurcations of piecewise linear maps studied by Avrutin et al. [32] result from a “reinjection” mechanism [33]. Here the orbit of a map performs multiple iterations on one side of the discontinuity, before jumping to the other side and being *reinjected* back into the initial side of the discontinuity. The stark difference of such a map to our map is that reinjection allows a *single* scalar map to produce periodic solutions of varying periods. In contrast, we rely on n different maps Π_n to describe the burst dynamics without explicitly capturing the period increment dynamics. It is therefore conceivable that despite the complexity and non-linearity of the dynamics of our two-cell network, a single piecewise-linear map might be already sufficient to capture the mechanisms that shape the parameter space of the full system. In their discussion, Bose and Booth [6] briefly outline ideas about how such a linear map could be constructed.

In addition to stable $n:n$ solutions, the numerical continuation by Bose and Booth [6] also revealed branches of unstable $n:n$ solutions. While we have identified fold bifurcations of our burst map, we have not found corresponding bifurcations of the flow ODE system, and have generally ignored the significance of unstable map fixed points. However, the quadratic nature of the period bifurcation curve is reminiscent of a saddle-node on an invariant circle (SNIC) bifurcation, where the oscillation period lengthens and finally becomes infinite as a limit cycle coalesces with a saddle point. SNIC bifurcations have been studied in great detail [e.g., 34], and a

next step would be to provide a rigorous explanation of not only the map dynamics, but also of the flow dynamics of the ODE system.

We have shown that when the strength of the maximum synaptic conductance is varied, synaptic depression of inhibition can enable our two-cell network to produce burst solutions of different periods. This result is in line with the idea that one role of synaptic depression in the nervous system may be to allow a finite size neuronal network to participate in different tasks by producing a large number of rhythms [6, 11, 35]. To change from one rhythm to another would only require a reconfiguration of the network through changes in synaptic coupling strength. Thus short-term synaptic depression of inhibition may provide means for a network to adapt to environmental challenges without changing its topology, that is without the introduction or removal of neurons.

DATA AVAILABILITY STATEMENT

The original contributions presented in the study are included in the article/**Supplementary Material**, further inquiries can be directed to the corresponding author. The source code to replicate all figures is available at <https://github.com/markolenik/poincare-map-paper>.

REFERENCES

- Manor Y, Nadim F, Abbott L, Marder E. Temporal dynamics of graded synaptic transmission in the lobster stomatogastric ganglion. *J Neurosci.* (1997) 17:5610–21. doi: 10.1523/JNEUROSCI.17-14-05610.1997
- Rabbah P, Nadim F. Distinct synaptic dynamics of heterogeneous pacemaker neurons in an oscillatory network. *J Neurophysiol.* (2007) 97:2239–53. doi: 10.1152/jn.01161.2006
- Donovan M, Wenner P, Chub N, Tabak J, Rinzel J. Mechanisms of spontaneous activity in the developing spinal cord and their relevance to locomotion. *Ann N Y Acad Sci.* (1998) 860:130–41. doi: 10.1111/j.1749-6632.1998.tb09044.x
- Nadim F, Manor Y. The role of short-term synaptic dynamics in motor control. *Curr Opin Neurobiol.* (2000) 10:683–90. doi: 10.1016/S0959-4388(00)00159-8
- Nadim F, Manor Y, Kopell N, Marder E. Synaptic depression creates a switch that controls the frequency of an oscillatory circuit. *Proc Natl Acad Sci USA.* (1999) 96:8206–11. doi: 10.1073/pnas.96.14.8206
- Bose A, Booth V. Co-existent activity patterns in inhibitory neuronal networks with short-term synaptic depression. *J Theor Biol.* (2011) 272:42–54. doi: 10.1016/j.jtbi.2010.12.001
- Brown TG. The intrinsic factors in the act of progression in the mammal. *Proc R Soc Lond Series B.* (1911) 84:308–19. doi: 10.1098/rspb.1911.0077
- Reiss RF. A theory and simulation of rhythmic behavior due to reciprocal inhibition in small nerve nets. In: *Proceedings of the May 1-3 1962 Spring Joint Computer Conference*. San Francisco, CA: ACM (1962). p. 171–94.
- Perkel DH, Mulloney B. Motor pattern production in reciprocally inhibitory neurons exhibiting postinhibitory rebound. *Science.* (1974) 185:181–3. doi: 10.1126/science.185.4146.181
- Friesen WO. Reciprocal inhibition: A mechanism underlying oscillatory animal movements. *Neurosci Biobehav Rev.* (1994) 18:547–53. doi: 10.1016/0149-7634(94)90010-8

AUTHOR CONTRIBUTIONS

MO and CH contributed to conception and design of the study. MO performed numerical computation and analysis. Both authors contributed to manuscript writing and revision.

FUNDING

This work was supported by the Wellcome Trust Doctoral Training Programme in Neural Dynamics, grant no. 102374/Z/13/Z.

ACKNOWLEDGMENTS

MO thanks the Wellcome Trust for financial support of his Ph.D. study. We thank Alan Champneys for sharing his insights on non-continuous maps during the course of this research. We are also grateful to Alan Roberts and Stephen R. Soffe for their comments on earlier versions of the manuscript.

SUPPLEMENTARY MATERIAL

The Supplementary Material for this article can be found online at: <https://www.frontiersin.org/articles/10.3389/fams.2022.822782/full#supplementary-material>

- Li WC, Sautois B, Roberts A, Soffe SR. Reconfiguration of a vertebrate motor network: Specific neuron recruitment and context-dependent synaptic plasticity. *J Neurosci.* (2007) 27:12267–76. doi: 10.1523/JNEUROSCI.3694-07.2007
- Morris C, Lecar H. Voltage oscillations in the barnacle giant muscle fiber. *Biophys J.* (1981) 35:193–213. doi: 10.1016/S0006-3495(81)84782-0
- Matveev V, Bose A, Nadim F. Capturing the bursting dynamics of a two-cell inhibitory network using a one-dimensional map. *J Comput Neurosci.* (2007) 23:169–87. doi: 10.1007/s10827-007-0026-x
- Bose A, Manor Y, Nadim F. Bistable oscillations arising from synaptic depression. *SIAM J Appl Math.* (2001) 62:706–27. doi: 10.1137/S0036139900378050
- Tsodyks MV, Markram H. The neural code between neocortical pyramidal neurons depends on neurotransmitter release probability. *Proc Natl Acad Sci USA.* (1997) 94:719–23. doi: 10.1073/pnas.94.2.719
- Ermentrout B. Simulating, Analyzing, and Animating Dynamical Systems. In: *Simulating, Analyzing, and Animating Dynamical Systems: A Guide to XPPAUT for Researchers and Students*. (2002) doi: 10.1137/1.9780898718195
- Virtanen P, Gommers R, Oliphant TE, Haberland M, Reddy T, Cournapeau D, et al. SciPy 1.0: fundamental algorithms for scientific computing in python. *Nat Methods.* (2020) 17:261–72. doi: 10.1038/s41592-020-0772-5
- Olenik M. PyXPP. (2021). Available online at: <https://github.com/markolenik/PyXPP> (accessed May 05, 2022).
- Wang XJ, Rinzel J. Alternating and synchronous rhythms in reciprocally inhibitory model neurons. *Neural Comput.* (1992) 4:84–97. doi: 10.1162/neco.1992.4.1.84
- Skinner FK, Kopell N, Marder E. Mechanisms for oscillation and frequency control in reciprocally inhibitory model neural networks. *J Comput Neurosci.* (1994) 1:69–87. doi: 10.1007/BF00962719
- Gonzalez AS. Pynverse. (2021). Available online at: <https://github.com/alvarosg/pynverse> (accessed May 05, 2022).

22. Gardini L, Avrutin V, Schanz M, Granados A, Sushko I. Organizing centers in parameter space of discontinuous 1D maps. The case of increasing/decreasing branches. *ESAIM: Proc.* (2012) 36:106–20. doi: 10.1051/proc/201236009
23. Tramontana F, Gardini L, Avrutin V, Schanz M. Period adding in piecewise linear maps with two discontinuities. *Int J Bifurcat Chaos.* (2012) 22:1250068. doi: 10.1142/S021812741250068X
24. Avrutin V, Granados A, Schanz M. Sufficient conditions for a period incrementing big bang bifurcation in one-dimensional maps. *Nonlinearity.* (2011) 24:2575–2598. doi: 10.1088/0951-7715/24/9/012
25. Mangan P, Cometa A, Friesen W. Modulation of swimming behavior in the medicinal leech. IV. Serotonin-induced alteration of synaptic interactions between neurons of the swim circuit. *J Compar Physiol A Sens Neural Behav Physiol.* (1994) 175:723–36. doi: 10.1007/BF00191844
26. Calabrese RL, Nadim F, Olsen ØH. Heartbeat control in the medicinal leech: A model for understanding the origin, coordination, and modulation of rhythmic motor patterns. *J Neurobiol.* (1995) 27:390–402. doi: 10.1002/neu.480270311
27. Akcay Z, Bose A, Nadim F. Effects of synaptic plasticity on phase and period locking in a network of two oscillatory neurons. *J Math Neurosci.* (2014) 4:8. doi: 10.1186/2190-8567-4-8
28. Akcay Z, Huang X, Nadim F, Bose A. Phase-locking and bistability in neuronal networks with synaptic depression. *Physica D.* (2018) 364:8–21. doi: 10.1016/j.physd.2017.09.007
29. Liao G, Diekmann C, Bose A. Entrainment dynamics of forced hierarchical circadian systems revealed by 2-dimensional maps. *SIAM J Appl Dyn Syst.* 19:2135–261. (2020) doi: 10.1137/19M1307676
30. Kuehn C. Multiple Time Scale Dynamics. vol. 191 of *Applied Mathematical Sciences*. Springer International Publishing;. (2015) doi: 10.1007/978-3-319-12316-5
31. Izhikevich EM. Which model to use for cortical spiking neurons? *IEEE Trans Neural Netw.* (2004) 15:1063–70. doi: 10.1109/TNN.2004.832719
32. Avrutin V, Schanz M, Schenke B. Breaking the continuity of a piecewise linear map. *ESAIM: Proc.* (2012) 36:73–105. doi: 10.1051/proc/201236008
33. Perez JM. Mechanism for global features of chaos in a driven nonlinear oscillator. *Phys Rev A.* (1985) 32:2513–6. doi: 10.1103/PhysRevA.32.2513
34. Ermentrout G, Kopell N. Parabolic bursting in an excitable system coupled with a slow oscillation. *SIAM J Appl Math.* (1986) 46:233–53. doi: 10.1137/0146017
35. Jilil S, Grigull J, Skinner FK. Novel bursting patterns emerging from model inhibitory networks with synaptic depression. *J Comput Neurosci.* (2004) 17:31–45. doi: 10.1023/B:JCNS.0000023870.23322.0a

Conflict of Interest: The authors declare that the research was conducted in the absence of any commercial or financial relationships that could be construed as a potential conflict of interest.

Publisher's Note: All claims expressed in this article are solely those of the authors and do not necessarily represent those of their affiliated organizations, or those of the publisher, the editors and the reviewers. Any product that may be evaluated in this article, or claim that may be made by its manufacturer, is not guaranteed or endorsed by the publisher.

Copyright © 2022 Olenik and Houghton. This is an open-access article distributed under the terms of the Creative Commons Attribution License (CC BY). The use, distribution or reproduction in other forums is permitted, provided the original author(s) and the copyright owner(s) are credited and that the original publication in this journal is cited, in accordance with accepted academic practice. No use, distribution or reproduction is permitted which does not comply with these terms.



OPEN ACCESS

APPROVED BY
Frontiers Editorial Office,
Frontiers Media SA, Switzerland

*CORRESPONDENCE
Mark Olenik
m.olenik@bristol.ac.uk

SPECIALTY SECTION
This article was submitted to
Dynamical Systems,
a section of the journal
Frontiers in Applied Mathematics and
Statistics

RECEIVED 03 July 2022
ACCEPTED 04 July 2022
PUBLISHED 02 August 2022

CITATION
Olenik M and Houghton C (2022)
Corrigendum: A scalar poincaré map
for anti-phase bursting in coupled
inhibitory neurons with synaptic
depression.
Front. Appl. Math. Stat. 8:985106.
doi: 10.3389/fams.2022.985106

COPYRIGHT
© 2022 Olenik and Houghton. This is
an open-access article distributed
under the terms of the [Creative
Commons Attribution License \(CC BY\)](#).
The use, distribution or reproduction
in other forums is permitted, provided
the original author(s) and the copyright
owner(s) are credited and that the
original publication in this journal is
cited, in accordance with accepted
academic practice. No use, distribution
or reproduction is permitted which
does not comply with these terms.

Corrigendum: A scalar poincaré map for anti-phase bursting in coupled inhibitory neurons with synaptic depression

Mark Olenik^{1*} and Conor Houghton²

¹School of Biological Sciences, Faculty of Life Sciences, University of Bristol, Bristol, United Kingdom, ²School of Computer Science, Electrical and Electronic Engineering, and Engineering Mathematics, Faculty of Engineering, University of Bristol, Bristol, United Kingdom

KEYWORDS

Poincaré map, neuronal bursting, dynamical system (DS), synaptic depression, central pattern generator

A corrigendum on

A scalar poincaré map for anti-phase bursting in coupled inhibitory neurons with synaptic depression

by Olenik M, and Houghton C. (2022). *Front. Appl. Math. Stat.* 8:822782.
doi: 10.3389/fams.2022.822782

In the published article, there was an error in [Figure 10](#) as published. The analytically derived graph was plotted orange, and the numerically computed graph was plotted blue. In the correct version the analytically computed graph is blue, and the numerically computed graph is orange. The corrected [Figure 10](#) and its caption appear below.

In the published article there is a typo in section 1, paragraph 5, where the singular form “parameter” was used, instead of the correct plural “parameters”. The last sentence of the paragraph previously stated:

“Because our map is fully explicit, it lays the framework for studying the effects of other model parameter on network dynamics without the need to run expensive numerical integrations of the ODEs.”

The corrected sentence appears below:

“Because our map is fully explicit, it lays the framework for studying the effects of other model parameters on network dynamics without the need to run expensive numerical integrations of the ODEs.”

A correction has been made to section 1.

In the original article, Equations 31 and 32 miss the differential in the denominator. A correction has been made to **Results**, “Construction of the Scalar Poincaré Map,” Equations 31, 32:

$$\frac{d\Pi_n}{d\bar{g}} > 0, \quad (31)$$

$$\frac{d\Pi_n}{dd^*} > 0, \quad (32)$$

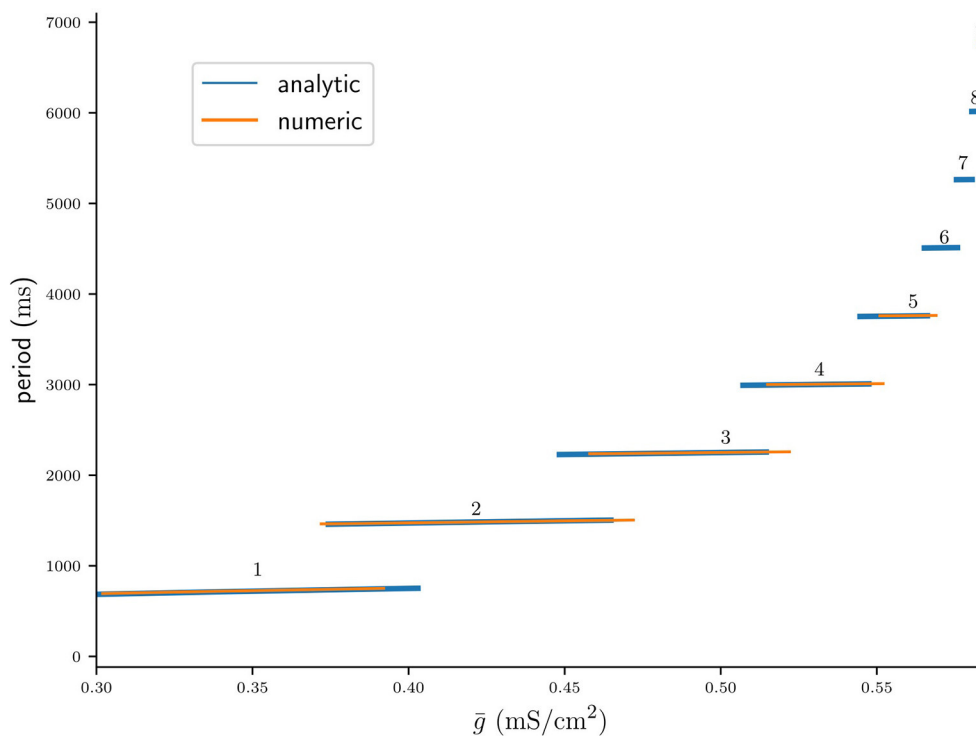


FIGURE 10

Bifurcation diagram of the period of stable $n:n$ solutions computed analytically from fixed points of Π_n , plotted on the respective intervals of $\bar{g} \in [\bar{g}_{\mathcal{L}}(n), \bar{g}_{\mathcal{R}}(n)]$ (blue), and computed from numerical integrations of the ODEs (orange).

Moreover, in the published article Equation 36 misses the differential symbol in the denominator. A correction has been made to **Results**, “Existence and Stability of Fixed Points,” Equation 36:

$$\frac{d}{dd^*} \Pi_n(d^*_b, \bar{g}_b) = 1. \quad (36)$$

In the published article in Equation 47, the symbol δ_n in the denominator is written incorrectly, the n should be a subscript. The correct Equation 47 is:

$$\frac{\partial F_n}{\partial d_f^*} = \tau_\kappa \frac{(\lambda\rho)^{n-1}}{\delta_n(d_f^*)} > 0. \quad (47)$$

A correction has been made to section 3.5.

In the published article in Equations 41 and 42, the “smaller than” and “greater than” signs appear in the wrong order. The correct Equations 41 and 42 are:

$$\frac{dG_n}{dd_f^*} > 0, \quad \text{for } d_f^* > d_b^*(n) \text{ stable}, \quad (41)$$

$$\frac{dG_n}{dd_f^*} < 0, \quad \text{for } d_f^* < d_b^*(n) \text{ unstable}, \quad (42)$$

In the published article in the Equations 51–54 some symbols have incorrect subscripts. The correct Equations 51–54 are:

$$\bar{g}_{\mathcal{L}}(n) < \bar{g}_{\mathcal{R}}(n) \quad (51)$$

$$\bar{g}_{\mathcal{L}}(n) < \bar{g}_{\mathcal{L}}(n+1) \text{ and } \bar{g}_{\mathcal{R}}(n) < \bar{g}_{\mathcal{R}}(n+1) \quad (52)$$

$$\bar{g}_{\mathcal{L}}(n+1) < \bar{g}_{\mathcal{R}}(n) \quad (53)$$

$$\bar{g}_{\mathcal{R}}(n+1) - \bar{g}_{\mathcal{L}}(n+1) < \bar{g}_{\mathcal{R}}(n) - \bar{g}_{\mathcal{L}}(n) \quad (54)$$

A correction has been made to section 3.6.

Finally, in the published article in **Results**, “Stable Solution Branch Borders,” paragraph 4, Equation 58 was quoted instead of Equation 54. The corrected sentence is:

Here $g_{\mathcal{L}}(n)$ and $\bar{g}_{\mathcal{R}}(n)$ were computed from Equations (56) and (54), respectively.

In the published article in the last sentence of section 4, paragraph 2, a wrong type of citation format was used. The original sentence previously stated “Our results are also in line with [7] rhythmogenesis hypothesis, namely that synaptic depression of inhibition is a mechanism by which anti-phase bursting may arise.”

The corrected sentence appears below:

“Our results are also in line with Brown’s [7] rhythmogenesis hypothesis, namely that synaptic depression of inhibition is a mechanism by which anti-phase bursting may arise.”

In the published article there was a typo in the acknowledgments. The first sentence previously stated: “MO thank the Wellcome Trust for financial support of his Ph.D. study.”

The corrected sentence appears below: “MO thanks the Wellcome Trust for financial support of his Ph.D. study.”

The authors apologize for these errors and state that this does not change the scientific conclusions

of the article in any way. The original article has been updated.

Publisher’s note

All claims expressed in this article are solely those of the authors and do not necessarily represent those of their affiliated organizations, or those of the publisher, the editors and the reviewers. Any product that may be evaluated in this article, or claim that may be made by its manufacturer, is not guaranteed or endorsed by the publisher.



Transmissibility in Interactive Nanocomposite Diffusion: The Nonlinear Double-Diffusion Model

Amit K. Chattopadhyay^{1*}, Bidisha Kundu², Sujit Kumar Nath^{3,4} and Elias C. Aifantis⁵

¹ Nonlinearity and Complexity Research Group, Department of Mathematics, Aston University, Birmingham, United Kingdom, ² School of Life Sciences, University of Lincoln, Lincoln, United Kingdom, ³ School of Computing, University of Leeds, Leeds, United Kingdom, ⁴ Faculty of Biological Sciences, University of Leeds, Leeds, United Kingdom, ⁵ Laboratory of Mechanics and Materials, Aristotle University of Thessaloniki, Thessaloniki, Greece

OPEN ACCESS

Edited by:

Erik Andreas Martens,
Lund University, Sweden

Reviewed by:

Alain Miranville,
University of Poitiers, France
Constantinos Siettos,
University of Naples Federico II, Italy

*Correspondence:

Amit K. Chattopadhyay
a.k.chattopadhyay@aston.ac.uk

Specialty section:

This article was submitted to
Dynamical Systems,
a section of the journal
Frontiers in Applied Mathematics and
Statistics

Received: 10 January 2022

Accepted: 10 May 2022

Published: 03 June 2022

Citation:

Chattopadhyay AK, Kundu B,
Nath SK and Aifantis EC (2022)
Transmissibility in Interactive
Nanocomposite Diffusion: The
Nonlinear Double-Diffusion Model.
Front. Appl. Math. Stat. 8:852040.
doi: 10.3389/fams.2022.852040

Model analogies and exchange of ideas between physics or chemistry with biology or epidemiology have often involved inter-sectoral mapping of techniques. Material mechanics has benefitted hugely from such interpolations from mathematical physics where dislocation patterning of plastically deformed metals and mass transport in nanocomposite materials with high diffusivity paths such as dislocation and grain boundaries, have been traditionally analyzed using the paradigmatic Walgraef-Aifantis (W-A) double-diffusivity (D-D) model. A long standing challenge in these studies has been the inherent nonlinear correlation between the diffusivity paths, making it extremely difficult to analyze their interdependence. Here, we present a novel method of approximating a closed form solution of the ensemble averaged density profiles and correlation statistics of coupled dynamical systems, drawing from a technique used in mathematical biology to calculate a quantity called the *basic reproduction number* R_0 , which is the average number of secondary infections generated from every infected. We show that the R_0 formulation can be used to calculate the correlation between diffusivity paths, agreeing closely with the exact numerical solution of the D-D model. The method can be generically implemented to analyze other reaction-diffusion models.

Keywords: double diffusion, reproduction number, autocorrelation, spatiotemporal correlation, Fick's diffusion

1. INTRODUCTION

Transport of mass, heat or electricity in inhomogeneous media has been modeled [1–3] involving distinct conducting paths such as diffusion in metals containing a large number of dislocations and/or grain boundaries [4], fluid flows in fissured rocks and media with double porosity [5, 6], heat or electricity conduction in fiber reinforced composites [10] have been addressed by Aifantis through continuous models, typically based on coupled sets of linear partial differential equations (the double diffusivity or D-D model) involving 4 phenomenological constants: 2 diffusion coefficients for each one of the two paths and two mass exchange constants between the paths. The above two-state idea was also utilized later in developing the first dynamical model of dislocation patterning, commonly known as the Walgraef-Aifantis (W-A) model [1, 2] that could distinguish between two dislocation populations: slow or “immobile” dislocation and fast or “mobile” ones that brings plastic deformation about. It turns out that the linearized version of the W-A model is identical in form to the D-D model variant of the two-state reaction-diffusion (R-D) formulation

used to describe transport of multiple families of species such as vacancies and interstitials in crystalline lattices, impurity, segregation in dislocation and grain boundaries or trapping and precipitation process in alloys.

Over the last two decades, the D-D and W-A models have become quite popular in both the applied mathematics [11] and the material science [12] communities due to the interesting mathematical properties of the former and robust interpretation of experimental observations of the latter groups of models. This includes implementation of D-D type models in interpreting molecular and mesoscopic transport in condensed matter and cosmological systems [13], i.e., Most of such models though overlooked the contribution of stochastic forcing or spatial randomness, e.g., surface impurities in materials, restricting the implementation of such models in explaining experimental observations. A recent series of stochastically driven D-D models [7–9] have not only addressed this issue of steering qualitative phenomenological models closer to experimental descriptions, technically these have opened up further possibilities of cross-disciplinary implementation of these models from material science to other fields and vice versa.

Anomalous diffusion involving multiple species and media has for long remained an interesting field of research. The diffusive behavior changes their characteristics depending on the choice of medium. There are many plausible reasons for this. One of them is that there exists some void grain boundary in the medium which represents an especially high diffusivity path inside the medium. Also, there are relatively narrow domains in the medium where the diffusion rate is slower. Simultaneous diffusion in multiple media has been traditionally analyzed using double-diffusion models [4–6, 10, 14] that is a coupled system of partial differential equations involving interacting variables. These D-D models considered two species of diffusive elements, one that follows the regular path, another following a high-diffusive path, with eventual dynamics determined by a dynamical equilibrium of these competing paths.

1.1. State of the Art

Elias C. Aifantis developed and introduced the concept of double diffusion step by step in Aifantis and Hill [5, 6] and Aifantis [15, 16]. A continuum basis for diffusion in regions with multiple diffusivity was introduced in Aifantis [15]. Simultaneously, in Aifantis [17], the diffusion in media with a continuous distribution of high-diffusivity paths was modeled. Finally, Aifantis provided a formulation generalizing this idea of the diffusion in solid media for wide range of applicability in different physical process, in double porosity [18], from metallurgy to soil science [14] polymer physics and geophysics, in Aifantis and Hill [5, 6]. Another explanation of this double diffusion model was provided in Hill [19] using the concept of discrete random walk model. In [5, 6]–[19], Aifantis and Hill studied the basic mathematical questions of the model. Mainly they studied uniqueness, maximum principles and basic source solutions in Aifantis [20] and Hill [19] and boundary value problems in Hill [19]. Kuttler and Aifantis studied the existence and uniqueness of the weak form of the nonclassical diffusion equation in Kuttler and Aifantis [21].

The diffusion process in a media is not deterministic. Indeed there are stochastic effects initiated and controlled by several factors. Randomness can be related to thermal fluctuations, grain size changes, impurity effects, etc. Recent studies of a type of non-equilibrium system involving multiple states of diffusion of a diffusing species, called stochastic resetting, is governed by a dynamics similar to a double-diffusion system [22]. These types of interactive features play an important role in the process and it became necessary to take into account of the stochastic agents. In nanoscales or nanopolycrystals, the diffusion near the grain boundary following two paths, regular and high diffusive, can be affected by stochastic fluctuations [7]. Deterministic internal length gradient method can not completely explain relaxation time for diffusion in nanopolycrystals. Considering boundary layer fluctuations, stochasticity was added in the modeling and first stochastic gradient nanomechanics (SGNM) model was proposed in Chattopadhyay and Aifantis [8]. Using SGNM model, relaxation time is discussed thoroughly for a specific superconductors [23] in Chattopadhyay and Aifantis [9]. Also, linear stochastic resonance has been predicted and how stochastic effects start affecting the system is explained in Chattopadhyay and Aifantis [9].

1.2. Open Questions

The present article is the first in line to provide a closed form approximate perturbative solution of the nonlinear model (close to the linearized stationary state) resulting from a combination of the D-D and W-A models. The D-D:W-A composite model leads to a coupled system of reaction-diffusion (R-D) equations where the diffusion terms are identical to those contained in both models, the linear terms as in the D-D model [7, 8] while the nonlinear terms resemble the W-A model (3rd order). In addition, the composite model contain second order cross-coupled terms that do not lend themselves to an exact analytical solution, not even in their linearized form. The underlying physical picture represents a system of multiple diffusive relaxation, including boundary layer shear (nonlinear terms), and driven by stochastic forcing as in the two models. The present model considers simultaneous diffusion in the lattice or grain interior along the grain boundaries but also allow for trapping and impurity effects. In other words, diffusing species can be trapped in both grain interiors along dislocation cores and dislocation dipoles as well as in the counterparts of the defects within the grain boundary space, as also impurity of lattice imperfection that are stochastically distributed and hence extremely difficult to account for.

While diffusion mediated interaction between multiple species is intrinsically nonlinear, traditional analyzes have relied on the dual approach of numerical modeling (nonlinear systems) and exactly solvable linear models (approximate only). Most of these studies are deterministic with occasional stochastic models strictly restricted to linear models. The present study outlines a generic approach, repurposed from the field of mathematical biology, to provide approximate closed form solutions of inherently nonlinear coupled systems irrespective of their origin. While there is no paucity of numerical estimation of nonlinear models, including those for double diffusion ([8] and

references therein), from the perspective of theoretical modeling, analytical clarity had to give way to quantitative precision. More importantly, a closed form solution offers a direct methodological link between the process and its parameters that is not available from brute numerical evaluation in a multi-parameter space. The present study is thus a major breakaway from the linearity assumption, retaining closer proximity to experiments while also comparing favorably with numerical solutions, as we will later show.

Nonlinear diffusion equations, a classical example of parabolic type equations, play an important role in the modeling of diffusion equations with nonlinearity [24], in particular, for stochastically driven diffusive systems. One is for free boundary problems such as the distribution of temperature in a homogeneous material during phase-transition [25], i.e., the time evolution of the phase boundaries, the so called Stefan problem.

Another is for reaction-diffusion problems, such as the Fisher-Kolmogorov-Petrovsky-Piskunov (Fisher-KPP) model for propagation of an advantageous gene in a population [26, 27], Gray Scott Model for diffusion of chemical species [28]. Similar style of modeling can be found for dislocation profiles in a material. Walgraef and Aifantis (WA model) proposed a model of a system of Reaction-Diffusion equations considering two profiles of dislocation flows, immobile dislocation for slow moving and mobile for relatively speedy moving [1]. The W-A model has been studied extensively numerically, toward bifurcation analysis and pattern formation in Pontes et al. [11] and Spiliotis et al. [12]. None of these were targeting a closed form analysis, as is the target in this study.

The article provides a generic technique, repurposed from a diverse domain (mathematical biology), to solve systems of coupled nonlinear equations. Following a general introduction and pointers to open questions in Section 1, Section 2 summarizes the model equation and provides a physical explanation of the mechanisms involved. Section 3 represents the nondimensionalized representation of the model in Section 2, the relevant non-dimensional governing equations and their linear stability analysis. Section 4 first discusses a popular method used in mathematical epidemiology in the calculation of the time varying reproduction number R_0 , then identifies the phenomenology as one of analyzing the covariance of two (or more) coupled variables in a dynamical system, and then uses this hypothesis to connect with the cross-coupling between D-D variables. Section 5 provides the anatomy of the time (t) evolution of the reproduction number $R_0(t)$ in the equivalent D-D model as one measuring the strength of cross-correlation between the different diffusing species. Finally, Section 6 summarizes the outcomes of this continuum (approximate) mapping that then is compared against direct numerical evaluation of this model.

2. THE MODEL

In this work, we focus on a closed-form, albeit approximate, solution of the D-D model for nano polycrystal diffusion by considering nonlinear source terms in the original W-A model, representing additional exchange of diffusion species between the

two paths. These new non-linear exchange terms represent the transfer of diffusion species through dislocation atmosphere i.e., diffusing species segregated in dislocation cores and dislocation dipoles. We study in particular how the “transmissibility” of the species affect their diffusion and corresponding trapping processes. We observe how their internal interactions can affect their behavior. We study how the transmissibility of the species affects their diffusion.

Considering $\tilde{\rho}_1$ and $\tilde{\rho}_2$ as the concentrations/densities for the two distinct D-D species along two different paths, the governing equations of diffusion are given by

$$\frac{\partial \tilde{\rho}_1}{\partial \tilde{t}} = D_1 \frac{\partial^2 \tilde{\rho}_1}{\partial \tilde{x}^2} - k_1 \tilde{\rho}_1 + k_2 \tilde{\rho}_2 + \lambda_1 \tilde{\rho}_1 \tilde{\rho}_2 + \sigma_1 \tilde{\rho}_1^2 \tilde{\rho}_2 \quad (1a)$$

$$\frac{\partial \tilde{\rho}_2}{\partial \tilde{t}} = D_2 \frac{\partial^2 \tilde{\rho}_2}{\partial \tilde{x}^2} + k_1 \tilde{\rho}_1 - k_2 \tilde{\rho}_2 + \lambda_2 \tilde{\rho}_1 \tilde{\rho}_2 + \sigma_2 \tilde{\rho}_1 \tilde{\rho}_2^2 \quad (1b)$$

where D_1, D_2 are diffusion coefficients, k_1, k_2 are the rate mass exchange between different paths. The nonlinear terms represent the interactions between different species (or dislocation paths, in case of two diffusive paths in the material body) when the density of one species influences the creation or annihilation of the other.

3. NON-DIMENSIONALIZATION OF THE DOUBLE DIFFUSING WALGRAEF-AIFANTIS MODEL

Let $\tilde{x} = ax$, $\tilde{t} = bt$, $\tilde{\rho}_1 = c_1 \rho_1$, $\tilde{\rho}_2 = c_2 \rho_2$. Substituting in Equations (1a–1b), then assuming that the diffusion coefficients remain unchanged after scaling, and choosing coefficients of nonlinear product terms as unity after scaling, for $\sigma_1 = \sigma_2 = \sigma$, we have

$$\frac{\partial \rho_1}{\partial t} = D_1 \frac{\partial^2 \rho_1}{\partial x^2} - \left(\frac{k_1 \sigma}{\lambda_1 \lambda_2} \right) \rho_1 + \left(\frac{k_2 \sigma}{\lambda_1^2} \right) \rho_2 + \rho_1 \rho_2 + \rho_1^2 \rho_2 \quad (2a)$$

$$\frac{\partial \rho_2}{\partial t} = D_2 \frac{\partial^2 \rho_2}{\partial x^2} + \left(\frac{k_1 \sigma}{\lambda_2^2} \right) \rho_1 - \left(\frac{k_2 \sigma}{\lambda_1 \lambda_2} \right) \rho_2 + \rho_1 \rho_2 + \rho_1 \rho_2^2. \quad (2b)$$

Note, the variables ρ_1 and ρ_2 , representing Equations (2a, 2b), are non-dimensional. The numerical model uses this system of a non-dimensional dynamical system.

3.1. Linear Stability Analysis

Equations (2a,2b) can be represented as the following coupled reaction-diffusion model

$$\frac{\partial \rho_1}{\partial t} = D_1 \frac{\partial^2 \rho_1}{\partial x^2} + F_1(\rho_1, \rho_2) \quad (3a)$$

$$\frac{\partial \rho_2}{\partial t} = D_2 \frac{\partial^2 \rho_2}{\partial x^2} + F_2(\rho_1, \rho_2), \quad (3b)$$

where $F_1(\rho_1, \rho_2) = - \left(\frac{k_1 \sigma}{\lambda_1 \lambda_2} \right) \rho_1 + \left(\frac{k_2 \sigma}{\lambda_1^2} \right) \rho_2 + \rho_1 \rho_2 + \rho_1^2 \rho_2$, and $F_2(\rho_1, \rho_2) = \left(\frac{k_1 \sigma}{\lambda_2^2} \right) \rho_1 - \left(\frac{k_2 \sigma}{\lambda_1 \lambda_2} \right) \rho_2 + \rho_1 \rho_2 + \rho_1 \rho_2^2$. We analyze the system stability near the *Homogeneous Equilibrium* (HE) state

or at the uniform steady state (ρ_1^*, ρ_2^*) [1, 12], in line with the approach used in Spillotis et al. [12], i.e., where

$$F_1(\rho_1^*, \rho_2^*) = 0, \quad (4a)$$

$$F_2(\rho_1^*, \rho_2^*) = 0 \quad (4b)$$

Solving these equations we get the HE state, $(\rho_1^*, \rho_2^*) = (0, 0)$. Perturbing around this equilibrium state, perturbations defined as $(\hat{\rho}_1, \hat{\rho}_2)$, we get $\rho_1 = \rho_1^* + \hat{\rho}_1$, $\rho_2 = \rho_2^* + \hat{\rho}_2$.

Now near the HE states, the linearized version of the Equations (3a, 3b) are

$$\frac{\partial \bar{\rho}}{\partial t} = \begin{pmatrix} D_1 & 0 \\ 0 & D_2 \end{pmatrix} \frac{\partial^2 \bar{\rho}}{\partial x^2} + J_F \bar{\rho} \quad (5)$$

where $\bar{\rho} = \begin{pmatrix} \hat{\rho}_1 \\ \hat{\rho}_2 \end{pmatrix}$, and J_F is the Jacobian of $\begin{pmatrix} F_1(\rho_1, \rho_2) \\ F_2(\rho_1, \rho_2) \end{pmatrix}$ at the equilibrium states (ρ_1^*, ρ_2^*) . We consider $\bar{\rho} = \begin{pmatrix} \phi_1(t) \\ \phi_2(t) \end{pmatrix} e^{i\omega x}$ for real ω and get

$$\begin{pmatrix} \frac{d\phi_1}{dt} \\ \frac{d\phi_2}{dt} \end{pmatrix} = (J_F - \omega^2 D) \begin{pmatrix} \phi_1(t) \\ \phi_2(t) \end{pmatrix}, \quad (6)$$

where $D = \begin{pmatrix} D_1 & 0 \\ 0 & D_2 \end{pmatrix}$. As this is a system of two variables, the signatures of trace and determinant of the matrix $(J_F - \omega^2 D)$ defines the stability of the system. The determinant should be always positive and trace should be always negative for all real values of ω . We test these conditions for the HE state at $(0, 0)$ and arrive at the following closed form expressions for the Trace (Tr) and Determinant (Det) of the model:

$$\text{Tr}(J_F - \omega^2 D) = -D_1\omega^2 - D_2\omega^2 - \frac{k_1\sigma}{\lambda_1\lambda_2} - \frac{k_1\sigma}{\lambda_1\lambda_2} \quad (7a)$$

$$\text{Det}(J_F - \omega^2 D) = D_1D_2\omega^4 + \frac{D_1k_2\sigma\omega^2}{\lambda_1\lambda_2} + \frac{D_2k_1\sigma\omega^2}{\lambda_1\lambda_2} \quad (7b)$$

For $D_1 > 0, D_2 > 0, k_1 > 0, k_2 > 0, \sigma > 0, \lambda_1 > 0, \lambda_2 > 0, \omega^2 > 0$, Trace is always negative and determinant is always positive. Hence, the HE state at $(0, 0)$ is a stable state.

4. BIOLOGY TO MATERIALS' MODELING

It is usual practice in infectious disease epidemiology and modeling to measure the “speed” of the propagation of the infection. This measurement is generally called the *basic reproduction number* R_0 that effectively equates to the number of secondary infections generated from each infected member of the population. R_0 depends on the numbers of currently infected, susceptible and the rate of infection in the population. This R_0 is the threshold parameter for an infectious disease, determining whether it becomes an epidemic, pandemic, or extinct in a community. The epidemiologists follow several methods to

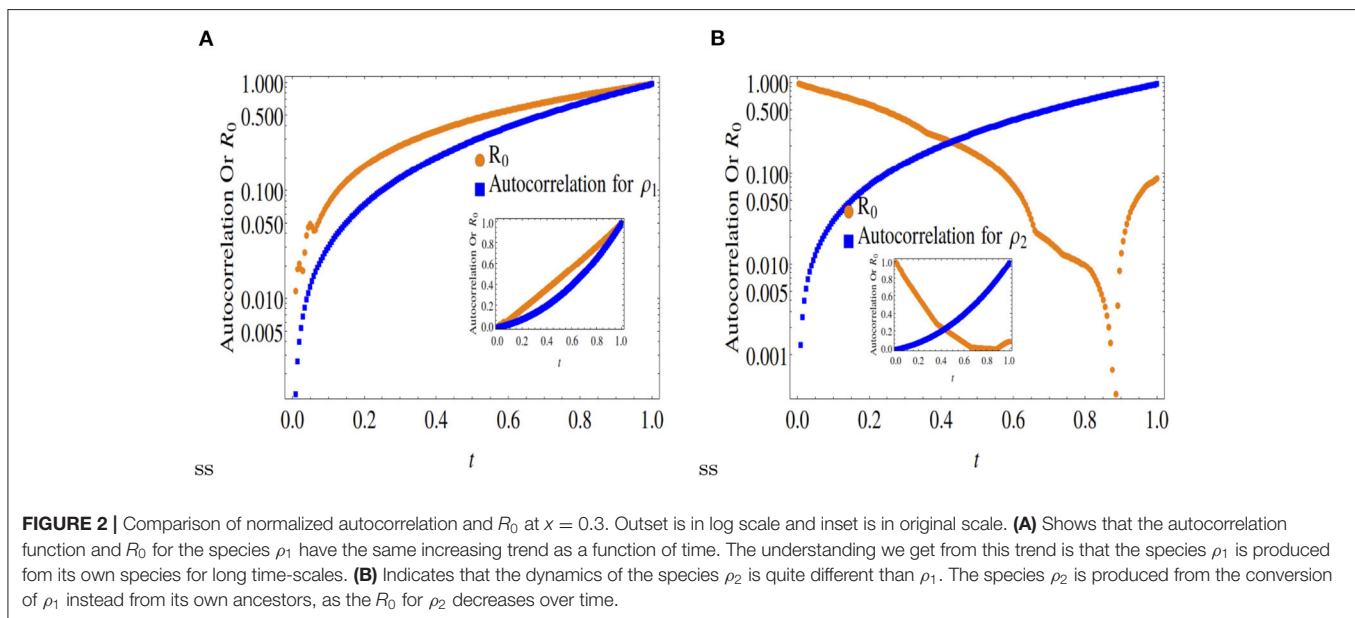
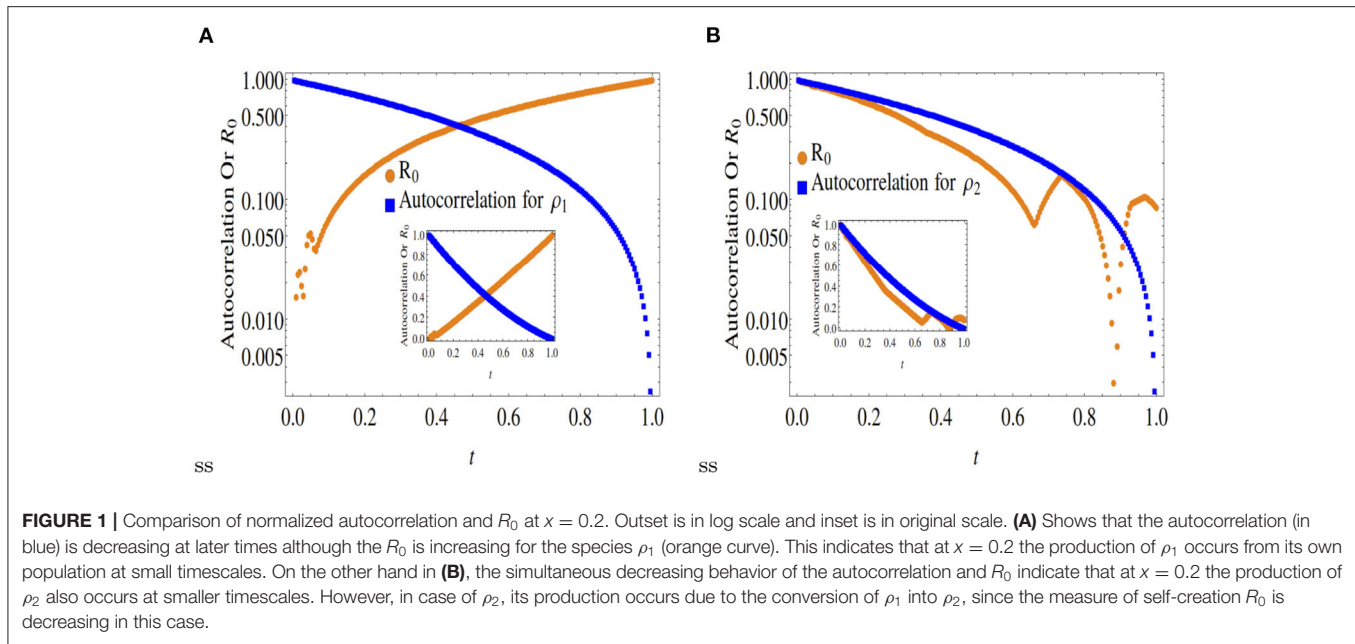
calculate R_0 . Two of these, referred to as the *next generation method* and the *age-structured method* [29–31] are widely used. Both are effective and popular in infection modeling studies.

In this work, we show how the concept of R_0 can be made an auxiliary method in studying the diffusion process in a medium. We show how the profile of time evolution of R_0 can help us to understand the diffusion-dynamics of two species, and can be used as a substitute to the enumeration of correlation functions.

Our starting point in this “reverse mapping” scheme from mathematical biology to material science relates to the origin of the concept of *basic reproduction number* R_0 . Let $I(t)$ be a time-evolving quantity whose value at time t is dependent on its values at previous time points. This essential non-Markovian distribution ensures non-trivial values for all $I(t - \tau)$, where $0 \leq \tau \leq t$, as long as $I(t)$ is defined. Representing $I(t)$ as the number of infected individuals at time t in a population, non-Markovian kinetics ensures that $I(t)$ should depend on the number of infected, present in the population, at time $t - \tau$, since the new infections can only be generated by the previous infections. The time required for an infected individual to generate a new infection, from the onset of its infection, is called the generation time τ . Clearly, τ is a non-negative continuous random variable which has a probability density function, say $g(\tau)$. In the case of infectious diseases, $g(\tau)$ is generally taken as Gamma or a lognormal distribution.

5. “GENERATION TIME” IN DOUBLE DIFFUSION: COMPARISON WITH RANDOM WALK MODEL

We can think of double diffusion as the continuum limit of a random walk model where the random walker diffuses along two different diffusive paths, occasionally jumping between them [19]. Here, by different diffusivity of paths we mean the probability of left jump (p_i), right jump (q_i), staying at same position without making any jump (r_i) are different for the two paths, where $i = 1, 2$ for path-1 and path-2. Let us introduce a random time interval τ , having a probability density function $g(\tau)$, during which the walker diffuses along the same path before making any jump to the other path. The time τ can be thought of as the generation time for the double diffusion model, in parallel with the well defined generation time for an infectious disease. For this random walk model of double diffusion, let the probability of jumping from path-1 to path-2 be $\mathbb{P}(1 \rightarrow 2) = s_1$ and same for path-2 to path-1 be $\mathbb{P}(2 \rightarrow 1) = s_2$. Therefore, the generation time in case of our double diffusion model can be compared to the survival time of the random walker on a single path before making a jump to the other. Now, for the random walk model of double diffusion we must have $p_i + q_i + r_i + s_i = 1$ for $i = 1, 2$. Therefore, the probability that the random walker continues on path i , in two consecutive jumps, is $(1 - s_i)$. Hence the corresponding survival probability on path i is given by a geometric distribution. More explicitly, the probability that the walker will stay on path i for n consecutive jumps is $(1 - s_i)^n s_i$. Motivated by the fact that the geometric distribution has memoryless property, and exponential distribution is the



only continuous distribution having memoryless property, it is reasonable to assume that the generation time is exponentially distributed in the continuum limit of this random walk model of double diffusion.

5.1. The Reproduction Number R_0 and Its Mapping to the D-D Model

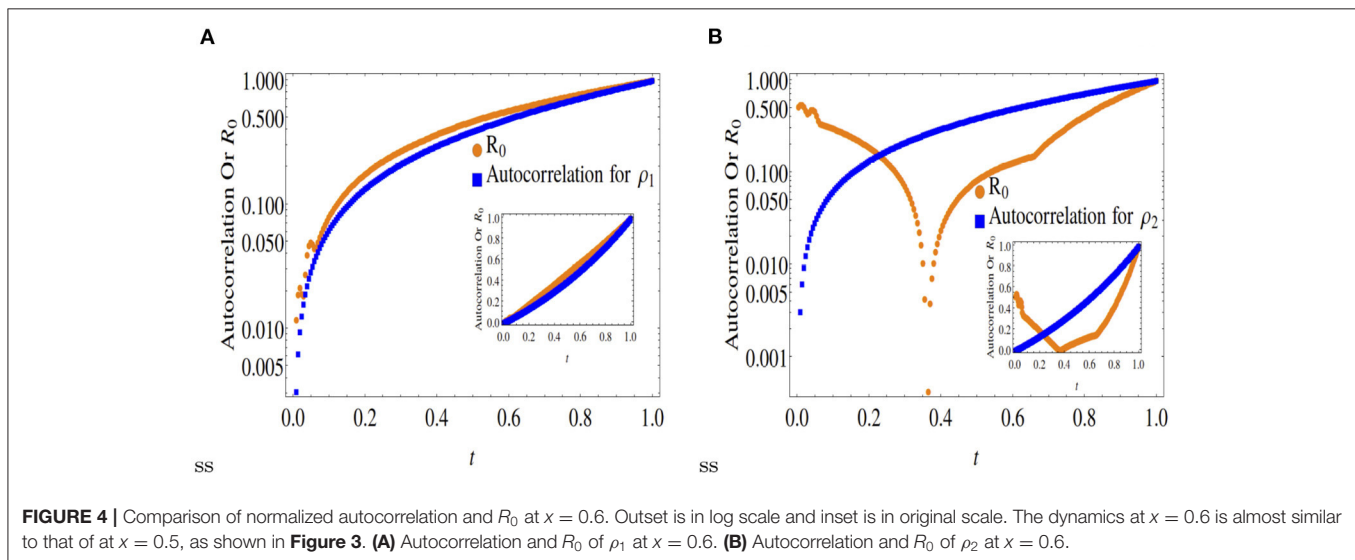
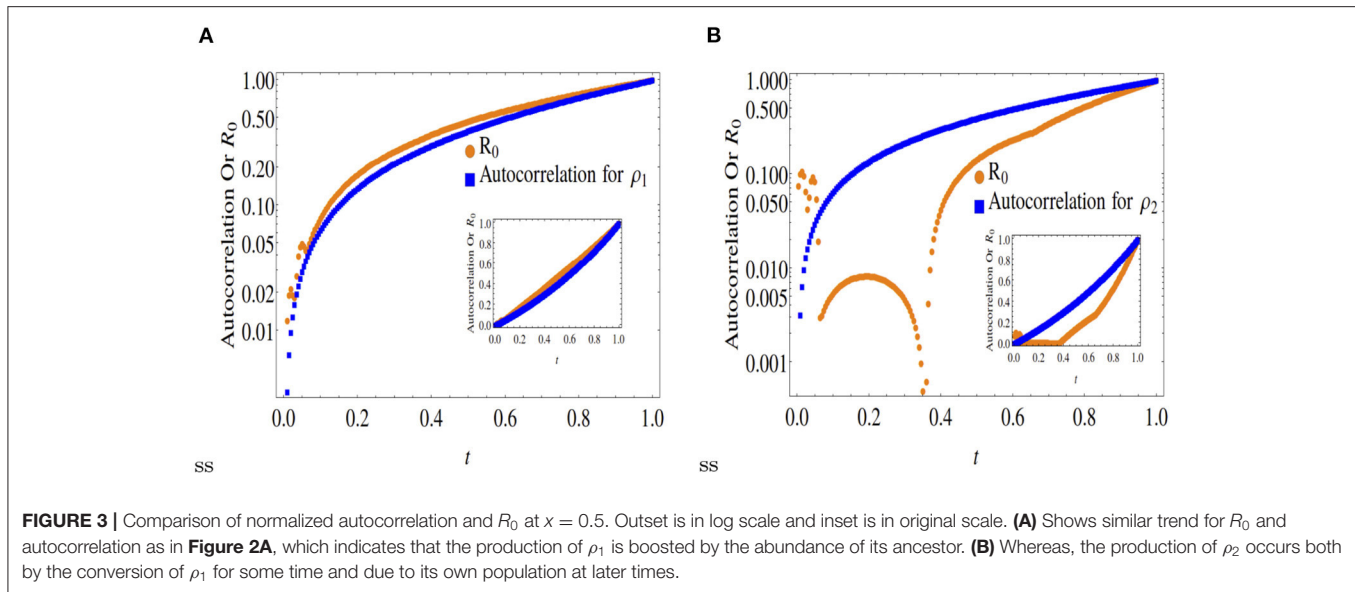
Following the similar concept in the case of double diffusion, we can think of the density $\rho(t)$ of certain species is dependent on its density $\rho(t - \tau)$ at earlier times ($0 \leq \tau \leq t$). The time required for generating new particles of the same species from the old ones is a continuous random variable τ with some density

function $g(\tau)$. Therefore, in the same token, as defined in case of infectious diseases, we can define a quantity R_0 for a species in a double-diffusive process as

$$R_0(t) = \frac{\rho(t)}{\int_0^\infty \rho(t - \tau) g(\tau) d\tau}. \quad (8)$$

where $g(\tau)$ is the generation time.

Figures 1–4 compare the R_0 equivalent of an equivalent epidemic rate model with that of the autocorrelation function (Equations (2a, 2b) at the quantitative level, providing interesting insights into the D-D reaction-diffusion model. It can be easily



understood from the mathematical expression of $R_0(t)$ that it is a measure of the production rate of a species from the population of the same species at an earlier epoch, rather than due the conversion of other species. On the other hand, autocorrelation is a measure of the abundance of a species as a whole, aggregating the production of a species from its own population as well as due to the conversion of other species. Therefore, the autocorrelation function together with the time-varying $R_0(t)$, gives us interesting spatio-temporal insights about the observed abundance.

A comparison between **Figures 1, 2** with **Figure 3** clearly indicates that while asymmetric cases ($x < 0.5$) ensure only partial convergence between the R_0 and autocorrelation profiles, i.e., only one of the two double diffusing variables match both profiles, at

$x = 0.5$, the profiles match (approximately) for both variables.

Note, the dynamics of ρ_1 as shown in **Figure 5** matches those for $x = 0.3, 0.5, 0.6$. However, the species ρ_2 is mostly created by the conversion of the species ρ_1 . These 5 figures clearly indicate that only for the symmetric case $x = 0.5$, the time dynamical evolution of the reproductive number for an epidemic model matches the average energy dissipation rate of individual variables (expressed as autocorrelation functions), not otherwise. This is not unexpected as the point $x = 0.5$ (spatial scale $0 < x < 1$) represents the point of dynamical equilibrium between two diffusing species, that also represents infection flux equilibrium between susceptible-infected-recovered species in an epidemic model. In other words, a fair quantitative comparison between the R_0 vs. the D-D model is only ensured at $x = 0.5$.

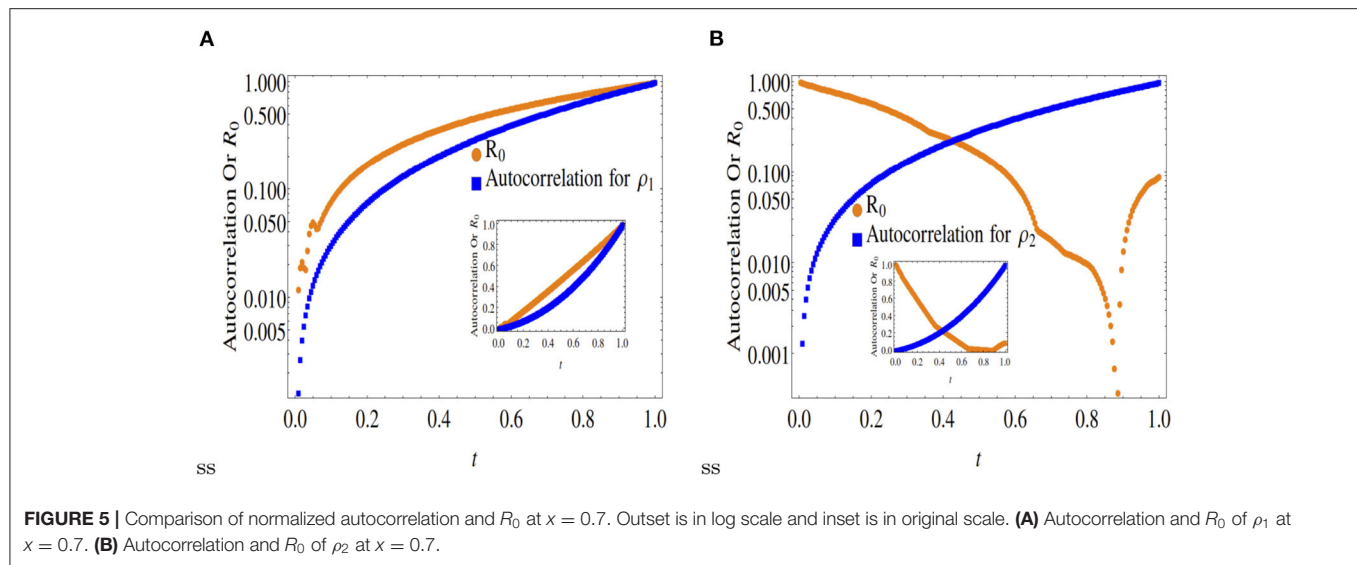


FIGURE 5 | Comparison of normalized autocorrelation and R_0 at $x = 0.7$. Outset is in log scale and inset is in original scale. **(A)** Autocorrelation and R_0 of ρ_1 at $x = 0.7$. **(B)** Autocorrelation and R_0 of ρ_2 at $x = 0.7$.

6. CONCLUSIONS

Clearly, a comparison of the dynamical variable $R_0(t)$, motivated by the epidemiological literature, with the autocorrelation function reveals the richness of the dynamics of a reaction-diffusion system which offers an option of interpolating the results from the epidemic model into the double-diffusion domain, in the process providing a closed form solution of the latter that has remained elusive thus far. Comparing the time evolution of R_0 with the autocorrelation function gives the information of the origin of the observed abundance of different species in a reaction-diffusion system as explained in **Figures 1–5**. The analogy is strictly restricted to the spatially symmetric ($x = 0.5$) conformation though, a point of dynamical equilibrium between two (or multiple) diffusing species, an analogy with the stationary state fixed point of an epidemic model in dynamical equilibrium.

Therefore, the introduction of the epidemiologically motivated quantity $R_0(t)$ into the studies of the reaction-diffusion systems can play a crucial role in understanding such systems in more depth. Since this interpolation between two unrelated disciplines only uses the mathematical similarity between two (or multiple) reaction-diffusion species, expressed as double-diffusion in material science, as compared to infection rate growth in epidemiology, the approach is generic enough to be applied to all coupled reaction-diffusion models. At the point of symmetry ($x = 0.5$ in our model), both quantities (R_0 and autocorrelation) will asymptotically match their values with evolving time allowing for a closed form mapped (from mathematical biology) solution of the R-D model. As a comparison with the numerical solution confirms close convergence with the approximate mapped solution (based on

the $R_0(t)$ formula as a descriptor of the correlation strength of the diffusing variables), the solution provides handle to studies analyzing higher order perturbations and relevant bifurcations, also including stochastic terms. Future studies involving calculation of correlated superconducting fluxes would be presented using the same method.

DATA AVAILABILITY STATEMENT

All data that support the findings of this study are included within the article (and any supplementary files).

AUTHOR CONTRIBUTIONS

AC led the project, conceived the model, and the mapping between mathematical biology to material science. BK and SKN executed the analytical calculations, model simulations, and introduced the connection with statistical physics. EA provided the material science backbone. All authors jointly wrote the paper and contributed equally to this manuscript.

FUNDING

The authors gratefully acknowledge partial financial support from the H2020-MSCA-RISE-2016 program, Grant No. 734485, entitled Fracture Across Scales and Materials, Processes and Disciplines (FRAMED). BK acknowledges funding by UKRI Grant No. (MR/T046619/1), part of the NSF/CIHR/DFG/FRQ/UKRI-MRC Next Generation Networks for Neuroscience Program. SKN acknowledges the Leverhulme Trust (RPG-2018-137) for supporting his time and resources for research in the UK.

REFERENCES

- Walgraef D, Aifantis EC. Dislocation patterning in fatigued metals as a result of dynamical instabilities. *J Appl Phys.* (1985) 58:688. doi: 10.1063/1.336183
- Walgraef D, Aifantis EC. Dislocation patterning in fatigued metals: labyrinth structures and rotational effects. *Int J Eng Sci.* (1986) 24:1789–98. doi: 10.1016/0020-7225(86)90127-8
- Aifantis EC. On the dynamical origin of dislocation patterns. *Mater Sci Eng.* (1986) 81:563–74. doi: 10.1016/0025-5416(86)90293-4
- Aifantis EC. Gradient nanomechanics: applications to deformation, fracture, and diffusion in nanopolycrystals. *Metall Mater Trans A.* (2011) 42:2985–98. doi: 10.1007/s11661-011-0725-9
- Aifantis EC, Hill JM. On the theory of diffusion in media with double diffusivity I–Basic mathematical results. *Q J Mech Appl Math.* (1980) 33:1.
- Aifantis EC, Hill JM. On the theory of diffusion in media with double diffusivity II–Basic mathematical results. *Q J Mech Appl Math.* (1980) 33:1.
- Chattopadhyay K, Aifantis EC. Double diffusivity model under stochastic forcing. *Physical Review E.* (2017) 95:052134. doi: 10.1103/PhysRevE.95.052134
- Chattopadhyay K, Aifantis EC. On stochastic resonance in a model of double diffusion. *Mater Sci Technol.* (2018) 34:1606–13. doi: 10.1080/02670836.2018.1507697
- Chattopadhyay K, Aifantis EC. Stochastically forced dislocation density distribution in plastic deformation. *Phys Rev E.* (2016) 94:022139. doi: 10.1103/PhysRevE.94.022139
- Vardoulakis J, Aifantis EC. A gradient flow theory of plasticity for granular materials. *Acta Mech.* (1991) 87:197–217. doi: 10.1007/BF01299795
- Pontes J, Walgraef D, Aifantis EC. On dislocation patterning: multiple slip effects in the rate equation approach. *Intl J Plasticity.* (2006) 22:1488–505. doi: 10.1016/j.ijplas.2005.07.011
- Spiliotis KG, Russo L, Aifantis EC. Analytical and numerical bifurcation analysis of dislocation pattern formation of the Walgraef-Aifantis model. *Int J Non Linear Mech.* (2018) 102:41–52. doi: 10.1016/j.ijnonlinmec.2018.03.002
- Aifantis EC. Gradient extension of classical material models: from nuclear & condensed matter scales to earth & cosmological scales. In: Ghavanloo E, Fazlzadeh SA, Marotti de Sciarra F, editor. *Size-Dependent Continuum Mechanics Approaches*. Springer; Cham: Springer Tracts in Mechanical Engineering.
- Tsambali A, Konstantinidis A, Aifantis EC. Modeling double diffusion in soils and materials. *J Mech Behav Mater.* (2018) 27:5–6. doi: 10.1515/jmbm-2018-2003
- Aifantis EC. A new interpretation of diffusion in high-diffusivity paths—a continuum approach. *Acta Metallurgica.* (1979) 27:683–91. doi: 10.1016/0001-6160(79)90019-1
- Aifantis EC. Comments on the calculation of the formation volume of vacancies in solids. *Phys Rev B.* (1979) 19:6622. doi: 10.1103/PhysRevB.19.6622
- Aifantis EC. Continuum basis for diffusion in regions with multiple diffusivity. *J Appl Phys.* (1979) 50:1334. doi: 10.1063/1.326167
- Wilson RK, Aifantis EC. On the theory of consolidation with double porosity. *Int J Eng Sci.* (1982) 20:1009–35. doi: 10.1016/0020-7225(82)90036-2
- Hill JM. A discrete random walk model for diffusion in media with double diffusivity. *ANZIAM J.* (1980) 22:58–74. doi: 10.1017/S0334270000002551
- Aifantis EC. On the problem of diffusion in solids. *Acta Mech.* (1980) 37:265–96. doi: 10.1007/BF01202949
- Kuttler K, Aifantis EC. Existence and uniqueness in nonclassical diffusion. *Q Appl Math.* (1987) 45:549–60. doi: 10.1090/qam/910461
- Santra I, Das S, Nath SK. Brownian motion under intermittent harmonic potentials. *J Phys A Math Theor.* (2021) 54:334001. doi: 10.1088/1751-8121/ac12a0
- Konstantinidis D, Eleftheriadis I, Aifantis EC. Application of double diffusivity model to superconductors. *J Mater Process Technol.* (2001) 108:185–7. doi: 10.1016/S0924-0136(00)00750-0
- Vázquez JL, Arturo P, Fernando Q, Ana R. Classical solutions and higher regularity for nonlinear fractional diffusion equations. *J Eur Math Soc.* (2017) 19:1949–75. doi: 10.4171/JEMS/710
- Rubinstein LI. *The Stefan Problem*. Translations of Mathematical Monographs. (2010).
- El-Hachem M, McCue SW, Jin W, Du Y, Simpson MJ. Revisiting the Fisher-Kolmogorov-Petrovsky-Piskunov equation to interpret the spreading-extinction dichotomy. *Proc Roy Soc A.* (2019) 475:20190378. doi: 10.1098/rspa.2019.0378
- Murray JD. *Mathematical Biology, 2nd Edn*. New York, NY: Springer-Verlag New York Inc. (1994).
- Pearson JE. Complex patterns in a simple system. *Science.* (1993) 261:189–92. doi: 10.1126/science.261.5118.189
- Nishiura H. Correcting the actual reproduction number: a simple method to estimate r_0 from early epidemic growth data. *Int J Environ Res Public Health.* (2010) 7:291–302. doi: 10.3390/ijerph7010291
- Cori A, Ferguson NM, Fraser C, Cauchemez S. A new framework and software to estimate time-varying reproduction numbers during epidemics. *Am J Epidemiol.* (2013) 178:1505–12. doi: 10.1093/aje/kwt133
- Chattopadhyay K, Choudhury D, Ghosh G, Kundu B, Nath SK. Infection kinetics of COVID-19 and containment strategy. *Scientific Rep.* (2021) 11:11606. doi: 10.1038/s41598-021-90698-2

Conflict of Interest: The authors declare that the research was conducted in the absence of any commercial or financial relationships that could be construed as a potential conflict of interest.

Publisher's Note: All claims expressed in this article are solely those of the authors and do not necessarily represent those of their affiliated organizations, or those of the publisher, the editors and the reviewers. Any product that may be evaluated in this article, or claim that may be made by its manufacturer, is not guaranteed or endorsed by the publisher.

Copyright © 2022 Chattopadhyay, Kundu, Nath and Aifantis. This is an open-access article distributed under the terms of the Creative Commons Attribution License (CC BY). The use, distribution or reproduction in other forums is permitted, provided the original author(s) and the copyright owner(s) are credited and that the original publication in this journal is cited, in accordance with accepted academic practice. No use, distribution or reproduction is permitted which does not comply with these terms.



Resource-Efficient Use of Modern Processor Architectures For Numerically Solving Cardiac Ionic Cell Models

Kristian Gregorius Hustad^{1*} and Xing Cai^{1,2}

¹Simula Research Laboratory, Oslo, Norway, ²Department of Informatics, University of Oslo, Oslo, Norway

OPEN ACCESS

Edited by:

Krasimira Tsaneva-Atanasova,
University of Exeter, United Kingdom

Reviewed by:

Luca Franco Pavarino,
University of Pavia, Italy
Mark Endrei,
The University of Queensland,
Australia

*Correspondence:

Kristian Gregorius Hustad
kghustad@simula.no

Specialty section:

This article was submitted to
Computational Physiology and
Medicine,
a section of the journal
Frontiers in Physiology

Received: 25 March 2022

Accepted: 27 April 2022

Published: 28 June 2022

Citation:

Hustad KG and Cai X (2022)
Resource-Efficient Use of Modern
Processor Architectures For
Numerically Solving Cardiac Ionic
Cell Models.
Front. Physiol. 13:904648.
doi: 10.3389/fphys.2022.904648

A central component in simulating cardiac electrophysiology is the numerical solution of nonlinear ordinary differential equations, also called cardiac ionic cell models, that describe cross-cell-membrane ion transport. Biophysically detailed cell models often require a considerable amount of computation, including calls to special mathematical functions. This paper systematically studies how to efficiently use modern multicore CPUs for this costly computational task. We start by investigating the code restructurings needed to effectively enable compiler-supported SIMD vectorisation, which is the most important performance booster in this context. It is found that suitable OpenMP directives are sufficient for achieving both vectorisation and parallelisation. We then continue with an evaluation of the performance optimisation technique of using lookup tables. Due to increased challenges for automated vectorisation, the obtainable benefits of lookup tables are dependent on the hardware platforms chosen. Throughout the study, we report detailed time measurements obtained on Intel Xeon, Xeon Phi, AMD Epyc and two ARM processors including Fujitsu A64FX, while attention is also paid to the impact of SIMD vectorisation and lookup tables on the computational accuracy. As a realistic example, the benefits of performance enhancement are demonstrated by a 10^9 -run ensemble on the Oakforest-PACS system, where code restructurings and SIMD vectorisation yield an 84% reduction in computing time, corresponding to 63,270 node hours.

Keywords: cardiac electrophysiology, ionic cell models, multicore CPUs, lookup tables (LUTs), SIMD vectorisation

1 INTRODUCTION

Computer simulation has firmly established itself as an important approach to studying cardiac electrophysiology, see e.g. Vigmond et al. (2009); Trayanova (2011). One essential component of any heart simulator is the computation of the total transmembrane *ionic current density*, conventionally denoted by I_{ion} . The importance of I_{ion} is due to its close interaction with the *transmembrane potential* v , i.e., the difference between the intra- and extracellular potentials. A coordinated evolution of $v(\vec{x}, t)$ in space and time is a prerequisite for the proper functioning of the heart. Physiologically, I_{ion} is intricately determined by various transmembrane currents through ionic channels, pumps and exchangers, even subcellular calcium handling. Thus, mathematical modeling of I_{ion} is challenging and still remains an active research field. Many cell models have been developed

over the years, where two examples of widely used cell models are the ten Tusscher–Panfilov model (see ten Tusscher and Panfilov (2006)) and the Grandi–Pasqualini–Bers model (see Grandi et al. (2010)).

The majority of the cell models take the form of a system of nonlinear first-order ordinary differential equations (ODEs) with initial conditions:

$$\frac{d\vec{s}(t)}{dt} = \vec{f}(t, \vec{s}(t)), \quad \vec{s}(0) = \vec{s}_0, \quad (1)$$

where $\vec{s}(t)$ is a vector of so-called state variables including the transmembrane potential itself, a set of individual ionic concentrations, and a set of gating variables, see e.g. Alonso et al. (2016) for a review. The evolution of $\vec{s}(t)$ determines the total transmembrane ionic current density I_{ion} , which in turn contributes to the dynamic change of v . The particular ODE inside the system in **Eq. (1)** that describes the dynamics of v has its simplest form as follows:

$$\frac{dv}{dt} = -\frac{1}{C_m} I_{\text{ion}}, \quad (2)$$

where C_m denotes the membrane capacitance. If electrophysiology is simulated over a cardiac tissue or the entire heart, then **Eq. (2)** can be incorporated into a partial differential equation (PDE) of the reaction-diffusion type, such as in the monodomain and bidomain models, see e.g. Colli Franzone et al. (2014).

1.1 Need for Huge Amounts of Computation

Many of the right-hand side functions in **Eq. (1)**, i.e., f_1, f_2, \dots, f_N , where N denotes the number of state variables of a cell model, are nonlinear and involve special mathematical functions such as the exponential, logarithmic and power functions. For example, the ten Tusscher–Panfilov model [see ten Tusscher and Panfilov (2006)] adopts $N = 19$ state variables and the authors' own C++ source code [see ten Tusscher (2021)] counts 77 calls to the exponential function and 4 calls to the logarithmic function. On a computer, these calls to the special mathematical functions will be translated into a large number of basic floating-point operations (FLOPs). For example, profiling tools have revealed that typical compilers will generate in total around 1500 FLOPs each time the 19 right-hand side functions of the ten Tusscher–Panfilov model are evaluated on a computer (see **Section 3.2**).

ODE computations can use substantial time of a heart simulator. Inside a monodomain or bidomain simulator of a cardiac tissue or an entire heart, an ODE system of form **Eq. (1)** exists “everywhere”, i.e., with the same spatial resolution as for the intra- and extracellular potential fields. For the latest simulation strategy based on the EMI (extracellular-membrane-intracellular) approach, see e.g., Tveito et al. (2017); Jæger et al. (2021a), a high spatial resolution is still needed to resolve the cell membrane surfaces, resulting in considerable computational effort needed to solve the individual ODE systems. Multiple studies have investigated how simulations using the monodomain model or the bidomain model can be scaled to thousands of compute nodes [see e.g., Niederer et al. (2011); Mirin et al. (2012); Colli Franzone et al. (2018)]. Operator splitting is typically used with the monodomain, bidomain, and EMI models

such that the non-linear ODE part is decoupled from the linear PDE part [see Clayton et al. (2011); Tveito et al. (2017)]. Thus, the performance of the ODE part, which does not require any communication, may be studied independently of the PDE part. For whole-heart simulations using the monodomain or bidomain model with reasonably accurate meshes, the number of ODE systems is in the millions, even ranging as high as 370 million [see Mirin et al. (2012)], whereas the time step is typically limited to around 25 μs [see Niederer et al. (2011)]. In other words, 40,000 time steps must be solved for each second of simulated time.

Besides the above *simulation scenario*, an *ensemble scenario* can also require solving many instances of a cell model. This is needed to study the sensitivity of a cell model with respect to its internal parameters, or to fit the model parameters with real-world cellular measurements [see e.g., Jæger et al. (2021b)]. The number of instances can easily be colossal, if the number of parameters of interest is large and/or the resolution needed to study each parameter is high.

No matter which scenario, when the required temporal/spatial/parameter resolution is high, there arises the need for numerically solving a large number of ODE system instances over a large number of time steps. This can lead to a gargantuan amount of computing time even on a supercomputer. The present paper thus aims to investigate how the modern multicore CPU architectures can be efficiently used for this purpose.

1.2 Need for Effective Use of Modern Processor Architectures

The primary design goal of a modern multicore CPU is to execute FLOPs fast. This is in principle a good match with numerically solving cardiac ionic cell models, which typically have a high computational intensity, i.e., the number of FLOPs executed per byte of memory traffic. Effective utilisation of the floating-point capability of a multicore CPU requires employing all the processor cores while each delivers a sizeable portion of its theoretical peak floating-point performance. Achieving the latter is not straightforward, because it requires each processor core to execute, most of the time, in a single-instruction-multiple-data (SIMD) style. The individual ODE system instances, in both simulation and ensemble scenarios, can be computed independently and thus readily offer parallelisation across the processor cores. However, inappropriate data structures, memory access patterns and/or code structure can seriously limit or even prohibit SIMD vectorisation. This important topic will be addressed in **Section 2.3**.

Executing FLOPs using SIMD vectorisation alone does not necessarily lead to the best computing speed. Another concern is the necessity of the FLOPs. Modern compilers are good at common subexpression elimination, thus avoiding unnecessary repetitions of FLOPs, but they are unable to decide the most economical way of evaluating the special mathematical functions. A classical method is to pre-evaluate a costly function for a certain value range and resolution, and store these pre-computed values in a *lookup table*. Later evaluations of the function are then replaced by reading (approximate) values from the table. The number of arithmetic operations is reduced at the cost of extra memory usage by the lookup table itself and extra memory traffic

due to repeatedly accessing the lookup table. Moreover, using lookup tables may prohibit a compiler from vectorising the other parts of the computation. **Section 2.4** will thus discuss the considerations and programming details about lookup tables.

The contribution of this paper is not about devising new ODE solvers with lower algorithmic complexity, higher accuracy or better stability. Instead, our approach to getting fast computing speed is rooted in a resource-efficient usage of modern multicore processor architectures. We discuss the code restructurings that are needed to help modern compilers automatically enable SIMD vectorisation. The speed improvement due to vectorisation is thoroughly investigated by both time measurements and profiling. To our knowledge, these aspects have not been systematically studied in the literature.

Another novelty of this paper is a deep dive into the pros and cons of using lookup tables, where we also study some related programming nuances. Although a number of choices concerning the trade-off between accuracy and speed may be considered when using lookup tables, we have devoted our attention to the programming details. We report accuracy results to verify the correctness of our implementation and contrast with the error associated with the use of SIMD vectorisation.

The ODE models used in this paper for performance study in **Section 3** are realistic cardiac ionic cell models (see **Table 1**), whereas we have only adopted the simplest ODE solvers. The rationale is that more sophisticated ODE solvers often use simple ODE solvers as the building blocks. Thus, a thorough understanding of how to obtain hardware resource efficiency for simple ODE solvers is readily extended to the wealth of advanced ODE solvers.

The remainder of this paper is organised as follows. **Section 2.1** briefly explains the basic steps of implementing ODE solvers, including directive-based parallelisation. **Section 2.2** points out the inefficiency of naïvely implemented ODE solvers. **Section 2.3** carefully examines the topic of SIMD vectorisation on modern multicore processors. **Section 2.4** is devoted to the details of using lookup tables as an alternative to getting fast computing speed. **Section 2.5** demonstrates how SIMD vectorisation and lookup tables can be combined. Thereafter, **Section 3** contains an extensive set of numerical experiments about the benefits due to, respectively, SIMD vectorisation and lookup tables. The topic of accuracy also receives close attention in **Section 3**. Finally, **Section 4** comments on the related work and provides some concluding remarks.

2 SIMD VECTORISATION AND LOOKUP TABLES FOR DELIVERING PERFORMANCE

As argued in **Section 1.1**, huge amounts of computation may arise from numerically solving many instances of a cell model, in both simulation and ensemble scenarios. At the same time, as discussed in **Section 1.2**, utilising the computational potential of modern processors can be non-trivial. This section thus aims to investigate two strategies for enhancing the performance of typical solvers of a cell model, specifically, use of SIMD

vectorisation and lookup tables. We will start with explaining the basic steps of implementing an ODE solver, for the purpose of setting the programming scene needed to dive into the two strategies.

2.1 Basic Steps of Implementing an ODE Solver

The basic steps of implementing an ODE solver are largely generic, such that automated code generation can allow an easy plug-and-play of the solution strategy and cell model, while keeping manual coding to a minimum level. We will use as an illustrating example the simplest ODE solver, namely, the forward Euler method. This choice is motivated by both its simplicity and its relevance as building blocks in many advanced ODE solvers. Simplicity is also the reason for choosing, later in this section, the FitzHugh-Nagumo cell model [see FitzHugh (1961); Nagumo et al. (1962)] that has only two state variables, for the ease of presentation. We remark that the same (automated) programming process applies to other ODE solvers and cell models.

Specifically, to numerically solve a system of ODEs in the form of **Eq. (1)**, the computational work per time step of the forward Euler (FE) method is as follows:

$$\vec{s}(t_{\ell+1}) \approx \vec{s}(t_{\ell}) + \Delta t \cdot \vec{f}(t_{\ell}, \vec{s}(t_{\ell})). \quad (3)$$

This simple numerical scheme only requires evaluating the right-hand functions \vec{f} with the latest state variables. The downside of FE is that it may require a very small time step size $\Delta t = t_{\ell+1} - t_{\ell}$, and thereby a tremendous number of steps, to produce a stable solution of a stiff ODE system.

2.1.1 Algorithmic Skeletons

The algorithmic skeleton for solving individual ODE system instances in a simulation scenario will differ from that in an ensemble scenario (see **Section 1.1**). Suppose the computational work of an ODE solver (e.g., FE) per time step is coded as a subroutine named `COMPUTE_ODE_STEP($\vec{s}, t, \Delta t$)`, these two algorithmic skeletons can be found, respectively, in **Algorithm 1** and **Algorithm 2**. Moreover, a realistic simulation scenario can also have a PDE component per time step, due to operator splitting used for solving e.g. the monodomain or bidomain equations. This is shown in **Algorithm 3** where the v values from all the cells are jointly updated per time step additionally to accommodate the PDE contribution.

Algorithm 1. Simple skeleton for the simulation scenario (outer loop over time).

```

1:  $t \leftarrow T_{\text{start}}$ 
2: while  $t < T_{\text{end}}$  do
3:   for each cell  $i$  do
4:     call COMPUTE_ODE_STEP( $\vec{s}_i, t, \Delta t$ )
5:   end for
6:    $t \leftarrow t + \Delta t$ 
7: end while

```

Algorithm 2. Simple skeleton for the ensemble scenario (outer loop over cells).

```

1: for each cell  $i$  do
2:    $t \leftarrow T_{\text{start}}$ 
3:   while  $t < T_{\text{end}}$  do
4:     call COMPUTE_ODE_STEP( $\vec{s}, t, \Delta t$ )
5:      $t \leftarrow t + \Delta t$ 
6:   end while
7: end for

```

Algorithm 3. Operator-splitting skeleton for the simulation scenario (outer loop over time).

```

1:  $t \leftarrow T_{\text{start}}$ 
2: while  $t < T_{\text{end}}$  do
3:   for each cell  $i$  do
4:     call COMPUTE_ODE_STEP( $\vec{s}, t, \Delta t$ )
5:   end for
6:   Gather the  $v$  value from each cell to form a vector  $\vec{v}$ 
7:   call COMPUTE_PDE_STEP( $\vec{v}, \vec{v}_{\text{new}}, t, \Delta t$ )
8:    $t \leftarrow t + \Delta t$ 
9:   Scatter the values of vector  $\vec{v}_{\text{new}}$  to the corresponding cells
10: end while

```

2.1.2 Automated Code Generation

Mathematical models of the ionic current density are typically very complex, involving many parameters and internal variables. Manual coding of COMPUTE_ODE_STEP, which is needed in any of the algorithmic skeletons, can therefore be nontrivial and error-prone. Here, two factors support an approach of automated code generation. First, most ODE solution strategies are generic and independent of a specific cell model. Second, the research community has developed several domain-specific standards to facilitate sharing of the existing cell models, thus offering standardised input to automated code generators. One such open standard is the CellML language [see Cuellar et al. (2003)] based on XML. The benefits of automation include avoidance of human programming errors, a flexible choice of the programming language for the generated code, and easy experimentation with different cell models.

As an example, we will show in **Listing 2** a piece of auto-generated code that implements a single FE step for the two-variable FitzHugh-Nagumo (FHN) cell model [see FitzHugh (1961); Nagumo et al. (1962)]:

$$\begin{aligned}
 \frac{dv}{dt} &= v(v - \alpha)(1 - v) - w + I_{\text{stim}}, \\
 \frac{dw}{dt} &= \varepsilon(v - \gamma w),
 \end{aligned}
 \quad I_{\text{stim}} = \begin{cases} -80 & 0 \leq t \leq 0.5, \\ 0 & \text{otherwise,} \end{cases}$$

(4)

where v and w are state variables, and α , ε and γ are model parameters. Correspondingly, **Listing 1** contains two assisting enum types that are used instead of integer literals when indexing arrays in order to improve readability. The FHN model is used in code listings in this section due to its simplicity. The results presented in **Section 3** use the more realistic models listed in **Table 1**.

Listing 1: Auto-generated enum declarations for the FHN model.

```

enum state {
    STATE_V,    // = 0
    STATE_w,    // = 1
    NUM_STATES, // = 2
};

enum parameter {
    PARAM_alpha,    // = 0
    PARAM_epsilon,  // = 1
    PARAM_gamma,    // = 2
    NUM_PARAMS,     // = 3
};

```

Listing 2: Auto-generated code of one FE step applied to the FHN model.

```

void FHN_step_FE_single(double *_restrict states, const double t,
                        const double dt, const double *_restrict parameters)
{
    // Assign states
    const double V = states[STATE_V];
    const double w = states[STATE_w];

    // Assign parameters
    const double alpha = parameters[PARAM_alpha];
    const double epsilon = parameters[PARAM_epsilon];
    const double gamma = parameters[PARAM_gamma];

    // Expressions for the Main component
    const double I = (t <= 0.5 && t >= 0. ? -80. : 0.);
    const double dV_dt = -w + (1. - V) * (-alpha + V) * V + I;
    states[STATE_V] = dt * dV_dt + V;
    const double dw_dt = epsilon * (-gamma * w + V);
    states[STATE_w] = dt * dw_dt + w;
}

```

The C code in **Listing 2** is auto-generated by Gotran [see Hake et al. (2020)]: a code generation framework for cell models and the associated ODE solvers. The input format of the FHN model can be found at the CellML website [see CellML (2022)].

2.1.3 Shared-Memory Parallelisation Using OpenMP

The need for parallelisation arises when the number of ODE system instances involved in a simulation or ensemble scenario is large. For both cases, parallelisation is straightforward because the ODE system instances can be computed independently. An automated code generator, such as Gotran, can easily create a subroutine that uses OpenMP directives for this purpose. **Listing 3** is such an example, which loops over a collection of cells and invokes FHN_step_FE_single (implemented in **Listing 2**) for each cell. The code in **Listing 3** is typically used in a simulation scenario, wrapped within an outer loop over time.

Listing 3: Example of OpenMP parallelisation (simulation scenario).

```

void FHN_step_FE_naive(double *_restrict states, const double t,
                      const double dt, const double *_restrict parameters,
                      int num_cells)
{
    #pragma omp parallel for
    for (int i = 0; i < num_cells; i++) {
        /* use pointer arithmetic to pass disjoint parts of the states
         * array for each cell */
        FHN_step_FE_single(states + i * NUM_STATES, t, dt, parameters);
    }
}

```

2.2 Issues of Inefficiency

The auto-generated code shown in **Listings 2** and **3** can be readily used in any simulation scenario. A corresponding version of **Listing 3** for an ensemble scenario can also easily be auto-generated. Switching to another cell model and/or a different explicit ODE solver will in general pose no challenge. Thanks to the automated insertion of OpenMP directives, the generated code can use all the CPU cores of a shared-memory system. **Listings 2** and **3** can also be used without change inside a distributed-memory parallel monodomain or bidomain simulator. (Here, we assume that each MPI process is assigned with a partition of the cells.)

However, we can only label the above auto-generated code as naïve, because the obtained performance will be considerably lower than the ideally achievable level. The main reason is the inability of compilers to enable SIMD vectorisation for this code. Specifically, the first argument to function `FHN_step_FE_single` in **Listing 2** assumes that the N state variables for each cell are stored contiguously in memory. This means that the state variables of all the cells are stored logically as an “array of structs”, as used by **Listing 3**. Although such a data structure makes sense by grouping the state variables of each cell, the downside is that compiler-supported SIMD vectorisation will fail completely. Code restructuring needed for auto-vectorisation will be addressed in **Section 2.3**, whereas the potential performance benefits of using lookup tables will be the topic of **Section 2.4**.

2.3 SIMD Vectorisation

2.3.1 Computing with Vectors

Modern CPUs use special registers and instructions for SIMD vectorised operations. For example, the AVX-512 vector instruction set provides 512-bit vectors, so that eight double-precision (64-bit) floating-point numbers may be stored together in a vector register, and arithmetic operations such as addition and multiplication can be performed simultaneously to all the numbers stored in these vectors. To efficiently read and store vector registers, the content of a vector should lie *contiguously* and *aligned* in memory. The latter means that the start address of the vector in memory is a multiple of the vector width.

Conceptually, simultaneous solution of multiple instances of the same cell model suits perfectly for SIMD vectorisation. This is because the identical computation takes place in the different cells, i.e., the same operations are applied to different values. The rare situation of conditional branching (e.g., the outcome of an `if` test depends on the actual value of a state variable) can also be vectorised through masking. In the following, we will discuss how to restructure the auto-generated naïve code, so that compilers can automatically

carry out the SIMD vectorisation, by using suitable compiler options/hints and vectorised math libraries.

2.3.2 Restructuring for Optimal Memory Layout

As discussed in **Section 2.2**, the auto-generated naïve code (as shown in **Listings 2** and **3**) adopts a natural but vectorisation-unfriendly data structure, where the state variables of each cell are stored contiguously in memory. For effective use of the vector registers, a vectorisation-friendly data structure should let the same state variable from all the cells be stored contiguously. The entire data structure thus has the layout of a “struct of arrays”. To guarantee memory alignment, each state-variable array may need to be padded. Suppose the number of cells is C , the number of no-use 64-bit values padded at the end of each array can be calculated as $8 - \text{modulo}(C, 8)$ for the case of 512-bit vector width. In practice, all the state-variable arrays (with padding) are concatenated into a very long 1D array. This can be seen in **Listing 4**.

2.3.3 Compiler-Supported Auto Vectorisation for the Simulation Scenario

When the memory-related code restructuring is done, SIMD vectorisation can be automatically enabled by a compiler. There are multiple ways of providing vectorisation hints to a C compiler, but we will focus on the `simd` construct of OpenMP as it is supported by all the major compilers. (The code examples given in this paper require OpenMP version 4.5 or newer.) In **Listing 3**, we used the compiler directive of `#pragma omp parallel for` to parallelise the for loop. **Listing 4** shows a modified version based on a restructured SIMD-friendly data layout, where we have also added the necessary compiler hints to enable auto-vectorisation. Specifically, the additional `simd` clause suggests to the compiler that multiple iterations of the loop could be computed together as a vector.

The `simd` clause may be followed by additional clauses: The `simdlen` clause specifies the preferred number of lanes per SIMD vector. In the following code listings, we assume that the user has defined the constant `VECTOR_LENGTH` which is passed as the argument to `simdlen`. The `aligned` clause can be used to provide information about the alignment of arrays, so that the compiler can employ aligned vector load/store instructions.

When using the Clang compiler, however, specifying only OpenMP pragmas does not lead to successful vectorisation, because Clang is unable to prove that vectorisation can safely be applied. We therefore specify an additional Clang-specific pragma, see **Listing 4**, where we instruct the compiler to assume memory safety, relieving Clang of the requirement to prove that there are no overlapping memory accesses. For the sake of brevity, we only show the vectorisation hints based on OpenMP in the remaining listings.

Listing 4: Step function for the FitzHugh-Nagumo model (simulation scenario) with SIMD-friendly data layout restructuring.

```
void FHN_step_FE(double *__restrict states, const double t,
                const double dt, const double *__restrict parameters,
                const long num_cells, const long padded_num_cells)
{
    #pragma omp parallel
    {
        // Assign parameters
        const double alpha = parameters[PARAM_alpha];
        const double epsilon = parameters[PARAM_epsilon];
        const double gamma = parameters[PARAM_gamma];

        #if defined(HINT_CLANG_SIMD)
            #pragma omp for
            #pragma clang loop vectorize(assume_safety)
        #elif defined(HINT_OMP_SIMD)
            #pragma omp for simd aligned(states : ALIGNMENT_BYTES) \
                simklen(VECTOR_LENGTH)
        #else
            #pragma omp for
        #endif

        for (long i = 0; i < num_cells; i++) {
            // Assign states
            const double V = states[STATE_V * padded_num_cells + i];
            const double w = states[STATE_w * padded_num_cells + i];

            // Compute FE step
            const double I = (t <= 0.5 && t >= 0. ? -80. : 0.);
            const double dV_dt = -w + (1. - V) * (-alpha + V) * V + I;
            states[STATE_V * padded_num_cells + i] = dt * dV_dt + V;
            const double dw_dt = epsilon * (-gamma * w + V);
            states[STATE_w * padded_num_cells + i] = dt * dw_dt + w;
        } // end of parallel region
    }
}
```

2.3.4 Compiler-Supported Auto Vectorisation for the Ensemble Scenario

The `simd` OpenMP clause works best when applied to the inner loop. In case the outer loop is over the cells, vectorisation becomes more complicated as the compiler will have to perform *outer loop vectorisation*. **Listing 5** shows how to restructure the code in the ensemble scenario to enable auto vectorisation. When the loops are structured in this manner with cells in the outer loop and time in the inner loop (we refer to this loop structure as Cell–Time), we minimise memory traffic, as the parameters and state variables can easily fit in cache between two time steps. Furthermore, expressions that are not a function of the state variables or time will not change between time steps and can therefore be reused such that the total amount of computation is reduced. Since the number of iterations in the inner loop over time (i.e., the number of time steps) is the same for all cells, outer loop vectorisation can safely be applied in this scenario. However, we observed that only the Intel compiler was able to perform vectorisation for the function in **Listing 5**. We therefore investigated two alternative loop structures in order to achieve vectorisation with the other compilers.

Listing 6 uses a Time–Cell loop structure similar to the simulation scenario, with the difference being that the parameters are no longer shared between all cells. This loop structure can lead to very high memory traffic, because all parameters must be read and all state variables read and written for each inner iteration in the loop. The three code blocks following the comments “Assign parameters”, “Assign states”, and “Compute FE step” are the same as in **Listing 5** and were omitted for brevity.

If we solve the model for smaller batches of cells, we facilitate caching of both arrays and reduce the memory traffic. **Listing 7**

shows a Cell–Time–Cell loop structure where the outermost loop divides the work into batches that are mapped to different OpenMP threads with the “parallel for” directive, and then the middle loop iterates over time, whereas the innermost loop iterates over the elements in a batch. We should choose the batch size to be a multiple of the hardware SIMD vector length, and the batch size is here controlled *via* a compile-time defined constant `VECTOR_LENGTH`. In practice, all vector lengths are a power of 2, so $2^5 = 32$ would be a reasonable choice of batch size that would work well on any CPU. Note that some extra bookkeeping is needed to handle the case where the total number of cells does not evenly divide the batch size. The performance of the different loop structures is discussed in **Section 3.4**.

Listing 5: Cell–Time loop structure in FE solution of the FitzHugh-Nagumo model (ensemble scenario) with SIMD-friendly data layout restructuring.

```
void FHN_solve_FE_ensemble_CT(double *__restrict states,
                              const double t_start, const double dt,
                              const double *__restrict parameters, const long num_cells,
                              const long padded_num_cells, const int num_timesteps)
{
    #pragma omp parallel for simd aligned(states : ALIGNMENT_BYTES) \
        simklen(VECTOR_LENGTH)
    for (long i = 0; i < num_cells; i++) {
        // Assign parameters
        const double alpha =
            parameters[PARAM_alpha * padded_num_cells + i];
        const double epsilon =
            parameters[PARAM_epsilon * padded_num_cells + i];
        const double gamma =
            parameters[PARAM_gamma * padded_num_cells + i];

        double t = t_start;
        for (int ti = 0; ti < num_timesteps; ti++) {
            // Assign states
            const double V = states[STATE_V * padded_num_cells + i];
            const double w = states[STATE_w * padded_num_cells + i];

            // Compute FE step
            const double I = (t <= 0.5 && t >= 0. ? -80. : 0.);
            const double dV_dt = -w + (1. - V) * (-alpha + V) * V + I;
            states[STATE_V * padded_num_cells + i] = dt * dV_dt + V;
            const double dw_dt = epsilon * (-gamma * w + V);
            states[STATE_w * padded_num_cells + i] = dt * dw_dt + w;

            t += dt;
        } // end of for loop over time
    } // end of for loop over cells
}
```

Listing 6: Time–Cell loop structure in FE solution of the FitzHugh-Nagumo model (ensemble scenario) with SIMD-friendly data layout restructuring.

```
void FHN_solve_FE_ensemble_TC(double *__restrict states,
                              const double t_start, const double dt,
                              const double *__restrict parameters, const long num_cells,
                              const long padded_num_cells, const int num_timesteps)
{
    double t = t_start;
    for (int ti = 0; ti < num_timesteps; ti++) {
        #pragma omp parallel for simd aligned(states:ALIGNMENT_BYTES) \
            simklen(VECTOR_LENGTH)
        for (long i = 0; i < num_cells; i++) {
            // Assign parameters (code block omitted, see Listing 5)
            // Assign states (code block omitted, see Listing 5)
            // Compute FE step (code block omitted, see Listing 5)
        } // end of for loop over cells
        t += dt;
    } // end of for loop over time
}
```


Listing 7: Cell–Time–Cell loop structure in FE solution of the FitzHugh–Nagumo model (ensemble scenario).

```
void FHN_solve_FE_ensemble_CTC(double *_restrict states,
    const double t_start, const double dt,
    const double *_restrict parameters, const long num_cells,
    const long padded_num_cells, const int num_timesteps)
{
    // spread work across threads in outer loop over (chunks of) cells
    #pragma omp parallel for
    for (long v = 0; v < num_cells; v += VECTOR_LENGTH) {
        long v_len = VECTOR_LENGTH;
        // ensure that v + v_len <= num_cells
        if (v + v_len > num_cells)
            v_len = num_cells - v;
        double t = t_start;
        for (int ti = 0; ti < num_timesteps; ti++) {
            // annotate inner loop over chunk/vector with simd hints
            #pragma omp simd aligned(states : ALIGNMENT_BYTES) \
                simdlen(VECTOR_LENGTH)
            for (long i = v; i < v + v_len; i++) {
                // Assign parameters (code block omitted, see Listing 5)
                // Assign states (code block omitted, see Listing 5)
                // Compute FE step (code block omitted, see Listing 5)
            } // end of vectorised for loop over cells
            t += dt;
        } // end of for loop over time
    } // end of for loop over cells
}
```

2.3.5 Using Vectorised Math Libraries

The cell models often involve calls to the exponential function (`exp`), the logarithmic function (`log`), and the power function (`pow`). The `expm1` function is also relevant in the context of some numerical schemes that require evaluating $e^x - 1$ where x may be close to zero, in which case `exp(x) - 1` is prone to rounding errors and `expm1(x)` produces more accurate results. In the standard C library, these are defined as functions with a scalar input and output, but we need to evaluate these functions on all the elements in a vector simultaneously to achieve SIMD. Fortunately, there are vectorised math libraries that provide C functions that use SIMD instructions to evaluate these math functions for selected vector lengths.

Intel's Short Vector Math Library (SVML) and the GNU C library, *glibc*, both provide vectorised versions of the relevant math functions for the x86 instruction set. Shibata and Petrogalli [see Shibata and Petrogalli (2020)] developed a vector math library, *SLEEF*, that supports the ARMv8 instruction set in addition to x86. There are also other vector math libraries, but these three libraries all integrate with compiler auto-vectorisation when used with a compatible compiler.

As vectorised implementations of `expm1` are not available for all libraries, we have used a preprocessor macro to control whether `expm1(x)` or `(exp(x) - 1)` is used. `expm1(x)` is used in the naïve implementations, and `(exp(x) - 1)` is used in all vectorised code unless otherwise stated.

We should note that the libraries vary slightly in the accuracy to which the functions are evaluated, and the instructions used (and thereby the total number of floating point operations) may also vary. Our goal in this study is not to compare the vector math libraries, but they are a necessary component when using auto-vectorisation on cell models that contain calls to math functions. When studying the

performance and accuracy of cell models, we will therefore have to consider the influence of the math libraries used. Time measurements of using vectorised math libraries, as well as an accuracy analysis will be provided in **Section 3.3**.

2.3.6 Explicit Control of the Vector Length

In some instances, the compiler may generate instructions with a shorter vector length than the maximal supported vector length, often resulting in sub-optimal performance. There are mechanisms that allow the user to instruct the compiler to target a specific vector length, but the exact mechanism varies for each compiler. For the Intel compiler on Oakbridge (see **Table 2**), we observed that 256-bit vectors would be used by default when targeting the Cascade Lake CPU, although the hardware vector length is 512 bits. When we appended `simdlen(8)` to the `simd` clause, the compiler would instead use 512-bit instructions (8 SIMD lanes with 64-bit floating-point values). For GCC, the flag `-mprefer-vector-width=512` can be used to the same effect.

For the Fujitsu compiler on Wisteria, we pass the flags `-msve-vector-bits=512` and `-ffj-interleave-loop-insns=4`. The second flag instructs the compiler to interleave 4 iterations of the loop such that 4×8 cells are processed in parallel in each OpenMP thread. Interleaving loop iterations increases the amount of instruction-level parallelism at the cost of an increased register pressure, which seems to be very beneficial on the A64FX CPU with somewhat higher latencies for arithmetic instructions than the CPUs found in the other systems. We found that interleaving 4 loop iterations yielded the best performance on Wisteria.

2.4 Lookup Tables

The rationale for using *lookup tables* is to reduce the amount of computation, by repeatedly referring to tables of pre-computed values. Most cell models contain a number of expressions that are functions of the transmembrane potential v , so these expressions may be pre-evaluated for a chosen sampling of the expected v values, before the ODE solution procedure. For instance, we may assume $v \in [-100 \text{ mV}, 50 \text{ mV}]$ in the healthy heart, and we can thus pre-evaluate the expressions at equally spaced points in this interval with a resolution of v_{step} . Expressions that are a function of more than one state variable are usually not considered for using lookup tables, because the memory footprint (and setup cost) of the tables grows exponentially with the number of input variables.

Let $f(v)$ denote an expression that depends on v and assume that a lookup table has been pre-computed for the interval $[v_{\min}, v_{\max}]$ with resolution v_{step} . When the lookup table is later repeatedly used, the actual v values may not coincide with the pre-chosen sampling values. Suppose a particular v value lies between two consecutive sampling points: $v_a \leq v < v_b = v_a + v_{\text{step}}$. The typical strategy is to use a linear interpolation by computing $w_a = \frac{v_b - v}{v_{\text{step}}}$ and $w_b = 1 - w_a$, and then use $w_a \cdot f(v_a) + w_b \cdot f(v_b)$ as the approximation of $f(v)$. The two values of $f(v_a)$ and $f(v_b)$ are fetched from the pre-computed lookup table that is stored in memory. Note that if multiple expressions use the same input variable, the weights w_a and w_b remain the same for all these expressions. For memory efficiency, the pre-evaluated values of

TABLE 1 | Cell models used in the numerical experiments of this paper. The “FLOPs” column lists the number of floating-point operations required to compute a single time step for a naïve implementation using the Forward Euler scheme. **Section 3.2** describes how performance counters were used to obtain the operation counts.

Model	Name	State variables	FLOPs	References
ten Tusscher–Panfilov (2006)	TP06	19	1500	ten Tusscher and Panfilov (2006)
Jæger–Tveito (2021)	JT21	25	1322	Jæger et al. (2020, 2021a)
Grandi–Pasqualini–Bers (2010)	GPB	39	2149	Grandi et al. (2010)

TABLE 2 | Hardware specifications (compute node level) of the five target platforms. ISA is an abbreviation of “instruction set architecture”.

Name	CPU	ISA	SIMD width (bits)	Memory	Peak memory bandwidth
Oakforest	1 × Intel Xeon Phi 7250 Peak performance: 3 TFLOPS	x86-64	512	16 GiB MCDRAM + 96 GiB DDR4	MCDRAM: > 400 GB/s DDR4: 125 GB/s
Oakbridge	2 × Intel Xeon Platinum 8280 Peak performance: 4.8 TFLOPS	x86-64	512	192 GiB DDR4	281 GB/s
Wisteria	1 × Fujitsu A64FX Peak performance: 3.4 TFLOPS	ARM v8.2-A	512	32 GiB HBM	1024 GB/s
Milan	2 × AMD EPYC 7763 Peak performance: 5.0 TFLOPS	x86-64	256	2 TiB DDR4	410 GB/s
ThunderX2	2 × Cavium ThunderX2 CN9980 Peak performance: 1.0 TFLOPS	ARM v8.1-A	128	1 TiB DDR4	341 GB/s

TABLE 3 | Compiler flags used to enable auto-vectorisation.

Compiler	Version	System	Flags
ARMClang	21.0	ThunderX2	-O3 -fopenmp -ffast-math -fsimdmath -fno-math-errno
Fujitsu	4.7.0	Wisteria	-Nclang -Ofast -fopenmp
GCC	11.1.0	Milan	-O3 -fopenmp -ffast-math -march=native
Intel	19.1.3.304	Oakbridge/ Oakforest	-O3 -qopenmp -fp-model fast=2 -march=native

these expressions can be collected as a large 2D table where each column corresponds to one expression.

2.4.1 The Rush–Larsen Scheme and Lookup Tables

When solving stiff ODE systems, the forward Euler scheme may require a very small Δt in order to maintain stability. Rush and Larsen [see Rush and Larsen (1978)] proposed the use of an exponential integrator for the gate variables, which are governed by quasi-linear equations on the form:

$$\frac{dw}{dt} = \frac{w_{\infty}(v) - w}{\tau_w(v)}, \quad (5)$$

where w_{∞} and τ_w are functions of the transmembrane potential. Let v_i denote the latest computed transmembrane potential. If v is assumed to be constant when updating w , Eq. (5) becomes a linear ODE with an analytical solution:

$$w(t_i + \Delta t) = [w(t_i) - w_{\infty}(v_i)]e^{-\Delta t/\tau_w(v_i)} + w_{\infty}(v_i). \quad (6)$$

The Rush–Larsen scheme (RL) applies Eq. (6) to all the gating equations, whereas the FE scheme in Eq. (3) is used for the remaining equations.

When using lookup tables in the context of RL, it is convenient to rewrite Eq. (6) on the form:

$$w(t_i + \Delta t) = a(v_i) \cdot w(t_i) + b(v_i), \quad (7)$$

where $a(v_i)$ and $b(v_i)$ are two pre-tabulated expressions:

$$a(v_i) = e^{-\Delta t/\tau_w(v_i)}, \quad (8)$$

$$b(v_i) = -w_{\infty}(v_i)[e^{-\Delta t/\tau_w(v_i)} - 1]. \quad (9)$$

Sundnes et al. [see Sundnes et al. (2009)] showed that the RL scheme can be generalised to equations that are not quasi-linear by performing an additional linearisation step. This leads to a first-order accurate generalised Rush–Larsen scheme, which we will simply refer to as GRL1. Both RL and GRL1 schemes will be used in the numerical experiments later.

2.4.2 Memory Layout of a Multi-Expression Lookup Table

A lookup table containing M expressions evaluated at S points, can be represented as an $S \times M$ array in memory. This choice of memory layout suits well for the row-major storage scheme used by the C programming language. To find linear interpolations of the M expressions with the same input

TABLE 4 | Single-threaded performance of scalar and vectorised math library calls. The units for the Scalar and SIMD columns is millions of function evaluations per second.

System	Function	Scalar	SIMD	Speedup
Oakbridge	exp	261.0	760.6	2.91
Oakbridge	expm1	167.4	648.8	3.88
Oakbridge	log	202.4	663.6	3.28
Oakbridge	pow	83.4	427.1	5.12
Oakforest	exp	43.9	260.0	5.92
Oakforest	expm1	23.7	223.4	9.44
Oakforest	log	38.5	247.1	6.41
Oakforest	pow	13.9	103.9	7.50
Milan	exp	91.7	743.6	8.11
Milan	expm1	151.8	138.3	0.91
Milan	log	73.9	583.6	7.89
Milan	pow	26.8	159.7	5.96
Wisteria	exp	85.6	633.1	7.40
Wisteria	expm1	25.3	24.3	0.96
Wisteria	log	79.1	534.7	6.76
Wisteria	pow	16.4	113.4	6.92
ThunderX2	exp	88.4	123.0	1.39
ThunderX2	expm1	45.6	27.1	0.59
ThunderX2	log	64.8	102.9	1.59
ThunderX2	pow	25.6	22.6	0.88

variable, we need to extract two consecutively tabulated values for each expression. Accessing two consecutive rows of the tabulated values (when the table is $S \times M$) is much more efficient than accessing two columns that are not contiguous in memory (if the table is $M \times S$).

We have implemented the ten Tusscher–Panfilov (TP06) model [see ten Tusscher and Panfilov (2006)] using lookup tables. Our selection of tabulated expressions is based on the implementation found in the openCARP cardiac simulator [see Plank et al. (2021)], which also makes use of the RL scheme. In total 12 out of the 19 state variables are gating variables that can be solved with Eq. (7). Eleven of the gating variables are functions of v , and the last one is a function of Ca_{ss} (free diadic subspace calcium concentration). We have therefore created one lookup table for the 11 expressions related to v and another table for Ca_{ss} . The v table also contains 6 expressions that appear on the right hand side of the equations for the non-gating variables.

2.5 Combining SIMD Vectorisation and Lookup Tables

Reconciling the scattered memory access patterns arising from the use of lookup tables with the need for contiguous memory accesses for effective use of SIMD vectorisation is non-trivial. We propose a partitioned method for the TP06 model where lookup tables are used for the 12 gating variables, and the non-gating variables are computed using SIMD vectorisation. The rationale for this partitioned method is that computing the gating equations using lookup tables is very effective. Specifically, updating each gating variable requires only eight FLOPs: two FLOPs for Eq. (7), in addition to the three FLOPs required for the linear interpolation of each of the two pre-tabulated expressions (a and b). Listing 8 shows the code skeleton with two inner loops.

Listing 8: Combined use of SIMD vectorisation and lookup tables when solving the ten Tusscher–Panfilov model with the RL scheme (simulation scenario).

```
void TP06_solve_RL_SIMD_LUT(double *_restrict states, const double t,
    const double dt, const double *_restrict parameters,
    const long num_cells, const long padded_num_cells, LUT *lut_V,
    LUT *lut_Ca_ss)
{
    // spread work across threads in outer loop over (chunks of) cells
    #pragma omp parallel for
    for (long v = 0; v < num_cells; v += VECTOR_LENGTH) {
        // declare and initialise v_len (see Listing 7)

        // save old values of V and Ca_ss (input variables for LUT)
        double V_old[VECTOR_LENGTH], Ca_ss_old[VECTOR_LENGTH];
        memcpy(V_old, &states[STATE_V * padded_num_cells + v],
            sizeof(double) * v_len);
        memcpy(Ca_ss_old, &states[STATE_Ca_ss * padded_num_cells + v],
            sizeof(double) * v_len);

        /* update non-gating variables with SIMD vectorisation
         * (including V and Ca_ss) */
        #pragma omp simd aligned(states : ALIGNMENT_BYTES) \
            simdlen(VECTOR_LENGTH)
        for (long i = v; i < v + v_len; i++) {
            // Assign parameters
            // Assign states
            // Compute RL step for non-gating variables
        }

        // update gating variables with LUT
        for (long i = v; i < v + v_len; i++) {
            // Assign states (only gating variables)
            /* Use previously saved values of V and Ca_ss to map into
             * rows in the lookup table */
            // Compute RL step for gating variables
        }
    } // end of outer for loop over cells
}
```

TABLE 5 | Maximum error of vectorised math library calls when evaluating input values in the prescribed ranges. The error is reported in units of least precision (ULPs).

Function (value range)	exp (−700, 700)	expm1 (−700, 700)	log (10^{-300} , 10^{300})	pow (−30, 30) × (−30, 30)
Oakbridge	2.623	2.753	1.496	0.998
Oakforest	1.471	2.008	1.276	1.035
Milan	2.623	0.735	1.343	0.998
Wisteria	1.923	0.753	1.343	1.62×10^{13}
ThunderX2	2.313	0.992	1.883	0.998

TABLE 6 | Single-threaded performance of naïve and auto-vectorised implementations. The FE scheme is used; $C = 11688851$ cells. “SoA” refers to the “struct of arrays” memory layout discussed in **Section 2.3.2**.

System	Model	Throughput ($10^6 \cdot \frac{\text{cell steps}}{\text{second}}$)			Speedup	
		Naïve	SoA	SIMD	SIMD naïve	SIMD SoA
Oakbridge	TP06	2.917	3.039	15.070	5.2	5.0
Oakbridge	JT21	3.622	3.559	17.970	5.0	5.0
Oakbridge	GPB	2.039	2.047	8.204	4.0	4.0
Oakforest	TP06	0.499	0.525	4.081	8.2	7.8
Oakforest	JT21	0.645	0.651	5.116	7.9	7.9
Oakforest	GPB	0.351	0.406	3.526	10.0	8.7
Milan	TP06	1.186	1.336	5.910	5.0	4.4
Milan	JT21	1.590	1.624	6.712	4.2	4.1
Milan	GPB	1.094	1.103	4.073	3.7	3.7
Wisteria	TP06	0.578	0.694	6.604	11.4	9.5
Wisteria	JT21	0.532	0.871	7.649	14.4	8.8
Wisteria	GPB	0.413	0.475	4.211	10.2	8.9
ThunderX2	TP06	0.911	0.951	1.509	1.7	1.6
ThunderX2	JT21	1.629	1.080	1.849	1.1	1.7
ThunderX2	GPB	0.747	0.787	1.179	1.6	1.5

TABLE 7 | Multi-threaded performance of naïve and auto-vectorised implementations; The FE scheme is used; $C = 11688851$ cells. “SoA” refers to the “struct of arrays” memory layout discussed in **Section 2.3.2**.

System	Model	Throughput ($10^6 \cdot \frac{\text{cell steps}}{\text{second}}$)			Speedup	
		Naïve	SoA	SIMD	SIMD naïve	SIMD SoA
Oakbridge	TP06	127.8	134.0	481.7	3.8	3.6
Oakbridge	JT21	148.8	147.2	444.7	3.0	3.0
Oakbridge	GPB	87.4	91.1	239.4	2.7	2.6
Oakforest	TP06	55.7	59.8	398.7	7.2	6.7
Oakforest	JT21	68.3	66.1	376.6	5.5	5.7
Oakforest	GPB	36.4	39.5	234.2	6.4	5.9
Milan	TP06	199.4	219.8	920.8	4.6	4.2
Milan	JT21	250.4	256.0	833.5	3.3	3.3
Milan	GPB	170.2	164.5	518.9	3.0	3.2
Wisteria	TP06	27.8	33.2	296.6	10.7	8.9
Wisteria	JT21	25.1	41.0	321.0	12.8	7.8
Wisteria	GPB	19.5	22.4	167.5	8.6	7.5
ThunderX2	TP06	94.1	97.6	137.1	1.5	1.4
ThunderX2	JT21	142.5	114.2	169.3	1.2	1.5
ThunderX2	GPB	75.5	83.1	109.1	1.4	1.3

The complete source code for the experiments in this paper is available online at <https://github.com/KGHustad/cell-model-cpu-code>.

3 EXPERIMENTS AND PERFORMANCE MEASUREMENTS

3.1 Overview of Hardware Testbeds

As our aim in this paper is to compare different optimisation strategies for a wide range of CPU architectures, we have used

TABLE 8 | Multi-threaded performance of an ensemble simulation using the JT21 model; $C = 11688851$ cells. The most performant implementation for each system is in boldface.

System	SIMD	Cell-Time		Time-Cell		Cell-Time-Cell	
		FE	GRL1	FE	GRL1	FE	GRL1
Oakbridge	On	631.1	358.9	154.3	132.2	375.2	257.5
Oakbridge	Off	150.5	90.0	85.3	57.8	110.1	71.1
Oakforest	On	422.4	237.6	108.2	89.1	114.1	94.7
Oakforest	Off	63.5	37.8	16.1	13.7	16.0	14.1
Milan	On	271.8	161.2	292.1	275.2	729.3	499.0
Milan	Off	269.2	158.7	151.2	105.9	167.4	116.8
Wisteria	On	41.4	19.4	104.5	70.3	125.1	79.1
Wisteria	Off	40.8	19.6	17.8	12.0	17.5	11.9
ThunderX2	On	103.5	58.6	83.5	60.9	112.2	76.6
ThunderX2	Off	111.4	62.6	64.1	40.6	79.6	47.9

five different hardware testbeds. The first three testbeds are using the supercomputers Oakforest-PACS, Oakbridge-CX and Wisteria-O operated by the Information Technology Center at the University of Tokyo, whereas the “Milan” and “ThunderX2” testbeds are part of the eX3 infrastructure hosted at Simula Research Laboratory. Each testbed consists of a single compute node with one or two multicore CPUs. An overview of the CPU and memory specifications for the testbeds is given in **Table 2**.

Table 3 lists the compiler flags we used to enable auto-vectorisation. Since **Listing 4** makes use of preprocessor conditionals, we have provided additional flags to define constants controlling which code path is compiled. With ARMClang and the Fujitsu compiler (running in Clang mode) we pass the flag `-DHINT_CLANG_SIMD`, and with the other compilers we pass the flag `-DHINT_OMP_SIMD`.

3.2 Counting Floating-Point Operations with Performance Counters

Some CPU architectures provide performance counters that enable the programmer to count the number of floating-point instructions executed for each vector length. The set of performance counters available is highly architecture-dependent, and we will limit our discussion here to the Intel Cascade Lake CPU architecture found on the “Oakbridge” system in **Table 2**. **Listing 9** demonstrates how the `perf` command in Linux can be used to count number of floating-point operations (FLOPs). Note that the performance counters must be multiplied by the number of SIMD lanes and summed up in order to obtain the total FLOP count. Written out, the total number of floating-point operations is computed as

$$\begin{aligned}
 &\text{floating-point operations} \\
 &= 8 \cdot \text{FP_ARITH_INST_RETIRED.512B_PACKED_DOUBLE} \\
 &\quad + 4 \cdot \text{FP_ARITH_INST_RETIRED.256B_PACKED_DOUBLE} \\
 &\quad + 2 \cdot \text{FP_ARITH_INST_RETIRED.128B_PACKED_DOUBLE} \\
 &\quad + 1 \cdot \text{FP_ARITH_INST_RETIRED.SCALAR_DOUBLE}.
 \end{aligned}$$

TABLE 9 | RRMS error when solving the TP06 model using SIMD and vectorised math functions. For each ODE solver scheme a reference solution is computed on Milan using scalar math functions and with compiler optimisations disabled. The model is solved for 1 s with a time step $\Delta t = 1 \mu s$.

System	FE	RL	GRL1
Oakbridge (with expm1)	2.11×10^{-16}	1.34×10^{-16}	9.47×10^{-17}
Oakbridge	2.00×10^{-16}	1.48×10^{-14}	1.29×10^{-12}
Oakforest	3.40×10^{-16}	2.40×10^{-11}	1.17×10^{-11}
Milan	2.67×10^{-16}	2.48×10^{-14}	1.07×10^{-12}
Wisteria	2.33×10^{-16}	2.49×10^{-14}	8.43×10^{-13}
ThunderX2	1.85×10^{-16}	2.48×10^{-14}	7.94×10^{-13}

Listing 9: Command used to count number of floating point operations on Intel Cascade Lake CPUs.

```
perf stat \
-e FP_ARITH_INST_RETIRED.SCALAR_DOUBLE \
-e FP_ARITH_INST_RETIRED.128B_PACKED_DOUBLE \
-e FP_ARITH_INST_RETIRED.256B_PACKED_DOUBLE \
-e FP_ARITH_INST_RETIRED.512B_PACKED_DOUBLE \
./bin/bench_FHN_naive
```

In **Table 1** we have used performance counters to count the number of floating-point operations required to solve a single step with a naïve FE implementation for each of the three cell models that are used in this section.

3.3 Speed and Accuracy of Vectorised Math Libraries

We measured the performance of selected scalar and vectorised math functions for each of the testbeds. The math function is called for every element in an array of length 30,000, and then this is repeated 20,000 times in an outer loop. We annotate the inner loop with `#pragma omp for simd` to enable vectorisation via OpenMP. We have selected the `exp()`, `expm1()`, `log()`, `pow()` functions for this benchmark, as these are the only math functions that are used when solving the cell models in this paper. The benchmark is single-threaded, and the number of function evaluations per second is reported in **Table 4**.

The Intel-based systems (Oakbridge and Oakforest) both see a speedup when using SIMD, and although the speedup is more pronounced on Oakforest, the absolute performance is 2.5–4 times higher on Oakbridge, despite having only 1.6 times the theoretical peak performance. The last x86 system, Milan, achieves speedup that exceeds expectations, considering that its 256-bit vector length would allow it to perform arithmetic at 4 times the rate of a scalar implementation. The theoretical peak performance of Milan and Oakbridge are comparable, and it seems likely that the high speedup is explained by the scalar implementations performing poorly on Milan. As there is no vectorised implementation of `expm1()` in libmvec version 2.27, we see no speedup for that function.

On Wisteria, we observe a reasonable 6–8 times speedup for all functions except `expm1()`. ThunderX2 achieves a modest speedup only for the `exp()` and `log()` functions, whereas the vectorised `expm1()` function sees a substantial degradation in performance.

We also measured the accuracy of the vectorised math libraries by calling each function with 1 million different input values, and then comparing the result with reference solutions with the MPFR library [see Fousse et al. (2007)] computed using 120 bits of accuracy. **Table 5** reports the maximum error in units of least precision (ULPs). If the true, infinite-precision value is located on the midpoint between two floating-point values of similar magnitude, the error would be 0.5 ULPs. The input values were generated by interpreting randomly generated bytes as a double-precision floats, and then we discarded values outside the desired domain (the input domains are listed in **Table 5**) and subnormal values (that are too small to represent in full precision). For the `pow()` function, we also omit values where the answer would have been subnormal.

`pow()` on Wisteria has very poor accuracy for two input values where the correct answers (6.11×10^{-308} , 2.48×10^{-307}) are small but not subnormal (as they are greater than 2.23×10^{-308}). If those two values are ignored, the maximum error was 36.206 ULPs, which is still significantly greater than the other systems. The remaining errors reported in **Table 5** are all below 3 ULPs, which should be well within the accuracy requirements for the solution of cell models.

3.4 Performance of Vectorised ODE Solvers

In our performance measurements of the ODE solver, we use the throughput metric “cell steps per second”, which is simply defined as

$$\text{cell steps per second} = \frac{\text{number of cells} \times \text{number of time steps}}{\text{solution time in seconds}} \quad (10)$$

The advantage of a such a throughput metric is that it simplifies the comparison of results with differing numbers of cells or time steps, and it can easily be used to estimate the solution time for a problem with a given number of cells and time steps.

Table 6 and **Table 7** show the single-threaded and multi-threaded performance of the naïve and auto-vectorised implementations using the FE scheme, where we have used it to solve three realistic ODE models as shown in **Table 1**. We set `OMP_NUM_THREADS=1` in the environment when measuring single-threaded performance, and we set it to the number of logical cores when measuring the multi-threaded performance. The “SoA” column uses a “struct of arrays” memory layout, as discussed in **Section 2.3.2**, but it does not provide any SIMD hints to the compiler. The “SIMD” column adds SIMD hints to the SoA implementation. We also report speedup factors comparing the SIMD implementation to both the naïve and the SoA implementation. The CPU clock speed is typically somewhat lower when executing vector instructions than when execution scalar instructions, especially when all cores are under heavy load, and this is one of the reasons why the speedup is generally higher in the single-threaded case. The other reason would be that we are more likely to encounter a memory bandwidth bottleneck

TABLE 10 | Multi-threaded performance of naïve, auto-vectorised and LUT implementations for the TP06 model in a simulation scenario. The Rush–Larsen scheme is used with $\Delta t = 0.1 \mu s$, $C = 1168851$ cells. “SoA” refers to the “struct of arrays” memory layout discussed in **Section 2.3.2**. The most performant implementation is in boldface.

System	Throughput ($10^6 \cdot \frac{\text{cell steps}}{\text{second}}$)					Speedup		
	Naïve	SoA	SIMD	LUT	SIMD & LUT	SIMD Naïve	LUT Naïve	SIMD & LUT Naïve
Oakbridge	96.0	96.3	374.3	393.4	552.4	3.9	4.1	5.8
Oakforest	46.9	47.8	354.3	196.3	423.5	7.6	4.2	9.0
Milan	163.2	170.9	754.5	762.3	1198.0	4.6	4.7	7.3
Wisteria	17.5	21.3	245.0	74.3	206.5	14.0	4.2	11.8
ThunderX2	71.8	79.7	116.0	250.1	199.3	1.6	3.5	2.8

when using all threads. For the JT21 model on the ThunderX2, we see a pronounced reduction in performance for the SoA implementation compared to the naïve implementation, but the other system–model combinations generally show a slight improvement for SoA over naïve.

Table 8 shows the multi-threaded performance in an ensemble simulation with the JT21 model using the FE and GRL1 schemes. The three loop-structures discussed in **Section 2.3.4** are shown in separate columns, and we also report the performance when vectorisation is disabled. When the Cell–Time loop structure is successfully auto-vectorised, it outperforms the other two loop structures, as we observe for Oakbridge and Oakforest. Both of the other loop structures are successfully auto-vectorised on all systems, but the Cell–Time–Cell loop structure is more cache friendly and performs better than the Time–Cell loop structure.

To quantify the error of the vectorised code relative to the scalar code, we use the relative root-mean-square (RRMS) norm given by

$$\|e\|_{\text{RRMS}} = \sqrt{\frac{\sum_{i=1}^N (v_i - v_i^{\text{ref}})^2}{\sum_{i=1}^N (v_i^{\text{ref}})^2}}, \quad (11)$$

where N is the number of time steps. We have solved the TP06 model for one second using a time step $\Delta t = 1 \mu s$ for the FE, RL and GRL1 schemes. The RRMS error for the transmembrane potential is reported in **Table 9**. The RL and GRL1 schemes exhibit a larger error when $(\exp(x) - 1)$ is used instead of $\expm1(x)$.

3.5 Speed and Accuracy Related to Using Lookup Tables

Table 10 reports the multi-threaded performance of naïve, auto-vectorised and lookup table (LUT) implementations for the TP06 model. Across all systems the LUT implementation is 3.5–4.7 times faster than naïve. ThunderX2 clearly favours LUT, which we attribute to its 128-bit vector length. Oakforest and Wisteria, on the other hand, clearly favour SIMD with their 512-bit vector length. On Oakbridge, which also has 512-bit vector units, LUT is marginally faster than SIMD. The fact that SIMD doesn’t perform better on Oakbridge is likely due

to the somewhat low speedup of the vectorised math library (see **Table 4**). On Milan, SIMD and LUT perform very similarly, which is roughly in line with expectations.

When solving the non-gating equations with SIMD vectorisation and the gating equations with LUT, we see an improvement over only SIMD or LUT on the three x86-based systems. As ThunderX2 has a very limited speedup from the use of SIMD vectorisation, the combination of SIMD and LUT performs worse than the LUT implementation. On Wisteria, the use of SIMD vectorisation leads to much greater speedups than the use of LUT, and shifting parts of the computation from SIMD to LUT leads to a loss in performance compared to the pure SIMD variant.

Whereas the speedup of the LUT implementation is largely insensitive to the CPU vector width and depends more on the model formulation, the speedup of the SIMD implementation strongly depends on the vector width. For the TP06 model, it seems that we need more than 4 SIMD lanes for the SIMD implementation to outperform the LUT implementation. However, the observations we have made regarding the speedup solving the TP06 model with a LUT does not generalise to all cell models, and other models may see smaller or larger gains from using a LUT.

Figure 1 compares the accuracy of the LUT implementation to the naïve implementation. The two solutions are plotted together in the top panel, and the difference is plotted in the bottom panel. The error introduced by the LUT is greatest during the upstroke, but the absolute error does not exceed $5 \times 10^{-5} \text{ mV}$ at any point.

3.6 Speeding up a 10^9 -Ensemble Computation

Recent studies [see e.g., Tveito et al. (2018); Jæger et al. (2020, 2021a)] have used cardiac cell models to decode the observed effect of a drug on a chip of human induced pluripotent stem cell-derived cardiomyocytes. In these studies, the assumption is that there is a set of model parameters corresponding to the drug effect, and the computational problem consists of searching through the higher-dimensional parameter space. The optimisation problem is particularly expensive because one has to solve the cell model for a long time period until steady state is reached.

In this section, we have set up an ensemble simulation where we try to optimise 11 parameters by pre-computing solutions for

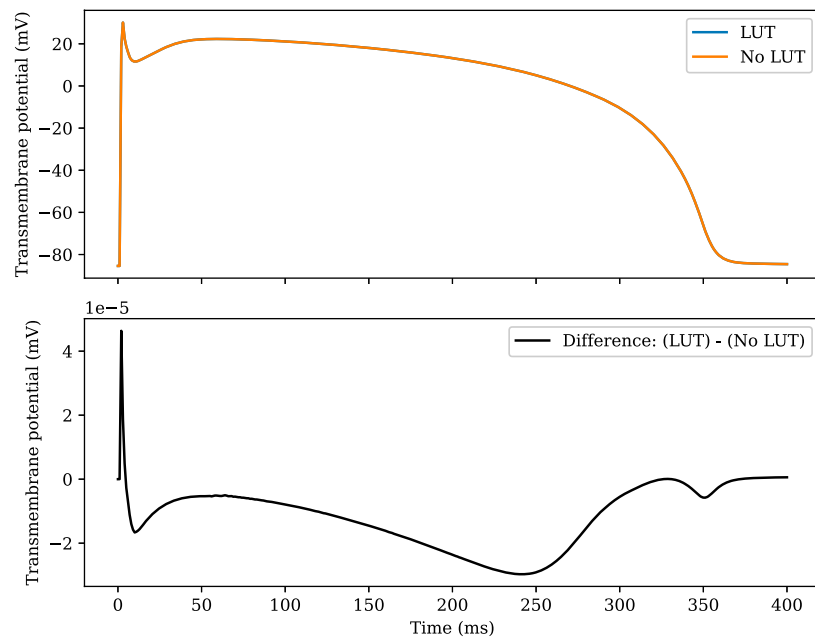


FIGURE 1 | Comparison of the TP06 model solved with and without the use of lookup tables. The RL scheme is used with $\Delta t = 1 \mu s$. In the upper plot, the two numerical solutions cannot be distinguished by eye. The RRMS error of the LUT solution compared with the non-LUT solution is 1.36×10^{-7} .

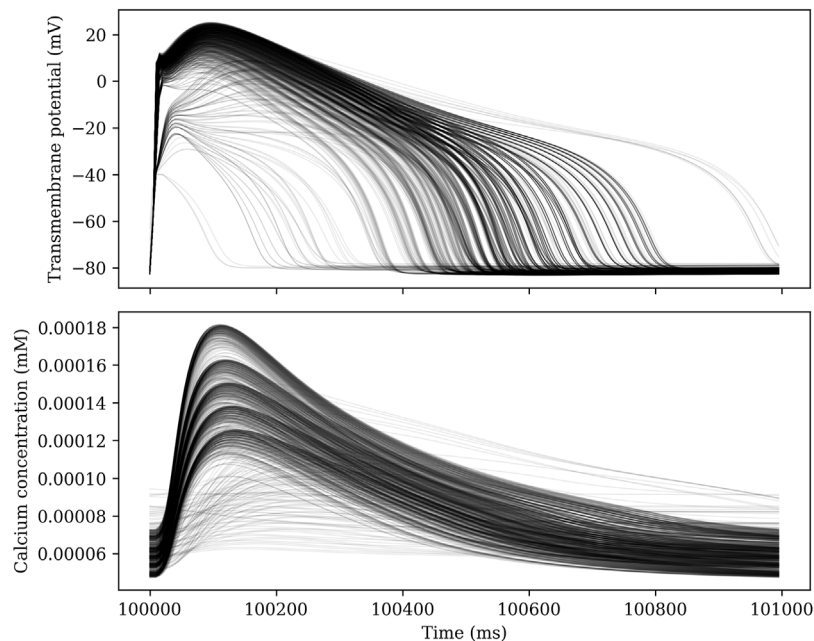


FIGURE 2 | Traces of the transmembrane potential and calcium concentration for 1000 different sets of parameters in an ensemble simulation.

a cartesian grid in the parameter space. Note that we treat the remaining model parameters as constant, similar to how all parameters are essentially constant in the simulation scenario. With 5–12 grid points for each parameter, the total number of parameter sets was 1,020,937,500. This parameter mesh can be used directly to solve the optimisation problem by taking the

parameter mesh point that minimises the cost function as the solution, or it can be used to guide the search of another optimisation algorithm.

Each parameter set is solved for 102 seconds using a GRL1 scheme with a time step $\Delta t = 10 \mu s$. The model is paced at 1 Hz, and the 100 first seconds are intended to allow the model to reach

steady state. We then record the solution for the last 2 seconds at a temporal resolution of 5 ms. By comparing the two last action potentials, we can determine whether steady state has indeed been reached. For some choices of parameters, there is no steady state solution with a period equal to the pacing period. **Figure 2** shows traces of the transmembrane potential for 1000 different sets of parameters for $t \in [100 \text{ s}, 101 \text{ s}]$.

The 1,020,937,500 parameter sets were divided into batches of size 50,048 so that we could use a batch job in the queue system on Oakforest to achieve task-level parallelism. Each of the 20,400 batches was solved on a single node, and the resource limits on Oakforest allowed us to use up to 2048 nodes concurrently. This job expended 11,990 tokens (and one token equals an hour of compute time for a single node). We ran one of the batches both with and without SIMD vectorisation so that we can extrapolate an estimate for how many tokens we would have needed if we had run the entire job with a scalar implementation. The codes differ only in the absence of vectorisation compiler hints for the non-SIMD version, i.e. the line `#pragma omp for simd` is replaced by `#pragma omp for`. The `expm1` function was used to evaluate expressions on the form $(e^x - 1)$. Without SIMD, the solver achieved a throughput of 37.0 million cell steps per second, whereas the SIMD version reached 232.25 million cell steps per second, equating to a speedup by a factor of 6.28. If we extrapolate from this speedup factor, we can estimate the cost of running the whole simulation without vectorisation to 75,260 node hours. In other words, the use of vectorisation lead to a reduction in compute time of approximately 63,270 node hours. Since the power draw per compute node on Oakforest is approximately 331 W [see TOP500 (2021)], 63,270 node hours translates to an energy consumption of approximately 20,942 kW h.

4 RELATED WORK AND CONCLUSION

4.1 Related Work

The code vectorisation in this work is automatically enabled by the compilers, with the help of a few hints that are provided in the form of compiler directives and additional clauses. Such an implicit vectorisation approach is programmer-friendly and portable, except perhaps a few `#if defined (XXX)` directives to accommodate compiler-specific details. The downside is that concerns over safety or efficiency may prevent the compiler from vectorising more complicated code, such as a loop body containing scattered memory accesses due to the use of lookup tables. To handle such situations will require explicit vectorisation. The first alternative is to directly program with SIMD intrinsics. The challenge is that different processor architectures may support different intrinsic instruction sets. For example, AMD CPUs currently only support (extended) SSE instructions with 128-bit and 256-bit vector widths [see AMD64 Technology (2021)], whereas high-end Xeon and Xeon Phi processors also support AVX-512 instructions with 512-bit vector width [see Intel (2021)]. On Arm processors, the diversity is even larger with respect to SIMD vectorisation. There are currently three SIMD instruction

set architectures applicable: SVE, Neon and Helium [see Arm Intrinsics (2022)]. However, a specific Arm processor may only support one of them. An explicit vectorisation of the ten Tusscher–Panfilov model for IBM A2 CPUs was developed as part of the “Cardioid” monodomain simulator [see Mirin et al. (2012)]. As a second approach to explicit vectorisation, there are high-level wrapper libraries that offer portability and improved programmability. Two such examples are VCL [see Fog (2017; 2022)] and MIPP [see Cassagne et al. (2018); MIPP (2021)]. Both are implemented using C++ and support various SSE and AVX/AVX-512 instructions, whereas the latter also supports Arm Neon instructions. The single-instruction-multiple-thread (SIMT) execution model found on graphics processing units (GPUs), which resembles CPU-based SIMD execution in some respects, has been applied to cardiac cell models [see e.g., Neic et al. (2012); Sachetto Oliveira et al. (2018)].

Using lookup tables is a widely used approach to saving the computational cost of directly evaluating mathematical functions. The different scientific domains that have used this performance enhancing strategy are summarised in a recent publication [see Marsh et al. (2021)], which also discusses a methodology for predicting the speedup due to using lookup tables. For cardiac simulations in particular, the topic of using lookup tables has been addressed in e.g. Cooper et al. (2006); Mirin et al. (2012); Green et al. (2019), where the latter contains a detailed study about the accuracy loss caused by lookup tables.

4.2 Conclusion

We have seen that the largest performance improvement of the ODE solvers arises from using SIMD, and the code vectorisation in this work has been automatically enabled by the compilers. There are two conditions for this “easy” approach. First, some restructurings of a naïve implementation are needed. The most important code restructuring is to re-organise the overall data structure as a “struct of arrays” with padding, see **Section 2.3.2**. The other code restructurings include swapping the cell-time loop ordering or adding an additional loop level for the ensemble scenario, see **Section 2.3.4**. Second, appropriate compiler hints are needed inside the source code. We have chosen to use the OpenMP `simd` construct together with the `#pragma omp parallel for` directive, as illustrated in **Listings 4, 5, 6** and **7**. This choice has the benefit of simultaneously enabling SIMD vectorisation and multi-threaded parallelisation, both are essential for achieving the full potential of multi-core CPUs for the ODE solving procedure.

In connection with the compiler-enabled auto-vectorisation, we have presented the necessary compiler options for the different compilers, see **Table 3**. We have also studied the performance gain (or even loss) due to vectorisation of four frequently used mathematical functions on five hardware testbeds (see **Table 4**), as well as the appropriate vectorised math libraries to be used. We have found that the relative benefit of using SIMD is correlated with the peak SIMD floating-point throughput of the hardware platform. Moreover, the minor accuracy loss due to using vectorised math libraries can be found in **Table 5**. It has been shown through actual ODE computations, see **Table 9**,

that the slightly inaccurate vectorised math libraries will not affect the overall accuracy.

The use of lookup tables may interfere with the auto-vectorisation, but we have demonstrated that the two techniques can be used to solve different parts of the cell model, which on some of the target platforms yielded higher performance than using either technique by itself. The decision about whether to use lookup tables is hardware specific. On platforms that only support small vector widths or have no high-quality vectorised math libraries, the speedup potential due to lookup tables can be large. The exact performance benefit, however, depends on the size and resolution of the lookup tables, which may affect the computational accuracy. A direction for future work is to investigate whether explicit vectorisation (using high-level wrapper libraries) can be used to combine SIMD parallelism with lookup tables without partitioning the state variables. In particular, such a combination should be attempted with the help of automated code generation, e.g., inside the modern cardiac simulator openCARP [see Plank et al. (2021); openCARP (2022)].

DATA AVAILABILITY STATEMENT

The original contributions presented in the study are included in the article/Supplementary Material, further inquiries can be directed to the corresponding author.

REFERENCES

- Alonso, S., Bär, M., and Echebarria, B. (2016). Nonlinear Physics of Electrical Wave Propagation in the Heart: A Review. *Rep. Prog. Phys.* 79, 096601. doi:10.1088/0034-4885/79/9/096601
- AMD64 Technology (2021). “AMD64 Architecture Programmer’s Manual, Volume 4: 128-Bit and 256-Bit Media Instructions,” in *Tech. Rep.* (Santa Clara, California: AMD).
- [Dataset] Arm Intrinsics (2022). Arm Developer – SIMD ISAs. Available at: <https://developer.arm.com/architectures/instruction-sets/simd-isas>.
- Cassagne, A., Aumage, O., Barthou, D., Leroux, C., and Jégo, C. (2018). “Mipp,” in Proceedings of the 2018 4th Workshop on Programming Models for SIMD/Vector Processing (ACM). doi:10.1145/3178433.3178435
- [Dataset] CellML (2022). Model: Nagumo, Arimoto, Yoshizawa, 1962. Available at: <https://models.cellml.org/exposure/7430333335941b3b0130d3a3d983d846>.
- Clayton, R. H., Bernus, O., Cherry, E. M., Dierckx, H., Fenton, F. H., Mirabella, L., et al. (2011). Models of Cardiac Tissue Electrophysiology: Progress, Challenges and Open Questions. *Prog. Biophysics Mol. Biol.* 104, 22–48. doi:10.1016/j.pbiomolbio.2010.05.008
- Colli Franzzone, P., Pavarino, L. F., and Scacchi, S. (2018). A Numerical Study of Scalable Cardiac Electro-Mechanical Solvers on Hpc Architectures. *Front. Physiol.* 9. doi:10.3389/fphys.2018.00268
- Colli Franzzone, P., Pavarino, L. F., and Scacchi, S. (2014). *Mathematical Cardiac Electrophysiology, Vol. 13 of Modeling, Simulation and Applications*. Berlin, Germany: Springer.
- Cooper, J., McKeever, S., and Garny, A. (2006). “On the Application of Partial Evaluation to the Optimisation of Cardiac Electrophysiological Simulations,” in Proceedings of the 2006 ACM SIGPLAN Symposium on Partial Evaluation and Semantics-Based Program Manipulation (ACM), 12–20. doi:10.1145/1111542.1111546
- Cuellar, A. A., Lloyd, C. M., Nielsen, P. F., Bullivant, D. P., Nickerson, D. P., and Hunter, P. J. (2003). An Overview of CellML 1.1, a Biological Model Description Language. *Simulation* 79, 740–747. doi:10.1177/0037549703040939

AUTHOR CONTRIBUTIONS

KH performed the software development and simulations. Both authors designed the study, wrote the manuscript, and approved the submitted version.

FUNDING

This work was partially supported by the European High-Performance Computing Joint Undertaking EuroHPC under grant agreement No 955495 (MICROCARD) co-funded by the Horizon 2020 programme of the European Union (EU) and the Research Council of Norway. The research presented in this paper has also benefited from the Experimental Infrastructure for Exploration of Exascale Computing (eX3), which is financially supported by the Research Council of Norway under contract 270053.

ACKNOWLEDGMENTS

This research was conducted using the Fujitsu PRIMERGY CX600M1/CX1640M1 (Oakforest-PACS), Fujitsu PRIMERGY CX400M1/CX2550M5 (Oakbridge-CX), and Fujitsu PRIMEHPC FX1000 (Wisteria-O) provided by The University of Tokyo through Joint Usage/Research Center for Interdisciplinary Large-scale Information Infrastructures and High Performance Computing Infrastructure in Japan (Project ID: jh210021).

- FitzHugh, R. (1961). Impulses and Physiological States in Theoretical Models of Nerve Membrane. *Biophysical J.* 1, 445–466. doi:10.1016/S0006-3495(61)86902-6
- [Dataset] Fog, A. (2022). GitHub Repositories for Vectorclass. Available at: <https://github.com/vectorclass>.
- [Dataset] Fog, A. (2017). VCL – C++ Vector Class Library. Available at: <https://www.agner.org/optimize/vectorclass.pdf>.
- Fousse, L., Hanrot, G., Lefèvre, V., Pélissier, P., and Zimmermann, P. (2007). MPFR: A Multiple-Precision Binary Floating-Point Library With Correct Rounding. *ACM Trans. Math. Softw.* 33, 13. doi:10.1145/1236463.1236468
- Grandi, E., Pasqualini, F. S., and Bers, D. M. (2010). A Novel Computational Model of the Human Ventricular Action Potential and Ca Transient. *J. Mol. Cell. Cardiol.* 48, 112–121. doi:10.1016/j.yjmcc.2009.09.019
- Green, K. R., Bohn, T. A., and Spiteri, R. J. (2019). Direct Function Evaluation versus Lookup Tables: When to Use Which? *SIAM J. Sci. Comput.* 41, C194–C218. doi:10.1137/18M1201421
- [Dataset] Hake, J., Finsberg, H., Hustad, K. G., and Bahij, G. (2020). Gotran – General ODE TRANslator. Available at: <https://github.com/ComputationalPhysiology/gotran> (Accessed July 1, 2020).
- [Dataset] Intel (2021). Intel Intrinsics Guide. Available at: <https://www.intel.com/content/www/us/en/docs/intrinsics-guide/index.html>.
- Jæger, K. H., Charwat, V., Charrez, B., Finsberg, H., Maleckar, M. M., Wall, S., et al. (2020). Improved Computational Identification of Drug Response Using Optical Measurements of Human Stem Cell Derived Cardiomyocytes in Microphysiological Systems. *Front. Pharmacol.* 10, 1648. doi:10.3389/fphar.2019.01648
- Jæger, K. H., Charwat, V., Wall, S., Healy, K. E., and Tveito, A. (2021b). Identifying Drug Response by Combining Measurements of the Membrane Potential, the Cytosolic Calcium Concentration, and the Extracellular Potential in Microphysiological Systems. *Front. Pharmacol.* 11, 2085. doi:10.3389/fphar.2020.569489
- Jæger, K. H., Hustad, K. G., Cai, X., and Tveito, A. (2021a). Efficient Numerical Solution of the EMI Model Representing the Extracellular Space (E), Cell Membrane (M) and Intracellular Space (I) of a Collection of Cardiac Cells. *Front. Phys.* 8. doi:10.3389/fphys.2020.579461

- Marsh, C. B., Green, K. R., Wang, B., and Spiteri, R. J. (2021). Performance Improvements to Modern Hydrological Models via Lookup Table Optimizations. *Environ. Model. Softw.* 139, 105018. doi:10.1016/j.envsoft.2021.105018
- [Dataset] MIPP (2021). GitHub Repository for MyIntrinsics++ (MIPP). Available at: <https://github.com/aff3ct/MIPP>.
- Mirin, A. A., Richards, D. F., Glosli, J. N., Draeger, E. W., Chan, B., Fattebert, J.-I., et al. (2012). "Toward Real-Time Modeling of Human Heart Ventricles at Cellular Resolution: Simulation of Drug-Induced Arrhythmias," in SC '12: Proceedings of the International Conference on High Performance Computing, Networking, Storage and Analysis, 1–11. doi:10.1109/SC.2012.108
- Nagumo, J., Arimoto, S., and Yoshizawa, S. (1962). An Active Pulse Transmission Line Simulating Nerve Axon. *Proc. IRE* 50, 2061–2070. doi:10.1109/JRPROC.1962.288235
- Neic, A., Liebmman, M., Hoetzl, E., Mitchell, L., Vigmond, E. J., Haase, G., et al. (2012). Accelerating Cardiac Bidomain Simulations Using Graphics Processing Units. *IEEE Trans. Biomed. Eng.* 59, 2281–2290. doi:10.1109/TBME.2012.2202661
- Niederer, S., Mitchell, L., Smith, N., and Plank, G. (2011). Simulating Human Cardiac Electrophysiology on Clinical Time-Scales. *Front. Physio.* 2, 14. doi:10.3389/fphys.2011.00014
- [Dataset] openCARP (2022). openCARP: Cardiac Electrophysiology Simulator. Available at: <https://opencarp.org>.
- Plank, G., Loewe, A., Neic, A., Augustin, C., Huang, Y.-L., Gsell, M. A. F., et al. (2021). The openCARP Simulation Environment for Cardiac Electrophysiology. *Comput. Methods Programs Biomed.* 208, 106223. doi:10.1016/j.cmpb.2021.106223
- Rush, S., and Larsen, H. (1978). A Practical Algorithm for Solving Dynamic Membrane Equations. *IEEE Trans. Biomed. Eng.* 25, 389–392. doi:10.1109/tbme.1978.326270
- Sachetto Oliveira, R., Martins Rocha, B., Burgarelli, D., Meira, W., Jr., Constantinides, C., and Weber dos Santos, R. (2018). Performance Evaluation of GPU Parallelization, Space-Time Adaptive Algorithms, and Their Combination for Simulating Cardiac Electrophysiology. *Int. J. Numer. Meth Biomed. Engng* 34, e2913. doi:10.1002/cnm.2913
- Shibata, N., and Petrogalli, F. (2020). SLEEF: A Portable Vectorized Library of C Standard Mathematical Functions. *IEEE Trans. Parallel Distrib. Syst.* 31, 1316–1327. doi:10.1109/TPDS.2019.2960333
- Sundnes, J., Artebrant, R., Skavhaug, O., and Tveito, A. (2009). A Second-Order Algorithm for Solving Dynamic Cell Membrane Equations. *IEEE Trans. Biomed. Eng.* 56, 2546–2548. doi:10.1109/TBME.2009.2014739
- [Dataset] ten Tusscher, K. H. W. J. (2021). Source Code Second Version Human Ventricular Cell Model. Available at: <http://www.binf.bio.uu.nl/khwjtuss/SourceCodes/HVM2/> (Accessed July 23, 2021).
- ten Tusscher, K. H. W. J., and Panfilov, A. V. (2006). Alternans and Spiral Breakup in a Human Ventricular Tissue Model. *Am. J. Physiology-Heart Circulatory Physiology* 291, H1088–H1100. doi:10.1152/ajpheart.00109.2006
- [Dataset] TOP500 (2021). Top500: Oakforest-PACS. Available at: <https://www.top500.org/system/178932/>.
- Trayanova, N. A. (2011). Whole-Heart Modeling. *Circ. Res.* 108, 113–128. doi:10.1161/CIRCRESAHA.110.223610
- Tveito, A., Jæger, K. H., Huebsch, N., Charrez, B., Edwards, A. G., Wall, S., et al. (2018). Inversion and Computational Maturation of Drug Response Using Human Stem Cell Derived Cardiomyocytes in Microphysiological Systems. *Sci. Rep.* 8, 17626. doi:10.1038/s41598-018-35858-7
- Tveito, A., Jæger, K. H., Kuchta, M., Mardal, K.-A., and Rognes, M. E. (2017). A Cell-Based Framework for Numerical Modeling of Electrical Conduction in Cardiac Tissue. *Front. Phys.* 5. doi:10.3389/fphys.2017.00048
- Vigmond, E., Vadakkumpadan, F., Gurev, V., Arevalo, H., Deo, M., Plank, G., et al. (2009). Towards Predictive Modelling of the Electrophysiology of the Heart. *Exp. Physiol.* 94, 563–577. doi:10.1113/expphysiol.2008.044073

Conflict of Interest: The authors declare that the research was conducted in the absence of any commercial or financial relationships that could be construed as a potential conflict of interest.

Publisher's Note: All claims expressed in this article are solely those of the authors and do not necessarily represent those of their affiliated organizations, or those of the publisher, the editors and the reviewers. Any product that may be evaluated in this article, or claim that may be made by its manufacturer, is not guaranteed or endorsed by the publisher.

Copyright © 2022 Hustad and Cai. This is an open-access article distributed under the terms of the Creative Commons Attribution License (CC BY). The use, distribution or reproduction in other forums is permitted, provided the original author(s) and the copyright owner(s) are credited and that the original publication in this journal is cited, in accordance with accepted academic practice. No use, distribution or reproduction is permitted which does not comply with these terms.



Novel Global Asymptotic Stability and Dissipativity Criteria of BAM Neural Networks With Delays

Mei Liu^{1*}, Haijun Jiang², Cheng Hu², Binglong Lu¹ and Zhanfeng Li¹

¹School of Mathematics and Statistics, Zhoukou Normal University, Zhoukou, China, ²College of Mathematics and System Sciences, Xinjiang University, Urumqi, China

In this article, issues of both stability and dissipativity for a type of bidirectional associative memory (BAM) neural systems with time delays are investigated. By using generalized Halanay inequalities and constructing appropriate Lyapunov functionals, some novelty criteria are obtained for the asymptotic stability for BAM neural systems with time delays. Also, without assuming boundedness and differentiability for activation functions, some new sufficient conditions for proving the dissipativity are established by making use of matrix theory and inner product properties. The received conclusions extend and improve some previously known works on these problems for general BAM neural systems. In the end, numerical simulation examples are made to show the availability of the theoretical conclusions.

OPEN ACCESS

Edited by:

Erik Andreas Martens,
Lund University, Sweden

Reviewed by:

Baogui Xin,
Shandong University of Science and
Technology, China
Shaobo He,
Central South University, China

*Correspondence:

Mei Liu
meiyiruoya@163.com

Specialty section:

This article was submitted to
Statistical and Computational Physics,
a section of the journal
Frontiers in Physics

Received: 25 March 2022

Accepted: 26 April 2022

Published: 30 June 2022

Citation:

Liu M, Jiang H, Hu C, Lu B and Li Z
(2022) Novel Global Asymptotic
Stability and Dissipativity Criteria of
BAM Neural Networks With Delays.
Front. Phys. 10:898589.
doi: 10.3389/fphy.2022.898589

Keywords: BAM neural network, global asymptotic stability, dissipativity, inner product, generalized Halanay inequalities, matrix theory

1 INTRODUCTION

The BAM neural network model, proposed by Kosko in [1], consists of neurons in two layers, the x -layer and the y -layer. The neurons of the same layer are sufficiently interconnected to the neurons arranged in the other layer, but neurons do not interconnect among the same layer. A useful feature of BAM is its ability to invoke stored pattern pairs in the case of noise. For detailed memory structure and examples of the BAM neural network, please refer to [2]. In recent years, BAM neural systems have received significant attention due to their wide applications in a lot of fields such as pattern recognition, image processing, signal processing, associative memories, optimization problems, and other engineering areas [3–6].

In general, due to the limited switching speed and signal propagation speed of neuron amplifiers, the implementation of a neural network will inevitably have a time delay. We also know that using a delayed version of the neural network is very important to solve some motion-related optimization problems. However, research shows that time delay may lead to divergence, oscillation, and instability, which may be bad for BAM neural systems [7, 8]. Therefore, these applications of the BAM neural systems with delays greatly rely on the dynamical behavior of the neural systems. For these reasons, it is necessary to study the dynamical behavior of the neural systems with delays, and it has been widely studied by a great number of researchers [9, 10].

In the design and analysis of neural networks, stability analysis is a very important and essential link. As small as a specific control system or as large as a social system, financial system, and ecosystem, it is always carried out under various accidental or continuous disturbances. After bearing this kind of interference, it is very important whether the system can keep running or working without losing control or swinging. For neural networks, because the output of the network is a

function of time, for a given input, the response of the network may converge to a stable output, oscillate, increase infinitely, or follow a chaotic mode. Therefore, if a neural network system wants to play a role in engineering, it must be stable.

The notion of global dissipativity proposed in the 1970s is a common notion in dynamical systems, and it is applied in the fields of chaos and synchronization theory, stability theory, and robust control and system norm estimation [11–14]. Hence, it is a special and interesting problem to study the dissipativity of dynamical networks. Up to now, the dissipativity for several classes of simple neural networks with delays has begun to attract initial interest in investigation, and some sufficient conditions have been received [15–17]. Yet, to our knowledge, only a few articles have not been used for Lyapunov–Krasovskii functionals or Lyapunov functionals [18–22]. In this study, a few dissipativity conclusions have been received for BAM neural networks with varying delays *via* inner product properties and matrix theory, which are different from the neural systems' model investigated in [23, 24].

Inspired by the previous discussion, the global asymptotic stability and dissipativity of BAM neural systems with time delays are investigated. Some new criteria to ensure the dissipation and stability of the BAM neural system are received. Compared with the previous results, our main results are more general and less conservative. The innovations of the study are at least the following aspects.

- 1) The BAM neural network model studied in this article has a time-varying delay.
- 2) In our article, the nonlinear activation functions we assumed are not differentiable and bound.
- 3) In this article, the sufficient conditions for the dissipativity of BAM neural networks with time-varying delay are obtained by using only the inner product property and matrix theory.
- 4) Moreover, the global attraction sets, namely, positive invariant sets, are obtained.

The structure of the article is organized in the following. The model description and some preliminary knowledge with some necessary definitions and lemmas are given in **Section 2**. In **Section 3**, by constructing Lyapunov functionals, we discussed the global asymptotic stability for the equilibrium point of delayed BAM neural systems. Some sufficient criteria are obtained and discussed to guarantee the global dissipativity by using inner product properties in **Section 4**. Two examples and their simulation conclusions are provided in **Section 5**. In the end, some results are reached in **Section 6**.

2 PRELIMINARIES

Notations: In this article, let R^n be a Euclidean space with the inner product $\langle x, y \rangle = y^T x$ and the norm $\|x\|_2 = \sqrt{\langle x, x \rangle}$, where $x = (x_1, x_2, \dots, x_n)^T$ and $y = (y_1, y_2, \dots, y_n)^T \in R^n$. The matrix norm is $\|A\|_2 = \sqrt{\lambda_{\max}(A^T A)}$ for $A \in R^{n \times n}$, where $\lambda_{\max}(A^T A)$ denotes the maximum eigenvalue of $A^T A$. $\lambda_{\min}(A)$

denotes the minimum eigenvalue of A . $A > 0$ denotes that matrix A is symmetric positive definite. E is a unit matrix.

In this article, the model of delayed BAM neural networks is investigated.

$$\begin{cases} \dot{x}(t) = -Ax(t) + Cf(y(t)) + \tilde{C}f(y(t-\tau)) + I, \\ \dot{y}(t) = -By(t) + Dg(x(t)) + \tilde{D}g(x(t-\sigma)) + J, \end{cases} \quad (1)$$

for $t > 0$, $x(t) = (x_1(t), x_2(t), \dots, x_n(t))^T$ represents neuron in the first layer at time t , and $y(t) = (y_1(t), y_2(t), \dots, y_n(t))^T$ represents neuron in the second layer at time t ; $A = \text{diag}(a_1, a_2, \dots, a_n)$ and $B = \text{diag}(b_1, b_2, \dots, b_n)$, in which $a_i > 0$ and $b_j > 0$ ($i, j \in \mathcal{I} = \{1, 2, \dots, n\}$) denote passive decay rates, respectively; $C = (c_{ij})_{n \times m}$, $D = (d_{ij})_{n \times m}$, $\tilde{C} = (\tilde{c}_{ij})_{n \times m}$ and $\tilde{D} = (\tilde{d}_{ij})_{n \times m}$ are synaptic connection strengths; $f(y(t)) = (f_1(y_1(t)), f_2(y_2(t)), \dots, f_n(y_n(t)))^T$ and $g(x(t)) = (g_1(x_1(t)), g_2(x_2(t)), \dots, g_n(x_n(t)))^T$ denote nonlinear activation functions; $I = (I_1, I_2, \dots, I_n)^T$, $J = (J_1, J_2, \dots, J_n)^T$ represents the external inputs to the neurons; $\tau = (\tau_1, \tau_2, \dots, \tau_n)^T$, $\sigma = (\sigma_1, \sigma_2, \dots, \sigma_n)^T$ which are required for axonal transmission and neural processing of signals are time delays.

In this study, we considered the following continuous activation functions:

(**H**₁): $\forall x, y \in R, x \neq y, i, j \in \mathcal{I}$, activation functions $f_j(\cdot)$ and $g_i(\cdot)$ satisfy $f_j(0) = g_i(0) = 0$, and there exist constants $l_j, m_i > 0$ such that

$$0 \leq \frac{f_j(x) - f_j(y)}{x - y} \leq l_j, \quad 0 \leq \frac{g_i(x) - g_i(y)}{x - y} \leq m_i.$$

Remark 1: The hypothesis of activation function H_1 in this study has been widely used in some references. In particular, when discussing the stability, synchronization, and dissipation of neural networks, H_1 is a common assumption. In the study, the activation function is Lipschitz continuous, so it is monotonously increasing. But it may not be differentiable or bounded. However, in [8, 13], the activation function should not only satisfy the hypothesis H_1 of this study but also satisfy the boundedness. In [15], the derivative of the activation function also satisfies boundedness. In this study, the activation function only needs to satisfy the hypothesis H_1 . Compared with [8, 13, 15], the assumption of excitation function in this study is more general.

The initial condition of the system (1) is considered as

$$\begin{cases} x(s) = \varphi(s), & s \in [-\alpha + t_0, t_0], \\ y(s) = \psi(s), & s \in [-\alpha + t_0, t_0], \end{cases}$$

where $\bar{\tau} = \max_{j \in \mathcal{I}} \{\tau_j\}$, $\bar{\sigma} = \max_{i \in \mathcal{I}} \{\sigma_i\}$, $\alpha = \max\{\bar{\tau}, \bar{\sigma}\}$, and $\varphi(s), \psi(s) \in C([-\alpha + t_0, t_0], R^n)$.

Definition 1: [25]. The neural system (1) is globally dissipative if there exists a compact set $S \subseteq R^{2n}$, such that $\forall z_0 \in S, \exists T(z_0) > 0$, when $t \geq t_0 + T(z_0)$, $z(t, t_0, z_0) \subseteq S$, in which $z(t, t_0, z_0)$ represents the solution for (1) from initial time t_0 and initial state z_0 . A set S is said to be forward invariant if $\forall z_0 \in S$ indicates $z(t, t_0, z_0) \subseteq S$ for $t \geq t_0$.

Definition 2: [26]. The point $(x^*, y^*)^T$ with $x^* = (x_1^*, x_2^*, \dots, x_n^*)^T$ and $y^* = (y_1^*, y_2^*, \dots, y_n^*)^T$ is the equilibrium of system (1) if

$$\begin{cases} -Ax^* + Cf(y^*) + \tilde{C}f(y^*) + I = 0, \\ -By^* + Dg(x^*) + \tilde{D}g(x^*) + J = 0. \end{cases}$$

Lemma 1: [27]. For every positive $k > 0$ and every $a, b \in \mathbb{R}^n$,

$$2a^T b \leq ka^T Xa + k^{-1}b^T X^{-1}b$$

holds, in which $X > 0$.

Lemma 2: (Generalized Halanay inequalities) [28]. If $V(t) \geq 0$, $t \in (-\infty, +\infty)$ and

$$D^+V(t) \leq \gamma(t) + \xi(t)V(t) + \eta(t) \sup_{t-\tau(t) \leq s \leq t} V(s), \quad t \geq t_0,$$

for $t \in [t_0, +\infty)$, in which $\gamma(t) \geq 0$, $\eta(t) \geq 0$, and $\xi(t) \leq 0$ are continuous functions and $\tau(t) \geq 0$, and there exists $\alpha > 0$ such that

$$\xi(t) + \eta(t) \leq -\alpha, \quad \text{for } t \geq t_0.$$

Then,

$$V(t) \leq \frac{\gamma^*}{\alpha} + \left(\sup_{-\infty \leq s \leq t_0} V(s) - \frac{\gamma^*}{\alpha} \right) \cdot e^{-\mu^*(t-t_0)},$$

where

$$\gamma^* = \sup_{t \geq t_0} \gamma(t), \quad \mu^* = \inf_{t \geq t_0} \{\mu(t) : \mu(t) + \xi(t) + \eta(t)e^{\mu(t)\tau(t)} = 0\},$$

$$\text{and the upper-right Dini derivative } D^+ \gamma(t) = \lim_{h \rightarrow 0^+} \frac{\gamma(t+h) - \gamma(t)}{h}.$$

3 GLOBAL ASYMPTOTIC STABILITY FOR BAM NEURAL NETWORKS

First of all, under condition (H_1) , neural system (1) always at least has an equilibrium point. In the following, the asymptotic stability of the equilibrium point will be proved. For simplicity, we transformed the equilibrium point of system (1) to the origin. We assumed that $z^* = (x_1^*, x_2^*, \dots, x_n^*, y_1^*, y_2^*, \dots, y_n^*)^T$ is an equilibrium of neural system (1). By the transformation $u_i(\cdot) = x_i(\cdot) - x_i^*$, $w_j(\cdot) = y_j(\cdot) - y_j^*$, one can transform system (1) into the system as follows:

$$\begin{cases} \dot{u}(t) = -Au(t) + C\tilde{f}(w(t)) + \tilde{C}\tilde{f}(w(t-\tau)), \\ \dot{w}(t) = -Bw(t) + D\tilde{g}(u(t)) + \tilde{D}\tilde{g}(u(t-\sigma)), \end{cases} \quad (2)$$

where $\tilde{f}(w(t)) = (\tilde{f}_1(w_1(t)), \tilde{f}_2(w_2(t)), \dots, \tilde{f}_n(w_n(t)))^T$, $\tilde{g}(u(t)) = (\tilde{g}_1(u_1(t)), \tilde{g}_2(u_2(t)), \dots, \tilde{g}_n(u_n(t)))^T$, in which $\tilde{f}_j(w_j(t)) = f_j(w_j(t) + y_j^*) - f_j(y_j^*)$, and $\tilde{g}_i(u_i(t)) = g_i(u_i(t) + x_i^*) - g_i(x_i^*)$. Functions $\tilde{f}_j(\cdot)$, $\tilde{g}_i(\cdot)$ satisfy the condition (H_1) ; hence, $\tilde{f}_j(\cdot)$, $\tilde{g}_i(\cdot)$ satisfy

$$\begin{cases} \tilde{f}_j^2(w_j(\cdot)) \leq l_j w_j(\cdot) \tilde{f}_j(w_j(\cdot)), \\ \tilde{f}_j^2(w_j(\cdot)) \leq l_j^2 w_j^2(\cdot), \quad \tilde{f}_j(0) = 0, \end{cases} \quad (3)$$

$$\begin{cases} \tilde{g}_i^2(u_i(\cdot)) \leq m_i u_i(\cdot) \tilde{g}_i(u_i(\cdot)), \\ \tilde{g}_i^2(u_i(\cdot)) \leq m_i^2 u_i^2(\cdot), \quad \tilde{g}_i(0) = 0. \end{cases} \quad (4)$$

Remark 2: It is easy to verify that systems (1) and (2) have the same stability. Therefore, to prove the stability of the equilibrium point z^* of the system (1), it is sufficient to prove the stability of the trivial solution of the system (2).

Theorem 1: Under condition (H_1) , if there exist positive definite diagonal matrices $P = \{p_i\} \in \mathbb{R}^{n \times n}$, $N = \{n_i\} \in \mathbb{R}^{n \times n}$ and constants $\varsigma_1, \varsigma_2, \beta_1, \beta_2 > 0$ such that

$$\begin{aligned} -2PA + \varsigma_1^{-1}P\tilde{C}N^{-1}\tilde{C}^T P + \beta_1^{-1}PCC^T P + \beta_2 M^2 + \varsigma_2 PM^2 &< 0, \\ -2NB + \varsigma_2^{-1}N\tilde{D}P^{-1}\tilde{D}^T N + \beta_2^{-1}NDD^T N + \beta_1 L^2 + \varsigma_1 NL^2 &< 0, \end{aligned}$$

where $M = \text{diag}\{m_1, \dots, m_n\}$, $L = \text{diag}\{l_1, \dots, l_n\}$; then the zero solution of neural system (2) is a unique equilibrium point and is globally asymptotically stable. Proof. Now, we chose Lyapunov functional.

$$\begin{aligned} V(u(t), w(t)) &= \sum_{i=1}^n p_i u_i^2(t) + \varsigma_1 \sum_{j=1}^n \int_{t-\tau_j}^t n_j \tilde{f}_j^2(w_j(s)) ds \\ &\quad + \sum_{j=1}^n n_j w_j^2(t) + \varsigma_2 \sum_{i=1}^n \int_{t-\sigma_i}^t p_i \tilde{g}_i^2(u_i(s)) ds. \end{aligned}$$

Then,

$$\begin{aligned} \dot{V}(u(t), w(t)) &= 2 \sum_{i=1}^n p_i u_i(t) \dot{u}_i(t) + \varsigma_1 \sum_{j=1}^n n_j [\tilde{f}_j^2(w_j(t)) - \tilde{f}_j^2(w_j(t-\tau_j))] \\ &\quad + 2 \sum_{j=1}^n n_j w_j(t) \dot{w}_j(t) + \varsigma_2 \sum_{i=1}^n p_i [\tilde{g}_i^2(u_i(t)) - \tilde{g}_i^2(u_i(t-\sigma_i))] \\ &= 2u^T(t)P\dot{u}(t) + \varsigma_1 \tilde{f}^T(w(t))N\tilde{f}(w(t)) - \varsigma_1 \tilde{f}^T(w(t-\tau))N \\ &\quad \times \tilde{f}(w(t-\tau)) + 2w^T(t)N\dot{w}(t) + \varsigma_2 \tilde{g}^T(u(t))P\tilde{g}(u(t)) \\ &\quad - \varsigma_2 \tilde{g}^T(u(t-\sigma))P\tilde{g}(u(t-\sigma)) \\ &= 2u^T(t)P(-Au(t) + C\tilde{f}(w(t)) + \tilde{C}\tilde{f}(w(t-\tau))) + \varsigma_1 \tilde{f}^T(w(t))N \\ &\quad \times \tilde{f}(w(t)) - \varsigma_1 \tilde{f}^T(w(t-\tau))N\tilde{f}(w(t-\tau)) + 2w^T(t)N(-Bw(t) \\ &\quad + D\tilde{g}(u(t)) + \tilde{D}\tilde{g}(u(t-\sigma))) + \varsigma_2 \tilde{g}^T(u(t))P\tilde{g}(u(t)) \\ &\quad - \varsigma_2 \tilde{g}^T(u(t-\sigma))P\tilde{g}(u(t-\sigma)). \end{aligned} \quad (5)$$

By Lemma 1, we obtained

$$\begin{aligned} -\varsigma_1 \tilde{f}^T(w(t-\tau))N\tilde{f}(w(t-\tau)) \\ + 2u^T(t)P\tilde{C}\tilde{f}(w(t-\tau)) \leq \varsigma_1^{-1}u^T(t)P\tilde{C}N^{-1}\tilde{C}^T Pu(t), \end{aligned} \quad (6)$$

$$\begin{aligned} -\varsigma_2 \tilde{g}^T(u(t-\sigma))P\tilde{g}(u(t-\sigma)) \\ + 2w^T(t)N\tilde{D}\tilde{g}(u(t-\sigma)) \leq \varsigma_2^{-1}w^T(t)N\tilde{D}P^{-1}\tilde{D}^T Nw(t). \end{aligned} \quad (7)$$

From Eqs 6, 7, then

$$\begin{aligned} \dot{V}(u(t), w(t)) &\leq -2u^T(t)PAu(t) + 2u^T(t)PC\tilde{f}(w(t)) + \varsigma_1^{-1}u^T(t)P\tilde{C}N^{-1}\tilde{C}^T Pu(t) \\ &\quad + \varsigma_1 \tilde{f}^T(w(t))N\tilde{f}(w(t)) - 2w^T(t)NBw(t) + 2w^T(t)N\tilde{D}\tilde{g}(u(t)) \\ &\quad + \varsigma_2^{-1}w^T(t)N\tilde{D}P^{-1}\tilde{D}^T Nw(t) + \varsigma_2 \tilde{g}^T(u(t))P\tilde{g}(u(t)) \\ &\leq -2u^T(t)PAu(t) + \beta_1^{-1}u^T(t)PCC^T Pu(t) + \beta_1 \tilde{f}^T(w(t))\tilde{f}(w(t)) \\ &\quad + \varsigma_1^{-1}u^T(t)P\tilde{C}N^{-1}\tilde{C}^T Pu(t) + \varsigma_1 w^T(t)NL^2 w(t) - 2w^T(t)NBw(t) \\ &\quad + \beta_2^{-1}w^T(t)NDD^T Nw(t) + \beta_2 \tilde{g}^T(u(t))\tilde{g}(u(t)) \\ &\quad + \varsigma_2^{-1}w^T(t)N\tilde{D}P^{-1}\tilde{D}^T Nw(t) + \varsigma_2 u^T(t)PM^2 u(t) \\ &= u^T(t) \left(-2PA + \varsigma_1^{-1}P\tilde{C}N^{-1}\tilde{C}^T P + \beta_1^{-1}PCC^T P + \beta_2 M^2 + \varsigma_2 PM^2 \right) u(t) \\ &\quad + w^T(t) \left(-2NB + \varsigma_2^{-1}N\tilde{D}P^{-1}\tilde{D}^T N + \beta_2^{-1}NDD^T N + \beta_1 L^2 \right. \\ &\quad \left. + \varsigma_1 NL^2 \right) w(t) \\ &< 0, \quad \forall u(t) \neq 0, w(t) \neq 0. \end{aligned} \quad (8)$$

This implies that the origin solution of system (2) is asymptotically stable. So the equilibrium point of system (1) is asymptotically stable.

Corollary 1: Under condition (H_1) , suppose $L = M = E$, $\varsigma_1 = \varsigma_2 = \beta_1 = \beta_2 = 1$, if there exist positive definite diagonal matrices $P = \{p_i\} \in R^{n \times n}$, $N = \{n_i\} \in R^{n \times n}$ such that

$$\begin{aligned} -2PA + \tilde{P}\tilde{C}N^{-1}\tilde{C}^T P + PCC^T P + E + P &< 0, \\ -2NB + N\tilde{D}P^{-1}\tilde{D}^T N + NDD^T N + E + N &< 0, \end{aligned}$$

then, the origin solution of network (2) is a unique equilibrium point, and it is globally asymptotically stable.

4 GLOBAL DISSIPATIVITY FOR BAM NEURAL NETWORKS

In this part, the global dissipativity for the BAM neural system (1) is considered.

Theorem 2: Under assumption (H_1) , suppose $z(t) = (x_1(t), \dots, x_n(t), y_1(t), \dots, y_n(t))^T$ is a solution of system (1) and

$$\xi(t) + \eta(t) \leq -\alpha < 0,$$

then for any given $\varepsilon > 0$, there exists T such that for all $t \geq T$

$$\|z(t)\|_2 \leq \sqrt{\frac{\gamma^2}{\alpha}} + \varepsilon.$$

So, network (1) is dissipative, and the closed ball $E = E(0, \sqrt{\frac{\gamma^2}{\alpha}} + \varepsilon)$ is an absorbing set, where $\gamma = \delta_3 \|I\|_2^2 + \rho_3 \|J\|_2^2$, $\xi(t) = \max\{-2\lambda_{\min}(A) + \delta_1^{-1} + \delta_2^{-1} + \rho_1 m^2 \|D\|_2^2 + \delta_3^{-1}, -2\lambda_{\min}(B) + \rho_1^{-1} + \rho_2^{-1} + \delta_1 l^2 \|C\|_2^2 + \rho_3^{-1}\}$, $\eta(t) = \max\{\delta_2 l^2 \|\tilde{C}\|_2^2, \rho_2 m^2 \|\tilde{D}\|_2^2\}$, $\delta_1, \delta_2, \delta_3, \rho_1, \rho_2, \rho_3 > 0$, $l = \max_{j \in I} \{l_j\}$, and $m = \max_{i \in I} \{m_i\}$. Proof. The Lyapunov functional should be considered:

$$V(t) = \|x(t)\|_2^2 + \|y(t)\|_2^2. \quad (9)$$

Then,

$$\begin{aligned} \dot{V}(t) &= 2\langle x(t), \dot{x}(t) \rangle + 2\langle y(t), \dot{y}(t) \rangle \\ &= 2\langle x(t), -Ax(t) \rangle + 2\langle x(t), Cf(y(t)) \rangle + 2\langle x(t), \tilde{C}f(y(t-\tau)) \rangle \\ &\quad + 2\langle x(t), I \rangle + 2\langle y(t), -By(t) \rangle + 2\langle y(t), Dg(x(t)) \rangle \\ &\quad + 2\langle y(t), \tilde{D}g(x(t-\sigma)) \rangle + 2\langle y(t), J \rangle \\ &\leq -2\lambda_{\min}(A)\|x(t)\|_2^2 + 2f^T(y(t))C^T x(t) + 2f^T(y(t-\tau))\tilde{C}^T x(t) + 2I^T x(t) \\ &\quad - 2\lambda_{\min}(B)\|y(t)\|_2^2 + 2g^T(x(t))D^T y(t) + 2g^T(x(t-\sigma))\tilde{D}^T y(t) + 2J^T y(t). \end{aligned} \quad (10)$$

By $\langle x, y \rangle = y^T x$, (H_1) , and Lemma 1, there exists $\sigma_1, \sigma_2, \sigma_3, \rho_1, \rho_2, \rho_3 > 0$ such that

$$\begin{aligned} 2f^T(y(t))C^T x(t) &\leq \delta_1 f^T(y(t))C^T Cf(y(t)) + \delta_1^{-1} x^T(t)x(t) \\ &\leq \delta_1 \lambda_{\max}(C^T C) \|f(y(t))\|_2^2 + \delta_1^{-1} \|x(t)\|_2^2 \\ &\leq \delta_1 \lambda_{\max}(C^T C) l^2 \|y(t)\|_2^2 + \delta_1^{-1} \|x(t)\|_2^2 \\ &\leq \delta_1 l^2 \|C\|_2^2 \|y(t)\|_2^2 + \delta_1^{-1} \|x(t)\|_2^2, \end{aligned} \quad (11)$$

$$\begin{aligned} 2f^T(y(t-\tau))\tilde{C}^T x(t) &\leq \delta_2 f^T(y(t-\tau))\tilde{C}^T \tilde{C} f(y(t-\tau)) + \delta_2^{-1} x^T(t)x(t) \\ &\leq \delta_2 \lambda_{\max}(\tilde{C}^T \tilde{C}) \|f(y(t-\tau))\|_2^2 + \delta_2^{-1} \|x(t)\|_2^2 \\ &\leq \delta_2 \lambda_{\max}(\tilde{C}^T \tilde{C}) l^2 \|y(t-\tau)\|_2^2 + \delta_2^{-1} \|x(t)\|_2^2 \\ &\leq \delta_2 l^2 \|\tilde{C}\|_2^2 \|y(t-\tau)\|_2^2 + \delta_2^{-1} \|x(t)\|_2^2, \end{aligned} \quad (12)$$

$$\begin{aligned} I^T x(t) &\leq \delta_3 I^T I + \delta_3^{-1} x^T(t)x(t) \\ &\leq \delta_3 \|I\|_2^2 + \delta_3^{-1} \|x(t)\|_2^2. \end{aligned} \quad (13)$$

Similar to Eqs 11–13, then

$$2g^T(x(t))D^T y(t) \leq \rho_1 m^2 \|D\|_2^2 \|x(t)\|_2^2 + \rho_1^{-1} \|y(t)\|_2^2, \quad (14)$$

$$2g^T(x(t-\sigma))\tilde{D}^T y(t) \leq \rho_2 m^2 \|\tilde{D}\|_2^2 \|x(t-\sigma)\|_2^2 + \rho_2^{-1} \|y(t)\|_2^2, \quad (15)$$

$$J^T y(t) \leq \rho_3 \|J\|_2^2 + \rho_3^{-1} \|y(t)\|_2^2. \quad (16)$$

By using Eqs 11–16 in Eq. 10, it is easy to obtain

$$\begin{aligned} \dot{V}(t) &\leq (-2\lambda_{\min}(A) + \delta_1^{-1} + \delta_2^{-1} + \rho_1 m^2 \|D\|_2^2 + \delta_3^{-1}) \|x(t)\|_2^2 \\ &\quad + (-2\lambda_{\min}(B) + \rho_1^{-1} + \rho_2^{-1} + \delta_1 l^2 \|C\|_2^2 + \rho_3^{-1}) \|y(t)\|_2^2 \\ &\quad + \delta_2 l^2 \|\tilde{C}\|_2^2 \|y(t-\tau)\|_2^2 + \rho_2 m^2 \|\tilde{D}\|_2^2 \|x(t-\sigma)\|_2^2 \\ &\quad + \delta_3 \|J\|_2^2 + \rho_3 \|J\|_2^2 \\ &\leq \gamma + \xi(t) (\|x(t)\|_2^2 + \|y(t)\|_2^2) + \eta(t) (\|x(t-\sigma)\|_2^2 + \|y(t-\tau)\|_2^2) \\ &\leq \gamma + \xi(t)V(t) + \eta(t) \sup_{t-\max\{\tilde{\tau}, \tilde{\sigma}\} \leq s \leq t} V(s). \end{aligned} \quad (17)$$

Then, by Lemma 2, we obtain

$$\begin{aligned} \|z(t)\|_2^2 &\leq \|x(t)\|_2^2 + \|y(t)\|_2^2 = V(t) \leq \frac{\gamma^*}{\alpha} \\ &\quad + \left(\sup_{-\infty \leq s \leq 0} V(s) - \frac{\gamma^*}{\alpha} \right) e^{-\mu^* t}, \end{aligned}$$

where $\mu^* = \inf_{t \geq 0} \{\mu(t) : \mu(t) + \xi(t) + \eta(t) e^{\mu(t) \max\{\tilde{\tau}, \tilde{\sigma}\}} = 0\}$.

So, for the given sufficient small $\varepsilon > 0$, there exists $T \geq 0$ such that

$$\|z(t)\|_2 \leq \sqrt{\frac{\gamma^*}{\alpha}} + \varepsilon, \quad \forall t \geq T,$$

where $\varepsilon > 0$ is sufficiently small. \square

Corollary 2: If taking $\delta_1, \delta_2, \delta_3, \rho_1, \rho_2, \rho_3 = 1$, under assumptions (H_1) , suppose that $z(t) = (x_1(t), \dots, x_n(t), y_1(t), \dots, y_n(t))^T$ is a solution of network (1) and

$$\xi(t) + \eta(t) \leq -\alpha < 0,$$

then network (1) is dissipative, and the closed ball $E = E(0, \sqrt{\frac{\gamma^2}{\alpha}} + \varepsilon)$ is an absorbing set for any $\varepsilon > 0$, where $\gamma = \|I\|_2^2 + \|J\|_2^2$, $\xi(t) = \max\{-2\lambda_{\min}(A) + m^2 \|D\|_2^2 + 3, -2\lambda_{\min}(B) + l^2 \|C\|_2^2 + 3\}$, $\eta(t) = \max\{l^2 \|\tilde{C}\|_2^2, m^2 \|\tilde{D}\|_2^2\}$.

Corollary 3: Under assumptions (H_1) , suppose that $z(t) = (x_1(t), \dots, x_n(t), y_1(t), \dots, y_n(t))^T$ is a solution of network (1), if

$$\xi(t) + \eta(t) \leq -\alpha < 0$$

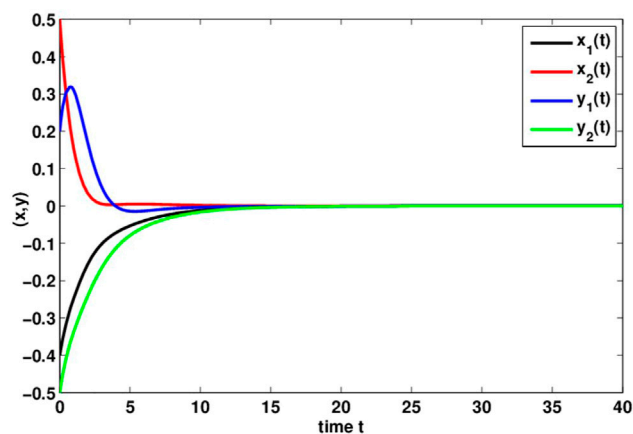


FIGURE 1 | Trajectories of system (18) for $[x(0), y(0)]^T = (-0.4, 0.5, 0.2, -0.5)^T$.

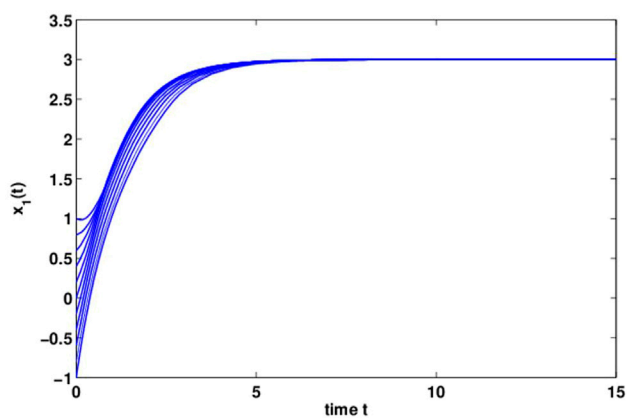


FIGURE 2 | Time response of the state variable $x_1(t)$ with different initial values.

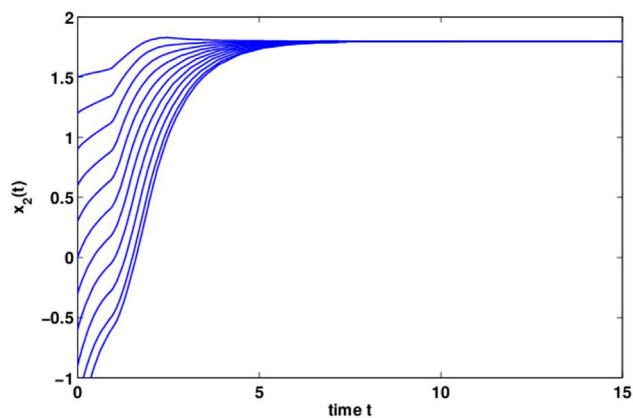


FIGURE 3 | Time response of the state variable $x_2(t)$ with different initial values.

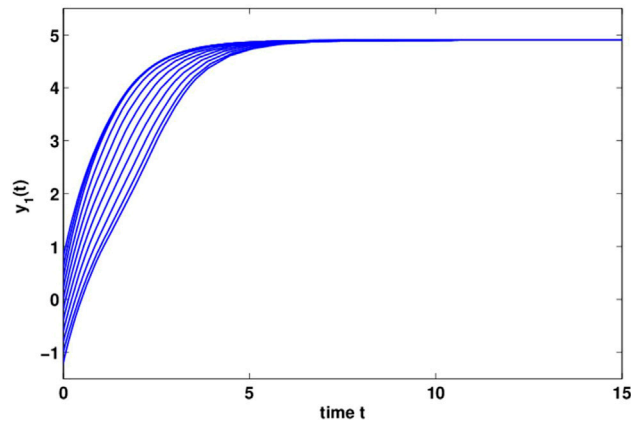


FIGURE 4 | Time response of the state variable $y_1(t)$ with different initial values.

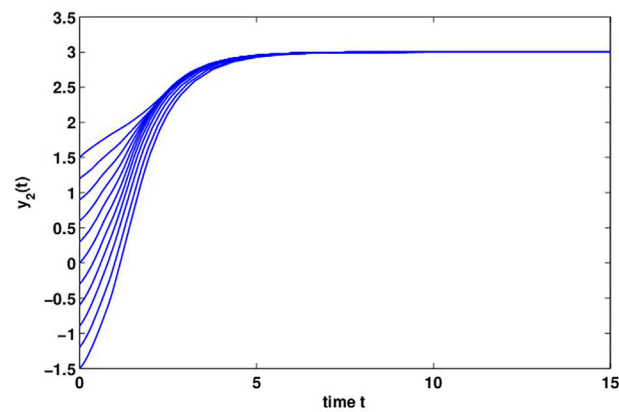


FIGURE 5 | Time response of the state variable $y_2(t)$ with different initial values.

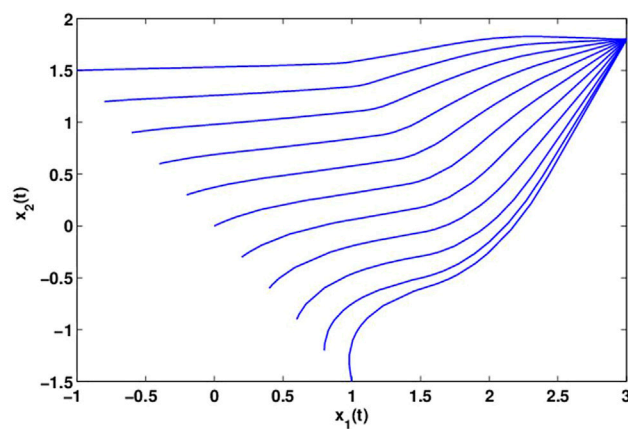


FIGURE 6 | Time response of the state variable $x_1(t)$ and $x_2(t)$ with different initial values.

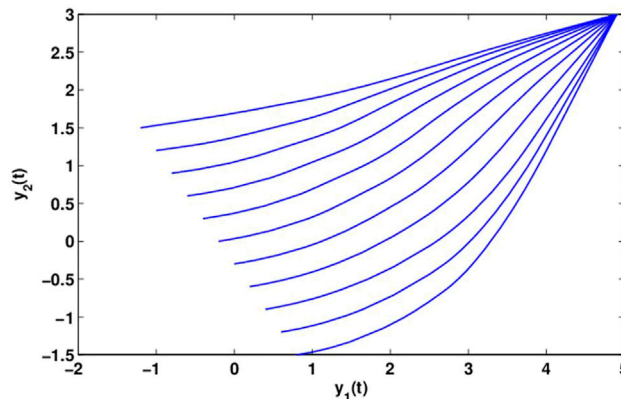


FIGURE 7 | Time response of the state variable $y_1(t)$ and $y_2(t)$ with different initial values.

and

$$\lim_{t \geq 0} \{\delta_3 \|I\|_2^2 + \rho_3 \|J\|_2^2\} = 0,$$

then system (1) is globally stable, where $\gamma = \delta_3 \|I\|_2^2 + \rho_3 \|J\|_2^2$, $\xi(t) = \max\{-2\lambda_{\min}(A) + \delta_1^{-1} + \delta_2^{-1} + \rho_1 m^2 \|D\|_2^2 + \delta_3^{-1}, -2\lambda_{\min}(B) + \rho_1^{-1} + \rho_2^{-1} + \delta_1 l^2 \|C\|_2^2 + \rho_3^{-1}\}$, $\eta(t) = \max\{\delta_2 l^2 \|\tilde{C}\|_2^2, \rho_2 m^2 \|\tilde{D}\|_2^2\}$, $\delta_1, \delta_2, \delta_3, \rho_1, \rho_2, \rho_3 > 0$.

Remark 3: In the existing articles, a lot of researchers studied the qualitative behaviors of neural systems *via* the Lyapunov function with linear matrix inequality techniques [26, 29, 30]. However, in this article, some new sufficient criteria of dissipativity of BAM neural networks with time delays are given by only using the property of matrix theory and inner product.

5 NUMERICAL SIMULATIONS

In the part, two examples are presented to show the effectiveness.

Example 1. Investigation of the delayed BAM neural network model.

$$\begin{cases} \dot{x}(t) = -Ax(t) + Cf(y(t)) + \tilde{C}f(y(t-\tau)) + I, \\ \dot{y}(t) = -By(t) + Dg(x(t)) + \tilde{D}g(x(t-\sigma)) + J, \end{cases} \quad (18)$$

in which $x(t) = (x_1(t), x_2(t))^T$ and $y(t) = (y_1(t), y_2(t))^T$. Let $\tau_1 = 1$, $\tau_1 = 0.9$, $\sigma_1 = 0.8$, $\sigma_2 = 0.7$, $A = B = E$, $I = J = 0$ and

$$C = \begin{pmatrix} 0 & 0.2 \\ -0.2 & 0.1 \end{pmatrix}, \tilde{C} = \begin{pmatrix} 0.1 & 0.2 \\ 0 & -0.1 \end{pmatrix}, D = \begin{pmatrix} 0.2 & 1 \\ 1 & 0.4 \end{pmatrix}, \tilde{D} = \begin{pmatrix} 0.2 & 0.5 \\ 0 & -0.1 \end{pmatrix}.$$

Choose $f_j(y_j) = (|y_j + 1| + |y_j - 1|)/2$, $g_j(x_j) = (|x_j + 1| + |x_j - 1|)/2$, $j = 1, 2$, $l_1 = l_2 = m_1 = m_2 = l = m = \delta_1 = \delta_2 = \delta_3 = \rho_1 = \rho_2 = 1$.

By computing, we can get

$$-2PA + \zeta_1^{-1} P \tilde{C} N^{-1} \tilde{C}^T P + \beta_1^{-1} P C C^T P + \beta_2 M^2 + \zeta_2 P M^2 < 0,$$

$$-2NB + \zeta_2^{-1} N \tilde{D} P^{-1} \tilde{D}^T N + \beta_2^{-1} N D D^T N + \beta_1 L^2 + \zeta_1 N L^2 < 0.$$

So, from Theorem 1, network (18) has a unique equilibrium, and it is globally asymptotically stable. By MATLAB, a unique equilibrium of network (18) $(0,0,0,0)^T$ is given, and the simulation results are given in **Figure 1**.

Example 2. The BAM neural model with delays is considered as (Eq. 18), where $x(t) = (x_1(t), x_2(t))^T$, $y(t) = (y_1(t), y_2(t))^T$ and $x(0) = (-1, 1.5)^T$, $y(0) = (0.8, -1.5)^T$. Let $\tau_1 = 0.9$, $\tau_2 = 0.9$, $\sigma_1 = 0.8$, $\sigma_2 = 0.8$, $A = B = E$, $I = (1, 0.5)^T$, $J = (2.5, 0.5)^T$ and

$$C = \begin{pmatrix} 1 & 0.2 \\ -0.2 & 0.1 \end{pmatrix}, \tilde{C} = \begin{pmatrix} 0.1 & 0.2 \\ 1 & -0.1 \end{pmatrix}, D = \begin{pmatrix} 0.2 & 1 \\ 1 & 0.4 \end{pmatrix}, \tilde{D} = \begin{pmatrix} 0.2 & 0.5 \\ 1 & -0.1 \end{pmatrix}.$$

Choose $f_j(y_j) = (|y_j + 1| + |y_j - 1|)/2$, $g_j(x_j) = (|x_j + 1| + |x_j - 1|)/2$, $j = 1, 2$ and $l_1 = l_2 = m_1 = m_2 = l = m = \delta_1 = \delta_2 = \delta_3 = \rho_1 = \rho_2 = \rho_3 = 1$.

By computing, we can get $\gamma = 7.75$, $\xi(t) = 2.703$, $\eta(t) = 1.04$. Let $\alpha = 4$, $\varepsilon = 0.98$, it follows from Theorem 2 and is observed that system (18) is global dissipativity. **Figures 2, 3** reflect the behaviors for the states $x_1(t)$ and $x_2(t)$ with different initial conditions. **Figures 4, 5** show the phase plane behaviors of $y_1(t)$ and $y_2(t)$ with different initial conditions. **Figures 6, 7** demonstrate the behaviors of the time domain for the states $x_1(t)$, $x_2(t)$ and $y_1(t)$, $y_2(t)$ with different initial conditions. System (18) is globally dissipative from the numerical simulations.

Remark 4: In the numerical simulation part of [13], the author only gives the simulation diagram of the BAM neural network model with one node. This article presents the simulation diagram of the BAM neural network model with two nodes. Moreover, in [13], the values of $\sigma(t)$ and $\tau(t)$ are all 1, while the values of $\sigma_1(t)$, $\sigma_2(t)$, $\tau_1(t)$, and $\tau_2(t)$ in this study are different. Therefore, in numerical simulation, this study is more general in the value of the model and time delay. In addition, the

unique equilibrium point $(0,0,0,0)^T$ of the system (18) is obtained by MATLAB. **Figure 1** shows an image which is globally asymptotically stable of the system (18) under initial conditions $(x_1(t), x_2(t), y_1(t), y_2(t))^T = (-0.4, 0.5, 0.2, -0.5)^T$. **Figures 2–5** show the state diagram of $x_1(t)$, $x_2(t)$, $y_1(t)$, and $y_2(t)$ under different initial conditions with respect to time t . **Figures 6, 7** show the state diagrams of $x_1(t)$, $x_2(t)$ and $y_1(t)$, $y_2(t)$ under different initial conditions with respect to time t . The previous figures given in this study can more intuitively reflect the stability and dissipation of the BAM neural network model.

6 CONCLUSION

In this study, by using matrix theory, inner product properties, generalized Halanay inequalities, and constructing appropriate Lyapunov functionals, novel sufficient criteria of the global asymptotic stability of the system and the global dissipativity of the equilibrium point have been derived for a type of BAM neural systems with delays. The given results might have an impact on investigating the instability, the existence of periodic solutions, and the stability of BAM neural networks. A comparison between the results and the correspondingly previous works implies that the derived criteria are less conservative and more general through numerical simulations.

REFERENCES

- Kosko B. Adaptive Bidirectional Associative Memories. *Appl Opt* (1987) 26: 4947–60. doi:10.1364/ao.26.004947
- Rajivganthi C, Rihan FA, Lakshmanan S. Dissipativity Analysis of Complex Valued BAM Neural Networks with Time Delay. *Neural Comput. Applic.* (2019). 31:127–137. doi:10.1007/s00521-017-2985-9
- Kosko B. Bidirectional Associative Memories. *IEEE Trans Syst Man Cybern* (1988) 18(10):49–60. doi:10.1109/21.87054
- Hopfield JJ. Neural Networks and Physical Systems with Emergent Collective Computational Abilities. *Proc Natl Acad Sci U.S.A* (1982) 79:2554–8. doi:10.1073/pnas.79.8.2554
- Hopfield JJ. Neurons with Graded Response Have Collective Computational Properties like Those of Two-State Neurons. *Proc Natl Acad Sci U.S.A* (1984) 81:3088–92. doi:10.1073/pnas.81.10.3088
- Kosto B. *Neural Networks and Fuzzy Systems-A Dynamical System Approach Machine Intelligence*. Englewood Cliffs, NJ: Prentice-Hall (1992).
- Abdurahman A, Jiang H. Nonlinear Control Scheme for General Decay Projective Synchronization of Delayed Memristor-Based BAM Neural Networks. *Neurocomputing* (2019) 357:282–91. doi:10.1016/j.neucom.2019.05.015
- Xu G, Bao H. Further Results on Mean-Square Exponential Input-To-State Stability of Time-Varying Delayed BAM Neural Networks with Markovian Switching. *Neurocomputing* (2020) 376:191–201. doi:10.1016/j.neucom.2019.09.033
- Liu J, Jian J, Wang B. Stability Analysis for BAM Quaternion-Valued Inertial Neural Networks with Time Delay via Nonlinear Measure Approach. *Mathematics Comput Simulation* (2020) 174:134–52. doi:10.1016/j.matcom.2020.03.002
- Priya B, Ali MS, Thakur GK, Sanober S, Dhupia B. Pth Moment Exponential Stability of Memristor Cohen-Grossberg BAM Neural Networks with Time-Varying Delays and Reaction-Diffusion. *Chin J Phys* (2021) 74:184–94. doi:10.1016/j.cjph.2021.06.027

DATA AVAILABILITY STATEMENT

The original contributions presented in the study are included in the article/Supplementary Material; further inquiries can be directed to the corresponding author.

AUTHOR CONTRIBUTIONS

ML established the mathematical model, theoretical analysis, and wrote the original draft; HJ provided modeling ideas and analysis methods; CH checked the correctness of theoretical results; BL and ZL performed the simulation experiments. All authors read and approved the final manuscript.

FUNDING

This work was supported by the National Natural Science Foundation of China (Grants No. 62003380).

ACKNOWLEDGMENTS

The authors are grateful to the editors and referees for their valuable suggestions and comments, which greatly improved the presentation of this article.

- Fang T, Ru T, Fu D, Su L, Wang J. Extended Dissipative Filtering for Markov Jump BAM Inertial Neural Networks under Weighted Try-Once-Discard Protocol. *J Franklin Inst* (2021) 358:4103–17. doi:10.1016/j.jfranklin.2021.03.009
- Yan M, Jiang M. Synchronization with General Decay Rate for Memristor-Based BAM Neural Networks with Distributed Delays and Discontinuous Activation Functions. *Neurocomputing* (2020) 387:221–40. doi:10.1016/j.neucom.2019.12.124
- Wu Z-G, Shi P, Su H, Lu R. Dissipativity-Based Sampled-Data Fuzzy Control Design and its Application to Truck-Trailer System. *IEEE Trans Fuzzy Syst* (2015) 23:1669–79. doi:10.1109/tfuzz.2014.2374192
- Xu C, Aouiti C, Liu Z. A Further Study on Bifurcation for Fractional Order BAM Neural Networks with Multiple Delays. *Neurocomputing* (2020) 417: 501–15. doi:10.1016/j.neucom.2020.08.047
- Yan M, Jian J, Zheng S. Passivity Analysis for Uncertain BAM Inertial Neural Networks with Time-Varying Delays. *Neurocomputing* (2021) 435:114–25.
- Li R, Cao J. Passivity and Dissipativity of Fractional-Order Quaternion-Valued Fuzzy Memristive Neural Networks: Nonlinear Scalarization Approach. *IEEE Trans Cybern* (2022) 52 (99) 2821–2832. doi:10.1109/tcyb.2020.3025439
- Li Y, He Y. Dissipativity Analysis for Singular Markovian Jump Systems with Time-Varying Delays via Improved State Decomposition Technique. *Inf Sci* (2021) 580:643–54. doi:10.1016/j.ins.2021.08.092
- Zhou L. Delay-dependent Exponential Stability of Cellular Neural Networks with Multi-Proportional Delays. *Neural Process Lett* (2013) 38(3):321–46. doi:10.1007/s11063-012-9271-8
- Zhou L, Chen X, Yang Y. Asymptotic Stability of Cellular Neural Networks with Multiple Proportional Delays. *Appl Maths Comput* (2014) 229(1):457–66. doi:10.1016/j.amc.2013.12.061
- Zhou L. Global Asymptotic Stability of Cellular Neural Networks with Proportional Delays. *Nonlinear Dyn* (2014) 77(1):41–7. doi:10.1007/s11071-014-1271-y
- Zhou L. Delay-dependent Exponential Synchronization of Recurrent Neural Networks with Multiple Proportional Delays. *Neural Process Lett* (2015) 42(3): 619. doi:10.1007/s11063-014-9377-2

22. Cong Z, Li N, Cao J. Matrix Measure Based Stability Criteria for High-Order Networks with Proportional Delay. *Neurocomputing* (2015) 149:1149. doi:10.1016/j.neucom.2014.09.016
23. Zhang T, Li Y. Global Exponential Stability of Discrete-Time Almost Automorphic Caputo-Fabrizio BAM Fuzzy Neural Networks via Exponential Euler Technique. *Knowledge-Based Syst* (2022) 246:108675. doi:10.1016/j.knosys.2022.108675
24. Wang S, Zhang Z, Lin C, Chen J. Fixed-time Synchronization for Complex-Valued BAM Neural Networks with Time-Varying Delays via Pinning Control and Adaptive Pinning Control. *Chaos, Solitons & Fractals* (2021) 153:111583. doi:10.1016/j.chaos.2021.111583
25. Cai Z, Huang L. Functional Differential Inclusions and Dynamic Behaviors for Memristor-Based BAM Neural Networks with Time-Varying Delays. *Commun Nonlinear Sci Numer Simulation* (2014) 19:1279–300. doi:10.1016/j.cnsns.2013.09.004
26. Zhou L. Novel Global Exponential Stability Criteria for Hybrid BAM Neural Networks with Proportional Delays. *Neurocomputing* (2015) 161:99–106. doi:10.1016/j.neucom.2015.02.061
27. Ren F, Cao J. LMI-based Criteria for Stability of High-Order Neural Networks with Time-Varying Delay. *Nonlinear Anal Real World Appl* (2006) 7:967–79. doi:10.1016/j.nonrwa.2005.09.001
28. Bo Liu B, Wenlian Lu W, Tianping Chen T. Generalized Halanay Inequalities and Their Applications to Neural Networks with Unbounded Time-Varying Delays. *IEEE Trans Neural Netw* (2011) 22(9):1508–13. doi:10.1109/tnn.2011.2160987
29. Wang Z, Huang L. Global Stability Analysis for Delayed Complex-Valued BAM Neural Networks. *Neurocomputing* (2016) 173:2083–9. doi:10.1016/j.neucom.2015.09.086
30. Rajchakit G, Saravanakumar R, Ahn CK, Karimi HR. Improved Exponential Convergence Result for Generalized Neural Networks Including Interval Time-Varying Delayed Signals. *Neural Networks* (2017) 86:10–7. doi:10.1016/j.neunet.2016.10.009

Conflict of Interest: The authors declare that the research was conducted in the absence of any commercial or financial relationships that could be construed as a potential conflict of interest.

Publisher's Note: All claims expressed in this article are solely those of the authors and do not necessarily represent those of their affiliated organizations, or those of the publisher, the editors, and the reviewers. Any product that may be evaluated in this article, or claim that may be made by its manufacturer, is not guaranteed or endorsed by the publisher.

Copyright © 2022 Liu, Jiang, Hu, Lu and Li. This is an open-access article distributed under the terms of the Creative Commons Attribution License (CC BY). The use, distribution or reproduction in other forums is permitted, provided the original author(s) and the copyright owner(s) are credited and that the original publication in this journal is cited, in accordance with accepted academic practice. No use, distribution or reproduction is permitted which does not comply with these terms.



Optimal Resonances in Multiplex Neural Networks Driven by an STDP Learning Rule

Marius E. Yamakou^{1,2*}, Tat Dat Tran^{3,2} and Jürgen Jost^{2,4}

¹Department of Data Science, Friedrich-Alexander-Universität Erlangen-Nürnberg, Erlangen, Germany, ²Max-Planck-Institut für Mathematik in den Naturwissenschaften, Leipzig, Germany, ³Fakultät für Mathematik und Informatik, Universität Leipzig, Leipzig, Germany, ⁴Santa Fe Institute for the Sciences of Complexity, Santa Fe, NM, United States

OPEN ACCESS

Edited by:

André H. Erhardt,
Weierstrass Institute for Applied
Analysis and Stochastics (LG),
Germany

Reviewed by:

Manish Dev Shrivastava,
Central University of Rajasthan, India
Rico Berner,
Humboldt University of Berlin,
Germany

*Correspondence:

Marius E. Yamakou
yamakoumaris@gmail.com

Specialty section:

This article was submitted to
Statistical and Computational Physics,
a section of the journal
Frontiers in Physics

Received: 31 March 2022

Accepted: 08 June 2022

Published: 04 July 2022

Citation:

Yamakou ME, Tran TD and Jost J
(2022) Optimal Resonances in
Multiplex Neural Networks Driven by an
STDP Learning Rule.
Front. Phys. 10:909365.
doi: 10.3389/fphy.2022.909365

In this paper, we numerically investigate two distinct phenomena, coherence resonance (CR) and self-induced stochastic resonance (SISR), in multiplex neural networks in the presence of spike-timing-dependent plasticity (STDP). The high degree of CR achieved in one layer network turns out to be more robust than that of SISR against variations in the network topology and the STDP parameters. This behavior is the opposite of the one presented by Yamakou and Jost (Phys. Rev. E 100, 022313, 2019), where SISR is more robust than CR against variations in the network parameters but in the absence of STDP. Moreover, the degree of SISR in one layer network increases with a decreasing (increasing) depression temporal window (potentiation adjusting rate) of STDP. However, the poor degree of SISR in one layer network can be significantly enhanced by multiplexing this layer with another one exhibiting a high degree of CR or SISR and suitable inter-layer STDP parameter values. In addition, for all inter-layer STDP parameter values, the enhancement strategy of SISR based on the occurrence of SISR outperforms the one based on CR. Finally, the optimal enhancement strategy of SISR based on the occurrence of SISR (CR) occurs via long-term potentiation (long-term depression) of the inter-layer synaptic weights.

Keywords: coherence resonance, self-induced stochastic resonance, small-world network, multiplex network, STDP

1 INTRODUCTION

Spiking activity in neural systems can be induced and affected by noise, which can be internally produced by the system itself and/or externally by processes acting on the system. The sources of neural noise include 1) synaptic noise, which is externally produced, and is caused by the quasi-random release of neurotransmitters by synapses and/or random synaptic input from other neurons, and 2) channel noise, which is internally produced and comes from the random switching of ion channels [47, 49]. Synaptic and channel noise have been found to give rise to peculiar dynamical behavior in neural networks, including various resonance phenomena. The most prominent forms of these noise-induced resonance phenomena include: stochastic resonance (SR) [3, 28], coherence resonance (CR) [36], self-induced stochastic resonance (SISR) [10, 34], and inverse stochastic resonance (ISR) [18, 42]. The emergence and the dynamics of SR, CR, SISR, and ISR are quite different from each other, and therefore, they have mostly been separately investigated in previous research works. It might nevertheless be possible that fundamental relationships exist between some or even all of these noise-induced resonances and that efficient enhancement schemes for

information processing could emerge from their co-existence in a neural network. Some research works have shown intriguing results about the interplay between some of these noise-induced resonance phenomena. The bifurcation and stochastic analysis in [48] revealed that the parameter that changes the relative geometric positioning (and stability) of the fixed point (the quiescent state of the neuron) with respect to the fold point of the cubic nullcline of the FitzHugh-Nagumo (FHN) model [11] can cause a switch between SISR and ISR in the same synaptic weak-noise limit. Experiments have frequently shown that real biological neurons with similar physiological features, excited by identical stimuli, may spike quite differently, thus expressing different neuro-computational properties [40]. The analysis presented in [48] may, therefore, provide a qualitative explanation for this particular behavior. Zamani et al. [51] later showed a similar behavior between SR and ISR in a minimal bistable spiking neural circuit, where both mechanisms could co-exist under careful preparations of the neural circuit. Whether and if so, how all of these different types of noise-induced resonance mechanisms are related and what efficient enhancement schemes for information processing emerge from their interactions is far from being completely understood.

In this paper, CR and SISR will be the phenomena of interest. In fact, in both CR and SISR, small random perturbations of an excitable neural system with a large time scale separation ratio may lead to the emergence of coherent spiking activity. The mechanisms behind these noise-induced resonance phenomena, however, are entirely different, see [10]. CR [36] occurs when a maximal degree of regularity in the neuron's spiking activity is achieved at an optimal noise intensity without a periodic input signal, provided the neuron's bifurcation parameters are tuned near the Hopf bifurcation [25, 26, 36] or the saddle-node bifurcation [17, 19, 20, 27] threshold. In this case, a relatively small noise amplitude can easily (without overwhelming the entire dynamics) drive the neuron towards a coherent spiking activity that emerges right after the bifurcation threshold. Thus, during CR, noise plays a relatively passive role. In the FitzHugh-Nagumo neuron model (that will be used in this work), CR requires that the noise source is attached to the slow recovery variable—mimicking the dynamics of channel noise [10].

SISR, on the other hand, occurs when a vanishingly small noise intensity perturbing the fast variable of an excitable system results in the onset of a limit cycle behavior that is absent without noise [34]. SISR combines a coherence resonance-type mechanism with an intrinsic reset mechanism, and no external periodic driving is required. The period of the coherent oscillations created by the noise has a non-trivial dependence on the noise intensity and the timescale between the fast variable and slow variable of the excitable system. SISR essentially depends on the interplay between three different timescales: the two timescales of the deterministic part of the excitable system (i.e., the fast and slow timescale of the fast and slow variable, respectively), plus a third timescale characteristic of the noise, which plays an active role in the mechanism of SISR, in contrast to CR. Thus, the mechanism behind SISR is different from that of CR (see [10]), and remarkably, it can also occur away from bifurcation

thresholds in a parameter regime where the zero-noise (deterministic) dynamics do not display a limit cycle nor even its precursor. The properties of the limit cycle that SISR induces are controlled by both the noise intensity and the time scale separation ratio. Moreover, unlike CR, SISR requires a strong timescale separation ratio between the variables of the excitable system. In the FitzHugh-Nagumo neuron model, SISR (in contrast to CR) requires that the noise source is attached to the fast membrane potential variable—mimicking the dynamics of synaptic noise [10].

Of course, it is worth pointing out that a neuron can have both channel and synaptic noise simultaneously. In this case, CR and SISR will compete with each other. The dominant phenomenon will correspond to the one whose conditions are met first. It is shown in [10, 34] that SISR will dominate CR because the oscillations due to SISR are contained in those of CR. Thus, the conditions necessary for SISR can always be met first. In the current work, we shall not consider the situations where we have both channel and synaptic noise in a given layer. Just one type of noise will be considered in a given layer, and thus the competition between CR and SISR in a given layer will also not be considered.

The characteristic features of CR and SISR based on (1) time-delayed feedback couplings and network topology [1, 15, 30], 2) the multiplexing of layer networks [6, 31, 39, 46, 50], and 3) the use of one type of noise-induced resonance mechanism to optimize another type [50] have been established. It has been shown that appropriate selection of the time-delayed feedback parameters of FHN neurons coupled in a ring network can modulate CR: with a local coupling topology, synaptic time delay weakens CR, while in cases of non-local and global coupling, only appropriate synaptic time delays can strengthen or weaken CR [1, 15, 30, 38]. The enhancement of CR and SISR in neural systems with multiplex layer networks has recently attracted attention. In a multiplex network [5], the nodes participate in several networks simultaneously, and the connections and interaction patterns are different in the different networks, although the nodes preserve their identities across the different networks or layers. Since there may exist different types of relations between neurons or brain regions, multiplex networks have also been proposed as neurophysiological models [8]. For instance, functional couplings, like synchronization, between brain regions can be realized in different frequency bands. And each such frequency band can process a different type of information, for instance in language processing, phonetic, semantic and prosodic information [13]. But the main purpose of our paper is a formal investigation of the interplay between different types of stochastic resonance in a model where the individual units follow FHN dynamics, as FHN has become a paradigmatic model system for nonlinear dynamics [24] where many features can be studied in rather explicit terms.

In particular, the enhancement of CR in one layer of a multiplex network of FHN neurons based on the occurrence of SISR in another layer was established in [50]. In this case, two enhancement schemes for CR were compared: In one scheme (CR-CR scheme), one layer of the multiplex network is configured so that CR is optimal and the other layer

configured so that CR is non-optimal in isolation. In the other scheme (SISR-CR scheme), one layer of the multiplex network is configured so that SISR is optimal, and the other layer is configured so that CR is non-optimal in isolation. It was then shown that depending on which optimal resonance mechanism (CR or SISR) we had in one layer of the multiplex network, the best enhancement of CR in the other layer would depend on the multiplexing time delay and strength between the two layers. With weaker multiplexing strength and shorter time delays between the layers, the CR-CR scheme performs better than the SISR-CR scheme. But with stronger multiplexing connections, the SISR-CR scheme outperforms the CR-CR scheme, especially at weaker noise amplitudes and longer multiplexing time delays. This result suggests that the interactions between different noise-induced resonance mechanisms in neural networks could open up new possibilities for control and enhancement of information processing. These enhancement schemes could allow us to enhance information processing in neural networks more efficiently, using the interplay between different noise-induced resonance mechanisms and the multiplexing of layer networks. Enhancement schemes based on multiplexing (or, in general, on connecting several layers to form a multilayer network) are advantageous because the dynamics of one layer can be controlled by adjusting the parameters of another layer. So far, the enhancement of CR and SISR based on the multiplexing of neural layer networks has been established only in regular networks in the absence of STDP [6, 31, 39, 46, 50].

Adaptive (or learning) rules in biological neural networks have been linked to an important mechanism, namely, spike-timing-dependent plasticity (STDP) [16, 29]. STDP describes how the synaptic weights get modified by repeated pairings of pre- and postsynaptic action potentials (spikes) with the sign and the degree of the modification dependent on the relative timing of the firing of neurons. Depending on the precise timing of pre- and postsynaptic action potentials, the synaptic weights can exhibit long-term potentiation (LTP, i.e., persistent strengthening of synapses) or long-term depression (LTD, i.e., persistent weakening of synapses). There are two main types of STDP—Hebbian excitatory STDP (eSTDP) and anti-Hebbian inhibitory STDP (iSTDP). In this paper, we will focus only on eSTDP.

The ubiquity and importance of STDP in neural dynamics require us to investigate the enhancement of CR and SISR in adaptive neural networks driven by STDP. Such an investigation should be instrumental both theoretically and experimentally. Some previous works have shown the crucial role of adaptivity in network of coupled oscillators. For example, in [2] it is shown that the plasticity of the connections between oscillators plays a facilitatory role for inverse stochastic resonance (ISR), where adaptive couplings guide the dynamics of coupled oscillators to parameter domains in which noise effectively enhances ISR. In [12], it is shown how the interaction of noise and multiscale dynamics, induced by slowly adapting feedback, may affect an excitable system, giving rise to a new mode of behavior based on switching dynamics which allows for an efficient control of the properties of CR.

In the current work, the main questions we want to address are the following: 1) How do network topology and STDP parameters affect the degree of coherence due to CR and SISR? 2) In the presence of STDP, which of these noise-induced resonance phenomena is more robust to parametric perturbations? 3) In the presence of STDP, is an enhancement of the less robust phenomenon in an isolated layer network still possible via multiplexing? 4) Can the occurrence of one resonance phenomenon in one layer be used to enhance the other phenomenon in another layer in the presence of STDP? 5) If the answers to the previous questions are affirmative, then what behavior (LTP or LTD) of the STDP learning rule optimizes the multiplexing enhancement strategy?

Here is an outline of the remainder of this article: In **Section 2**, we present the mathematical model of the stochastic neural networks and give a brief description of the STDP learning rule and the dynamical differences in the emergent nature of the two noise-induced resonance phenomena that are of interest. In **Section 3**, we present the numerical methods used in our numerical simulations. In **Section 3.1**, we discuss the results of the dynamics of CR and SISR in isolated layer networks. In **Section 3.2**, we discuss the results of the enhancement of SISR using the multiplexing technique. Finally, we summarize our findings and conclude in **Section 4**.

2 MATHEMATICAL MODEL

We consider the following two-layer multiplex network, where each layer represents a network of N diffusively coupled FHN neurons in the excitable regime and the presence of noise:

$$\begin{cases} dv_{1i} &= \left[v_{1i} - \frac{v_{1i}^3}{3} - w_{1i} - I_{1i}^s(t) + I_{2i}^m(t) \right] dt + \sigma_1 dW_{1i}, \\ dw_{1i} &= \left[\varepsilon_1 (v_{1i} + \alpha - \gamma_1 w_{1i}) \right] dt + \sigma_2 dW_{2i}, \\ dv_{2i} &= \left[v_{2i} - \frac{v_{2i}^3}{3} - w_{2i} - I_{2i}^s(t) + I_{1i}^m(t) \right] dt + \hat{\sigma}_1 dW_{3i}, \\ dw_{2i} &= \left[\varepsilon_2 (v_{2i} + \alpha - \gamma_2 w_{2i}) \right] dt + \hat{\sigma}_2 dW_{4i}, \end{cases} \quad (1)$$

$v_{1i} \in \mathbb{R}$ and $w_{1i} \in \mathbb{R}$ represent the fast membrane potential variables and the slow recovery current variables in the first layer, respectively. Similarly, $v_{2i} \in \mathbb{R}$ and $w_{2i} \in \mathbb{R}$, respectively represent the membrane potential and recovery current variables for the neurons in the second layer. The index $i = 1, \dots, N$ stands for the i th neuron in the network of N neurons. $0 < \varepsilon_1 \ll 1$ and $0 < \varepsilon_2 \ll 1$ are the time-scale separation ratios between the fast membrane potential and the slow recovery current variables in the first and second layers, respectively. $\gamma_1 > 0$ and $\gamma_2 > 0$ are co-dimension-one Hopf bifurcation parameters in each of the layers and thus define the excitability threshold. $\alpha \in (0, 1)$ is a constant parameter. $\sigma_1 W_{1i}$ is the uncorrelated Gaussian white noise with standard deviation σ_1 , and similarly for $\sigma_2 W_{2i}$, $\hat{\sigma}_1 W_{3i}$, and $\hat{\sigma}_2 W_{4i}$. $\sigma_1 W_{1i}$ and $\hat{\sigma}_1 W_{3i}$ which are attached to the fast membrane

potential variables should be interpreted as representing synaptic noise sources, while $\sigma_2 W_{2i}$ and $\hat{\sigma}_2 W_{4i}$ which are attached to the slow recovery variables both represent channel noise sources.

The terms $I_{1i}^s(t)$, $I_{2i}^s(t)$, $I_{1i}^m(t)$, and $I_{2i}^m(t)$ in **Eq. 1** represent synaptic currents (modelled by diffusive electrical couplings) and also govern the STDP learning rule between connected neurons. We point out that we are using adaptive (based on STDP) electrical synapses so that we can directly compare our results to those in [50] where non-adaptive electrical synapses are used to study CR and SISR. The intra-layer synaptic currents $I_{1i}^s(t)$ and $I_{2i}^s(t)$ of the i th neuron in the layer 1 and layer 2 at time t are respectively given by

$$\begin{cases} I_{1i}^s(t) = \frac{1}{c_i} \sum_{j \neq i} a_{ij}^1 K_{ij}^1(t) (v_{1j}(t - \tau_1) - v_{1i}(t)), \\ I_{2i}^s(t) = \frac{1}{c_i} \sum_{j \neq i} a_{ij}^2 K_{ij}^2(t) (v_{2j}(t - \tau_2) - v_{2i}(t)), \end{cases} \quad (2)$$

where the synaptic connectivity matrices $A^1 = \{a_{ij}^1\}_{i,j=1}^N$ and $A^2 = \{a_{ij}^2\}_{i,j=1}^N$ of the layer 1 and layer 2, respectively, have $a_{ij}^1 = 1 = a_{ij}^2$ if the neuron j is pre-synaptic to the neuron i ; otherwise, $a_{ij}^1 = 0 = a_{ij}^2$. The synaptic connections in each layer, represented by the connectivity matrices A^1 and A^2 , are modeled in terms of the time-invariant Watts-Strogatz small-world network [41, 43, 44], where the in-degree of the i th neuron in the ℓ th layer (i.e., the number of synaptic inputs to the neuron i in layer ℓ) is given by $c_i^\ell = \sum_{j \neq i} a_{ij}^\ell$, ($\ell = 1, 2$). The intra-layer time delays of the electric synaptic coupling in layer 1 and layer 2 are represented by τ^1 and τ^2 , respectively.

The inter-layer synaptic currents $I_{1i}^m(t)$ and $I_{2i}^m(t)$ (which we shall also sometimes refer to as multiplexing currents) of the i th neuron in layer 1 and layer 2 at time t are respectively given by

$$\begin{cases} I_{1i}^m(t) = K_{ii}^{12}(t) (v_{2i}(t - \tau_{12}) - v_{1i}(t)), \\ I_{2i}^m(t) = K_{ii}^{12}(t) (v_{1i}(t - \tau_{12}) - v_{2i}(t)), \end{cases} \quad (3)$$

where τ_{12} represents the multiplexing (inter-layer) time delay of the electrical synaptic coupling between layer 1 and layer 2. With increasing time t , the intra-layer synaptic strengths $K_{ij}^1(t)$ and $K_{ij}^2(t)$, and the multiplexing (inter-layer) synaptic strength $K_{ii}^{12}(t)$ for each synapse are updated with a nearest-spike pair-based STDP rule [33]. To prevent unbounded growth, negative conductances (i.e., negative coupling strength) and elimination of synapses (i.e., $K_{ij}^1 = K_{ij}^2 = K_{ii}^{12} = 0$), we set a range with the lower and upper bounds: $\{K_{ij}^1, K_{ij}^2, K_{ii}^{12}\} \in [0.0001, 1]$. The initial intra-layer synaptic weights (i.e., $K_{ij}^1(t=0)$ and $K_{ij}^2(t=0)$), are normally distributed with mean and standard deviation equal to 0.1 and 0.02, respectively. And each of the N initial inter-layer synaptic weights $K_{ii}^{12}(t=0)$ is uniformly distributed in the interval $[0.0001, 1]$. They are updated according to the rule

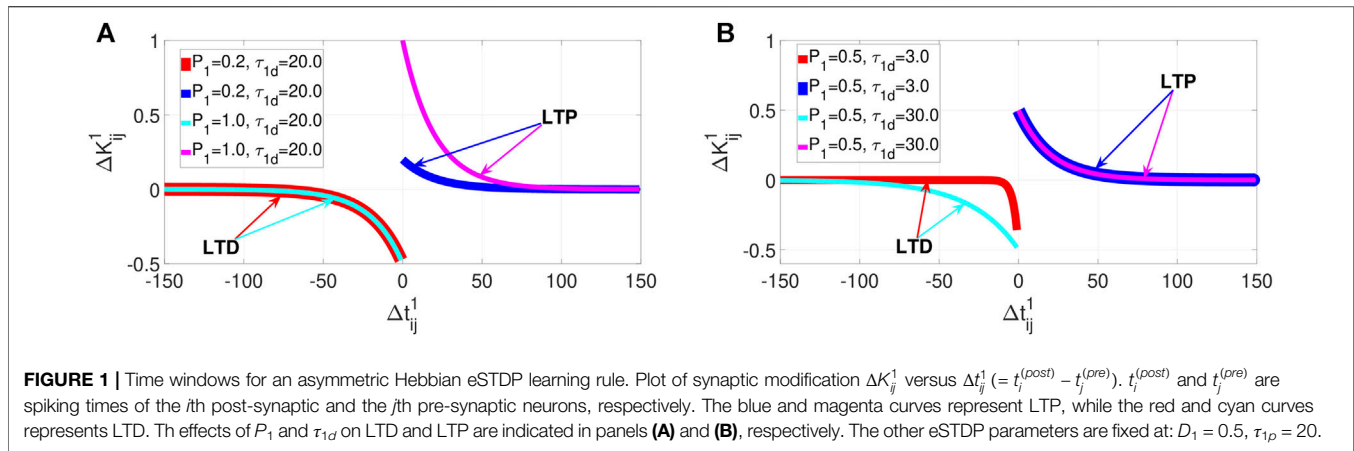
$$\begin{cases} K_{ij}^1 \rightarrow K_{ij}^1 + \lambda \Delta K_{ij}^1(\Delta t_{ij}^1), \\ K_{ij}^2 \rightarrow K_{ij}^2 + \lambda \Delta K_{ij}^2(\Delta t_{ij}^2), \\ K_{ii}^{12} \rightarrow K_{ii}^{12} + \lambda \Delta K_{ii}^{12}(\Delta t_{ii}^{12}), \end{cases} \quad (4)$$

The intra-layer synaptic modifications $\Delta K_{ij}^1(\Delta t_{ij}^1)$ and $\Delta K_{ij}^2(\Delta t_{ij}^2)$ depend on the relative time difference $\Delta t_{ij} = (t_i^{(post)} - t_j^{(pre)})$ ($\Delta t_{ij} = \Delta t_{ij}^1, \Delta t_{ij}^2$) between the nearest-spike times of the post-synaptic neuron i and the pre-synaptic neuron j . The inter-layer synaptic modification $\Delta K_{ii}^{12}(\Delta t_{ii}^{12})$ depends on the relative time difference $\Delta t_{ii}^{12} = (t_2^{(post)} - t_1^{(pre)})$ between the nearest-spike times of the i th post-synaptic neuron in layer 2 and the i th pre-synaptic neuron in layer 1. The parameter λ represents the learning rate. It was found that small learning rates lead to more robust learning [32]. Hence, in this work, we choose a small learning rate (i.e., $\lambda = 0.0001$) which, by the way, also simulates the effect of STDP on the long-term evolution of a neural network [37]. In the numerical simulations, we will consider eSTDP with an asymmetric Hebbian time window for the synaptic modifications given by [4, 22]:

$$\begin{cases} \Delta K_{ij}^1(\Delta t_{ij}^1) = \begin{cases} P_1 \exp(-\Delta t_{ij}^1 / \tau_{1p}) & \text{if } \Delta t_{ij}^1 > 0 \\ -D_1 \exp(\Delta t_{ij}^1 / \tau_{1d}) & \text{if } \Delta t_{ij}^1 < 0 \\ 0, & \text{if } \Delta t_{ij}^1 = 0 \end{cases} \\ \Delta K_{ij}^2(\Delta t_{ij}^2) = \begin{cases} P_2 \exp(-\Delta t_{ij}^2 / \tau_{2p}) & \text{if } \Delta t_{ij}^2 > 0 \\ -D_2 \exp(\Delta t_{ij}^2 / \tau_{2d}) & \text{if } \Delta t_{ij}^2 < 0 \\ 0, & \text{if } \Delta t_{ij}^2 = 0 \end{cases} \\ \Delta K_{ii}^{12}(\Delta t_{ii}^{12}) = \begin{cases} P_{12} \exp(-\Delta t_{ii}^{12} / \tau_{12p}) & \text{if } \Delta t_{ii}^{12} > 0 \\ -D_{12} \exp(\Delta t_{ii}^{12} / \tau_{12d}) & \text{if } \Delta t_{ii}^{12} < 0 \\ 0 & \text{if } \Delta t_{ii}^{12} = 0, \end{cases} \end{cases} \quad (5)$$

where LTP occurs if $\Delta t_{ij}^1 > 0$, $\Delta t_{ij}^2 > 0$, and $\Delta t_{ii}^{12} > 0$ (i.e., a post-synaptic spike follows a pre-synaptic spike); LTD if $\Delta t_{ij}^1 < 0$, $\Delta t_{ij}^2 < 0$, and $\Delta t_{ii}^{12} < 0$ (i.e., a post-synaptic spike precedes a pre-synaptic spike); and no synaptic modification if $\Delta t_{ij}^1 = \Delta t_{ij}^2 = \Delta t_{ii}^{12} = 0$. In **Eq. 5**, P_1 , P_2 , and P_{12} (D_1 , D_2 , and D_{12}) represent the potentiation (depression) adjusting rate parameters in layer 1, layer 2, and between layer 1 and 2, respectively. And τ_{1p} , τ_{2p} , and τ_{12p} (τ_{1d} , τ_{2d} , and τ_{12d}) represent the potentiation (depression) temporal window parameters in layer 1, layer 2, and between layer 1 and 2, respectively. The amount of synaptic modification (i.e., strengthening or weakening) is controlled by the adjusting rate parameters P_1 , P_2 , P_{12} , D_1 , D_2 , and D_{12} , while the time window for the synaptic modification is controlled by τ_{1p} , τ_{2p} , τ_{12p} , τ_{1d} , τ_{2d} , and τ_{12d} .

Experimental investigations [7, 9, 14, 45, 52] have shown that for a fixed stimulus, $D_1 \tau_{1d} > P_1 \tau_{1p}$ ensures dominant depression of synapses, otherwise (i.e., $D_1 \tau_{1d} \leq P_1 \tau_{1p}$) dominant potentiation. In **Figures 1A,B**, we show the asymmetric Hebbian time window for the synaptic modification $\Delta K_{ij}^1(\Delta t_{ij}^1)$ given by **Eq. 5** ($\Delta K_{ij}^2(\Delta t_{ij}^2)$ and $\Delta K_{ii}^{12}(\Delta t_{ii}^{12})$ have the same behavior). We see that $\Delta K_{ij}^1(\Delta t_{ij}^1)$ varies, depending on the relative time difference Δt_{ij}^1 between the nearest spike times of the post-synaptic neuron i and the pre-synaptic neuron j . In **Figure 1A**, for a fixed value of $D_1 (= 0.5)$, $\tau_{1d} (= 20)$, and $\tau_{1p} (= 20)$, we show the effects of P_1 on LTP and LTD. In **Figure 1B**, for a fixed value of $D_1 (= 0.5)$, $\tau_{1d} (= 20)$, and $P_1 (= 0.5)$, we show the effects of τ_{1d} on LTP and LTD. In the same way, fixing P_1 and τ_{1d} and varying D_1 and τ_{1p} show similar effects on LTD and LTP. Thus, for a particular noise intensity, when we fix parameter values of D_1 and τ_{1p} , the



inequality $D_1\tau_{1d} > P_1\tau_{1p}$ ($D_1\tau_{1d} \leq P_1\tau_{1p}$) can switch from LTD (LTP) to LTP (LTD) by changing the values of the parameters P_1 and τ_{1d} . Hence, the synapses can exhibit LTD and LTP if we vary only two parameters (i.e., P_1 and τ_{1d} or D_1 and τ_{1p}) and keep the other two constant. Therefore, throughout our studies, we fix the depression adjusting rate parameter at $D_1 = 0.5$ and the potentiation temporal window parameter at $\tau_{1p} = 20$, and choose the potentiation adjusting rate parameter $P_1 \in [0.1, 1]$ and the depression temporal window parameter $\tau_{1d} \in [0.2, 30]$ as the alterable (control) parameters of the eSTDP learning rule.

3 NUMERICAL RESULTS

To quantify the degree of SISR (i.e., the degree of coherence of the spiking activity induced by the mechanism of SISR), we use the normalized standard deviation of the mean interspike interval, commonly known as the coefficient of variation [36]. Because the coefficient of variation is based on the time intervals between spikes, it does relate to the timing precision of information processing in neural systems [35] and naturally becomes an essential statistical measure in neural coding. The coefficient of variation (CV) of N coupled neurons is defined as [30]:

$$CV = \frac{\sqrt{\langle ISI^2 \rangle - \langle ISI \rangle^2}}{\langle ISI \rangle}, \quad (6)$$

where

$$\begin{cases} \langle ISI \rangle &= \frac{1}{N} \sum_{i=1}^N \langle ISI_i \rangle, \\ \langle ISI^2 \rangle &= \frac{1}{N} \sum_{i=1}^N \langle ISI_i^2 \rangle. \end{cases} \quad (7)$$

$\langle ISI_i \rangle$ and $\langle ISI_i^2 \rangle$ are respectively the mean and the mean squared (over time) inter-spike intervals (ISI) of the i th neuron (i.e., $ISI_i = t_i^{m+1} - t_i^m > 0$, where t_i^m and t_i^{m+1} two consecutive spike times bounding the m th interval). We determine the spike occurrence times by the upward crossing of the membrane potential variable v_{ei} past the spike detection

threshold of $v_{th} = 0.0$. If $CV = 1$, we get a Poissonian spike train (rare and incoherent spiking). If $CV < 1$, the spike sequence becomes more regular, and CV vanishes for periodic deterministic spikes. $CV > 1$ corresponds to a spike point process that is more variable than a Poisson process. Thus, a neural network undergoing a high degree of CR or SISR will show a pronounced minimum in the values of CV [36].

For our investigations, we numerically integrate the set of stochastic differential equations in Eq. 1 with the Hebbian eSTDP rule of Eq. 4 by using the fourth-order Runge-Kutta algorithm for stochastic processes [21] and the Box-Muller algorithm [23]. The integration time step is fixed at $dt = 0.01$ for a total time of $T = 1.0$, $\times 10^6$ unit. Averages are taken over 20 different realizations of the initial conditions. For each realization, we choose random initial points $[v_{ei}(0), w_{ei}(0)]$ for the i th neuron in the ℓ th layer with uniform probability in the range of $v_{ei}(0) \in (-2, 2)$ and $w_{ei}(0) \in (-2/3, 2/3)$. The initial synaptic weights $K_{ij}^1(t=0)$, $K_{ij}^2(t=0)$, and $K_{ij}^{12}(t=0)$ are normally distributed with mean and standard deviation equal to 0.1 and 0.02, respectively. Furthermore, in our simulations, we use small-world networks generated by the Watts-Strogatz algorithm [41, 43, 44]. The average degree $\langle s_\ell \rangle$ and the rewiring probability $\beta_\ell \in [0, 1]$ will be taken as the network parameters to control the degrees of CR and SISR. We note that in the context of small-world networks with rewiring probability $\beta_\ell \in (0, 1)$, it is possible to interpolate between a regular ring network by setting $\beta_\ell = 0$ and a random network by setting $\beta_\ell = 1$ in the Watts-Strogatz algorithm.

Following the work in [10, 50], we note that while CR and SISR generally require an excitable regime (achieved by fixing $\gamma_1 = \gamma_2 = 0.75$) for their occurrence, for the particular case of the FHN neuron model, the occurrence of CR requires the presence of only channel noise. Thus, when investigating CR in a given layer of Eq. 1, we will set all synaptic noises to zero (i.e., $\sigma_1 = \hat{\sigma}_1 = 0$) in that layer. Secondly, because the CR has been shown [10] to be rather insensitive against variations of the timescale separation ratio, we will fix these parameters at the standard and most commonly used value $\varepsilon_\ell = 0.01$, ($\ell = 1, 2$) in the layer in which we investigate CR. On the other hand, the occurrence of SISR in a given layer network of Eq. 1 requires 1) presence of only synaptic noise, and thus, when investigating SISR in a given layer, we will set all

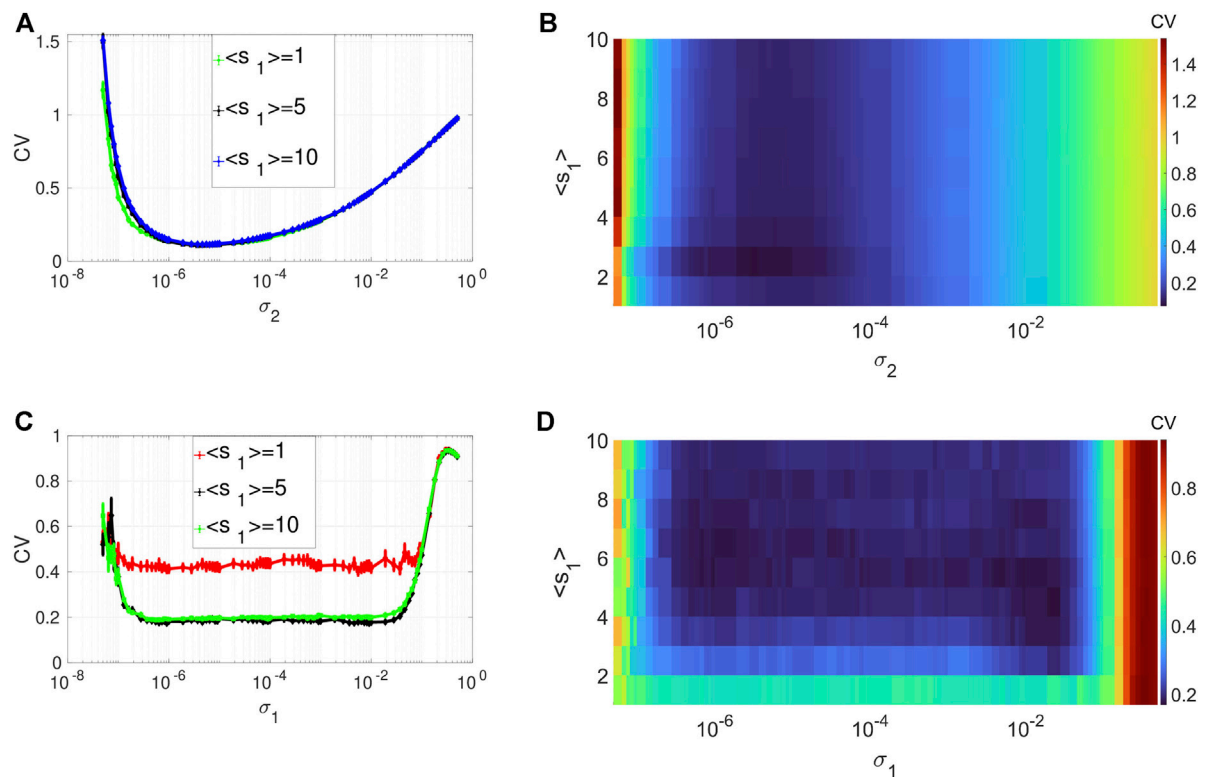


FIGURE 2 | Variation of CV w.r.t. the average degree $\langle s_1 \rangle$ and the noise intensity σ_2 for CR or σ_1 for SISR. Panels (A) and (B) show CR characterized by a family of non-monotonic CV curves w.r.t. σ_2 ($\sigma_1 = 0$) at $\varepsilon_1 = 0.01$. Panels (C) and (D) show SISR characterized by a family of non-monotonic CV curves w.r.t. σ_1 ($\sigma_2 = 0$) at $\varepsilon_1 = 0.001$. In both phenomena, the other parameters of the layer 1 are fixed at: $\beta_1 = 0.1$, $\tau_1 = 1$, $P_1 = 0.1$, $\tau_{1d} = 20$, $D_1 = 0.5$, $\tau_{1p} = 20$, $N = 50$.

channel noises to zero (i.e., $\sigma_2 = \hat{\sigma}_2 = 0$) in that layer, and 2) a stronger timescale separation ratio between the fast and slow variables of the FHN model. Thus, we will set $\varepsilon_\ell = 0.001$ ($\ell = 1, 2$) in the layer in which we investigate SISR—a much smaller value than for CR. The constant parameter $\alpha \in (0, 1)$ is fixed at 0.5 throughout our simulations.

3.1 Optimal CR and SISR in an Isolated Layer

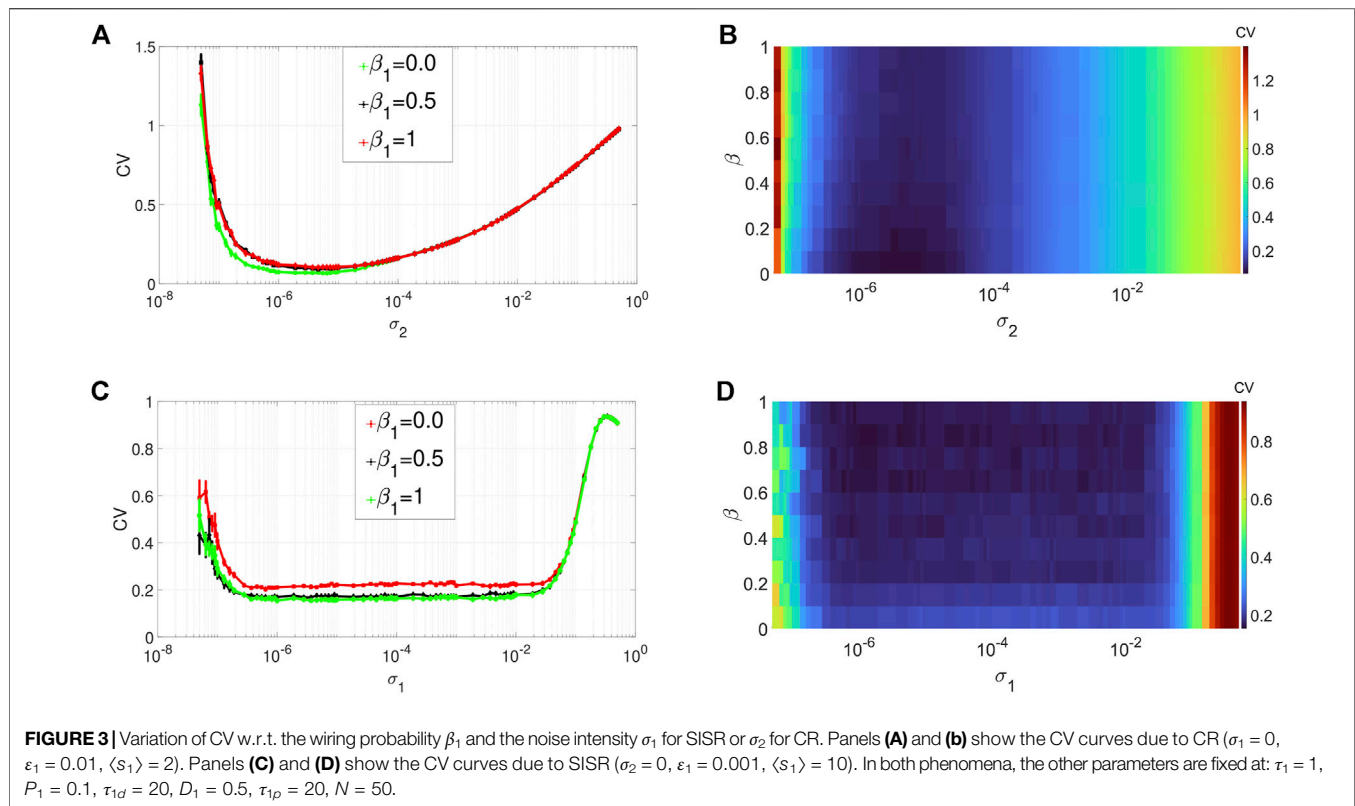
Before investigating the dynamics of CR and SISR in the multiplex network of Eq. 1, we should first understand their dynamics in an isolated layer network. Thus, this subsection is devoted to the investigation of CR and SISR in a single isolated layer of Eq. 1. We present the numerical results on the dynamics of CR and SISR in terms of the network parameters (i.e., the average degree $\langle s_1 \rangle$, the rewiring probability β_1 , and the intra-layer time delay τ_1) and the parameters of the eSTDP learning rule (i.e., the potentiation adjusting rate P_1 and depression temporal window τ_{1d}) in layer 1 of Eq. 1.

3.1.1 With respect to Network Parameters: $\langle s_1 \rangle$, β_1 , τ_1

The average number of synaptic inputs per neuron (i.e., the average degree connectivity) in layer 1 is given by $\langle s_1 \rangle = \frac{1}{N} \sum_{i=1}^N c_i^1$, where the in-degree of the i th neuron in layer 1 (i.e., the number

of synaptic inputs to the neuron i in layer 1) is given by $c_i^1 = \sum_{j \neq i} a_{ij}^1$. The higher (lower) the value of $\langle s_1 \rangle$, the denser (sparser) the network in layer 1. The rewiring probability β_1 of layer 1, satisfying $0 \leq \beta_1 \leq 1$, reflects the degree of randomness in the network. The network is 1) regular for $\beta_1 = 0$ with a high clustering high mean geodesic distance between neurons, 2) random for $\beta_1 = 1$ with a low clustering and low mean geodesic distance between neurons, and 3) small-world for $\beta_1 \in (0, 1)$ with a relatively high clustering but low mean geodesic distance between neurons. The time delay τ_1 between the signal transfer between any pair of connected neurons originates from the finite transmission speed of the neural signal along the axon pre-synaptic neuron.

Figures 2A,B depicts the variation in the degree of CR in layer 1 (in isolation) of Eq. 1. We show the variation of CV as a function of the channel noise intensity σ_2 (with $\sigma_1 = 0$) and the average degree $\langle s_1 \rangle$ of this layer. In these panels, CR is characterized by a family of non-monotonic CV curves as a function of the noise intensity σ_2 . Panels A and B also indicate that the phenomenon of CR is robust to changes in the average degree of the network connectivity $\langle s_1 \rangle$. As $\langle s_1 \rangle$ increases, the minimum of the CV curves (taking the value $CV_{\min} = 0.1108$ at $\sigma_2 = 7.3 \times 10^{-6}$) does not change. However, when the network is very sparse, i.e., when $\langle s_1 \rangle = 1$, we can see that the green line in Figure 2A extends a little more to the left compared to the denser



network configurations. This indicates that when $\langle s_1 \rangle = 1$, a relatively weaker noise intensity can enhance the degree of CR. Therefore, in the rest of our simulations, to have the best degree of CR while also allowing the network to have a small-world topology, we will fix the average degree of the layer networks at $\langle s_1 \rangle = 2$.

Figures 2C,D show the variation in the degree of SISR in layer 1 (in isolation) of **Eq. 1**. In this case, we switched on the synaptic noise intensity σ_1 (and turned off the channel noise, i.e., $\sigma_2 = 0$), decreased the timescale separation parameter from $\varepsilon = 0.01$ to $\varepsilon = 0.001$, and kept the rest of the parameters at the same values as in **Figures 2A,B**. In contrast to CR, SISR is sensitive to changes in the average degree parameter $\langle s_1 \rangle$. In particular, when the network is very sparse, i.e., when $\langle s_1 \rangle = 1$, the degree of SISR becomes significantly lower, with a minimum value of the CV curve around $CV_{\min} = 0.4$ for a wide range of the noise intensity, i.e., $\sigma_1 \in (3.7 \times 10^{-7}; 1.9 \times 10^{-2})$. As the network becomes denser, i.e., $\langle s_1 \rangle$ increases, the degree of SISR also increases with the minimum value of the CV curves occurring at $CV_{\min} \approx 0.1903$ for $\sigma_1 \in (3.7 \times 10^{-7}; 1.9 \times 10^{-2})$. Thus, in the rest of our simulations, to have a high (low) degree of SISR, we will fix the average degree of the layer networks at $\langle s_1 \rangle = 10$ ($\langle s_1 \rangle = 1$), in contrast to CR.

Interestingly, in **Figure 2**, we see that the best degree of coherence is higher for CR (with $CV_{\min} = 0.1108$) than for SISR (with $CV_{\min} \approx 0.1903$). In previous work [50], where we investigated CR and SISR in one isolated layer of **Eq. 1** in the absence of STDP, the opposite behavior occurs, i.e., SISR produces a higher degree of coherence (with $CV_{\min} = 0.012$) than CR (with $CV_{\min} = 0.130$), when all the other parameters are

at their optimal values. This means that in the presence (absence) of STDP, the degree of coherence due to CR (SISR) is higher than that of SISR (CR). Furthermore, while the degree of CR is higher than that of SISR, the range of values of the noise intensity in which the degree of CR is high is significantly smaller than that of SISR. This is explained by the fact that high coherence due to SISR emerges due to the asymptotic matching of the deterministic and stochastic timescales. While the high coherence due to CR emerges as a result of the proximity to the Hopf bifurcation [10, 50]. **Figures 2C,D** indicate that this matching of timescales occurs for a wider range of values of the synaptic noise intensity (with flat-bottom CV curves), hence the larger interval for coherence. On the other hand, **Figures 2A,B** show a smaller interval of the channel noise intensity in which the degree CR is highest. In this case, the noise intensity has to be just right (not too weak or strong) to let the systems oscillate between the excitable and the oscillatory regimes via a noise-induced Hopf bifurcation, leading to the emergence of a limit cycle behavior (i.e., noise-induced coherent oscillations). The noise channel noise should not be too weak so that the systems do not stay for too long in the excitable regime, thereby destroying the coherence. Nor should it be too strong to overwhelm the entire oscillations in the oscillatory regime, hence the relatively smaller noise interval for the highest coherence in the case of CR.

Figures 3A,B depict the variation in the degree of CR in layer 1 (in isolation) of **Eq. 1** as a function of the channel noise intensity σ_2 and the network rewiring probability β_1 at an optimal value of the average degree (i.e., $\langle s_1 \rangle = 1$) chosen from **Figure 2A**. The other parameters are kept fixed at the values given in **Figure 2**.

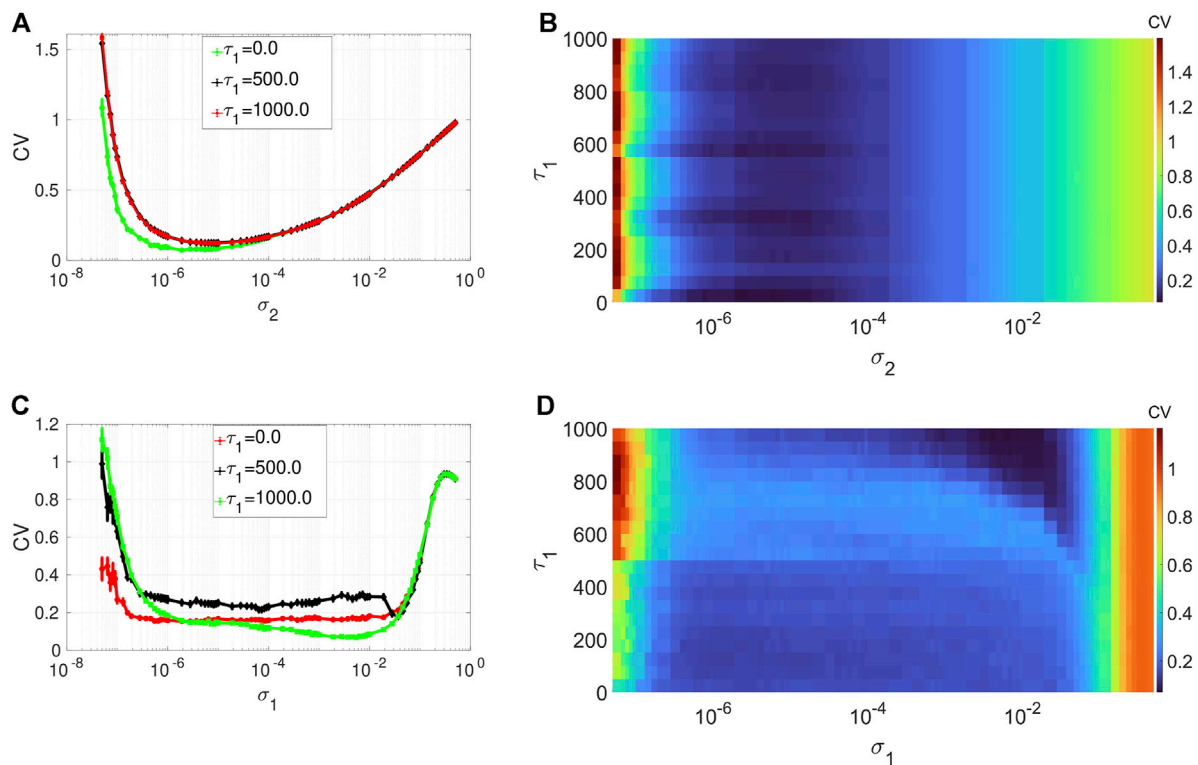


FIGURE 4 | Variation of CV w.r.t. the time delay τ_1 and noise intensity σ_1 for SISR or σ_2 for CR. Panels (A) and (B) show the CV curves due to CR ($\sigma_1 = 0$, $\epsilon_1 = 0.01$, $\langle s_1 \rangle = 2$). Panels (C) and (D) show the CV curves due to SISR ($\sigma_2 = 0$, $\epsilon_1 = 0.001$, $\langle s_1 \rangle = 10$). In both phenomena, the other parameters are fixed at: $\tau_1 = 1$, $P_1 = 0.1$, $\tau_1 d = 20$, $D_1 = 0.5$, $\tau_1 \rho = 20$, $N = 50$.

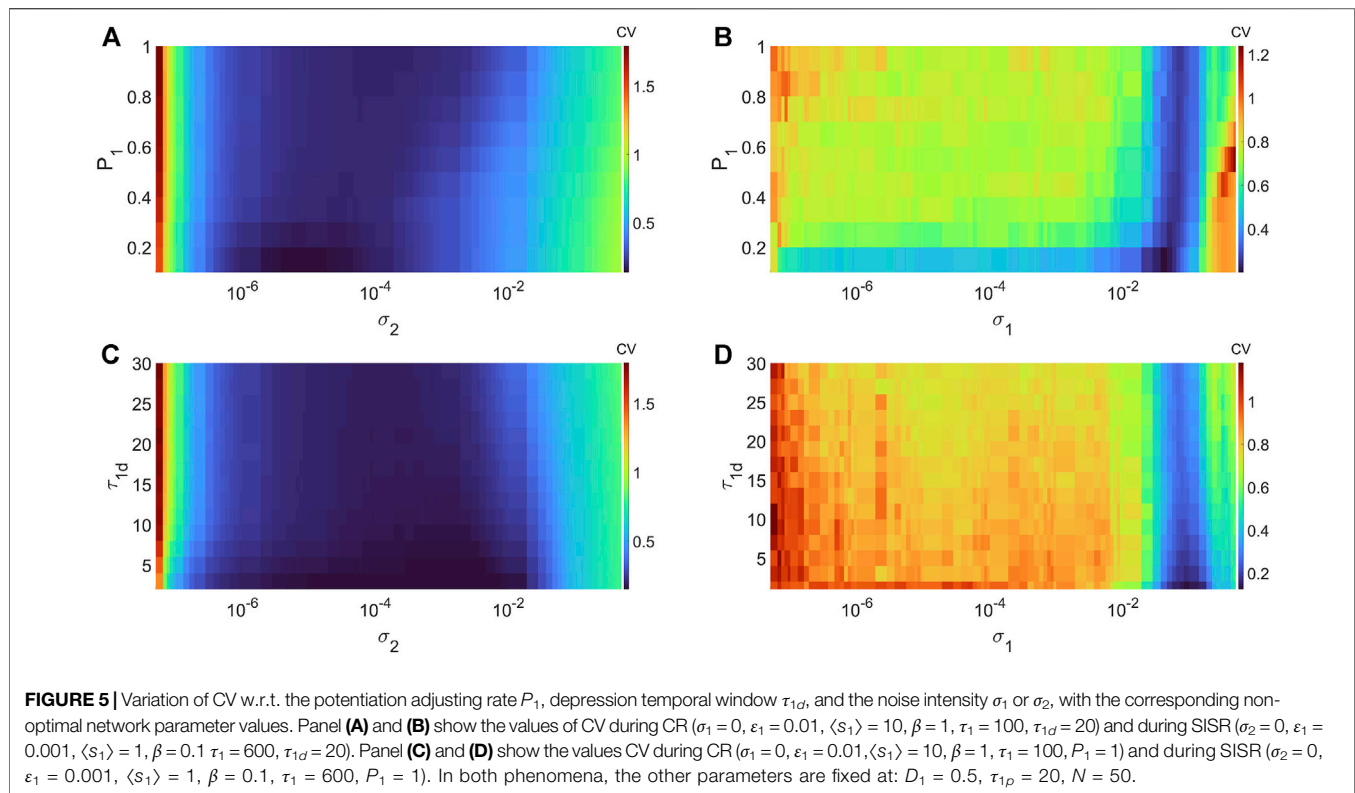
From **Figures 3A,B**, we notice that variations in the rewiring probability do not destroy the high degree of CR. Here the minimum of the CV curves remain very low. However, we can observe that when the network is regular, i. e., when $\beta_1 = 0.0$, the minimum of the CV curve (see, e.g., the green curve in **Figure 3A**) is noticeably lower than when we have small-world (with $\beta_1 \in (0, 1)$) and the random network (with $\beta_1 = 1$) topology. Nevertheless, because in this work we are interested in non-regular networks (i.e., $\beta_1 \in (0, 1]$), we will fix β_1 to a very low, but non-zero value (i.e., $\beta_1 = 0.1$) to have a high degree of CR in a small-world network. Hence, in the rest of our simulations, to have the best degree of CR in our small-world network, we will fix the rewiring probability of the layer networks at $\beta_1 = 0.1$.

Figures 3C,D show the variation in the degree of SISR in layer 1 (in isolation) of **Eq. 1** as a function of the synaptic noise intensity σ_1 and the network rewiring probability β_1 at the optimal value of the average degree (i.e., $\langle s_1 \rangle = 10$) chosen from **Figure 2C**. The rest of the parameter values are the same as in **Figures 3A,B**. We observe again that the degree of SISR is more sensitive to changes in the parameter β_1 than the degree of CR. Furthermore, we observe that varying the rewiring probability β_1 has the opposite effect on the degree of SISR compared to its effect on the degree of CR. The more regular the network is (see, e.g., the red curve in **Figure 3C**), the higher the CV curve and hence the lower the degree of SISR. Thus, in the rest of our simulations, to have the best degree of SISR in our

network, we will fix the rewiring probability of the layer networks at $\beta_1 = 1$ (see the green curve in **Figure 3C**).

Figures 4A,B depict the variation in the degree of CR in layer 1 (in isolation) of **Eq. 1** as a function of channel noise intensity σ_2 and the intra-layer time delay τ_1 of the network, at an optimal value of the average degree (i.e., $\langle s_1 \rangle = 2$) and the network rewiring probability (i.e., $\beta_1 = 0.1$) chosen from **Figure 2A** and **Figure 3A**, respectively. Again we notice, from the low values of the minimum of the CV curves, the robustness of the degree of CR to variations of a network parameter, i.e., τ_1 . Nonetheless, with the low degree of CR, we can still observe that when the synaptic connections between the neurons are instantaneous (i.e., when $\tau_1 = 0$), the CV curve (see the green curve in) is slightly lower than the rest of the curves. Further increase in the time delay does not affect the degree of CR. In the rest of the simulations, to have the best degree of CR in our network, we will fix the intra-layer time delay at a low but non-zero value, i.e., at $\tau_1 = 1$.

Figures 4C,D show the variation in the degree of SISR in layer 1 (in isolation) of **Eq. 1** as a function of synaptic noise intensity σ_1 and the intra-layer time delay τ_1 at an optimal value of the average degree (i.e., $\langle s_1 \rangle = 10$) and the network rewiring probability (i.e., $\beta_1 = 1$) chosen from **Figure 2C** and **Figure 3C**, respectively. We observe that the degree of SISR is again more sensitive to parametric perturbations than the degree CR. Moreover, the variation in the degree of SISR as a function of the intra-layer



time delay τ_1 is not linear and significantly depends on values of the synaptic noise σ_1 . In **Figure 4A**, for $\tau_1 = 0.0$, we have CV values which are higher and lower than those at $\tau_1 = 1,000$ and $\tau_1 = 500$, respectively. Thus, in the rest of the simulations, to have the best degree of SISR in our network, we will fix the intra-layer time delay at $\tau_1 = 1,000$.

3.1.2 With respect to STDP Parameters: P_1 , τ_{1d}

Using the insight from the previous section on the effects of each network parameter (i.e., $\langle s_1 \rangle$, β_1 , and τ_1) on the degree of CR and SISR, we now investigate the effects of STDP on the degree of CR and SISR by varying the parameters P_1 of the potentiation adjusting rate and τ_{1d} of the depression temporal window. To do this, we first note that the results in **Figures 2–4** are obtained when the parameters of STDP (i.e., P_1 and τ_{1d}) are kept fixed at the values indicated in the captions. So in the sequel, we fix the network parameters at their non-optimal values, i.e., at values at which each phenomenon produces the lowest degree of coherence. Then, we vary the parameters (P_1 and τ_{1d}) of the STDP learning rule in layer 1.

Extensive numerical simulations (not shown) have indicated that the variations in the degree of CR and SISR with respect to P_1 and τ_{1d} are higher at the corresponding optimal network parameter values indicated in **Figures 2–4** than at the non-optimal network parameter values. Qualitatively, however, the variations in the degrees of both phenomena are essentially the same when we have optimal or non-optimal network parameter values. Because we are interested in the highest degree of CR and SISR, we present the results on the effects of STDP on the degree

of CR and SISR when the network parameters are non-optimal. We will then investigate the enhancement strategies of the degree of each phenomenon using the multiplexing technique.

In **Figures 5A,B**, we show the variations in degree of CR and SISR in layer 1 (in isolation) of **Eq. 1** as a function of the channel (σ_2) and synaptic (σ_1) noise intensity and the potentiation adjusting rate parameter P_1 at corresponding non-optimal values of the network parameters, respectively. **Figure 5A** shows that the higher (compared to the degree of coherence induced by SISR in **Figure 5B**) degree of coherence induced by CR is more (compared to the robustness of the coherence induced by SISR in **Figure 5B**) robust to variations in the potentiation adjusting rate parameter P_1 . Even though the lowest CV values for each value of P_1 are relatively close to each other, we have the lowest (highest) $CV_{\min} = 0.1363$ ($CV_{\min} = 0.1804$) occurring at $P_1 = 0.1$ ($P_1 = 1$). For SISR, we the lowest (highest) $CV_{\min} = 0.2009$ ($CV_{\min} = 0.2588$) occurs at $P_1 = 0.1$ ($P_1 = 1$).

In **Figures 5C,D**, we show the variations in degree of CR and SISR in layer 1 (in isolation) of **Eq. 1** as a function of the channel (σ_2) and synaptic (σ_1) noise intensity and the depression temporal window τ_{1d} at corresponding non-optimal values both of the network parameters and the potentiation adjusting rate parameter P_1 (obtained from **Figures 5A,B**), respectively. For CR, we the lowest (highest) $CV_{\min} = 0.0254$ ($CV_{\min} = 0.1849$) occurs at $\tau_{1d} = 0.01$ ($\tau_{1d} = 30$). For SISR, we the lowest (highest) $CV_{\min} = 0.1245$ ($CV_{\min} = 0.2632$) occurs at $\tau_{1d} = 0.01$ ($\tau_{1d} = 30$). Thus, unlike the opposite effects of the variations in each network parameter on the degree of CR and SISR, the variations in the

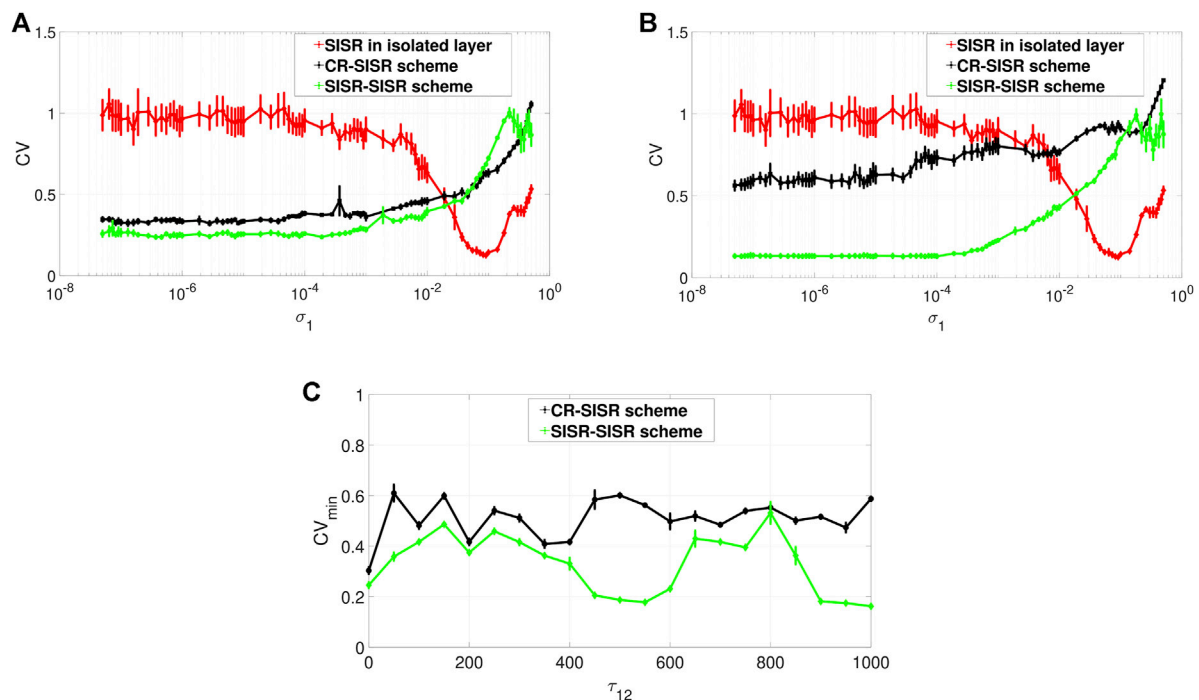


FIGURE 6 | Variation of CV of the controlled layer (exhibiting SISR) w.r.t. the noise intensity σ_1 and the inter-layer time delay τ_{12} . Panels (A) and (B) show the CV curves in the absence ($\tau_{12} = 0$) and presence ($\tau_{12} = 1,000$) of the inter-layer time delay τ_{12} , respectively. The red curves represent the variation in the degree of SISR in layer 1 when in isolation. The black and the green curves show the enhancement performances of the CR-SISR and SISR-SISR schemes, respectively. Panel (C) shows that for the same value of the inter-layer time delay, the SISR-SISR scheme always outperforms the CR-SISR scheme. Parameters of layer 2 in the CR-SISR scheme: $\hat{\sigma}_1 = \hat{\sigma}_2 = 0$, $\hat{\sigma}_2 = \sigma_1 \neq 0$, $\varepsilon_2 = 0.01$, $\langle s_2 \rangle = 2$, $\beta_2 = 0.1$, $\tau_2 = 1$, $P_2 = 0.1$, $\tau_{2d} = 20$. Parameters of layer 2 in the SISR-SISR scheme: $\hat{\sigma}_2 = \sigma_2 = 0$, $\hat{\sigma}_1 = \sigma_1 \neq 0$, $\varepsilon_2 = 0.001$, $\langle s_2 \rangle = 10$, $\beta_2 = 1$, $\tau_2 = 1$, $P_2 = 0.1$, $\tau_{2d} = 20$. Parameters of layer 1 in isolation and in both schemes: $\varepsilon_1 = 0.001$, $\langle s_1 \rangle = 1$, $\beta_1 = 0.1$, $\tau_1 = 600$, $P_1 = 1$, $\tau_{1d} = 0.01$, $N = 50$. Parameters of the inter-layer STDP: $P_{12} = 1$, $\tau_{12d} = 30$, $D_{12} = 0.5$, $\tau_{12p} = 20$.

STDP parameters have similar effects on the degree of CR and SISR.

In previous work [50], we aimed at enhancing CR (and not SISR) via the multiplexing technique because CR showed more sensitivity to parametric perturbations than SISR in the absence of the STDP learning rule. The results in **Figures 2–5** indicate that the degree of CR becomes more robust to parametric perturbations than the degree of SISR, which is particularly sensitive to the variations in the parameters of the STDP learning rule. For this reason, in the next section, we focus only on the enhancement of the more sensitive phenomenon, i.e., SISR, via the multiplexing technique used in [50].

3.2 Enhancement of SISR via the Multiplexing Technique

It has been shown in [50] that in a two-layer multiplex network with static (non-adaptive) synaptic couplings, CR or SISR in one layer could induce and enhance CR in the other layer. Here, we address whether enhancing a low degree of SISR in one layer of a multiplex network is possible using an enhanced CR or SISR in the other layer when adaptive synaptic couplings drive the network. Then, we investigate which enhancement scheme is best: 1) the CR-SISR scheme or 2) the SISR-SISR scheme.

In the CR-SISR scheme, we use the results from **Section 3.1** and we set layer 1 such that it has a low degree of SISR, i.e., we choose the network and STDP parameter values ($\langle s_1 \rangle = 1$, $\beta_1 = 0.1$, $\tau_1 = 600$, $P_1 = 1$, $\tau_{1d} = 0.01$) so that the CV curve is high—indicating a poor degree of SISR in layer 1 in isolation. We also set layer two such that it has a high degree of CR, i.e., we choose the network and the STDP parameter values ($\langle s_1 \rangle = 2$, $\beta_2 = 0.1$, $\tau_2 = 1$, $P_2 = 0.1$, $\tau_{2d} = 20$) so that the CV curve is low—indicating a high degree of CR in layer 2 in isolation. Then, we couple the two layers in a multiplex fashion, i.e., each neuron in a layer is coupled only to its replica neuron in the other layer via a synaptic coupling driven by STDP. In the SISR-SISR scheme, we have the same settings as in the CR-SISR scheme, except that in layer 2, we set the network and STDP parameter values ($\langle s_2 \rangle = 10$, $\beta_2 = 1$, $\tau_2 = 1$, $P_2 = 0.1$, $\tau_{2d} = 20$) so that the CV curve is high—in indicating a high degree of SISR in layer 2 in isolation.

The STDP driving the multiplexing (inter-layer) synaptic connections is governed by synaptic weight $K_{ii}^{12}(t)$ that evolves according **Eqs. 4, 5**. Similarly to the intra-layer synaptic weights of the isolated layer networks of **Section 3.1**, we will fix the depression adjusting rate parameter at $D_{12} = 0.5$ and the potentiation temporal window parameter at $\tau_{12p} = 20$, and vary only the potentiation adjusting rate $P_{12} \in [0.05, 1]$, the

depression temporal window $\tau_{12d} \in [0.2, 30]$, and the inter-layer time delay $\tau_{12} \in [0.0, 1,000]$ parameters in the intervals indicated.

In **Figure 6**, we show the performance of each scheme in enhancing the low degree of SISR in layer 1. **Figures 6A,B** depict the performances for an instantaneous (i.e., $\tau_{12} = 0$) multiplexing and for a time-delayed ($\tau_{12} = 1,000$) multiplexing between layer 1 and layer 2, respectively. We recall that layer 1 is the layer of interest, i.e., the layer with a low degree of SISR when it is in isolation. The red curve in **Figures 6A,B** represents the degree of coherence due to SISR in layer 1 when it is in isolation. We can see that for the selected set of network and STDP parameters (i.e., $\langle s_1 \rangle = 1$, $\beta_1 = 0.1$, $\tau_1 = 600$, $P_1 = 1$, $\tau_{1d} = 0.01$), the degree of coherence due to SISR is very low as indicated by the high values of the red CV curve for values of the synaptic noise intensity in some interval, i.e., $\sigma_1 \in (5.0, \times, 10^{-8}, 3.5 \times 10^{-2})$.

When layer 1, with its poor degree of SISR, is multiplexed with layer 2 exhibiting a high degree of CR, the performance of this CR-SISR scheme is depicted by the black curve in **Figures 6A,B** which represent the new degree of SISR in layer 1. We see that the multiplexing of layer 1 with another layer exhibiting a strong CR can significantly improve the degree of SISR in layer 1 by lowering the red CV curve, which becomes black. On the other hand, when layer 1, with its poor degree of SISR, is multiplexed with layer 2 exhibiting a high degree of SISR, the performance of this SISR-SISR scheme is depicted by the green curve in **Figures 6A,B** which represent the new degree of SISR in layer 1. We see that the multiplexing of layer 1 with another layer exhibiting a strong SISR can significantly improve the degree of SISR in layer 1 by lowering the red CV curve, which becomes green. However, in both schemes, this enhancement of SISR in layer 1 fails when the synaptic noise intensity is larger than 1.9×10^{-2} , a point from which the black and the green CV curves of the CR-SISR and SISR-SISR schemes lie above the red CV curve of layer 1 in isolation.

Furthermore, we observe that even though the degree of the coherence induced by CR can be higher than the degree of coherence induced by SISR in an isolated layer network driven by STDP, the degree of SISR induced via a multiplexing SISR-SISR enhancement scheme is higher than that induced by a CR-SISR enhancement scheme. This is clearly indicated by the black and green curves simulated with no inter-layer time delay in **Figure 6A** and with an inter-layer time delay in **Figure 6B**. For the majority of values of the synaptic noise intensity of layer 1, the green curve lies entirely below the black one.

To further investigate the effect of the inter-layer time delay τ_{12} on the degree of coherence due to SISR in layer 1, we computed the minimum value of the CV curve, (i.e., CV_{\min}) for a wide range of values of the inter-layer time delay τ_{12} . The result is shown in **Figure 6C**, where the green curve representing the enhancement performance of the SISR-SISR scheme always lies below the black curve, which represents the performance of the CR-SISR scheme, as the inter-layer time delay changes in $\tau_{12} \in [0, 1,000]$. **Figure 6C** also indicates that when the inter-layer time delay is at $\tau_{12} = 550$ and $\tau_{12} = 1,000$, the SISR-SISR scheme performs significantly better than at other values of the inter-layer time delay and the CR-SISR scheme. The best inter-layer time delay values in the CR-SISR scheme occur at $\tau_{12} = 0$ and at $\tau_{12} =$

350. The results presented in **Figure 6** are for fixed values of the alterable parameters of the inter-layer STDP learning rule, i.e. $P_{12} = 0.05$ and $\tau_{12d} = 30$.

Now we investigate the effects of varying these two parameters on the performances of the CR-SISR and SISR-SISR enhancement schemes. To implement this, we fix, from **Figure 6C**, the inter-layer time delay at the optimal value for each scheme, i.e., $\tau_{12} = 350$ and $\tau_{12} = 1,000$ for the CR-SISR and the SISR-SISR scheme, respectively. **Figures 7A,B** show the performances of the CR-SISR and SISR-SISR schemes as a function of the multiplexing STDP parameters, i.e., P_{12} and τ_{12d} , respectively. For the CR-SISR scheme, we observe that a larger depression temporal window (i.e., $\tau_{12d} \rightarrow 30$) and a smaller potentiation adjusting rate ($P_{12} \rightarrow 0.05$) yield the lowest minimum CV value, given by $CV_{\min} = 0.2989$ which occurs at the synaptic noise intensity of $\sigma_1 = 1.9, \times, 10^{-4} = \hat{\sigma}_2$.

The SISR-SISR scheme in **Figure 7B** shows better overall performance compared to the CR-SISR scheme with respect to these inter-layer STDP parameters. First, we observe that the surface of the graph CV_{\min} in the SISR-SISR scheme (with the highest value at $CV_{\min} = 0.2098$, occurring at $P_{12} = 0.5$ and $\tau_{12} = 0.5$) lies *entirely* below the surface of the graph CV_{\min} in the CR-SISR scheme (with the lowest value at $CV_{\min} = 0.2989$, occurring at $P_{12} = 0.05$ and $\tau_{12d} = 30$). Secondly, from **Figure 7B**, we observe that small (i.e., $P_{12} = 0.1$), but not *too* small values (unlike in the CR-SISR scheme in **Figure 7A** with $P_{12} = 0.05$) of the potentiation adjusting rate and large values of the depression temporal window (i.e., $\tau_{12} = 30$) parameters yield the lowest minimum CV value, given by $CV_{\min} = 0.1005$ which occurs at the synaptic noise intensity of $\sigma_1 = 7.3 \times 10^{-5} = \hat{\sigma}_1$.

In [50], the synaptic connections between the FHN neurons are static, and the effects of STDP on the strength of synaptic couplings are entirely ignored. The results [50] show that intermediate and strong multiplexing between the layer networks is required for the enhancement of the coherence, irrespective of the enhancement scheme. However, in the current paper, the inter-layer synaptic strength may not be static. Thus, we cannot choose *a priori* the strength of the inter-layer synaptic connections because this is entirely controlled by the STDP rule, which depends on the neurons' random spiking times. The best performance of the CR-SISR scheme (indicated by the lowest of value of CV_{\min} in **Figure 7A**) occurs when $P_{12} = 0.05$, $\tau_{12d} = 30$, $\tau_{12} = 350$, and $\sigma_1 = 1.9, \times, 10^{-4}$. While the best performance of the SISR-SISR scheme (indicated by the lowest value CV_{\min} in **Figure 7B**) occurs when $P_{12} = 0.1$, $\tau_{12d} = 30$, $\tau_{12} = 1,000$, and $\sigma_1 = 7.3 \times 10^{-5}$. Now, using these two sets of parameter values, we computed the time-evolution of the population-averaged multiplexing synaptic weights $\langle K_{ii}^{12} \rangle$ with an initial normal distribution of mean 0.1 and standard deviation of 0.02. The results are depicted in **Figure 7C** where the green curve shows that the best enhancement of SISR via the SISR-SISR scheme occurs via LTP, i.e., the strengthening of the inter-layer synapses from the initial value. In contrast, the red curve shows that the best enhancement of SISR via the CR-SISR scheme occurs via LTD, i.e., the weakening of the inter-layer synapses from the initial value. We note that the red curve in **Figure 7C** is close to zero, but not exactly zero (since the elimination of synapses has

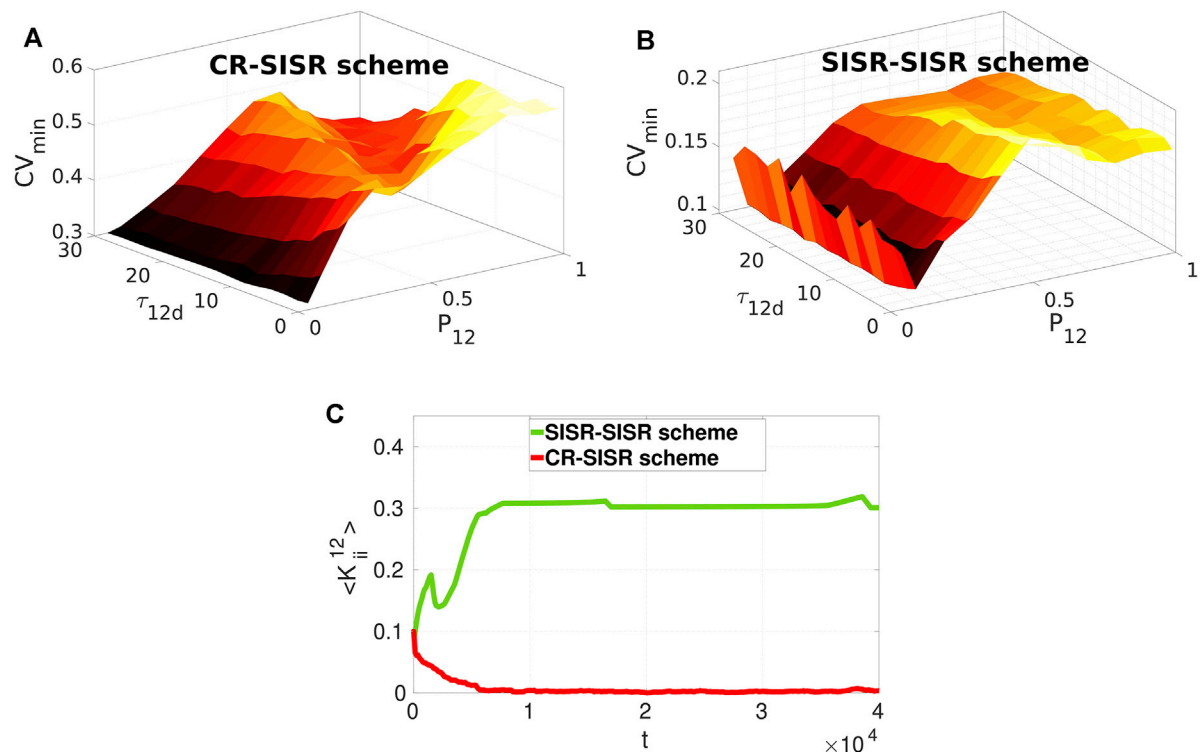


FIGURE 7 | Minimum CV against the multiplexing potentiation adjusting rate P_{12} and depression temporal window τ_{12d} for layer 1 exhibiting SISR when multiplexed to layer 2 exhibiting CR and SISR in Panels (A) and (B), respectively. The SISR-SISR scheme outperforms the CR-SISR scheme in enhancing SISR in layer 1 in the entire (τ_{12d}, P_{12}) plane. Parameter values in panels (A) and (B) are the same as in (Figure 6A) with $\tau_{12} = 350$ and $\tau_{12} = 1,000$ in the CR-SISR and SISR-SISR scheme, respectively. Panel (C) shows the time-evolution of population-averaged inter-layer synaptic weights $\langle K_{ii}^{12} \rangle$ with an initial normal distribution of mean 0.1 and standard deviation 0.02 at the values of P_{12} , τ_{12d} , and σ_1 (see main text) at which CV_{\min} achieves its lowest value in CR-SISR and the SISR-SISR schemes. LTP (LTD) favours the SISR-SISR scheme (CR-SISR scheme).

been avoided by bounding $\langle K_{ii}^{12} \rangle \in [0.0001, 1]$). The fact that the weak multiplexing of layer networks could enhance resonance phenomena in one of the layers was already discovered in [39]. However, this remains an observed behavior as the precise mechanism behind it is still elusive. A theoretical explanation of weak-multiplexing-induced resonance phenomena should be rewarding in theoretical studies and applications, e.g., in neuroengineering.

4 SUMMARY AND CONCLUSION

In this paper, we have numerically investigated the effects of varying the network and STDP parameters on the degree of CR and SISR in isolated and coupled (multiplexed) layer networks consisting of electrically connected FHN model neurons. In the isolated layer networks and for a fixed set of parameters, the results indicate that: 1) in the presence of STDP, the degree and the robustness of the coherence due to CR are always higher than those of the coherence due to SISR, unlike in the absence of STDP where the opposite behaviors occur [50], 2) the degree of coherence due to SISR increases with the average degree of the network connectivity and the rewiring probability of the network topology. While the degree of the

coherence due to SISR shows a nonlinear response to the variation in the electric time delay between the neurons—smaller and significantly larger time delays yield a higher degree of coherence than intermediate values, and 3) the degree of coherence due to SISR increases with a decreasing (increasing) value of the depression temporal window (potentiation adjusting rate) parameter of the STDP learning rule, especially at (relatively) larger synaptic noise intensities.

In the multiplex networks, we set up two enhancement schemes for the more sensitive phenomenon, i.e., SISR in layer 1, based on the multiplexing with layer 2 and using SISR and CR acting as the enhancing phenomena each with a high degree of coherence in layer 2. In the first enhancement scheme (termed the CR-SISR scheme), we have SISR with a low degree of coherence, achieved with specific values of the network and STDP parameter in layer 1 obtained in advance. And in layer 2 we have CR with a high degree of coherence, achieved with specific values of the network and STDP parameters obtained in advance. In the second enhancement scheme, termed the SISR-SISR scheme, we have SISR with a low degree of coherence in layer 1. And in layer 2 we have SISR with a high degree of coherence. Our results showed that: 1) both schemes can significantly enhance (as indicated by the relatively lower value of the CV curves) the poor degree of SISR in layer 1,

2) at the optimal inter-layer time delay (τ_{12}) of each scheme, a larger depression temporal window (τ_{12d}) and a smaller potentiation adjusting rate (P_{12}) parameters of the inter-layer STDP learning rule improve the CR-SISR and SISR-SISR enhancement schemes. However, for the SISR-SISR scheme, the potentiation adjusting rate parameter should not be too small, 3) the SISR-SISR scheme outperforms the CR-SISR scheme in the enhancement of SISR in layer 1 for all the parameter values of the inter-layer STDP learning rule, and 4) at their respective optimal inter-layer time delay, synaptic noise intensity, potentiation adjusting rate, and depression temporal window parameter values, the SISR-SISR scheme enhances SISR in layer 1 via long-term potentiation (LTP) of the synaptic strength between the layers. In contrast, the CR-SISR scheme enhances SISR in layer 1 via long-term depression (LTD) of the synaptic strength between the layers.

Interesting future research directions on the topic would be to investigate the robustness of the results presented in this paper when the topologies of the layer and multiplex networks are different and when the networks are driven by homeostatic structural plasticity.

REFERENCES

1. Aust R, Hövel P, Hizanidis J, Schöll E. Delay Control of Coherence Resonance in Type-I Excitable Dynamics. *Eur Phys J Spec Top* (2010) 187:77–85. doi:10.1140/epjst/e2010-01272-5
2. Bačić I, Klinshov V, Nekorkin V, Perc M, Franović I. Inverse Stochastic Resonance in a System of Excitable Active Rotators with Adaptive Coupling. *EPL (Europhysics Letters)* (2018) 124:40004.
3. Benzi R, Sutera A, Vulpiani A. The Mechanism of Stochastic Resonance. *J Phys A: Math Gen* (1981) 14:L453–L457. doi:10.1088/0305-4470/14/11/006
4. Bi G-q., Poo M-m. Synaptic Modifications in Cultured Hippocampal Neurons: Dependence on Spike Timing, Synaptic Strength, and Postsynaptic Cell Type. *J Neurosci* (1998) 18:10464–72. doi:10.1523/jneurosci.18-24-10464.1998
5. Bianconi GM. *Multilayer Networks: Structure and Function*. Oxford University Press (2018).
6. Bönsel F, Krauss P, Metzner C, Yamakou ME. Control of Noise-Induced Coherent Oscillations in Three-Neuron Motifs. *Cogn Neurodynamics* (2021) 1–20. doi:10.1007/s11571-021-09770-2
7. Dan Y, Poo M-M. Spike Timing-dependent Plasticity: from Synapse to Perception. *Physiol Rev* (2006) 86:1033–48. doi:10.1152/physrev.00030.2005
8. De Domenico M. Multilayer Modeling and Analysis of Human Brain Networks. *Gigascience* (2017) 6:1–8. doi:10.1093/gigascience/gix004
9. Debanne D, Gähwiler BH, Thompson SM. Long-term Synaptic Plasticity between Pairs of Individual Ca3 Pyramidal Cells in Rat Hippocampal Slice Cultures. *J Physiol* (1998) 507:237–47. doi:10.1111/j.1469-7793.1998.237bu.x
10. DeVille RE, Vanden-Eijnden E, Muratov CB. Two Distinct Mechanisms of Coherence in Randomly Perturbed Dynamical Systems. *Phys Rev E Stat Nonlin Soft Matter Phys* (2005) 72:031105. doi:10.1103/PhysRevE.72.031105
11. FitzHugh R. Mathematical Models of Threshold Phenomena in the Nerve Membrane. *Bull Math Biophys* (1955) 17:257–78. doi:10.1007/bf02477753
12. Franović I, Yanchuk S, Eydam S, Bačić I, Wolfrum M. Dynamics of a Stochastic Excitable System with Slowly Adapting Feedback. *Chaos: Interdiscip J Nonlinear Sci* (2020) 30:083109.
13. Friederici AD, Singer W. Grounding Language Processing on Basic Neurophysiological Principles. *Trends Cognitive Sciences* (2015) 19:329–38. doi:10.1016/j.tics.2015.03.012
14. Froemke RC, Dan Y. Spike-timing-dependent Synaptic Modification Induced by Natural Spike Trains. *Nature* (2002) 416:433–8. doi:10.1038/416433a

DATA AVAILABILITY STATEMENT

The original contributions presented in the study are included in the article/Supplementary Material, further inquiries can be directed to the corresponding author.

AUTHOR CONTRIBUTIONS

MY designed the study, conducted the numerical simulations, analyzed the results, and wrote the manuscript. TT analyzed the results and wrote the manuscript. JJ analyzed the results and wrote the manuscript. All the authors have approved the submitted version.

ACKNOWLEDGMENTS

MY acknowledges support from the Deutsche Forschungsgemeinschaft (DFG, German Research Foundation)—Project No. 456989199.

15. Geffert PM, Zakharova A, Vüllings A, Just W, Schöll E. Modulating Coherence Resonance in Non-excitable Systems by Time-Delayed Feedback. *Eur Phys J B* (2014) 87:291. doi:10.1140/epjb/e2014-50541-2
16. Gerstner W, Kempter R, Van Hemmen JL, Wagner H. A Neuronal Learning Rule for Sub-millisecond Temporal Coding. *Nature* (1996) 383:76–8. doi:10.1038/383076a0
17. Gu H, Zhang H, Wei C, Yang M, Liu Z, Ren W. Coherence Resonance-Induced Stochastic Neural Firing at a Saddle-Node Bifurcation. *Int J Mod Phys B* (2011) 25:3977–86. doi:10.1142/s0217979211101673
18. Gutkin BS, Jost J, Tuckwell HC. Inhibition of Rhythmic Neural Spiking by Noise: the Occurrence of a Minimum in Activity with Increasing Noise. *Naturwissenschaften* (2009) 96:1091–7. doi:10.1007/s00114-009-0570-5
19. Hizanidis J, Schöll E. Control of Coherence Resonance in Semiconductor Superlattices. *Phys Rev E Stat Nonlin Soft Matter Phys* (2008) 78:066205. doi:10.1103/PhysRevE.78.066205
20. Jia B, Gu H-G, Li Y-Y. Coherence-resonance-induced Neuronal Firing Near a Saddle-Node and Homoclinic Bifurcation Corresponding to Type-I Excitability. *Chin Phys. Lett.* (2011) 28:090507. doi:10.1088/0256-307x/28/9/090507
21. Kasdin NJ. Runge-kutta Algorithm for the Numerical Integration of Stochastic Differential Equations. *J Guidance, Control Dyn* (1995) 18:114–20. doi:10.2514/3.56665
22. Kim S-Y, Lim W. Stochastic Spike Synchronization in a Small-World Neural Network with Spike-timing-dependent Plasticity. *Neural Networks* (2018) 97: 92–106. doi:10.1016/j.neunet.2017.09.016
23. Knuth DE. *The Art of Computer Programming*, 2. Reading, MA: Addison-Wesley (1973). p. 51.
24. Kuehn C. *Multiple Time Scale Dynamics*, 191. Springer (2015).
25. Lindner B, Garcia-Ojalvo J, Neiman A, Schimansky-Geier L. Effects of Noise in Excitable Systems. *Phys Rep* (2004) 392:321–424. doi:10.1016/j.physrep.2003.10.015
26. Lindner B, Schimansky-Geier L. Analytical Approach to the Stochastic Fitzhugh-Nagumo System and Coherence Resonance. *Phys Rev E* (1999) 60:7270–6. doi:10.1103/physreve.60.7270
27. Liu Z-Q, Zhang H-M, Li Y-Y, Hua C-C, Gu H-G, Ren W. Multiple Spatial Coherence Resonance Induced by the Stochastic Signal in Neuronal Networks Near a Saddle-Node Bifurcation. *Physica A: Stat Mech its Appl* (2010) 389: 2642–53. doi:10.1016/j.physa.2010.02.029
28. Longtin A. Stochastic Resonance in Neuron Models. *J Stat Phys* (1993) 70: 309–27. doi:10.1007/bf01053970

29. Markram H, Lübke J, Frotscher M, Sakmann B. Regulation of Synaptic Efficacy by Coincidence of Postsynaptic Aps and Epsps. *Science* (1997) 275:213–5. doi:10.1126/science.275.5297.213
30. Masoliver M, Malik N, Schöll E, Zakharova A. Coherence Resonance in a Network of Fitzhugh-Nagumo Systems: Interplay of Noise, Time-Delay, and Topology. *Chaos* (2017) 27:101102. doi:10.1063/1.5003237
31. Masoliver M, Masoller C, Zakharova A. Control of Coherence Resonance in Multiplex Neural Networks. *Chaos, Solitons & Fractals* (2021) 145:110666. doi:10.1016/j.chaos.2021.110666
32. Masquelier T, Guyonneau R, Thorpe SJ. Spike Timing Dependent Plasticity Finds the Start of Repeating Patterns in Continuous Spike Trains. *PloS one* (2008) 3:e1377. doi:10.1371/journal.pone.0001377
33. Morrison A, Aertsen A, Diesmann M. Spike-timing-dependent Plasticity in Balanced Random Networks. *Neural Comput* (2007) 19:1437–67. doi:10.1162/neco.2007.19.6.1437
34. Muratov CB, Vanden-Eijnden E, E. W. Self-induced Stochastic Resonance in Excitable Systems. *Physica D: Nonlinear Phenomena* (2005) 210:227–40. doi:10.1016/j.physd.2005.07.014
35. Pei X, Wilkens L, Moss F. Noise-mediated Spike Timing Precision from Aperiodic Stimuli in an Array of hodgekin-huxley-type Neurons. *Phys Rev Lett* (1996) 77:4679–82. doi:10.1103/physrevlett.77.4679
36. Pikovsky AS, Kurths J. Coherence Resonance in a Noise-Driven Excitable System. *Phys Rev Lett* (1997) 78:775–8. doi:10.1103/physrevlett.78.775
37. Ren Q, Kolwankar KM, Samal A, Jost J. Hopf Bifurcation in the Evolution of Networks Driven by Spike-timing-dependent Plasticity. *Phys Rev E Stat Nonlin Soft Matter Phys* (2012) 86:056103. doi:10.1103/PhysRevE.86.056103
38. Semenov V, Feoktistov A, Vadvivasova T, Schöll E, Zakharova A. Time-delayed Feedback Control of Coherence Resonance Near Subcritical Hopf Bifurcation: Theory versus experiment. *Chaos* (2015) 25:033111. doi:10.1063/1.4915066
39. Semenova N, Zakharova A. Weak Multiplexing Induces Coherence Resonance. *Chaos* (2018) 28:051104. doi:10.1063/1.5037584
40. Shepherd GM. *The Synaptic Organization of the Brain*. Oxford University Press (2004).
41. Strogatz SH. Exploring Complex Networks. *nature* (2001) 410:268–76. doi:10.1038/35065725
42. Tuckwell HC, Jost J, Gutkin BS. Inhibition and Modulation of Rhythmic Neuronal Spiking by Noise. *Phys Rev E Stat Nonlin Soft Matter Phys* (2009) 80:031907. doi:10.1103/PhysRevE.80.031907
43. Watts DJ. *Small Worlds: The Dynamics of Networks between Order and Randomness*. Princeton University Press Princeton (2000).
44. Watts DJ, Strogatz SH. Collective Dynamics of 'small-World' Networks. *nature* (1998) 393:440–2. doi:10.1038/30918
45. Wolters A, Sandbrink F, Schlottmann A, Kunesch E, Stefan K, Cohen LG, et al. A Temporally Asymmetric Hebbian Rule Governing Plasticity in the Human Motor Cortex. *J Neurophysiol* (2003) 89:2339–45. doi:10.1152/jn.00900.2002
46. Yamakou ME, Hjorth PG, Martens EA. Optimal Self-Induced Stochastic Resonance in Multiplex Neural Networks: Electrical vs. Chemical Synapses. *Front Comput Neurosci* (2020) 14:62. doi:10.3389/fncom.2020.00062
47. Yamakou ME, Inack EM (2022). Coherence Resonance and Stochastic Synchronization in a Small-World Neural Network: An Interplay in the Presence of Spike-timing-dependent Plasticity. *arXiv preprint arXiv:2201.05436*.
48. Yamakou ME, Jost J. A Simple Parameter Can Switch between Different Weak-Noise-Induced Phenomena in a Simple Neuron Model. *Epl* (2017) 120:18002. doi:10.1209/0295-5075/120/18002
49. Yamakou ME, Jost J. Weak-noise-induced Transitions with Inhibition and Modulation of Neural Oscillations. *Biol Cybern* (2018) 112:445–63. doi:10.1007/s00422-018-0770-1
50. Yamakou ME, Jost J. Control of Coherence Resonance by Self-Induced Stochastic Resonance in a Multiplex Neural Network. *Phys Rev E* (2019) 100:022313. doi:10.1103/PhysRevE.100.022313
51. Zamani A, Novikov N, Gutkin B. Concomitance of Inverse Stochastic Resonance and Stochastic Resonance in a Minimal Bistable Spiking Neural Circuit. *Commun Nonlinear Sci Numer Simulation* (2020) 82:105024. doi:10.1016/j.cnsns.2019.105024
52. Zhang LI, Tao HW, Holt CE, Harris WA, Poo M-m. A Critical Window for Cooperation and Competition Among Developing Retinotectal Synapses. *Nature* (1998) 395:37–44. doi:10.1038/25665

Conflict of Interest: The authors declare that the research was conducted in the absence of any commercial or financial relationships that could be construed as a potential conflict of interest.

Publisher's Note: All claims expressed in this article are solely those of the authors and do not necessarily represent those of their affiliated organizations, or those of the publisher, the editors and the reviewers. Any product that may be evaluated in this article, or claim that may be made by its manufacturer, is not guaranteed or endorsed by the publisher.

Copyright © 2022 Yamakou, Tran and Jost. This is an open-access article distributed under the terms of the Creative Commons Attribution License (CC BY). The use, distribution or reproduction in other forums is permitted, provided the original author(s) and the copyright owner(s) are credited and that the original publication in this journal is cited, in accordance with accepted academic practice. No use, distribution or reproduction is permitted which does not comply with these terms.



OPEN ACCESS

EDITED BY

André H. Erhardt,
Weierstrass Institute for Applied Analysis
and Stochastics (LG), Germany

REVIEWED BY

Stefan Gahbauer,
University of California, San Francisco,
United States

*CORRESPONDENCE

Ana-Nicoleta Bondar,
nbondar@fizica.unibuc.ro,
a.bondar@fz-juelich.de

SPECIALTY SECTION

This article was submitted to Biophysics,
a section of the journal
Frontiers in Physics

RECEIVED 07 June 2022

ACCEPTED 09 August 2022

PUBLISHED 06 September 2022

CITATION

Bondar A-N and Alfonso-Prieto M
(2022), Hydrogen-bond networks for
proton couplings in G-Protein
coupled receptors.
Front. Phys. 10:963716.
doi: 10.3389/fphy.2022.963716

COPYRIGHT

© 2022 Bondar and Alfonso-Prieto. This
is an open-access article distributed
under the terms of the [Creative
Commons Attribution License \(CC BY\)](#).
The use, distribution or reproduction in
other forums is permitted, provided the
original author(s) and the copyright
owner(s) are credited and that the
original publication in this journal is
cited, in accordance with accepted
academic practice. No use, distribution
or reproduction is permitted which does
not comply with these terms.

Hydrogen-bond networks for proton couplings in G-Protein coupled receptors

Ana-Nicoleta Bondar^{1,2*} and Mercedes Alfonso-Prieto²

¹Faculty of Physics, University of Bucharest, Bucharest, Romania, ²Computational Biomedicine (IAS-5/INM-9), Forschungszentrum Jülich, Jülich, Germany

G-protein signaling pathways mediate communication across cell membranes. The first steps of this communication occur at the cell membrane, where upon receiving an external signal –the binding of an agonist ligand– the membrane-embedded G-Protein Coupled Receptor adopts a conformation recognized by a cytoplasmatic G protein. Whereas specialized GPCRs sense protons from the extracellular milieu, thus acting as pH sensors in specialized cells, accumulating evidence suggests that pH sensitivity might be common to distinct GPCRs. In this perspective article we discuss general principles of protonation-coupled protein conformational dynamics and how these apply to GPCRs. To dissect molecular interactions that might govern the protonation-coupled conformational dynamics of GPCRs, we use graph-based algorithms to compute graphs of hydrogen bond networks. We find that the internal H-bond networks contain sites where structural rearrangements upon protonation change could be transmitted throughout the protein. Proton binding to bulk-exposed clusters of titratable protein sidechains ensures the pH sensing mechanism is robust.

KEYWORDS

G-protein coupled receptor (GPCR), G protein, pH, hydrogen bond (H-bond), graph theory—graph algorithms

Introduction

G-Protein Coupled Receptors (GPCRs) mediate communication between eukaryotic cells and their environments. Signals sensed by GPCRs can be of external origin, such as light or odors, or endogenous, such as hormones or neurotransmitters. Humans have >750 GPCRs [1], and about 30–35% of the drugs target GPCRs that respond to endogenous signals (endo-GPCRs)—though just a minority (10%) of the known GPCRs are used as targets [2–4]. As endo-GPCRs are significantly conserved between human and mouse, and are expressed preferentially in the brain [1], they are of tremendous interest in expanding the repertoire of GPCRs used for therapeutics [4]. Moreover, since the majority of the GPCRs that are currently targeted by approved drugs couple to cytoplasmatic G proteins G_s or G_i [4], in the future G proteins might also become drug targets [5, 6], e.g., by using ligands that can modulate interactions between G proteins and their upstream/downstream interaction partners and thus impact signal transduction pathways.

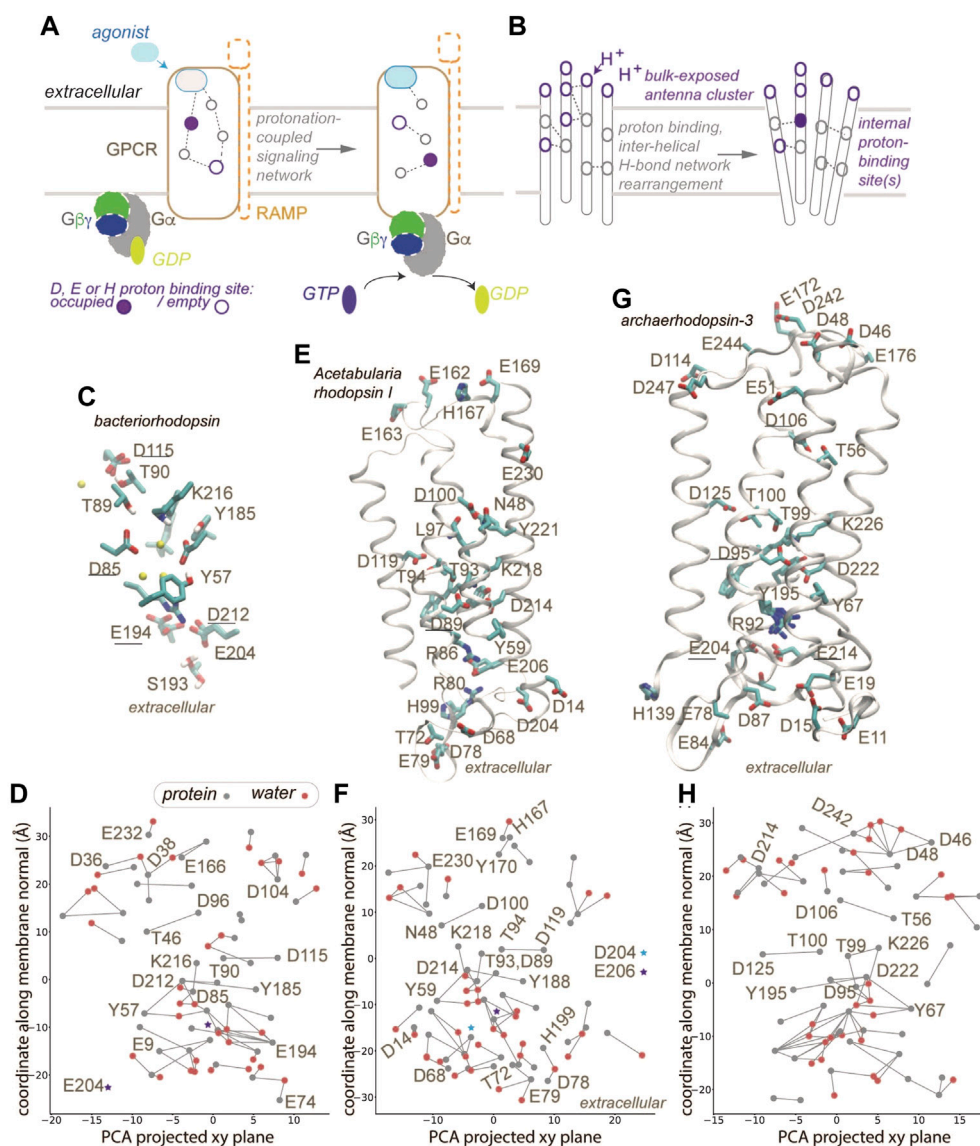


FIGURE 1

GPCR activation and protonation-coupled conformational dynamics with H-bond networks. **(A)** Agonist and G-protein binding may associate with protonation-coupled formation of a continuous H-bond network inside the GPCR. **(B)** Schematic representation of a membrane protein with a bulk-exposed proton antenna cluster and an internal proton-binding site. **(C,D)** Close view of the internal H-bond network **(C)** and H-bond graph **(D)** computed for bacteriorhodopsin, pdb 7z09 [39]. Gray and red nodes represent, respectively, protein sidechains and water oxygen atoms; only selected nodes are labeled. **(E,F)** Molecular graphics **(E)** and H-bond graph **(F)** computed for *Acetabularia* rhodopsin I, pdb 5awz [40]. **(G,H)** Molecular graphics **(G)** and H-bond graph computed for archaerhodopsin-3, pdb 6gux [41]. Only some helices are displayed in panels E,G. Groups underlined in panels C,E,G were implicated in proton binding [40, 41, 78]. Molecular graphics included in Figure 1 and Figure 2 were prepared with Visual Molecular Dynamics, VMD [79]. H-bond graphs in panels D, E, H were computed with C-Graphs [19] using structures aligned with OPM [80].

The general principles of how GPCRs interact with G proteins to effect cell signaling are illustrated in Figure 1A. Upon binding of an agonist the GPCR changes conformation and binds to the G protein (Figure 1A). Some class B GPCRs alter their ligand specificity upon interactions with receptor activity-modifying proteins, RAMPS, which are single-pass transmembrane proteins with an extracellular domain [7]. Both GPCRs and G proteins are

dynamic [8, 9]. GPCRs can couple to lipids [10, 11], can bind sodium ions [12, 13], and change protonation during their function [14, 15]. Indeed, recent data were interpreted to suggest that “proton-sensing and H^+ -gated agonism are recurring features of GPCR signaling biology” [16]; however it remains unclear how GPCRs couple proton binding with protein conformation. Mechanisms for protonation-coupled function have been

dissected for microbial rhodopsins –which, similar to GPCRs, are seven-helical membrane proteins, and pass through discrete intermediate conformations during their reaction cycles. Here, we rely on GPCRs and microbial rhodopsin structures to dissect interactions potentially important for protonation-coupled conformational change. We computed H-bond networks using the graph-based algorithms Bridge [17, 18] and C-Graphs [19] and as H-bond criterion a distance of ≤ 3.5 Å between the donor and acceptor heavy atoms; the graph computations included all H-bonding protein sidechains, and water-mediated bridges between sidechains with up to three water molecules in a bridge. Thus, nodes of an H-bond graph are H-bonding protein sidechains, and edges, sidechain-sidechain H-bonds or water-mediated bridges between sidechains. We suggest that GPCRs that couple proton binding with conformational change might use mechanisms similar to other membrane proteins (Figure 1B).

Internal H-bond networks of static GPCR structures depend on the resolution

Analyses of H-bonds in static experimental structures of GPCRs are commonly used to formulate hypotheses about reaction mechanisms. As summarized below, the view of internal H-bond networks of GPCRs depends drastically on the resolution at which structures were solved, and on the internal number of water molecules.

The structure of the (inactive) visual rhodopsin GPCR from squid presented a remarkable internal protein-water H-bond network hypothesized to mediate propagation of structural change during receptor activation [20]. Much of this H-bond network remains present in structures of the early intermediates batho and lumi [19]. Moreover, some of the internal water molecules of squid rhodopsin are conserved in structures of jumping-spider rhodopsin-1 and adenosine A2A receptor (AA2AR), suggesting conserved roles of water molecules in propagating structural change [19].

A difficulty with identifying protein-water H-bond networks of GPCRs based on static structures is that the number of internal water molecules tends to depend on the resolution: GPCR structures solved at resolutions of 2 Å or higher typically have at least 30 internal water molecules, some of which are found at conserved sites [21]. A dataset of 63 GPCR structures solved at a resolution of 2.5 Å or better, and with at least 10 internal water molecules, were found to host a conserved, core protein-water H-bond network that inter-connects functionally important regions of GPCRs [21]; within this dataset, structures solved at resolution of at least 2.3 Å and with more internal water molecules had additional local H-bond clusters [21]. In stark contrast with the extended H-bond network of the inactive squid rhodopsin structure, two recent structures of G-protein bound GPCRs solved at resolutions of 2.9–3.15 Å [22, 23], which lack internal water molecules, have only small, localized

H-bond clusters of up to 3–4 protein sidechains [24]. This suggests that both the resolution and internal water content need to be accounted for in hypotheses about putative roles of H-bond networks for conformational couplings of GPCRs [21, 24].

Protonation change during GPCR function and pH-sensing GPCRs: Lessons from microbial rhodopsins and other proton-binding membrane proteins

GPCRs that change protonation during function include bovine rhodopsin –two internal Glu groups, one at the ligand binding site (E3.28 in the standard Ballesteros-Weinstein numbering scheme for class A GPCRs), and one at a conserved functional motif (E3.49) [14]; the M2 muscarinic receptor –two conserved carboxylic groups, D2.50 and D3.32, might change protonation [25]; the calcium receptor –whose activity might be modulated by proton binding to carboxylic sidechains [26]; the μ -opioid receptor –the propensity of the ligand to H-bond to H6.52 could explain pH sensitivity [27]; AA2ARs –ligand binding depends on pH-sensitive interactions of E169 and H264 at the extracellular side [28, 29].

Other GPCRs signal changes in extracellular pH to ensure cell homeostasis, i.e., their biological function is to sense pH, and they have been implicated in disease conditions associated with acidic pH –cancer, inflammatory disease, and ischemia [30, 31]. As no three-dimensional structures have been solved for these canonical pH-sensing GPCRs, their reaction mechanism remains elusive. Central roles for proton sensing have been assigned to H-bonding extracellular His sidechains [32], or to a triad of internal carboxylic groups [33]. How the protonation change of external His sidechains would cause receptor structural changes, and how protons from the extracellular bulk would make their way to internal carboxylic groups, are key open questions. As summarized below, we suggest that mechanisms used by microbial rhodopsins, and by other proton-binding membrane proteins, provide clues about common principles of action for protonation-coupled membrane proteins.

Membrane proteins are commonly thought to rely on internal H-bond networks to couple protein conformation with a change in protonation, typically of a carboxylate and/or His sidechains, as these moieties titrate in a pH range relevant to biology [34, 35]. Protonation change at internal sites of membrane proteins involves H-bond paths that transiently inter-connect proton donor and acceptor pairs. In the bacteriorhodopsin proton pump (Figures 1C,D 2A), a few internal carboxylic groups, including D85, D96 and E194/E204 (Figures 1C,D) change protonation during bacteriorhodopsin's function. In the resting state, the primary proton acceptor D85 H-bonds with T89 and water, protonated D115 with T90, D212 with Y57 and Y185, and the

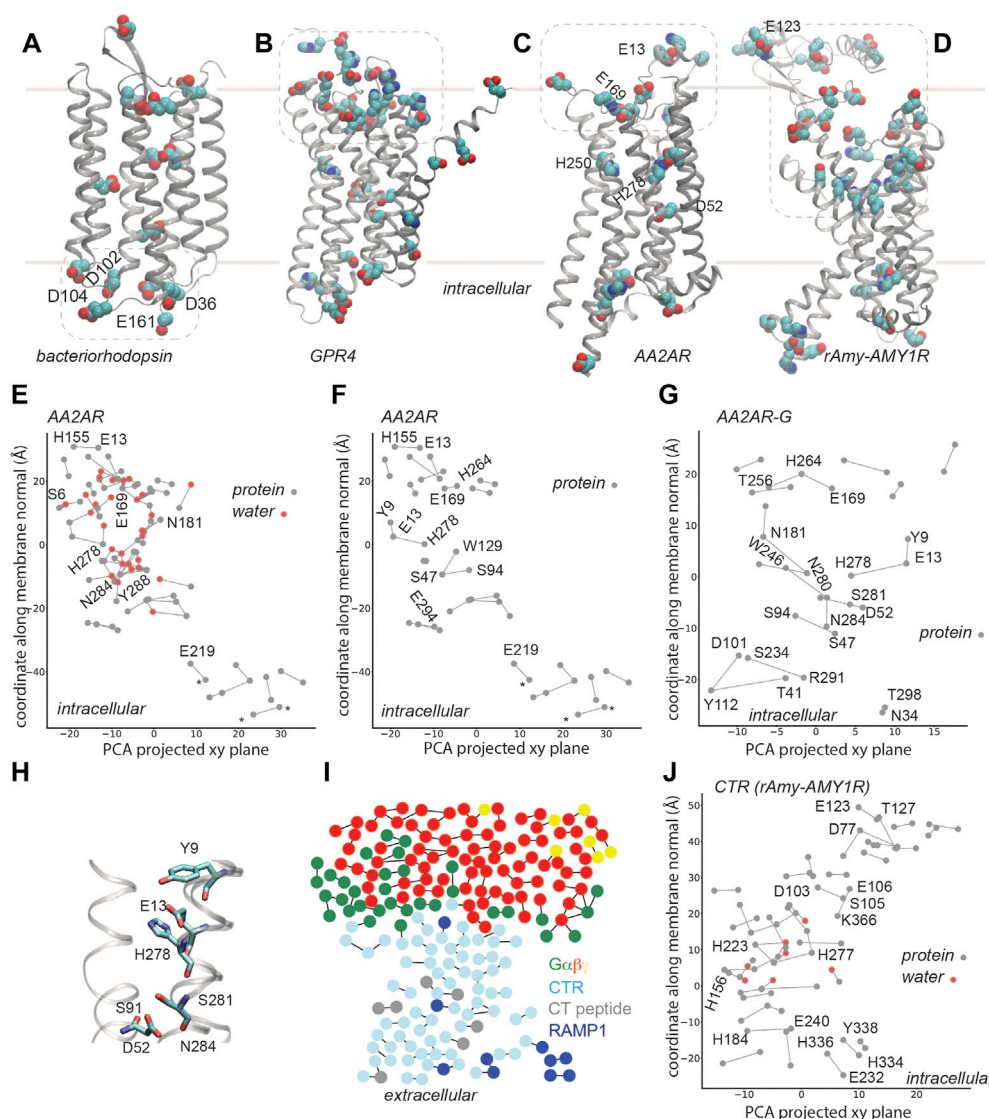


FIGURE 2

H-bond networks of GPCRs. Dotted lines indicate selected clusters of bulk-exposed carboxylic and His groups. (A) Carboxylic groups of bacteriorhodopsin, based on pdb 5zim [81]; Asp/Glu groups labeled are part of the proton-collecting antenna [37, 38]. (B) Carboxylic and His groups of human GPR4 from model AF-P46093-F1-model_v2, UniProt entry P46093 [61]. (C,D) Carboxylic and His groups of AA2AR (panel B, pdb 5nm4, 1.7 Å resolution [63]) and of rAmy-AMY1R (pdb 7tyf [72]). (E–G) C-Graphs H-bond graphs computed with water bridges (E) vs. for protein sidechains (F) for AA2AR based on pdb 5 nm4, and for G-protein bound AA2AR, pdb 5g53, 3.4 Å resolution [82] (G). H-bond networks of AA2ARs were reported in Refs. [19, 21]. In panels (E,F), stars indicate groups of a synthetic construct. (H) Selected H-bonds of AA2AR. (I) Bridge2 H-bond graph of the CTR-G protein complex, pdb 6e3y, 3.3 Å resolution [70]. (J) C-Graphs H-bond graph for the CTR, pdb 7tyf, 2.2 Å resolution [72]. Panels (E–G,J) use structures with the receptor domain oriented along the membrane normal using VMD and OPM [80].

proton-release site E194-E204 with S193. At the cytoplasmic side, a cluster of carboxylic groups might function as a proton-collecting antenna [36–38] that picks up protons and delivers them to an internal carboxylic group [37, 38] (Figure 2A).

The protein-water H-bond graph computed from a high-resolution structure (1.05 Å) of bacteriorhodopsin [39] contains 79 H-bonding sidechains and water molecules, and 73 H-bonds between these groups (Figure 1D); when we computed the

H-bond graph of the same structure without water molecules, only 19 H-bonds remained. We obtained similar results for a 1.6 Å resolution structure of *Acetabularia* rhodopsin I [40] (Figure 1E), whose H-bond graph has about 3.7-fold more H-bonds when both protein sidechains and water molecules are included (Figure 1F), than when water was excluded. Likewise, for the 1.3 Å resolution structure of archaerhodopsin-3 [41] (Figure 1G) the protein-water H-bond graph has about

3.8-fold more H-bonds than when (Figure 1H), vs. 24 H-bonds when only sidechains were included in computations.

The H-bond graphs above of microbial rhodopsins have H-bonds that are common at proton-binding sites of membrane transporters and receptors, including GPCRs [42, 43]. In class A GPCRs, the conserved D2.50 is paired with S7.46 [21, 44, 45]. In bacteriorhodopsin, for which proton binding has been studied extensively, including with Fourier Transform Infrared Spectroscopy [38, 46–50], Nuclear Magnetic Resonance [51], time-resolved serial femtosecond crystallography [52, 53], and computations [54–56], the internal proton donor D96 H-bonds to T46, and D115, which remains protonated throughout the reaction cycle, H-bonds to T90 (Figure 1D). Interhelical H-bonds of the corresponding Asp are present in *Acetabularia* rhodopsin-1 and archaerhodopsin-3, though in the former D100 (corresponding to bacteriorhodopsin D96) H-bonds to an Asn (N48) instead of a Ser/Thr. More generally, Asp/Glu-Ser/Thr and Asp-Asn H-bonds are rather common in membrane transporters and receptors [42]. Similarly, bulk-exposed proton antenna clusters that deliver/release a proton to/from an internal site (Figures 1B, 2A), as proposed for bacteriorhodopsin, have also been discussed for cytochrome *c* oxidase and for photosystem II [36–38, 44, 57–59].

The AlphaFold [60] model deposited for the pH-sensing GPR4 [61] suggests that a large cluster of Asp, Glu, and His groups is located at the extracellular site, where pH must be sensed, and several carboxylic and histidine sidechains, at the core of the receptor (Figure 2B). Although details of the predicted structural model might be debatable, we suggest that, qualitatively, the overall arrangement with a bulk-exposed carboxylic-histidine cluster and several internal titratable sidechains resembles that of bacteriorhodopsin (Figures 1B, 2A,2B) and other microbial rhodopsins (Figures 1E–H).

Given the lack of experimental structures for pH-sensing GPCRs, below we further dissect internal H-bond networks of AA2AR as a class A receptor for which activation upon proton binding was recently discovered [16], and the calcitonin receptor (CTR), as a class B GPCR involved in cell signaling paths likely to depend on pH; as proton sensing appears to be rather common to GPCRs, studies of H-bond networks of GPCRs susceptible of pH sensitivity could inform on general principles of function.

Internal H-bond networks of the adenosine A2A receptors

AA2ARs are targeted by one of the most consumed substances in the world, caffeine, and by drugs against Parkinson's disease [62]. Very recently, experimental data were interpreted to suggest that acidic pH can activate AA2AR [16], but it remains unclear how AA2ARs may couple proton binding to protein conformational change for receptor activation.

AA2AR (Figure 2C) contains relatively few internal carboxylic and His sidechains; there are, however, numerous other charged and polar sidechains within the transmembrane region of AA2AR, such that its protein-water H-bond graph computed for the highest-resolution structure [63] has no fewer than 82 H-bonds (Figure 2E). An extended H-bond cluster with 19 H-bonding protein sidechains and water molecules extends across >20 Å along the membrane normal, from S6 (1.32) to N181; a few other relatively large protein-water H-bond clusters are present, such that the entire receptor is spanned by H-bond clusters. H250 (6.52) and H278 (7.42) are located in the ligand binding site [64], with H278 part of an H-bond cluster with Y9 (1.35) and E13 (1.39) (Figures 2F,G). In an active-like structure, D52 (2.50) is H-bonded to S91 (3.39), S281 (7.46) and N284 (7.49) (Figure 2H), thus being part of a network that connects several GPCR motifs involved in ligand binding and receptor activation. For detailed analyses and discussions of GPCR H-bond networks of GPCRs, including of the adenosine A2A receptor we refer the reader to [21].

Without water molecules, the H-bond graph of the same AA2AR structure consists of just 29 H-bonds, and the largest H-bond cluster has 4 H-bonding sidechains (compare Figure 2E with Figure 2F). Likewise, the H-bond graph obtained for AA2AR in the AA2AR-G complex has 21 H-bonds, with local H-bond clusters of up to 4 H-bonding sidechains (Figure 2G). This finding is compatible with the aforementioned observations on the chemokine [23] and cannabinoid [24] receptors bound to G proteins, with the graph computations presented above for microbial rhodopsins (Figure 1), and with computations suggesting important roles of water-mediated interactions in GPCR activation [21, 65, 66]. That is, internal water molecules might be needed to establish extended connections throughout active-like, G-protein bound GPCRs. Moreover, the H-bond networks at the extracellular side, where bulk water molecules could visit the receptor at least transiently, are likely dynamic and could rearrange upon binding of an agonist, including –in the recently proposed acid sensor AA2AR [16]– upon proton binding.

Internal His, Asp and Glu of AA2AR mentioned above are conserved in the non-proton-sensing adenosine A1 and A2B receptors, which suggests that details of the intra-molecular interactions of titratable groups might determine pH sensitivity. Further studies that integrate high-resolution static structures with spectroscopy, site-directed mutagenesis, and computation, will be needed to unravel mechanisms of proton binding to adenosine receptors.

H-bond networks for allosteric regulation of the calcitonin receptor

The CTR is among the best-studied class B GPCRs that are regulated by RAMPs. By itself, the CTR has high affinity for calcitonin (CT), being implicated in bone homeostasis. In

complex with one of the three RAMPs, CTR forms amylin receptors, $AMY_{1-3}R$, which have high affinity for the peptide amylin (Amy) and are involved in the control of food intake [7]; in addition to Amy, AMY_1R binds the neuropeptide calcitonin gene-related peptide [7] and could be involved in migraines [67]. Whether and how pH impacts CTRs is unclear, though observations of an increased expression of the CTR at acidic pH [68] and of pH-dependent interactions between calcitonin and model membranes [69], suggest that CTR could be among GPCRs whose functioning is influenced by pH.

A structure of the human(h) CTR bound to $G\alpha_s\beta\gamma$ and to salmon calcitonin (sCT) was initially solved with cryo-EM at a resolution of 4.1 Å [70] and then refined to a resolution of 3.3 Å [71]. Although some ambiguity remained in the CTR-CT interactions, the structure suggested polar receptor-ligand contacts and a number of H-bonds within the CTR and at the CTR-G protein interface [71]. The transmembrane region of the refined CTR structure contains several local H-bond clusters, but they are localized, with at most 4-5 sidechains in a cluster, and most of the H-bond graph consists of singular H-bonds (Figure 2I). Such a picture is compatible with the findings for AA2AR and other GPCRs, which need internal water molecules to establish extended H-bond clusters.

Cryo-EM structures solved were recently at resolutions of 2.0–3.3 Å for ligand-bound G_s -CTR and G_s - $AMY_{1-3}R$ [72]. Protein-water H-bonds were suggested to help stabilize the active conformation of the receptor, and to contribute to the binding of sCT [72]. The H-bond graph we computed for the CTR domain contains 51 sidechain-sidechain and water-mediated H-bonds; the largest H-bond clusters contain two water molecules each and 5-6 protein sidechains (Figure 2J). Several Asp, Glu, and His sidechains are part of the internal H-bond network, and thus of interest for potential couplings between protonation change and protein conformation. A large cluster of carboxylic and His sidechains that faces the extracellular bulk (Figure 2D) could couple protonation change with ligand binding.

Conclusion

Protonation is of general importance for the post-translational regulation of protein function [35], and a number of GPCRs bind protons during function [25, 73] or function as pH sensors implicated in cancer [32]. H-bond graphs of GPCRs and microbial rhodopsins suggest that GPCRs might share with other protonation-coupled membrane proteins common principles of how protonation change couples with protein conformation (Figure 1B). In the future, given the rapid pace at which GPCR structures are solved, H-bond graph computations could help identify H-bond networks and sites where the H-bond network is interrupted –which could guide, e.g., the placing of internal water molecules in GPCR structures.

H-bond graphs of high-resolution structures of GPCRs trapped in distinct intermediates could help interpret spectroscopic fingerprints for putative proton-binding sites of GPCRs. We anticipate that future studies will capitalize on improvements in cryo-EM structure solving [74], computational modeling of GPCR conformational intermediates [75], and public repositories for GPCRs [76, 77].

Data availability statement

The raw data supporting the conclusion of this article will be made available by the authors, without undue reservation.

Author contributions

A-NB designed and performed research, wrote the original draft and edited the manuscript. MA-P performed research and edited the manuscript.

Acknowledgments

Open-access publication funded by the Deutsche Forschungsgemeinschaft (DFG, German Research Foundation)—491111487. We thank the Central Library of the Forschungszentrum Jülich for making the open access publication possible. MA-P acknowledges financial support in part from the DFG Research Unit FOR2518 “Functional Dynamics of Ion Channels and Transporters—DynIon” Project P6. A-NB acknowledges financial support in part from the European Union’s Horizon 2020 Research and Innovation Program under the Marie Skłodowska-Curie grant agreement No 860592, Innovative Training Network “Proton and proton-coupled transport”.

Conflict of interest

The authors declare that the research was conducted in the absence of any commercial or financial relationships that could be construed as a potential conflict of interest.

Publisher’s note

All claims expressed in this article are solely those of the authors and do not necessarily represent those of their affiliated organizations, or those of the publisher, the editors and the reviewers. Any product that may be evaluated in this article, or claim that may be made by its manufacturer, is not guaranteed or endorsed by the publisher.

References

- Vassilatis DK, Hohmann JG, Zeng H, Li F, Ranchalis JE, Mortrud MT, et al. The G protein-coupled receptor repertoires of human and mouse. *Proc Natl Acad Sci U S A* (2003) 100:4903–8. doi:10.1073/pnas.0230374100
- Wise A, Gearing K, Rees S. Target validation of G-protein coupled receptors. *Drug Discov Today* (2002) 7:235–46. doi:10.1016/s1359-6446(01)02131-6
- Hauser A, Attwood MM, Rask-Andersen M, Schiöth HB, Gloriam DE. Trends in GPCR drug discovery: New agents, targets and indications. *Nat Rev Drug Discov* (2017) 16:829–42. doi:10.1038/nrd.2017.178
- Sriram K, Insel PAG. Protein-coupled receptors as targets for approved drugs: How many targets and how many drugs? *Mol Pharmacol* (2018) 93:251–8. doi:10.1124/mol.117.111062
- Höller C, Freissmuth M, Nanoff CG. G proteins as drug targets. *CMLS Cel Mol Life Sci* (1999) 55:257–70. doi:10.1007/s000180050288
- Nubbemeyer B, Pepanian A, George AAP, Imhof D. Strategies towards targeting Gai/s proteins: Scanning of protein-protein interaction sites to overcome inaccessibility. *ChemMedChem* (2021) 16:1697–716. doi:10.1002/cmdc.202100039
- Gingell JJ, Simms J, Barwell J, Poyner DR, Watkins HA, Pioszak AA, et al. An allosteric role for receptor activity-modifying proteins in defining GPCR pharmacology. *Cell Discov* (2016) 2:16012. doi:10.1038/celldisc.2016.12
- Deupi X, Kobilka B. Energy landscapes as a tool to integrate GPCR structure, dynamics, and function. *Physiology* (2010) 25:293–303. doi:10.1152/physiol.00002.2010
- Alhadeff R, Vorobyov I, Yoon HW, Warshel A. Exploring the free-energy landscape of GPCR activation. *Proc Natl Acad Sci U S A* (2018) 115:10327–32. doi:10.1073/pnas.1810316115
- Brown MF. Modulation of rhodopsin function by properties of the membrane bilayer. *Chem Phys Lipids* (1994) 73:159–80. doi:10.1016/0009-3084(94)90180-5
- Oates J, Watts A. Uncovering the intimate relationship between lipids, cholesterol and GPCR activation. *Curr Opin Struct Biol* (2011) 21:802–7. doi:10.1016/j.sbi.2011.09.007
- Katritch V, Fenalti G, Abola EE, Roth BL, Cherezov V, Stevens RC. Allosteric sodium in class A GPCR signaling. *Trends Biochem Sci* (2014) 39:233–44. doi:10.1016/j.tibs.2014.03.002
- Selent J, Sanz F, Pastor M, De Fabritiis G. Induced effects of sodium ions on dopaminergic G-protein coupled receptors. *Plos Comput Biol* (2010) 6:e1000884. doi:10.1371/journal.pcbi.1000884
- Mahalingam M, Martínez-Mayorga K, Broen MF, Vogel R. Two protonation switches control rhodopsin activation in membranes. *Proc Natl Acad Sci U S A* (2008) 105:17795–800. doi:10.1073/pnas.0804541105
- Madathil S, Fahmy K. Lipid protein interactions couple protonation to conformation in a conserved cytosolic domain of G Protein-Coupled Receptors. *J Biol Chem* (2009) 284:28801–9. doi:10.1074/jbc.m109.002030
- Kapolka NJ, Rowe JB, Taghon GJ, Morgan WM, OShea CR, Isom DG. Proton-gated coincidence detection is a common feature of GPCR signaling. *Proc Natl Acad Sci U S A* (2021) 118:e2100171118. doi:10.1073/pnas.2100171118
- Siemers M, Lazaratos M, Karathanou K, Guerra F, Brown LS, Bridge BA-N. Bridge: A graph-based algorithm to analyze dynamic H-bond networks in membrane proteins. *J Chem Theor Comput* (2019) 15:6781–98. doi:10.1021/acs.jctc.9b00697
- Siemers M, Bondar A-N. Interactive interface for graph-based analyses of dynamic H-bond networks: Application to spike protein S. *J Chem Inf Model* (2021) 61:2998–3014. doi:10.1021/acs.jcim.1c00306
- Bertalan E, Lesca E, Schertler GFX, Bondar A-N. C-Graphs tool with graphical user interface to dissect conserved hydrogen-bond networks: Applications to visual rhodopsins. *J Chem Inf Model* (2021) 61:5692–707. doi:10.1021/acs.jcim.1c00827
- Murakami M, Kouyama T. Crystal structure of squid rhodopsin. *Nature* (2008) 453:363–7. doi:10.1038/nature06925
- Bertalan É, Lešnik S, Bren U, Bondar A-N. Protein-water hydrogen-bond networks of G protein-coupled receptors: Graph-based analyses of static structures and molecular dynamics. *J Struct Biol X* (2020) 212:107634. doi:10.1016/j.jsb.2020.107634
- Hua T, Li X, Wu L, Iliopoulos-Tsoutsouvas C, Yuxia W, Wu M, et al. Activation and signaling mechanisms revealed by cannabinoid receptor-G_i complex structures. *Cell* (2020) 180:1–11. doi:10.1016/j.cell.2020.01.008
- Isaïkina P, Tsai C-J, Dietz N, Pamula F, Grahl A, Goldie KN, et al. Structural basis of the activation of the CC chemokine receptor 5 by a chemokine agonist. *Sci Adv* (2021) 7:eabg8685. doi:10.1126/sciadv.abg8685
- Bondar A-N. Graphs of hydrogen-bond networks to dissect protein conformational dynamics. *J Phys Chem B* (2022) 126:3973–84. doi:10.1021/acs.jpbc.2c00200
- Vickery ON, Carvalheda CA, Zaidi SA, Pisiakov AV, Katritch V, Zachariae U. Intracellular transfer of Na⁺ in an active-state G-Protein-Coupled Receptor. *Structure* (2018) 26:171–80.e2. doi:10.1016/j.str.2017.11.013
- Quinn SJ, Bai M, Brown EM. pH sensing by the calcium-sensing receptor. *J Biol Chem* (2004) 279:37241–9. doi:10.1074/jbc.m404520200
- Meyer J, del Vecchio G, Steitz V, Massaly N, Stein C. Modulation of μ -opioid receptor activation by acidic pH is dependent on ligand structure and an ionizable amino acid residue. *Br J Pharmacol* (2019) 176:4510–20. doi:10.1111/bph.14810
- Carpenter B, Lebon G. Human adenosine A_{2A} receptor: Molecular mechanism of ligand binding and activation. *Front Pharmacol* (2017) 8:898. doi:10.3389/fphar.2017.00898
- Cao R, Giorgietti A, Bauer A, Neumaier B, Rosetti G, Carloni P. Role of extracellular loops and membrane lipids for ligand recognition in the neuronal adenosine receptor type 2A: An enhanced sampling simulation study. *Molecules* (2018) 23:2616. doi:10.3390/molecules23102616
- Klatt W, Wallner S, Brochhausen C, Stolwijk JA, Schreml S. Expression profiles of proton-sensing G-protein coupled receptors in common skin tumors. *Sci Rep* (2020) 10:15327. doi:10.1038/s41598-020-71700-9
- Silva PHI, Wagner CA. Physiological relevance of proton-activated GPCRs. *Pflugers Arch - Eur J Physiol* (2022) 474:487–504. doi:10.1007/s00424-022-02671-1
- Ludwig M-G, Vanek M, Guerini D, Gasser JA, Jones CE, Junker U, et al. Proton-sensing G-protein-coupled receptors. *Nature* (2003) 425:93–8. doi:10.1038/nature01905
- Rowe JB, Kapolka NJ, T GJ, Morgan WM, Isom DG. The evolution and mechanism of GPCR proton sensing. *J Biol Chem* (2020) 296:100167–13. doi:10.1074/jbc.ra120.016352
- Thurlkill RA, Grimsley GR, Scholtz JM, Pace CN. pK values of the ionizable groups of proteins. *Protein Sci* (2006) 15:1214–8. doi:10.1110/ps.051840806
- Schönichen A, Webb BA, Jacobson MP, Barber DL. Considering protonation as a posttranslational modification regulating protein structure and function. *Annu Rev Biophys* (2013) 42:289–314. doi:10.1146/annurev-biophys-050511-102349
- Sacks V, Marantz Y, Aagaard A, Checover S, Nachliel E, Gutman M. The dynamic feature of the proton collecting antenna of a protein surface. *Biochim Biophys Acta - Bioenerg* (1998) 1365:232–40. doi:10.1016/s0005-2728(98)00073-5
- Checover S, Marantz Y, Nachliel E, Gutman M, Pfeiffer M, Tittor J, et al. Dynamics of the proton transfer reaction on the cytoplasmic surface of bacteriorhodopsin. *Biochemistry* (2001) 40:4281–92. doi:10.1021/bi002574m
- Riesle J, Oesterhelt D, Dencher NA, Heberle J. D38 is an essential part of the proton translocation pathway in bacteriorhodopsin. *Biochemistry* (1996) 35:6635–43. doi:10.1021/bi9600456
- Borschchevskiy V, Kovalev K, Round E, Efremov R, Astashkin R, Bourenkov G, et al. True-atomic-resolution insights into the structure and functional role of linear chains and low-barrier hydrogen bonds in proteins. *Nat Struct Mol Biol* (2022) 29:440–50. doi:10.1038/s41594-022-00762-2
- Furuse M, Tamogami J, Hosaka T, Kikukawa T, Shinya N, Hato M, et al. Structural basis for the slow photocycle and late proton release in *Acetabularia* rhodopsin I from the marine plant *Acetabularia acetabulum*. *Acta Crystallogr D Biol Crystallogr* (2015) 71:2203–16. doi:10.1107/s1399004715015722
- Bada Juarez JF, Judge PJ, Adam S, Axford D, Vinals J, Birch J, et al. Structures of the archaeorhodopsin-3 transporter reveal that disordering of internal water networks underpins receptor sensitization. *Nat Commun* (2021) 12:629. doi:10.1038/s41467-020-20596-0
- Lazaratos M, Siemers M, Brown LS, Bondar A-N. Conserved hydrogen-bond motifs of membrane transporters and receptors. *Biochim Biophys Acta - Biomembranes* (2022) 1864:183896. doi:10.1016/j.bbmem.2022.183896
- Bondar A-N, Lemieux HJ. Reactions at biomembrane interfaces. *Chem Rev* (2019) 119:6162–83. doi:10.1021/acs.chemrev.8b00596
- Bondar A-N. Proton-binding motifs of membrane-bound proteins: From bacteriorhodopsin to spike protein S. *Front Chem* (2021) 9:685761. doi:10.3389/fchem.2021.685761
- Bondar A-N. Mechanisms of long-distance allosteric couplings in proton-binding membrane transporters. *Adv Protein Chem Struct Biol* (2022) 128:199–239. doi:10.1016/bs.apcsb.2021.09.002
- Gerwert K, Hess B, Soppa J, Oesterhelt D. Role of aspartate-96 in proton translocation by bacteriorhodopsin. *Proc Natl Acad Sci U S A* (1989) 86:4943–7. doi:10.1073/pnas.86.13.4943

47. Balashov SP, Govindjee R, Imasheva ES, Misra S, Ebrey TG, Feng Y, et al. The two pKa's of aspartate-85 and control of thermal isomerization and proton release in the arginine-82 to lysine mutant of bacteriorhodopsin. *Biochemistry* (1995) 34: 8820–34. doi:10.1021/bi00027a034
48. Dioumaev AK, Brown LS, Needleman R, Lanyi JK. Fourier Transform infrared spectra of a late intermediate of the bacteriorhodopsin photocycle suggest transient protonation of asp-212. *Biochemistry* (1999) 38:10070–8. doi:10.1021/bi990873+
49. Metz G, Siebert F, Engelhardt M. Asp85 is the only internal aspartic acid that gets protonated in the M intermediate and the purple-to-blue transition of bacteriorhodopsin. A solid-state ¹³C CP-MAS NMR investigation. *FEBS Lett* (1992) 303:237–41. doi:10.1016/0014-5793(92)80528-o
50. Kandori H, Belenki M, Herzfeld J. Vibrational frequency and dipolar orientation of the protonated Schiff base in bacteriorhodopsin before and after photoisomerization. *Biochemistry* (2002) 41:6026–31. doi:10.1021/bi025585j
51. Ni QZ, Can Tv ED, Belenki M, Griffin RG, Herzfeld J. Primary transfer step in the light-driven ion pump bacteriorhodopsin: An irreversible U-turn revealed by Dynamic Nuclear Polarization-Enhanced Magic Angle Spinning NMR. *J Am Chem Soc* (2018) 140:4085–91. doi:10.1021/jacs.8b00022
52. Nango E, Royant A, Kubo M, Nakane T, Wickstrand C, Kimura T, et al. A three-dimensional movie of structural changes in bacteriorhodopsin. *Science* (2016) 354:1552–7. doi:10.1126/science.aah3497
53. Weinert T, Skopintsev P, James D, Dworkowski F, Panepucci E, Kekilli D, et al. Proton uptake mechanism in bacteriorhodopsin captured by serial synchrotron crystallography. *Science* (2019) 365:61–5. doi:10.1126/science.aaw8634
54. Bondar A-N, Elstner M, Suhai S, Smith JC, Fischer S. Mechanism of primary proton transfer in bacteriorhodopsin. *Structure* (2004) 12:1281–8. doi:10.1016/j.str.2004.04.016
55. Hayashi S, Ohmine I. Proton transfer in bacteriorhodopsin: Structure, excitation, IR spectra, and potential energy surface analyses by an *ab initio* QM/MM method. *J Phys Chem B* (2000) 104:10678–91. doi:10.1021/jp001508r
56. Goyal P, Ghosh N, Phatak P, Clemens M, Gaus M, Elstner M, et al. Proton storage site in bacteriorhodopsin: New insights from quantum mechanics/molecular mechanics simulations of microscopic pK_a and infrared spectra. *J Am Chem Soc* (2012) 133:14981–97. doi:10.1021/ja201568s
57. Ådelroth P, Brzezinski P. Surface-mediated proton-transfer reactions in membrane-bound proteins. *Biochim Biophys Acta - Bioenerg* (2004) 1655: 102–15. doi:10.1016/j.bbabi.2003.10.018
58. Shutova T, Klimov VV, Andersson B, Samuelsson G. A cluster of carboxylic groups in PsbO protein is involved in proton transfer from the water oxidizing complex of Photosystem II. *Biochim Biophys Acta - Bioenerg* (2007) 1767:434–40. doi:10.1016/j.bbabi.2007.01.020
59. Lorch S, Capponi S, Pieront F, Bondar A-N. Dynamic carboxylate/water networks on the surface of the PsbO subunit of photosystem II. *J Phys Chem B* (2015) 119:12172–81. doi:10.1021/acs.jpcc.5b06594
60. Jumper J, Evans R, Pritzel A, Green T, Figurnov M, Ronneberger O, et al. Highly accurate protein structure prediction with AlphaFold. *Nature* (2021) 596: 583–9. doi:10.1038/s41586-021-03819-2
61. The UniProt Consortium UniProt: A hub for protein information. *Nucleic Acid Res* (2015) 43:D204–D212. doi:10.1093/nar/gku/989
62. Jacobson KA, Gao ZG, Matricon P, Eddy MT, Carlsson J. Adenosine A2A receptor antagonists: From caffeine to selective non-xanthines. *Br J Pharmacol* (2020) 179:3496–511. doi:10.1111/bph.15103
63. Weinert T, Olieric N, Cheng R, Brünle S, James D, Ozerov D, et al. Serial millisecond crystallography for routine room-temperature structure determination at synchrotrons. *Nat Commun* (2017) 8:542. doi:10.1038/s41467-017-00630-4
64. Jespers W, Schiedel AC, Heitman LH, Cooke RM, van Westen GJP, Gloriam DE, et al. Structural mapping of adenosine receptor mutations: Ligand binding and signaling mechanisms. *Trends Pharmacol Sci* (2018) 39:75–89. doi:10.1016/j.tips.2017.11.001
65. Yuan S, Filipek S, Palczewski K, Vogel H. Activation of G-protein-coupled receptors correlates with the formation of a continuous internal water pathway. *Nat Commun* (2014) 5:4733. doi:10.1038/ncomms5733
66. Lee Y, Kim S, Choi S, Hyeon C. Ultraslow water-mediated transmembrane interactions regulate the activation of A_{2A} adenosine receptor. *Biophys J* (2016) 111: 1180–91. doi:10.1016/j.bpj.2016.08.002
67. Walker CS, Eftekhari S, Bower RL, Wilderman A, Insel PA, Edvinsson L, et al. A second trigeminal CGRP receptor: Function and expression of the AMY1 receptor. *Ann Clin Transl Neurol* (2015) 2:595–608. doi:10.1002/acn3.197
68. Biskobing DM, Fan D. Acid pH increases carbonic anhydrase II and calcitonin receptor mRNA expression in mature osteoclasts. *Calcif Tissue Int* (2000) 67: 178–83. doi:10.1007/s00223001107
69. Micelli S, Melelo D, Picciarelli V, Gallucci E. Effect of pH-variation on insertion and ion channel formation of human calcitonin into planar lipid bilayers. *Front Biosci* (2006) 11:2035–44. doi:10.2741/1945
70. Liang Y-L, Khoshouei M, Radjainia M, Zhang Y, Glukhova A, Tarrasch J, et al. Phase-plate cryo-EM structure of a class B GPCR-G-protein complex. *Nature* (2017) 546:118–23. doi:10.1038/nature22327
71. dal Maso E, Glukhova A, Zhu Y, Garcia-Nafria J, Tate CG, Atanasio S, et al. The molecular control of calcitonin receptor signaling. *ACS Pharmacol Transl Sci* (2019) 2:31–51. doi:10.1021/acsptsci.8b00056
72. Cao J, Belousoff J, Liang Y-L, Johnson RM, Josephs TM, Fletcher MM, et al. A structural basis for amylin receptor phenotype. *Science* (2022) 375:eabm9609. doi:10.1126/science.abm9609
73. Zhang XC, Cao C, Zhou Y, Zhao Y. Proton transfer-mediated GPCR activation. *Protein Cell* (2015) 6:12–7. doi:10.1007/s13238-014-0106-4
74. Garcia-Nafria J, Tate CG. Structure determination of GPCRs: Cryo-EM compared with X-ray crystallography. *Biochem Soc Trans* (2021) 49:2345–55. doi:10.1042/bst20210431
75. Del Alamo S, Sala D, McHaorab HS, Miller J. Sampling alternative conformational states of transporters and receptors with AlphaFold2. *ELife* (2022) 11:e75751. doi:10.7554/elife.75751
76. Rodriguez-Espigares I, Torrens-Fontanals M, Tiemann JKS, Aranda-Garcia D, Ramirez-Anguita JM, Stepniowski TM, et al. GPCRmd uncovers the dynamics of the 3D-GPCRome. *Nat Methods* (2020) 17:777–87. doi:10.1038/s41592-020-0884-y
77. Kooistra AJ, Mordalski S, Pándy-Szekeres P, Esguerra M, Mamyrbekov A, Munk C, et al. GPCRdb in 2021: Integrating GPCR sequence, structure and function. *Nucleic Acids Res* (2021) 49:D335–D43. doi:10.1093/nar/gkaa1080
78. Lanyi JK. Bacteriorhodopsin. *Int Rev Cytol* (1999) 187:161–202. doi:10.1016/s0074-7696(08)62418-3
79. Humphrey W, Dalke W, Schulten K. VMD: Visual molecular dynamics. *J Mol Graph* (1996) 14:33–8. doi:10.1016/0263-7855(96)00018-5
80. Lomize M, Pogozheva ID, Joo H, Mosberg HI, Lomize AL. OPM database and PPM web server: Resources for positioning of proteins in membranes. *Nucleic Acids Res* (2011) 40:D370–6. doi:10.1093/nar/gkr703
81. Hasegawa N, Jonotsuka H, Miki K, Takeda K. X-ray structure analysis of bacteriorhodopsin at 1.3 Å resolution. *Sci Rep* (2018) 8:13123. doi:10.1038/s41598-018-31370-0
82. Carpenter B, Nehmé R, Warne T, Leslie AGW, Tate CG. Structure of the adenosine A2A receptor bound to an engineered G protein. *Nature* (2016) 536: 104–7. doi:10.1038/nature18966



OPEN ACCESS

EDITED BY

Glenn Terje Lines,
Simula Research Laboratory, Norway

REVIEWED BY

Sarangam Majumdar,
University of L'Aquila, Italy
Blouza Adel,
Université de Rouen, France

*CORRESPONDENCE

Christina Kuttler
kuttler@ma.tum.de

SPECIALTY SECTION

This article was submitted to
Mathematical Biology,
a section of the journal
Frontiers in Applied Mathematics and
Statistics

RECEIVED 24 May 2022

ACCEPTED 29 August 2022

PUBLISHED 21 September 2022

CITATION

Kuttler C and Maslovskaya A (2022)
Computer-assisted modeling of
Quorum sensing in bacterial
population exposed to antibiotics.
Front. Appl. Math. Stat. 8:951783.
doi: 10.3389/fams.2022.951783

COPYRIGHT

© 2022 Kuttler and Maslovskaya. This
is an open-access article distributed
under the terms of the [Creative
Commons Attribution License \(CC BY\)](#).
The use, distribution or reproduction
in other forums is permitted, provided
the original author(s) and the copyright
owner(s) are credited and that the
original publication in this journal is
cited, in accordance with accepted
academic practice. No use, distribution
or reproduction is permitted which
does not comply with these terms.

Computer-assisted modeling of Quorum sensing in bacterial population exposed to antibiotics

Christina Kuttler^{1*} and Anna Maslovskaya²

¹Fakultät für Mathematik, Technische Universität München, Garching bei München, Germany,

²Mathematics and Computer Sciences Department, Amur State University, Blagoveshchensk, Russia

A mathematical model for bacterial growth and control by antibiotics treatment, including Quorum sensing as a special kind of communication, is introduced. We aim in setting up a flexible model structure allowing for fast simulations and overview about the general behavior. The deterministic approach can be used for *in silico* studies of bacterial cooperative behavior in the special case of Quorum sensing. Since antibiotic treatment is the basic and vital way to fight pathogenic bacteria, in the present study, we propose a modification of a reaction-diffusion model of communication processes in a bacterial population exposed to antibiotics. The dynamical biological system is formalized by a system of semilinear parabolic PDEs. The numerical solution of the 2D problem is based on a hybrid computing procedure, which includes a finite difference method combined with a Monte-Carlo simulation of population dynamics. Computational experiments are performed to describe space-time distributions of key chemical compounds characterizing Quorum sensing during the growth of a bacterial population and its decrease resulting from the predetermined strategy of antibiotic treatment.

KEYWORDS

bacterial communication, antibiotics action, reaction-diffusion process, model of Quorum sensing, stochastic bacterial dynamics, computer simulation of signal substances

1. Introduction

Bacteria are not just single cells and acting individually, but have been discovered to form successful communities which have various possibilities to interact, within colonies but also beyond. One such mechanism, detected in more and more bacterial species, is the so-called “Quorum sensing” [1]. It is based on an intracellular gene regulation system and uses signal molecules, the so-called, which are produced inside the cells and can be transported and diffuse in the extracellular space.

Quorum sensing systems are known to control many important phenotypic changes of the bacteria. Historically first luminescence of the marine bacterial species *Vibrio fischeri* was found in the light organ of the squid *Euprymna scolopes*. Later, more and more species were found to use similar systems for different purposes, like pathogenicity and biofilm production [2]. Furthermore, Quorum sensing may even influence the

resistance against several stressors like antibiotics to some extent, as considered e.g., in [3].

More concretely, we consider the Gram-negative bacterial species *Pseudomonas putida* IsoF, whose Quorum sensing system is quite well-known and has been used in many previous publications as a model organism for this purpose. Even though, this sounds very specific, *P. putida* uses a type of Quorum sensing system as many other Gram-negative bacteria also do, with slight differences in the molecule structure, but analogous architecture of the gene regulation system [4]. Usually, they use so-called Acyl-homoserine lactones (short: AHL) as autoinducer molecules. Thus, the *ppu* system of *P. putida* can be taken as prototype system, and the mathematical modeling can easily be transferred also to other species and their Quorum sensing systems. As a special property, *P. putida* also produces an enzyme which can degrade autoinducers, the so-called Lactonase [5]. Corresponding models have been considered in previous publications and can be taken as standard [6, 7].

However, as a main treatment of bacterial infections in patients since many decades, antibiotics are used, fight against bacterial infections and to kill or at least reduce growth of the bacteria. We aim in setting up a simple and fast to calculate model. This means, we focus on the most essential parts: growth of whole colonies, decrease during the presence of antibiotics. To keep it as simple as possible, we neglect any refined structures of the colony growth, as they may play a minor role for our purposes. Based on this, we want to keep the basic Quorum sensing model in, including the Lactonase in the model setup. By that we can always check, if (and when) the Quorum sensing system, including the behavioral changes controlled by it, is active or not, given a certain antibiotics treatment.

For our *in silico* study, we focus on the situation of bacterial colonies, e.g., on surfaces of medical devices or on laboratory equipment. They can be easier “treated” than bacterial infections in a living host, where many side aspects may play a role. We want to set up a prototype model which is easy to handle, but already provides the structure to be adapted to more concrete situations. The hybrid structure contains a time-dependent colony growth including an explicit saturation and the effect of the antibiotics treatment on the one hand side, as well as a classic reaction-diffusion model to describe the spread of AHL and Lactonase molecules on a surface layer. For the antibiotics treatment we assume for simplification that it can be applied on the whole surface at once, e.g., by putting a water-based layer above which contains the antibiotics in a homogeneous concentration. Thus, it is sufficient to use one homogeneous time-dependent variable for the antibiotics for the whole system.

The model approach allows to easily make simulations, to place the bacterial colonies, also to handle many of them at once. It provides a simplified structure, which can also be easily used to control such systems, e.g., how a treatment should look like to keep a bacterial population under control, such that it

doesn’t activate its Quorum sensing system and by that doesn’t become pathogenic.

The present study aims in the development of the mathematical model of Quorum sensing in a Gram-negative bacterial population under the inhibitory action of antibiotics. The overall goal is to design a hybrid model that provides a quick approach by combining the continuous deterministic approach (expressed by the reaction-diffusion model of bacterial communication) and the discrete stochastic simulation of vital activity of bacteria exposed to antibiotics. By that, we keep the model as simple as possible to focus on the essential behavior. The paper is organized as follows. The mathematical statement of the reaction-diffusion problem, the applied numerical method, and the computational setup are presented in Section 2. Section 3 focuses on the computer simulations of space-time distributions of key characteristics of Quorum sensing for *P. putida* bacterial species. We will perform a full cycle of mathematical modeling and computer simulation to explore the changes in chemical compounds characterizing bacterial communication at varying strategies of antibiotic treatment.

2. Mathematical problem statement and computational details

2.1. Governing equations for modeling of bacterial Quorum sensing

The basic model of the bacterial communication process describes the dynamics of changes in concentrations of key chemical compounds such as AHL and Lactonase, which characterize the “quorum level” in a bacterial population and the “level” of its degradation, respectively [8]. The bacterial Quorum sensing model can be referred to as a reaction-diffusion dynamical system. In the two-dimensional case, the mathematical model is expressed by an initial-boundary value problem for a system of partial differential equations:

$$\frac{\partial U}{\partial t} = D_U \Delta U - \gamma_U U - \gamma_{L \rightarrow U} L U + F_1(x, y, t, U), \quad (1)$$

$$\begin{aligned} \frac{\partial L}{\partial t} &= D_L \Delta L - \gamma_L L + F_2(x, y, t, U), \\ 0 < x < l, \quad 0 < y < l, \quad 0 < t \leq t_{ob}, \end{aligned} \quad (2)$$

$$U(x, y, 0) = 0, \quad L(x, y, 0) = 0, \quad 0 \leq x \leq l, \quad 0 \leq y \leq l, \quad (3)$$

$$U(0, y, t) = 0, \quad U(l, y, t) = 0, \quad L(0, y, t) = 0, \quad L(l, y, t) = 0,$$

$$\begin{aligned} U(x, 0, t) &= 0, \quad U(x, l, t) = 0, \quad L(x, 0, t) = 0, \\ L(x, l, t) &= 0, \quad 0 < t \leq t_{ob}, \end{aligned} \quad (4)$$

where $U(x, y, t)$ is the AHL concentration and $L(x, y, t)$ is the Lactonase concentration produced by bacteria, both given in mol/l; l is the linear size of the solution domain in μm ; t_{ob} is the observation time in h; γ_U , $\gamma_{L \rightarrow U}$, γ_L , D_U , D_L are model parameters (detailed description below) associated with the processes of diffusion and degradation of main chemical compounds.

The governing Equations (1)–(2) describe the dynamics and diffusion of AHL and Lactonase concentrations, the natural degradation of AHL and Lactonase, degradation of AHL by Lactonase due to the negative feedback, the production of AHL and the reaction of Lactonase resulting from the positive feedback. The generation terms $F_1(x, y, t, U)$ and $F_2(x, y, t, U)$ are defined by the assumed normal distribution of bacterial population density and the Hill function taking into account the possible changes in bacterial concentration:

$$F_m(x, y, t, U) = N(t) \sum_{v=1}^V f_m \exp \left(-\frac{(x - x_c^v)^2 + (y - y_c^v)^2}{\sigma^2} \right), \quad m = 1, 2, \quad (5)$$

$$\begin{aligned} f_1(U) &= \alpha_U + \beta_U \frac{U^n}{((U_{th})^n + U^n)}, \\ f_2(U) &= \beta_L \frac{U^n}{((U_{th} + \varepsilon)^n + U^n)}, \end{aligned} \quad (6)$$

where (x_c^v, y_c^v) is the position of the bacterial colony with the number v ; $N(t)$ is the normalized function defined the dynamics of a bacterial population density; $\sigma = \sigma(t)$, ε , α_U , β_U , β_L , U_{th} , n are model parameters, which specify the principles underlying the time dependence of the bacterial population density and its spatial distribution in the solution domain.

Therefore, the mathematical model is formalized by an initial-boundary value problem for the system of semilinear reaction-diffusion PDEs. Some remarks devoted to the existence and uniqueness of solutions can be found in [8] supported by theoretical reviews [9, 10]. Obviously, the construction of analytical solutions for the considered problem meets essential difficulties. Thus, we focus in our present study on the application of numerical methods, namely a finite difference method combined with a stochastic procedure for the simulation of the bacterial population dynamics, to obtain solutions of the problem (1)–(6).

2.2. Numerical scheme for solving the problem

The equations of the system (1)–(2) could be written in the following general form:

$$\frac{\partial u}{\partial t} = D \left(\frac{\partial^2 u}{\partial x^2} + \frac{\partial^2 u}{\partial y^2} \right) - qu + F, \quad (7)$$

where $u = U$, $q = \gamma_U + \gamma_{L \rightarrow U} L$, $D = D_U$, $F = F_1$ for Equation (1) and $u = L$, $q = \gamma_L$, $D = D_L$, $F = F_2$ for Equation (2).

To solve the problem numerically, we apply a splitting finite-difference method [11]. For instance, we use the concept of the Peaceman-Rachford alternating direction method. Notice that the main advantage of the method is a fairly good correlation between accuracy and computational costs. This method is quite simple in programming, at the same time, for standard problems it is absolutely stable and has the second order of accuracy with respect to space and time variables. For small Courant numbers, this method is used even to test other schemes. The disadvantages of this scheme include conditional convergence when the number of spatial variables is more than two. In addition, this method is conditionally stable when solving problems with the Neumann and Robin boundary conditions [11, 12]. Since our particular problem does not have such limitations, the alternating direction method turned out to be a promising candidate for constructing a numerical algorithm.

Here, let us introduce Ω_{h_1, h_2}^τ as a space-time grid covering the solution domain:

$$\begin{aligned} \Omega_{h_1, h_2}^\tau &= \{x_i = (i-1)h_1, i = \overline{1, N+1}, y_j = (j-1)h_2, \\ &\quad j = \overline{1, M+1}, t^k = (k-1)\tau, k = \overline{1, K+1}\}. \end{aligned}$$

To deal properly with functions, we introduce the discrete function space of grid functions, which is isomorphic to finite dimensional Euclidean spaces. Further, the space of grid functions is equipped with an appropriate discrete norm (for instance, l_2 norm is further used).

Therefore, we have the following finite difference approximation on the first temporal semi-step $k + 1/2$ for $i = 2, 3, \dots, N$, $j = 2, 3, \dots, M$, $k = 1, 2, \dots, K$:

$$\begin{aligned} &\left[-\frac{D\tau}{2h_1^2} \right] u_{i-1,j}^{(s+1)} + \left[1 + \frac{D\tau}{2h_1^2} + \frac{\tau q_{i,j}^{k+1/2}}{2} \right] u_{i,j}^{(s+1)} \\ &+ \left[-\frac{D\tau}{2h_1^2} \right] u_{i+1,j}^{(s+1)} = u_{i,j}^k + \frac{D\tau}{2h_2^2} [u_{i,j-1}^k - 2u_{i,j}^k + u_{i,j+1}^k] \\ &+ \frac{\tau}{2} \tilde{F}, \end{aligned} \quad (8)$$

where the iterative sequence $u_{i,j}^{(s)}$, $s = 1, 2, \dots$, converges to the $u_{i,j}^{k+1/2}$, starting with $u_{i,j}^{(1)} = u_{i,j}^k$; $q_{i,j}^{k+1/2} = \gamma_U + \gamma_{L \rightarrow U} L_{i,j}^{k+1/2}$ for the Equation (1) and $q_{i,j}^{k+1/2} = \gamma_L$ for the Equation (2).

In this case, we supplement the computational scheme by the iterative procedure due to the presence of nonlinear terms in the generation parts of equations. In order to calculate the Lactonase concentration, we set $\tilde{F} = F(x_i, y_j, t^k, U_{i,j}^k)$ for the Equation (2). Further, we suppose that $\tilde{F} = F(x_i, y_j, t^k, U_{i,j}^{(s)})$ to calculate the AHL concentration with the Equation (1). And then, we again solve Equation (2) with $\tilde{F} = F(x_i, y_j, t^k, U_{i,j}^{(k+1/2)})$ to obtain the update distribution of the Lactonase concentration.

In a similar way, we can derive the computational scheme for the second time semi-step $k + 1$:

$$\left[-\frac{D\tau}{2h_2^2} \right] u_{i,j-1}^{(s+1)} + \left[1 + \frac{D\tau}{2h_2^2} + \frac{\tau q_{i,j}^{k+1}}{2} \right] u_{i,j}^{(s+1)} + \left[-\frac{D\tau}{2h_2^2} \right] u_{i,j+1}^{(s+1)} \\ = u_{i,j}^{k+1/2} + \frac{D\tau}{2h_1^2} \left[u_{i-1,j}^{k+1/2} - 2u_{i,j}^{k+1/2} + u_{i+1,j}^{k+1/2} \right] + \frac{\tau}{2} \tilde{F}, \quad (9)$$

where the iterative sequence $u_{i,j}^{(s)}$, $s = 1, 2, \dots$, converges to the $u_{i,j}^{k+1}$, starting with $u_{i,j}^{(1)} = u_{i,j}^{k+1/2}$; $q_{i,j}^{k+1} = \gamma_U + \gamma_{L \rightarrow U} L_{i,j}^{k+1}$ for the Equation (1); $q_{i,j}^{k+1} = \gamma_L$ for the Equation (2); $\tilde{F} = F(x_i, y_j, t^{k+1}, U_{i,j}^{(k+1)})$ for (2) and $\tilde{F} = F(x_i, y_j, t^k, U_{i,j}^{(s)})$ for (1). The systems defined by (8)–(9) are supplemented by discrete initial and boundary conditions:

$$u_{i,j}^1 = 0, \quad i = 1, 2, \dots, N + 1, \quad j = 1, 2, \dots, M + 1, \quad (10)$$

$$u_{i,1}^k = 0, \quad u_{i,M+1}^k = 0, \quad i = 1, 2, \dots, N + 1, \quad k = 2, 3, \dots, K + 1,$$

$$u_{1,j}^k = 0, \quad u_{N+1,j}^k = 0, \quad j = 1, 2, \dots, M + 1, \quad k = 2, 3, \dots, K + 1, \quad (11)$$

To solve the systems of linear equations on each time layer, we apply the Thomas algorithm.

2.3. Computational algorithm for simulation of bacterial population dynamics

The mathematical problem statement allows us to calculate the space-time distributions of chemical compounds regulating Quorum sensing for bacterial colonies, which are located at *a priori* defined positions in the computational domain. At the same time, we can provide simulations in a more realistic manner by including the algorithm of modeling bacterial population dynamics into the general computation scheme. In the present study, we use the ideas of a stochastic generation and the logistic growth of a bacterial population. The approach to constructing a hybrid scheme combining a deterministic model and stochastic modeling of bacterial evolution has been proposed before and successfully tested in our previous studies [7, 13, 14].

The computational algorithm is based on the following assumptions. During the observation process, bacteria colonies of circular shapes are growing stochastically on the plane OXY according to the logistic law. First, up to three bacterial colonies start to grow simultaneously from randomly chosen points (x_c^v, y_c^v) , and besides, with different probabilities, i.e. the probability of appearance of one colony is essentially greater

than for two and three (for example, for one colony $p^1 = 0.6$, for two colonies $p^2 = 0.3$, and for three colonies $p^3 = 0.1$). According to the Monte-Carlo method, a new bacterial colony can appear at a random time, but with a small probability on each time layer (for instance, $p^v = 0.1$). The linear size (radius) of each bacterial colony is denoted by $R(x_c^v, y_c^v, t)$. The time-dependent value of R is calculated by the logistic law of growth:

$$R^v(t) = \frac{IR_0 \exp(rt)}{I + R_0(\exp(rt) - 1)}, \quad v = 1, 2, \dots, V, \quad (12)$$

where R_0 is the initial linear size of a bacterial colony, which can grow up by assumption to a limiting linear size of I , in μm , and r is the parameter related to the rate of bacterial growth in $1/\text{h}$.

Here, we suppose that all bacterial colonies grow with a similar velocity. If the colonies are overlapping, the source functions F_1 and F_2 are determined by a superposition of corresponding contributions. Note also that the parameter σ in (5) is approximately estimated according to the “3-Sigma rule,” specifically, as $R^v(t)/3$.

Further, we start the degradation of a bacterial population by simulating the action of antibiotics at a defined time, when the total bacterial concentration reaches $4.6 \cdot 10^{11}$ cells/l. This value corresponds to the normalized value of $N(t)$ equaled to the unit. At the same time, we stop “generating” new bacterial colonies.

In addition, we need to formalize the relation between the linear size of bacterial colonies and the antibiotic action. In the present study, we apply a simplified approach. We suppose that the concentration of antibiotics does not depend on spatial coordinates, but is homogeneous on the whole surface, and it can be specified as a time-dependent function. To be precise, let us consider the antibiotics of ciprofloxacin as an example [15]. An approximation of concentration dynamics for ciprofloxacin can be plotted with the use of empirical data: the maximum value reaches at time moment 4–8 h and approximately after 12–24 h the concentration falls to a certain level. We use the Rayleigh distribution for the approximation:

$$A(t) = A_0 t \exp\left(\frac{-t^2}{A_1}\right). \quad (13)$$

Hence, we can assume for simplicity that the linear size of each bacterial colony reduced due to antibiotic action can be expressed as follows:

$$R^v(t) = \tilde{R}^v(t) \left(1 - \theta \frac{A^2(t)}{A^2(t) + m} \right), \quad v = 1, 2, \dots, V, \quad (14)$$

where $\tilde{R}^v(t)$ is the current value of the linear size of v colony; θ is the empirical constant provided the certain density of alive population; the parameter m corresponds to the maximum value of antibiotic concentration.

Further, to determine the time-dependent bacterial density $N(t)$ (the normalized value) we assume here for simplicity that this function can be described by the formula for the growth range:

$$N(t) = (1 + \exp(-\mu(t - b_1)))^{-1}, \quad t \leq t_d, \quad (15)$$

and we use the following expression to approximate decreasing in the bacterial population density as a result of the degradation due to a single antibiotic treatment:

$$N(t) = a + b(1 + \exp(\mu(t - b_2)))^{-1}, \quad t > t_d, \quad (16)$$

where a , b_1 , b_2 , μ are approximation parameters, which, in particular, provide a smooth behavior of $N(t)$ at time moment t_d .

Notice that the Equations (15)–(16) provide a model description of time-dependent behavior of the bacterial concentration (namely, the periods of bacterial growth and degradation to equilibrium values, the velocity of changes in concentration, the relative level of degradation). The “height” of the bacterial concentration is influenced by the parameters α_U , β_U , α_L , and the corresponding dimensions are correspondent to the basic Equations (5)–(6).

Therefore, the space distribution of a bacterial population is stochastically simulated on each time layer, taking into account the mechanisms of growth and degradation. At the same time, for all bacterial colonies, we calculate the corresponding bacterial concentration in view of the growth or degradation phase.

3. Computational experiments results and discussions

3.1. General algorithm, specification of the model object, and computational setup

By construction, the procedure of model implementation includes the Monte-Carlo simulation of bacterial population growth, the finite difference iterative scheme to solve PDEs and calculate the chemical compounds, the algorithm for simulation of the degradation of a bacterial population due to antibiotic action, and the functional dependence for bacterial concentration, taking into account the time-dependent decrease of the bacterial amount. The flowchart of the general computational algorithm is shown in Figure 1.

The program implementation of 2D model of bacterial Quorum sensing was performed in Matlab. The designed software is intended for computer simulations of space-time distributions of chemical compounds such as AHL and Lactonase concentrations at given parameters. Figure 2 illustrates the program application architecture diagram. In these terms, conducting simulations requires initialization

of the model as well as computational parameters. The graphical user interface (GUI) permits to submit all parameters and options that are necessary to accomplish a quorum sensing simulation. The GUI provides options to access the core system and modules that compute and visualize the antibiotic strategy (as time-dependent function of an antibiotic concentration), characteristics of bacterial populations (location at each moment, summarized linear size, total amount, etc.), and space-time distributions of main characteristics of quorum sensing, namely AHL and Lactonase concentrations during the observation process.

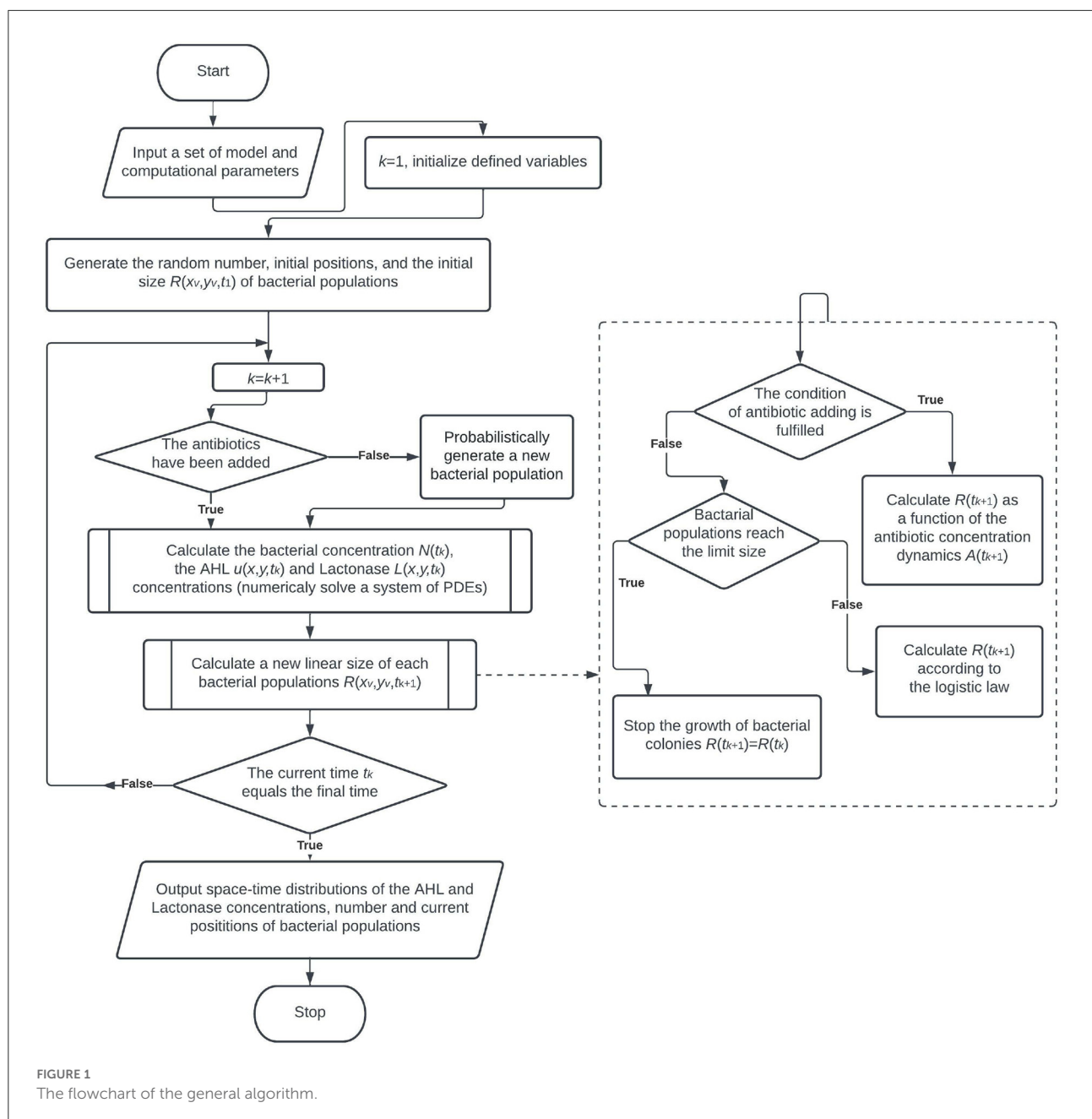
For instance, we will consider *Pseudomonas putida* IsoF as an object of mathematical modeling [16].

Pseudomonas putida is a Gram-negative rod-shaped bacterium of *Pseudomonas* genus, that lives in soils, waters, and plants. Generally, *P. putida* is defined as a nonpathogenic bacterium due to the lack of virulence-related genes [17]. *P. putida* IsoF is considered as an object due to its versatility and ease of handling to examine Quorum sensing. Note also that recent research suggests that *P. putida* can be a human pathogen causing nosocomial infections in patients with a weakened immune system like cancer patients and newborns [18]. *P. putida* can provide the exchange platform for more virulent and antibiotic resistant microorganisms such as deadly *Pseudomonas aeruginosa* [19]. Most infections caused by *P. genus* demonstrate resistance to certain antibiotics and their combinations. Therefore, *P. putida* represents an important model organism to perform simulations of Quorum sensing characteristics in a bacterial population under antibiotic action.

Let us assume that we have a two-dimensional domain limited by $0 \leq x \leq 100 \mu\text{m}$ and $0 \leq y \leq 100 \mu\text{m}$. The time of observation is up to 50–100 h. We choose the model parameter values as listed in Table 1 using previously estimated values [8]. The empirical parameter θ in (14) is fixed to be 0.2. The time of start of antibiotic action is estimated as $t_d = 10 - 16$ h.

The values of the parameters for bacterial density approximation (15)–(16) are established empirically from microbiological experiments for *Pseudomonas* bacterial species [20, 21]. We specify a following set of approximation parameters for the bacterial dynamics: $b_1 = 6$ h, $b_2 = 18$ h, $\mu = 1.4$ 1/h. Figure 3 illustrates the time-dependent behavior of bacterial density for the species *P. putida*. In this case, we suppose 30% decreasing in the bacterial population density within 10 h due to a single antibiotic action.

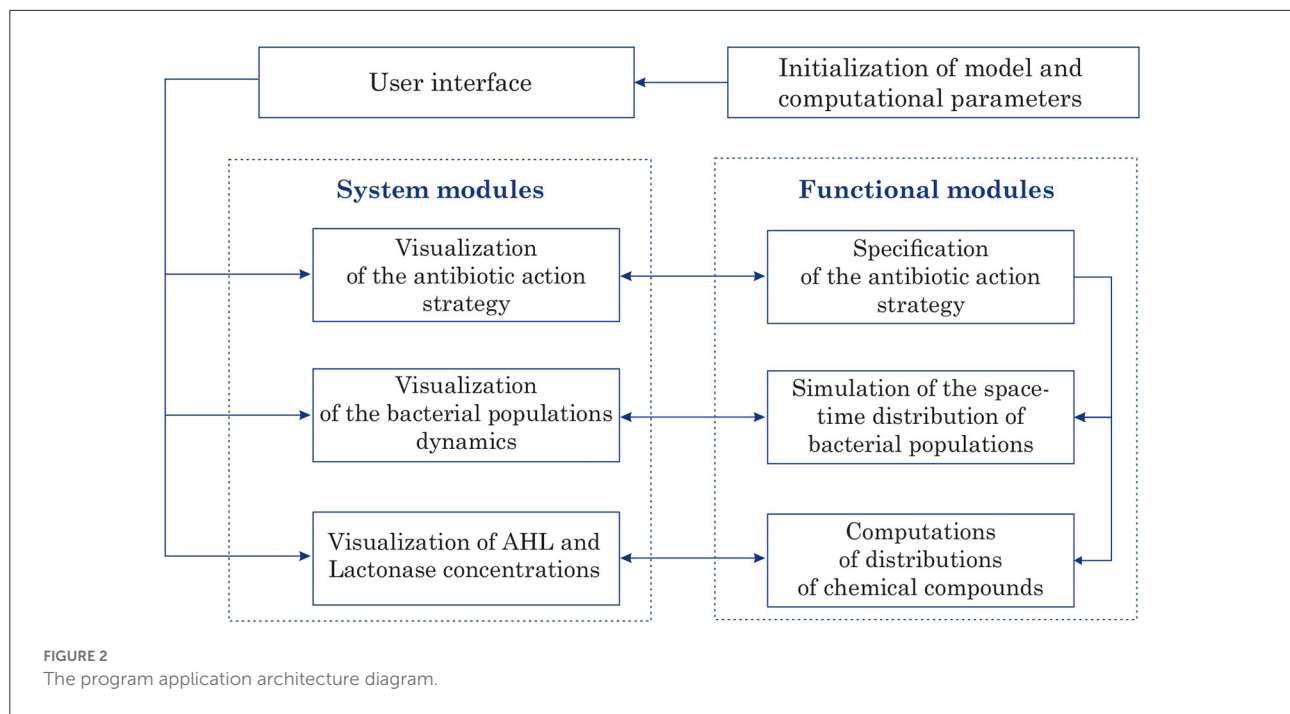
In addition, we conducted a numerical study of the stability of a constructed computational scheme. As far as the initial and boundary conditions are strictly defined for the corresponding chemical substances, here we examine the stability of the computational scheme by variation of the “amplitude part” of the generating terms defined by F_m . In more detail, we vary the parameters of α_U , β_U , and β_L . Here we assume that the parameters of α_U , β_U , and β_L alternately increase by 20, 30, 40, 50% while the others remain the same



(with respect to the initial values as listed in Table 1). In order to estimate the perturbations of grid functions under the “amplitude parameters” variation, we use the following estimations: $\xi_m = \|\bar{U}_m - U_{m-1}\|_2 / \|U_{m-1}\|_2$, $\varphi_m = \|\bar{L}_m - L_{m-1}\|_2 / \|L_{m-1}\|_2$, $m = 2, 3, 4, 5$, where $m = 1$ corresponds to the AHL and Lactonase concentrations calculated for the last time moment at $h_1 = h_2 = 1 \mu\text{m}$ and $\tau = 0.01 \text{ h}$ at initial parameters listed in Table 1. For these computations we suppose that there is only one bacterial colony located at the

central position of the computational domain with a linear size of $10 \mu\text{m}$.

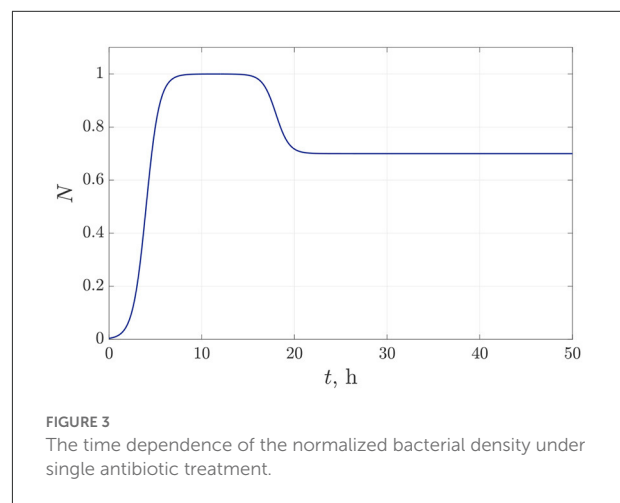
Figure 4 shows the estimation of the perturbation of corresponding grid functions. These data suggest an appearance of slight perturbations of the AHL and Lactonase concentrations under the variation of the “source functions.” The almost linear growth of the estimations indicates the numerical stability of the computational algorithm.

TABLE 1 Parameter values estimated for the bacterium *P. putida*.

Name	Meaning of parameter	Value
D_U	Diffusion rate of AHL	$100 \mu\text{m}^2/\text{h}$
D_L	Diffusion rate of Lactonase	$1 \mu\text{m}^2/\text{h}$
γ_U	Abiotic degradation rate of AHL	0.005545 1/h
γ_L	Abiotic degradation rate of Lactonase	0.5 1/h
$\gamma_{L \rightarrow U}$	Degradation rate of AHL by Lactonase	$0.65 \cdot 10^9 \text{ l/(mol}\cdot\text{h)}$
α_U	Low production rate of AHL	$1.058 \cdot 10^{-7} \text{ mol/(l}\cdot\text{h)}$
β_U	Increased production rate of AHL	$1.058 \cdot 10^{-6} \text{ mol/(l}\cdot\text{h)}$
β_L	Production rate of Lactonase	$1.38 \cdot 10^{-6} \text{ mol/(l}\cdot\text{h)}$
U_{th}	Threshold of AHL concentration between low and increased activity	$7 \cdot 10^{-8} \text{ mol/l}$
ε	Threshold shift for Lactonase production	$5 \cdot 10^{-9} \text{ mol/l}$
n	Degree of polymerization	2.5

3.2. Time-dependent simulations of Quorum sensing characteristics in bacterial population of *P. putida* under antibiotics action

We conducted numerical experiments for the 2D reaction-diffusion model combined with the procedure of the Monte-Carlo simulation of bacterial growth and further degradation



of the population due to antibiotic action. According to the above algorithm, one, two or three bacterial colonies with a circular shape can start to grow at an initial time. The initial radius R_0 of each bacterial colony is set to be $1 \mu\text{m}$. The parameter of the rate of logistics population growth is assumed to be $r = 0.4 \text{ 1/h}$, the limiting value of linear size is $I = 20 \mu\text{m}$. During the bacterial evolution process, a new bacterial colony appears with a small probability specified as 0.1 per time step of the simulation, chosen to be 0.5 h . Concretely, for the first simulation, we had two bacterial colonies at the start moment and the total amount V , equaled to 4.

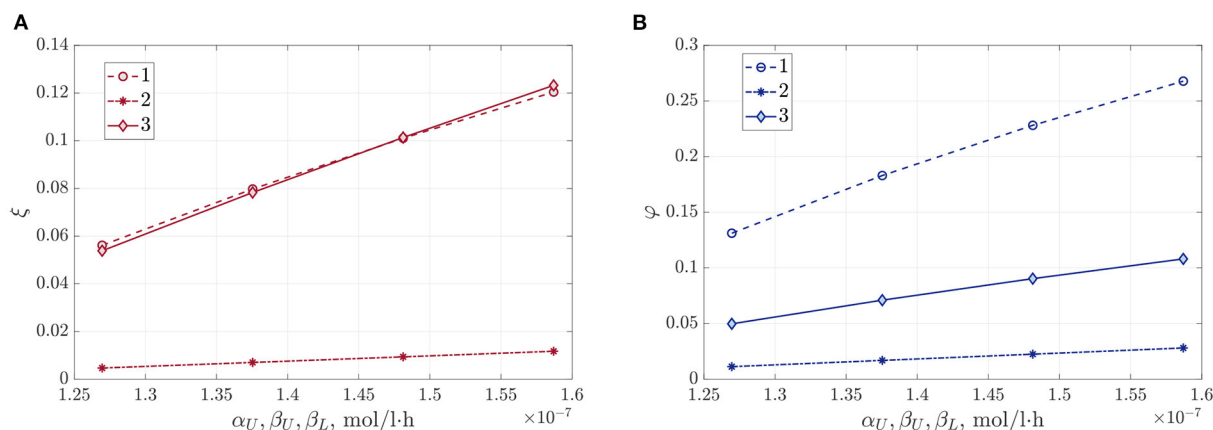


FIGURE 4

The estimation of the perturbations of grid functions for AHL concentration (A), and the Lactonase concentration (B) under the variation of the parameters of generating terms α_U (1), β_U (2), and β_L (3).

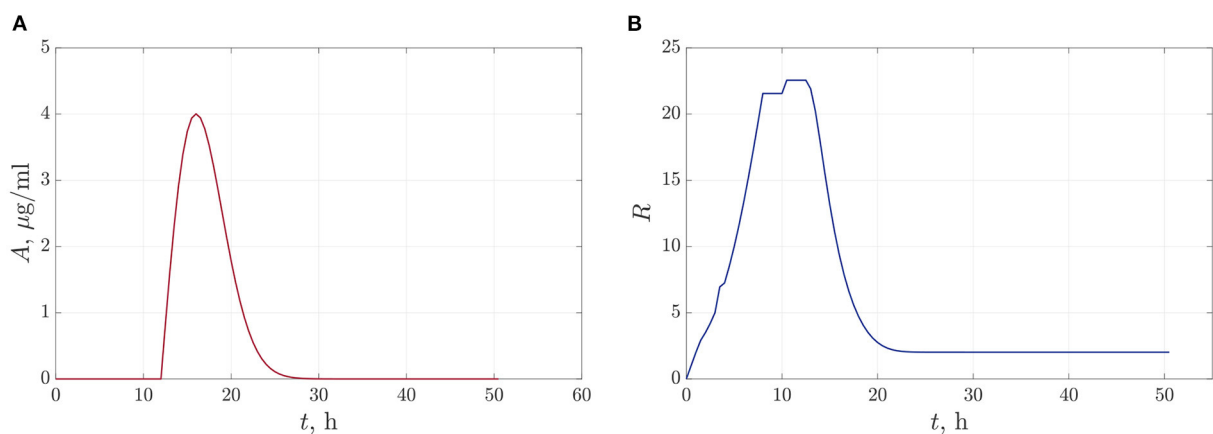


FIGURE 5

The dynamics of changes in antibiotic concentration (A), and the total linear size of bacterial colonies at single antibiotic treatment (B).

In the first case, we suppose that we do a single antibiotic treatment when the bacteria reach the critical value of population density. The time-dependent function (13) defining the dynamics of antibiotic concentration during the observation time is shown in Figure 5A. The parameters of the approximation (13) are set to be $A_0 = 1.65$ and $A_1 = 32$. Here we can claim that antibiotics reach an acting maximum concentration after 3.5–4 h after adding and acting during 10–13 h. Figure 5B illustrates the dynamics of the total value of linear size $R(t) = \sum_{v=1}^V R^v(t)$ of bacterial colonies. We see that the bacterial population has time to reach the equilibrium value before we start the degradation by antibiotics at $t = 12$ h. After that, the $R(t)$ leveled off at $2.017 \mu\text{m}$.

The following figures (Figures 6A,B) present the space distributions of key chemical compounds characterizing Quorum sensing in the bacterial community, namely the AHL and Lactonase concentrations calculated at a fixed time 12 h. In addition, graphs in Figure 7 visualize the maximum values of the AHL and Lactonase concentrations as time dependencies. These data indicate that the Lactonase concentration reached a maximum value before adding antibiotics, whereas the AHL concentration declined slightly due to the interaction between these players. The results suggest that the AHL concentration fell gradually, followed by a stabilization to the level of $4.89 \cdot 10^{-10}$ mol/l, at the same time, the Lactonase concentration decreases more essential and leveled to the value of $6.76 \cdot 10^{-13}$ mol/l. The average value of the

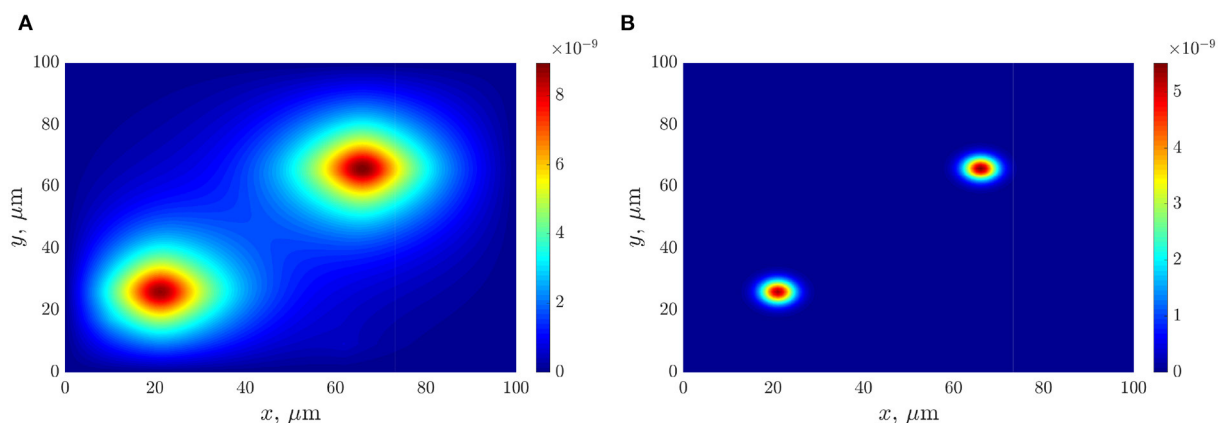


FIGURE 6
The distributions of chemical compounds calculated at time 12 h: (A)—the AHL concentration; (B)—the Lactonase concentration.

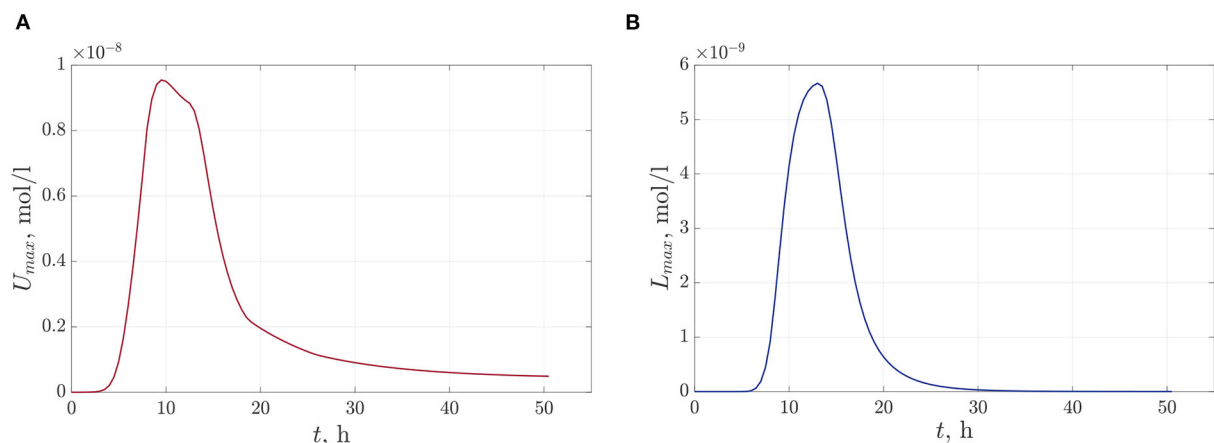


FIGURE 7
The time-dependent profiles of maximum values of chemical compounds during the observation time 50 h: (A)—the AHL concentration and (B)—the Lactonase concentration at single antibiotic treatment.

AHL concentration equals $1.36 \cdot 10^{-10}$ mol/l at the final time point.

This means that antibiotic action affects the enzyme, preventing the bacterial quorum to a greater extent than the signaling substance that provides the quorum itself. We can observe that a small bacterial population that has been reduced by a factor of ten is still producing signaling molecules. This effect can be referred to as the emergence of increasing the resistance of reduced bacterial population. Hence, we can conclude that a single antibiotic treatment leads to a reduction in the bacterial population under the assumed conditions of computational experiments. However, the Quorum sensing level in a reduced population remains very high compared to a saturated population, and a bacterial population will be able to quickly restore their numbers in the presence

of a nutrient medium. Therefore, the obvious strategies for suppressing Quorum sensing are to use a multiple antibiotic treatments strategy, an increasing antibiotic dose, a combination of different antibiotics, or even combining application of antibiotics and natural degrading enzymes.

3.3. A multiple antibiotic treatment strategy: Numerical experiments

Note that due to the stochasticity underlying the simulation of population generation and growth an exact reproduction of the computational experiments is not possible. Let us consider a computational experiment in which we apply a multiple antibiotic treatment strategy. For instance, we assume that

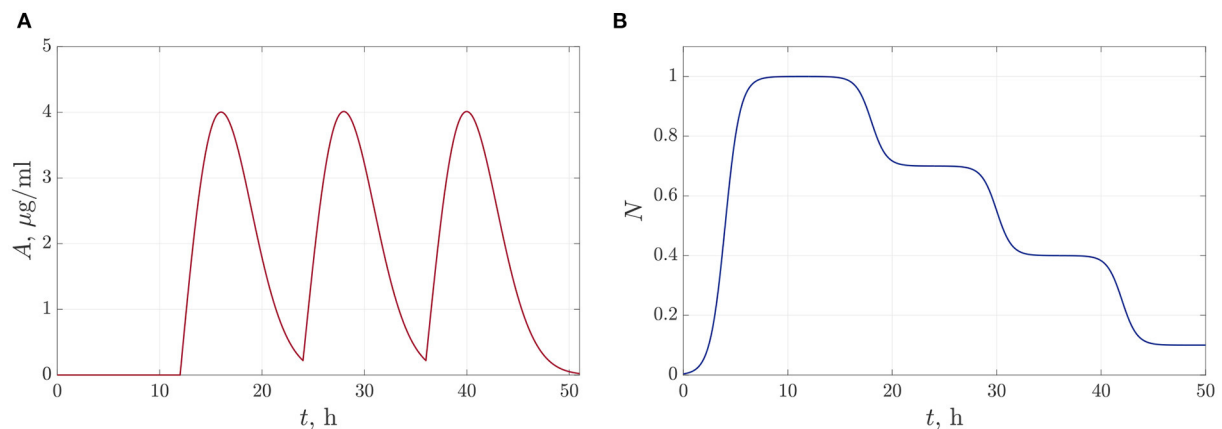


FIGURE 8

The dynamics of changes in the antibiotic concentration—(A) and the normalized bacterial concentration dynamics—(B) under multiple exposure to antibiotics.

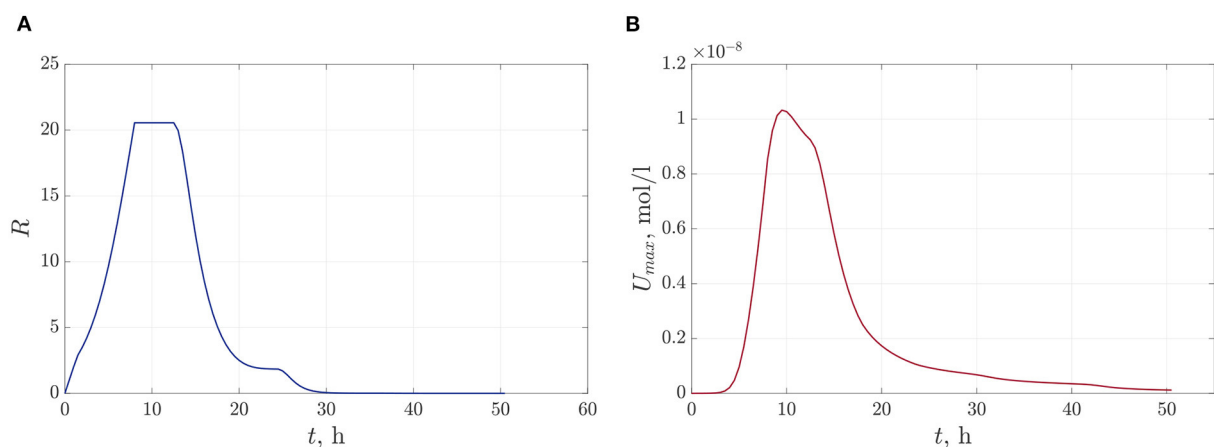


FIGURE 9

The time dependence of total linear size of bacterial colonies—(A) and the dynamics of the maximum values of the AHL concentration—(B) at the multiple antibiotic treatment.

antibiotic treatment was done three times, specifically at 12, 24, and 36 h (Figure 8A). In these terms, the function of bacterial density dynamics $N(t)$ includes three degradation phases as presented in Figure 8B. Figure 9A shows the changes in the total bacterial linear size $R(t)$ during the observation time. The graph is characterized by a sharp decline to the value of $4.8 \cdot 10^{-5} \mu\text{m}$. The simulations suggest a more significant decrease in the AHL concentration as presented in Figure 9B, where the maximum value corresponds to $1.78 \cdot 10^{-10} \text{ mol/l}$ at the final time $t = 50$ h. Nevertheless, the quorum level remains considerable even for a negligible population size. Concretely, the average value of AHL concentration is equal to $4.26 \cdot 10^{-11} \text{ mol/l}$ at the last moment. This effect is caused by the diffusion processes

and long relaxation time of the AHL concentration. Moreover, as we mentioned above, antibiotic adding has a strong effect on the Lactonase concentration, resulting in the suppression of this enzyme, which in turn does not essentially inhibit the AHL concentration.

We conducted a series of computational experiments, varying the interval between antibiotic treatment: 4, 8, 12, 16 h with a triple sequential addition of the same concentration. The findings allow us to conclude that all applied strategies lead to significant degradation of the bacterial population and a decrease in the AHL concentration. The total linear size of the population varies in the range of $2 \cdot 10^{-5} - 4 \cdot 10^{-4} \mu\text{m}$ and the average value of the AHL concentration changes from

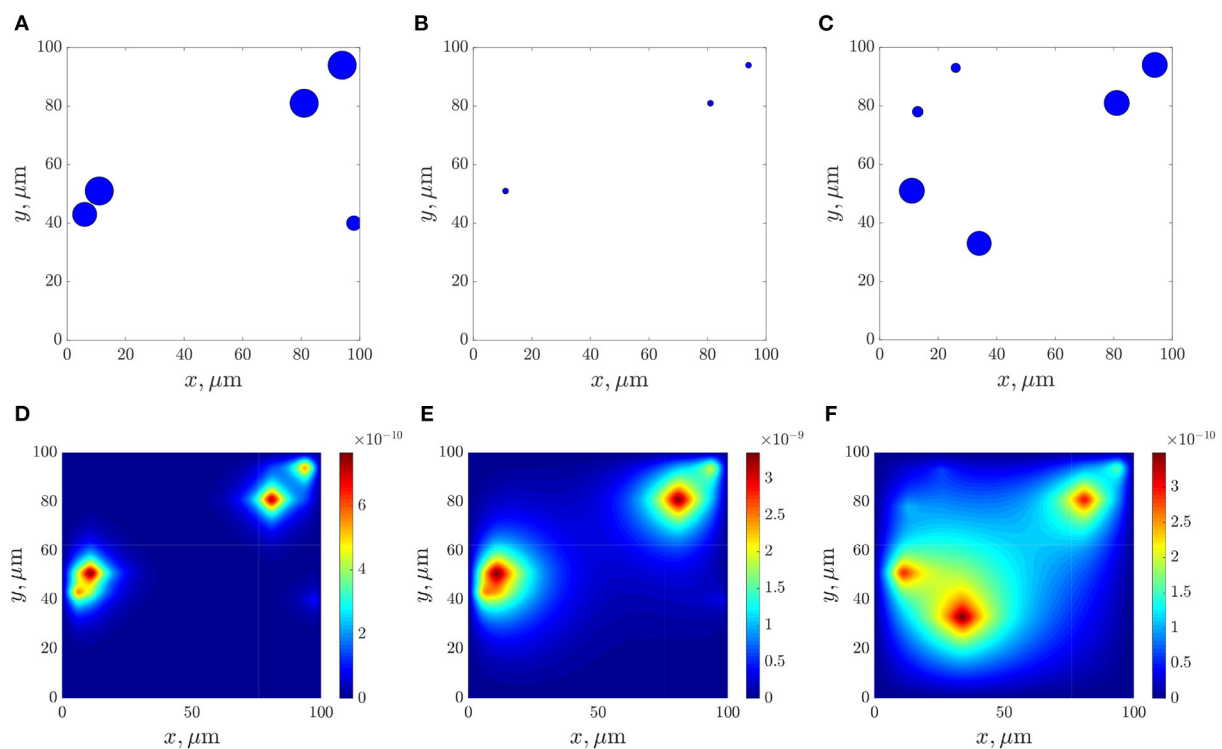


FIGURE 10
The dynamics of bacterial population (A–C), and the space distributions of the AHL concentration—(D–F), calculated at the corresponding moments 5, 12, and 100 h.

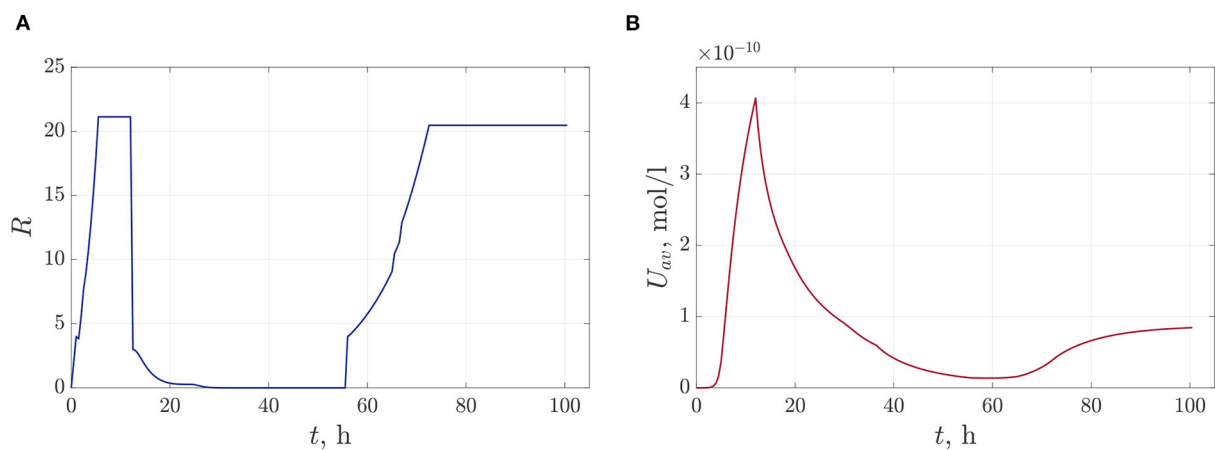


FIGURE 11
The time dependence of the total linear size of bacterial colonies—(A) and the dynamics of the average value of the AHL concentration—(B).

$2 \cdot 10^{-11}$ to $8 \cdot 10^{-11}$ mol/l at $t = t_{ob}$. It follows that the frequent use (within the considered range) of antibiotics does not confer treatment benefits.

It should be pointed out that we simulate the effect of a powerful antibiotic action in a simplified situation, excluding the

growth of the population after treatment. However, as known, pathogenic species of the *P. genus* exhibit resistant behavior [22], i.e., capable of continuing their vital activity under antibiotic treatment. Obviously, the intervals of antibiotic exposure should not exceed the duration of the antibiotic action (in our case, it

is about 16 h), otherwise the surviving population will strive to restore equilibrium amount.

Figures 10A–C show frames of evolution of a typical bacterial population growing in colonies under triple antibiotic treatment 12 h apart (12, 24, 36 h, respectively). In this computational experiment, we assume that the bacterial population can continue to grow after antibiotic action (for example, after 55 h), but more slowly than in the initial case (the parameter of the logistic growth $r = 0.1$). Also, new bacterial colonies can appear during simulations. The space distributions of the AHL concentration are presented in Figures 10D–F computed at fixed moments: at the beginning of bacterial evolution—5 h, at the beginning of antibiotic action—12 h, and at the final time 100 h. Figure 11 gives a detailed visualization of time-dependence of the total linear size of the population and the average value of the AHL concentration. Our data indicate that after 17 h, the population restored its numbers. At the same time, the “communication level” of the bacterial population is only 20% of the equilibrium value in the absence of inhibition due to antibiotics. This effect is caused by a long relaxation time of the AHL concentration and an additional increase in the Lactonase concentration.

4. Conclusions

In summary, we have shown that the developed hybrid mathematical model allows to examine the behavior of key chemical compounds characterizing bacterial communication during antibiotic treatment. We have proposed suitable computational techniques to conduct time-dependent simulations of bacterial quorum sensing. The computational procedure for the model implementation includes the following points: First, we performed the Monte-Carlo simulation of bacterial maturation and population growth. Then, to estimate chemical compounds, the system of PDEs was numerically solved with the finite difference iterative scheme. Finally, we conducted simulations of the degradation of a bacterial population due to antibiotic action, taking into account the time-dependent decrease in the number of bacteria.

The continued *in silico* studies of bacterial cooperative behavior hold great promise in microbiology. Computational experiments based on the mathematical model of Quorum sensing in pathogenic bacteria provide a set of tools for building a new level of understanding of the mechanisms of response formation to external influences. The obtained data suggest that even a small bacterial population maintains an essential quorum, which will be able to restore the equilibrium population size provided the nutrient medium and in the absence of further external inhibitors (or, for

example, a weak immune system). The big advantage of the presented approach is that it allows for a quick overview and estimate of the system behavior, what was our purpose here. Additional studies are required to modify the mathematical model, e.g., by introducing space-time distributions of bacterial biomass and antibiotic concentration, providing more details and accuracy, but requiring more computational effort and more detailed knowledge about the biological system. This general approach can be useful for further studies of optimal modes of antibiotic and other treatments.

Data availability statement

The original contributions presented in the study are included in the article/supplementary material, further inquiries can be directed to the corresponding author/s.

Author contributions

CK and AM designed the conceptualization, performed the numerical simulations, validation, analysis of results, and wrote the original manuscript. AM derived computational scheme and designed the computer program. All authors contributed to the article and approved the submitted version.

Funding

This research was supported by TUM Publishing Fund and also partially supported by the Ministry of Science and Higher Education of the Russian Federation (project no. 122082400001-8, AM).

Conflict of interest

The authors declare that the research was conducted in the absence of any commercial or financial relationships that could be construed as a potential conflict of interest.

Publisher's note

All claims expressed in this article are solely those of the authors and do not necessarily represent those of their affiliated organizations, or those of the publisher, the editors and the reviewers. Any product that may be evaluated in this article, or claim that may be made by its manufacturer, is not guaranteed or endorsed by the publisher.

References

1. Fuqua C, Greenberg EP. Listening on bacteria: acyl-homoserine lactone signalling. *Nat Rev Mol Cell Biol.* (2002) 3:685–95. doi: 10.1038/nrm907
2. Williams P, Winzer K, Chan W, Camara M. Look who's talking: communication and quorum sensing in the bacterial world. *Philos Trans R Soc B.* (2007) 362:1119–34. doi: 10.1098/rstb.2007.2039
3. Lin LH, Wang JH, Yo JL, Li YY, Liu GX. Effects of Allacin on the formation of *Pseudomonas aeruginosa* biofilm and the production of Quorum-sensing controlled virulence factors. *Pol J Microbiol.* (2013) 62:243–51. doi: 10.33073/pjm-2013-032
4. Whitehead NA, Barnard AML, Slater H, Simpson NJL, Salmond GPC. Quorum-sensing in Gram-negative bacteria. *FEMS Microbiol Rev.* (2001) 25:365–404. doi: 10.1111/j.1574-6976.2001.tb00583.x
5. Fekete A, Kuttler C, Rothballer M, Hense BA, Fischer D, Buddrus-Schiemann K, et al. Dynamic regulation of N-acyl-homoserine lactone production and degradation in *Pseudomonas putida* IsoF. *FEMS Microbiol Ecol.* (2010) 72:22–34. doi: 10.1111/j.1574-6941.2009.00828.x
6. Buddrus-Schiemann K, Rieger M, Muhlbauer M, Barbarossa MV, Kuttler C, Hense BA, et al. Analysis of N-acyl-homoserine lactone dynamics in continuous cultures of *Pseudomonas putida* IsoF by use of ELISA and UHPLC/qTOF-MS-derived measurements and mathematical models. *Anal Bioanal Chem.* (2014) 406:6373–83. doi: 10.1007/s00216-014-8063-6
7. Kuttler C, Maslovskaya A. Computer simulation of communication in bacterial populations under external impact of signal-degrading enzymes. *Proc CEUR Worksh Proc.* (2020) 2783:163–79.
8. Kuttler C. Reaction-diffusion equations and their application on bacterial communication. In: Rao ASRS, Pyne S, Rao CR, editors. *Handbook of Statistics.* Amsterdam: Elsevier (2017). p. 55–91. doi: 10.1016/bs.host.2017.07.003
9. Lions JL, Magenes E. *Non-Homogeneous Boundary Value Problems and Applications.* Berlin; Heidelberg; New York, NY: Springer-Verlag (1972). doi: 10.1007/978-3-642-65161-8
10. Evans LC. *Partial Differential Equations.* Providence, RI: American Mathematical Society (2010).
11. Samarskii AA. *The Theory of Difference Schemes.* Boca Raton, FL: CRC Press (2001). doi: 10.1201/9780203908518
12. Glowinski R, Osher SJ, Yin W. *Splitting Methods in Communication, Imaging, Science, and Engineering.* Cham: Springer International Publishing (2016). doi: 10.1007/978-3-319-41589-5
13. Kuttler C, Maslovskaya A. Hybrid stochastic fractional-based approach to modeling bacterial quorum sensing. *Appl Math Model.* (2021) 93:360–75. doi: 10.1016/j.apm.2020.12.019
14. Kuttler C, Maslovskaya A, Moroz L. Numerical simulation of time-fractional diffusion-wave processes applied to communication in bacterial populations. In: *Proceedings of the IEEE Days on Diffraction.* St. Petersburg: IEEE (2021) p. 114–9. doi: 10.1109/DD52349.2021.9598648
15. Rakhmawatie DD, Mustofa M, Sholikhah EN. Effects of ciprofloxacin concentrations on the resistance of uropathogen *Escherichia coli*: in vitro kinetics and dynamics simulation model. *J Med Sci.* (2020) 52:191–204. doi: 10.19106/JMedSci005203202001
16. Cárcamo-Oyarce G, Lumjiaktase P, Kümmerli R, Eberl L. Quorum sensing triggers the stochastic escape of individual cells from *Pseudomonas putida* biofilms. *Nat Commun.* (2015) 6:5945. doi: 10.1038/ncomms6945
17. Weimer A, Kohlstedt M, Volke DC, Nikel PI, Wittmann C. Industrial biotechnology of *Pseudomonas putida*: advances and prospects. *Appl Microbiol Biotechnol.* (2020) 104:7745–66. doi: 10.1007/s00253-020-10811-9
18. Fernández M, Porcel M, de la Torre J, Molina-Henares MA, Daddaoua A, Llamas MA, et al. Analysis of the pathogenic potential of nosocomial *Pseudomonas putida* strains. *Front Microbiol.* (2015) 6:871. doi: 10.3389/fmicb.2015.00871
19. Peter S, Oberhettinger P, Schuele L, Dinkelacker A, Vogel W, Dörfel D, et al. Genomic characterization of clinical and environmental *Pseudomonas putida* group strains and determination of their role in the transfer of antimicrobial resistance genes to *Pseudomonas aeruginosa*. *BMC Genomics.* (2017) 18:859. doi: 10.1186/s12864-017-4216-2
20. Shen N, Jiang M, Wei P. The kinetic study on the production of hydantoinase and n-carbamoylase by *Pseudomonas* JS-01. *J Nanjing Univ Chem Technol.* (2001) 23:36–9.
21. Ditmarsch D, Xavier JB. High-resolution time series of *Pseudomonas aeruginosa* gene expression and rhamnolipid secretion through growth curve synchronization. *BMC Microbiol.* (2011) 11:1409. doi: 10.1186/1471-2180-11-140
22. Žiemytė M, Carda-Diéguez M, Rodríguez-Díaz JC, Ventero MP, Mira A, Ferrer MD. Real-time monitoring of *Pseudomonas aeruginosa* biofilm growth dynamics and persister cells' eradication. *Emerg Microbes Infect.* (2021) 10:2062–75. doi: 10.1080/22221751.2021.1994355



OPEN ACCESS

EDITED BY

André H. Erhardt,
Weierstrass Institute for Applied Analysis
and Stochastics (LG), Germany

REVIEWED BY

Omar Abu Arqub,
Al-Balqa Applied University, Jordan
Harsha Vaddireddy,
Oklahoma State University Stillwater,
United States, in collaboration with
reviewer SP

*CORRESPONDENCE

Fukang Yin,
yinfukang@nudt.edu.cn

SPECIALTY SECTION

This article was submitted to Statistical
and Computational Physics,
a section of the journal
Frontiers in Physics

RECEIVED 17 June 2022

ACCEPTED 01 September 2022

PUBLISHED 30 September 2022

CITATION

Xiao C, Zhu X, Yin F, Cao X, Peng K and
Nie J (2022), Fourier filter-based
physics- information convolutional
recurrent network for 2D
incompressible flow.
Front. Phys. 10:971722.
doi: 10.3389/fphy.2022.971722

COPYRIGHT

© 2022 Xiao, Zhu, Yin, Cao, Peng and
Nie. This is an open-access article
distributed under the terms of the
[Creative Commons Attribution License](https://creativecommons.org/licenses/by/4.0/)
(CC BY). The use, distribution or
reproduction in other forums is
permitted, provided the original
author(s) and the copyright owner(s) are
credited and that the original
publication in this journal is cited, in
accordance with accepted academic
practice. No use, distribution or
reproduction is permitted which does
not comply with these terms.

Fourier filter-based physics-information convolutional recurrent network for 2D incompressible flow

Chaohao Xiao¹, Xiaoqian Zhu¹, Fukang Yin^{1*}, Xiaoqun Cao¹,
Kecheng Peng^{1,2} and Jun Nie³

¹College of Meteorology and Oceanography, National University of Defense Technology, Changsha, China, ²College of Computer, National University of Defense Technology, Changsha, China, ³PLA, Beijing, China

Physics-informed convolutional recurrent network (PhyCRNet) can solve partial differential equations without labeled data by encoding physics constraints into the loss function. However, the finite-difference filter makes the solution of 2D incompressible flow challenging. Hence, this paper proposes a Fourier filter-based physics-informed convolution recurrent network (named Fourier filter-based PhyCRNet), which replaces the finite-difference filter in PhyCRNet with the Fourier filter to solve the 2D incompressible flow problem. The suggested network improves the accuracy of the partial derivatives, solves the inverse Laplacian operator, and has similar generalization ability due to inheriting the framework of PhyCRNet. Four examples, including the 2D viscous Burger, FitzHugh–Nagumo RD, vorticity and the two-dimensional Navier–Stokes (N-S) equations, validate the correctness and reliability of the proposed Fourier filter-based PhyCRNet.

KEYWORDS

fourier filter, convolutional recurrent network, 2D incompressible flow, inverse laplacian operator, physics-informed

1 Introduction

Partial differential equations (PDEs), play a crucial role in modeling a wide variety of problems in applied mathematics, physics, biology, chemistry, and engineering technology and thus are widely used to express and interpret the laws involved [1,2]. Although many phenomena can be analyzed and solved through PDEs modeling, such as weather forecasting [3], communication technology [4] and electromagnetic induction [5], in many cases, the analytical solution of PDEs is unavailable, and researchers solve PDEs by numerical methods, i.e., finite-difference, finite volume, and finite element methods [6]. Although some classic numerical methods achieve very high accuracy, the balance between computational cost and accuracy is still a vital issue.

Recently, the rapid development and application of deep learning have provided an alternative solution to PDEs of positive and inverse problems. Theoretically, the universal

approximation theorem proves that deep neural networks can simulate arbitrarily complex functions [7]. Due to the development of deep learning and the improvement of computing power, several studies have been proposed utilizing deep learning to solve PDEs [8–15]. The latest related research can be mainly divided into discovering PDEs from data and solving PDEs. The pioneering work in inverse problem research is the sparse regression method introduced by Rudy et al. [8]. On this basis, Long et al. [11] proposed an improved neural network, the PDE-Net, to obtain the PDE coefficients and solve PDE. The Physics-informed Neural Network (PINN) proposed by Rassi et al. [16] introduced an innovative approach to encoding physical constraints into loss functions, with many improved PINN versions being used to solve problems in different scenarios [17–21]. Other researchers propose operator schemes to solve PDEs. For example, Lu et al. [22] introduced a neural network of DeepONets for learning nonlinear operators, while Li et al. [23] proposed the Fourier neural operator (FNO) utilizing the Fourier transform, which afforded a much faster solution rate and a stronger generalization ability than other neural networks. Recent research fused neural operators and PINNs to improve the interpretability and speed up the network's fitting [24,25]. Nevertheless, such a strategy requires quantitative and high-quality training data.

Recent studies have revealed that PDEs can be solved by training the network constraints, such as physical constraints [26,27], without labeled data. However, due to limitations of the network training process, the time extrapolation results are often unsatisfactory. Therefore, researchers have introduced time series prediction deep learning networks in the study to solve PDEs [28–30] with the help of classical numerical methods to solve time-dependent PDEs [31–33]. For instance, the physics-informed based convolutional recurrent network (PhyCRNet) introduced by Ren et al. [30] considers all aspects. Indeed, it starts from the initial conditions without any labeled data, extracts spatial features using a convolutional neural network (CNN) [34], utilizes a convolutional long and short term memory network (ConvLSTM) [35] to learn its evolution, and finally encodes the output values into the loss function through the finite-difference filter for physical constraints. Hence, PhyCRNet solves PDEs using the equations as constraints and supervises the network's convergence, without high-quality training data.

However, the 2D incompressible flow refers to a flow in which the density remains constant in two-dimensional fluid parcel, which is characterized by stream function and the associated velocity fields and vorticity, as defined by the stream function's partial derivatives. Typical numerical methods use pseudo-spectral methods to balance the solution rate and accuracy by using the vorticity as the initial field, calculating the partial derivatives in the spectral space, and solving the equations using time iterations [36–38].

Nevertheless, calculating the stream function from the vorticity involves calculating the inverse Laplace operator, which is difficult to solve by the finite-difference method. Overall, PhyCRNet has the following disadvantages in solving the 2D incompressible flow problem.

1. The differential accuracy of the finite-difference is not high, resulting in an inaccurate calculation loss function and affecting the convergence speed and accuracy of the solution.
2. Calculating the inverse Laplace operator is challenging when using the finite-difference filter and in the case of calculating the stream function.
3. Finite-difference differential calculation accuracy is related to the grid spacing and the number of cells, and the computational overhead is higher in high-resolution calculations.

Based on these shortcomings, it is necessary to improve the PhyCRNet.

Hence, this paper employs the discrete Fourier transform [39] in the pseudo-spectral method [40] to replace the finite-difference filter in the PhyCRNet and optimize PhyCRNet. The main contribution of this method is solving the problem of efficient solution of the differential operator and the inverse Laplace operator during the vorticity calculation of the stream function in PhyCRNet. In the Fourier filter-based PhyCRNet, we first transform the network's output into the Fourier space for partial differentiation and calculate the Laplace and the inverse operators, followed by the inverse Fourier transform. Finally, the physical constraints are achieved by encoding and thus effectively solving PhyCRNet's problem. This improved network has a faster solution than the finite-difference method in large-scale calculations [23].

The remainder of the paper is organized as follows: **Section 2** introduces the Fourier filter-based PhyCRNet, while **Section 3** provides two examples of two-dimensional viscous Burger's equation and FitzHugh–Nagumo RD equations to verify the performance of the Fourier filter-based PhyCRNet in solving some basic PDEs. Then, two examples, including the vorticity equation and the 2D incompressible Navier-Stokes equation, demonstrate the advantages of the Fourier filter-based PhyCRNet, finally, **Section 5** concludes this work.

2 Methodology

This section introduces the proposed Fourier filter-based PhyCRNet, whose structure describes the PDEs to be solved and then introduces the related algorithms and network frameworks. Finally, the related content of the improved PhyCRNet (namely, Fourier filter-based PhyCRNet) is introduced.

2.1 Problem statement

Our proposed method focuses on the time series prediction and solution of spatiotemporal PDEs. Numerical experimental equations such as Burger's equation are widely used to verify the method and have the following general form [41,42].

$$u_t + \mathcal{F}[u; \lambda] = 0, x \in \Omega, t \in [0, T] \quad (1)$$

where $u(t, x)$ represents the possible solutions found in the time range $t \in [0, T]$ and the physical space $x \in \Omega$ and $\mathcal{F}[*; \lambda]$ is the nonlinear operator parameterized with λ . Also, for the initial and boundary conditions, there are characterizations of the form $I(u, \mathcal{F}[*; \lambda]; \text{with } t = 0, x \in \Omega) = 0$ and $(u, \mathcal{F}[*; \lambda]; t \in [0, T], x \in \partial\Omega) = 0$, where $x \in \partial\Omega$ represents the boundary interval. The boundary conditions such as Dirichlet and Neumann have not been discussed in this work for the time being.

2.2 PhyCRNet

PhyCRNet proposed by Ren et al adopts ConvLSTM to learn temporal evolution and constructs the network loss function with PDE constraints. It propagates information into future times and solves equations without labeled data as PINN. It has stable extrapolability after training which makes it better than other deep learning methods. For more detailed work on PhyCRNet, refer to the work [30].

2.3 The discrete fourier transform

The discrete Fourier transform (DFT), a fundamental transformation in digital signal processing, is widely used in convolution, image processing, and frequency analysis [43–45]. Its implementation is similar to the continuous Fourier transform, which for a given certain sequence of real numbers $\{x_n, n = 0, 1, 2, \dots, N-1\}$, it is represented as a sequence of complex numbers $\{X_n, n = 0, 1, 2, \dots, N-1\}$ utilizing the discrete Fourier transform. DFT is defined as follows:

$$X_k = \sum_{n=0}^{N-1} x_n e^{-2\pi i \frac{nk}{N}}, k = 0, 1, \dots, N-1 \quad (2)$$

where $e^{-2\pi i \frac{nk}{N}} = \cos(2\pi \frac{nk}{N}) + i \sin(2\pi \frac{nk}{N})$. At the same time, the original discrete function can also be reconstructed by the inverse discrete Fourier transform (IDFT), defined as:

$$x_n = \frac{1}{N} \sum_{k=0}^{N-1} X_k e^{2\pi i \frac{nk}{N}}, k = 0, 1, \dots, N-1 \quad (3)$$

By considering the 2-dimensional function $f(x, y)$ as an example, according to Eqs 2, 3:

$$f(x, y) \xrightarrow{DFT} DFT \hat{F}(x, y); \hat{F}(x, y) \xrightarrow{IDFT} IDFT f(x, y) \quad (4)$$

For the function after the discrete Fourier transform, its corresponding derivative can be quickly obtained in the Fourier space.

$$\begin{aligned} \frac{\partial f}{\partial x} &\xleftarrow{IDFT} 2\pi i \frac{n}{N} \hat{F}(x, y); \frac{\partial f}{\partial y} \xleftarrow{IDFT} 2\pi j \frac{n}{N} \hat{F}(x, y) \\ n &= -\frac{N}{2}, \dots, \frac{N}{2} - 1 \end{aligned} \quad (5)$$

Different from the finite difference filter in PhyCRNet to solve the derivative, the spatial derivative is calculated as the product of spectrum and ik in the wave number domain after the discrete Fourier transforms the function. So, the Fourier filter proposed in this paper is used to calculate spatial derivatives of loss function by discrete Fourier transform. This strategy is more adaptable to solving many PDEs types.

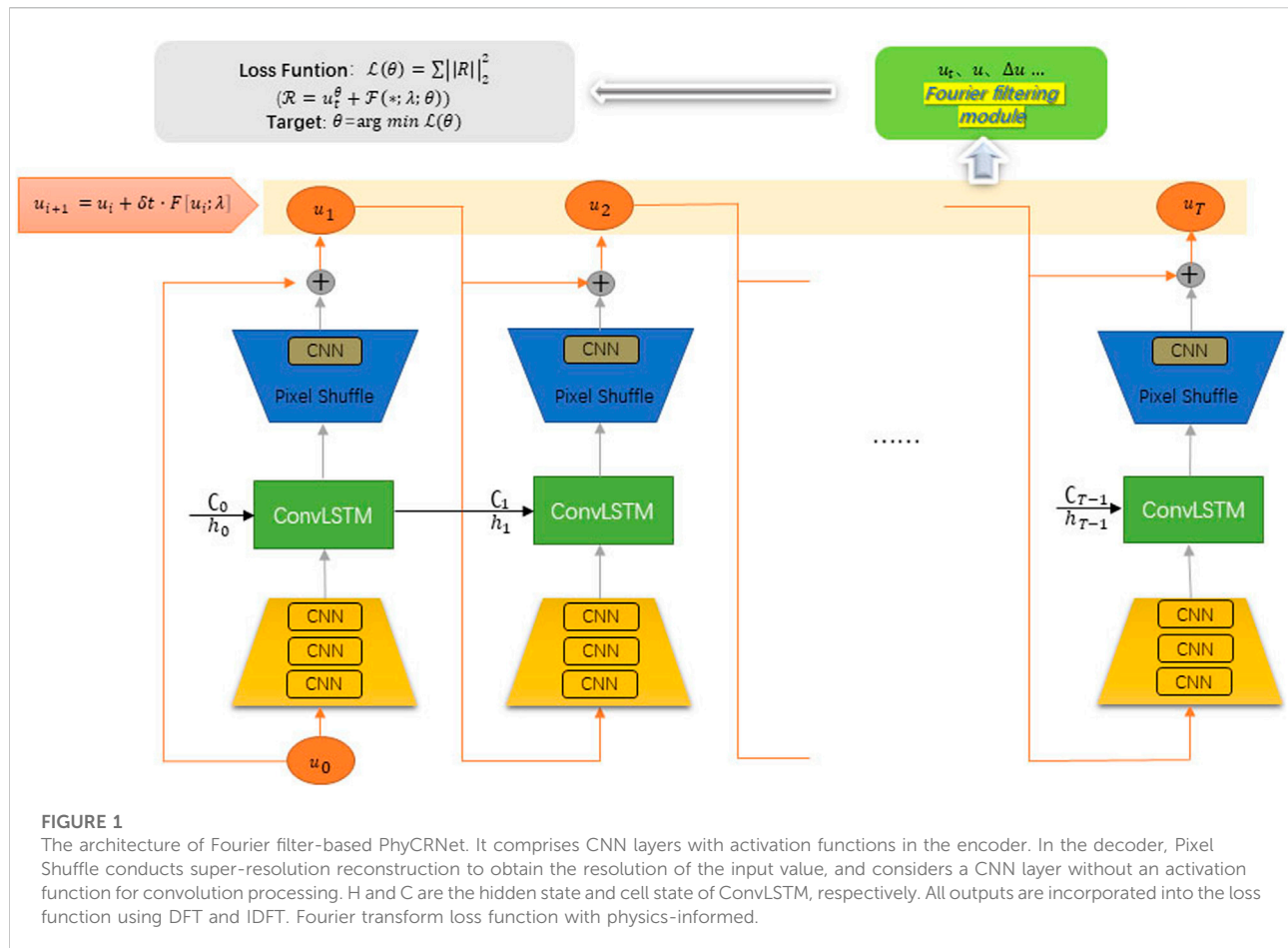
Moreover, the pseudo-spectral method has advantages in solving the 2-dimensional incompressible flow equation [46]. Indeed, given vorticity (ζ) and the stream function (ψ) at time t , this method first updates ζ forward at time $t + \delta t$. Then the Poisson equation with periodic boundary is considered as a relationship between the two to update ψ forward at time $t + \delta t$. The Poisson equation involves the inverse Laplace operator calculation, which is trivial to implement by the discrete Fourier transform when its mean state is known [47]. This is why the discrete Fourier transform is superior to the finite-difference. Assuming that the mean state is one, the inverse Laplace operator is computed as follows:

$$\begin{aligned} K &= \begin{cases} \left(2\pi i \frac{n}{N}\right)^2 + \left(2\pi j \frac{n}{N}\right)^2 & n = -\frac{N}{2}, \dots, -1, 1, \dots, \frac{N}{2} - 1 \\ 1 & n = 0 \end{cases} \\ &f \xleftarrow{IDFT} \Delta \hat{F}(x, y) / K \end{aligned} \quad (6)$$

The improvement proposed in this work is to replace the finite-difference filter in the PhyCRNet with the discrete Fourier transform, and then perform the PDE residual connection to integrate the physical constraints into the neural network (further details are presented in Section 2.4). The resulting network has two advantages. First, it overcomes the inability of PhyCRNet to efficiently solve the inverse Laplace operator. Indeed, the Fourier filter-based PhyCRNet can solve PDEs similar to describing 2D incompressible flows, enhancing the network's generalization ability. Second, the Fourier transform has higher accuracy than the finite-difference method when calculating high-order partial derivatives, and its computational efficiency is faster in large-scale scientific computing.

2.4 Fourier filter-based PhyCRNet

This section introduces the structure of proposed network. As illustrated in Figure 1, the network consists of the encoding



module, time series module, decoding module, input and output connection module and Fourier filtering module. Firstly, the encoding module is used to extract spatial features through CNN and then output to the time series module. Secondly, the time series module captures the time dependence of spatial features and establishes time series relationships. In this way, the network generates the predicted values only under the initial condition. Then, the decoding module reconstructs the discrete output of the time series module by the sub-pixel convolutional layer (pixel shuffle) to achieve the same resolution as the input. In addition, a convolution layer without activation function is added at the end of the module. Finally, the input-output connection module adopts a forward Eulerian method to establish the relationship of u_{i+1} and u_i . The Fourier filtering module calculates the spatial derivative involved in the computation of loss function. The Fourier filter calculates the spatial partial derivatives by transforming the input to the spectral space, which turns into a simple multiplication in the frequency domain compared with the finite difference. For more details, please refer to 2.3 for the idea of Fourier filtering and 2.5 for loss construction.

2.5 Fourier transform loss function with physics-informed

Given that the Fourier filter-based PhyCRNet is trained without labeled data, the loss function construction controlled by the PDEs is significant and must preserve high accuracy and efficiency. The loss function accuracy depends on the partial derivatives, which unlike the chained derivatives of Physics-informed Neural Network (PINN) [16], the Fourier filter-based PhyCRNet uses the Fourier filter formed by the discrete Fourier transform (as introduced in Section 2.3) to calculate the partial derivatives in the PDEs. Hence, we calculate $F[u; \lambda]$ in Eq. 1 and construct the PDEs residual connection to integrate the physical constraints into the loss function of the neural network. Then the PDEs residual connection is formed and the physical constraints are integrated into the loss function in the neural network. As an example, solving the 2-dimensional PDEs, $f(x, y, t; \theta)$ can be defined according to the left side of Eq. 1:

$$f(x, y, t; \theta) = u_t(x, y, t; \theta) + \mathcal{F}[u(x, y, t; \theta); \lambda] \quad (7)$$

where $u_t(x, y, t; \theta)$ is obtained by traditional numerical methods. The shared network parameter θ is obtained during training by using the minimization loss function $\mathcal{L}(\theta)$ in Eqs 8, 9, defined as the sum of squares of the discrete values of $f(x, y, t; \theta)$ over all spatial and temporal periods

$$\mathcal{L}(\theta) = \sum_{i=1}^n \sum_{j=1}^m \sum_{k=1}^T \|f(x_i, y_j, t_k; \theta)\|_2^2 \quad (8)$$

$$\theta = \arg \min \mathcal{L}(\theta) \quad (9)$$

where $\| \cdot \|_2$ denotes the ℓ_2 norm.

3 Numerical experiments

This section validates the proposed Fourier filter-based PhyCRNet by utilizing nonlinear PDEs and two PDEs for describing the 2D incompressible fluid flow. The trial involving two nonlinear PDE (2D viscous Burger's equations and FitzHugh–Nagumo RD equations) verifies that the Fourier filter-based PhyCRNet possesses the capabilities of PhyCRNet. And two 2D incompressible fluid flow PDEs test the feasibility and advantages of Fourier filter-based PhyCRNet. All numerical implementations and constructed networks are coded using Pytorch [48], and all models are trained on an NVIDIA GeForce GTX 3090 with 24 GB of memory.

3.1 Network parameters

The main difference between Fourier filter-based physics-informed convolutional recurrent network (PhyCRNet) and PhyCRNet is the calculation of the partial derivatives, while the other remaining structure is the same. In the encoding part, three convolutional layers are used for feature extraction, with 8, 32, 128 units respectively using a convolutional kernel (4×4) and a stride of 2 and ReLU function as the activation function. In the decoding part, for the standard connection between the input and output, sub-pixel convolution is performed through pixel shuffle to complete super-resolution reconstruction. Then a convolutional layer is added, using a convolutional kernel (5×5) and a stride of one to ensure constant resolution without an activation function. The convolution operation in ConvLSTM involves a convolution kernel (3×3) and a stride of 1. At the same time, the training of both networks are trained using the stochastic gradient descent Adam optimizer [49].

3.2 Evaluation metrics

Three evaluation metrics, mean absolute error (MAE), mean absolute percentage error (MAPE), and root mean square error

(RMSE), are widely used in the evaluation of deep learning networks. In order to evaluate the solution accuracy of the network in this paper, an accumulative root mean square error (a-RMSE) is defined and the same evaluation metric is used for training and extrapolation.

$$\epsilon_\tau = \sqrt{\frac{1}{N_t} \sum_{k=1}^{N_t} \frac{\|u(x_{i,j}, t_k) - u(x_{i,j}, \theta, t_k)\|_2^2}{mn}} \quad (10)$$

where N_t represents the number of time steps in the period $[0, \tau]$, and ϵ_τ represents the full-field a-RMSE. m and n are the resolutions in the spatial region, while $u(x_{i,j}, t_k)$ and $u(x_{i,j}, \theta, t_k)$ represent the reference solution and the prediction, respectively.

3.3 2D viscous Burger's equations

Considering the following 2D viscous Burger's equations with periodic conditions:

$$\begin{aligned} u_t + u(x, y, t) \nabla u(x, y, t) &= \nu \Delta u(x, y, t), x, y \in [0, 1], t \in (0, T] \\ u(x, y, 0) &= u_0(x, y, 0), x, y \in [0, 1] \end{aligned} \quad (11)$$

where u is the fluid's velocity (u and v), ν is the viscosity coefficient, Δ is the Laplace operator, ∇ is the gradient operator, and $u_0(x, y, 0)$ denotes the initial condition. Here, we set $\nu = 0.005$, and the spatial region is $\Omega \in [0, 1]^2$ with a resolution of $[128 \times 128]$.

The initial condition $u_0(x, y, 0)$ is generated in a Gaussian random field, according to $u_0 \sim \mu$ where $\mu \sim \mathcal{M}(0, 625(-\Delta + 25I)^{-2})$. The experimental reference value is obtained by a pseudo-spectral method with a fourth-order Runge-Kutta method ($\delta t = 1 \times 10^{-4}$). PhyCRNet and the Fourier filter-based PhyCRNet both are trained with a relatively large time step ($\delta t = 0.002$) for iterative calculation. In the finite-difference filter module of PhyCRNet, Eq. 12 is used to calculate Δ , and the following difference filter Eq. 13 is used to calculate ∇ :

$$D_{lap} = \begin{bmatrix} 0 & 0 & -1 & 0 & 0 \\ 0 & 0 & 16 & 0 & 0 \\ -1 & 16 & -60 & 16 & -1 \\ 0 & 0 & 16 & 0 & 0 \\ 0 & 0 & -1 & 0 & 0 \end{bmatrix} \times \frac{1}{12(\delta x)^2} \quad (12)$$

$$D_1 = \begin{bmatrix} 0 & 0 & 1 & 0 & 0 \\ 0 & 0 & -8 & 0 & 0 \\ 1 & -8 & 0 & 8 & -1 \\ 0 & 0 & 8 & 0 & 0 \\ 0 & 0 & -1 & 0 & 0 \end{bmatrix} \times \frac{1}{12\delta x} \quad (13)$$

$$D_t = [-1, 0, 1] \times \frac{1}{2\delta t} \quad (14)$$

However, in Fourier filter-based PhyCRNet, Eq. 5 is used to calculate ∇ , and Δ is calculated by a method similar to Eq. 6, while u_t

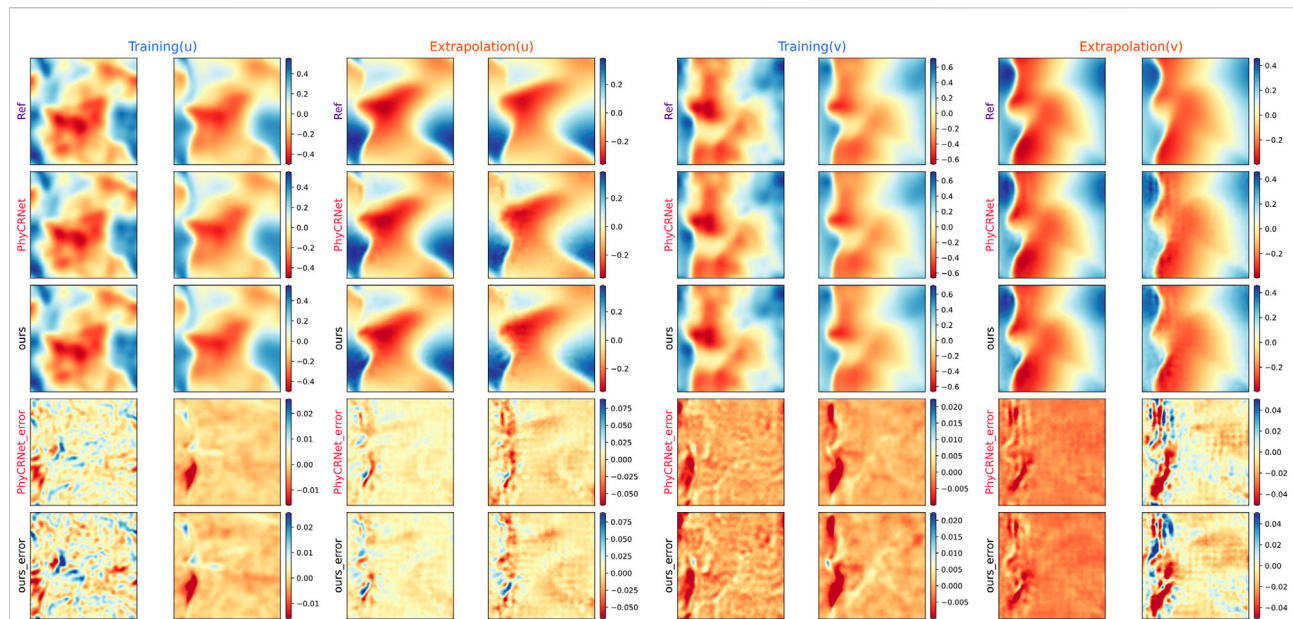


FIGURE 2

The results of Fourier filter-based PhyCRNet and PhyCRNet network solving the two-dimensional viscous Burger's equation. Four representative moments are selected for comparison as training ($t = 0.1, 0.3$ s) and extrapolation ($t = 0.6, 0.8$ s), and the errors across the interval are compared. The subfigures from top to bottom are reference solutions, predictions by PhyCRNet and ours, and errors of PhyCRNet and ours, respectively.

is calculated by the difference filter in Eq. 14 uniformly. Except for the calculation of spatial derivatives, all parameters are the same as Ref. [30]. The learning rate starts at 6×10^{-4} and decays to 99% every 50 epochs. During the period $[0, 0.4]$, PhyCRNet and Fourier filter-based PhyCRNet are trained separately to obtain the numerical solution of the two-dimensional viscous Burger's equation for 200 time steps. Then, based on the trained model, the solution for the last 200 time steps (within time $[0.4, 0.8]$) is predicted to verify the model's extrapolation performance. According to the training method mentioned in [30], we pretrain the model from 100 and then 200 time steps, then extrapolate for another 200 time steps. The relevant codes and data come from open source [30].

Figure 2 depicts four snapshots of u taken from the training phase ($t = 0.1, 0.3$ s) and the extrapolation phase ($t = 0.6, 0.8$ s), respectively. Each snapshot from top to bottom are reference solutions, predictions by PhyCRNet and ours, and errors of PhyCRNet and ours, respectively. From Figure 2, it can be found that the results of both networks are very agreement with the reference in training and extrapolation. It verifies that the Fourier filter-based PhyCRNet has the same capability to solve basic PDEs as PhyCRNet.

3.4 FitzHugh–Nagumo RD equations

Considering the following the FitzHugh–Nagumo (FN) RD equations:

$$\begin{aligned} u_t &= \gamma_u \Delta u + u - u^3 - v + \alpha \\ v_t &= \gamma_v \Delta v + \beta(u - v) \end{aligned} \quad (15)$$

Same as 3.2, except for the Fourier filter, the network hyperparameters and equation coefficients are the same as [30]. u and v are two interactive components. γ_u , γ_v , α and β are equation coefficients by $\gamma_u = 1$, $\gamma_v = 100$, $\alpha = 0.01$ and $\beta = 0.25$, respectively. The IC is IC_FN1 and the reference solution is calculated using a method in 2D domain of $[0, 1.28]$ for 12,000 time steps ($\delta t = 2 \times 10^{-4}$) [30]. Two model are trained to solve this PDEs for 200 time steps with time duration of $[0, 1.2]$ and used to achieve the inference for $[1.2, 2.4]$, where $\delta t = 0.006$. The learning rate is set as 5×10^{-5} and decays by 0.5% every 50 epochs. Besides, we pretrain the model from 100 and then 200 time steps to extrapolate for another 200 time steps.

During training ($t = 0.6, 1.2$ s) and extrapolation ($t = 1.8, 2.4$ s) phases, the reference solutions, predicted solutions and error maps are shown in Figure 3. Although FitzHugh–Nagumo RD equations are more complex than Burger's equation, Fourier filter-based PhyCRNet and PhyCRNet have the same outstanding performance with the truth reference both in training and extrapolation. The error maps of two model exhibit near-perfect results, especially the extrapolation error of the field variable v is smaller. Considering that this PDEs has a more complex nonlinear form, the above two neural network methods capture the dynamic evolution process in the long-term,

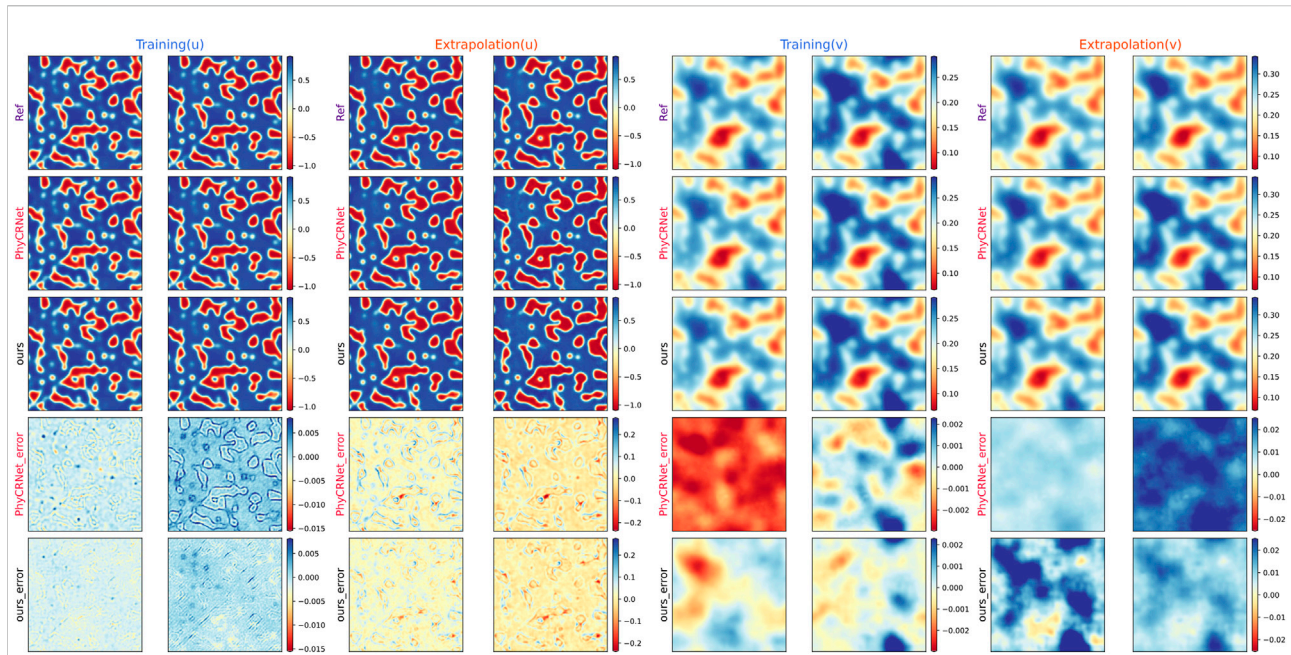


FIGURE 3

The results of Fourier filter-based PhyCRNet and PhyCRNet network solving the FitzHugh–Nagumo RD equations. Four representative moments are selected for comparison as training ($t = 0.6, 1.2$ s) and extrapolation ($t = 1.8, 2.4$ s), and the errors across the interval are compared. The subfigures from top to bottom are reference solutions, predictions by PhyCRNet and ours, and errors of PhyCRNet and ours, respectively.

which is different from the traditional forward Euler integration scheme.

3.5 Vorticity equation

This section focuses on the experimental validation of the Fourier filter-based PhyCRNet to solve the problems that the finite-difference filter of PhyCRNet cannot solve. Since the finite-difference filter cannot solve problems like inverse Laplace operators and there is a time iteration relationship between the input and output modules, the finite-difference method imposes the solution of some PDEs not to have a good propagation relationship between the input and output.

Consider a simple equation for describing 2D incompressible nonviscous fluid flow, namely the vorticity equation, which takes the following form

$$\begin{aligned} \frac{D\zeta}{Dt} &= \zeta_t - \psi_y \zeta_x + \psi_x \zeta_y = 0 \quad x, y \in [0, 1], t \in (0, T) \\ \zeta(x, y, t) &= v_x - u_y = \psi_{xx} + \psi_{yy} \quad x, y \in [0, 1], t \in (0, T) \\ u &= -\psi_y \quad v = \psi_x \quad u_x + v_y = 0 \quad x, y \in [0, 1] \end{aligned} \quad (16)$$

where $\zeta(x, y, t)$ represents the vorticity, the stream function $\psi(x, y, t)$ is used to describe the flow of the fluid, and u, v represent the velocity of the fluid in the x and y directions, respectively. The initial flow function for the equation is:

$$\psi(x, y, 0) = -0.25 \exp \left(\left[-4(x - 0.5)^2 - (y - 0.5)^2 / 2\sigma^2 \right] \right) \quad (17)$$

where $\sigma = 0.15$. When calculating the reference solution, we calculate ζ and ψ of the initial state from Eq. 17. On the 2D region $\Omega \in [0, 1]^2$ with a resolution of 256×256 , a pseudo-spectral method with a fourth-order Runge-Kutta time integral ($\delta t = 1 \times 10^{-4}$) is used to solve the vorticity equation. The solution reveals that the vorticity ζ moves forward first, then uses the method of Eq. 6 to update the stream function ψ , and then calculates u, v . Using vorticity as a bridge between the input-output connection modules of the network can more effectively capture the time evolution. During network training and extrapolation, the time step is chosen to be $\delta t = 0.001$. Fourier filter-based PhyCRNet is trained for 100 time steps within $[0, 0.1]$ to solve the vorticity equation, and the solution is extrapolated based on the training model for another 100 time steps within time $[0.1, 0.2]$. The learning rate starts at 5×10^{-3} and then decays to 99% every 100 epochs. The entire training time is 6.5 h.

Figures 4, 5 compare the vorticity and velocity fields predicted by Fourier filter-based PhyCRNet and the ground-truth reference values. Four representative time instances are selected for the training ($t = 0.025, 0.075$ s) and extrapolation ($t = 0.125, 0.175$ s) phases. From Figures 4, 5, we conclude the following. First, we can see in figures that both the vorticity

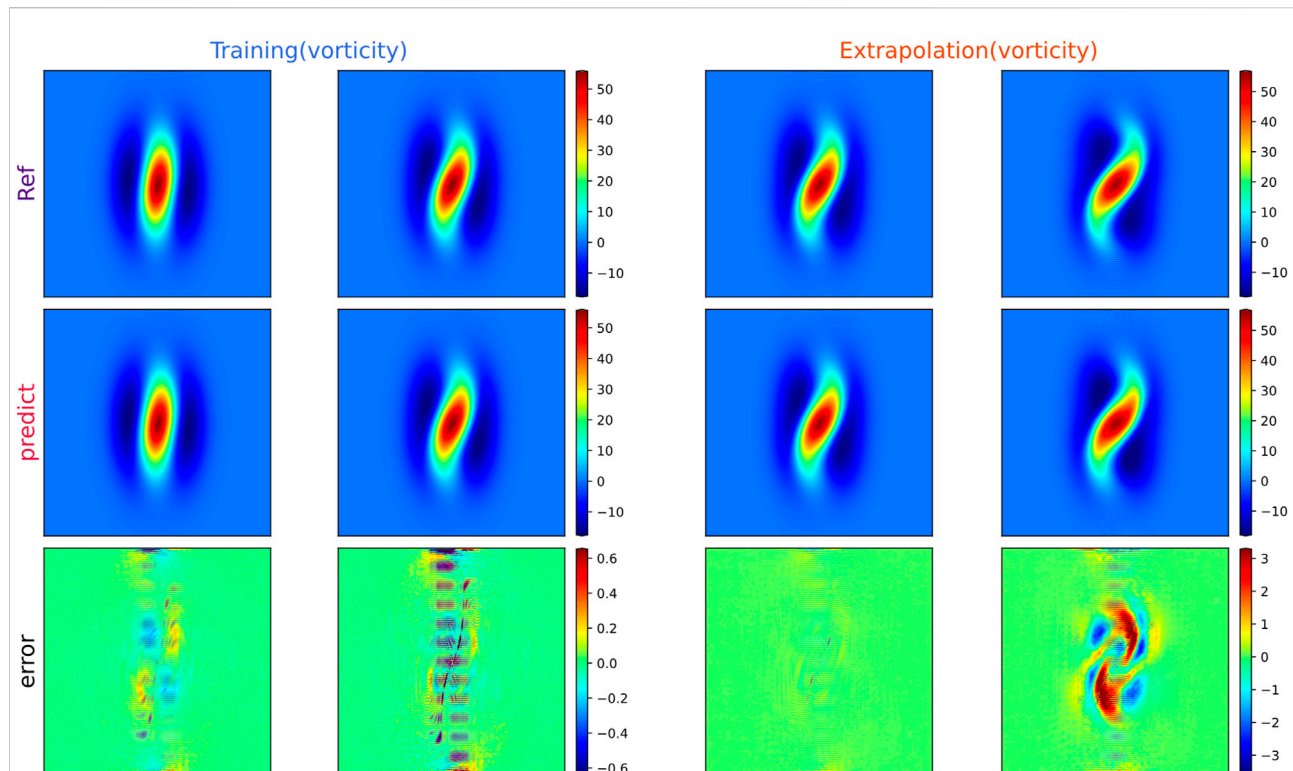


FIGURE 4

The vortex results for solving the vorticity equation with Fourier filter-based PhyCRNet. Four representative moments are selected for comparison, presenting the training ($t = 0.025, 0.075$ s) and extrapolation ($t = 0.125, 0.175$ s) maps, and compare the errors across the interval. From top to bottom are reference solutions, predictions and errors.

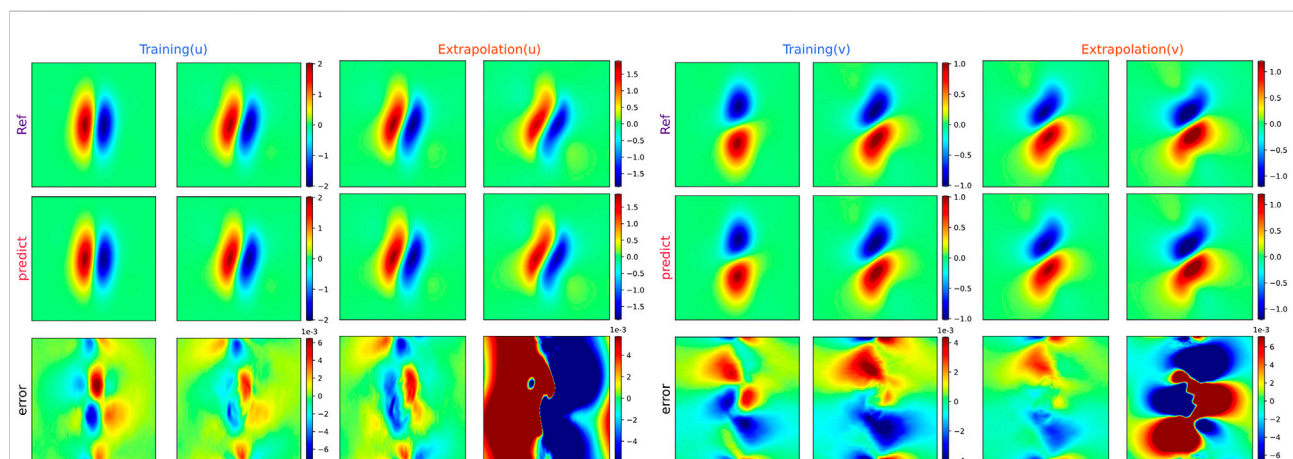


FIGURE 5

The velocity results for solving the vorticity equation with Fourier filter-based PhyCRNet. Four representative moments are selected for comparison, presenting the training ($t = 0.025, 0.075$ s) and extrapolation ($t = 0.125, 0.175$ s) maps, and compare the errors of the entire interval. From top to bottom are reference solutions, predictions and errors.

and velocity fields are close to the true reference during the training and extrapolation phases. Especially in the training phase, many errors are close to zero. As the extrapolation

period increases, the error also increases. However, when the extrapolation is at the same training time, the shape of the rotation is still the same. In the region with a larger value, the

error becomes larger, but the evolution trend of the solution can still be used as a reference. As the extrapolation time increases, the error also increases. This conclusion is also verified in Figure 8C according to the time-varying a-RMSE.

3.6 Two-dimensional Navier-Stokes equation

We consider the 2D Navier-Stokes equations for a incompressible viscous fluid in the form of vorticity on the unit torus [23]:

$$\begin{aligned} \partial_t \zeta(x, y, t) + u(x, y, t) \cdot \nabla \zeta(x, y, t) &= \nu \Delta \zeta(x, y, t) + f(x, y) \\ x, y &\in [0, 1], t \in (0, T] \nabla \cdot u(x, y, t) \\ &= 0, x, y \in [0, 1], t \in (0, T] \end{aligned} \quad (18)$$

The reference is all from the open source code of [23]. The initial condition $\zeta(x, y, 0)$ with periodic boundary condition are generated according to $\zeta(x, y, 0) \sim \mu$, where $\mu = N(0, 7^{3/2}(-\Delta + 25I)^{-2.5})$. We set $\nu = 1e-3$, and the forcing is kept fixed $f(x, y) = 0.1(\sin(2\pi(x+y)) + \cos(2\pi(x+y)))$. The equation is solved by a pseudo-spectral method, where first, the velocity field is calculated in the Fourier space. The vorticity field is then differentiated, and the nonlinear term is calculated in the physical space. In terms of time, we use the Crank-Nicolson scheme, and the time step is $\delta t = 1 \times 10^{-4}$. All data are generated on a grid with 256×256 resolution. The model is trained for 200 timesteps within the $[0, 2]$ period, and we extrapolate over $[2, 4]$, where $\delta t = 0.01$. The entire training time process lasts 12.5 h.

The vorticity and velocity field predicted by the Fourier filter-based PhyCRNet and the ground-truth are illustrated in Figures 6, 7, respectively. The figures clearly show that the velocity and vorticity fields agree with the ground truth during the training phase. According to the error distribution, the error is minimal and, on many occasions, close to zero. In the extrapolation stage, although the error is increased compared to the training phase, the evolution of the vorticity and velocity fields can still be predicted accurately by the trained model of Fourier filter-based PhyCRNet. This reveals that Fourier filter-based PhyCRNet affords appealing stability.

3.7 Errors comparison

The error propagation maps of 2D viscous Burger's equations and FitzHugh-Nagumo RD equations are shown in Figures 8A,B, respectively. The performance of the proposed methods is different in the two experiments. There may be caused by the Fourier filter performs smooth filtering when calculating spatial derivatives and the setting of hyperparameters which is not the optimal setting of Fourier filter based PhyCRNet for solving 2D viscous Burger's equations. Overall, the errors of both models are

on the same level, which indicates that Fourier filter-based PhyCRNet has the same capability to solve the basic PDEs as PhyCRNet.

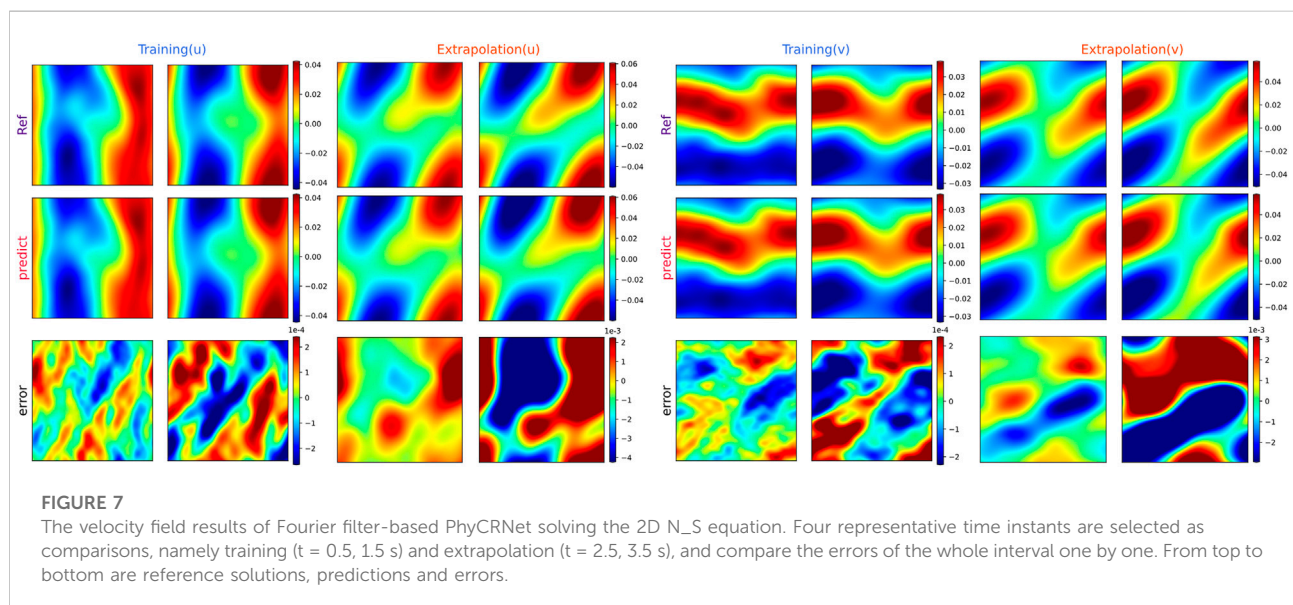
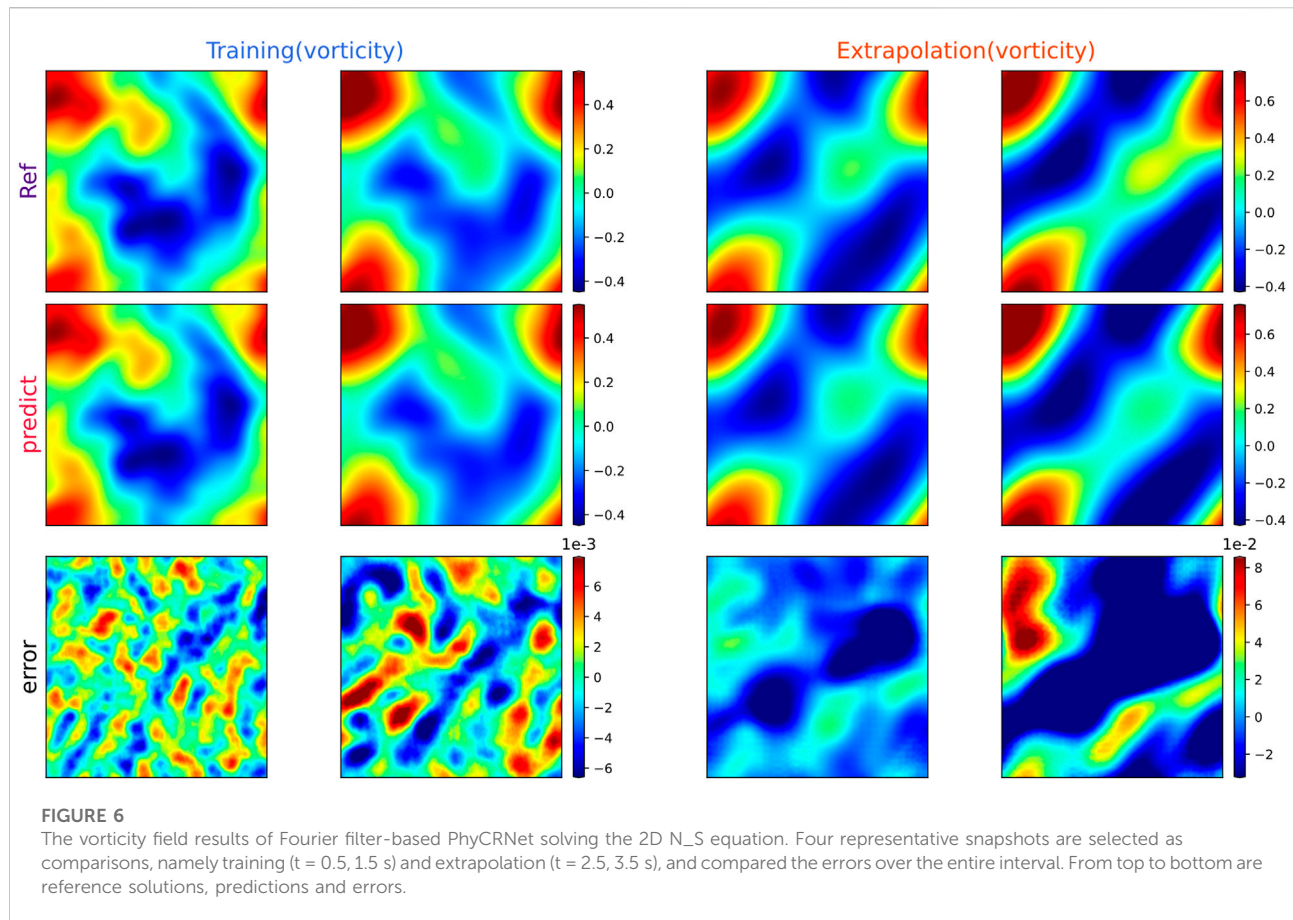
In Figure 8C, we observe that the errors of vorticity and velocity are very small during the training phase, and the errors gradually increase as the extrapolation time increases. Since both values are not in the same order of magnitude, the a-RMSE of the vorticity is significantly larger than the velocity field, below 0.7 and 0.02, respectively. As shown in Figure 8D, the a-RMSE of vorticity and velocity during the training and extrapolation phases is below 0.04 and 0.01, respectively. This further verifies the effectiveness of the Fourier filter-based PhyCRNet in solving 2D N-S equations.

3.8 Convergence study

It is significant to conduct the convergence study of the Fourier filter-based PhyCRNet. Fourier method is widely used to solve PDEs, and its convergence has been verified in previous studies (Hald, 1981; Tadmor, 1989; Bardos and Tadmor, 2015). Besides, the convergence of PhyCRNet has been verified. The Fourier filter that replaces the finite difference filter has a higher solution accuracy, so the calculation of the loss function is more accurate. The loss function is used to evaluate the error between the predicted value of the network and the target value. The trained network reaches convergence by back-propagation algorithm [50–52]. According to Eqs 7, 8, the loss function with physical constraints is trained to converge to an acceptable error range, which guarantees the convergence of the network. Therefore, we focus on the loss history of the neural network. Since the loss histories of the four experiments are similar at training phases, we choose the 2D Navier-Stokes equation as the representative example to show the convergence history of the proposed method in Figure 9. It is obvious that as the number of iterations increases, the loss value decreases. However, the convergence trend gradually becomes stable with the iteration. More precisely, the network training has reached a reasonable convergence range after training.

4 Discussion

As a widely used fluid model, incompressible flow has many variants for different scenarios and there are many traditional numerical methods [53–58]. The development of deep learning in recent years has also made rapid progress in the exploration and solution of incompressible flow models [59–61]. This paper develops the Fourier filter-based PhyCRNet to solve PDEs. Through four numerical



experiments, we verify the capability of our proposed method in the solution of general PDEs and equations describing 2D incompressible flows, respectively. By comparing the

predicted values of the Fourier filter-based PhyCRNet with the reference solution, it shows that the proposed network inherits the advantages of PhyCRNet, that is, the ability of

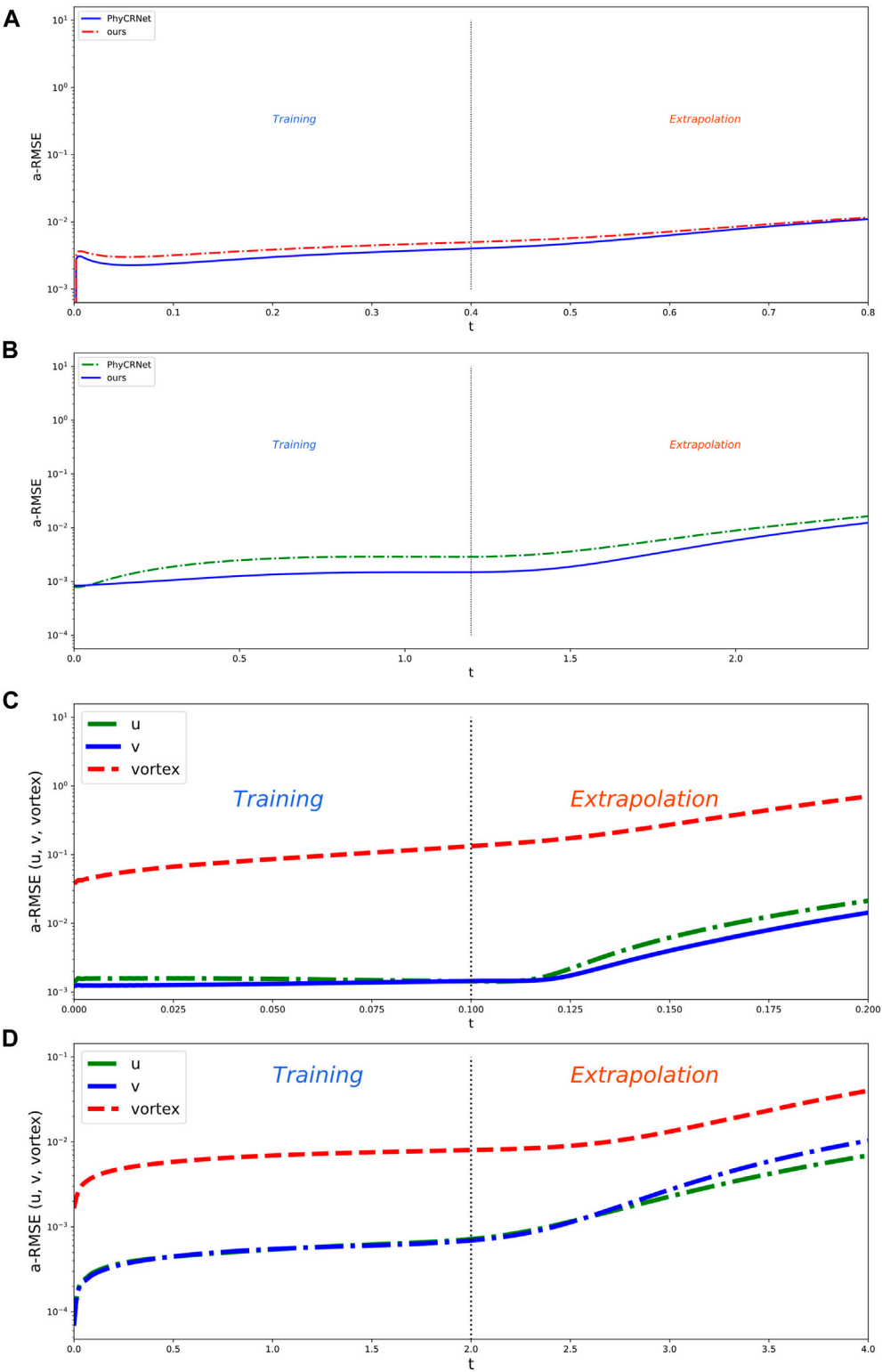


FIGURE 8
The a-RMSE of the four Equations. (A) 2D viscous Burger's equations; (B) FitzHugh–Nagumo RD equations; (C) Vorticity equation; (D) 2D Navier-Stokes equation.

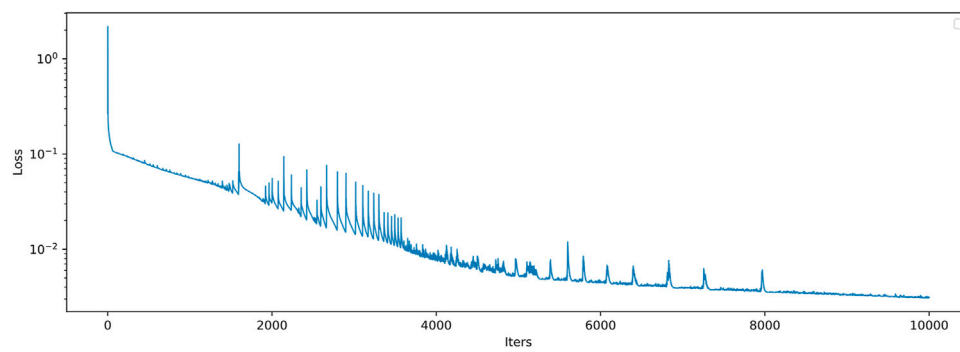


FIGURE 9
The convergence history of Fourier filter-based PhyCRNet.

extrapolate and encode physical constraints into loss function, and has the following strengths:

1. The calculation of the inverse Laplace operator. It introduces the Fourier filter to calculate the inverse Laplace operator, which the finite-difference filter cannot achieve. In the 2D incompressible flows, the solution is to iterate forward on the vorticity field and update the velocity field after the Laplace inverse operation. The Fourier filter-based PhyCRNet can efficiently solve 2D incompressible flows with the inverse Laplace operator.
2. The accuracy of partial derivatives. It adopts a discrete Fourier transform to calculate partial derivatives improving the solution accuracy. Here we only consider numerical experiments in the periodic domain, but after processing the output with methods such as periodic extension [62,63], the Fourier filter can extend the proposed method to the aperiodic domain.
3. The computational efficient of network. Because of Fourier method, the calculation of the inverse Laplace operator and partial derivatives is very efficient. Due to the small amount of experimental computation and the computational cost of the time series module dominates the entire training process, there is no noticeable performance in the solution of the 2D viscous Burger's equation and FitzHugh–Nagumo RD equations.
4. The proposed network exploits the powerful fitting capabilities of deep learning, while avoiding the dependence of the quality of training data. When carrying out network constraints, the fusion of physics-informed adopts the classical numerical method, so the prediction accuracy after training cannot be better than that of the traditional numerical method. Overall, the proposed method provides a reference deep learning method for scientific computing.

5 Conclusion

In this paper, a Fourier filter-based PhyCRNet is proposed by replacing the finite-difference filter with the Fourier filter to improve the accuracy of derivatives and overcome the difficulty of solving the inverse Laplacian operator. The proposed method integrates the physics-informed into the loss function by traditional numerical method to enhance the interpretability and improve the convergence rate. Numerical results demonstrate that the Fourier filter based PhyCRNet not only has the ability to solve general partial differential equations with PhyCRNet, but also is very effective, accurate and easy to implement for 2D incompressible flow. Certainly, the method proposed is not to replace the classical numerical method, but as an emerging field of deep learning to solve partial differential equations, it can bring a new method to scientific computing.

In the future, the proposed network can extend to the solution of problem with irregular regions and various boundary conditions. Furthermore, the graph neural network can be used to replace the convolutional network to extract spatial features more effectively.

Data availability statement

The original contributions presented in the study are included in the article/supplementary material, further inquiries can be directed to the corresponding author.

Author contributions

CX, XZ, FY, XC, KP, and JN contributed to the writing of the manuscript and to the interpretation of results. CX: Conceptualization, Writing-Original draft preparation. CX and

FY: Software, Validation. XZ, XC, KP, and JN: Writing-Reviewing and Editing.

Conflict of interest

The authors declare that the research was conducted in the absence of any commercial or financial relationships that could be construed as a potential conflict of interest.

References

- Renardy M, Rogers RC. *An introduction to partial differential equations*. Berlin, Germany: Springer Science & Business Media (2006).
- Petrovsky IG. *Lectures on partial differential equations*. Chelmsford, MA, USA: Courier Corporation (2012).
- Müller EH, Scheichl R. Massively parallel solvers for elliptic partial differential equations in numerical weather and climate prediction. *Q J R Meteorol Soc* (2014) 140(685):2608–24. doi:10.1002/qj.2327
- Nielsen AS, Brunner G, Hesthaven JS. Communication-aware adaptive parareal with application to a nonlinear hyperbolic system of partial differential equations. *J Comput Phys* (2018) 371:483–505. doi:10.1016/j.jcp.2018.04.056
- Rabczuk T, Ren H, Zhuang X. A nonlocal operator method for partial differential equations with application to electromagnetic waveguide problem. *Comput Mater Continua* (2019) 59:31–55. doi:10.32604/cmc.2019.04567
- Hughes TJ. *The finite element method: Linear static and dynamic finite element analysis*. Chelmsford, MA, USA: Courier Corporation (2012).
- Hornik K, Stinchcombe M, White H. Multilayer feedforward networks are universal approximators. *Neural networks* (1989) 2(5):359–66. doi:10.1016/0893-6080(89)90020-8
- Rudy SH, Brunton SL, Proctor JL, Kutz JN. Data-driven discovery of partial differential equations. *Sci Adv* (2017) 3(4):e1602614. doi:10.1126/sciadv.1602614
- Long Z, Lu Y, Ma X, Dong B. Pde-net: Learning pdes from data. In: International Conference on Machine Learning: PMLR (2018). p. 3208–16.
- Zhu Y, Zabaras N. Bayesian deep convolutional encoder-decoder networks for surrogate modeling and uncertainty quantification. *J Comput Phys* (2018) 366: 415–47. doi:10.1016/j.jcp.2018.04.018
- Lu L, Jin P, Karniadakis GE. *Deeponet: Learning nonlinear operators for identifying differential equations based on the universal approximation theorem of operators* (2019). arXiv preprint arXiv:1910.03193.
- Brunton SL, Noack BR, Koumoutsakos P. Machine learning for fluid mechanics. *Annu Rev Fluid Mech* (2020) 52:477–508. doi:10.1146/annurev-fluid-010719-060214
- Guo Y, Cao X, Liu B, Gao M. Solving partial differential equations using deep learning and physical constraints. *Appl Sci* (2020) 10(17):5917. doi:10.3390/app10175917
- Raissi M, Yazdani A, Karniadakis GE. Hidden fluid mechanics: Learning velocity and pressure fields from flow visualizations. *Science* (2020) 367(6481): 1026–30. doi:10.1126/science.aaw4741
- Lu L, Meng X, Mao Z, Karniadakis GE. DeepXDE: A deep learning library for solving differential equations. *SIAM Rev Soc Ind Appl Math* (2021) 63(1):208–28. doi:10.1137/19m1274067
- Raissi M, Perdikaris P, Karniadakis GE. Physics-informed neural networks: A deep learning framework for solving forward and inverse problems involving nonlinear partial differential equations. *J Comput Phys* (2019) 378:686–707. doi:10.1016/j.jcp.2018.10.045
- Meng X, Li Z, Zhang D, Karniadakis GE. PPINN: Parareal physics-informed neural network for time-dependent PDEs. *Comput Methods Appl Mech Eng* (2020) 370:113250. doi:10.1016/j.cma.2020.113250
- Wight CL, Zhao J. *Solving allen-Cahn and Cahn-Hilliard equations using the adaptive physics informed neural networks* (2020). arXiv preprint arXiv:2007.04542.
- Bai Y, Chaolu T, Bilige S. Solving Huxley equation using an improved PINN method. *Nonlinear Dyn* (2021) 105(4):3439–50. doi:10.1007/s11071-021-06819-z
- Haghighat E, Raissi M, Moure A, Gomez H, Juanes R. A physics-informed deep learning framework for inversion and surrogate modeling in solid mechanics. *Comput Methods Appl Mech Eng* (2021) 379:113741. doi:10.1016/j.cma.2021.113741
- Yang L, Meng X, Karniadakis GE. B-PINNs: Bayesian physics-informed neural networks for forward and inverse PDE problems with noisy data. *J Comput Phys* (2021) 425:109913. doi:10.1016/j.jcp.2020.109913
- Lu L, Jin P, Pang G, Zhang Z, Karniadakis GE. Learning nonlinear operators via DeepONet based on the universal approximation theorem of operators. *Nat Mach Intell* (2021) 3(3):218–29. doi:10.1038/s42256-021-00302-5
- Li Z, Kovachki N, Azizzadenesheli K, Liu B, Bhattacharya K, Stuart A, et al. *Fourier neural operator for parametric partial differential equations* (2020). arXiv preprint arXiv:2010.08895.
- Li Z, Zheng H, Kovachki N, Jin D, Chen H, Liu B, et al. *Physics-informed neural operator for learning partial differential equations* (2021). arXiv preprint arXiv:2111.03794.
- Wang S, Wang H, Perdikaris P. Learning the solution operator of parametric partial differential equations with physics-informed DeepONets. *Sci Adv* (2021) 7(40):eabi8605. doi:10.1126/sciadv.abi8605
- Zhu Y, Zabaras N, Koutsourelakis P-S, Perdikaris P. Physics-constrained deep learning for high-dimensional surrogate modeling and uncertainty quantification without labeled data. *J Comput Phys* (2019) 394:56–81. doi:10.1016/j.jcp.2019.05.024
- Rao C, Sun H, Liu Y. Physics-informed deep learning for computational elastodynamics without labeled data. *J Eng Mech* (2021) 147(8):04021043. doi:10.1061/(asce)em.1943-7889.0001947
- Geneva N, Zabaras N. Modeling the dynamics of PDE systems with physics-constrained deep auto-regressive networks. *J Comput Phys* (2020) 403:109056. doi:10.1016/j.jcp.2019.109056
- Hu Y, Zhao T, Xu S, Xu Z, Lin L. *Neural-PDE: A rnn based neural network for solving time dependent PDEs* (2020). arXiv preprint arXiv:2009.03892.
- Ren P, Rao C, Liu Y, Wang JX, Sun H. PhyCRNet: Physics-informed convolutional-recurrent network for solving spatiotemporal PDEs. *Comput Methods Appl Mech Eng* (2022) 389:114399. doi:10.1016/j.cma.2021.114399
- Zhong W, Jianing Z, Zhong XX. On a new time integration method for solving time dependent partial differential equations. *Comput Methods Appl Mech Eng* (1996) 130(1–2):163–78. doi:10.1016/0045-7825(95)00876-4
- El-Ajou A, Arqub OA, Momani S, Baleanu D, Alsaedi A. A novel expansion iterative method for solving linear partial differential equations of fractional order. *Appl Maths Comput* (2015) 257:119–33. doi:10.1016/j.amc.2014.12.121
- Arqub OA, Hayat T, Alhodaly M. Analysis of lie symmetry, explicit series solutions, and conservation laws for the nonlinear time-fractional phi-four equation in two-dimensional space. *Int J Appl Comput Math* (2022) 8(3):145–17. doi:10.1007/s40819-022-01334-0
- Albawi S, Mohammed TA, Al-Zawi S. Understanding of a convolutional neural network. In: 2017 international conference on engineering and technology (ICET). Antalya, Turkey: IEEE (2017). p. 1–6.
- Shi X, Chen Z, Wang H, Yeung DY, Wong WK, Woo WC. Convolutional lstm network: A machine learning approach for precipitation nowcasting. *Adv Neural Inf Process Syst* (2015) 28.
- Merilees PE. The pseudospectral approximation applied to the shallow water equations on a sphere. *Atmosphere* (1973) 11(1):13–20. doi:10.1080/00046973.1973.9648342
- Ku HC, Hirsh RS, Taylor TD. A pseudospectral method for solution of the three-dimensional incompressible Navier-Stokes equations. *J Comput Phys* (1987) 70(2):439–62. doi:10.1016/0021-9991(87)90190-2
- Ku HC, Taylor TD, Hirsh RS. Pseudospectral methods for solution of the incompressible Navier-Stokes equations. *Comput Fluids* (1987) 15(2):195–214. doi:10.1016/s0045-7930(87)80004-x

Publisher's note

All claims expressed in this article are solely those of the authors and do not necessarily represent those of their affiliated organizations, or those of the publisher, the editors and the reviewers. Any product that may be evaluated in this article, or claim that may be made by its manufacturer, is not guaranteed or endorsed by the publisher.

39. Fornberg B. *A practical guide to pseudospectral methods*. Cambridge: Cambridge University Press (1998).
40. Bracewell RN, Bracewell RN. *The Fourier transform and its applications*. New York: McGraw-Hill (1986).
41. Gourlay A. Some recent methods for the numerical solution of time-dependent partial differential equations. *Proc R Soc Lond A. Math Phys Sci* (1971) 323(1553):219–35.
42. Kreiss HO, Ortiz OE. *Introduction to numerical methods for time dependent differential equations*. Hoboken, NJ, USA: John Wiley & Sons (2014).
43. Cooley JW, Lewis PA, Welch PD. The fast Fourier transform and its applications. *IEEE Trans Ed* (1969) 12(1):27–34. doi:10.1109/te.1969.4320436
44. Parks T. *DFT/FFT and convolution algorithms*. New York: John Wiley & Sons (1985).
45. Blahut RE. *Fast algorithms for signal processing*. Cambridge: Cambridge University Press (2010).
46. Matyka M. *Solution to two-dimensional incompressible Navier-Stokes equations with simple, simpler and vorticity-stream function approaches. driven-lid cavity problem: Solution and visualization* (2004). arXiv preprint physics/0407002.
47. Fuka V. Poissfft—a free parallel fast Poisson solver. *Appl Maths Comput* (2015) 267:356–64. doi:10.1016/j.amc.2015.03.011
48. Paszke A, Gross S, Chintala S, Chanan G, Yang E, DeVito Z, et al. *Automatic differentiation in pytorch* (2017).
49. Da K. A method for stochastic optimization (2014). arXiv preprint arXiv:1412.6980.
50. Rumelhart DE, Hinton GE, Williams RJ. *Learning internal representations by error propagation*. California, USA: California Univ San Diego La Jolla Inst for Cognitive Science (1985).
51. LeCun Y, Touresky D, Hinton G, Sejnowski T. A theoretical framework for back-propagation. In: *Proceedings of the 1988 connectionist models summer school* (1988). p. 21–8.
52. Goh AT. Back-propagation neural networks for modeling complex systems. *Artif intelligence Eng* (1995) 9(3):143–51. doi:10.1016/0954-1810(94)00011-s
53. Solonnikov V. Solvability of the initial-boundary-value problem for the equations of motion of a viscous compressible fluid. *J Math Sci* (1980) 14(2): 1120–33. doi:10.1007/bf01562053
54. Giga Y. Solutions for semilinear parabolic equations in L_p and regularity of weak solutions of the Navier-Stokes system. *J differential equations* (1986) 62(2): 186–212. doi:10.1016/0022-0396(86)90096-3
55. Pedlosky J. *Geophysical fluid dynamics*. Berlin, Germany: Springer (1987).
56. Lions P. *Mathematical topics in fluid mechanics. Incompressible models, vol. 1*. Oxford: Clarendon (1996).
57. Danchin R. Local and global well-posedness results for flows of inhomogeneous viscous fluids. *Adv differential equations* (2004) 9(3-4): 353–86.
58. Zhang P. Global smooth solutions to the 2-D nonhomogeneous Navier–Stokes equations. *Int Maths Res Notices* (2008). doi:10.1093/imrn/rnn098
59. Jin X, Cai S, Li H, Karniadakis GE. NSFnets (Navier-Stokes flow nets): Physics-informed neural networks for the incompressible Navier-Stokes equations. *J Comput Phys* (2021) 426:109951. doi:10.1016/j.jcp.2020.109951
60. Ebrahimijahan A, Dehghan M, Abbaszadeh M. Simulation of the incompressible Navier–Stokes via integrated radial basis function based on finite difference scheme. *Eng Comput* (2022) 2022:1–22. doi:10.1007/s00366-021-01543-z
61. Kashefi A, Mukerji T. *Physics-informed PointNet: A deep learning solver for steady-state incompressible flows and thermal fields on multiple sets of irregular geometries* (2022). arXiv preprint arXiv:2202.05476.
62. Eckhoff KS. Accurate reconstructions of functions of finite regularity from truncated Fourier series expansions. *Math Comput* (1995) 64(210):671–90. doi:10.1090/s0025-5718-1995-1265014-7
63. Huybrechs D. On the Fourier extension of nonperiodic functions. *SIAM J Numer Anal* (2010) 47(6):4326–55. doi:10.1137/090752456



OPEN ACCESS

EDITED BY
Krasimira Tsaneva-Atanasova,
University of Exeter, United Kingdom

REVIEWED BY
Qingyun Wang,
Beihang University, China
Helmut Schmidt,
Institute of Computer Science, Czech
Academy of Sciences Praha (Prague),
Czechia

*CORRESPONDENCE
Jens Starke
jens.starke@uni-rostock.de

SPECIALTY SECTION
This article was submitted to Biophysics,
a section of the journal
Frontiers in Physics

RECEIVED 24 May 2022
ACCEPTED 29 September 2022
PUBLISHED 18 October 2022

CITATION
Spiliotis K, Butenko K, van Rienen U,
Starke J and Köhling R (2022), Complex
network measures reveal optimal
targets for deep brain stimulation and
identify clusters of collective
brain dynamics.
Front. Phys. 10:951724.
doi: 10.3389/fphy.2022.951724

COPYRIGHT
© 2022 Spiliotis, Butenko, van Rienen,
Starke and Köhling. This is an open-
access article distributed under the
terms of the [Creative Commons
Attribution License \(CC BY\)](#). The use,
distribution or reproduction in other
forums is permitted, provided the
original author(s) and the copyright
owner(s) are credited and that the
original publication in this journal is
cited, in accordance with accepted
academic practice. No use, distribution
or reproduction is permitted which does
not comply with these terms.

Complex network measures reveal optimal targets for deep brain stimulation and identify clusters of collective brain dynamics

Konstantinos Spiliotis¹, Konstantin Butenko^{2,3},
Ursula van Rienen^{2,4,5}, Jens Starke^{1*} and Rüdiger Köhling⁶

¹Institute of Mathematics, University of Rostock, Rostock, Germany, ²Institute of General Electrical Engineering, University of Rostock, Rostock, Germany, ³Movement Disorders and Neuromodulation Unit, Department for Neurology, Charité—Universitätsmedizin Berlin, Berlin, Germany, ⁴Department Life, Light and Matter, University of Rostock, Rostock, Germany, ⁵Department of Ageing of Individuals and Society, University of Rostock, Rostock, Germany, ⁶Oscar-Langendorff-Institute of Physiology, Rostock University Medical Center, Rostock, Germany

An important question in computational neuroscience is how to improve the efficacy of deep brain stimulation by extracting information from the underlying connectivity structure. Recent studies also highlight the relation of structural and functional connectivity in disorders such as Parkinson's disease. Exploiting the structural properties of the network, we identify nodes of strong influence, which are potential targets for Deep Brain Stimulation (DBS). Simulating the volume of the tissue activated, we confirm that the proposed targets are reported as optimal targets (sweet spots) to be beneficial for the improvement of motor symptoms. Furthermore, based on a modularity algorithm, network communities are detected as set of nodes with high-interconnectivity. This allows to localise the neural activity, directly from the underlying structural topology. For this purpose, we build a large scale computational model that consists of the following elements of the basal ganglia network: subthalamic nucleus (STN), globus pallidus (external and internal parts) (GPe-GPi), extended with the striatum, thalamus and motor cortex (MC) areas, integrating connectivity from multimodal imaging data. We analyse the network dynamics under Healthy, Parkinsonian and DBS conditions with the aim to improve DBS treatment. The dynamics of the communities define a new functional partition (or segregation) of the brain, characterising Healthy, Parkinsonian and DBS treatment conditions.

KEYWORDS

electric field volume conductor model, dynamical systems, Hodgkin Huxley neurons, complex networks, movement disorder

1 Introduction

Movement disorders like Parkinson's disease and dystonia are characterised by abnormal functioning of the whole basal ganglia (BG) - thalamocortical network. In Parkinson's disease, one of the main characteristics of the altered BG network behaviour is a synchronised abnormal β - activity (12–35 Hz) Kühn et al. [1]; Neumann et al. [2]. This enhanced BG rhythm also affects thalamic activity by sending strong inhibitory signals via GPi (internal segment of the globus pallidus). The hyperpolarisation of thalamic neurons due to increased inhibitory BG output increases the burst discharges Kim et al. [3]; Galvan et al. [4], which in turn triggers motor dysfunction through the thalamocortical pathway Kim et al. [3].

Deep brain stimulation (DBS) of the BG was shown to be an efficient treatment for movement disorders Deuschl et al. [5]; Vidailhet et al. [6], but its therapeutic mechanism is still not fully understood. The application of DBS leads to firing pattern alterations, and in particular, to disruption of hypersynchronised β -band oscillations Kühn et al. [1]; Kim et al. [3]; Crompe et al. [7]. Indeed, recordings in animal models Xu et al. [8]; Kim et al. [3]; Crompe et al. [7] and observations from computational network models Rubin and Terman [9]; Popovych and Tass [10]; So et al. [11]; Galvan and Wichmann [12] suggest that DBS in the subthalamic nucleus (STN) results in more periodic and regular firing at higher frequencies in the BG-thalamic network.

Two important questions arise concerning the structural connectivity and DBS effectiveness. The first question is how to determine those electrode positions which are the most effective for the activation of neural pathways to improve DBS outcome. The second question which naturally arises, is which differences in neural activation patterns will emerge within the brain's structural network when simulating different conditions (i.e., Healthy, Parkinsonian and DBS). Due to the strongly heterogeneous nature of the connection topology and the stochastic and nonlinear large scale interactions of the underlying units/neurons, the emergent macroscopic behavior usually is far from trivial to predict Spiliotis and Siettos [13]; Siettos and Starke [14]; Deco et al. [15,16]; Bassett and Bullmore [17]; Bullmore and Sporns [18]; Iliopoulos and Papasotiriou [19]. Self-organisation, sustained oscillations, travelling waves, multiplicity of stationary states and spatio-temporal chaos are paradigms of the rich nonlinear behaviour at the coarse-grained systems level Spiliotis and Siettos [13]; Siettos and Starke [14]; Deco et al. [15,16]; De Santos-Sierra et al. [20]; Crowell et al. [21]; Spiliotis et al. [22], indicating thus that a precise structure–function relation remains a major open problem Deco et al. [16].

As the primary aim of this paper, we identify positions of nodes of high functional impact using network analysis. We test then the hypothesis that such high-connectivity nodes are pivotal in shaping network activity and are highly effective stimulation

targets for restoring the normal network function. Notably, the electric field-based approximation of the volume of tissue activated (VTA) Butson et al. [23]; Butenko et al. [24], computed at these nodes for a monopolar DBS, overlapped with target areas previously shown to be effective against akinetic symptoms of Parkinson's disease Dembek et al. [25].

The critical high-connectivity nodes were identified according to three different, but interrelated measures:

- 1) Using the measure of “clustering coefficient,” nodes are identified which form triplet interactions. This triangular interconnection allows for circular information flow and information feedback. This triplet organisation constitutes the complex level of connectivity, and is speculated to play a role in e.g. effective information distribution but also complex oscillatory network rhythm formation.
- 2) Using the measure of “betweenness centrality,” high-connectivity nodes are identified (also known as hubs and defined by their so-called nodal efficiency van Hartevelt et al. [26]). This nodal efficiency is related to the degree of influence of nodes in the network and can be interpreted as the amount of flow that passes through these nodes. Such hubs act as central crossroads, enhancing the ability of parallel information transfer and the functional integration in brain networks van Hartevelt et al. [26].
- 3) Using the measure of “eigencentrality” (or eigenvector centrality), nodes are identified which specifically connect with other nodes of high centrality. In this way, targeting such nodes will likely influence a large population of other nodes. In many cases, centrality measures correlate strongly Li et al. [27]; nodes with extreme values of “betweenness centrality” also show high “eigencentrality” values.

The second aim of this study was to explore the relationship between anatomical structure and neural activity (i.e., functional connectivity) using modified Hodgkin-Huxley models Terman et al. [28]; Rubin and Terman [9]; So et al. [11]; Spiliotis et al. [22]. In the current study, we address this question by combining the community structures (i.e., sets of high-connectivity nodes as identified using modularity measures, Newman [29]) and a large scale biophysical model which produces virtual neural activity. We study three different conditions: Healthy, Parkinsonian state and Parkinsonian conditions with DBS. In the latter case, we extend the previous computational model Spiliotis et al. [22] in order to simulate specific spatial positions of DBS electrodes Mandali et al. [30].

Predicting DBS outcome using neural networks is not novel Rubin and Terman [9]; Popovych and Tass [10]; Spiliotis et al. [22]; Fleming et al. [31], in the cited studies, however, smaller networks were studied without taking into account connectivity structure and VTA. In the current study, we follow a different approach: initially, we integrate the high dimensional nonlinear system, which produces spatiotemporal patterns consistent with

either Healthy (normal) or Parkinsonian states. Then we average the activity over the different community structures that have been previously identified using modularity network measures.

The second main result of the study shows that in all areas (the detected communities), including neocortical ones, Parkinsonian conditions alter power spectrograms, but mainly subcortical structures, with e.g., slowing of activity in the thalamus and faster activity in pathways connecting pallido-thalamic and subthalamic-pallidal nodes. Under DBS, in turn, the simulation reveals that this stimulation at high-connectivity nodes is able to restore thalamic activity, and partly also cortical one, while on the one hand, hyperdirect-pathway associated nodes remain largely unaffected, and on the other, structures in close vicinity of the electrode mainly follow the stimulation.

2 Network connectivity from data sources

To describe the structural connectivity of the network, data from different studies on human brain anatomy were utilised.

2.1 Data sources

For the current model, published data on anatomical and fiber tract positions were used from different sources: The basal ganglia nuclei and their substructures were taken from the DISTAL Atlas Ewert et al. [32]; Chakravarty et al. [33]. The Melbourne Subcortex Atlas Tian et al. [34] was used to define substructures of the thalamus, while the relevant cortical regions were selected using the Brainnetome Atlas parcellation Fan et al. [35]. Fiber tracts classified to pathways in the vicinity of the STN were taken from Petersen et al. [36], and projections of the ventral anterior nucleus to motor cortical regions, required to complete the BG-thalamo-cortical network, were extracted from the structural group connectome of 90 PPMI Parkinson's disease-patients GQI Marek et al. [37], post-processed in Ewert et al. [32]. All data were represented in MNI (Montreal Neurological Institute) space.

2.2 Structural connectivity of the basal ganglia-thalamo-cortical network

To investigate DBS network effects in Parkinson's disease, the classic circuit model of the BG-thalamo-cortical network was employed Milardi et al. [38] (Figure 1A). It consists of three inputs from motor cortical regions: the direct pathway that involves the striatum and continues as a GABAergic projection to the GPi and SNr (substantia nigra pars reticulata); the indirect pathway that also involves the striatum, but has GABAergic projections to the GPe (external segment of the globus pallidus), which in turn inhibits the STN, GPi and SNr. In

addition to these pathways, there is the hyperdirect pathway through which the STN receives a direct excitatory input from the cortical areas. The glutamatergic efferents of the STN innervate the GPe, GPi and SNr. GABAergic projections of the two latter nuclei to the ventral anterior (VA) and ventral lateral (VL) regions of the thalamus represent the output of the BG circuit to the thalamo-cortical network Bosch-Bouju et al. [39].

The interstructural connectivity of the network was simulated using data based on the pathway atlas of human motor network obtained from multimodal imaging, including diffusion, histological and structural MRI data, fused to a virtual 3D rendering Petersen et al. [36] or classified based on their position relative to the involved structures (thalamo-cortical projections), see Figure 1. Note that the grouping of fibers leads to an emergence of network nodes. In the current study, the simulated network (Figure 1B) does not include the substantia nigra (SN). The reason for this omission is that the dopaminergic projections of the SNc (substantia nigra pars compacta) are not myelinated, and hence less excitable (by approx. two orders of magnitude) by extracellular fields Tarnaud et al. [40], yielding a very low chance that DBS actually would affect them directly. Furthermore, to ensure homogeneity of the BG pathways, only those present in Petersen et al. [36] were employed, which did not include the striatonigral and the nigrothalamic projections. For the same reason, only the VA neurons were simulated, as they predominantly receive the pallidal output, unlike the VL nucleus that is mostly innervated by the SNr afferents Lanciego et al. [41]. Note that although the projections from the VL to the motor cortex exist, we excluded them to avoid modelling of intrinsic dynamics between subregions of the thalamus.

3 Modelling structural basal ganglia-thalamo-cortical neuronal network using complex network theory and pathway classification

Structural brain connectivity refers to the set of anatomical links (or axonal tracts) which join different brain regions. The connectivity can be described and simplified employing elements of complex network theory Bullmore and Sporns [18]; Stam and Reijneveld [42], where the neural elements at the beginning and the end of a tract serve as nodes of the network, while the anatomical tract is described as edge of the network. The topological structure of the network plays an important role in the emergent neural activity and brain functionality, however it is not well understood how the structure or topology shapes the dynamics Deco et al. [15,43]. The knowledge of the network structural properties is important since it allows to build realistic computational models and to shed light

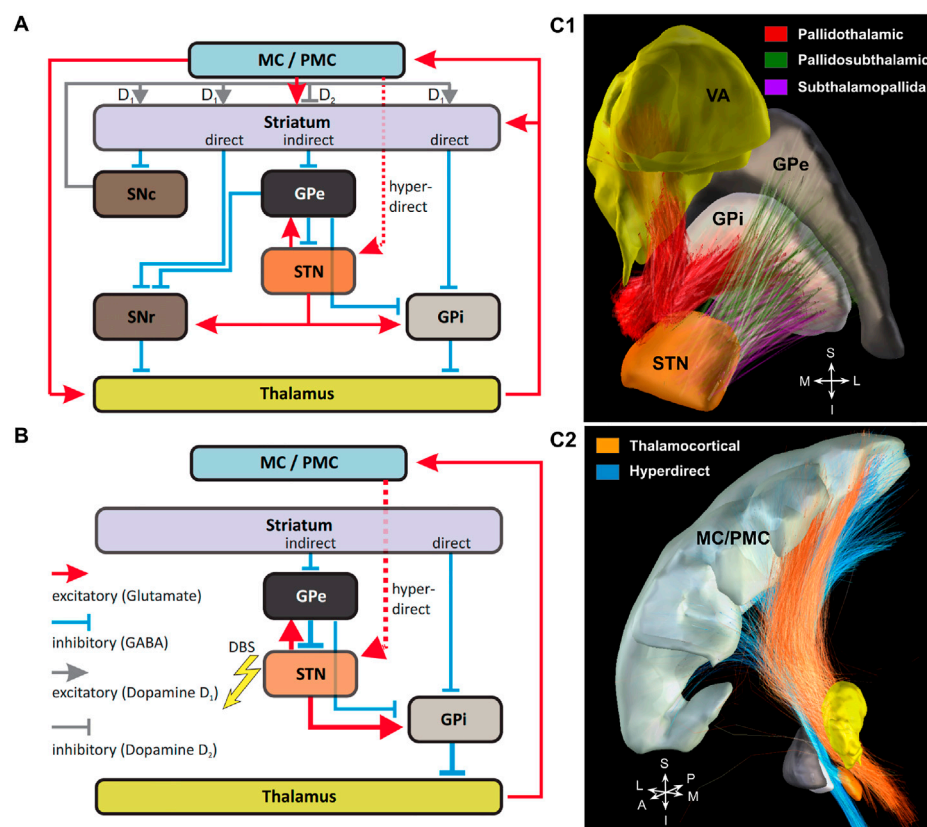


FIGURE 1

Basal ganglia-thalamo-cortical circuits. (A): Circuit model comprising all main connections. MC/PMC—motor and premotor cortical regions, respectively. For explanations, please see the main text. (B): Simulated reduced circuit model with highlighted (bold arrows) connections possibly affected by STN-DBS. The synaptic connection between Striatum and Globus Pallidus pars externa/interna (GPe and GPi) were modelled by different constant currents. (C): Structural connectivity of the simulated network is based on the pathway atlas of human motor network constructed from multimodal data including diffusion, histological and structural MRI data, fused to a virtual 3D rendering Petersen et al. [36]. (C1): Projections from GPi to thalamus (VA nucleus) are shown in red, connections between subthalamic nucleus (STN) and GPe are shown in green, projections from STN to GPi are shown in violet. (C2): Connections between motor cortex (MC/PMC) and the thalamus projections were obtained by classifying fiber tracts from Marek et al. [37] and are shown in orange. Projections from motor cortex to STN (hyperdirect pathway) are shown in blue. Nuclei are shown in the following colours: GPe in light grey, GPi in dark grey, STN in dark orange, thalamus (VA nucleus) in yellow and motor cortex (M1) in light grey.

on mechanisms underlying brain functionality or dysfunctionality (i.e., movement disorders), and to predict the neural dynamics on multiple scales Honey et al. [44,45]. Using the structural connectivity of Section 2, we build a directed network. The internal connectivity structure within the areas STN, GPe, GPi, thalamus and motor cortex areas had to be defined using complex network theory Stam and Reijneveld [42]; Watts and Strogatz [46].

3.1 Construction of complex network using the structural connectivity

The resulting structure of Section 2.2 is used to obtain the connectivity network in the form $G = (V, E)$, where V is the set

of nodes and E represents the set of edges. The nodes of the structural network are defined as points in three-dimensional space and correspond to the starting and ending point of a fiber tract. The resolution is set at 1mm^3 , meaning that if two (or more) ending (or starting) points lying within the same cube of 1mm^3 , they are considered as one node. The connectivity information is included in the adjacency (or connectivity) matrix A : if there is a fiber tract starting at position $\mathbf{x} = (x_1, y_1, z_1)$ and ending at $\mathbf{y} = (x_2, y_2, z_2)$ then $A(\mathbf{x}, \mathbf{y}) = 1$, otherwise $A(\mathbf{x}, \mathbf{y}) = 0$. The resulting connectivity constitutes a graph $G = (V, E)$, where the V is the set of nodes and E is the set of edges or tracts. At the given resolution of 1mm^3 , the network contains 134 STN nodes, 244 and 246 GPe and GPi nodes, respectively, 833 thalamic nodes and 2070 cortical nodes.

3.2 Intrastructural small-world network connectivity

The pathway classification analysis in [Section 2.2](#) does not contain information about the internal connectivity of each region (i.e., how the nodes are connected within a region). We model connectivity within each area using small-world structures Watts and Strogatz [46]; Bassett and Bullmore [47]; Bullmore and Sporns [18]; Stam and Reijneveld [42]; Spiliotis and Siettos [13], thus increasing overall network connectivity beyond the interstructural projections. In such small-world complex networks Mark [48]; Watts and Strogatz [46], each node interacts with its k nearest neighbours; additionally, a few randomly chosen remote connections (with a small probability p) within the area are also formed Watts and Strogatz [46]. Small-world structures are commonly used in computational neuroscience Netoff et al. [49]; Berman et al. [50]; She et al. [51]; Bassett and Bullmore [17,47]; Fang et al. [52]; De Santos-Sierra et al. [20] as a result of two main characteristics which they show: highly clustered property together with short path length Bullmore and Sporns [18]; Watts and Strogatz [46]; Newman [29], enhancing in this way the signal or rhythm propagation within the network and the synchronizability in the network.

The GPe/GPi, thalamus and MC layers were modelled as separate small-world networks. Each node increases the initial number of connections (or the degree of the node) by $k = 20$ degrees on average. The local internal connections lay in a distance less than 5 mm (these are the local neighbours); however, the small-world topology Watts and Strogatz [46] allows remote connections (in a distance greater than 5 mm) with a small probability $p = 0.05$. The choices of k and p in this model are phenomenologically extracted. These values turn out to be successful i.e. the values k and p are chosen such that the network will give high values of clustering coefficient compared to a random network (where the clustering coefficient is very low and simultaneously a low value of the characteristic path length, see also Watts and Strogatz [46]). Similar values have been used in other studies and with the chosen values, the connectivity structure resembles real-neuronal connectivity as it is shown for example, in the work of De Santos-Sierra et al. [20] and Netoff et al. [49].

For the STN, we chose a modified small world approach which results from the experimental findings of Gouty-Colomer et al. [53]; Ammari et al. [54]. The STN area is characterised by sparse connectivity, where local and remote connections coexist. Specifically, only 20% of the STN neurons develop connections (collaterals) within the other STN neurons Gouty-Colomer et al. [53]. Almost 80% of these connections are local within a distance of 200–400 μ m radius, and the other 20% are contacts which occur farther away, i.e., >500 μ m. In this sense, the 20% of neurons, which form STN connections, have both local and remote connections analogous to the small-world property Spiliotis et al. [22]. Similar to the previous connectivity, in our

model, only the 20% of STN neurons show an average of 25 connections each, while few of these are randomly chosen remote connections Spiliotis et al. [22]; Gouty-Colomer et al. [53]).

3.3 Network properties: Degree distributions, path distances and centralities

Network measures such as a quantification of homogeneity are used to identify structural properties of the underlying neuronal network. These measures allow to categorise structural elements according to connectivity properties (i.e., profiles), segregating them into discrete entities. The main categories are clustering and distancing measures, centralities and communities detection Bullmore and Sporns [18]; Stam and Reijneveld [42]. Another subdivision of the network measures is the local and global description. The local description refers to the individual property of the i -th node, while the ensemble over the whole set of nodes in the network defines the global description (or distribution) for the network. The statistical distribution of a network property in this paper is characterised by its mean (the first-order statistical measure).

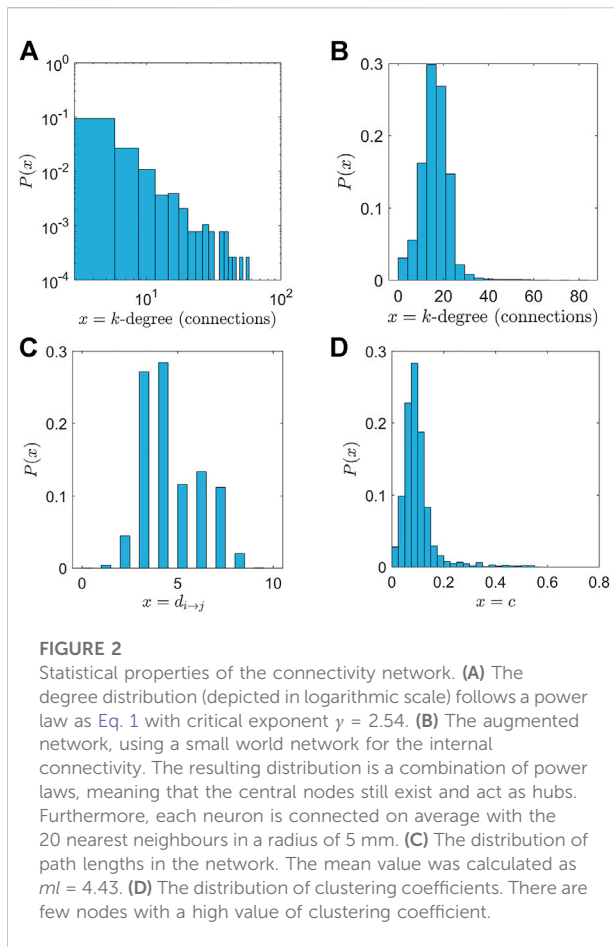
3.3.1 Degree distribution

The degree of a node i refers to the number of edges connected to it Bullmore and Sporns [18]. In directed networks, a node has both an in-degree and out-degree, which are the numbers of in-coming and out-going edges, respectively. A high degree of connectivity (increased numbers of links) of the i -th node defines the importance of a node in the network. The degree distribution $P(k)$ defines the probability of a randomly selected node to have specific degree k . Averaging over all the nodes of the network, we obtain the mean degree, the first characteristic of the connectivity. The degree distribution after pathway classification analysis ([Section 2.1](#)), as long as internal connectivity is not considered, follows a power law of the form.

$$P(K) = ck^{-\gamma} \quad (1)$$

where the exponent γ was calculated as $\gamma \approx 2.5$.

The main characteristic of a power-law degree distribution is that only a few high-connectivity nodes acting as central nodes or hubs (nodes with a high number of connections) exist, while the majority of nodes show little connectivity. The high-connectivity nodes or hubs are responsible for an effective and fast spreading of information or signals in the network. [Figure 2A](#) depicts the degree distribution of $P(k)$ in the network, while [Figure 2B](#) shows the degree distribution of the network including internal connections. In the latter case, the network thus combines both power law properties (describing connections among nuclei) and small world characteristics (describing local



connectivity within nuclei). This generates an almost symmetric distribution of $P(k)$.

3.3.2 Paths lengths, efficacy, and clustering coefficient

In graph theory, a path is a sequence of successive steps between two nodes, assuming that it is never intersecting a single node more than once. The minimum distance (i.e., the minimum steps in case of binary networks) between two nodes defines the shortest path length. Averaging over the set of all shortest paths, we obtain the mean path length of the network:

$$\bar{m} = \frac{\sum_{i,j} d_{i \rightarrow j}}{N(N-1)}, \quad (2)$$

The mean path length shows the ability of the network to spread information between any two nodes. A low mean shortest path length \bar{m} signifies that any two randomly chosen nodes can interchange information via just very few intermediate nodes (in our case ≈ 4 nodes).

Another similar measure which is applied in the case where there is no connecting path between two nodes (i.e., $d_{i \rightarrow j} = \infty$), is the global efficacy \bar{G} :

$$\bar{G} = \frac{\sum_{i,j} \frac{1}{d_{i \rightarrow j}}}{N(N-1)}. \quad (3)$$

This measure avoids calculating with infinity, since if there is no pathway between two nodes i.e., $d_{i \rightarrow j} = \infty \Rightarrow 1/d_{i \rightarrow j} = 0$. The \bar{m} is comparable with inverse \bar{G} , and according to the Cauchy inequality for the arithmetic and harmonic mean, we obtain

$$\bar{m} \geq \frac{1}{\bar{G}}. \quad (4)$$

For the augmented network, the mean path length was computed to be $\bar{m} = 4.435$, while the inverse global efficacy resulted in $1/\bar{G} = 3.91$. Figure 2C shows the distribution of distances between any two nodes (i.e., $d_{i \rightarrow j}$).

Beyond the information flow between any two nodes, information flow among three nodes in a circular path, with the first node communicating with the second, and the second with the third, but the third communicating back to the first, another quality of information is made possible, i.e. feedback information. This would enable a circuitry to act in control loops, allowing for rhythm generation. To quantify this property, we introduce the clustering coefficient, which measures the local property of a node i to form triangle motifs. The clustering coefficient of a node i is defined as ratio:

$$c(i) = \frac{\sum_{j,k} a_{ij} a_{jk} a_{ki}}{k_i(k_i - 1)}. \quad (5)$$

The higher the number of triangles (that exist) with respect to the i -th node, the higher the clustering coefficient. Figure 2D depicts the distribution of clustering coefficients. The mean clustering coefficient is computed as $\bar{c} = 0.1$. The distribution shows the existence of few nodes with high values of c .

3.3.3 Betweenness centrality

Besides the ability to generate feedback-loops, information flow within a network is governed by the degree of interconnectivity between nodes. Centrality measures are used to identify such high-interconnectivity nodes in the network. The significance of a node is related to the degree of influence which it exerts in the network. For example, the influence can be interpreted as the amount of flow which passes from this node. Important nodes act as central crossroad or hubs in the network.

“Betweenness centrality” measures the amount of influence which a node has with respect to the total information flow in the network (serving as a bridge between subgraphs, i.e., sets of nodes of the network). The “betweenness centrality” (B_c) mathematically is defined as the fraction of all shortest paths

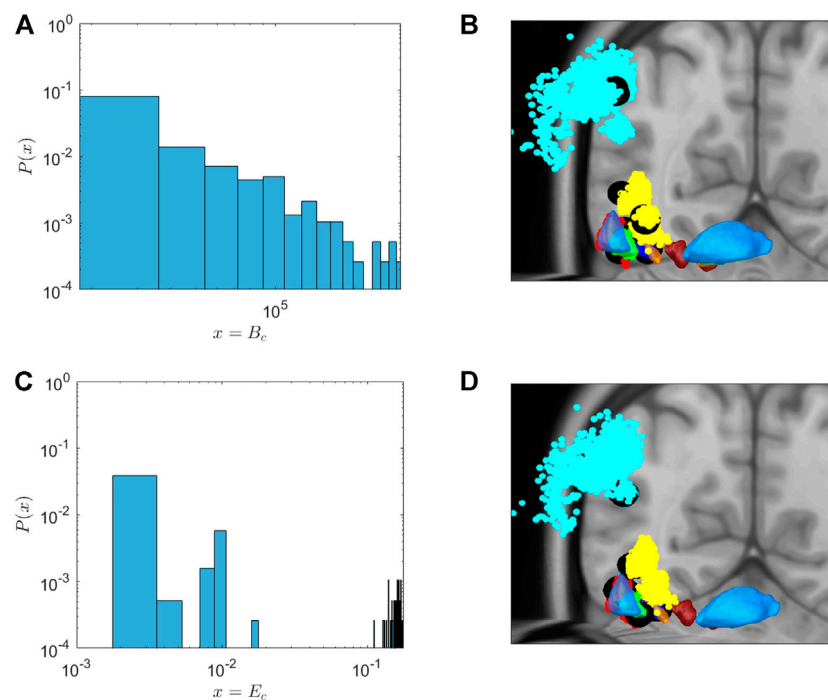


FIGURE 3

Probability distribution (A,C) and position (B,D) of nodes with high centrality measures. (A,C): Probability distribution of centrality nodes. (A) The distribution of “betweenness centrality” follows a power law distribution. Thus, > 90% of the nodes have a “betweenness centrality” < 20,000, and only 0.5% a centrality value of 200,000. (C) The distribution of “eigencentrality” also follows a power law distribution. Thus, again > 99% of the nodes have a value < 0.2, and only 0.2% an “eigencentrality” value of 0.17. (B,D) Position of high centrality nodes (i.e., the nodes with the highest B_c or E_c values in each region, usually with a $B_c > 200,000/E_c > 0.17$) in MNI brain space coordinates shown as black dots. Brain regions are colour-coded as given in the figure. Most of these nodes are located in STN and GPi, thalamus (Tha) and GPe, but also some in the motor cortex (MC).

in the network that pass through a given node, specifically the “betweenness centrality” of a node i is defined as:

$$B_c(i) = \sum_{j \neq i \neq k} (g_{jk}(i)) / g_{jk}, \quad (6)$$

where $g_{jk}(i)$ is the number of shortest paths from j to k passing from node i , and g_{jk} is the number of shortest paths between nodes j and k . Bridging nodes that connect disparate parts of the network often have a high ‘betweenness centrality’. Higher values of $B_c(i)$ indicate that the node acts as a central node influencing most of the other nodes in the network. The importance of these hubs is also highlighted pathophysiologically in the sense that therapeutic intervention in, e.g., Parkinson’s disease alters both the structural and functional connectivity profile in patients (a study which, however, obviously does not have any data on the Healthy state of the network as a basis of comparisons) van den Heuvel and Sporns [55].

Figure 3 depicts the distribution of B_c of the network. Indeed, the large majority of nodes shows very low centrality. However, there are few nodes with high B_c . In Figure 3B, black filled circles depict the spatial localisation of these central nodes in the network. As can be seen in this figure, these high-centrality

nodes can be found in the STN, GPe and GPi, as well as the thalamus, but also in the motor cortex. We propose these nodes as very promising targets for DBS treatment. The coordinates of these hubs in MNI space, and the brain area they belong to, are given in Table 1.

3.3.4 Eigencentrality

Beyond betweenness centrality, identifying nodes with high-connectivity, nodes with high connectivity connected to other nodes with high connectivity represent a special type of network information distribution, since nodes with such high “eigencentrality” (E_c), are hypothesised to play an important role in fast and effective signal distribution within the network.

For each node in the network, a positive number x_i is assigned. The number x_i is set to be proportional to the sum of the weights of all nodes connected to i :

$$x_i = \lambda^{-1} \sum_j A_{ij} x_j \Leftrightarrow Ax = \lambda x, \quad (7)$$

where λ has to be identified. The last equation shows that the element x_i is the i -th element of the eigenvector of the adjacency matrix (corresponds to the eigenvalue λ). The eigencentrality (or

TABLE 1 High centrality nodes, which might have high effectiveness in the DBS treatment.

Centrality measure	Subthalamic nucleus (STN)	Globus pallidus externa (GPe)	Globus pallidus interna (Gpi)	Thalamus (Tha)	Motor cortex areas (MC)
Betweenness centrality	(15, -13, -4), (13, -14, -7), (13, -11, -6), (13, -13, -8) center: (13.5, -12.8, -6.3)	(18, -4, -7), (18, -6, -2), (19, -5, -1), (20, -6, -3) center: (18.8, -5.3, -3.3)	(18, -9, -1), (20, -9, -1), (19, -9, 0), (18, -10, -1) center: (18.8, -9.3, -0.8)	(19, -7, 13), (9, -5, 4), (9, -4, 6) (8, -4, 5) center: (11.25, -5.0, 7.0)	(16, 2, 51), (16, 1, 49), (20, 9, 46), (18, 2, 49) center: (17.5, 3.5, 48.8)
Eigencentrality	(15, -14, -8), (14, -15, -8), (11, -12, -7), (15, -13, -4) center: (13.8, -13.5, -6.8)	(23, -7, 1), (20, -6, 1), (22, -4, 1), (20, -2, 0) center: (21.3, -4.8, 0.8)	(20, -9, -1), (12, -1, -6), (13, -1, -6), (13, -2, -7) center: (14.5, -3.3, -5)	(19, -8, 10) (18, -8, 10), (18, -8, 9), (19, -9, 9) center: (18.5, -8.3, 9.5)	(29, -20, 34), (27, -19, 33), (28, -22, 33), (19, -1, 50) center: (25.8, -15.5, 37.5)
Clustering coefficient	(12, -11, -9), (17, -14, -4), (15, -10, -5), (15, -17, -7), center: (14.8, -13, -6.3)	(17, -6, 10), (21, -8, -10), (16, -3, -7), (16, -5, -12) center: (17.5, -5.5, -9.75)	(13, -4, -5), (15, -5, -6), (11, -1, -5), (14, -3, -7) center: (13.3, -3.3, -5.8)	(7, -6, 8), (7, -6, 6), (17, -13, 10) (10, -5, 3) center: (10.3, -7.5, 6.8)	(27, -7, 66), (47, -2, 37), (36, 20, 32), (44, -4, 53) center: (38.5, 1.8, 47)

eigenvector centrality) is defined when one chooses $\lambda = \lambda_1$ the highest eigenvalue of the adjacency matrix A . Then

$$E_c(i) = \lambda_1^{-1} \sum_j A_{ij} x_j, \quad (8)$$

which gives the eigenvector centrality the nice property that it can be large either because a vertex has many neighbours or because it has important neighbours (or both) Newman [56].

3.4 Detection of communities and modularity

Networks characteristically are made up of sets of nodes (subgraphs) which are densely connected among each other within the network, and which have sparse connections to other subgraphs Newman [29]. We hypothesise that such densely connected subgraph groups (or communities) play a significant role in information processing within the network. Assigning and allocating these densely connected communities to brain structures allows to construct a modular view of the network's dynamics Newman [29].

In this paper, the modality index identifies such densely connected communities. The modality index Newman [29] assigns a community numbers s_i to each node. For example, in the case of two communities, then $s_i = \pm 1$. Here, we seek the best network partition in order to optimise the modularity function Q :

$$Q = \frac{1}{4m} s^T B s \quad (9)$$

where $m = 1/2 \sum k_{ij}$ is the total number of edges in the network, and $B_{ij} = A_{ij} - k_i k_j / 2m$ is the resultant modularity matrix, also known as graph Laplacian matrix. In such matrices, the optimisations can be achieved using graph partitioning or

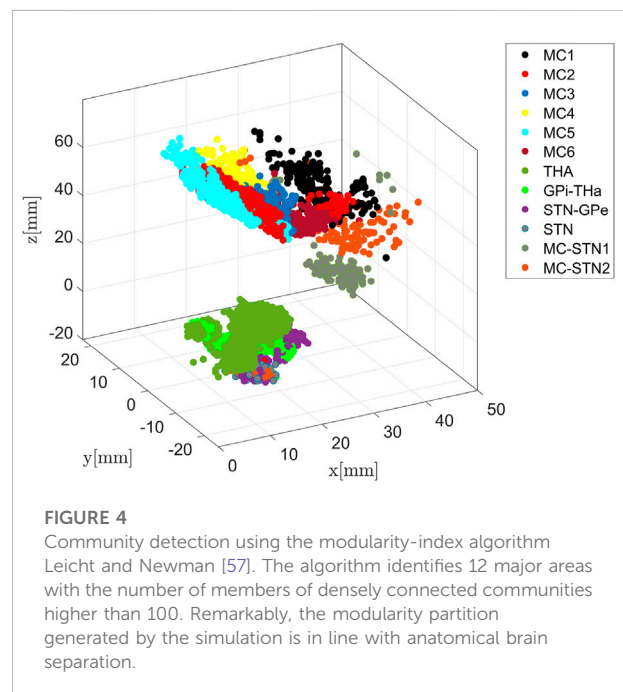


FIGURE 4
Community detection using the modularity-index algorithm Leicht and Newman [57]. The algorithm identifies 12 major areas with the number of members of densely connected communities higher than 100. Remarkably, the modularity partition generated by the simulation is in line with anatomical brain separation.

spectral partitioning (eigenvalues-eigenvectors decomposition) of the matrix B Newman [29]; Leicht and Newman [57].

Figure 4 shows the communities for the augmented network as determined by the optimisation of the Q function. Using structural brain segmentation and following anatomical partitioning, the resulting communities can be assigned to distinct brain areas. Specifically, six communities emerged from the simulation as populations with 294, 473, 189, 399, 290, and 330 members, all located in MC (see also Figure 7). Three important communities were detected in BG and the thalamus, the first one with 780 members in the thalamus, the second with 293 members connecting GPi and thalamus, and the third with 283 members connecting STN and GPe (see also

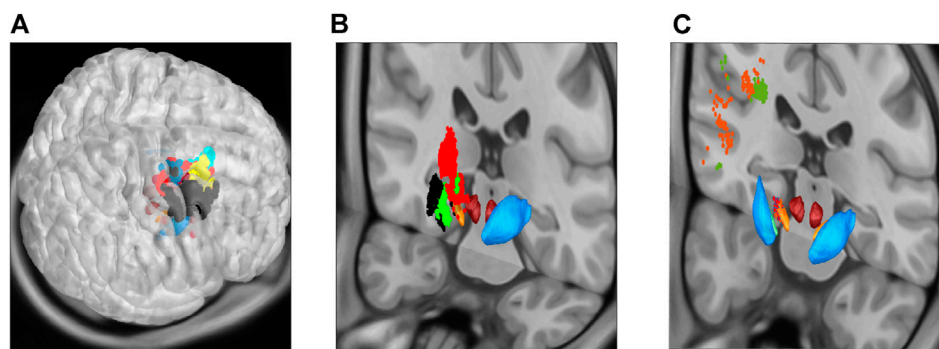


FIGURE 5

Community detection using the modularity-index algorithm Leicht and Newman [57], now projecting the same communities as in Figure 4 onto MNI space sections, showing motor cortical areas as surface projection (A), thalamus and basal ganglia as frontal cut projection (B) and STN-MC connections as hyperdirect pathway projected onto a frontal section (C). As in the previous figure, the 12 major areas are located in MC (6), thalamus (1) and basal ganglia (2), as well as three communities in locations associated with the hyperdirect pathway (one in STN in light orange, two connecting STN and MC; dark orange and green).

Figure 9). In addition, one community with 41 members was obtained in the STN itself, and further two communities with 184 and 107 members connecting MC and STN as hyperdirect pathway (see also Figure 10). The localisation of these communities in virtual space is given in Figure 4, as projection onto the MNI coordinate space in Figure 5.

4 Deep brain stimulation at centrality nodes: Electric field approximation

As outlined above, the centrality nodes (defined by the higher values of the “betweenness centrality” B_c and the “eigencentrality” E_c as well as the clustering coefficient c) can be hypothesised to be possible stimulation targets especially effective in neuromodulation. To evaluate this hypothesis, for each of the three measures (B_c , E_c and c), first the centre of mass was calculated for the four positions in or close to the STN with the highest values (see coordinates as given in Table 1). For centre of mass positions, next an approximation of the volume of tissue activated (VTA) for a conventional DBS signal (2 mA 90 μ s rectangular pulse with a 130 Hz repetition rate) was calculated. The stimulation was conducted in a monopolar mode, with the active contact placed at the coordinates of the centrality nodes, and the approximation was based on the electric field magnitude Åström et al. [58], thresholded at 150 V/m. Using the simulation platform OSS-DBS Butenko et al. [24], the field was computed in a heterogeneous and anisotropic volume conductor defined with data from Zhang and Arfanakis [59] and Horn [60]; Horn et al. [61].

Since the centrality nodes were located very close to each other, the three corresponding VTAs overlapped strongly; all three being located in the dorsolateral STN (Figure 6A), which

is a clinically established target for treating motor symptoms of Parkinson’s disease Benabid et al. [62]. It must be, however, noted that the employed structural connectivity of the network (Figure 1) was inherently biased towards the dorsolateral region. Next, we estimated the structural connectivity of these VTAs using the previously described pathway atlas, but now also including fibers beyond the motor circuit. In all three cases, nearly the same fibers were “recruited” by the stimulation, namely, the motor pallido-subthalamic projections, the hyperdirect pathway descending from the primary motor cortex (upper and lower extremity), and the dorso-lateral prefrontal cortex. Importantly, for the given stimulation amplitude, a recruitment of the corticofugal pathway was not predicted, allowing to avoid capsular side-effects Tommasi et al. [63]; Xu et al. [64]. Beyond this, no activation in the pallidothalamic projections was observed.

Noteworthy is the spatial relation of the centrality nodes obtained by our simulation to the target spots of the STN-DBS. The VTAs significantly overlapped with STN regions shown to be effective in treating hypokinetic symptoms of Parkinson’s disease, while a region implicated in side-effect occurrence was largely avoided Dembek et al. [25] (Figure 6B). Moreover, the VTAs of the present study contained the effective target points which were determined by projecting actual target coordinates of patients treated successfully with DBS for Parkinson’s disease onto MNI space in another study on a large cohort Horn et al. [65]. Such a coincidence of the centrality nodes and the so-called sweet spots might explain the efficiency of the STN as a target for various neurological disorders. This relatively small nucleus is a site of convergence of various neural circuits (even though not all of them include the STN itself). Hence, its stimulation allows a wide-spread neuromodulatory intervention.

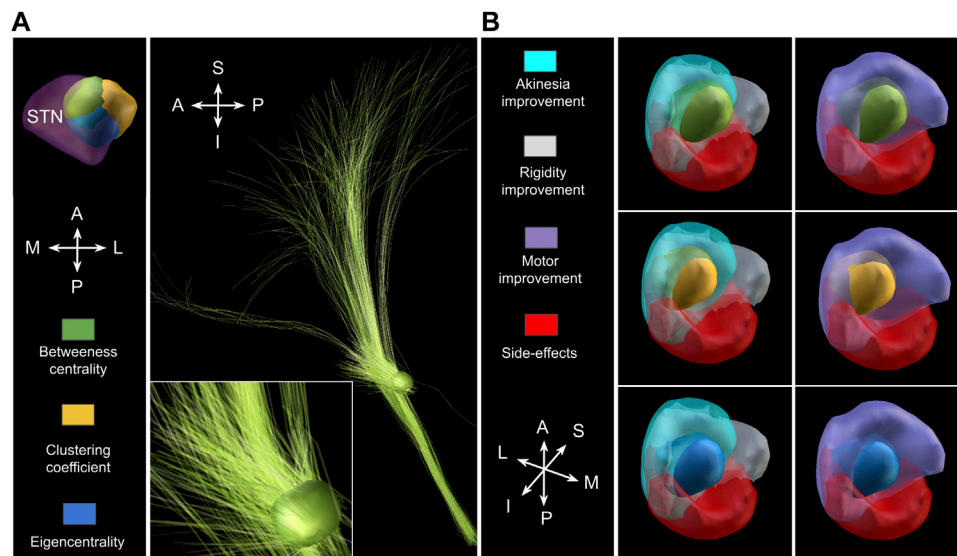


FIGURE 6

Recruitment of neural tissue by monopolar STN-DBS at the centrality nodes. **(A):** All three (overlapping) VTAs are located in the dorsolateral STN (left; green for between-centrality nodes, yellow for clustering coefficient, and blue eigencentality) and predominantly recruit motor pallidum subthalamic projections, the hyperdirect pathway from the primary motor cortex (upper and lower extremities), as well as its branch descending from the dorso-lateral prefrontal cortex (right). Note that the latter was not used to construct the network model. For the particular stimulation protocol (2 mA), no corticofugal fibers are recruited according to the computational model. **(B):** The VTAs (green for between-centrality nodes, yellow for clustering coefficient, and blue eigencentality) overlap with target areas, whose stimulation is clinically proven to improve motor symptoms, especially akinesia Dembek et al. [25]. While an overlap also with regions producing possible side-effects exists, this overlap is significantly smaller (note that the regions delineated in Dembek et al. [25] overlap as well).

5 Modelling the dynamics of the thalamo-cortical basal ganglia circuit

After establishing the structural components and determining promising target regions in the previous sections on structural simulation, we also wished to explore the functional consequences of DBS on network activity patterns. For this, we worked on the same structural model as above, and superimposed modified Hodgkin-Huxley modelling.

In the augmented network, each node serves as a neuron (hypothesising a homogeneous neural population on the 1 mm^3 cube), and the edges represent synaptic links between the neurons. Consequently, depending on the region, each node-neuron is modelled with a variation of Hodgkin-Huxley's current-balance equations Terman et al. [28]; Rubin and Terman [9]; Hodgkin and Huxley [66]. In this section, we present the mathematical description of the neurons from each area of the basal ganglia (BG), thalamus and cortex. Next, we couple the neural activity of neurons according to structural connectivity within and between the subthalamic nucleus (STN), globus pallidus externa (GPe) and interna (GPi), thalamus (Tha) and motor cortex (MC).

5.1 Modelling and simulations of neurons in STN-GPe-GPi nuclei

The properties of neurons are expressed using the conductance-based biophysical model of Hodgkin-Huxley's formalism as also has been used in previous work of Terman et al. [28]; Rubin and Terman [9]; Popovych and Tass [67]. The dynamics of each STN, GPe and GPi neuron are given by a current balance equation for the membrane potential: Terman et al. [28]; Bevan and Wilson [68]; Popovych and Tass [10]:

$$C \frac{dV_i}{dt} = -I_{\text{LEAK}} - I_K - I_{\text{Na}} - I_{\text{Ca}} - I_T - I_{\text{AHP}} - I_{\text{syn}} + I_{\text{DBS}} \quad (10)$$

$$\frac{dx_i}{dt} = (x_{\infty} - x_i) / \tau_{x_i} \quad (11)$$

$$\frac{d[\text{Ca}^{2+}]_i}{dt} = \epsilon_1 (-I_{\text{Ca}} - I_T - k_{\text{Ca}} [\text{Ca}^{2+}]_i), \quad (12)$$

where C is the membrane capacity, V_i is the membrane potential of the i th neuron, x_i denotes the gating variables n , h , r and x_{∞} is the steady state value for the gating variables. The quantity $[\text{Ca}^{2+}]_i$ is the intracellular concentration of calcium. The exact description of the ionic currents I_{LEAK} , I_K , I_{Na} , I_{Ca} and the synaptic current I_{syn} for the STN and GP neurons are given in the supplementary material. The current I_{DBS} in Eq. 10 models

DBS on STN neurons only and the form is described in the [Supplementary Material](#). In the absence of DBS treatment the value is: $I_{DBS} = 0$.

5.2 Synaptic suppression of pallido-thalamic projections

Here, we model the GABAergic short term depression. The functionality of the GABAergic synapse and the resulting release of neurotransmitters is dependent on the firing history of the presynaptic neuron Zucker and Regehr [69]; Farokhniaee and McIntyre [70]. High-frequency stimulation induces suppression of GPi GABAergic synaptic transmission Farokhniaee and McIntyre [70], which in turn, leads to a thalamic activity facilitation.

The synaptic activity is defined by the activation variable s_i , which is given by Laing and Chow [71]; Ermentrout and Terman [72]; Compté et al. [73]:

$$\frac{ds_i}{dt} = \alpha(1 - s_i)H(V_i - \theta_0) - \beta s_i, \quad (13)$$

where $H(V)$ is a smooth approximation of the step function, i.e., $H(V) = 1/(1 + e^{-(V - \theta_0)/\sigma_x})$, where α, β stands for the rate of activation and inactivation, respectively, and typically, $\alpha = O(1)$, $\beta = O(\epsilon)$ holds Laing and Chow [71]; Ermentrout and Terman [72]; Terman [74].

The inhibitory GABAergic synaptic current for the i th neuron is given, by

$$I_{i,GABA} = g_{GABA}(V_i - E_{GABA}) \sum_j A_{ij} s_j, \quad (14)$$

where A_{ij} has the value 1 or 0, depending on whether the neuron is connected or not. The summation is taken over all presynaptic neurons.

In case of existent synaptic suppression the GABAergic synaptic current changes to

$$I_{i,GABA} = g_{GABA}(V_i - E_{GABA}) \sum_j A_{ij} s_j P_j, \quad (15)$$

where the factor P_j describes the probability of a neurotransmitter release (in the $\{ij\}$ synapses), and follows the dynamics Benita et al. [75]:

$$\frac{dP_j}{dt} = \frac{P_0 - P_j}{\tau_D} \quad (16)$$

$$P_j(t_{sp}) \rightarrow P_j(t_{sp}) A_D,$$

where t_{sp} corresponds to the last spike-time of the presynaptic neuron and A_D is the depression factor ($0 < A_D < 1$), in our case, the value $A_D = 0.8$ was used. The value P_0 describes the steady state of P and in our case was set to 1. To simplify, when a presynaptic neuron fires at time t_{sp} the functionality of the synapse (the release of neurotransmitters) is reduced (suppressed by a factor A_D). In the absence of neural activity

the synapse returns to a full ability of release, in a time scale $1/\tau$ where $\tau = 400$ ms Benita et al. [75].

5.3 Modelling neurons in the thalamus

The mathematical description of the thalamic neurons is given by the following equation.

$$C \frac{dV_i}{dt} = -I_{LEAK} - I_K - I_{Na} - I_T - I_{syn} + I_{SM} \quad (17)$$

$$\frac{dx_i}{dt} = (x_{\infty} - x_i) / \tau_x, \quad (18)$$

where C is the membrane capacity and V_i is the membrane potential of the i th neuron, while the Eq. 18 describes the first order kinetics for the gating variables h, r . The currents I_{LEAK} , I_K and I_{Na} are the ionic currents, I_T is the T-type calcium channel. The synaptic current I_{syn} has the form $I_{syn} = I_{GPTH} + I_{THTH}$, where the GABAergic current I_{GPTH} represents the inhibition of the GPi area to the thalamus, while I_{THTH} represents the internal excitatory or inhibitory thalamic connections. The current I_{SM} represents sensorimotor excitation (from motor cortex areas to thalamus). The detailed description of the ionic and synaptic currents is given in the [Supplementary Material](#).

5.4 Modelling and simulations of neurons in the motor cortex

The motor cortex neurons MC, are described as one-compartment soma, and following the equations Pospischil et al. [76]:

$$C \frac{dV_i}{dt} = -I_{LEAK} - I_K - I_{Na} - I_M - I_{syn} + I_{app} \quad (19)$$

$$\frac{dx_i}{dt} = a_x(1 - x_i) - b_x x_i \quad (20)$$

$$\frac{dp_i}{dt} = (p_{\infty} - p_i) / \tau_p, \quad (21)$$

where V_i is the membrane potential, and x_i represents the gating variables for potassium and sodium current, of the i th neuron. The gating variable p_i represents the activation gate of the slow, voltage-dependent potassium current I_M . The current I_{app} is added to tune the oscillatory behaviour of MC neurons around 20Hz. Each MC neuron has different value of I_{app} which is extracted randomly from the interval $[2, 3]$. The synaptic activity is given from the current I_{syn} and the exact form is described at [Supplementary Material](#). The whole MC area is modelled as small world network. In this network, 20% of the neurons send inhibitory signals. i.e., replicate interneurons. The cortical neurons show a regular spiking activity Pospischil et al. [76]. The exact description is given in the [Supplementary Material](#).

5.5 Average over the detected communities macroscopic description

In this paper, we obtain a macroscopic description of the dynamics of the detected communities of [Section 3.4](#), by averaging the mean voltage activity \bar{V} of neurons over the population in the community; specifically, we define:

$$\bar{V}_x(t) = \frac{1}{N} \sum_{k=1}^N V_k(t). \quad (22)$$

The mean voltage activity \bar{V} is used for the characterisation of rhythmic activity using Fourier spectral analysis under different states (Healthy, Parkinsonian or DBS in Parkinsonian conditions). In all simulations, the Fourier power spectrum is normalised dividing by the highest absolute value. In this context, the Parkinsonian state was modelled, in brief, by increasing the activity of STN, decreasing the activity of GPe (D2 dopamine-mediated receptor activity effect in the indirect pathway), and simultaneously increasing the activation of GPi due to D1 dopamine-mediated activity in the direct pathway. The detailed description of is given in [Section 3](#) of the [Supplementary Material](#).

6 Collective dynamics of the structural clusters (communities)

Structural connectivity can have significant impact on the large-scale dynamics of the brain [Deco et al. \[43\]](#); [Papadopoulos et al. \[77\]](#); [Deco et al. \[15\]](#). However, the connection between anatomical-structural and functional brain connectivity is far from been trivial. Large-scale computational models and their complex nonlinear dynamics constitute an important method to explore this connection [Papadopoulos et al. \[77\]](#); [Schirner et al. \[78\]](#). Here, we propose a new method which correlates the structural and functional connectivity, specifically focusing on densely connected communities as identified by the modality index ([Section 3.4](#)).

6.1 Analysis of macroscopic activity in motor cortex clusters

The network analysis resulted in the identification of 6 MC areas consisting of 294, 473, 189, 399, 290 and 330 nodes, respectively. For each area, we extract the Fourier spectrum for the macroscopic variable of [Eq. 22](#), averaging all values of each member of the detected community. The results are depicted in [Figure 7](#). The first column depicts the six different cortical node sets (six clusters emerging from modularity analysis) in red on the virtual brain surface. The next three columns show the power

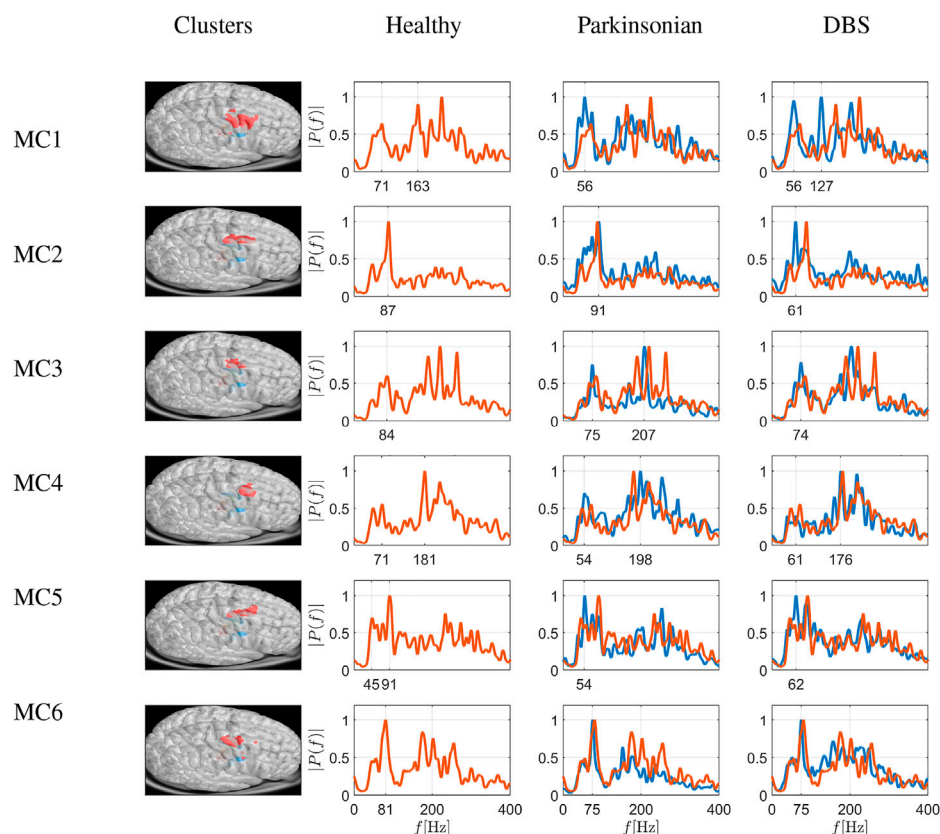
spectra in three different conditions (i.e., Healthy, Parkinsonian and DBS). Under healthy conditions, the activity peaks in the low and high γ band (i.e. ≈ 80 Hz and ≈ 190 – 290 Hz, with one to three peaks). Under Parkinsonian conditions, these peaks are often blunted, i.e., with less obvious peaks in e.g., MC1, MC3 and MC6 (Parkinsonian conditions depicted as blue curves, and healthy conditions depicted as red curves, for comparison see also column 1 of [Figure 8](#) which depicts the differences between Healthy and Parkinsonian cases).

To better estimate the differences between the conditions, we generated difference curves of the spectrograms of [Figure 7](#) based on the following subtraction pairs: $|P_X(f)| - |P_Y(f)|$, where $|P_X|$, $|P_Y|$, are the power spectra of the states X , Y , respectively, and represent: healthy, Parkinsonian or DBS conditions, see [Figure 8](#). By further calculating the area under the curve (AUC, [Valor et al. \[79\]](#)) for each of these difference pairs i.e.,

$$E = \int_a^b |P_X(f)| - |P_Y(f)| df \quad (23)$$

(numbers in insets in [Figure 8](#)) one can estimate the degree of change expected to occur when changing the condition. Comparing the difference between healthy and Parkinsonian conditions [Park-Healthy, [Eq. 23](#)], one can see that the spectrograms differ by ≈ 55 arbitrary units for most MC clusters, save in two locations (MC2 and MC6), where the values are below 50. Obviously, thus, the effect of Parkinsonian conditions is heterogeneous in the MC network, albeit within moderate boundaries; overall, the difference is in the range of 50 ± 5 (arbitrary units).

Comparing these differences now to differences DBS-Healthy, see [Eq. 23](#), the relative effect of DBS can be gauged: In two areas, DBS actually induced more differences than the disease condition alone (MC1, MC2, with values 62 and 49, compared to 55 and 45), in three areas, DBS reduces the differences (which might be interpreted as a normalisation of activity), i.e., in MC3, MC4 and MC5 (with values 47, 40 and 44 compared to 58, 55 and 53), and in one area, there is virtually no effect of DBS regarding this measure (MC6, with a value 49, compared to 49). Again, this leads to the conclusion that the effect of DBS is heterogeneous regarding cortical activity, with alterations by +18 and +8% (positive changes meaning that the frequency spectrogram digresses even more from healthy conditions under DBS than under Parkinsonian conditions alone) occurring in some regions (MC1, MC2), and -20 , -28 and -17% in others (MC3, MC4, MC5; negative values indicating that the spectrograms under DBS show less of a difference against healthy conditions than under Parkinsonian conditions without DBS), and in fact only a minimal change (+0.9%) in MC6, see [Figure 8](#) ([Supplementary Table S4](#)). Using repetitive analyses with the data, we did not see changes of $> 5\%$, while the effect sizes particularly of beneficial DBS effects in the order of 17%–28%. Therefore, we think that the

**FIGURE 7**

Simulation of frequency spectrograms of cortical sets of nodes as average neuronal activity (power on ordinate given as relative value) in a frequency range of 0–400 Hz. The six rows depict six different cortical node sets (six clusters emerging from modularity analysis) shown in red on the virtual brain surface. The spectrograms correspond to healthy conditions (red traces), Parkinsonian conditions and DBS in a Parkinson-affected network (both as blue traces), as shown in the different columns. Traces from healthy conditions are superimposed as fine red traces. Under healthy conditions, the activity peaks in the low and high γ band (i.e., ≈ 80 Hz and ≈ 190 – 290 Hz, with one to three peaks). Under Parkinsonian conditions, these peaks are generally blunted, and DBS is able to reverse this at least in some instances (e.g., clusters in MC3, MC4 and MC5, where spectrograms under DBS deviate less from healthy conditions than spectrograms under Parkinsonian conditions by as much as 17–28%, taking the overall area under the curve differences as a measure; see Figure 8).

differences are unlikely due to random sampling errors. Overall, just averaging these changes, this amounts to a change of cortical spectral activity by $\approx -7\%$. Where are the clusters positioned on the cortex? With MC1 and MC2, those regions where DBS seems to accentuate differences in spectral activity, we see the largest clusters forming (incidentally) a “W” or “ ∞ ” figure. With MC3, MC4 and MC5, it appears that these clusters are positioned very close to the frontal or dorsal end of the MC2 cluster, or indeed at fragmented positions of the MC1 cluster; those regions interestingly show a reduction in spectrogram difference induced by DBS. One might speculate that normalising effects of DBS are reflected in spatially fragmented changes in the cortex, but not when considering large networks. Overall, obviously, the reason for the heterogeneity in functional connectivity or for the impact of DBS remains unknown and we hope that the current analysis spurs further detailed investigations into this matter.

6.2 Analysis of macroscopic activity in basal ganglia-thalamic clusters

The second group of communities (clusters), identified by modularity measure, belongs to the basal ganglia or thalamus. Specifically, the first thalamic cluster contains 780 neurons, the second community contains 293 neurons connecting GPi and thalamus and the third cluster consists of 283 neurons connecting STN and GPe. For each cluster, we extract the Fourier spectrum for the macroscopic variable of Eq. 22. These Fourier spectra of all members of the detected communities were averaged. The results are depicted in Figure 9. The three rows depict node sets emerging from modularity analysis in the thalamus (top), in the GPi-thalamic pathway (middle) and the STN-GPe pathway (bottom), depicted as red dots on the virtual brain sections.

Under healthy conditions (column 2 in Figure 9), in the thalamus, the activity peaks in the low γ band (i.e., ≈ 46 Hz). In

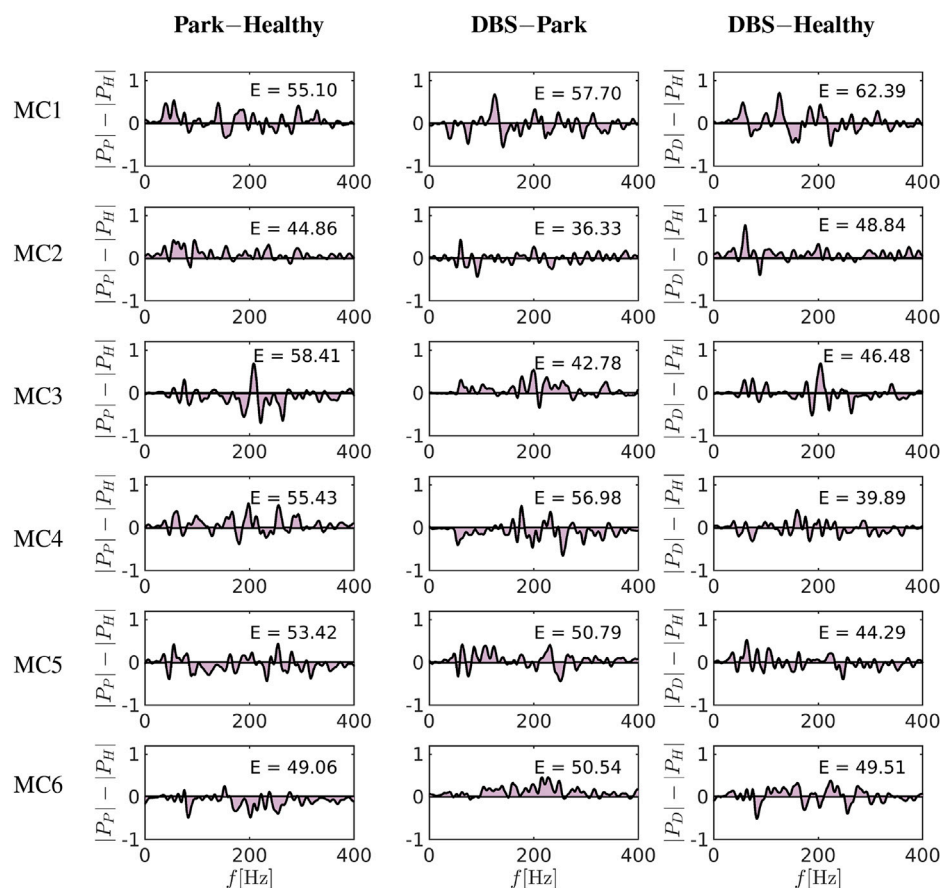


FIGURE 8

Differences of the spectrum between Park-Healthy and DBS-Healthy [subtracting the spectrum according to Eq. 23]. Each row represents one of six cortical sets of nodes as emergent from centrality measure modelling. The columns show the differences of these frequency spectra by subtracting Park vs. Healthy, DBS vs. Park and DBS vs. Healthy. The shaded area under the curve as a measure of frequency spectrum divergence is computed and depicted in columns 1, 2 and 3. The MC3, MC4 and MC5 areas in the cases of DBS vs. Healthy show a reduction in the computed area compared to Park vs. Healthy, indicating that DBS reduces the spectrum difference compared to Parkinsonian condition, although differences to the healthy condition remain.

the pallido-thalamic cluster (projections from GPi to thalamus; GPi-Thal), the neuronal activity is characterised by a slow β band rhythm (i.e., ≈ 13 –14 Hz). The third cluster comprises neurons projecting from the STN to GPe (STN-GPe), again showing a maximum of activity in the low β band (i.e., ≈ 13 –14 Hz).

Under Parkinsonian conditions, the situation reverses: in the thalamus, higher frequency γ activity is blunted, and low-frequency activity emerges (at ≈ 6 Hz, i.e., θ band), while in the cited pallidal pathways, peak frequencies are shifted to higher frequencies (≈ 25 and 50 Hz, i.e., in the β and low γ band). DBS clearly changes this situation: In the pathways directly connected to the STN (which is the stimulation target), the dominant frequencies are in the DBS frequency and harmonics (i.e., 130 and 260 Hz). Importantly, this leads to a restoration of thalamic activity, where again the activity is peaking in the low γ band (i.e., ≈ 38 Hz), not quite reaching the frequency under healthy conditions, but definitely different from low-frequency Parkinsonian activity.

6.3 Analysis of macroscopic activity in clusters associated with the hyperdirect pathway

The third group of communities emerging from the simulation were clusters associated with the hyperdirect pathway, as shown in Figure 10. These include one cluster in the STN, and two clusters connecting MC and STN. The first cluster is made of 41 neurons, and the other two of 184 and 107 neurons. Under healthy conditions, in a set of STN nodes quite different from the one projecting to the GPe of the BG-thalamic clusters (compare with Figure 9), the activity is also distinctly different as it peaks at 21 Hz (compared to 14 Hz in the BG-cluster), with a much wider frequency distribution into higher frequencies. These nodes probably relate to the hyperdirect pathway, as they are close to the nodes of MC-STN connections. In the latter, under

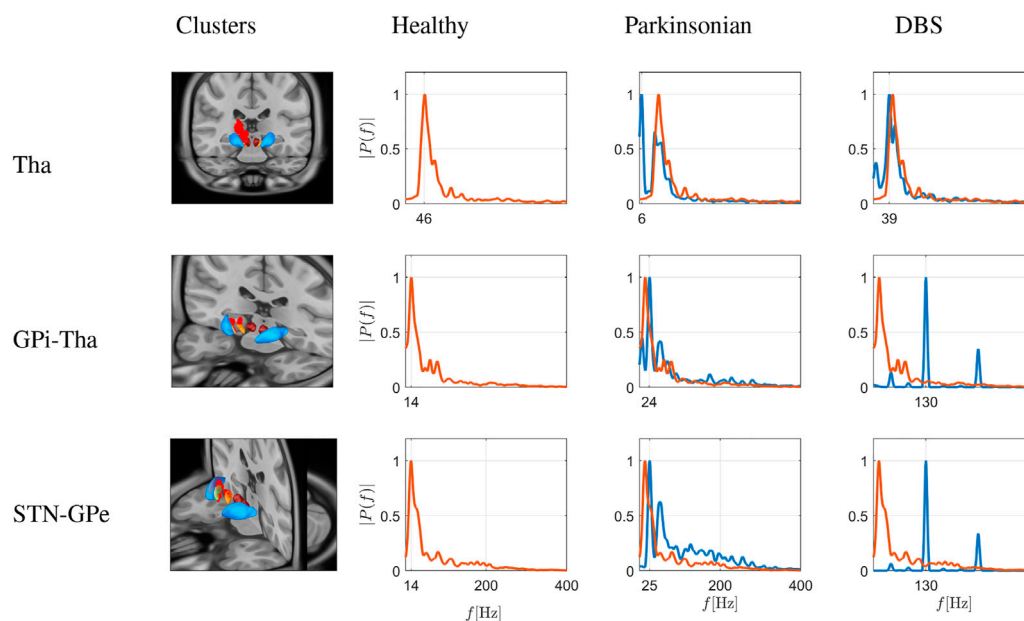


FIGURE 9

Simulation of frequency spectrograms of basal ganglia and thalamic sets of nodes as average neuronal activity (power on ordinate given as relative value) in a frequency range of 0–400 Hz. The three rows depict node sets emerging from modularity analysis in the thalamus (top), in the GPi-thalamic pathway (middle) and the STN-GPe pathway (bottom), depicted as red dots on the virtual brain sections. The spectrograms correspond to healthy conditions (red traces), Parkinsonian conditions and DBS in a Parkinson-affected network (both as blue traces), as shown in the different columns. Traces from healthy conditions are superimposed as fine red traces. Under healthy conditions, the activity peaks in the low γ band (i.e., ≈ 46 Hz) in the thalamus, while in the pathways projecting from GPi to the thalamus and projecting from the STN to GPe, low frequency activity in the low β band is seen (i.e., ≈ 13 –14 Hz). Under Parkinsonian conditions, the situation reverses: in the thalamus, higher frequency γ activity is blunted, and low-frequency activity emerges (at ≈ 6 Hz, i.e., θ band), while in the cited pathways, peak frequencies are shifted to higher frequencies (≈ 25 and 50 Hz, i.e., in the β and low γ band). DBS clearly changes this situation: In the pathways directly connected to the STN (which is the stimulation target), the dominant frequencies are in the DBS frequency and harmonics (i.e., 130 and 260 Hz). This leads to a restoration of thalamic activity, where again the activity is peaking in the low γ band (i.e., ≈ 38 Hz).

healthy conditions, peak activity emerges at ≈ 160 –180 Hz, i.e. in the high γ range.

Under Parkinsonian conditions, STN nodes narrow down their spectrum to two peaks (at 44 and 86 Hz), and a loss of the wide spectral activity. Under DBS, in the STN nodes a wider distribution of frequencies appears again, albeit as an appearance of peaks at harmonic frequencies of 44 Hz (44, 88, 172 Hz). In the hyperdirect pathway related nodes, however, DBS does not change much in the activity, save appearance of a 130 Hz peak (then stimulating frequency). In the first cluster (see middle row in Figure 10), the frequency distribution otherwise remains more or less similar, and in the second cluster (bottom row in Figure 10), the 160 Hz peak is blunted.

7 Discussion and conclusion

In this study, we provided insights into complex network processes in order to obtain a new approach gauging the effectiveness of DBS. Additionally, we investigated the relationship between structural and functional connectivity,

presenting a new *in silico* methodological approach to explore dynamics of brain motor area functions under healthy and Parkinsonian conditions, as well as the impact of Deep Brain Stimulation (DBS). Using a state-of-the-art network (constructed from data based on the pathway atlas of human motor network, obtained from various types of imaging, including diffusion, histological and structural MRI data, all fused to a virtual 3D rendering, Petersen et al. [36]) and integrating this network into advanced complex network measures, Bullmore and Sporns [18], we detected nodes, with high-connectivity and thus pivotal impact on the activity distribution within the network. These nodes are hypothesised to be ideal targets for DBS application. Our results based on betweenness centrality propose the following MNI coordinates (13.5, -12.8 , -6.3) as optimal STN target. The following optimal points (sweet spots) are suggested in other publications: (12.5, -12.72 , -5.38) in Dembek et al. [25]; (12.42, -12.58 , -5.92) in Horn et al. [65]; (11.83, -11.63 , -5.8) in Bot et al. [80] and (10.83, -13.31 , -7.01) in Akram et al. [81], see also Table 2 in Dembek et al. [25]. Remarkably, completely different methodologies [e.g., we use graph theory, while Dembek et al. [25] use VTA with Probabilistic Stimulation

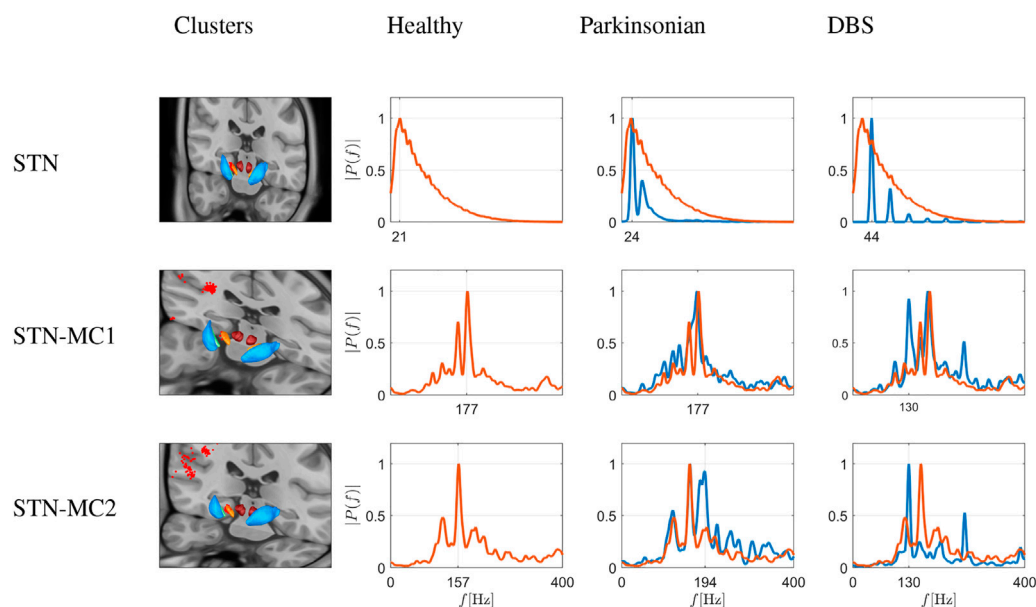


FIGURE 10

Simulation of frequency spectrograms of the STN (top row) and the hyperdirect pathway connections (two bottom rows) as average neuronal activity (power on ordinate given as relative value) in a frequency range of 0–400 Hz. The three rows thus depict node sets emerging from modularity analysis in the STN itself (top), and in nodes connecting MC and STN, i.e., two clusters of connections involving the hyperdirect pathway (middle and bottom), depicted as red dots on the virtual brain sections. The spectrograms correspond to healthy conditions (red traces), Parkinsonian conditions and DBS in a Parkinson-affected network (both as blue traces), as shown in the different columns. Traces from healthy conditions are superimposed as fine red traces. Under healthy conditions, in a set of STN nodes quite different from the one projecting to the GPe of the previous figure, the activity is also distinctly different as it peaks at 21 Hz, with a very wide frequency distribution into higher frequencies. These nodes probably relate to the hyperdirect pathway, as they are close to the nodes of the second row, i.e., MC–STN connections. In the latter, under healthy conditions, peak activity emerges at ~ 160 – 180 Hz, i.e., in the high γ range. Under Parkinsonian conditions, STN nodes narrow down their spectrum to two peaks (at 44 and 86 Hz), and a loss of the wide spectral activity. Under DBS, in the STN nodes a wider distribution of frequencies appears again, albeit as an appearance of peaks at harmonic frequencies of 44 Hz (44, 88, 172 Hz). In the hyperdirect pathway related nodes, however, DBS does not change much in the activity, save appearance of a 130 Hz peak (then stimulating frequency). In the first cluster (middle), the frequency distribution otherwise remains more or less similar, and in the second cluster (bottom), the 160 Hz peak is blunted.

Maps (PSM)] result in very similar STN sweet spots. The advantage of using a graph-theoretical approach, as in the current study, is that it is simple and takes only a few seconds to estimate the best stimulus target. Furthermore, this method could be combined in the future with already established statistical methods used e.g., Dembek et al. [25].

As a next step, we computed the volume of tissue activated (VTA) at the positions around the STN, which had emerged as pivotal nodes. Comparing these VTAs to clinically established DBS targets in Parkinson's disease, it is evident that the position of the nodes matches well with areas associated with alleviation of motor symptoms Benabid et al. [62]; Dembek et al. [25]; Horn et al. [65], suggesting that the high-connectivity nodes can infer potentially effective stimulation sites. Future studies should investigate whether a match between such nodes and neurosurgical targets also occurs when analysing networks constructed based on whole brain structural connectomes.

The second part of the current study addresses modelling of functional changes within a neuronal network. Specifically, here, we propose a new method to analyse network activity under

different conditions (i.e., Healthy, Parkinsonian and DBS), using knowledge of detailed structural network connectivity in a large scale Basal ganglia-thalamo-cortical model. This new approach is based on the detection of network communities or modules central to activity distribution. Network analysis of structural connectivity showed that the communities or groups of highly-connected nodes can be assigned to distinct anatomical regions (Figure 4). Such a modular network organisation, in comparison to a random distribution network, clearly shows advantages like greater robustness, adaptivity, and evolvability of network function Meunier et al. [82]. Although the relation of structural/functional connectivity and how neural activity could emerge from the brain's anatomical connections has been studied in several other experimental and computational studies Deco et al. [16,43]; Horn et al. [83], the current view of modular activity organisation is new.

Our analysis showed that in all modular areas, including neocortical ones, Parkinsonian conditions alter power spectrograms, but mainly subcortical structures, with e.g., slowing of activity in the thalamus and faster activity in

pathways connecting pallido-thalamic and subthalamic-pallidal nodes. Under DBS, in turn, simulations reveal that this stimulation at high-connectivity nodes is able to restore thalamic activity, and partly also cortical one, while on the other hand, hyperdirect-pathway associated nodes remain largely unaffected. Specifically, the simulations suggest that nuclei directly involved in DBS (STN, Pallidum) mainly follow the stimulation. The thalamus, in turn, translates this into a concordant shift of its activity to the low- γ frequency band (from θ under Parkinsonian conditions), while the motor cortex, in turn, shows a discrete, and inhomogeneous response. Thus, theoretically, the thalamus also under these conditions may serve as activity gate to the cortex, while the motor cortex only adjusts in a minor way—presumably thus preserving general functionality, which would likely be lost if strong rhythmicity were to emerge in the cortex. Importantly, at least a part of these conclusions is also clinically confirmed. In a recent study Neumann et al. [84] on Parkinson's disease patients receiving DBS, using clinical, behavioural and fiber tracking informed computational models, the hypokinetic state depends on suppressing indirect pathway activity and not on the hyperdirect pathway. By contrast, in that study, cognitive impairment in Parkinson's disease patients could be attributed to modulation of the hyperdirect pathway, suggesting that the hyperdirect and indirect pathways, converging in the subthalamic nucleus, are differentially involved in cognitive aspects of motor programming and kinematic gain control during motor performance.

The present study constitutes a computational approximation of the basal ganglia-thalamo-cortical network, with assumptions and limitations. Regarding the assumptions, synaptic coupling was tuned to be consistent to produce beta-band oscillatory activity within the basal ganglia, as a pathophysiological marker of Parkinson's disease. Further, an internal connectivity in the nuclei was assumed to take the form of small world complex structures. This novel approach in basal ganglia modelling has a reasonable justification in previous publications, both modelling and experimental Netoff et al. [49]; Berman et al. [50]; She et al. [51]; Bassett and Bullmore [17,47]; Fang et al. [52]; De Santos-Sierra et al. [20]. As a limitation of the model, the exact structure of the connectivity on this microscopic level is not known, and hence also it remains to be clarified in the future how this can be analogously modelled. In the current study, the striatal input to GPe and GPi was simplified as different, but homogeneous constant currents to all neurons in GPe and GPi, but with different values between GPe and GPi, as well as healthy and Parkinsonian conditions.

As a future modelling perspective, one important topic will be the investigation of how this structural separation of the network can help to construct a low-representation model of brain activity (also called neural

manifolds). The low representation will be tested under several DBS variations (i.e., functional connectivity) with respect to the parameters of DBS implantation (position, frequency, shape).

Data availability statement

The raw data supporting the conclusion of this article will be made available by the authors, without undue reservation.

Author contributions

KS, RK, and JS contributed to conceptualisation, methodology, model analysis and investigation. KS and KB contributed to model simulations and investigation. RK, JS, and UvR reviewing and editing the manuscript, and supervision. All authors contributed to the article, writing of the original draft, and approved the submitted version.

Funding

This research was funded by the Deutsche Forschungsgemeinschaft (DFG, German Research Foundation)—SFB 1270/2-299150580.

Conflict of interest

The authors declare that the research was conducted in the absence of any commercial or financial relationships that could be construed as a potential conflict of interest.

Publisher's note

All claims expressed in this article are solely those of the authors and do not necessarily represent those of their affiliated organizations, or those of the publisher, the editors and the reviewers. Any product that may be evaluated in this article, or claim that may be made by its manufacturer, is not guaranteed or endorsed by the publisher.

Supplementary material

The Supplementary Material for this article can be found online at: <https://www.frontiersin.org/articles/10.3389/fphy.2022.951724/full#supplementary-material>

References

- Kühn A, Kempf F, Brücke C, Doyle L, Martinez-Torres I, Pogossyan A, et al. High-frequency stimulation of the subthalamic nucleus suppresses oscillatory β activity in patients with Parkinson's disease in parallel with improvement in motor performance. *J Neurosci* (2008) 28:6165–73. doi:10.1523/jneurosci.0282-08.2008
- Neumann W-J, Staub-Bartelt F, Horn A, Schanda J, Schneider G-H, Brown P, et al. Long term correlation of subthalamic beta band activity with motor impairment in patients with Parkinson's disease. *Clin Neurophysiol* (2017) 128:2286–91. doi:10.1016/j.clinph.2017.08.028
- Kim J, Kim Y, Nakajima R, Shin A, Jeong M, Park A, et al. Inhibitory basal ganglia inputs induce excitatory motor signals in the thalamus. *Neuron* (2017) 95:1181–96.e8. doi:10.1016/j.neuron.2017.08.028
- Galvan A, Devergnas A, Wichmann T. Alterations in neuronal activity in basal ganglia-thalamocortical circuits in the parkinsonian state. *Front Neuroanat* (2015) 9:5. doi:10.3389/fnana.2015.00005
- Deuschl G, Schade-Brittinger C, Krack P, Volkmann J, Schäfer H, Bötzel K, et al. A randomized trial of deep-brain stimulation for Parkinson's disease. *N Engl J Med Overseas Ed* (2006) 355:896–908. doi:10.1056/nejmoa060281
- Vidalhet M, Jutras M-F, Grabli D, Roze E. Deep brain stimulation for dystonia. *J Neurol Neurosurg Psychiatry* (2013) 84:1029–42. doi:10.1136/jnnp-2011-301714
- Crompe B, Aristieta A, Leblois A, Elsherbiny S, Boraud T, Mallet N. The globus pallidus orchestrates abnormal network dynamics in a model of parkinsonism. *Nat Commun* (2020) 11:1570. doi:10.1038/s41467-020-15352-3
- Xu W, Russo G, Hashimoto T, Zhang J, Vitek J. Subthalamic nucleus stimulation modulates thalamic neuronal activity. *J Neurosci* (2008) 28:11916–24. doi:10.1523/jneurosci.2027-08.2008
- Rubin J, Terman D. High frequency stimulation of the subthalamic nucleus eliminates pathological thalamic rhythmicity in a computational model. *J Comput Neurosci* (2004) 16:21–35. doi:10.1023/b:jncs.0000025686.47117.67
- Popovych O, Tass P. Adaptive delivery of continuous and delayed feedback deep brain stimulation - a computational study. *Sci Rep* (2019) 9:10585. doi:10.1038/s41598-019-47036-4
- So R, Kent A, Grill W. Relative contributions of local cell and passing fiber activation and silencing to changes in thalamic fidelity during deep brain stimulation and lesioning: A computational modeling study. *J Comput Neurosci* (2012) 32:499–519. doi:10.1007/s10827-011-0366-4
- Galvan A, Wichmann T. Pathophysiology of parkinsonism. *Clin Neurophysiol* (2008) 119:1459–74. doi:10.1016/j.clinph.2008.03.017
- Spiliotis K, Siettos C. A timestepper-based approach for the coarse-grained analysis of microscopic neuronal simulators on networks: Bifurcation and rare-events micro- to macro-computations. *Neurocomputing* (2011) 74:3576–89. doi:10.1016/j.neucom.2011.06.018
- Siettos C, Starke J. Multiscale modeling of brain dynamics: From single neurons and networks to mathematical tools. *WIREs Mech Dis* (2016) 8:438–58. doi:10.1002/wsbm.1348
- Deco G, Jirsa V, Robinson P, Breakspear M, Friston K. The dynamic brain: From spiking neurons to neural masses and cortical fields. *Plos Comput Biol* (2008) 4:e1000092. doi:10.1371/journal.pcbi.1000092
- Deco G, Ponce-Alvarez A, Mantini D, Romani GL, Hagmann P, Corbetta M. Resting-state functional connectivity emerges from structurally and dynamically shaped slow linear fluctuations. *J Neurosci* (2013) 33:11239–52. doi:10.1523/jneurosci.1091-13.2013
- Bassett DS, Bullmore ET. Small-world brain networks revisited. *Neuroscientist* (2017) 23:499–516. doi:10.1177/1073858416667720
- Bullmore E, Sporns O. Complex brain networks: Graph theoretical analysis of structural and functional systems. *Nat Rev Neurosci* (2009) 10:186–98. doi:10.1038/nrn2575
- Iliopoulos A, Papanastasiou I. Functional complex networks based on operational architectonics: Application on eeg-based brain-computer interface for imagined speech. *Neuroscience* (2022) 484:98–118. doi:10.1016/j.neuroscience.2021.11.045
- De Santos-Sierra D, Sendiña-Nadal I, Leyva I, Almendral J, Anava S, Ayali A, et al. Emergence of small-world anatomical networks in self-organizing clustered neuronal cultures. *PLoS ONE* (2014) 9:e85828. doi:10.1371/journal.pone.0085828
- Crowell A, Ryapolova-Webb E, Ostrem J, Galifianakis N, Shimamoto S, Lim D, et al. Oscillations in sensorimotor cortex in movement disorders: An electrocorticography study. *Brain* (2012) 135:615–30. doi:10.1093/brain/awr332
- Spiliotis K, Starke J, Franz D, Richter A, Köhling R. Deep brain stimulation for movement disorder treatment: Exploring frequency-dependent efficacy in a computational network model. *Biol Cybern* (2021) 116:93–116. doi:10.1007/s00422-021-00909-2
- Butson CR, Cooper SE, Henderson JM, McIntyre CC. Patient-specific analysis of the volume of tissue activated during deep brain stimulation. *NeuroImage* (2007) 34:661–70. doi:10.1016/j.neuroimage.2006.09.034
- Butenko K, Bahls C, Schröder M, Köhling R, van Rienen U. OSS-DBS: Open-source simulation platform for deep brain stimulation with a comprehensive automated modeling. *Plos Comput Biol* (2020) 16:e1008023–18. doi:10.1371/journal.pcbi.1008023
- Dembek TA, Roediger J, Horn A, Reker P, Oehr C, Dafsari HS, et al. Probabilistic sweet spots predict motor outcome for deep brain stimulation in Parkinson disease. *Ann Neurol* (2019) 86:527–38. doi:10.1002/ana.25567
- van Hartevelt TJ, Cabral J, Deco G, Möller A, Green AL, Aziz TZ, et al. Neural plasticity in human brain connectivity: The effects of long term deep brain stimulation of the subthalamic nucleus in Parkinson's disease. *PLOS ONE* (2014) 9:e86496–13. doi:10.1371/journal.pone.0086496
- Li C, Li Q, Van Mieghem P, Stanley HE, Wang H. Correlation between centrality metrics and their application to the opinion model. *Eur Phys J B* (2015) 88:65–13. doi:10.1140/epjb/e2015-50671-y
- Terman D, Rubin J, Yew A, Wilson C. Activity patterns in a model for the subthalamopallidal network of the basal ganglia. *J Neurosci* (2002) 22:2963–76. doi:10.1523/jneurosci.22-07-02963.2002
- Newman MEJ. Modularity and community structure in networks. *Proc Natl Acad Sci U S A* (2006) 103:8577–82. doi:10.1073/pnas.0601602103
- Mandali A, Chakravarthy VS, Rajan R, Sarma S, Kishore A. Electrode position and current amplitude modulate impulsivity after subthalamic stimulation in Parkinson's disease—A computational study. *Front Physiol* (2016) 7:585. doi:10.3389/fphys.2016.00585
- Fleming J, Dunn E, Lowery M. Simulation of closed-loop deep brain stimulation control schemes for suppression of pathological beta oscillations in Parkinson's disease. *Front Neurosci* (2020) 14:166. doi:10.3389/fnins.2020.00166
- Ewert S, Plettig P, Li N, Chakravarty MM, Collins DL, Herrington TM, et al. Toward defining deep brain stimulation targets in MNI space: A subcortical atlas based on multimodal MRI, histology and structural connectivity. *NeuroImage* (2018) 170:271–82. doi:10.1016/j.neuroimage.2017.05.015
- Chakravarty MM, Bertrand G, Hodge CP, Sadikot AF, Collins DL. The creation of a brain atlas for image guided neurosurgery using serial histological data. *NeuroImage* (2006) 30:359–76. doi:10.1016/j.neuroimage.2005.09.041
- Tian Y, Margulies D, Breakspear M, Zalesky A. Topographic organization of the human subcortex unveiled with functional connectivity gradients. *Nat Neurosci* (2020) 23:1421–32. doi:10.1038/s41593-020-00711-6
- Fan L, Li H, Zhuo J, Zhang Y, Wang J, Chen L, et al. The human brainnetome atlas: A new brain atlas based on connective architecture. *Cereb Cortex* (2016) 26:3508–26. doi:10.1093/cercor/bhw157
- Petersen MV, Mlakar J, Haber S, Parent M, Smith Y, Strick P, et al. Holographic reconstruction of axonal pathways in the human brain. *Neuron* (2019) 104:1056–64.e3. doi:10.1016/j.neuron.2019.09.030
- Marek K, Jennings D, Lasch S, Siderowf A, Tanner C, Simuni T, et al. The Parkinson progression marker initiative (ppmi). *Prog Neurobiol* (2011) 95:629–35. doi:10.1016/j.pneurobio.2011.09.005
- Milardi D, Quartarone A, Bramanti A, Anastasi G, Bertino S, Basile GA, et al. The cortico-basal ganglia-cerebellar network: Past, present and future perspectives. *Front Syst Neurosci* (2019) 13:61. doi:10.3389/fnsys.2019.00061
- Bosch-Bouju C, Hyland B, Parr-Brownlie L. Motor thalamus integration of cortical, cerebellar and basal ganglia information: Implications for normal and parkinsonian conditions. *Front Comput Neurosci* (2013) 7:163. doi:10.3389/fncom.2013.00163
- Tarnaoud T, Joseph W, Martens L, Tanghe E. Dependence of excitability indices on membrane channel dynamics, myelin impedance, electrode location and stimulus waveforms in myelinated and unmyelinated fibre models. *Med Biol Eng Comput* (2018) 56:1595–613. doi:10.1007/s11517-018-1799-y
- Lanciego JL, Luquin N, Obeso JA. Functional neuroanatomy of the basal ganglia. *Cold Spring Harbor Perspect Med* (2012) 2:a009621. doi:10.1101/cshperspect.a009621
- Stam C, Reijneveld J. Graph theoretical analysis of complex networks in the brain. *Nonlinear Biomed Phys* (2007) 1:3. doi:10.1186/1753-4631-1-3
- Deco G, Senden M, Jirsa V. How anatomy shapes dynamics: A semi-analytical study of the brain at rest by a simple spin model. *Front Comput Neurosci* (2012) 6:68–7. doi:10.3389/fncom.2012.00068

44. Honey CJ, Sporns O, Cammoun L, Gigandet X, Thiran JP, Meuli R, et al. Predicting human resting-state functional connectivity from structural connectivity. *Proc Natl Acad Sci U S A* (2009) 106:2035–40. doi:10.1073/pnas.0811168106
45. Honey C, Thivierge J-P, Sporns O. Can structure predict function in the human brain? *NeuroImage* (2010) 52:766–76. doi:10.1016/j.neuroimage.2010.01.071
46. Watts D, Strogatz S. Collective dynamics of ‘small-world’ networks. *Nature* (1998) 393:440–2. doi:10.1038/30918
47. Bassett D, Bullmore E. Small-world brain networks. *Neuroscientist* (2006) 12: 512–23. doi:10.1177/1073858406293182
48. Mark N. The structure and function of complex networks. *SIAM Rev* (2003) 45:58. doi:10.1137/S003614450342480
49. Netoff T, Clewley R, Arno S, Keck T, White J. Epilepsy in small-world networks. *J Neurosci* (2004) 24:8075–83. doi:10.1523/jneurosci.1509-04.2004
50. Berman B, Smucny J, Wylie K, Shelton E, Kronberg E, Leehey M, et al. Levodopa modulates small-world architecture of functional brain networks in Parkinson’s disease. *Mov Disord* (2016) 31:1676–84. doi:10.1002/mds.26713
51. She Q, Chen G, Chan R. Evaluating the small-world-ness of a sampled network: Functional connectivity of entorhinal-hippocampal circuitry. *Sci Rep* (2016) 6:21468. doi:10.1038/srep21468
52. Fang J, Chen H, Cao Z, Jiang Y, Ma L, Ma H, et al. Impaired brain network architecture in newly diagnosed Parkinson’s disease based on graph theoretical analysis. *Neurosci Lett* (2017) 657:151–8. doi:10.1016/j.neulet.2017.08.002
53. Gouty-Colomer L-A, Michel F, Baude A, Lopez-Pauchet C, Dufour A, Cossart R, et al. Mouse subthalamic nucleus neurons with local axon collaterals. *J Comp Neurol* (2018) 526:275–84. doi:10.1002/cne.24334
54. Ammari R, Lopez C, Bioulac B, Garcia L, Hammond C. Subthalamic nucleus evokes similar long lasting glutamatergic excitations in pallidal, entopeduncular and nigral neurons in the basal ganglia slice. *Neuroscience* (2010) 166:808–18. doi:10.1016/j.neuroscience.2010.01.011
55. van den Heuvel MP, Sporns O. Rich-club organization of the human connectome. *J Neurosci* (2011) 31:15775–86. doi:10.1523/JNEUROSCI.3539-11.2011
56. Newman M. *Networks, an introduction*. New York: Oxford University Press (2010).
57. Leicht EA, Newman MEJ. Community structure in directed networks. *Phys Rev Lett* (2008) 100:118703. doi:10.1103/PhysRevLett.100.118703
58. Åström M, Diczfalussy E, Martens H, Wårdell K. Relationship between neural activation and electric field distribution during deep brain stimulation. *IEEE Trans Biomed Eng* (2015) 62:664–72. doi:10.1109/TBME.2014.2363494
59. Zhang S, Arfanakis K. Evaluation of standardized and study-specific diffusion tensor imaging templates of the adult human brain: Template characteristics, spatial normalization accuracy, and detection of small inter-group FA differences. *NeuroImage* (2018) 172:40–50. doi:10.1016/j.neuroimage.2018.01.046
60. Horn A. *MNI T1 6thGen NLIN to MNI 2009b NLIN ANTs transform* (2016). figshare. Dataset. doi:10.6084/m9.figshare.3502238.v1
61. Horn A, Li N, Dembek TA, Kappel A, Boulay C, Ewert S, et al. Lead-dbs v2: Towards a comprehensive pipeline for deep brain stimulation imaging. *NeuroImage* (2019) 184:293–316. doi:10.1016/j.neuroimage.2018.08.068
62. Benabid AL, Chabardes S, Mitrofanis J, Pollak P. Deep brain stimulation of the subthalamic nucleus for the treatment of Parkinson’s disease. *Lancet Neurol* (2009) 8:67–81. doi:10.1016/S1474-4422(08)70291-6
63. Tommasi G, Krack P, Fraix V, Le Bas J, Chabardes S, Benabid A, et al. Pyramidal tract side effects induced by deep brain stimulation of the subthalamic nucleus. *J Neurol Neurosurg Psychiatry* (2008) 79:813–9. doi:10.1136/jnnp.2007.117507
64. Xu W, Miocinovic S, Zhang J, Baker KB, McIntyre CC, Vitek JL. Dissociation of motor symptoms during deep brain stimulation of the subthalamic nucleus in the region of the internal capsule. *Exp Neurol* (2011) 228:294–7. doi:10.1016/j.expneurol.2010.08.007
65. Horn A, Kühn AA, Merkl A, Shih L, Alterman R, Fox M. Probabilistic conversion of neurosurgical dbs electrode coordinates into mni space. *NeuroImage* (2017) 150:395–404. doi:10.1016/j.neuroimage.2017.02.004
66. Hodgkin AL, Huxley AF. A quantitative description of membrane current and its application to conduction and excitation in nerve. *J Physiol* (1952) 117:500–44. doi:10.1113/jphysiol.1952.sp004764
67. Popovych O, Tass P. Multisite delayed feedback for electrical brain stimulation. *Front Physiol* (2018) 9:46. doi:10.3389/fphys.2018.00046
68. Bevan M, Wilson C. Mechanisms underlying spontaneous oscillation and rhythmic firing in rat subthalamic neurons. *J Neurosci* (1999) 19:7617–28. doi:10.1523/jneurosci.19-17-07617.1999
69. Zucker RS, Regehr WG. Short-term synaptic plasticity. *Annu Rev Physiol* (2002) 64:355–405. doi:10.1146/annurev.physiol.64.092501.114547
70. Farokhniaee A, McIntyre CC. Theoretical principles of deep brain stimulation induced synaptic suppression. *Brain Stimulation* (2019) 12:1402–9. doi:10.1016/j.brs.2019.07.005
71. Laing C, Chow C. A spiking neuron model for binocular rivalry. *J Comput Neurosci* (2002) 12:39–53. doi:10.1023/a:1014942129705
72. Ermentrout B, Terman D. *Neural networks as spatio-temporal pattern-forming systems*. New York: Springer (2012).
73. Compte A, Brunel N, Goldman-Rakic P, Wang X-J. Synaptic mechanisms and network dynamics underlying spatial working memory in a cortical network model. *Cereb Cortex* (2000) 10:910–23. doi:10.1093/cercor/10.9.910
74. Terman D. An introduction to dynamical systems and neuronal dynamics. *Lecture Notes Maths* (2005) 1860:21–68. doi:10.1007/978-3-540-31544-5_2
75. Benita JM, Guillamon A, Deco G, Sanchez-Vives M. Synaptic depression and slow oscillatory activity in a biophysical network model of the cerebral cortex. *Front Comput Neurosci* (2012) 6:64. doi:10.3389/fncom.2012.00064
76. Pospischil M, Toledo-Rodriguez M, Monier C, Piwkowska Z, Bal T, Frégnac Y, et al. Minimal Hodgkin-Huxley type models for different classes of cortical and thalamic neurons. *Biol Cybern* (2008) 99:427–41. doi:10.1007/s00422-008-0263-8
77. Papadopoulos L, Lynn CW, Battaglia D, Bassett DS. Relations between large-scale brain connectivity and effects of regional stimulation depend on collective dynamical state. *Plos Comput Biol* (2020) 16:e1008144–43. doi:10.1371/journal.pcbi.1008144
78. Schirner M, McIntosh AR, Jirsa V, Deco G, Ritter P. Inferring multi-scale neural mechanisms with brain network modelling. *eLife* (2018) 7:e28927. doi:10.7554/eLife.28927
79. Valor A, Arista Romeu EJ, Escobedo G, Campos-Espinosa A, Romero-Bello II, Moreno-González J, et al. Study of methionine choline deficient diet-induced steatosis in mice using endogenous fluorescence spectroscopy. *Molecules* (2019) 24:3150. doi:10.3390/molecules24173150
80. Bot M, Schuurman PR, Odekerken VJJ, Verhagen R, Contarino FM, De Bie RMA, et al. Deep brain stimulation for Parkinson’s disease: Defining the optimal location within the subthalamic nucleus. *J Neurol Neurosurg Psychiatry* (2018) 89: 493–8. doi:10.1136/jnnp-2017-316907
81. Akram H, Sotiropoulos SN, Jbabdi S, Georgiev D, Mählkecht P, Hyam J, et al. Subthalamic deep brain stimulation sweet spots and hyperdirect cortical connectivity in Parkinson’s disease. *NeuroImage* (2017) 158:332–45. doi:10.1016/j.neuroimage.2017.07.012
82. Meunier D, Lambiotte R, Bullmore E. Modular and hierarchically modular organization of brain networks. *Front Neurosci* (2010) 4:200. doi:10.3389/fnins.2010.00200
83. Horn A, Reich M, Vorwerk J, Li N, Wenzel G, Fang Q, et al. Connectivity predicts deep brain stimulation outcome in Parkinson disease. *Ann Neurol* (2017) 82:67–78. doi:10.1002/ana.24974
84. Neumann W, Schroll H, De Almeida Marcelino A, Horn A, Ewert S, Irmen F, et al. Functional segregation of basal ganglia pathways in Parkinson’s disease. *Brain* (2018) 141:2655–69. doi:10.1093/brain/awy206



OPEN ACCESS

EDITED BY

Glenn Terje Lines,
Simula Research Laboratory, Norway

REVIEWED BY

Sara Abdelsalam,
British University in Egypt, Egypt
Sankar M,
University of Technology and Applied
Sciences, Oman

*CORRESPONDENCE

Hasan Shahzad,
hasanshahzad99@hotmail.com
Xinhua Wang,
wxhemma2005@163.com

SPECIALTY SECTION

This article was submitted to Statistical
and Computational Physics,
a section of the journal
Frontiers in Physics

RECEIVED 20 July 2022

ACCEPTED 25 October 2022

PUBLISHED 10 November 2022


CITATION

Shahzad H, Wang X, Raizah Z, Riaz A,
Majeed AH, Anwar MA and Eldin SM
(2022), Fluid-structure interaction study
of bio-magnetic fluid in a wavy
bifurcated channel with elastic walls.
Front. Phys. 10:999279.
doi: 10.3389/fphy.2022.999279

COPYRIGHT

© 2022 Shahzad, Wang, Raizah, Riaz,
Majeed, Anwar and Eldin. This is an
open-access article distributed under
the terms of the [Creative Commons
Attribution License \(CC BY\)](https://creativecommons.org/licenses/by/4.0/). The use,
distribution or reproduction in other
forums is permitted, provided the
original author(s) and the copyright
owner(s) are credited and that the
original publication in this journal is
cited, in accordance with accepted
academic practice. No use, distribution
or reproduction is permitted which does
not comply with these terms.

Fluid-structure interaction study of bio-magnetic fluid in a wavy bifurcated channel with elastic walls

Hasan Shahzad^{1*}, Xinhua Wang^{1*}, Zehba Raizah^{2,3},
Arshad Riaz⁴, Afraz Hussain Majeed⁵,
Muhammad Adnan Anwar⁶ and Sayed M. Eldin ⁷

¹Faculty of Materials and Manufacturing, College of Mechanical Engineering and Applied Electronics Technology, Beijing University of Technology, Beijing, China, ²Department of Mathematics, College of Science, King Khalid University, Abha, Saudi Arabia, ³Research Center for Advanced Materials Science (RCAMS), King Khalid University, Abha, Saudi Arabia, ⁴Division of Science and Technology, Department of Mathematics, University of Education, Lahore, Pakistan, ⁵Department of Mathematics, Air University, Islamabad, Pakistan, ⁶Department of Mathematics, Syed Babar Ali School of Science and Engineering, Lahore, Pakistan, ⁷Center of Research, Faculty of Engineering, Future University in Egypt, New Cairo, Egypt

As a result of its wide range of applications, FSI has grabbed the attention of researchers and scientists. In this study we consider an incompressible, laminar fluid flowing through the bifurcated channel. The wavy walls of the channel are considered elastic. Moreover, a magnetic field is applied towards the axial direction of the flow. Using a two-way fluid-structure interaction, an Arbitrary Lagrangian-Eulerian (ALE) formulation is used for coupling the problem. The problem is discretized using P_2 and P_1 finite element methods to approximate the displacement, pressure, and velocity. The linearized system of equations is solved using Newton's iterative scheme. The analysis is carried out for the Reynolds number and Hartman number. The ranges of the studied parameters are Reynolds number $300 \leq Re \leq 1000$ and Hartmann number $0 \leq Ha \leq 10$. The hemodynamic effects on the bifurcated channel and elastic walls are calculated using velocity, pressure, wall shear stresses (WSS), and loads at the walls. The study shows there is an increase in boundary load as the values of the Hartman number increase hence WSS increases. On the other hand, an increase in the Reynolds number increases the resistance forces hence velocity and WSS decrease. Also, numerical values of WSS for rigid and elastic walls are calculated. Studies showed that WSS decreases for the FSI case when compare to CFD (computational fluid dynamic) case.

KEYWORDS

fluid-structure interaction, wall shear stress, finite element method, bifurcation, biomagnetic fluid, elastic walls

Introduction

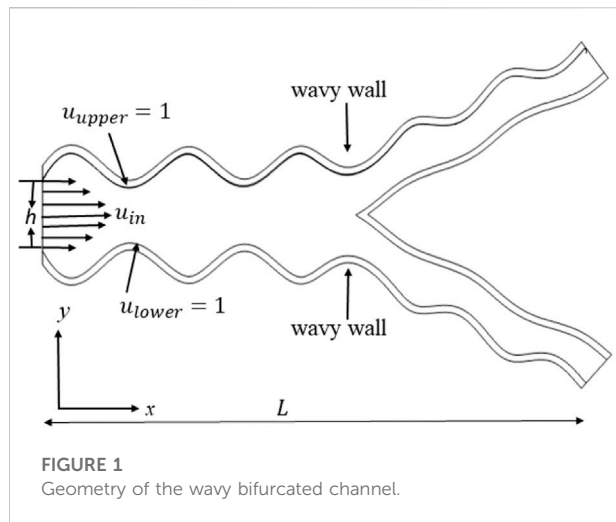
Cardiovascular disorders are now the leading cause of death worldwide, accounting for around a quarter of all deaths in the modern era [1–3]. Cardiovascular problems include atherosclerosis, carotid aneurysm, and deep vein thrombosis, which cause heart attack, stroke, and embolism all stem from platelet aggregation [4]. Recent years have seen a large number of theoretical and experimental studies on arterial blood flow [4]. To better understand how the cardiovascular system's physiological blood flow might be diagnosed, researchers are eager to examine how blood flows through an aortic artery bifurcation. The evaluation of blood flow through different types of geometries under different flow sites is highly essential because the leading cause of death in the world by arterial diseases is connected with the flow problems in the blood arteries. Viscosity, size, and form of arteries, as well as flow characteristics such as laminar, pulsatile, and turbulent all, have a significant impact on how blood moves through the vessels [5]. Numerous theoretical and experimental investigations on arterial blood flow have been conducted recently. Blood flow hemodynamics strongly depends upon the non-Newtonian characteristics, flow behavior, and shape of the artery. Fojas et al. [6] study the two-dimensional carotid artery model with bifurcation. An arbitrary Lagrangian-Eulerian (ALE) technique was used to solve the system of nonlinear equations. Comparisons were made between the findings of the hemodynamic simulations and the Doppler ultrasonography measurements of physiological blood velocity.

A literature review shows that many experiments were performed to measure the velocity field in bifurcation [7, 8], and the pressure drop model was proposed [9, 10]. Mekheimer [11] Proposed a theoretical investigation of a mixture of blood and synovial with heat distribution, volume fraction and concentration effects through stenosed concentric tubes. They concluded synovial fluid which has less friction than other fluids, can help to speed up the blood flow in the area of atherosclerosis. Flow past in a branching tube was analyzed by [12]. Yung et al. [13] numerically investigated the flow in bifurcation. For analytical and numerical research, basic “Y” type bifurcations with sharp corners were taken as assumptions, but experimental articles did not specify specific geometry employed in experiments. Thus, it is only possible to study the correlation between these theoretical and experimental results qualitatively. For the first time [14, 15], conducted thorough experiments to explore the primary and secondary flow field in a single bifurcation with smoothed corners and precisely defined geometric parameters. Numerical simulation performed by Zhao et al. [16] showed agreement between experimental and computational results by [14, 15].

Magnetohydrodynamics (MHD) is the study of fluids with magnetic characteristics. Human blood flow in the vascular system is greatly influenced by the use of MHD. Magnetic

devices have been developed for a variety of applications, including medication transporters, cancer treatment, cell separation, etc. In medical research, the theory of electromagnetic field was first introduced by Kolin [17]. Later, Korchevskii, Marochnik [18] offered the opportunity to control the blood flow in the arterial lumen system by spreading a magnetic field. Ahmed et al. [19] proposed a unique model of unsteady MHD fluid flow and heat transfer across carbon nanotubes utilizing variable viscosity. MHD effects on blood flow in bifurcated arteries with minor stenosis in the parent lumen were studied by Srinivasacharya and Rao [20]. They used the finite difference method to solve the resulting set of equations numerically. The hemodynamics effects like flow rate, shear stresses are calculated for the involved parameter. Abdelsalam et al. [21] investigated the effects of chemical interaction and laser radiation with MHD and electroosmotic flow of non-Newtonian hybrid fluid in a sinusoidal channel. The aim of the research is to help restrict the growth of bacteria, promote oxygen binding to the blood, transfer oxygen to organs, and activate white blood cells. Mekheimer et al. [11] used a vertical micro channel to investigate the effect of diamond and copper nanoparticles on the electro-magneto-hydro dynamically regulated peristaltic pumping of a couple stress fluid. They found the irreversibility process enhanced with the sphere shaped particles also, MHD reduced the bolus size. Further investigation on MHD flows and their applications can be seen in the articles [22–25] and references therein.

Researchers are eager to examine how blood flows through an aortic artery bifurcation to better understand how the cardiovascular system's physiological blood flow might be diagnosed. Blood flow across diverse geometries and flow sites are critical since arterial diseases are the leading cause of death in the globe, and because flow problems in the blood arteries are the primary cause of death. The blood flow is greatly affected by physical properties such as viscosity, vessel size and shape, and flow behaviour, such as laminar or pulsatile. Many vascular disorders can be linked back to abnormal blood flow dynamics in the arteries. Having a better knowledge of these dynamics could help in both healthy and pathological conditions. The hemodynamics of blood flow cannot be predicted accurately if we assume rigid walls. So this study is not effective in many practical cases. Therefore, FSI is taken into account [26]. FSI between blood and wall artery is difficult to model. Both modeling and computing efficiency is advancing rapidly in this discipline. Taking into consideration the FSI for the vessels and blood can be achieved by introducing a 2D or 3D elastic structure, utilizing a Lagrangian [27], Eulerian [28], or ALE (Arbitrary Lagrangian-Eulerian) framework [29]. Zhao et al. [30] studied the blood flow in the aortic arch using FSI. The system of equations is formed using the ALE frame. They studied the elasticity and wall stress in the aorta wall. Studies show that difference in the elastic characteristics of the different layer is responsible for the pathological state. Methods et al. [31]

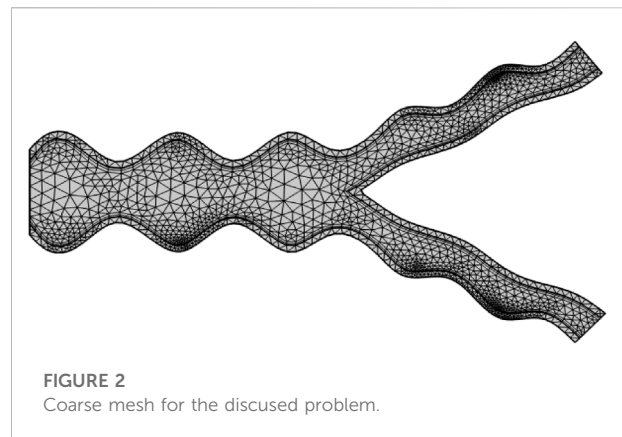


performed an FSI simulation in a patient-specific artery using the ALE concept. The fluid flow pattern and WSS were given special consideration in their study. In [32] the hemodynamics characteristic of blood flow using FSI were discussed. The coupling of the non-linear system of the equation with FSI is performed using the Gauss-Seidel iterative algorithm. Recently Shahzad et al. [33] studied the hemodynamics effects of non-Newtonian fluid flowing in the bifurcated artery. The theoretical model for stenosed bifurcated artery was constructed. They used an ALE technique to study the elastic wall behavior for non-Newtonian fluid.

In this study, a fluid-structure interaction simulation is performed for the bifurcated channel. The walls of the channel are considered wavy and elastic. The magnetic field is applied toward the axial direction of the flow. How Re and Ha affect the hemodynamics of the channel were studied. In the next section, physical configuration and mathematical modeling are performed. After that solution methodology is explained. The result and discussion section highlighted the major outcomes of the study. The conclusion based on the results is highlighted in the last section.

Physical configuration and mathematical modeling

The coordinate system and the geometry of the problem are shown in Figure 1. The wall of the channel is considered wavy with width $w = 0.08\text{cm}$. The total length of the channel is $L = 6\text{cm}$. The geometrical elements that influence the fluid dynamics in branching geometries are: change in cross-sectional area from mother to daughter branch, shape change in bifurcation module, flow driven at a bifurcation, and flow path curvature in the bifurcation module. Further, we suppose that walls of the bifurcated channel are constructed of linear elastic



and isotropic material with a particular Young's modulus and Poisson ratio. Which we defined as [34]

$$\nu = \frac{\lambda_l}{2(\lambda_l + \mu_m)}, \quad E = \frac{\mu(3\lambda_l + 2\mu_m)}{\lambda_l + \mu_m}, \quad (1)$$

$$\mu_m = \frac{E}{2(1 + \nu)}, \quad \lambda_l = \frac{\nu E}{(1 + \mu_m)(1 - 2\nu)}$$

where λ_l , Lamé coefficient; μ_m , Shear modulus; E , Young's Modulus; ν , Poisson ratio. Where $E = 5 \times 10^5$ and value of $\nu = 0.49$.

We consider the incompressible, two-dimensional, viscous, biomagnetic fluid flowing through the bifurcated channel. The walls of the bifurcated channel are considered wavy. The upper wall and lower walls move with velocity 1. The parabolic inlet with $U_{max} = 0.3$ is considered at the inlet. While at outlet boundaries pressure is assumed zero. The low magnetic Reynolds approximation is assumed [35].

Lagrangian and Eulerian descriptions are commonly used in continuum mechanics to describe solid and fluid motion, respectively. With regards to fluid and solid domains mixing (fluid structure interaction), ALE is a more generic approach. For the fluid-structure interaction, we can write the governing equations in two dimensions as [34].

TABLE 1 Grid convergence for various refinement levels at $Re = 200$ and $Ha = 0$.

Refinement level	WSS on the upper wall	Absolute error
1	0.473018	—
2	0.470492	0.0025
3	0.473178	0.0027
4	0.475150	0.0047
5	0.476230	0.0011
6	0.476365	0.0001

TABLE 2 WSS comparison for CFD and FSI case.

Ha	Re = 300		Re = 500		Re = 800	
	CFD case	FSI case	CFD case	FSI case	CFD case	FSI case
0	0.342855	0.334139	0.221536	0.218223	0.157072	0.155413
2	0.347158	0.338239	0.222788	0.219411	0.156423	0.154701
4	0.360056	0.350603	0.228537	0.224991	0.15612	0.154361
6	0.38257	0.372627	0.239482	0.235677	0.16016	0.158443
8	0.414214	0.403517	0.256632	0.252632	0.168657	0.166945
10	0.451058	0.439229	0.278059	0.273645	0.180917	0.179107

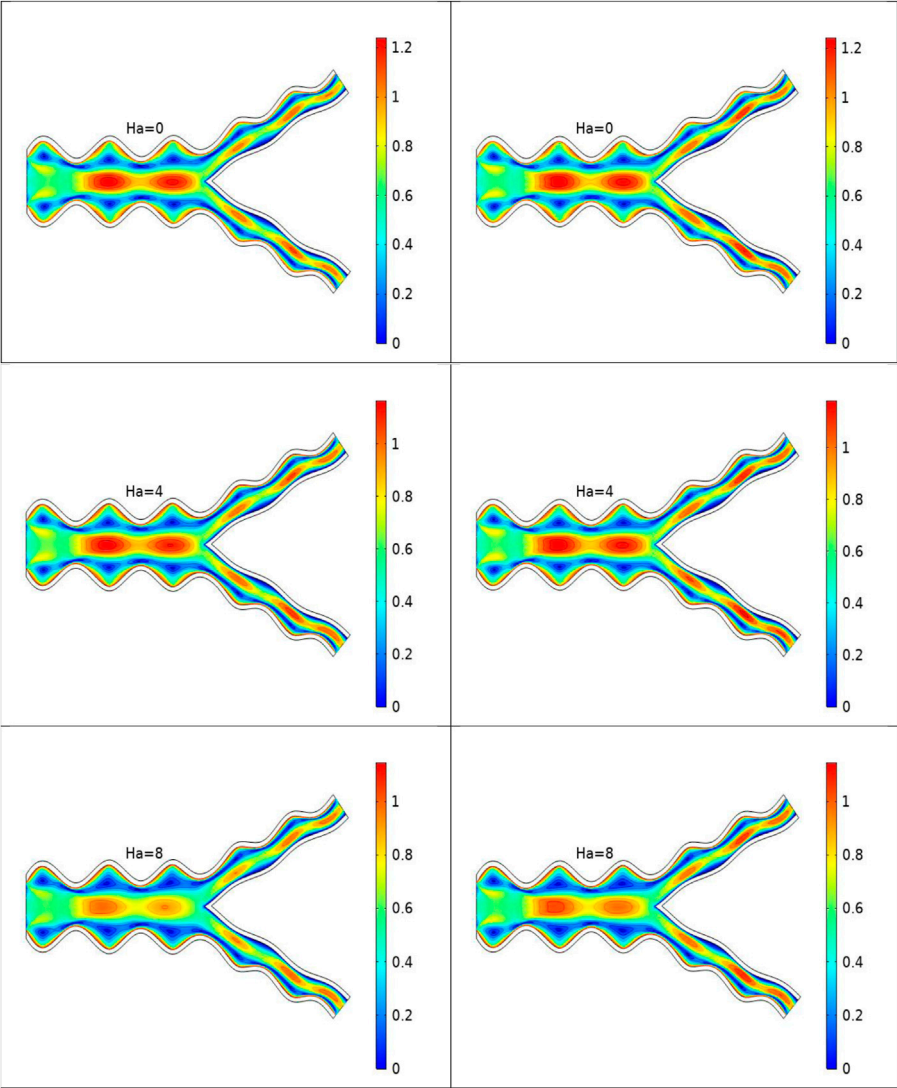


FIGURE 3
Velocity contours for Re 300 (left) and 500 (right).

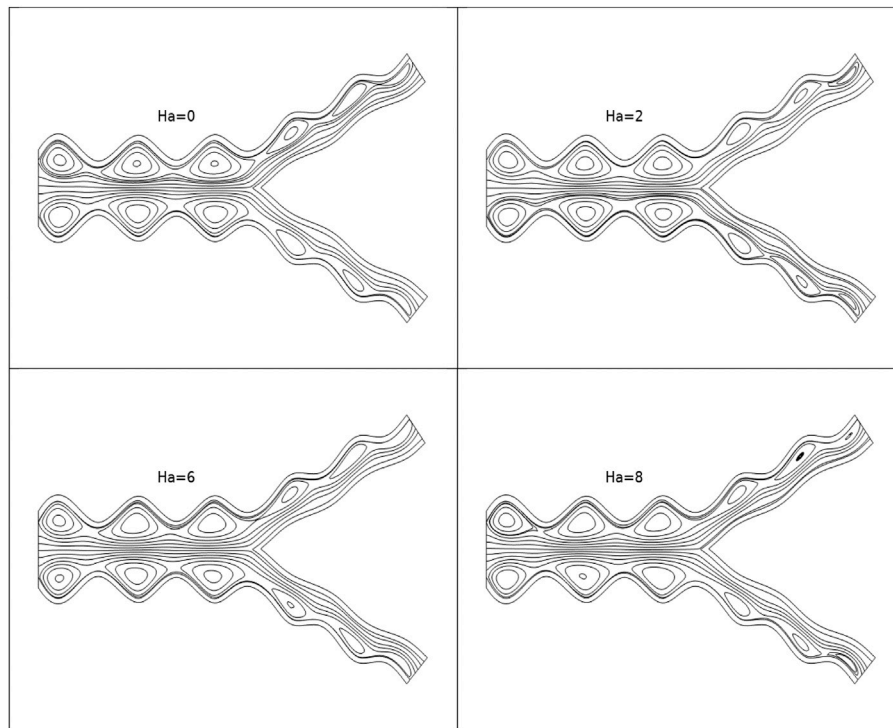


FIGURE 4
Streamlines for various Hartmann numbers at $Re = 300$.

Continuity equation

$$\frac{\partial u}{\partial x} + \frac{\partial v}{\partial y} = 0 \quad (2)$$

Momentum equations

$$\rho \left((u - u_s) \frac{\partial u}{\partial x} + (v - v_s) \frac{\partial u}{\partial y} \right) = -\frac{\partial p}{\partial x} + \mu \left(\frac{\partial^2 u}{\partial x^2} + \frac{\partial^2 u}{\partial y^2} \right) - \sigma^* B^2 u \quad (3)$$

$$\rho \left((u - u_s) \frac{\partial v}{\partial x} + (v - v_s) \frac{\partial v}{\partial y} \right) = -\frac{\partial p}{\partial y} + \mu \left(\frac{\partial^2 v}{\partial x^2} + \frac{\partial^2 v}{\partial y^2} \right) \quad (4)$$

The governing equation for the solid displacement is given by

$$\nabla \cdot \mathbf{Q}_s = 0 \quad (5)$$

where u , v , velocity component; u_s , v_s , mesh coordinate velocity; σ , electrical conductivity of the fluid; ρ , density of the fluid; μ , viscosity of the fluid; \mathbf{Q}_s , solid stress tensor; B , magnetic field strength.

The elastic deformation of the walls caused by the fluid and pressure forces can be represented in terms of the Kirchhoff stress tensor as [36].

$$\begin{aligned} \tau &= J \mathbf{Q}_s \\ \mathbf{Q}_s &= J^{-1} F S F^T \end{aligned}$$

where $F = (1 + \nabla d_s)$, $J = \det(F)$, S is related by the strain ϵ as $S = C(E, \nu)$: (ϵ), and

$$\epsilon = \frac{1}{2} (\nabla d_s + \nabla d_s^T + \nabla d_s^T \nabla d_s)$$

where S , second Piola-Kirchhoff stress tensor; E , Young's modulus; ν , Poisson's ratio; d_s , solid displacement vector.

Making use of the dimensionless variables listed below

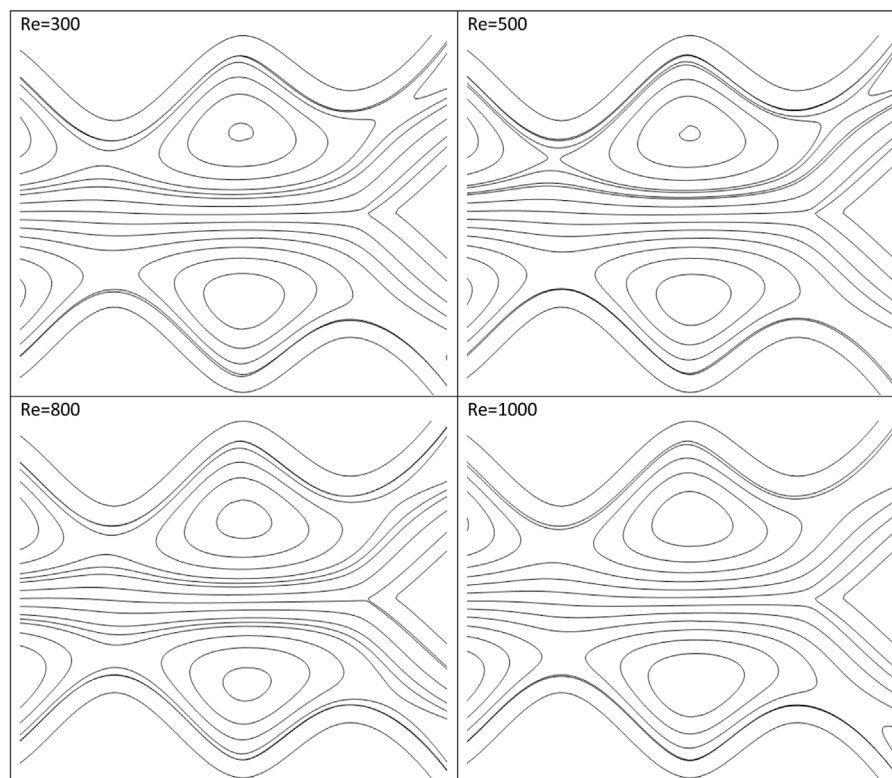
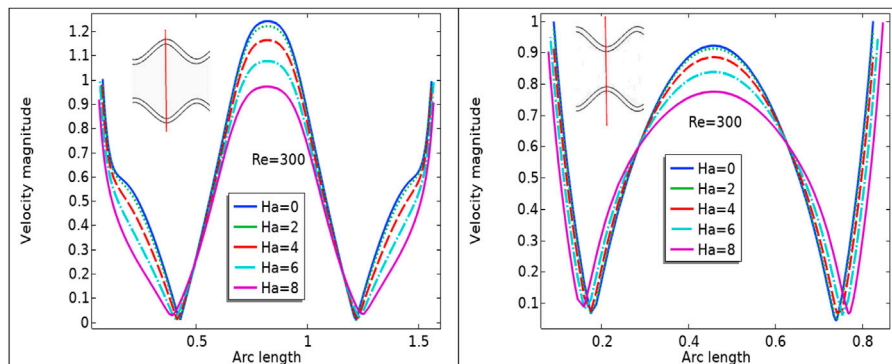
$$\begin{aligned} u &= \frac{\bar{u}}{u_0}, v = \frac{\bar{v}}{u_0}, x = \frac{\bar{x}}{h}, y = \frac{\bar{y}}{h}, u_s = \frac{u_s}{u_0}, v_s = \frac{v_s}{u_0}, p = \frac{\bar{p}}{\rho u_0^2}, Re = \frac{\rho h u_0}{\mu}, Ha = \frac{\sigma B^2 h}{\mu} \end{aligned} \quad (6)$$

where h , channel height; u_0 , inlet velocity; Re , Reynolds number; Ha , Hartmann number.

By taking a dimensionless parameter into account and omitting bar sign for simplicity, we can rewrite Eqs 2–5 as

$$\frac{\partial u}{\partial x} + \frac{\partial v}{\partial y} = 0 \quad (7)$$

$$\begin{aligned} \rho \left((u - u_s) \frac{\partial u}{\partial x} + (v - v_s) \frac{\partial u}{\partial y} \right) &= -\frac{\partial p}{\partial x} + \frac{1}{Re} \left(\frac{\partial^2 u}{\partial x^2} + \frac{\partial^2 u}{\partial y^2} \right) \\ &\quad - \frac{Ha^2}{Re} u \end{aligned} \quad (8)$$

**FIGURE 5**Streamlines for various Reynolds numbers at $Ha = 0$.**FIGURE 6**

Velocity profile for various cut lines defined.

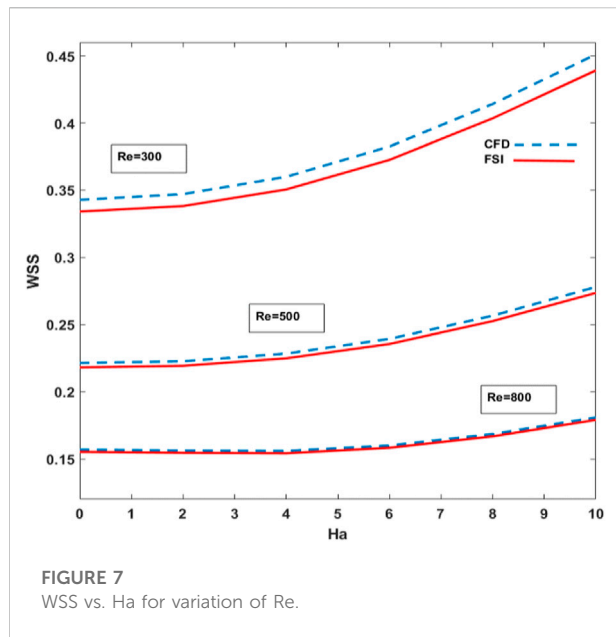
$$\rho \left((u - u_s) \frac{\partial v}{\partial x} + (v - v_s) \frac{\partial v}{\partial y} \right) = -\frac{\partial p}{\partial y} + \frac{1}{Re} \left(\frac{\partial^2 v}{\partial x^2} + \frac{\partial^2 v}{\partial y^2} \right) \quad (9)$$

$$\nabla q_s = 0 \quad (10)$$

At the inlet, a parabolic velocity profile is assumed as $u(x, y) = 3U_{max} y(1 - y)$. Pressure determines the outflow boundary conditions. The outlet's pressure is set to zero.

Solution methodology

To address the FSI problem, the interdependent system of partial differential Eqs 8–10 are solved with the ALE approach, based on FEM. Galerkin finite element method [35] was used to transform and discretize the equations. This approach combines the ability to move the boundary domain,

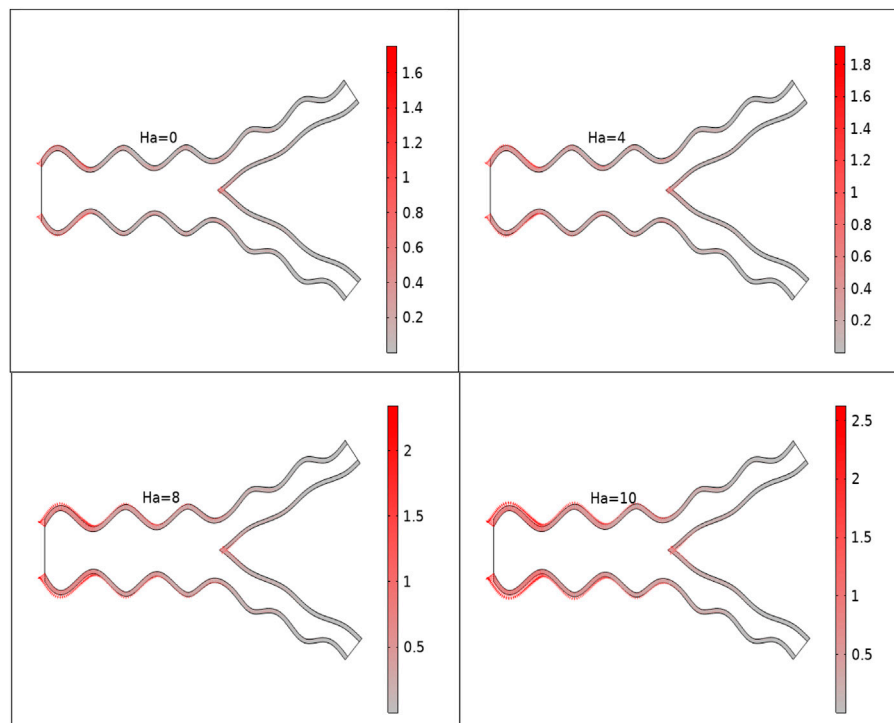


holding a moving domain with a moving procedure. The ALE approach is explained in greater detail in the articles [37–41]. A solution accuracy is improved by applying hybrid mesh

which consists of rectangular and triangular elements. The requirements for the nonlinear iteration's convergence are stated as

$$\left| \frac{\chi^{n-1} - \chi^n}{\chi^{n+1}} \right| < 10^{-6}$$

where χ is the general component of the solution. Figure 2 depicts the coarse level grid of the problem. The key steps to study the structural analysis of the domain using FEM are discretization, meshing, and mesh refinement. FEM schemes are used to address the complex fluid flow problems by dividing the domain into subdomains or elements. Since discretization of the domain into finite elements is a key step so meshing is performed at multiple levels but for optimization, only a coarse level is presented (see Figure 2). The first and second-order polynomial space (P_1 and P_2) is generated in the form of a hybrid grid consisting of quadrilateral and triangular elements to approximate the domain. Grid independence tests are performed to confirm that the results produced are independent of the number of mesh elements. The numerical values of WSS for the upper wall at $Re = 200$ and $Ha = 0$ are calculated for various refinement levels and shown in Table 1 (coarse to extremely fine). With the improvement of refinement



levels, the absolute error decreases and is minimum for extremely fine level. Therefore, the study is conducted at an extremely fine level.

Results and discussion

A two-dimensional theoretical model for bio-magnetic flow in a bifurcated channel with elastic wavy walls is proposed. The magnetic field is applied to the axial direction of the flow. The nonlinear differential equations are transformed into a dimensionless form by utilizing appropriate scales. The system of equations is discretized using ALE and is solved using the FEM approach. The numerical solution is obtained for the various values of the parameters involved. Results for various values of Ha and Re are produced to gain a physical understanding of the situation. The results are demonstrated by the mean of streamlines, velocity surfaces, displacements, and WSS.

In Table 2 WSS are calculated for the variation of Reynolds and Hartmann number. Also, a comparison is made for CFD (rigid wall) and FSI (elastic wall) cases. WSS decreases for the FSI case as compared to the CFD case where the walls of the channel are considered rigid. WSS decreases when the viscous forces inside the channel increase i.e. for increasing Reynolds number. The magnetic field has opposite effects on WSS as compared to Re . WSS is minimum for pure hydrodynamic cases i.e., $Ha = 0$, but when the value of Hartmann number increases the pressure at the walls increases hence WSS increases (see Table 1).

Figure 3 shows the variation of velocity magnitude for various values of Hartmann number at $Re = 300$ (left) and 500 (right). Due to an increase in viscous forces the velocity magnitude inside the channel decreases. Therefore, an increase in Reynolds number retards the velocity. On the other hand velocity magnitude inside the channel is maximum for the pure hydrodynamic case. An increase in magnetic field strength give rise to WSS, as a result, velocity magnitude inside the channel decreases. Due to the elastic nature of the walls, a reasonable distortion can be observed for the variation of Hartmann number (see Figure 3). In Figure 4 streamlines are drawn for various values of the Hartmann number. Recirculation near the walls is maximum for the pure hydrodynamic case ($Ha = 0$). As Hartmann varies, the recirculation pattern decreases. The fluid exerts more pressure on the wall, which results in to increase in WSS. In Figure 5 streamlines for the variation of Reynolds number are drawn and observed near the bifurcation region. As increase in Reynolds number increases the viscous forces which consequently retards the flow and thereby reduced the flow velocity. This can also be observed by the recirculation pattern of the fluid near the

walls (see Figure 5). Figure 6 plots the velocity profile for the expanded and contracted region for the variation of Hartmann number. An increase in Hartmann's number reduces the velocity. Moreover, due to the parabolic inlet, a parabolic profile of velocity is observed.

Mechanical properties of the bifurcated channel are very important because they are directly related to recirculation area, flow pattern, WSS, etc. Due to the elastic behavior of wavy walls, a noticeable deformation can be seen for the variation of Hartmann number, which results in to decrease in the recirculation which gives rise to the wall shear stress. Figure 7 plots the WSS against the Hartmann number for the variation of Re . Also, a comparison is made between the CFD and FSI cases. A significant decrease in WSS for the FSI case. A boundary load is simulated in Figure 8. A significant change in the load at the boundary is observed for the variation of the Hartmann number. At $Ha = 0$, due to parabolic inlet velocity, there is a negligible load at the boundary. But it gradually starts increasing for variation of Ha . A noticeable change can be seen at $Ha = 10$.

Conclusion

A fluid-structure interaction study of two-dimensional biomagnetic flow in a bifurcated channel is conducted. The walls of the channel are assumed elastic. The magnetic field is applied to the axial direction of the flow. The nonlinear differential equations are transformed into a dimensionless form by utilizing appropriate scales. The system of equations is discretized using ALE and is solved using the FEM approach. The major findings of the study are highlighted as.

- WSS is higher for CFD (rigid wall) case as compared to FSI (elastic wall) case.
- WSS decreases for increasing values of Reynolds number.
- Compared to the pure hydrodynamic scenario, the magnetic field reduces the gain in velocity.
- There is an increase in the recirculation patterns near the walls of the channel for the variation of Hartmann number. Hence pressure exerted by the fluid on the wall increases.
- The magnetic field increases the boundary load as compared to the pure hydrodynamic case.
- The magnetic field increases the WSS and hence the risk of atherosclerosis reduces.

Data availability statement

The raw data supporting the conclusion of this article will be made available by the authors, without undue reservation.

Author contributions

ZR: funding; HS and AHM computed the results; HS and SME wrote the original draft; XW has supervised; AR and AHM wrote the review draft; XW and MAA: modeling; Conceptualization and Validation, MAA.

Funding

This work was supported by the King Khalid University through a grant KKU/RCAMS/22 under the Research Center for Advance Materials (RCAMS) at King Khalid University, Saudi Arabia.

References

- Lloyd-Jones D, Adams RJ, Brown TM, Carnethon M, Dai S, De Simone G, et al. Heart disease and stroke statistics-2010 update: A report from the American heart Association. *Circulation* (2010) 121:e46–e215. doi:10.1161/CIRCULATIONAHA.109.192667
- Jackson SP. Arterial thrombosis-insidious, unpredictable and deadly. *Nat Med* (2011) 17:1423–36. doi:10.1038/nm.2515
- Davies MJ, Fulton WF, Robertson WB. The relation of coronary thrombosis to ischaemic myocardial necrosis. *J. Pathol.* (1979) 127:99–110. doi:10.1002/path.1711270208
- Srinivasacharya D, Madhava Rao G. Modeling of blood flow through a bifurcated artery using nanofluid. *Bionanoscience* (2017) 7:464–74. doi:10.1007/s12668-017-0402-6
- Ahmed A. Peristaltic flow of a magnetohydrodynamic nanofluid through a bifurcated channel. *Acta Mech* (2021) 232:575–89. doi:10.1007/s00707-020-02731-6
- Fojas JJR, De Leon RL. Carotid artery modeling using the Navier-Stokes equations for an incompressible, Newtonian and Axisymmetric flow. *APCBBE Proced* (2013) 7:86–92. doi:10.1016/j.apcbee.2013.08.017
- Chang HK, El Masry OA. A model study of flow dynamics in human central airways. Part I: Axial velocity profiles. *Respir Physiol* (1982) 49:75–95. doi:10.1016/0034-5687(82)90104-9
- Schroter RC, Sudlow MF. Flow patterns in models of the human bronchial airways. *Respir Physiol* (1969) 7:341–55. doi:10.1016/0034-5687(69)90018-8
- Pedley TJ, Schroter RC, Sudlow MF. Energy losses and pressure drop in models of human airways. *Respir Physiol* (1970) 9:371–86. doi:10.1016/0034-5687(70)90093-9
- Pedley TJ, Schroter RC, Sudlow MF. The prediction of pressure drop and variation of resistance within the human bronchial airways. *Respir Physiol* (1970) 9:387–405. doi:10.1016/0034-5687(70)90094-0
- Mekheimer KS, Abo-Elkhair RE, Abdelsalam SI, Ali KK, Moawad AMA. Biomedical simulations of nanoparticles drug delivery to blood hemodynamics in diseased organs: Synovitis problem. *Int Commun Heat Mass Transfer* (2021) 130:105756. doi:10.1016/j.icheatmasstransfer.2021.105756
- Smith FT. On entry-flow effects in bifurcating, blocked or constricted tubes. *J Fluid Mech* (1976) 78:709–36. doi:10.1017/S002211207600270X
- Yung CN, de Witt KJ, Keith TG. Three-dimensional steady flow through a bifurcation. *J Biomech Eng* (1990) 112:189–97. doi:10.1115/1.2891171
- Zhao Y, Lieber BB. Steady Inspiratory flow in a model Symmetric bifurcation. *J Biomech Eng* (2016) 116:488–96. doi:10.1115/1.2895800
- Zhao Y, Lieber BB. Steady expiratory flow in a model Symmetric bifurcation. *J Biomech Eng* (2016) 116:318–23. doi:10.1115/1.2895737
- Zhao Y, Brunskill CT, Lieber BB. Inspiratory and expiratory steady flow analysis in a model symmetrically bifurcating airway. *J Biomech Eng* (1997) 119:52–8. doi:10.1115/1.2796064
- Kolin A. An electromagnetic flowmeter: The principle of the method and its application to blood flow measurements. *Exp Biol Med* (Maywood) (1936) 35:53–6. doi:10.3181/00379727-35-8854p
- Korchevskii LS, Marochnik EM. Magnetohydrodynamic version of movement of blood. *Biophys* (1965) 10:411–3. doi:10.1016/j.asej.2016.04.023
- Ahmed Z, Nadeem S, Saleem S, Ellahi R. Numerical study of unsteady flow and heat transfer CNT-based MHD nanofluid with variable viscosity over a permeable shrinking surface. *Int J Numer Methods Heat Fluid Flow* (2019) 29:4607–23. doi:10.1108/HFF-04-2019-0346
- Srinivasacharya D, Rao M. Computational analysis of magnetic effects on pulsatile flow of couple stress fluid through a bifurcated artery. *Comput Methods Programs Biomed* (2016) 137:269–79. doi:10.1016/j.cmpb.2016.09.015
- Abdelsalam SI, Mekheimer KS, Zaher AZ. Dynamism of a hybrid Casson nanofluid with laser radiation and chemical reaction through sinusoidal channels. *Waves in Random and Complex Media* (2022). 2022. 1–22. doi:10.1080/17455030.2022.2058714
- Jagadeesha RD, Prasanna BMR, Sankar M. Double diffusive convection in an inclined parallelogrammic porous enclosure. *Proced Eng* (2015) 127:1346–53. doi:10.1016/j.proeng.2015.11.493
- Jagadeesha RD, Prasanna BMR, Younhae D, Sankar M. Natural convection in an inclined parallelogrammic porous enclosure under the effect of magnetic field. *J Phys : Conf Ser* (2017) 908:012076. doi:10.1088/1742-6596/908/1/012076
- Alsharif AM, Abdellateef AI, Elmaboud YA, Abdelsalam SI. Performance enhancement of a DC-operated micropump with electroosmosis in a hybrid nanofluid: Fractional Cattaneo heat flux problem. *Appl Math Mech* (2022) 43(6):931–44. doi:10.1007/s10483-022-2854-6
- Shahzad H, Ain QU, Pasha AA, Irshad K, Shah IA, Ghaffari A, et al. Double-diffusive natural convection energy transfer in magnetically influenced Casson fluid flow in trapezoidal enclosure with fillets. *Int Commun Heat Mass Transfer* (2022) 137:106236. doi:10.1016/j.icheatmasstransfer.2022.106236
- Crosetto P, Reymond P, Deparis S, Kontaxakis D, Stergiopoulos N, Quarteroni A. Fluid-structure interaction simulation of aortic blood flow. *Comput Fluids* (2011) 43:46–57. doi:10.1016/j.compfluid.2010.11.032
- Idelsohn SR, Oñate E, Del Pin F. A Lagrangian meshless finite element method applied to fluid-structure interaction problems. *Comput Struct* (2003) 81:655–71. doi:10.1016/S0045-7949(02)00477-7
- Cottet GH, Maitre E, Milcent T. Eulerian formulation and level set models for incompressible. *Fluid-Structure Interaction* (2008) 42:471–92. doi:10.1051/m2an
- Scovazzi G, Hughes TJR. Lecture Notes on continuum mechanics on arbitrary moving domains. *Solutions* (2007) 62.
- Zhao YC, Vatanikhah P, Goh T, Wang J, Chen XV, Kashani MN, et al. Computational fluid dynamics simulations at micro-scale stenosis for microfluidic thrombosis model characterization. *Mol Cel Biomech* (2021) 18:1–10. doi:10.32604/mcb.2021.012598

Conflict of interest

The authors declare that the research was conducted in the absence of any commercial or financial relationships that could be construed as a potential conflict of interest.

Publisher's note

All claims expressed in this article are solely those of the authors and do not necessarily represent those of their affiliated organizations, or those of the publisher, the editors and the reviewers. Any product that may be evaluated in this article, or claim that may be made by its manufacturer, is not guaranteed or endorsed by the publisher.

31. Methods C, Mech A, Bazilevs Y, Gohean JR, Hughes TJR, Moser RD, et al. Patient-specific isogeometric fluid-structure interaction analysis of thoracic aortic blood flow due to implantation of the Jarvik 2000 left ventricular assist device. *Comput Methods Appl Mech Eng* (2009) 198:3534–50. doi:10.1016/j.cma.2009.04.015
32. Nobile F. *Numerical approximation of fluid-structure interaction problems with applications to Haemodynamics*. Lausanne: EPFL (2001). doi:10.5075/epfl-thesis-2458
33. Shahzad H, Wang X, Sarris I, Iqbal K, Hafeez MB, Krawczuk M. Study of Non - Newtonian biomagnetic blood flow in a stenosed bifurcated artery having elastic walls. *Sci Rep* (2021) 11:23835. doi:10.1038/s41598-021-03426-1
34. Anwar MA, Iqbal K, Razzaq M. Analysis of biomagnetic blood flow in a stenosed bifurcation artery amidst elastic walls. *Phys Scr* (2021) 96:085202. doi:10.1088/1402-4896/abf67b
35. Sajid M, Shahzad H, Mughees M, Ali N. Mathematical modeling of slip and magnetohydrodynamics effects in blade coating. *J Plast Film Sheeting* (2019) 35: 9–21. doi:10.1177/8756087918777782
36. Ghalambaz M, Jamesahar E, Ismael MA, Chamkha AJ. Fluid-structure interaction study of natural convection heat transfer over a flexible oscillating fin in a square cavity. *Int J Therm Sci* (2017) 111:256–73. doi:10.1016/j.ijthermalsci.2016.09.001
37. Casadei F, Halleux JP. An algorithm for permanent fluid-structure interaction in explicit transient dynamics. *Comput Methods Appl Mech Eng* (1995) 128:231–89. doi:10.1016/0045-7825(95)00843-8
38. Donea J, Huerta A. *Finite element methods for flow problems*. Hoboken: Wiley (2003). p. 30.
39. Donea J, Giuliani S, Halleux JP. An arbitrary Lagrangian-Eulerian finite element method for transient dynamic fluid-structure interactions. *Comput Methods Appl Mech Eng* (1982) 33:689–723. doi:10.1016/0045-7825(82)90128-1
40. Kuhl E, Hulshof S, de Borst R. An arbitrary Lagrangian eulerian finite-element approach for fluid-structure interaction phenomena. *Int J Numer Methods Eng* (2003) 57:117–42. doi:10.1002/nme.749
41. Mazumder S. *Numerical methods for partial differential equations: Finite difference and finite volume methods*. Cambridge: Academic Press (2015).

Frontiers in Physics

Investigates complex questions in physics to understand the nature of the physical world

Addresses the biggest questions in physics, from macro to micro, and from theoretical to experimental and applied physics.

Discover the latest Research Topics

[See more →](#)

Frontiers

Avenue du Tribunal-Fédéral 34
1005 Lausanne, Switzerland
frontiersin.org

Contact us

+41 (0)21 510 17 00
frontiersin.org/about/contact

